The 13th International Conference of Young Scientists on Energy Issues

Kaunas, Lithuania, May 26-27, 2016

Organized by

Lithuanian Energy Institute

In cooperation with:

AGA

Biuro pasaulis

Kauno energija

Reo Investment

Chairman of the Conference dr. Sigitas Rimkevičius

Chairman of the Organizing Committee Vytautas Akstinas

INTERNATIONAL SCIENTIFIC COMMITTEE

Aleksandrs Ļvovs	Latvia	Mantas Marčiukaitis	Lithuania
Andres Siirde	Estonia	Namejs Zeltins	Latvia
Andris Kreslins	Latvia	Pierre-Etienne Labeau	Belgium
Anton Brin	Belarus	Panos M. Pardalos	USA
Alessandro Petruzzi	Italy	Ralf Ebinghaus	Germany
Bernhard Peters	Luxemburg	Sten Bergstrom	Sweden
Bjørn C. Hauback	Norway	Sigitas Rimkevičius	Lithuania
Darius Milčius	Lithuania	Sergej Zhdanok	Belarus
Enn Mellikov	Estonia	Svetlana Danilova-Tretiak	Belarus
Eugenijus Ušpuras	Lithuania	Victor A. Zhovyansky	Ukraine
Finn Ravndal	Norway	Vaclovas Miškinis	Lithuania
Florentin Paladi	Moldova	Virginijus Radziukynas	Lithuania
Luis E. Herranz	Spain	Vytautas Martinaitis	Lithuania
Myriam Lazard	France		

The Board of Reviewers was formed from the experts in the field of the Conference topics.

Board of Reviewers

Aleksandras Iljinas	Lithuania
Alessandro Petruzzi	Italy
Algirdas Gulbinas	Lithuania
Algirdas Jasinskas	Lithuania
Algirdas Maknickas	Lithuania
Andres Siirde	Estonia
Andris Kreslins	Latvia
Anupras Šlančiauskas	Lithuania
Artur Rogoža	Lithuania
Antanas Kavolynas	Lithuania
Antanas Markevičius	Lithuania
Anton Brin	Belarus
Arturas Klementavičius	Lithuania
Artūras Šmaižys	Lithuania
Arvaidas Galdikas	Lithuania
Arvydas Adomavičius	Lithuania
Asta Malakauskaitė	Lithuania
Asta Narkūnienė	Lithuania
Audrius Jonaitis	Lithuania
Aurimas Lisauskas	Lithuania
Aušra Pažėraitė	Lithuania
Benediktas Čėsna	Lithuania
Bernhard Peters	Luxemburg
Bjørn C. Hauback	Norway
Brigita Abakevičienė	Lithuania
Dainius Martuzevičius	Lithuania
Dainius Vaičiulis	Lithuania
Dalia Grigaliūnienė	Lithuania
Dalia Jankūnaitė	Lithuania
Dalia Štreimikienė	Lithuania
Dalius Tarvydas	Lithuania
Kristina Ukvalbergienė	Lithuania
Linas Miknius	Lithuania
Liudvikas Pranevičius	Lithuania
Liutauras Marcinauskas	Lithuania
Luis E. Herranz	Spain
Mantas Marčiukaitis	Lithuania
Marija Eidukevičiūtė	Lithuania
Marijus Šeporaitis	Lithuania
Martynas Lelis	Lithuania
Mindaugas Jakubčionis	Lithuania
Mindaugas Krakauskas	Lithuania
Mindaugas Vaišnoras	Lithuania
Mindaugas Valinčius	Lithuania
Myriam Lazard	France
Namejs Zeltins	Latvia
Narimantas Listopadskis	Lithuania
Nerijus Pedišius	Lithuania
Nerijus Striūgas	Lithuania
Panos M. Pardalos	USA
Pierre-Etienne Labeau	Belgium
Pranas Kuzas	Lithuania
Pranas Mierauskas	Lithuania
Raimondas Bliūdžius	Lithuania
Raimondas Pabarčius	Lithuania
Ralf Ebinghaus	Germany
Ramūnas Gatautis	Lithuania
Reda Čerapaitė-Trušinskienė	Lithuania
Regina Kalpokaitė-Dičkuvienė	Lithuania
Ričardas Krikštolaitis	Lithuania
Rimantas Pranas Deksnys	Lithuania
Rimantas Levinskas	Lithuania

Danas Ridikas	Lithuania
Darius Albrektas	Lithuania
Darius Biekša	Lithuania
Darius Milčius	Lithuania
Darius Virbukas	Lithuania
Diana Meilutytė-Barauskienė	Lithuania
Diana Adlienė	Lithuania
Diana Šarauskienė	Lithuania
Egidijus Norvaiša	Lithuania
Egidijus Saulius Juodis	Lithuania
Egidijus Urbonavičius	Lithuania
Eglė Biekšienė	Lithuania
Eglė Jaraminienė	Lithuania
Enn Mellikov	Estonia
Ernestas Narkūnas	Lithuania
Eugenija Farida Dzenajavičienė	Lithuania
Eugenijus Perednis	Lithuania
Eugenijus Ušpuras	Lithuania
Farida Dzenajavičienė	Lithuania
Feliksas Zinevičius	Lithuania
Finn Ravndal	Norway
Florentin Paladi	Moldova
Gediminas Vasiliauskas	Lithuania
Gediminas Vilkevičius	Lithuania
Giedrė Streckienė	Lithuania
Giedrius Laukaitis	Lithuania
Giedrius Šiupšinskas	Lithuania
Gintautas Miliauskas	Lithuania
Grigorijus Duškesas	Lithuania
Inga Konstantinavičiūtė	Lithuania
Inga Radžiūnienė	Lithuania
Inga Stasiulaitienė	Lithuania
Inga Valuntienė	Lithuania
Irina Kliopova	Lithuania
Jolanta Dvarionienė	Lithuania
Rita Plukienė	Lithuania
Robertas Alzbutas	Lithuania
Robertas Navakas	Lithuania
Robertas Poškas	Lithuania
Rolandas Jonynas	Lithuania
Rolandas Urbonas	Lithuania
Romualdas Kėželis	Lithuania
Romualdas Škėma	Lithuania
Saulė Milčiuvienė	Lithuania
Sergej Zhdanok	Belarus
Sigitas Kadiša	Lithuania
Sigitas Masaitis	Lithuania
Sigitas Rimkevičius	Lithuania
Simona Tučkutė	Lithuania
Stanislovas Vrubliauskas	Lithuania
Stasys Šinkūnas	Lithuania
Sten Bergstrom	Sweden
Svetlana Danilova Tretiak	Belarus
Tomas Deveikis	Lithuania
Tomas Sabonis	Lithuania
Vaclovas Kveselis	Lithuania
Vaclovas Miškinis	Lithuania
Vaidas Matuzas	Lithuania
Valdas Girdauskas	Lithuania
Valdas Ragaišis	Lithuania
Valentinas Klevas	Lithuania
Victor A. Zhovyansky	Ukraine
Vidas Lekavičius	Lithuania
Viktorija Grigaitienė	Lithuania
Vilma Čipinytė	Lithuania
Violeta Makarevičienė	Lithuania
Violeta Pukelienė	Lithuania
Violeta Vaitkevičienė	Lithuania
Virginijus Radziukynas	Lithuania
Virginijus Vileiniškis	Lithuania

Jonas Baltrušaitis	USA	Vitas Valinčius	Lithuania
Juozas Gudzinskas	Lithuania	Vykintas Šuksteris	Lithuania
Jūratė Karbauskaitė	Lithuania	Vytautas Martinaitis	Lithuania
Jūratė Kriaučiūnienė	Lithuania	Vytautas Stankus	Lithuania
Jurij Tonkonogij	Lithuania	Vytis Kopustinskas	Lithuania
Justas Kažys	Lithuania	Vladislovas Algirdas Katinas	Lithuania
Karolina Čepurnienė	Lithuania	Žaneta Simanavičienė	Lithuania
Kęstutis Čiuprinskas	Lithuania	Žaneta Stasiškienė	Lithuania
Kęstutis Valančius	Lithuania	Žilvinas Nakutis	Lithuania
Kęstutis Venslauskas	Lithuania	Živilė Rutkūnienė	Lithuania
Kristina Brinkienė	Lithuania	Žydrė Kadžiulienė	Lithuania

Dear Reader of the Conference proceedings,

The **International Conference of Young Scientists on Energy Issues** has been organized already for thirteen time since 2004, which became a nice annual tradition. We are very proud to bring together talented young scientists to participate in the **13th International Conference of Young Scientists on Energy Issues** (**CYSENI 2016**). We expect that this will contribute to exchange of ideas, improved knowledge of young researchers, development of their acquired abilities and contribute to increasing level of exercised research activities.

The initiative for such an event came from young and enthusiastic researchers of Lithuanian Energy Institute (LEI). They realised that there are a lot of young, smart and science-oriented young people who do research in the energy area and they do need a place and time to meet each other to share their views, generated ideas and

present the latest research results. The first Conference was organized by young researchers with the supervision of experienced scientists from LEI in 2004. In 2005, it became a national Conference with participants from Kaunas University of Technology, Vilnius Gediminas Technical University, Vilnius University, Vytautas Magnus University – in fact from all science and education institutions of Lithuania involved in energy-related topics. The next year (2006) was devoted to strengthening the status of the conference among young researchers and their experienced supervisors. In 2007, the Organising Committee decided to put emphasis both on regional and international dimensions of the conference. The participants from neighbouring countries – Belarus and Poland participated in the conference for the first time. In 2008, we welcomed the participants from Belarus, Estonia, India, Latvia, Lithuania and Russia. In 2009 the outcomes of the conference (in terms of scientific papers) was contributed by the young scientists from Belarus, Estonia, Italy, Latvia, Lithuania, Nigeria and Ukraine. With a growing attention to this annual event the conference proceedings included the papers with scientific results of researchers from various Lithuanian science and research institutions and foreign institutions (Belarus, Estonia, Germany, Italy, Latvia, Nigeria, Norway and Ukraine) in 2010. In total 69 papers of young scientists' from various Lithuanian science and research institutions and foreign institutions in Belarus, Estonia, Germany, Latvia, Nigeria, Poland, Taiwan and Ukraine were reviewed and accepted for the publication in 2011. In 2012, even 81 young scientists took part in the conference and presented the results of their research.

In 2013 conference celebrated its 10 years anniversary. This time there were submitted 130 abstracts, 100 papers were reviewed and 80 papers were accepted to the Conference. The authors were not just from Lithuanian institutions or neighbouring countries – Latvia, Estonia, Poland, Belarus, Ukraine, Moldova, Georgia, Romania, Nigeria, Indonesia and Taiwan.

Participants of CYSENI 2014 were from many different countries (United Kingdom, Denmark, USA, Lithuania, Latvia, Ukraine, Georgia, Belarus, Czech Republic, Estonia and India). In 2015 our conference, for scientific discussion, connect together even 129 participants from Czech Republic, Latvia, Estonia, Sweden, Switzerland, Malaysia, Morocco, Russia, Italy, Poland, Ukraine and Belarus.

This year we are pleased that young scientists further found the conference valuable to present their up to date research results and share scientific experience. Conference event in Institute is usually full of pleasant atmosphere, interesting and valuable discussions and cheerful social programme. For the best papers of this year we have provided an opportunity to be published in journal **Energetika** (ISSN 0235-7208). The greetings and acknowledgments of the participants encourage us to keep these moments in mind and improve the future CYSENI conferences.

Regarding the next year we already invite you to the **14th International Conference of Young Scientists on Energy Issues** (**CYSENI 2017**), which will be held on 25-26 May, 2017 in Kaunas, Lithuania.

Sincerely,
Conference Organizers

CONTENT

I HYDROGEN AND FUEL CELLS (5)

II RENEWABLE ENERGY SOURCES (12)

III SMART ENERGY NETWORKS (2)

IV ENERGY EFFICIENCY AND RELIABILITY (3)

V KNOWLEDGE FOR ENERGY POLICY MAKING (3)

VI INVESTIGATIONS IN THE FIELDS OF THERMAL PHYSICS, FLUID MECHANICS AND METROLOGY (4)

VII MATERIALS SCIENCES AND TECHNOLOGY (8)

VIII INVESTIGATIONS OF COMBUSTION AND PLASMA PROCESSES (10)

IX GLOBAL CHANGE AND ECOSYSTEMS (2)

X FUSSION ENERGY (1)

XI NUCLEAR FISSION AND RADIATION PROTECTION (1)

XII CROSS-CUTTING ENERGY ISSUES (4)

CYSENI 2016, May 26-27, Kaunas, Lithuania
ISSN 1822-7554, www.cyseni.com

POWER GENERATION BY PROTON EXCHANGE MEMBRANE FUEL CELL USING PLASMA MODIFIED ALUMINUM AND WATER REACTION

Marius Urbonavičius, Darius Milčius
Lithuanian Energy Institute
Breslaujos str. 3, LT-44403 Kaunas – Lithuania
Email: Marius.Urbonavicius@lei.lt

ABSTRACT

Currently, possibility of hydrogen use as an alternative to fossil fuel is widely discussed. Hydrogen fuel cells could be used as clean energy sources in portable devices because of zero carbon emission. The main obstacles associated with hydrogen-based energy systems are complex and expensive H_2 storage and transportation. Moreover, safety still remains a challenge because of very high H_2 reactivity. Overcoming those problems, on-board hydrogen production could be achieved from exothermic reaction between aluminum and water ($2Al + 6H_2O \rightarrow 2Al(OH)_3 + 3H_2$). Although the reaction is thermodynamically favorable, thin (5–10 nm) and dense alumina (Al_2O_3) film is spontaneously formed on metal surface and prevents Al-H_2O reaction at ambient conditions. One of the methods (discussed in previous papers) to bypass this issue is modification of aluminum powder under hydrogen gas plasma. This research is concentrated on experiments of electricity generation where hydrogen produced via plasma modified Al powder and water reaction has been channeled to a fuel cell. Plasma modified Al powder sinks and readily reacts with water releasing hydrogen after immersion. Aluminum powder was investigated by scanning electron microscopy (SEM) for surface morphology, X-ray diffraction (XRD) for microstructure analysis and gas content (O, N, H) analyser. Experiments of electric power generation were conducted using laboratory-built equipment which consists of Al-water reaction vessel, hydrogen gas filters, proton exchange membrane fuel cell, load (resistance) and energy meter. Generated energy and voltage of fuel cell were measured at constant resistance.

Keywords: aluminum powder, plasma, hydrogen generation, PEM fuel cell, electricity production

1. INTRODUCTION

Hydrogen fuel cells (FC) continue to be a promising power system for stationary and mobile applications in recent years [1]. The major challenges for widespread application of hydrogen are arising from lack of infrastructure, particularly from hydrogen storage techniques [2]. Conventional hydrogen storage methods still need lots of additional improvements in order to fulfill market requirements for hydrogen powered portable devices [3].

Aluminum reaction with water could be a solution for hydrogen generation on-board. It can eliminate the need for H_2 storage and hydrogen can be supplied to portable fuel cell whenever it is needed. Reaction between 1 g of aluminum and water yields 1245 ml of hydrogen [4]. Byproduct of metal-water reaction is metal oxide or hydroxide: $xM + yH_2O \rightarrow M_xO_y + yH_2$; or $xM + 2yH_2O \rightarrow xM(OH)_{2y/x} + yH_2$ [5]. Aluminum hydroxide is stable and evironmetally friendly product. Although aluminum-water reaction is thermodynamically favorable (exothermic) but it does not proceed due to passivation of aluminum surface by a protective natural oxide layer (5–10 nm) which prevents from direct contact between water and aluminum metal particles [2]. Numbers of suggestions have been proposed for disrupting the protective layer and accelerating hydrogen production, including usage of highly alkaline solution, oxide or inorganic salt additives, aluminum mixture with Ga, Bi, Zn, In, Li, Sn, Mg or Hg or ball milling with additives [6-9].

Energy generation using aluminum-water reaction is realy attractive due to low temperature, low cost of Al, its abundance in earth’s crust (8.1%) and high electron density.

In present research the reaction of plasma modified aluminum powder and water at different initial temperatures was investigated and application of this reaction to the proton exchange membrane was tested.

2. METHODOLOGY

2.1. Aluminum powder modification in plasma

Small amount of aluminum powder was located in vacuum chamber under the circular magnetron (Fig. 1a). Al powder has irregular shape with size varying up to 100 µm. The magnetron with aluminum cathode was used as plasma generator. Distance between magnetron and the sample was 0.07 m. Rotary and diffusion pumps enabled a base pressure of 0.2 Pa in a vacuum chamber. Surface modification of Al powder was performed at 13 Pa pressure by hydrogen gas plasma. Al powder was treated at 1 A current for 1 hour using DC power supply.

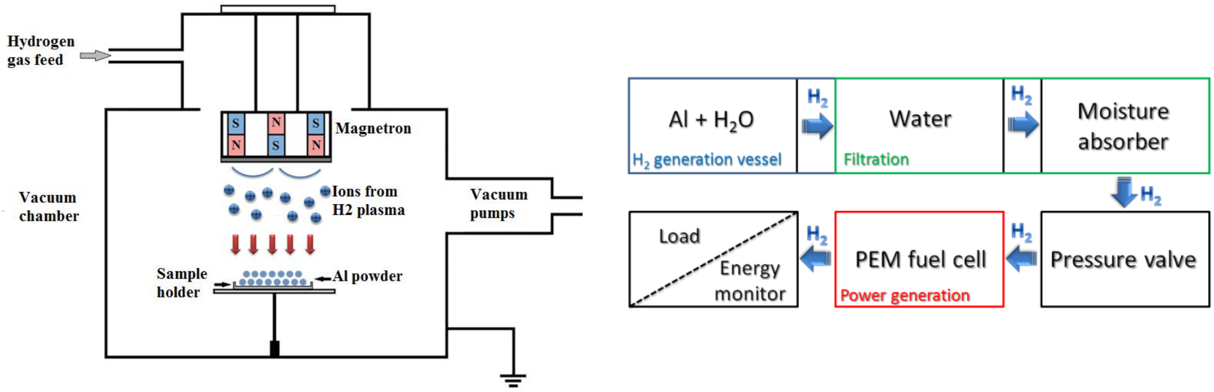

a) b)

Fig. 1. Experimental scheme of Al powder modification in plasma (a) and power generation using Al-water reaction (b)

2.2. Analysis methods

Surface morphology of untreated and plasma treated Al powder were investigated by the scanning electron microscope (SEM, Hitachi S-3400N). The microstructure of Al powder was characterized by X-ray diffraction analysis using Bruker diffractometer (Bruker D8). The radiation source is Cu Kα ($\lambda = 0.15406$ nm) at 40 kV and 40 mA. The measurements were performed at 2θ angle in the range 20°–70^{o} using PSD detector in steps of 0.01^{o}. XRD phases were identified using EVA *Search – Match* software. O/N/H gas analyser (Horiba EMGA 830) was used to identify gas content within the samples.

2.3. Hydrogen production and power generation

Volumetric analysis of hydrogen production was performed using inverted burette filled up with water which has graduated scale in steps of 1 ml. Quantity of H_2 gas was measured from water level change in the burette and complete hydrogen yield was defined by integrating H_2 flow with time until the Al-water reaction stopped. During the reaction, temperature of water was maintained using universal stirred water bath (BWT-U).

Investigation of electricity generation using produced H_2 after Al-water reaction was done according to the schematic illustration presented in Fig. 1b. Power generation system consisted of: hydrogen generation vessel for Al-water reaction; water unit and moisture sorbent for filtration of H_2 flow; pressure valve ensuring steady pressure of hydrogen flow supplied to the fuel cell; 1.5 W proton exchange membrane fuel cell (PEMFC) for electricity generation; Renewable energy monitor from Horizon and a constant load of 20 Ω concected to the energy monitor equipment.

3. RESULTS AND DISCUSSIONS

3.1. SEM views of Al powder and O/N/H analysis

SEM views of unmodified and plasma modified Al powder at 1 A for 1 hour are presented in Fig. 2. Irregular shape of Al particles is clearly seen in Fig. 2a. Surface of untreated powder seems to be relatively smooth (Fig. 2b). Morphological changes of modified Al powder were not observed at first sight (Fig. 2c). Though after magnification, some irregularities and cracks were observed which were distributed randomly in the sample (Fig. 2d). The width of crack observed in Fig. 2d is approximately 150 nm.

Although metal oxide layer is considered to be a diffusion barrier for hydrogen atoms, but small amount of hydrogen could be introduced through crystal defects induced by ion irradiation [10]. Hydrogen absorbtion and diffusion is strongly affected by structural defect sites such as grain boundaries, disorders and dislocations where hydrogen is trapped initially [11, 12]. It is possible that diffused hydrogen could create some cracks or irregularities by changing structure of very surface or native oxide density of Al particles.

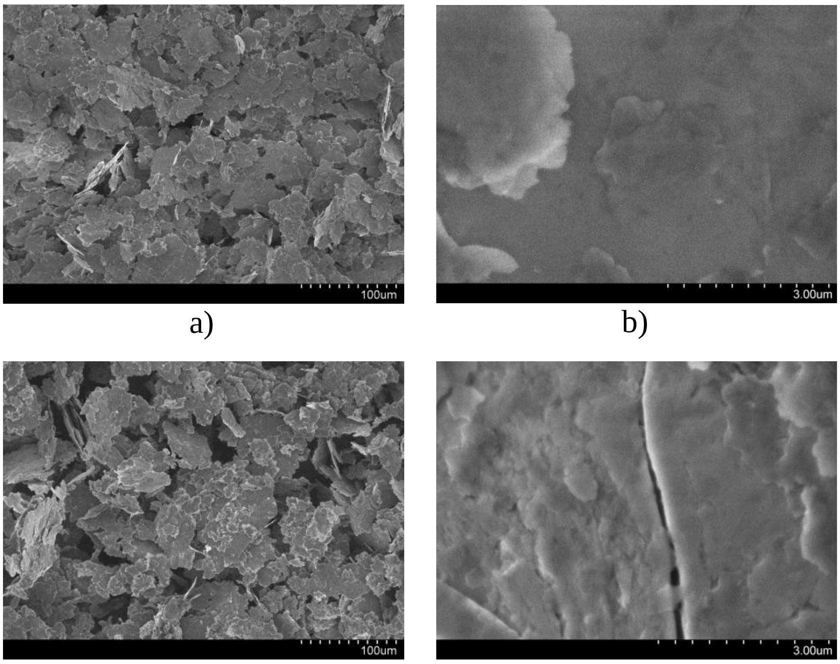

a) b)

c) d)

Fig. 2. SEM views of unmodified Al powder (a–b) and plasma modified Al powder at 1 A for 1 h (c–d)

Oxygen and hydrogen content of untreated Al powder was measured 2.718 and 0.314 wt. % respectively. Oxygen content of plasma modified Al powder slightly decreased to 2.460 wt. % but content of hydrogen deacreased to 0.117 wt. %. Needs to be mentioned that hydrogen concentration decreases approximately 3 times after every modification of Al powder in plasma. Higher hydrogen content of untreated powder indicates that not only native aluminum oxide is formed but aluminum surface is passivated by hydroxides as well. Additionally, Chai et al. [6] indicated that surface of aluminum is composed of Al_2O_3 layer and a thin layer of AlOOH or $Al(OH)_3$.

Plasma irradiation cleaned top surface which led to increased surface energy and hidrophilicity. Besides, it is worth to notice that hydrogen atoms and ions are very powerful reducing agent for most oxides [13, 14].

Presumably, in such manner hydrogen plasma reduce native oxide by changing its stechiometry (making mechanically weaker) and creates cracks which act like pathways for water molecules and hydroxyl ions to reach pure metal surface.

3.2. XRD analysis of Al powder

Fig. 3 includes X-ray diffraction patterns of unmodified and plasma modified Al powder at 1 A for 1 hour. Aluminum peaks with cubic crystallographic orientation (111), (200) and (220) were identified. Additionally, $Al(OH)_3$ and Kβ radiation were observed in both samples. Aluminum hydroxide could appear due to Al powder contact with air. Therefore no significant structural changes or formation of new phases were registered after plasma treatment. This is an argument that alteration is induced by hydrogen gas plasma only in the top surface of Al particles.

Structure refinement of XRD patterns ($R_{wp} = 2.88$) was performed using TOPAS software and cristallite size of untreated and plasma treated aluminum was calculated 119.6 nm and 126.2 nm, respectively. This minor increase could be related to the instrumental error. XRD did not registered any significant changes even after increasing plasma treatment up to 20 hours. Peaks intensity and full width at half maximum remained almost unchanged.

Generally hydrogen diffused in metals causes lattice expansion. However Buckley [15] observed that XRD analysis registered either small decrease or zero change in lattice parameter after charging Al foil under high concentration of hydrogen. Moreover formation of alane phase (AlH_3) is a challenge because of low decomposition temperature [16].

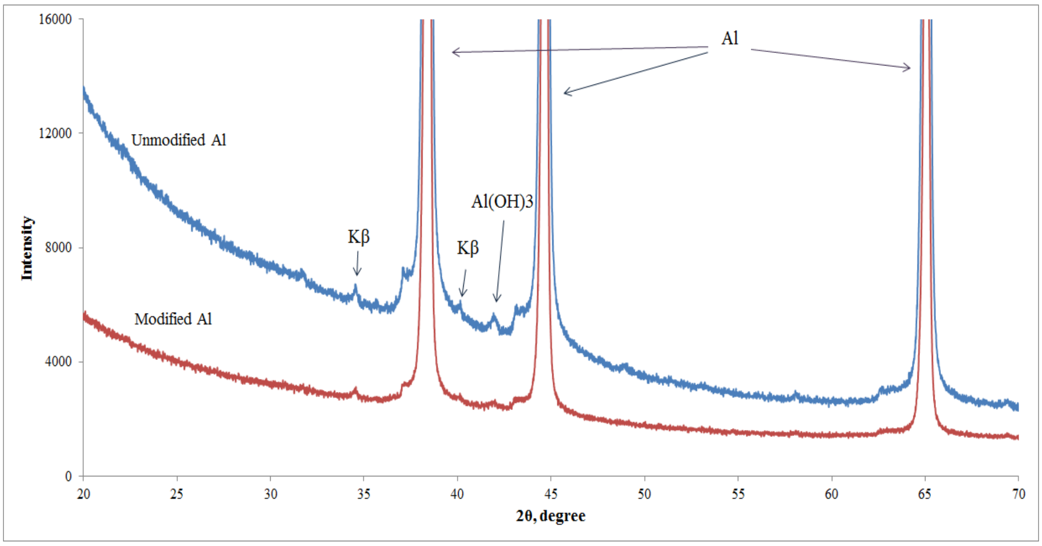

Fig. 3. XRD patterns of unmodified and plasma modified Al powder at 1 A for 1 h

3.3. Effect of water temperature on the kinetics of hydrogen generation

The yield of hydrogen produced (H_2 yield vs. time) after unmodified and plasma modified Al powder reaction with water is presented in Fig. 4a. Fig. 4b shows enlarged view of the reaction start. Small amount of sodium hydroxide (0.2 g of NaOH) was dissolved in 100 ml of pure water in order to increase concentration of OH groups slightly. The reaction was tested using 40 ml of water (with dissolved NaOH) in different initial temperatures (25°C, 30°C, 35°C and 40°C) reacting with 0.05 g Al powder.

Modified Al powder sank immediately after immersion into the water because of plasma induced hydrophilicity while unmodified Al powder floated on the top of water. Change of cumulative H_2 yield with increasing temperature was negligible in both cases. Modified Al powder produced 63 ml of H_2 at 25°C of initial water temperature and 66 ml at 40°C, whereas H_2 yield of unmodified Al rised from 15 ml to 20 ml increasing temperature from 25°C to 40°C, respectively (Fig. 4a). Theoretically, 1g of Al could generate about 1245 ml of H_2 after reaction with water. It is clearly seen (Fig. 4b), that induction time (until H_2 generation starts) is decreased from 44 s to 13 s for modified and from 190 s to 95 s for unmodified Al at water temperatures of 25°C and 40°C, respectively. Increasing the initial reaction temperature results in enhanced Al-water reaction and higher H_2 flow rate [17]. Also it is observed that Al corrosion is very slow in cold water and very fast in boiling water [18].

Al-water reaction is highly exothermic which increase water temperature during the reaction as well: $Al + 3H_2O \rightarrow Al(OH)_3 + 1.5H_2 + 426.5$ kJ [19].

Cracks and structural defects created by hydrogen ions from plasma leads to faster start and more effective reaction because aditional pathways are opened for water molecules and OH^- groups to pure metal surface. Furthermore, larger area of modified Al powder interacts with water due to hydrophilicity.

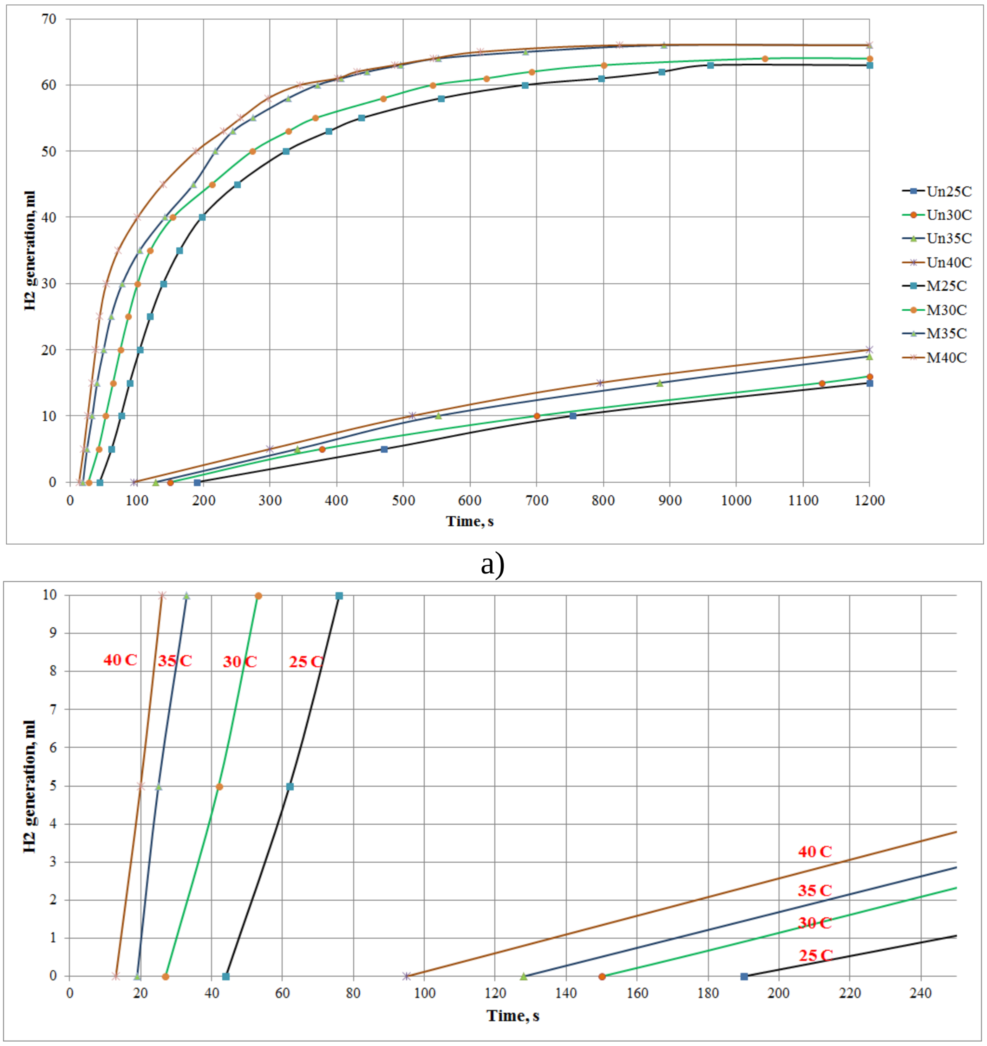

a)

b)

Fig. 4. Temperature influence on H_2 generation using 0.05 g of modified and unmodified Al powder with 40 ml of water (0.2 g of NaOH dissolved in 100 ml H_2O) (a) and enlarged view of reaction start (b)

3.4. Power generation using PEMFC

Hydrogen gas was produced during the reaction between 0.1 g of modified Al powder and 40 ml of water (0.2 g NaOH in 100 ml H_2O) and channeled to proton exchange membrane fuel cell, rated at 1.5 W power for electricity generation. Use of strong alkali should be avoided because it could lead to corrosion of fuel cell. Nevertheless filtration is needed to avoid contaminatiom of the FC membrane. More detailed scheme is presented in Fig. 1b. Voltage generation of fuel cell in different initial temperatures of reaction (25°C, 30°C, 35°C, 40°C) is presented in Fig. 5. Reaction temperature influenced the start of H_2 and voltage generation only. Increased temperature resulted faster reach of nominal voltage. As the hydrogen flow rate decreased, the voltage of fuel cell decreased as well.

However, the energy generated by PEM fuel cell was measured appoximately the same in all cases, 13.6 mWh at 25°C and the same value of 12.5 mWh at 30°C, 35°C, 40°C.

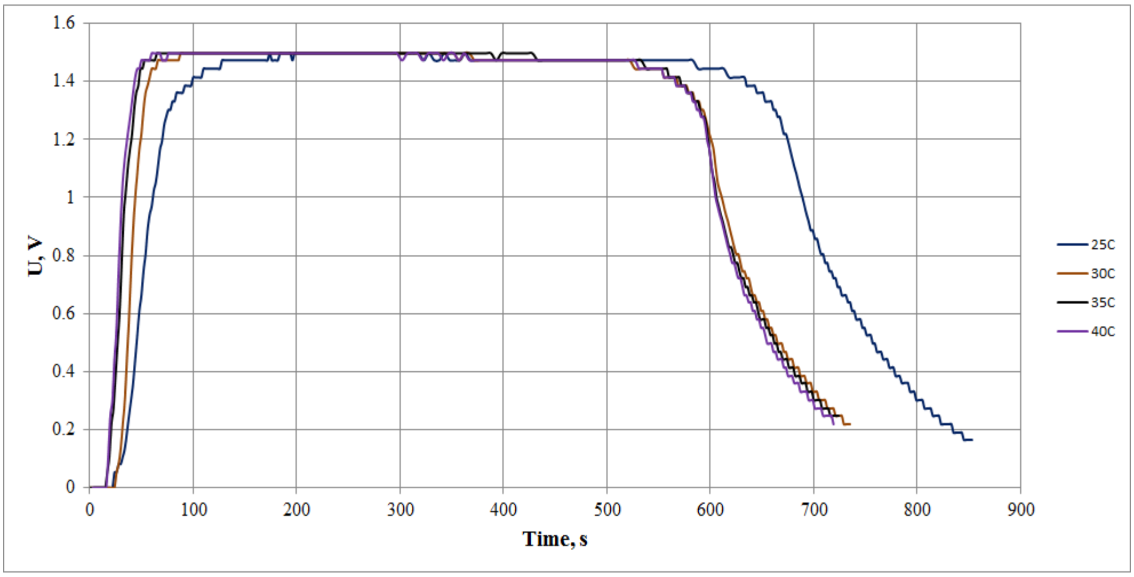

Fig. 5. Power generation after 0.1 g of Al reaction with 40 ml of water under different initial temperatures

When hydrogen is provided to the fuel cell, a contollable H_2 flow rate is generally required for stable power generation [9]. Control of reaction temperature could be one of the methods for regulation of H_2 flow. Yavor et al. [5] calculated aluminum activation energy (50 kJ/mol) indicating a higher temperature dependence of the reaction rate.

Such Al-water – Fuel cell system could be applied for marine or underwater propulsion or as battery replacement in remote communication posts [7, 20]. Some applications where hydrogen after Al-water reaction is fed to the fuel cell were investigated [21-23]. Further H_2 generation after Al-water reaction is commercialy available, mainly as lift gas for weather baloons or back-up power systems (used by military and meteorological users) [24].

Wang et al. [25] examined electricity production from aluminum based reactions and concluded that use of secondary Al (Al scrap) is economical and environmentally friendly way which provides H_2 at reasonable cost.

4. CONCLUSIONS

Surface of aluminum powder can be modified in H_2 plasma by cleaning hydroxides, reducing Al_2O_3 and inducing structural deffects (or cracks and ruptures) within native oxide layer. Such alterations were registered by scanning electron microscopy and gas analyser. Despite small increase in crystallite size which could be attributed to measurement error, XRD technique did not identify any significant structural changes. This result could be interpretated as plasma induced surface modification without structural changes in the bulk.

Considerable difference of produced H_2 after reaction between untreated ant plasma treated Al powder was observed. From 3 to 4 times more hydrogen was produced using modified Al powder. Increasing the initial water temperature resulted in higher H_2 flow rate and faster reaction start but cumulative hydrogen yield remained nearly the same.

Energy generated by PEM fuel cell was measured appoximately the same (13.6 mWh for 25°C and 12.5 mWh for increased temperature) after 0.1g of Al powder reacted with water at different initial temperatures. Energy generation (and H_2) could be increased using larger amount of Al powder or using more water. More water has more hydroxide groups. Highly increased pH level which could damage fuel cell should be avoided.

Kinetically controlled amounts of H_2 provided to fuel cell is considered to be essential factor for application of in-situ hydrogen generation.

5. REFERENCES

1. LI F., SUN L., ZHAO J., XU F., ZHOU H., ZHANG Q., HUANG F. Mechanisms of H_2 generation for metal doped $Al_{16}M$ (M = Mg and Bi) clusters in water. *International Journal of Hydrogen Energy*, Vol. 38, 2013, p. 6930–6937.
2. NIE H., SCHOENITZ M., DREIZIN E.L. Calorimetric investigation of the aluminum-water reaction. *International Journal of Hydrogen Energy*, Vol. 37, 2012 p. 11035–11045.
3. WANG E.D., SHI P.F., DU C.Y., WANG X.R. A mini-type hydrogen generator from aluminum for proton exchange membrane fuel cells. *Journal of Power Sources*, Vol. 181, 2008 p. 144–148.
4. HU X., ZU G., ZHANG Y., WANG Y., GU M., YANG S., SONG P., LI X., FANG H., JIANG G., WANG Z. Hydrogen generation through rolling using Al-Sn alloy. *International Journal of Hydrogen Energy*, Vol. 37, 2012, p. 11012–11020.
5. YAVOR Y., GOROSHIN S., BERGTHORSON J.M., FROST D.L. Comparative reactivity of industrial metal powders with water for hydrogen production. *International Journal of Hydrogen Energy*, Vol. 40, 2015, p. 1026–1036.
6. MENG H.X., WANG N., DONG Y.M., JIA Z.L., GAO L.J., CHAI Y.J. Influence of M-B (M = Fe, Co, Ni) on aluminum-water reaction. *Journal of Power Sources*, Vol. 268, 2014, p. 550–556.
7. ELITZUR, SH., ROSENBAND V., GANY A. Study of hydrogen production and storage based on aluminum-water reaction. *International Journal of Hydrogen Energy*, 2014, Vol. 39 (12), p. 6328–6334.
8. DUPIANO P., STAMATIS D., DREIZIN E.L. Hydrogen production by reacting water with mechanically milled composite aluminum-metal oxide powders. *International Journal of Hydrogen Energy*, Vol. 36, 2011, p. 4781–4791.
9. HUANG X., GAO T., PAN X., WEI D., LV C., QIN L., HUANG Y. A review: feasibility of hydrogen generation from the reaction between aluminum and water for fuel cell applications. *Journal of Power Sources*, Vol. 29, 2013, p. 133–140.
10. BEGRAMBEKOV L., DVOYCHENKOVA O., EVSIN A., KAPLEVSKY A., SADOVSKIY YA., SCHITOV N., VERGASOV S. AND YURKOV D. Hydrogen transport through oxide metal surface under atom and ion irradiation. *Journal of Physics: Conference Series*, Vol. 567, 2014, p. 1–5.
11. HEBERT K.R. Trapping of hydrogen absorbed in aluminum during corrosion. *Electrochimica Acta*, Vol. 168, 2015, p. 199–205.

12. PEDERSEN A., JONSSON H. Simulations of hydrogen diffusion at grain boundaries in aluminum. *Acta Materialia*, Vol. 57, 2009, p. 4036–4045.
13. KITAMURA T., SHIBATA K., TAKEDA K. In-flight reduction of Fe_2O_3, Cr_2O_3, TiO_2 and Al_2O_3 by Ar-H_2 and Ar-CH_4 plasma. *ISIJ International,* Vol. 33, No. 11, 1993, p. 1150–1158.
14. SABAT K.C., RAJPUT P., PARAMGURU R.K., BHOI B., MISHRA B.K. Reduction of oxide minerals by hydrogen plasma: an overview. *Plasma Chemistry and Plasma Processing,* Vol. 34, 2014, p. 1-23.
15. BUCKLEY C.E., BIRNBAUM H.K. Characterization of the charging techniques used to introduce hydrogen in aluminum. *Journal of Alloys and Compounds,* Vol. 330–332, 2002, p. 649–653.
16. GRAETZ J., REILLY J.J. Thermodynamics of the α, β, and γ polymorphs of AlH_3. *Journal of Alloys and Compounds,* Vol. 424, 2006, p. 262–265.
17. KOROSH M., ALINEJAD B. Enhancement of hydrogen generation rate in reaction of aluminum with water. *International Journal of Hydrogen Energy,* Vol. 35, 2010, p. 5227–5232.
18. CZECH E., TROCZYNSKI T. Hydrogen generation through massive corrosion of deformed aluminum in water. *International Journal of Hydrogen Energy,* Vol. 35, 2010, p. 1029-1037.
19. DAI H.D., MA G.L., KANG X.D., WANG P. Hydrogen generation from coupling reactions of sodium borohydride and aluminum powder with aqueous solution of cobalt chloride. *Catalysis Today,* Vol. 170, 2011, p. 50–55.
20. http://articles.maritimepropulsion.com/article/Hydrogen-From-Water-With-The-Help-Of-Aluminum14706.aspx
21. PARK J., XU X., WANG J., ZHU X. A small-scale and portable 50 W PEMFC system taht automatically generates hydrogen from a mixture of Al, CaO, NaOH and sodium CMC in water without external power supply. *International Journal of Hydrogen Energy,* 2013, Vol. 38 (12), p. 10511–10518.
22. FAN M., SUN L., XU F. Feasibility study of hydrogen production for micro fuel cell from activated Al-In mixture in water. *Energy,* Vol. 35, 2010, p. 1333–1337.
23. VLASKIN M.S., SHKOLNIKOV E.I., BERSH A.V., ZHUK A.Z., LISICYN A.V. SOROKOVIKOV A.I., PANKINA Y.V. An experimental aluminum-fueled power plant. *Journal of Power Sources,* Vol. 196, 2011, p. 8828–8835.
24. http://www.alumifuelpowertech.com/
25. WANG H., LEUNG D.Y.C., LEUNG M.K.H. Energy analysis of hydrogen and electricity production from aluminum-based processes. *Applied Energy,* Vol. 90, 2012, p. 100–105.

CYSENI 2016, May 26-27, Kaunas, Lithuania
ISSN 1822-7554, www.cyseni.com

CONVERSION OF THE IDLE WATER DISCHARGES FROM RESERVOIRS TO THE HYDROGEN PRODUCTION BY ELECTROLYSIS

M.T. Idiev, B.S. Safarov, U.N. Fayzulloev
Tajik National University
Rudaki Avenue 17, 734025 Dushanbe – Tajikistan
Email: idiev_64@mail.ru

ABSTRACT

The total hydropower resources of the Central Asia is estimated 457 TWh per year. Currently, it was used only 10% of total capacity. The main volume of regional hydroelectric potential is concentrated in Tajikistan (69%) and approximately 22% in Kyrgyzstan. It is known that due to the large volume of river flow during summer time all hydropower plants in Tajikistan carried idle discharge excess water. According to the information of Holding Company "Barqi Tojik", the idle discharge of water from the cascade hydropower plant on the Vakhsh River today is 600 m^3/s. Moreover, this process continues three months (early July – end of September) each year. A simple calculation shows that every summer idle discharge volume of excess water is more than 4.5 bln. m^3, which is almost half of the project value of the Nurek reservoir (10.5 km^3). The total amount of single dumping of water from reservoirs of Tajikistan in 2012 made on an electric power equivalent more than 6 TWh. The purpose of this work is to develop technology for the use of idle discharge of water for hydrogen production. Considering the substantial role of water chemistry on the electrolysis process the first priority is water clearing from mineral components. This paper presents the results of chemical analyses and the comparison of the results of electrolysis before and after water treatment.

Keywords: idle, reservoir, hydrogen, electrolysis

1. INTRODUCTION

The recent attention and interest of the world community to the so-called alternative and clean sources of energy and urgency of the implementation of green energy in all spheres of human activity are caused by two fundamental factors:

- Reduce fossil organic fuels coupled with global environmental problems;
- Air pollution and global climate change.

The widespread use of fossil fuels in industry and transport leads to the release of enormous amounts of greenhouse gases and pollutants into the airspace resulting in global climate change.

Now in the production structure of primary fuel and energy resources in the region of Central Asia, the leading place belongs to fossil fuels. More than half of the total energy volume correspond to the natural gas main reserves that are concentrated in Turkmenistan and Uzbekistan. In the structure of primary energy resources of the region the leading place also occupies the oil up to 80% of it's production which belongs to the Republic of Kazakhstan [1].

The power system of Uzbekistan is part of the integrated power system of Central Asia. The total installed capacity of the electricity sector of the Republic of Uzbekistan in 2013 was 127179 MW. In Uzbekistan there are 9 thermal power plants with cumulative capacityof 9819 MW. State joint stock company (SJSC) "UZBEKENERGO" is the largest producer of electric and thermal energy with an installed capacity of 11.238 GW which covers 98% of electric and 35% of thermal energy. The average annual balance of the fuel system of SJSC "UZBEKENERGO" consisted of natural gas – 86.7%, fuel oil – 10.26%, coal – 3.04%. Thus, the main emissions of toxic components into the atmosphere were 206.143 thousand t: coal ash – 47.94, sulfur dioxide – 120.12, nitrogen oxides – 37.166.

Consider the fact that the coal potential is widely involved in the energy sector of the Republic of Kazakhstan, the transition from coal to other fuels could reduce annual CO_2 emissions by 37 Mt. More than 12% of electric energy in Kazakhstan is produced by use of renewable energy sources on five hydropower stations. According to the National report, from 90 small hydropower plants in Kazakhstan 21 is in operation. Total output power of all stations is 78 MW and at rehabilitation of old hydropower plants total capacity can reach 450 MW.

According to UN Program provided the increase of the production of heat and electricity in thermal power plants of Kyrgyzstan up to 2020 by use of the coal Kara-Keche deposit and planned construction of power plants of Kara-Keche of 800 MW [2]. This will lead to a significant emission of CO_2 and the coal particles to the atmosphere and thereby to environmental degradation.

According to the UN Program for the economies of Central Asia renewable hydro potential in Central Asia is estimated 460 b per year that is now used only 10%. The main volume of hydropotential is concentrated in Tajikistan (69%) and Kyrgyzstan (22%) [3]. Tajikistan is rich in water resources. The total number of rivers in Tajikistan is 25,000 with a total length of about 90,000 km and more than 8492 glaciers which occupy 6% of the country. Total average annual hydropower potential is 527 b and about 40–50% are technically possible for development of hydropower.

The problem of environmental protection and global climate change caused by emissions of greenhouse gases and suspended particles in the atmosphere stimulates the search and the development of modern alternative and environmentally friendly technologies for the production of energy. The problem of reducing emissions of greenhouse gases in the atmosphere stimulates the search for alternative sources of energy to the existing fossil fuel. In this respect, hydrogen energy is a potential candidate for the development and widespread introduction of green energy [4–8].

Use the summer idle discharges of water from reservoirs for electrolysis creates a favorable condition for the generation and storage of hydrogen for application in winter

The present work is devoted to the production of hydrogen by electrolysis of river water and study of the degree of mineralization of water and the electrode materials on the electrolysis process.

2. EXPERIMENTAL PART

The electrolysis of water was performed using electrodes of stainless steel and copper at voltage in the range of 2.4–4.0 V. The volt-ampere characteristics of electrolytic cell with electrodes of stainless steel and copper were significantly different. The object of electrolysis was water of the Vakhsh River before and after electrosedimentation. Formation of the hydrogen was qualitatively determined by the formation of bubbles on the electrode surface and quantified by measuring manometer connected to the cell (Fig. 1).

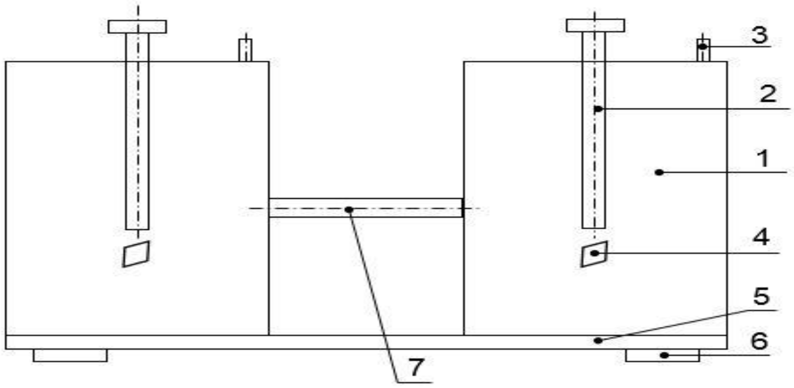

Fig. 1. Schematic diagram of electrolysis cell. 1 – cell; 2 – electrode holder; 3 – fitting for trapping of hydrogen and oxygen; 4 – electrodes; 5 – base of cell; 6 – feet; 7 – connecting tube

Electrolysis of river water without pre-treatment showed that after a certain time (about 15 min) begins the process of sediment formation on the bottom of the cell and the electrodes are covered with thin films. The formation of electrolysis products was negligible and remained constant even by increasing the voltage to 4.2 V.

3. RESULTS AND DISCUSSION

The field intensity between electrodes and the electric current in the circuit decreases due to the formation of gas bubbles on the surface of electrodes. To remove bubbles from the surface of the electrodes was used mechanical vibration. The V-I characteristic of river water electrolysis before and after chemical treatment showed on the Fig. 2.

However, after an abrupt initial increase of the electric current comes the process of saturation characterized by the appearance of impedance on the curve (Fig. 2). It is important to have information about the types and properties of chemical components to develop appropriate methods for removing foreign components leading to inhibition of the process of electrolysis. The results of the chemical analyses of the Vakhsh River are presented on the Fig. 3, that shows that the presence of anions and cations of river water naturally accompanied by deposition of deposits on the electrode surface at electrolysis.

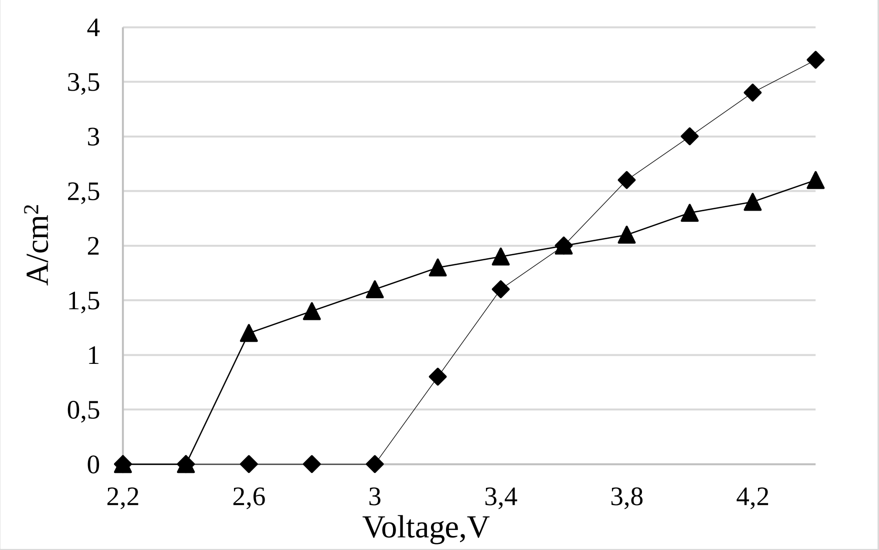

Fig. 2. Voltage-ampere characteristic of electrolyser with stainless steel electrodes at electrolysis of river water before (▲) and after electrosedimentation (■)

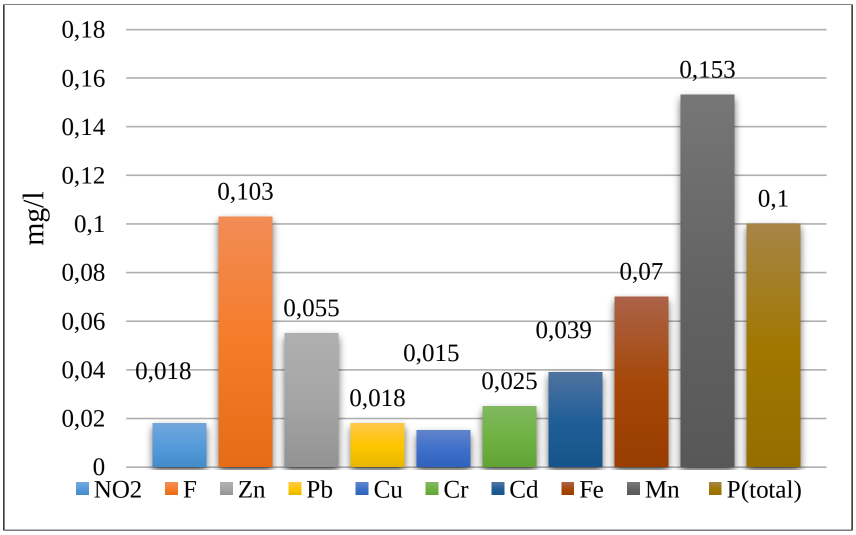

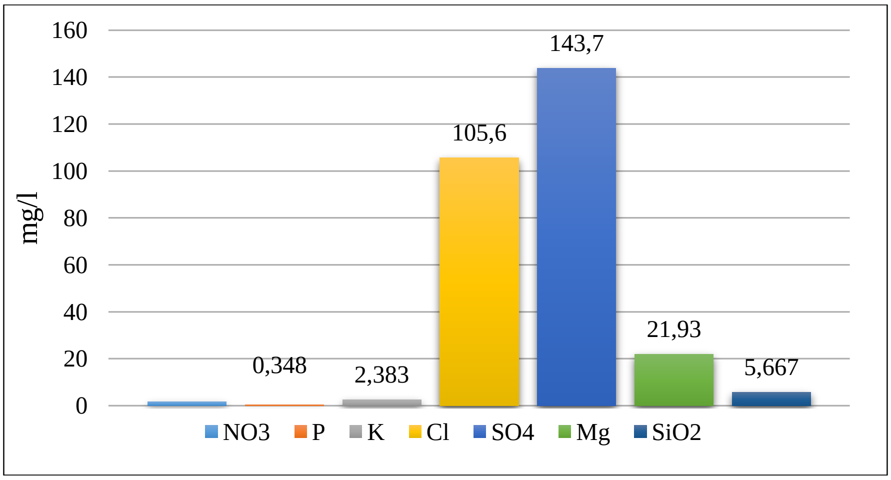

Fig. 3. Results of chemical analyses of the Vakhsh River water

Dynamics of changes of the hydrogen concentration vs voltage shown on the Fig. 4.

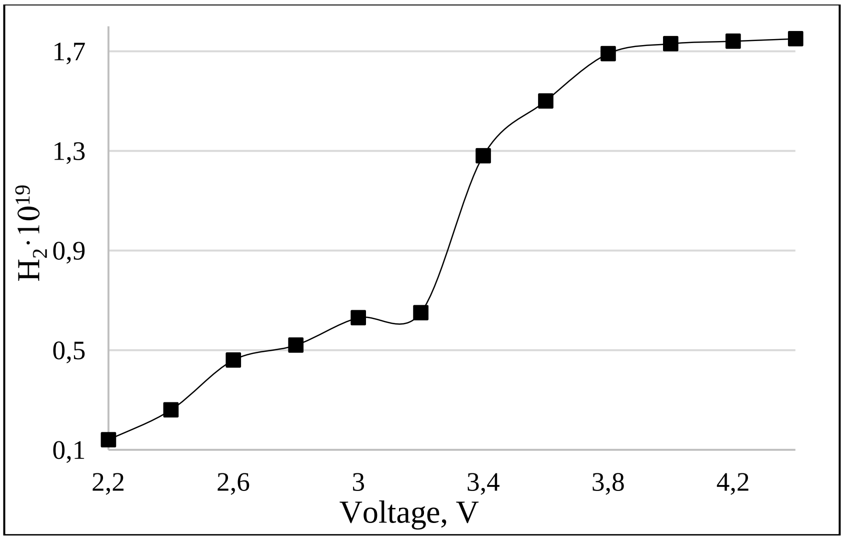

Fig. 4. The consentration of hydrogen at the electrolysis of water by use of electrodes of stainless steel for the 80 min

The change of hydrogen concentration depending on the voltage of the cell has a stepped character (Fig. 4). According to our assumption, this is primarily due to the formation of bubbles and their presence on the surface of the electrodes. The mechanical vibration of the electrolysis cell stimulated to increase of the number of hydrogen.

The voltage source that was used in the work had a scale 2.2–6.5 V. Therefore, in Fig. 4 and Fig. 5 the voltage begins from 2.2 V.

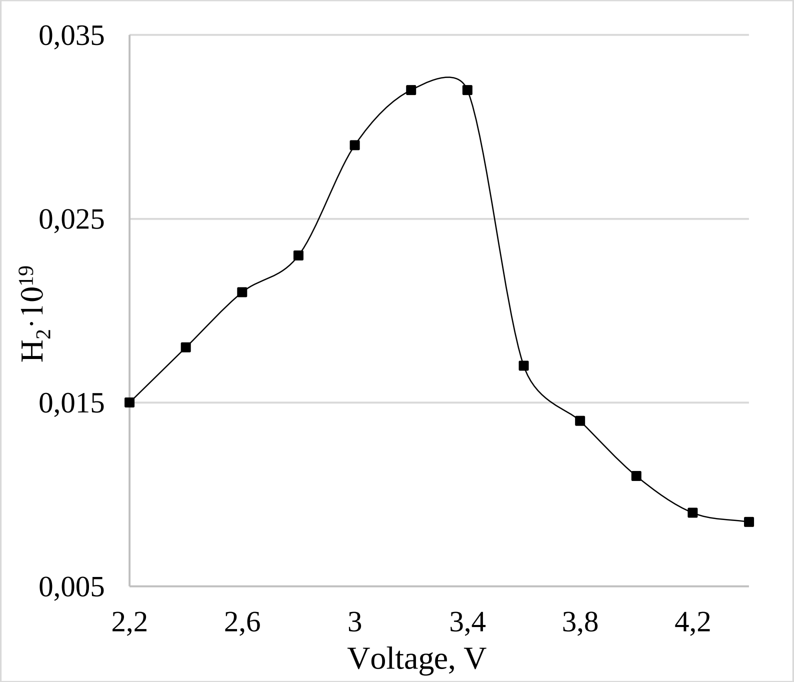

Fig. 5.The amount of hydrogen at electrolysis of water by use of copper electrodes

The sharp decrease of the rate of formation of hydrogen at electrolysis of water by copper electrodes for a given voltage value is associated with surface reactions on the electrodes. Therefore, it can be assumed, that copper reacts with hydrogen ions and partially goes into solution.

Believe that the use of noble metals for electrodes significantly improve the process of electrolysis of water. The electrolysis of water using electrodes from noble metals the plan of our further research

4. CONCLUSION

Thus, result of the research showed that surface phenomena of the electrodes and the degree of mineralization of water are the limiting factors in the processes of electrolysis of water. The stainless steel is a more versatile material for the electrolysis at high voltages and for aggressive media.

5. REFERENCES

1. NORMATOV, I. SH., NARZULLOEV,N., MUMINOV, A., PETROV, G.N. Estimation of the Carbon Dioxide Formation in Heat-Power Complex of the Central Asia and Prospektive of Development of Hydrogen Power Engineering. *Environment Science and Engineering*, 2013. Vol. B2. p.61–67.
2. <http://www.eabr.org>
3. KREUTER, W., HOFMANN, H. Electrolysis: the important energy transformer in a world of sustainable energy. *Hydrogen Energy*, 1998. Vol. 23. No. 8. p. 661–666.
4. NEAGU, C., JANSEN, H., GARDENIERS, H., ELWENSPOEK, M. The electrolysis of water: An actuation principle for MEMS with a big opportunity. *Mechatronics*, 2000. p. 571–581.
5. MILLET, P., ANDOLFATTO, F., DURAND, R. Design and performance of a solid polymer electrolyte water electrolyser. *Hydrogen Energy*, 1996. Vol. 21. p. 87–93.
6. STUCKI, S., SCHERER, G.G., SCHLAGOWSKI, S., FISCHER, E. PEM water electrolysers: evidence for membrane failure in 100 kW demonstration plants. *Applied Electrochemistry*, 1998. Vol. 28. p. 1041–1049.

7. ABOUATALLAH, R.M., KIRK, D.W., THORPE, S.J., GRAYDON, J.W. Reactivation of nickel cathodes by dissolved vanadium species during hydrogen evolution in alkaline media. *Electrochimica Acta*, 2001. Vol. 47. p. 613–621.
8. BOCUTTI, R., SAEKI, M.J., FLORENTINO, A.O., OLIVEIRA, C.L.F., ANGELO, A.C.D. The hydrogen evolution reaction on code posited Ni-hydrogen storage intermetallic particles in alkaline medium. *Hydrogen Energy*, 2000. Vol. 25. p. 1051–1058.

CYSENI 2016, May 26-27, Kaunas, Lithuania
ISSN 1822-7554, www.cyseni.com

DIRECT MEASUREMENTS OF DISSOLVED GAS NEAR THE CATHODE DURING PULSE ELECTROLYSIS

A. Volkovs, M. Vanags, J. Kleperis
Institute of Solid State Physics, University of Latvia
Kengaraga str. 8, LV-1063 Riga – Latvia
Email: ISSP@cfi.lu.lv

ABSTRACT

The study investigates dissolved gas concentrations produced by inductive voltage pulseswater electrolysis. Inductive voltage pulse in the electrolysis cell is characterized by fast-growing impulse front and a relatively slow discharge curve This type of impulse characteristics has been earlier described and associated with separation of cell's geometric capacitor charging process from electric double – layer charging and charge transfer processes.

Authors put forward the following hydrogen and oxygen reaction pattern – the long curve discharge period, Hydrogen Evolution Reaction (HER) is replaced by Oxygen Evolution Reaction (OER) due to increased OH^- ion concentration near the cathode.

A hand made water electrolysis cell with platinum wire electrodes was used. As for the electrolyte solution potassium hydroxide aqueous solution was used. The concentration of dissolved oxygen gas near the cathode was measured using Clark-type microsensor. Gas measurements revealed that during inductive voltage pulse, not only hydrogen but also oxygen was released in the vicinity of the cathode.

In addition, the dissolved oxygen concentration in the alkaline solution of electrolyser is higher than in acid solution. The appearance of oxygen at the vicinity of cathode shows oxygen evolution reaction (OER) in the time of the cathodic pulse.

Keywords: Electrolysis, hydrogen, pulse discharge, oxygen evolution reaction.

1. INTRODUCTION

Hydrogen has proven to be the best alternative energy carrier over the years due to its high energy density, chemical properties and abundance in nature. Hydrogen technologies have had many advancements since Adriaan Paets van Troostwijk and Johan Rudolph Deiman discovered water electrolysis in 1789 [1]. After more than hundred years, later approximately 400 industrial electrolyzers were used all over the world, and in 1939, the first large electrolysis plant was commissioned with the hydrogen production capacity of 10000 Nm^3/h [2]. Later high-pressure electrolyzers and solid state electrolytes were developed, as well as the first solid oxide high – temperature electrolyzer. At present, the hydrogen technologies are increasingly researched and improved along with the development of proton exchange membrane, which can be used in the water electrolyzers and fuel cells, along with the development of high-temperature solid oxide electrolyzers likewise the optimization of alkaline electrolyzers [3].

Along with the hydrogen generation techniques, hydrogen-storing methods also have had major advancements over the last century. Metal-hydride alloys allow hydrogen to be stored with maximum volumetric and gravimetric energy densities, for later use in transport and many other applications. Solar and wind energy power plants are generating green electrical energy for water splitting in hydrogen and oxygen, therefore obtaining clean and environmentally friendly hydrogen, but still, the electric power dissipation has the biggest share in the price of electrolytic hydrogen. The recent growth in hydrogen generation and storage infrastructure could be even higher, if the commonly used hydrogen PEM electrolyzes had an efficiency over the current value of only around 70% [4]. The biggest goal for electrolysis is to develop electrically effective system for hydrogen generation, which does not consume unnecessary electrical power. The electrolysis machinery has been operating since the end of the 19th century. The big drawback is the large loss of energy, which unnecessarily heats up the electrolyte. The voltage in practical devices of electrolysis is higher than thermo neutral cell voltage (1.48 V) [5]. Having such value of voltage some part of the electricity transforms into heat, which heats up the cell and requires additional cooling. The voltage, used in the process of DC electrolysis, is defined:

$$E = E_{atg} + loss \tag{1}$$

where the loss is:

$$loss = E_{anode} + E_{cathode} + E_{mt} + IR \tag{2}$$

where

E_{anode} – activation overvoltage of the anode,
$E_{cathode}$ – activation overvoltage of the cathode,
E_{mt} – overvoltage of the mass transfer,
IR – ohmic overvoltage (includes resistance in an electrolyte, on electrodes, leads).

Current density must be higher than 100 mA/cm^2 in industrial electrolyzers, that allows the industrial electrolyzer to be operated already in the voltage area, where the ohmic loss takes part, therefore a part of the supplied electricity transforms into the heat, becoming the loss of the water electrolysis.

Ghoroghchian and Bockris [6] in 1956 suggested that pulse DC electrolysis is more effective than conventional electrolysis. Many new patents appeared in 1970ties [7] stating to be invented over effective electrolysis, (i.e. the efficiency on current power is higher than 100%). The water splitting scheme described in patents initiated a huge interest, but nobody has succeeded in interpreting this scheme and its performance mechanisms up to now, and what is more important, nobody has succeeded in experimentally repeating devices described as well. In this paper authors describe the processes that hypothetically takes place in the electrolyte solution during pulse electrolysis.

2. EXPERIMENTAL TECHNIQUES

2.1. Observation of current oscilogram from the pulse electrolysis cell

In this work, the authors put forward a new hypothesis that in addition to normal DC electrolysis reaction, a similar reaction takes place creating the same final products. In previous experiments of impulse electrolysis authors have discovered that during a fast voltage pulse, negative current occurred in the discharge curve of the electrode oscilogram (Fig. 1) [8]. This means that the current flows in the opposite direction, and the solution gives back electrons to the opposite electrodes. It gives authors the opportunity to put forward the hypothesisthat parallel to DC electrolysis the pulse electrolysis takes place near the cathode only, and if so, then oxygen evolution reaction (OER) should be taking place near the cathode as well, unlike DC electrolysis.

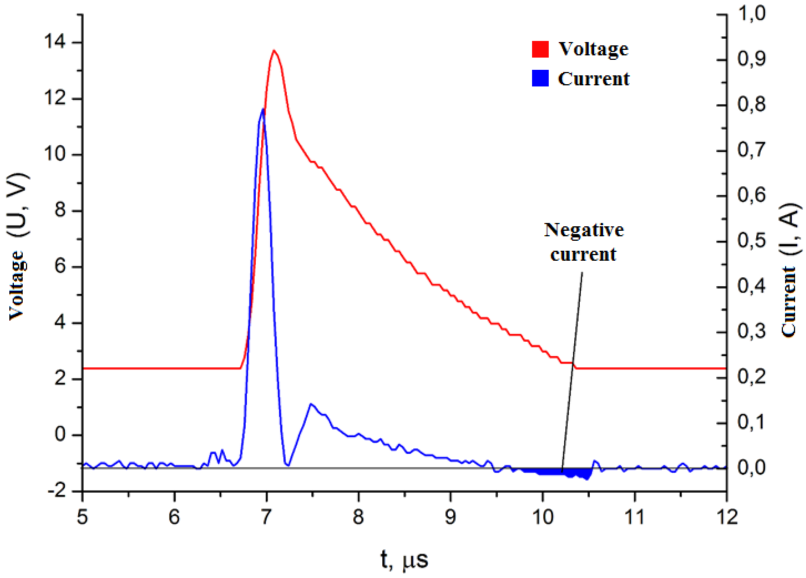

Fig. 1. Voltage and current ocilogram of the electrodes in electrolysis cell

For better understanding weneed to compare the processes that take place in normal DC electrolysis and pulse electrolysis, and explain the experimental setup.

2.2. Inductive reverse voltage pulse generator

A high frequency inductive pulse generator was built to initiate the pulse electrolysis (Fig. 2).

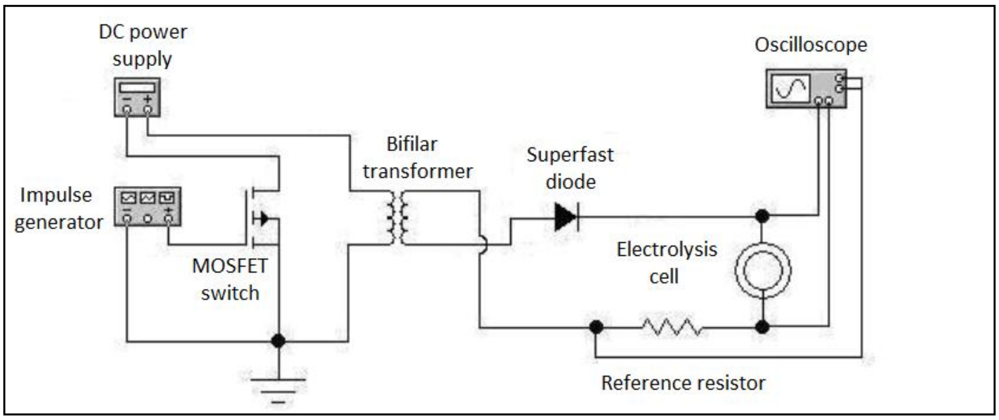

Fig. 2. High frequence inductive reverse voltage DC pulse generator

The pulse generator consisted of DC power supply, N channel MOSFET BUZ350 transistor, HF impulse generator, special broad-band bifilarly wound transformer, blocking diode and two beam digital oscilloscope. The impulse generator was set to 5 kHz, the frequency in which the bifilar transformer coils had reached their saturation current. When the gate drive voltage has been given to the MOSFET transistor from the impulse generator, a 2 V potential is initiated in the primary winding of the transformer. Then the transistor severs the primary circuit and a much bigger 14 V reverse voltage potential is initiated in the secondary winding, which is fed to the electrodes of the electrolysis cell. In order to protect the circuit from backfire pulses a high performance diode is used. To obtain current and voltage oscillogram, a two beam digital oscilloscope probes are connectedto the electrodes. A benchmark resistor is used to measure the current.

2.3. The hypothesis

As we analyze the voltage and current curves, we can see that they have a difference in phase, which means that the solution acts as a capacitor. Also the discharge part of the curve represents a capacitor. To better understand this process, form the electronic perspective, we need to look closer, to the events that take place in the cell. The current pulse in the pulse electrolysis cell can be explained using an equivalent electric circuit (Fig. 3). The circuit consists of C_G – geometrical cell capacity, C_{EDL} – electric double layer capacity, R_E – resistivity of the electrolyte, and R_{CT} – electric charge transfer resistivity. In Fig. 3 both cathode and anode are represented as a capacitor and resistor in parallel connection. Theoretically analyzing the current oscillogram, it is possible to conclude that after about 0.3 µs of fast charge, the cells geometrical capacity has reached saturation current. It is concluded so, because the capacity of the geometrical cell is much smaller, than the double layer capacity, the geometrical capacity starts to discharge, charging the electric double layer capacity on both electrodes [9]. After that, the double layer slowly discharges and the cycle starts over.

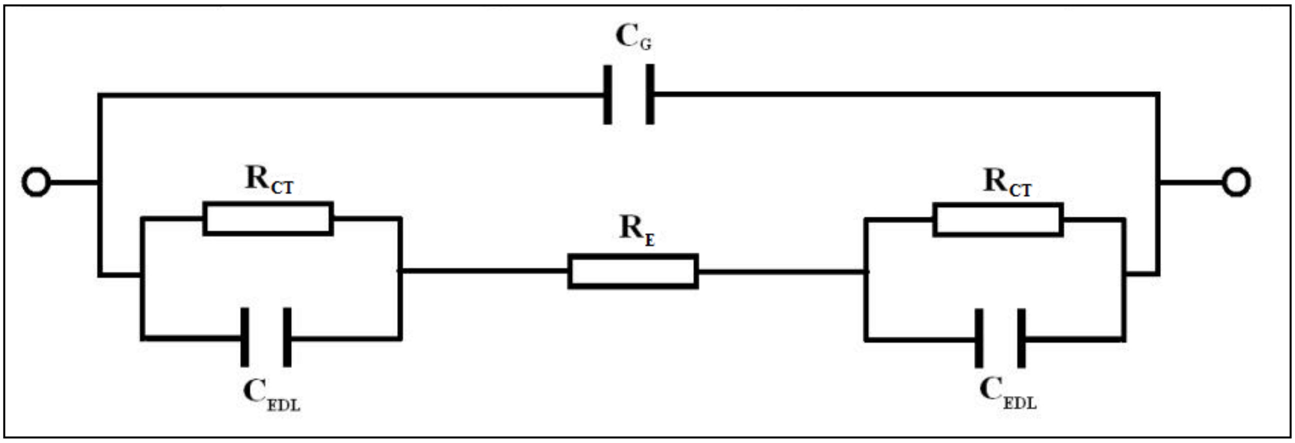

Fig. 3. Equivalent electrical circuit of the electrolysis cell

2.4. Pulse electrolysis principle

Keeping in mind the equivalent electrical circuit, we can begin to deduce the mechanism of the pulse electrolysis.

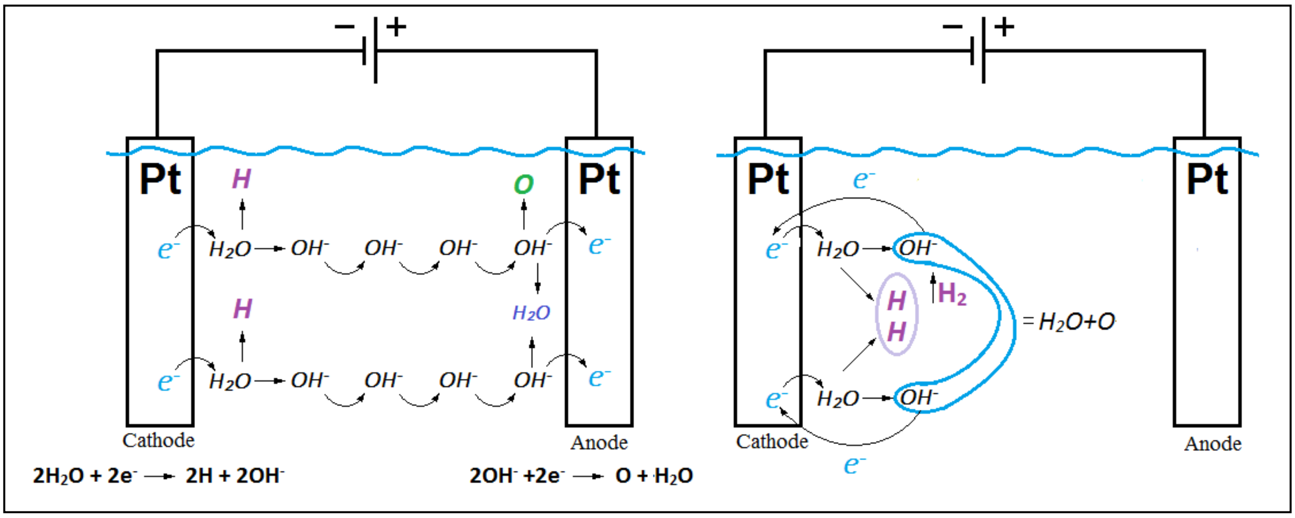

Fig. 4. Conventional DC electrolysis (left) and induced pulse DC electrolysis (right) principles

In the left part of Fig. 4 the conventional DC electrolysis mechanism is shown. When DC voltage is applied to the electrodes, it is known that a hydrogen evolution reaction (HER) takes place near the cathode and oxygen evolution reaction (OER) near the anode. In the HER reaction, electrons dissociate water molecules tohydrogen atoms and negative hydroxide ions. The two hydrogen atomsthen form a hydrogen molecule and bubble out of the solution. The negative hydroxide ions act as a charge transfer which transfer electrons to the anode, where they complete the electrochemical process. When the hydroxide ion gives away one electron, it can react with the other hydroxide ion forming water molecule and oxygen. However, when a high frequency pulse is initiated, another hypothetical process takes place parallel to the previous one. At 5 KHz frequency hydroxide ions cannot pass through the solution, since that process takes around 1 μs. When the pulse electrolysis is initiated, potential difference dissociate water molecules into hydrogen and hydroxide ions rapidly. At a suddenfall of the current pulse, the environment near the cathode is relatively more negative than electrode itself. Therefore, the electrons from the environment are forced to return back to the cathode in order to make the solution more electrically neutral. Hydrogen atoms bondforming hydrogen molecules and hydroxide ions react forming water and oxygen atoms as it happens in the normal DC electrolysis. Only this time all the reactions take place at only one of the electrodes.

2.5. Construction of the electrolysis cell

To check whether this process actually takes place in the pulse electrolysis, a special cell was built. The main goal for the cell was to ensure that the dissolved oxygen generated by electrolysis at electrodes could not godirectly from one electrode to another. A nonconductive diaphragm was glued inside the cell, so that a gap at the bottom of the cell was left open (Fig. 5), which allowed electrical contact of both sides through the electrolyte solution. The cell was sealed with a hermetic lid, which had a drilling for the Unisense oxygen microsensor (Fig. 5). Before the measurements were taken, the solution was bubbled with argon for 15 minutes to release any dissolved oxygen from the solution.

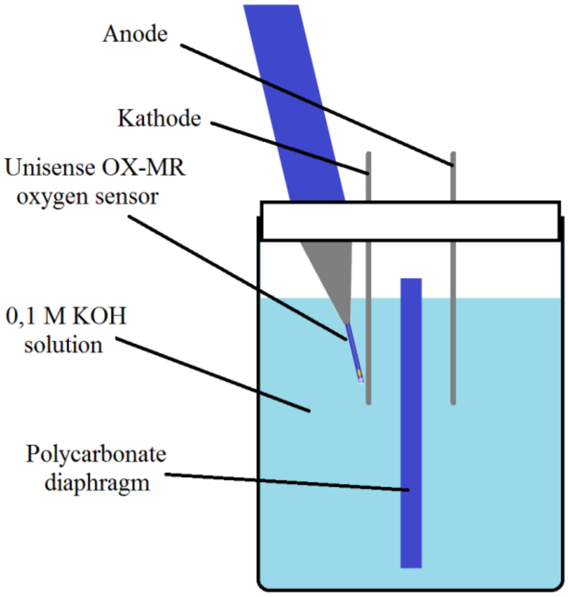

Fig. 5. Construction of the electrolysis cell

Platinum was chosen for both anode and cathode because it is stable material and it is less possible that oxygen orany other ions/compounds would be generated from the electrode material during the electrolysis process.

2.6. Clark type oxygen microsensor

This sensor measures the current resulting from reduction of oxygen on the gold electrode inside sensor capillary. The resulting current is measured by Unisense pico ammeter. Sensor current is linearly directly proportional to the partial pressure of the dissolved oxygen. Knowing the temperature and salinity of the solution, oxygen concentration can be measured with an accuracy of 0.1 µmol / L. For the measurement 0.1 M KOH solution was used, which provided a higher solution conductivity.

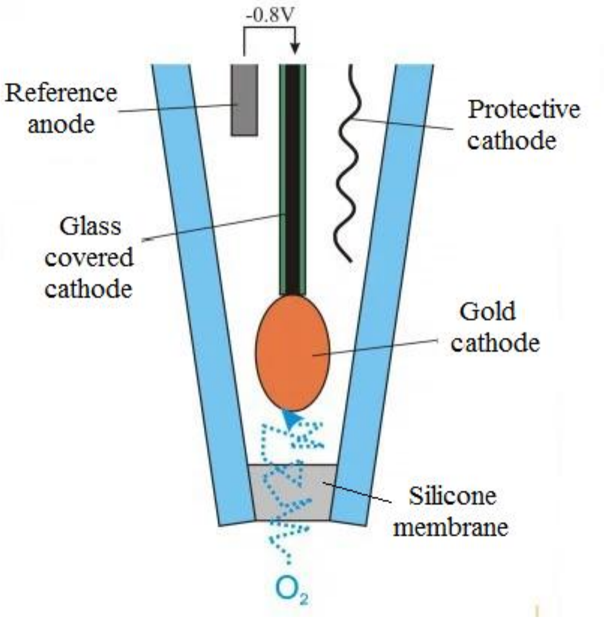

Fig. 6. Scheme of the Clark type oxygen sensor

3. RESULTS AND DISCUSSIONS

3.1. Oxygen sensor measurements

When the electrolysis cell is turned on, oxygen concentration near the cathode increases up to nearly 20 µmol/l confirming authors hypothesis. Next the polarity of the electrodes were switched so that the electrode near the oxigen sensor was the positively charged anode. The obtained data was linearly approximated and showed that the concentration of oxygen at the cathode grew slightly less than at the anode. To ensure that the oxygen concentration does not grow over the solubility limitthe pulse was periodically turned on and off. As it is shown in the graph (Fig. 7), when the pulse generator is turned on for 30 seconds, the oxygen concentration increases. As it was turned off the concentration started to decrease and stayed at a constant value. This leads the authors to think, that the OER reaction near the cathode takes place. As mentioned before, the accuracy of the clark type oxigen microsensor is 0.1 µmol / l, but in Fig. 7 the measured dissolved concentration shows a rather noisy result, at some points background fluctuations exceeds 5 µmol / l whereas signal values above background rises only by slightly more than 10 µmol / l. Since negative current in the voltage and current oscilogramm (Fig. 1) is very low, the concentration diference of dissolved oxigen, periodicaly switching the pulse electrolyse on and off is also low. The electrolyte was filled with small bubbles of hydrogen and oxigen and some of them were stuck on the microsensors capillary which distorted the measurement. The measurement could be taken more precise if the microsensor would be placed differently against the electrode.

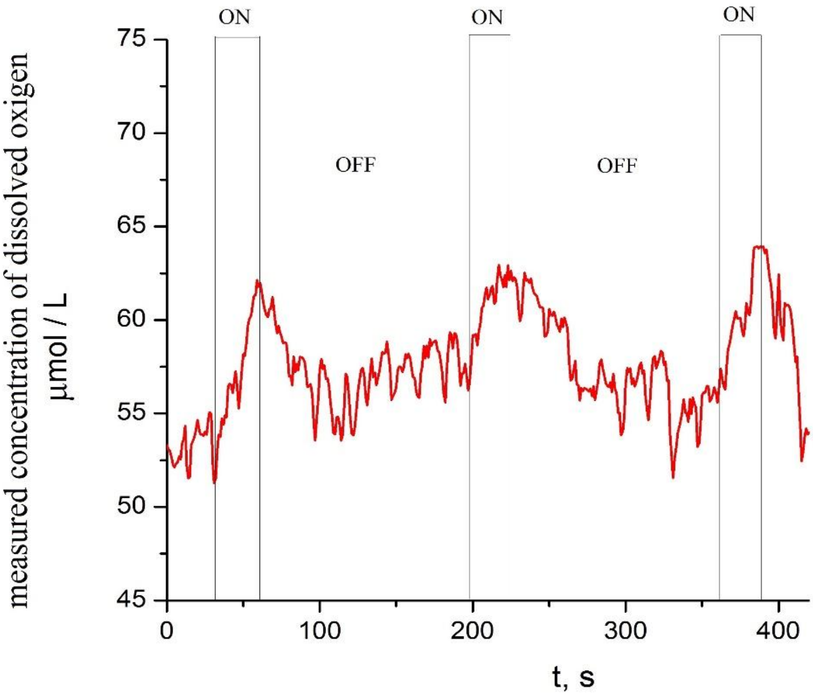

Fig. 7. Experimental results of the pulse electrolysis – capillary sensor is placed near cathode

4. CONCLUSIONS

During the reverse inductive voltage pulse electrolysis, at the discharge curve a negative current is obtained, which leads to hypothetical conclusion of OER reaction near the cathode. The oxygen measurements near the cathode show increase of oxygen concentration when the pulse electrolysis is initiated. To explain theresults, we offer the following reaction process model: parallel to the conventional DC electrolysis reaction the electric pulse rapidly generates an increase of OH^- ion and hydrogen concentration in the immediate vicinity of the cathode. The environment near the cathode is relatively more negative than the cathode itself and the electrons are forced to return to the cathode, which does not allow OER reaction on the anode due to the fast pulse time. At the end, both HER and OER happens at the vicinity of one electrode. The experiment could be conducted more precise by using Fourier transformation infrared spectroscopy (FTIR) and modifying the electrolysis cell, so that each electrode would be surrounded by a dielectric pipe in which the oxigen and hydrogen would accumulate for later gas absorption measurements in FTIR. This way it could be possible to make different pulse electrolyse measurements dependent on time.

5. REFERENCES

1. R. De LEVIE. The electrolyses of water. *Journal of Electroanalytical Chemistry*, 476 (1999), p. 92–93.
2. ZOULIAS E., VARKARAKI E., et all. A Review On Water Electrolysis. Centre for Renewable Energy Sources (CRES), Pikermi, Greece: http://www.cres.gr/kape/publications/papers/dimosieyseis/ydrogen/A%20REVIEW%20ON%20WATER%20ELECTROLYSIS.pdf.
3. KREUTER W, and HOFMANN H. Electrolysis: the important energy transformer in a world of sustainable energy. *Int. J. Hydrogen Energy* 23(8), 1998, p. 661–666.
4. Kaveh MAZLOOMI, Nasri B. SULAIMAN, Hossein MOAYEDI. Electrical efficiency of electrolytic hydrogen production. http://www.electrochemsci.org/papers/vol7/7043314.pdf.
5. OLDHAM K.B., MYLAND J. C. Fundamentals of Electrochemical Science. United Kingdom: Academic Press Limited, 1993, 474 p.
6. J. GHOROGHCHIAN, J, O'm. BOCKRIS. Use Of A Homopolar Generator In Hydrogen Production From Water, *International journal of Hydrogen energy*, Vol. 10, Iss. 2, 1985.
7. MEYER, S.A. Process and apparatus for the production of fuel gas and the enhanced release of thermal energy from such gas. US Patent 5149407 (1992).
8. VANAGS M, KLEPERIS J, BAJARS G. *Water electrolysis with inductive voltage pulses*, In Book: Electrolysis Editors Janis Kleperis, Vladimir Linkov 2012, ISBN: 978-953-51-0793-4.
9. VANAGS M. *Nanostructured iron oxide photoanode synthesis and properties, mechanisms of pulse electrolysis an photo electrolysis*, Riga Technical University, Latvia, 2015, 166 pp.

THE INFLUENCE OF POTASSIUM HYDROXIDE, STAINLESS AND GRAPHITE ELECTRODES ON EFFICIENCY OF THE WATER ELECTROLYSIS

A. O. Muminov, N. B. Kurbanov, B. A. Markaev
Tajik National University
Rudaki Avenue 17, 734025 Dushanbe – Tajikistan
Email: zar.rakhimov@mail.ru

ABSTRACT

This work is devoted to the development of technology for producing hydrogen by electrolysis using idle discharge of water from Nurek reservoir. The study of the electrolysis of river water and water after the softening process using stainless steel and graphite electrodes is presented. The beginning of the electrolysis process is characterized by the appearance of bubbles on the electrode surface. The mechanical vibration for removal of bubbles from the surface of electrodes was used. It was found that large amounts of hydrogen ($1.7{\cdot}10^{19}$) generated by the electrolysis of water were achieved using stainless steel electrodes. In the case of electrolysis of water at voltages on graphite electrodes of 4 V was obtained the maximum amount of hydrogen equal to $0.034{\cdot}10^{19}$ and further increase of the voltage on the electrode does not lead to the progress of electrolysis due to electrochemical reactions on the electrode surface.

Keywords: electrolysis, hydrogen, copper, stainless steel

1. INTRODUCTION

Recent attention and interest of the world community in the so-called alternative and clean sources of energy and urgency of implementation of green energy in all spheres of human activity are caused by two fundamental factors:

- the shortage of fossil fuels;
- air pollution and global climate change.

Now leading position belongs to fossil fuels in the production structure of primary fuel and energy resources in the region of Central Asia. More than a half of the total energy is produced using natural gas from the reserves located in Turkmenistan and Uzbekistan mainly. Another leading position of primary energy resources in the region is occupied by oil and Republic of Kazakhstan produces up to 80% of this fuel [1].

Water electrolysis is the most promising technology for producing hydrogen in the future, although at present due to the high cost of electricity the share of this method in the global production of hydrogen is less than 5% [2]. Naturally, for the implementation of the electrolysis of water and receiving products of electrolysis in sufficient quantities should the power source. The cost of electrical energy is the main parameter determining the efficiency of the electrolysis process. Now the cheapest form of electricity is hydropower. Sufficient stock of hydropower resources (527 TWh) and accordingly low cost of electricity opens wide prospects for the development of hydrogen energy in Tajikistan.

2. EXPERIMENTAL PART

This work is devoted to study the possibility to produce hydrogen by electrolysis of water and increased output of hydrogen in the presence of the potassium hydroxide solution by concentration of 0.1–0.8 M. For electrolysis of water was used the equipment principle scheme is shown on Fig. 1.

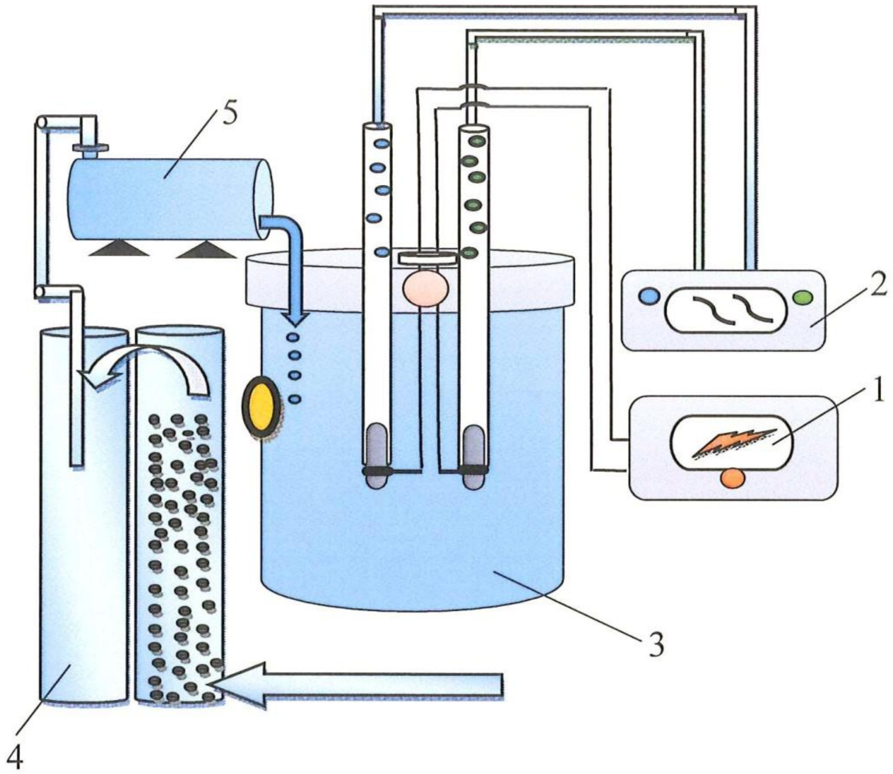

Fig. 1. Scheme of the technological line for production of hydrogen by electrolysis of water: 1 –power unit; 2 – manometer; 3 – cell; 4 – cleaning system; 5 – water tank

The river water after passing through the treatment systems (4), consisting of cylinders with active absorbents (activated coal) is flow to the tank (5). Further leaks into the cell (3). The rate of water flow from the tank to the electrolysis cell (3) is regulated by a flow meter. The distance between the electrodes is 4–8 mm. The hydrogen and oxygen volume at electrolysis is measured by oil pressure gauge (1). For study of the effect of potassium alkali on the electrolysis process were prepared solutions of KOH with a concentration of 0.1–0.8 M. The dependence of the rate of hydrogen formation at fixed concentration of KOH was investigated at voltages on the electrodes 18 V and 24 V.

3. RESULT AND DISCUSSION

In thin layers of solutions of sodium hydroxide, sulfuric acid and sodium sulfate the magnitude of the effective conductivity exceeds the conductivity in the volume of electrolyte in 1.5–2.5 times depending on the composition of the electrolyte [3]. It was suggested that the cause of abnormally high conductivity is an ordered arrangement of water dipoles at the phase boundary between gas-liquid and the ability of the relay mechanism of charge transfer without changing the orientation of dipoles of water. The amount of hydrogen was determined using the universal gas equation:

$$PV = n \cdot R; \cdot \tag{1}$$

$$N_{H2} = n \cdot N_A. \tag{2}$$

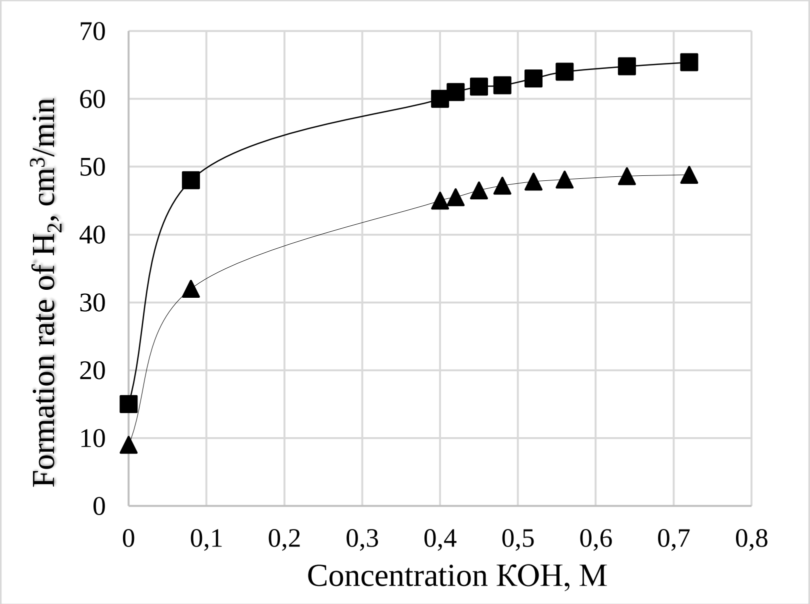

Fig. 2. The formation of H_2 at voltages of 18 V (▲) and 24 V (■) using graphite electrodes

The increase of KOH concentration in the electrolytic cell up to 0.4 M as seen from Fig. 2 leads to the acceleration of electrolysis. Further increase of its value almost does not affect to the rate of the process.It should be noted that blackening of the water and deposition of gray sediments at the bottom of the electrolysis cell was observed by increasing the concentration of KOH. The chemical analysis demonstrated that grey precipitate deposited on the bottom of the cell is a part of the graphite electrode immersed in the electrolyte solution. The observed phenomenon can be explained in framework of capillary model. Some amounts of KOH solution can be absorbed in graphite due to its high absorbtion capacity and this contributes to gradual fragility of the electrode and its deposition.

The increase of volume fraction of hydrogen or oxygen bubbles between electrodes- increase of void fraction and would cause the increase of electric resistance in aqueous solution resulting in efficiency decrease of water electrolysis [4].

While the current density is small, the efficiency of water electrolysis becomes larger as electrodes space decreases, since the electric resistance between electrodes decreases. When the current density is rather high and the space is rather small, however, the void fraction between electrodes gets rather large resulting in increasing electric resistance between electrodes, and then decreasing the efficiency of water electrolysis [5].

There is an optimum condition on water electrolysis efficiency due to the effects of generated bubbles between electrodes. In this paper, in order to explain the existence of the optimum condition a model of alkaline water electrolysis was established. The model can express void fraction and current density profiles along electrodes and show the existence of the optimum condition. For verification of this model, rising velocity, diameter distribution of bubbles between electrodes and current density profiles along electrodes were measured during water electrolysis of KOH solution [6].

From the Fig. 2 can see that at others equal conditions the voltage increase on the electrodes results to increasing the rate of the formation of hydrogen.The electrolysis of water was performed using electrodes of stainless steel are resistant to alkaline medium (Fig. 3).

Fig. 3 shows that as in the case of graphite at using steel electrodes on the dependence of the efficiency of electrolysis from the voltage the impedance is observed.

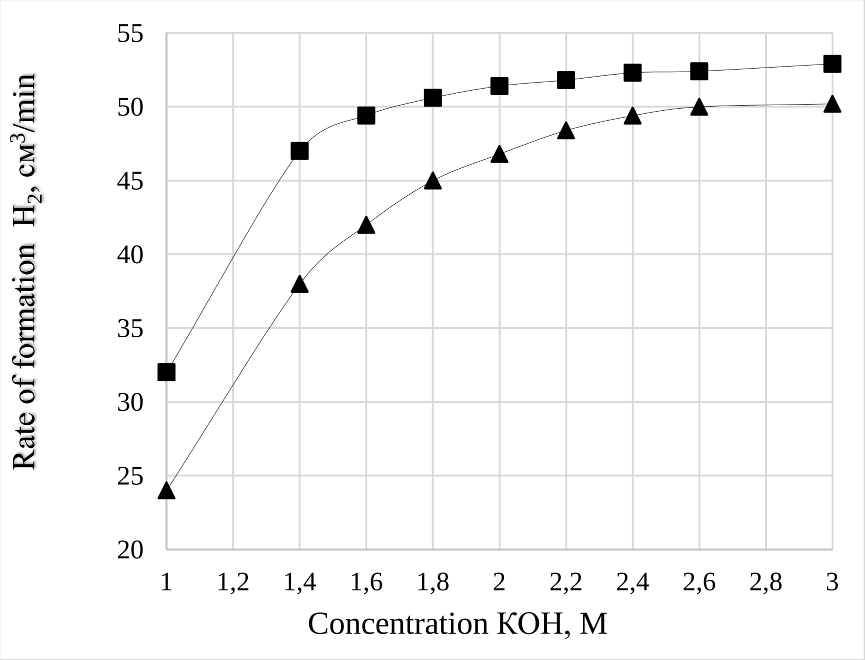

Fig. 3. The rate of formation of H_2 at voltages of 18 V (▲) and 24 V (■)
on the stainless steel electrodes

4. CONCLUSION

A significant increase of the water electrolysis efficiency in the presence of a potassium hydroxide solution was observed. Efficiency increasing of the electrolysis continues up to a certain value of the concentration of a potassium hydroxide. The graphite electrodes due to their porosity structure and sufficient content of micro- and macropores in an alkaline medium are destroyed.

5. REFERENCES

1. NORMATOV, I., NARZULLOEV, N., MUMINOV, A., PETROV, G. Estimation of the Carbon Dioxide Formation in Heat-Power Complex of the Central Asia and Prospective of Development of Hydrogen Power Engineering. *Environment Science and Engineering*, 2013. Vol. B2. p. 61–67.
2. TARASOV, B.P., LOTOSKY, M.T. Hydrogenenergy: last, present, views of the future. *Russ. Chem.Society named after D. I. Mendeleev*, 2006. Vol. L. No. 6. p. 5–18.
3. NEFEDOV, V. G., ZYUBENKO, T.O., BONDAR, D.V. Electrical conductivity anomalies in thin liquid layers at the surface of the air-electrolyte interface during electrolysis of water. *Questi*ons chemistry and chemical technology. *New ideology*, 2007. No. 3. p. 120–125.
4. LEROY, R.L., JANJUA, M.B.I., RENAUD, R., LEUENBERGER, U. Analysis of Time-Variation Effects in Wate*r Electrolyzes*. *Electrochem. Soc.*, 1979. Vol. 126, pp. 1674–1682.
5. NAGAI, N., TAKEUCHI, M., KIMURA, T., OKA, T. Existence of Optimum Space between Electrodes on Hydrogen Production by Water Electrolysis. *Hydrogen Energy*, 2003. Vol. 28. p. 35–41.
6. NAGAI, N., TAKEUCHI, M., NAKAO, M. Influences of Bubbles between Electrodes onto Efficiency of Alkaline Water Electrolysis. *Proceedings of PSFVIP-4,* June 3–5, 2003, Chamonix, France. p. 1–10.

CYSENI 2016, May 26-27, Kaunas, Lithuania
ISSN 1822-7554, www.cyseni.com

ELECTRICAL POWER GENERATION WITH PEM FC USING HYDROGEN SUPPLY THROUGH Mg-Ni REACTION WITH WATER

Dalius Girdzevičius, Darius Milčius
Lithuanian Energy Institute
Breslaujos str. 3, LT-44403, Kaunas – Lithuania
Email: dalius.girdzevicius@lei.lt

ABSTRACT

Hydrogen is considered as energy vector of the future because of its potential use for clean energy generation. Portable electronic devices can be powered when hydrogen is supplied to fuel cells. In order to avoid massive equipment for hydrogen storage, direct hydrogen production can be achieved on-site during the reaction between metals/metal alloys/metal hydrides and water. Magnesium hydride offers great perspective for widespread applications as its weight yield of hydrogen reaches 6.4% according to the reaction with water and it can even increase to 15.2% if water produced in fuel cell is used in the reaction again.

In the present work Mg powder with content of Ni was synthesized under low temperature hydrogen plasma conditions changing DC magnetron current from 0.5 to 1 A. As pure Mg powder was immersed into hydrogen plasma simultaneous hydrogenation process was ensured. Constant working pressure (7 Pa) and time of treatment (60 min) were maintained for all samples.

Nickel was chosen as catalyst capable to influence growth of hydride by creating its nucleation centres. Process of electric power generation was investigated when reaction between modified Mg powder and water was applied to laboratory-built equipment. Solutions of acetic acid and sodium chloride were used as promoters during powder-water reactions. Experiments of hydrogen production and energy generation confirmed that absence of MgO, morphological surface variations, presence of Ni and ratio of powder to water are essential for more efficient reactions.

Characterisation of predicted magnesium hydride powder was done using scanning electron microscopy, electron dispersive spectroscopy and X-ray diffraction. SEM revealed morphological changes of Mg powder after hydrogen plasma treatment compared to pure Mg. Inhomogenous distribution of Ni caused by size and spherical shape of primary powder was shown by EDS. XRD analysis showed only Mg, MgO and Ni peaks indicating that hydrogen generation during powder-water reaction was evoked because of microgalvanic corrosion at Mg-Ni intersections.

Keywords: hydrogen generation, Mg-Ni powder, water, electrical power generation

CYSENI 2016, May 26-27, Kaunas, Lithuania
ISSN 1822-7554, www.cyseni.com

THE INFLUENCE OF ACYL MOIETY OF CARBOXYLATE METHYL ESTERS ON RAPESEED OIL CHEMICAL INTERESTERIFICATION

Zane Sustere, Valdis Kampars
Institute of Applied Chemistry, Faculty of Materials Science and Applied Chemistry,
Riga Technical University, Paula Valdena 3/7, LV 1048, Riga – Latvia
Email: zanesustere@inbox.lv

ABSTRACT

In recent years much research has been aimed to improve biodiesel synthesis using interesterification reaction. In interesterification reaction of vegetable oil with short-chain aliphatic esters instead of glycerol short-chain triglyceride (triacylglycerols) are formed what can be considered a valuable additives for biodiesel and have not to be removed from the reaction mixture. Furthermore, it has been proven that the mixtures of fatty acid alkyl esters and triacylglycerols have no detrimental effects on fuel properties.

With the aim to ascertain the influence of the structure of acyl moiety of different methyl esters on the composition of obtained interesterification mixture in the present work rapeseed oil interesterification with methyl formate, acetate and propionate were studied using two different catalysts – the sodium methoxide in methanol (commercial catalyst) and the potassium *t*-butoxide in *t*-butanol solution. The second catalyst allows to minimize the side reactions, that usually occur when sodium methoxide in methanol are used.

To determine the influence of different acid moiety of carboxylate methyl esters reactions at assumed constant reaction conditions - 27°C temperature, carboxylate methyl ester to oil molar ratio 18 and catalyst amount 0.12 (molar ratio to oil) were performed. In order to increase the yield of products, reactions at boiling temperature of aliphatic esters and modification of other variables also has been made. The reactivity of the acyl moiety decrease in order methyl formate, methyl acetate, methyl propionate. The highest FAME content (82.8 wt.% from theoretically predicted 84 wt.%) was obtained with methyl formate, when potassium *t*-butoxide was used as catalyst and reactant to oil molar ratio was increased to 36:1.

Keywords: renewable fuel, chemical interesterification, methyl formate, methyl acetate, methyl propionate

1. INTRODUCTION

Biodiesel is a renewable fuel obtained mainly from the triglycerides contained in oils and fats, as well as in algae, via a transesterification reaction with methanol. The glycerol formed during this reaction is usually managed as a waste product [1]. The alternative process, that prevents glycerol synthesis is interesterification of oil. The interesterification of triglycerides with methyl acetate provides a promising alternative of transesterification because triacetin is formed instead of glycerol [2, 3]. When the triacetin is included in the formulation of biodiesel, the amount of biofuel obtained from triglyceride noticeably increase [4].

Interesterification of oils and fats to produce FAME (Fatty acid methyl esters) and triacetin are extensively studied in recent years. In order to improve process effectiveness, a lot of research capabilities are devoted to the interesterification studies which use waste cooking oils [5–7], heterogeneous biocatalysts [8] and supercritical methyl acetate [9, 10].

There are many reports on the influence of different alcohol moieties on transesterification [11, 12], but interesterification with different carboxylate esters are not studied widely. Since warious carboxylate ester are available, it is important to clarify the applicability of those esters in biodiesel production [13]. It has been shown that supercritical interesterification of rapeseed oil with methyl, ethyl, propyl and butyl acetates, propionates and butyrates high product yield (more than 50%) was obtained only when methyl acetate and ethyl acetate were used. Longer alkyl chains in both alcohol and acyl moieties of alkyl esters gave lower product yields [13].

The aim of this study is to supplement the carboxylate ester row with methyl formate, as there are no data about biodiesel production using methyl formate. Recent studies have shown that addition of triacetin to the biodiesel up to 10 wt% do not affect the quality of biofuel and it still meet the requirements of quality standard EN14214 [4]. Using methyl formate and methyl propionate, the byproducts in reaction are triformin and tripropionin, respectively, and the influence of these products to fuel properties had not been studied.

Interesterification reactions of rapeseed oil using chemical catalysts does not require high temperatures, pressure or long reaction times contrary to the enzymatic and/or supercritical interesterification. The main task of this study is to ascertain the influence of chemical structure of acyl moiety of carboxylate methyl esters (methyl formate, methyl acetate, methyl propionate) on the rapeseed oil chemical interesterification reaction. This reaction is composed of three consecutive reversible reactions, which are shown in Fig. 1.

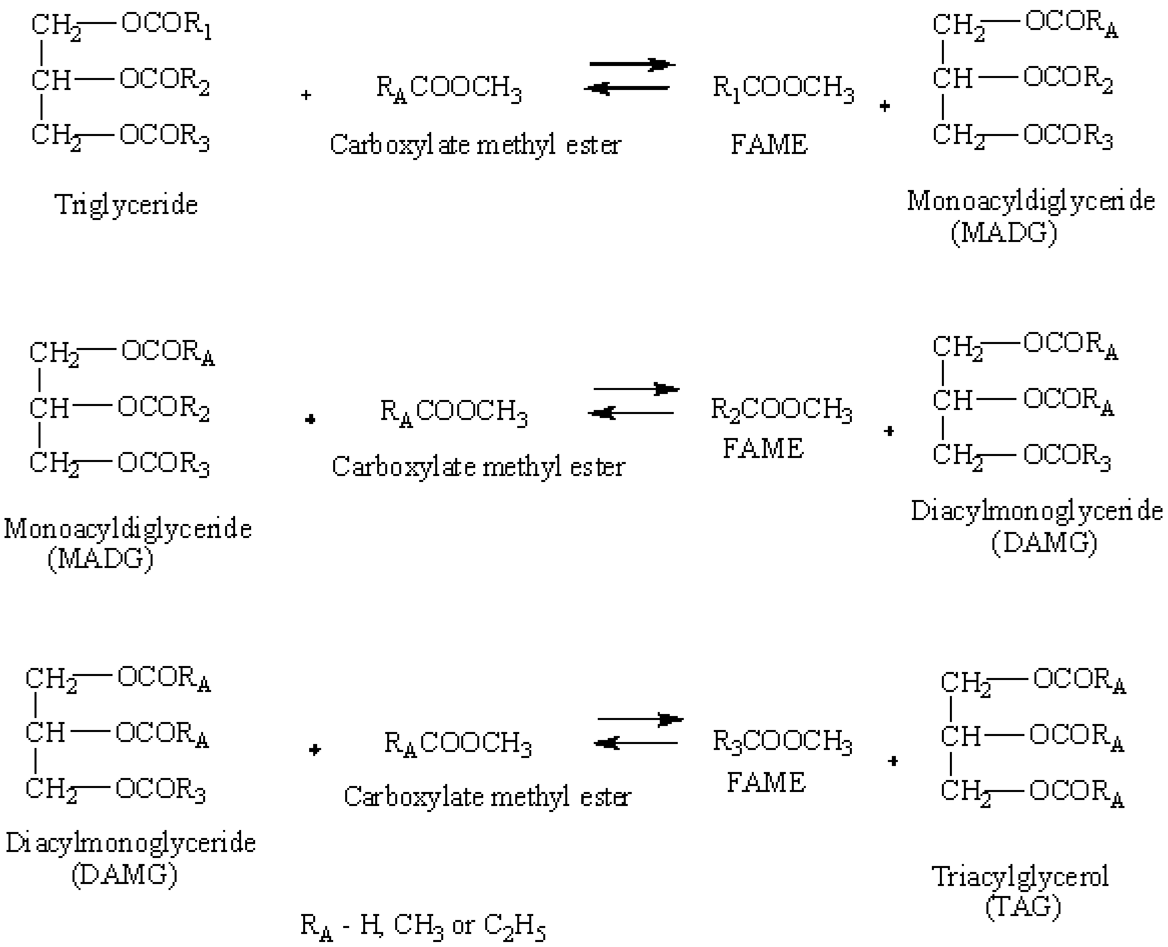

Fig. 1. The interesterification of triglycerides with carboxylate methyl esters

2. MATERIALS AND METHODS

2.1. Materials

The refined rapeseed oil was purchased from a local producer *Iecavnieks*. The methyl acetate (99%) were obtained from *ROTH*, methyl formate (99%) and methyl propionate (99%) were obtained from *Sigma-Aldrich*. Phosphoric acid (85%) was obtained from *Sigma-Aldrich.* Catalyst 28.6 wt.% sodium methoxide solution in methanol (MeONa) was supplied from *Sigma-Aldrich*. Catalyst potassium t-butoxide (BuOK) was obtained from *Sigma-Aldrich* and t-butanol was obtained from *ROTH* and 1M solution was made. Materials for GC analysis – methyl heptadecanoate (95%) were supplied from *Sigma-Aldrich*, 1,2,4-butanetriol (96%) and MSTFA (N-methyl-N-(trimethylsilyl)trifluoroacetamide, 97%) – from *Alfa Aesar,* tricaprin (> 98%) – from *TCI Europe*, heptane (> 95%), and dichloromethane (pure) – were supplied by *ROTH.*

2.2. Experimental procedure

The rapeseed oil and alkyl acetate were mixed and heated up to 27°C or close to boiling point temperature of monoesters (formate 27°C, acetate 55°C, propionate – 78°C) in the 250 mL or 500 mL 3-necked flask, equipped with a reflux condenser, thermometer and magnetic stirrer-heater. The rotational speed was set at 800 rpm. Then catalyst was added and the reaction time was started. Reaction mixture was quenched after 60 min by adding the stoichiometric amount of phosphoric acid. Then excess of reagent was removed by rotary evaporation and the sample was filtered and stored in refrigerator. Each experiment was carried out two times and the average value was calculated. As the concentration of both catalysts solutions in alcohols are different (see 2.1. section), the amount of catalyst used is measured as molar ratio to oil, to make them comparable with each other.

2.3. Analytical methods

The analysis of all components of each sample was carried out by using of an *Analytical Controls* biodiesel analyser based on *Agilent Technologies* gas chromatograph 7890A, equipped with 2 columns. Ester content was determined according to modified standard method EN 14103, using a methyl heptadecanoate as internal standard. The capillary column employed was a HP Innowax with a length of 30 m, an internal diameter of 0.25 mm and a film thickness of 0.25 µm. Oven temperature was set at 200°C.

Glycerol, mono-, di- and triglycerides, – diaACYLmonoglyceride (DAMG), monoacyldiglyceride (MADG), monoacylmonoglyceride (MAMG) and triacylglycerol (TAG – triformin, triacetin, tripopionin) were analysed using DB5-HT column (15 m, 0.32 mm, 0.10 µm) under conditions prescribed in standard EN 14105 and quantified as in our previous work [14]. The oven temperature was set to 50°C for 5 min and then temperature was first increased to 180°C at the rate of 15 °C/min, then to 230°C at the rate of 7 °C/min and finally to 370°C at the rate of 10 °C/min. Helium was used as carrier gas and detector temperature was set to 390°C in both methods. Each measurement was carried out twice and the average value was calculated.

The theoretically predicted content of FAME in reactions with methyl formate, methyl acetate and methyl propionate by full triglyceride conversion accordingly to the scheme represented in Fig. 1 are 84.0 wt.%, 80.9 wt.% and 78.0 wt.%, and the theoretically predicted content of triacylglycerols are 16.0 wt.%, 19.1 wt% and 22.0 wt.%, respectively.

3. RESULTS AND DISCUSSIONS

3.1. Reactions with sodium methoxide catalyst

3.1.1. Reactions with sodium methoxide catalyst at constat reaction conditions

To determine the influence of different acid moiety of carboxylate methyl esters on the composition of obtained interesterification mixture, experiments were carried out at assumed constant reaction conditions suitable for all reactants – 27°C temperature (as the boiling point of methyl formate is 32°C and it is much lower than for methyl acetate (57°C) and methyl propionate (80°C)), carboxylate methyl ester to oil molar ratio 18:1 (18), catalyst amount 0.12 (molar ratio to oil), reaction time 1 hour – on basis of our previous study.

As catalyst sodium methoxide dissolved in methanol has been used, simultaneously FAME during transesterification reaction with methanol and interesterification reaction with carboxylate methyl ester has been produced.

Table 1. Percentage composition of reaction mixtures obtained with methyl formate, methyl acetate, methyl propionate at constant reaction conditions using MeONa catalyst

Reactant	DAMG	MADG	TG	TAG	FAME
methyl formate	9.2	13.1	15.8	1.9	55.0
methyl acetate	5.4	2.3	0	8	70.5
methyl propionate	0	10.8	74	0	11.3

The interesterification reactions with methyl formate and methyl propionate do not proceed with full conversion of oil and the content of the FAME in reaction with methyl propionate is only 11.3 wt.%. The highest content is obtained with methyl acetate – 70.5 wt.% (the yield is 87.1%), but using methyl formate the content is lower as might be expected – 55%. It is known that using supercritical treatment with molar ratio of methyl acetate to oil of 42 the yield of FAME was 89.7%, what is almost the same as for methyl acetate with molar ratio 18 in our study [13]. It can be concluded, that under selected condition the higher reactivity has the methyl acetate but the yield is too low for practical interest and some modification of reaction variable are necessary.

3.1.2. The influence of sodium methoxide catalyst amount

Low yield of products in investigated interesterification reactions can be caused by low reactivity of used methyl esters at 27°C and therefore the chemical equilibrium during the 1 h can't be reached. In praxis the realization of chemical reaction near to the boiling temperature of reaction mixture is used, therefore we made the investigation of all reactions near the boiling point of carboxylate methyl ester. To clarify the influence of the catalyst amount on the proceeding of the chemical interesterification of rapeseed oil, experiments were carried out during 1 hour with molar ratio of carboxylate methyl ester to rapeseed oil equal to 18, and temperature of reaction near to the boiling point of corresponding methyl ester: formate 27°C, acetate 55°C, propionate – 78°C.

The highest FAME content were reached using methyl acetate, even with catalyst amount 0.08 molar ratio to oil 66.7 wt% of FAME were obtained. Increase of catalyst amount in all cases, caused increase of FAME content. It can be explained by larger amount of methanol introduction in reaction mixture with larger amount of catalyst used, see Fig. 2. The optimal amount for methyl acetate was chosen 0.08. The high content of FAME using methyl formate and methyl propionate could be obtained only with high amount of sodium methoxide used (0.4). And it can be concluded, that in methyl propionate reactions triglyceride transesterfication with methanol dominated.

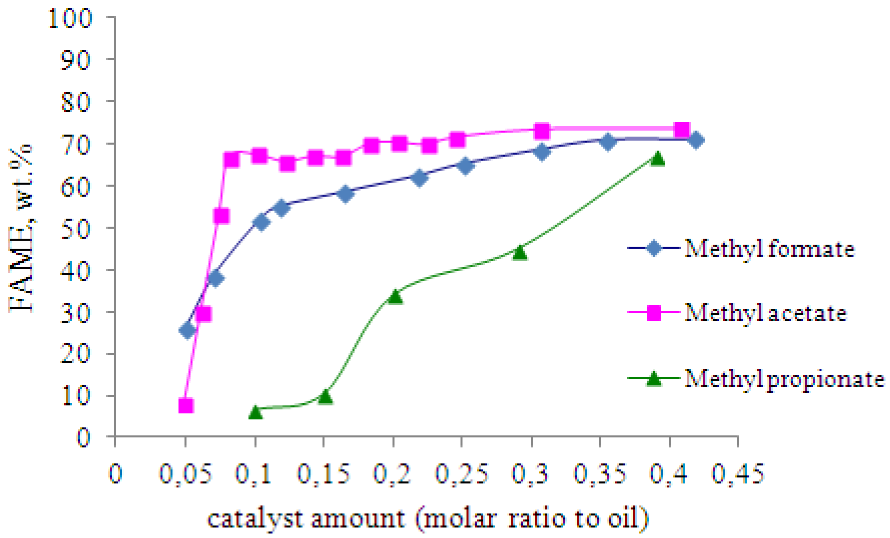

Fig. 2. The influence of MeONa catalyst amount on the FAME content. Reaction conditions: molar ratio of carboxylate methyl ester to oil 18, temperature – near boiling point of corresponding carboxylate methyl esters (formate 27°C, acetate 55°C, propionate – 78°C), reaction time – 1 hour

3.2. Reactions with potassium *t*-butoxide catalyst

3.2.1. Reactions with potassium t-butoxide catalyst at constat reaction conditions

The BuOK solution in t-butanol were used as catalyst, because the reactivity of t-butanol is low, and only interesterification reactions could proceed.

To determine the influence of different acid moiety of carboxylate methyl esters on the composition of obtained interesterification mixture, experiments were carried out at assumed constant reaction conditions: 27°C temperature, reaction time 1 hour, methyl ester to oil molar ratio 18 and catalyst amount 0.12 (the same conditions as in 2.1.1. section). Results are shown in Table 2.

Table 2. Percentage composition of reaction mixtures obtained with methyl formate, methyl acetate, methyl propionate at constant reaction conditions using BuOK catalyst

Reactant	DAMG	MADG	TG	TAG	FAME
methyl formate	7.1	2.7	1	3.3	72.7
methyl acetate	8	3.2	0.6	15.6	71
methyl propionate	0	4.8	94	0	1

As can be seen in Table 2, the highest FAME content was obtained with methyl formate – 72.7 wt.% and the shorter the alkyl residue in acyl moiety the higher yield of FAME. This result agreed with the known results of interesterification reaction of rapeseed oil using supercritical treatment [13**]**, where maximal content of FAME was obtained with methyl acetate, though methyl formate was not studied. In interesterification reactions with methyl acetate the use of BuOK catalyst gave almost the same content of FAME (71.0 wt.%) than use of MeONa (70.5 wt.%). Methyl propionate in presence of BuOK practically did not react (only 1.0 wt.% FAME obtained). As the reagent to oil molar ratio 18 had been used, the content of intermediates is high – almost 8.0 wt.% DAMG. But in methyl formate reactions the content of TAG is very low – 3.3 wt.%, that can be explained with possible low stability of TAG, during the rotary evaporation. To evaluate the possibility of increase the yield of FAME, the investigation of influence of catalyst amount, temperature and reactant amount is necessary.

3.2.2. The influence of potassium t-butoxide catalyst amount

Similarly like in MeONa case, to clarify the influence of the catalyst amount on the proceeding of the chemical interesterification of rapeseed oil, experiments were carried out during 1 hour with molar ratio of methyl ester to rapeseed oil equal to 18, and temperature of reaction near to the boiling point of corresponding methyl ester (formate 27°C, acetate 55°C, propionate – 78°C).

As can be seen in Fig.3., the shorter alkyl residue in acyl moiety resulted in the higher yield of FAME. The content of FAME in methyl acetate reactions are lower than in methyl formate reactions, despite, that the temperature in methyl acetate reactions is higher. The optimal amount for methyl formate was chosen 0.12 (FAME content 72.7 wt.%) and for methyl acetate 0.10 (FAME content 67.7 wt.%), see Fig. 3. The optimal amount of catalyst will increase with the increasing amount of carboxylate methyl esters used, because some part of catalyst always will be consumed for the neutralization of small amounts of the acid present, despite of the acid values of carboxylate methyl esters were insignificant (< 0.2 mg KOH/g). Based on the Fig. 3. and our previous results we have made the calculations [15]. For methyl formate to oil molar ratios 3, 9, 18, 27 and 36 the optimal amounts are 0.09, 0.10, 0.12, 0.14 and 0.16, respectively.

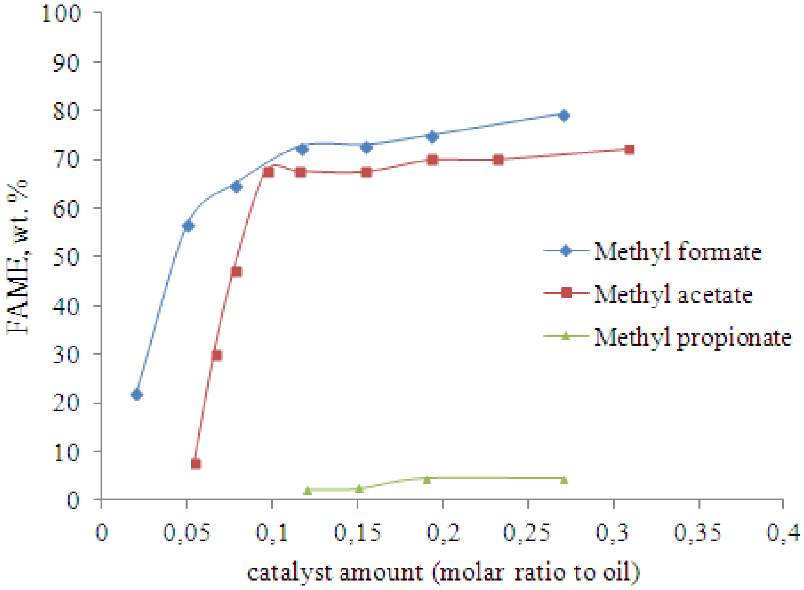

Fig. 3. The influence of BuOK catalyst amount on the FAME content. Reaction conditions: molar ratio of methyl ester to oil 18, temperature – near boiling point of corresponding carboxylate methyl esters (formate 27°C, acetate 55°C, propionate – 78°C), reaction time – 1 hour

The optimal amounts used in interesterification are similar to those used in transesterification. With reactant molar ratio to oil 18, used catalyst amount 0.12 (molar ratio to oil) is equal to 1.5 wt.% (mass percentage to oil) for BuOK catalyst and 0.7 wt.% for MeONa catalyst (as concentration of both solutions are different). In transesterification usually MeONa is used and the amount used are 0.7–1.0 wt.% with alcohol to oil molar ratio 6 [16, 17]. Also in industrial production of biodiesel using MeONa catalyst, 0.75 wt.% is used usually (local producer *Latraps*).

3.2.3. The influence of excess of methyl formate on reaction by use of BuOK catalyst

As optimal amount of catalyst was determined (see 3.2.2. section), the influence of excess of methyl formate can be clarified. To increase the yield, the excess of methyl formate had been increased, see Fig. 4.

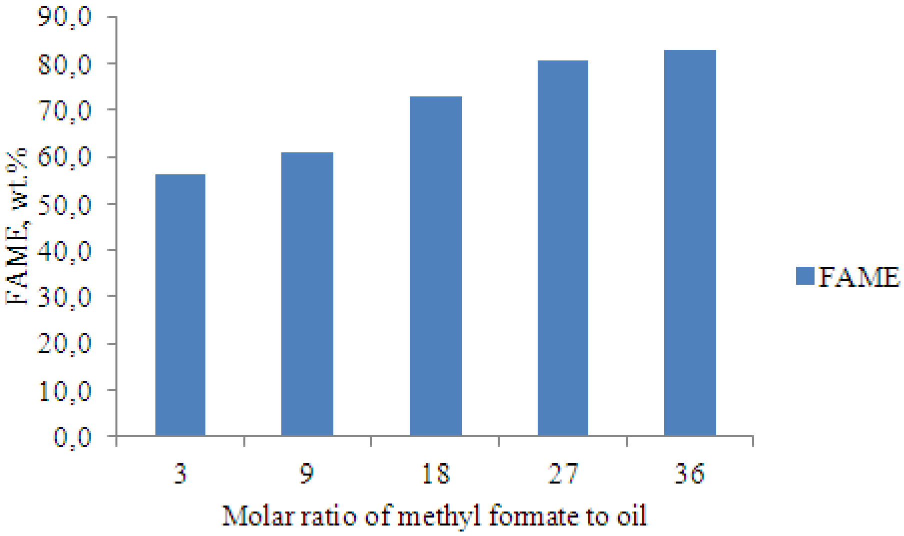

Fig. 4. The influence of excess of methyl formate on FAME content.
Reaction conditions: 27°C temperature and optimal amount of BuOK catalyst

Using molar ratio of methyl formate to oil equal 36, the content of FAME increased till 82.8 wt.%, that is very close to the theoretically predicted value (84.0 wt.%) and no further increase is necessary (and also from economical point further increase will not be interesting). It is much more than could be produced with MeONa catalyst, Casas et al obtained 77.0 wt.% with methyl acetate to oil molar ratio 48 and catalyst to oil molar ratio 0.1 [2].

4. CONCLUSIONS

To determine the influence of different acid moiety of carboxylate methyl esters in interesterification reactions two different catalysts – the sodium methoxide in methanol (commercial catalyst) and the potassium *t*-butoxide in *t*-butanol solution were studied. The use of sodium methoxide in methanol solution as a catalyst is not suitable, as triglyceride side reactions with methanol occur usually. The potassium *t*-butoxide solution in *t*-butanol (BuOK) ensures a domination of interesterification reaction, because the reactivity of *t*-butanol is low. The shorter the alkyl residue in acyl moiety, the higher yield of FAME using the BuOK catalyst. Using molar ratio of methyl formate to oil equal 36 and catalyst amount of 0.16, the content of FAME reached 82.8 wt.%, what is close to the theoretically predicted value (84.0 wt.%). Using methyl formate as reactant and small amounts of BuOK catalyst it is possible to obtain high percentage yield of FAME (99%) at low temperature (27°C).

5. ACKNOWLEDGMENTS

This work was supported by the National Research Programme of Latvia “LATENERGI”.

5. REFERENCES

1. CASAS, A., RAMOS, M., PEREZ, A. New trends in biodiesel production: Chemical interesterification of sunflower oil with methyl acetate. *Biomass Bioenergy*, 2011, 35(5), p. 1702–1709.
2. CASAS, A., RAMOS, M., PEREZ, A. Methanol-enhanced chemical interesterification of sunflower oil with methyl acetate. *Fuel*, 2013, 106, p. 869–872.
3. MADDIKERI, G. L., PANDIT, A. B., GOGATE, P. R. Ultrasound assisted interesterification of waste cooking oil and methyl acetate for biodiesel and triacetin production. *Fuel Process Technol*, 2013, 116, p. 241–249.
4. CASAS, A., RUIZ, J. R., RAMOS, M. J. Effects of triacetin on biodiesel quality. *Energy Fuels*, 2010, 24, p. 4481–4489.
5. MADDIKERI, G. L., GOGATE, P. R., PANDIT, A. B. Intensified synthesis of biodiesel using hydrodynamic cavitation reactors based on the interesterification of waste cooking oil. *Fuel*, 2014, 137, p. 285–292.
6. BHARATHIRAJA, B., JAYAMUTHUNAGAI, J., PRAVEENKUMAR, R., PALANI, M. J. Kinetics of interesterfication on waste cooking oil (Sunflower Oil) for the production of Fatty Acid Alkyl Esterase Using Whole cell biocatalyst(Rhizopus Oryzae) and Pure lipase enzyme. *Int J Green Energy*, 2015, 12(10), p. 1012–1017.
7. RAZACK, S. A., DURAIARASAN, S. Response surface methodology assisted biodiesel production from waste cooking oil using encapsulated mixed enzyme. *Waste Manage*. 2016, 47, p. 98–104.
8. KOVALENKO, G. A., PERMINOVA, L. V., BEKLEMISHEV, A. B., YAKOVLEVA, E. YU., PYKHTINA, M. B. Heterogeneous Biocatalytic Processes of Vegetable Oil Interesterification to Biodiesel. *Catal Ind*, 2015, 7(1), p. 73–81.
9. GOEMBIRA, F., SAKA, S. Effect of additives to supercritical methyl acetate on biodiesel production. *Fuel Process Technol*, 2014, 125, p. 114–118.
10. GOEMBIRA, F., SAKA, S. Advanced supercritical Methyl acetate method for biodiesel production from Pongamia pinnata oil. *Renew Energ*, 2015, 83, p. 1245–1249.
11. MALINS, K., KAMPARS, V., KAMPARE, R., PRILUCKA, J., BRINKS, J., MURNIEKS, R., et.al. Properties of rapeseed oil fatty acid alkyl esters derived from different alcohols. *Fuel*, 2014, 137, p. 28–35.
12. SANCHEZ, M., BERGAMIN, F., PENA, E., MARTINEZ, M., ARACIL, J. A comparative study of the production of esters from Jatropha oil using different short-chain alcohols: Optimization and characterization. *Fuel*, 2015 143, 183–188.
13. GOEMBIRA, F.,MATSUURA, K., SAKA, S. Biodiesel production from rapeseed oil by various supercritical carboxylate esters. *Fuel*, 2012, 97, p. 373–378.
14. SUSTERE, Z., KAMPARE, R., LIEPINS, E., KAMPARS, V. The composition of commercial acetylated glycerol samples determined by ^{13}C and ^{1}H NMR. The comparison with gas chromatography. *J Anal Chem*, 2014, 69(8), p. 838–843.
15. SUSTERE Z., KAMPARS V. Chemical Interesterification of the Rapeseed Oil with Methyl Acetate in the Presence of Potassium *tert*-Butoxide in *tert*-Butanol. *IJETR*, 2015, 3 (10), ISSN: p. 2321–0869.
16. PULLEN J., SAEED K. Investigation of the factors affecting the progress of base-catalyzed transesterification of rapeseed oil to biodiesel FAME. *Fuel Process Technol.*, 2015, 130, p. 127–135.
17. LIN Y.C., HSU K. H., LIN J. F. Rapid palm-biodiesel production assisted by a microwave system and sodium methoxide catalyst. *Fuel*, 2014, 115, p. 306–311.

CYSENI 2016, May 26-27, Kaunas, Lithuania
ISSN 1822-7554, www.cyseni.com

MULTI-CRITERIA DECISION ANALYSIS METHODS AIMING TO EVALUATE RENEWABLE ENERGY SOURCES TECHNOLOGY

Ilona Ališauskaitė-Šeškienė
Lithuanian Energy Institute
Breslaujos str. 3, LT-44403 Kaunas – Lithuania
Kaunas University of Technology
Gedimino str. 50, LT-44239 Kaunas – Lithuania
Email: i.alisauskaite@gmail.com

ABSTRACT

Although renewable energy is the inevitable choice for sustainable economic growth, many factors still need to be taken into consideration when investing in a renewable energy technology. Moving towards a sustainable future requires policy actions that solve existing problems without creating new ones and sustainability assessment of renewable energy technologies could be the key for reaching that goal successfully. Properly conducted sustainability assessment of RES and other electricity energy technologies can prevent potential barriers or limit them while implementing and using RES technologies, also creating an opportunity to prepare for possible consequences arising from feasible disadvantages of RES. Various tools and methods for sustainability assessment of RES technology exist as well as there are many different renewables, however many scientists propose Multi-Criteria Decision Analysis (MCDA) method as the appropriate one for sustainability assessment. The paper aims to systematise, analyze and generalize the newest existing literature about MCDA method its techniques and issues while evaluating renewable energy sources technology.

Keywords: renewable energy sources (RES), RES technology, sustainability assessment, Multi-Criteria Analysis (MCA), Multi-Criteria Decision Analysis (MCDA)

1. INTRODUCTION

Increased utilization of RES would solve many essential challenges in the world – ecological crisis, social tensions, unemployment and economic stagnation. However, various market failures and other RES barriers exist, which basicaly are the main reason utilization of RES is still far from its potential at global scale [1]. One might not forget, such a major barrier as the timing of RES targets and the uncertainty regarding future targets [2], not to mention, conventional fossil fuels, including oil, coal, and natural gas, continue to dominate the market due to its low cost and high availability, while at the same time challenging the principles of sustainability [3]. Furthermore, not only RES technologies have many advantages (great potential for sustainability, technically feasible, economically viable, socially acceptable alternative to traditional fuels), they have their own disadvantages as well [1], [4]. Common features to all RES are their usually higher cost and the fact that none of them is solely beneficial for the environment [5]. And although four of most common sources (wind power, hydropower, energy from wood and energy from crops) can replace CO_2 emissions in different degrees [5], unintended consequences emerging from the increased use of renewables exist, especially with respect to their effects on other valuable natural resources (e.g., water and land) in the long run [6]. According to Hadian & Madani, such RES as hydropower and biomass, affect water more than the others and additionally, the production of some energy (like ethanol and biomass) requires large land areas. These secondary impacts on water and land can establish barriers to sustainable development as the pressure on a major component of the ecosystem (e.g., land, water) can eventually yield to the failure of that component and even to the collapse of the whole system due to the strong interrelations of ecosystem components [6]. Wind power can also cause negative landscape effects and is detrimental to bird and bat populations [5]. Furthermore, bioenergy crop production (such as corn, wheat or barley for ethanol) is a source of nutrient leaching and it reduces biodiversity [5], [7]. However, regarding the ecological problems, world has crossed or at least has come close to that border where the space for the long-run survival of the human civilisation is doubtful [1], [8]. Humanity stands before two intrinsically linked global challenges – development and climate change [9], and scientists agree – ultimately, there is no alternative other than replacing traditional energy sources with renewables [6].

Because not all renewable energy technologies may always provide the most sustainable option, bearing in mind certain specific area [10], many factors need to be taken into consideration when investing in a renewable energy technology and lessons can be learnt from sustainable development when selecting the optimal solution for supplying clean energy. The important goal is trying to find the right balance between economic, social and environmental aspects of sustainable development, which together act as guiding principles to ensure that factors which are considered for a renewable energy technology is relevant for sustainable development [10]. Concept of sustainability is an integrative precondition for the assessment of energy technologies [11] and sustainability assessment can be used as a tool, helping decision-makers and policy-makers decide, which actions they should and should not take in an attempt to make society more sustainable [12].

Moving towards a sustainable future requires policy actions that solve existing problems without creating new ones [6], [13, 14] and sustainability assessment of renewable energy technologies could be the key for reaching that goal successfully. Properly conducted sustainability assessment of RES technologies can prevent potential barriers or limit them while implementing and using RES technologies, also creating an opportunity to prepare for possible consequences arising from feasible already mentioned disadvantages of RES.

1.1. Multi-criteria decision analysis used in sustainability assessment

Various tools and methods for sustainability assessment of RES technologies exist as well as there are many renewables which differ in their environmental and economic impacts, their stage of technology development and their technologies itself [5], [15]. Many scientists [1], [16–20] propose Multi-Criteria Analysis (MCA) method as the appropriate one for sustainability assessment. Multi-Criteria Analysis or Multi-Criteria Decision Analysis (MCDA) became increasingly popular in decision-making for sustainable energy because of multi-dimensionality of the sustainability goal and the complexity of socio-economic and biophysical systems [19]. The concept of multi-criteria sustainability assessment for evaluating energy systems in regards of sustainability was developed by Afgan & Carvalho [21]. According to them, energy system is a complex one with respective structure – it may interact with its surrounding by utilizing resources, exchanging conversion system products, utilizing economic benefits from the conversion process and absorbing the social consequences of the conversion process. Therefore, depending on the problem, energy system can be defined by different boundaries. While sustainability indicators take into account economic and environmental resources parameters, Afgan & Carvalho [21] have presented selection of criteria and options for new and renewable technologies assessment, which was based on the analysis and synthesis of parameters under information deficiency method. In their analysis indicators represented measure of different interactions between energy system and its surroundings. Thus, multi-criteria evaluation of new and renewable technologies established a measuring parameter, comprised of different above-mentioned interactions of system and its surroundings, demonstrated the potential analysis of complex systems and it was intended for use in the evaluation of different option of power plants [21].

Expression MCDA is being used as an umbrella term to describe a collection of formal approaches which seek to take explicit account of multiple criteria inhelping decision makers (individuals or groups) explore decision that matters [22]. According to Belton & Stewart [22], “decisions matter when the level of conflict between criteria, or of conflict between different stakeholders regarding what criteria are relevant and the importance of the different criteria, assumes such proportinions that intuitive "gut-feel" decision-making is no longer satisfactory". These scientists defined three main categories for MCA methods:

- value measurement models;
- goals, aspiration and reference level models;
- outranking models.

Furthermore, four different problems (typologies or cathegories of problems), which may be solved by MCDA, can be identified [23]:

- choice problem – occurs when one is needed to make a simple choice from a set of alternatives;
- sorting problem – occurs when one is in need to classify alterantives into relatively homogenious groups;
- ranking problems – occurs when one is in need to rank alternatives from best to worst;
- description problems – occurs when one is in need to describe actions and their concequences in a formalized and systematic manner.

According to other scientists [16], "in a decisional process the making of choices derives from complex hierarchical comparisons among alternative options, which are often based on conflictual criteria". A large number of external variables play a relevant role in orienting decisionmaking and while some of these variables can be manipulated by numerical models, such as cost-benefit analysis, market penetration strategies and environmental impacts, other factors dealing with social and cultural context, political drawbacks and aesthetic aspects, can be assessed only in a qualitative way or with subjective judgment [16]. Therefore, MCDA "gives the decision-maker considerable help in the selection of the most suitable innovative technologies in the energy sector, according to preliminary fixed objectives" [16].

Thus scientists [17] suggest multi-criteria decision making method as a solution for problems involving conflicting and multiple objectives. According to these sholars, MCA method can provide solutions to increase complex energy management options, whereas traditional single criteria approach is normally aimed at identifying the most efficient options at a low cost. Other scientists [19] describe MCA method as "a form of integrated sustainability evaluation", that can be used to eliminate the difficulty – "it is an operational evaluation and decision support approach that is suitable for addressing complex problems featuring high uncertainty, conflicting objectives, different forms of data and information, multi interests and perspectives, and the accounting for complex and evolving biophysical and socio-economic systems". However, one must not forget, as any other sustainability assessment method, MCDA has its' own disadvantages as well (Table 1). Thus it is highly important for decision makers to understand the risk of performing MCA method – after all, this particular method is created for decision makers to decide, which RES technologies to choose/select in the energy sector, according to preliminary fixed objectives.

Nonetheless, because multi-criteria decision making (MCDM) provides strong decision making in domains where selection of the best alternative is highly complex, it is the most well-known branch of decision making, with the techniques that differ in their theoretical background, type of questions asked and obtained results [29].

Table 1. Advantages and disadvantages of MCA method

Types	Cited authors	Advantages	Disadvantages
Multi-Criteria Analysis (MCA)	Dombi, M., Kuti, I., & Balogh, P. (2014); Stigka, E. K., Paravantis, J. A., & Mihalakakou, G. K. (2014); Hadian, S., & Madani, K. (2015);	• Indicators represent measure of different interactions between energy system and its surroundings; • Demonstrates the potential analysis of complex systems; • Helps to assess factors that can be assessed only in qualitative way or	• Lacks public input and opinion; • Doesn't take into account external costs and benefits of

	Beccali, M., Cellura, M., & Mistretta, M. (2003); Pohekar, S., & Ramachandran, M. (2004); Qin, X., Huang, G. H., Chakma, A., Nie, X., & Lin, Q. (2008); Wang, J., Jing, Y., Zhang, C., & Zhao, J. (2009); Wimmler, C., Hejazi, G., de Oliveira Fernandes, E., Moreira, C., & Connors, S. (2015); Afgan, N. H., & Carvalho, M. G. (2002); Ek, K. (2005); Gasparatos, A. (2010); Madani, K., Sheikhmohammady, M., Mokhtari, S., Moradi, M., & Xanthopoulos, P. (2014); Menegaki, A. (2008).	subjective judgment; • It is considerable help for decision makers while selecting the most suitable innovative technologies in the energy sector, according to preliminary fixed objectives; • Is suitable for addressing complex problems featuring high uncertainty, conflicting objectives, different forms of data and information, multi interests and perspectives, and the accounting for complex and evolving biophysical and socio-economic systems.	renewables; • Lacks a basic definition of sustainability; • Results indifferent optimal outcomes; • Study results are highly sensitive to the choice of multi-criteria assessment method.

1.2. Various MCA methods for RES technology evaluation

In recent years, due to increasing energy demand, use of renewable energy technologies has grown dramatically, naturally number of different MCA techniques has grown as well. Furthermore, “MCDM has been one of the fastest growing areas of operational research, as it is often realized that many concrete problems can be represented by several (conflicting) criteria” [30].

Doukas, Andreas & Psarras [31] presented direct and flexible multi-criteria decision making (MCDM) approach. Zangeneh, Jadid, & Rahimi-Kian [32] proposed a model for evaluation and ranking of various distributed technologies in Iran. Oberschmidt, Geldermann, Ludwig, & Schmehl [33] elaborated a multi-riteria methodology – PROMETHEE (Preference Ranking Organization Method for Enrichment Evaluations) – by assigning criteria weights depending on the actual development phase of a certain technology for the performance assessment of energy supply technologies. Shen, Lin, Li, & Yuan [34] used a fuzzy Analytic Hierarchy Process (FAHP) in order to reveal the suitable RES for the purposes of meeting goals that pertain to energy, the environment, and the economy in Taiwan. Streimikiene, Balezentis, Krisciukaitienė, & Balezentis [35] in their study applied two different MCA methods, Multi-objective Optimization on the Basis of Ratio Analysis pluss Full Multiplicative form (MULTIMOORA) techniques and Technique for Order of Preference by Similarity to ideal Solution (TOPSIS), for more robbust assessment of most sustainable electricity production technologies. Balezentiene, Streimikiene, & Balezentis [36] offered offers a multi-criteria decision making framework for prioritization of energy crops based on fuzzy MULTIMOORA method which enables to tackle imprecise information. Stein [37] in his research proposed a model, built by using Analytic Hierarchy Process (AHP), that ranked renewable and other technology for electricity production. Ren, Fedele, Mason, Manzardo, & Scipioni [38] in their paper developed as sustainability assessment method to rank the prior sequence of biomass-based technologies for hydrogen production by using novel fuzzy Multi-Criteria Decision Making (FMCDM) method which allows multiple groups of decision-makers to use linguistic variables to assess the biomass-based technologies. Van de Kaa, Rezaei, Kamp, & de Winter [39] decided to choose AHP in order to rank photovoltaic (PV) technological systems because this particular method, as a robust MCDM method, is used to compare factors and technological designs and to structure this decision-making situation. Furthermore, according to scientists, “because the AHP method uses simple scoring questions and a schematic overview of the factors, it is very useful in situations with respondents who are not familiar with the underlying theoretical concepts of the decision-making situation”. Troldborg, Heslop, & Hough [40], because of MCA’s attractiveness yet uncertainty considering its input information, decided to to develop and apply a MCA for a national-scale sustainability assessment and ranking of eleven renewable energy technologies in Scotland. Zhao & Guo [41] proposed fuzzy multi-attribute decision making approach (fuzzy entropy-TOPSIS) for selecting the proper green supplier of thermal power equipment in China. Luthra, Kumar, Garg, & Haleem [42] identified twenty-eigth barriers for adoption of renewable and sustainable energy technologies in India. Scientists used Analytic Hierarchy Process (AHP) as an appropriate methodology, which works as a multi-attribute decision-making methodology – it is a decision support tool that uses a multilevel hierarchical structure of objectives, criteria, sub-criteria and alternatives.

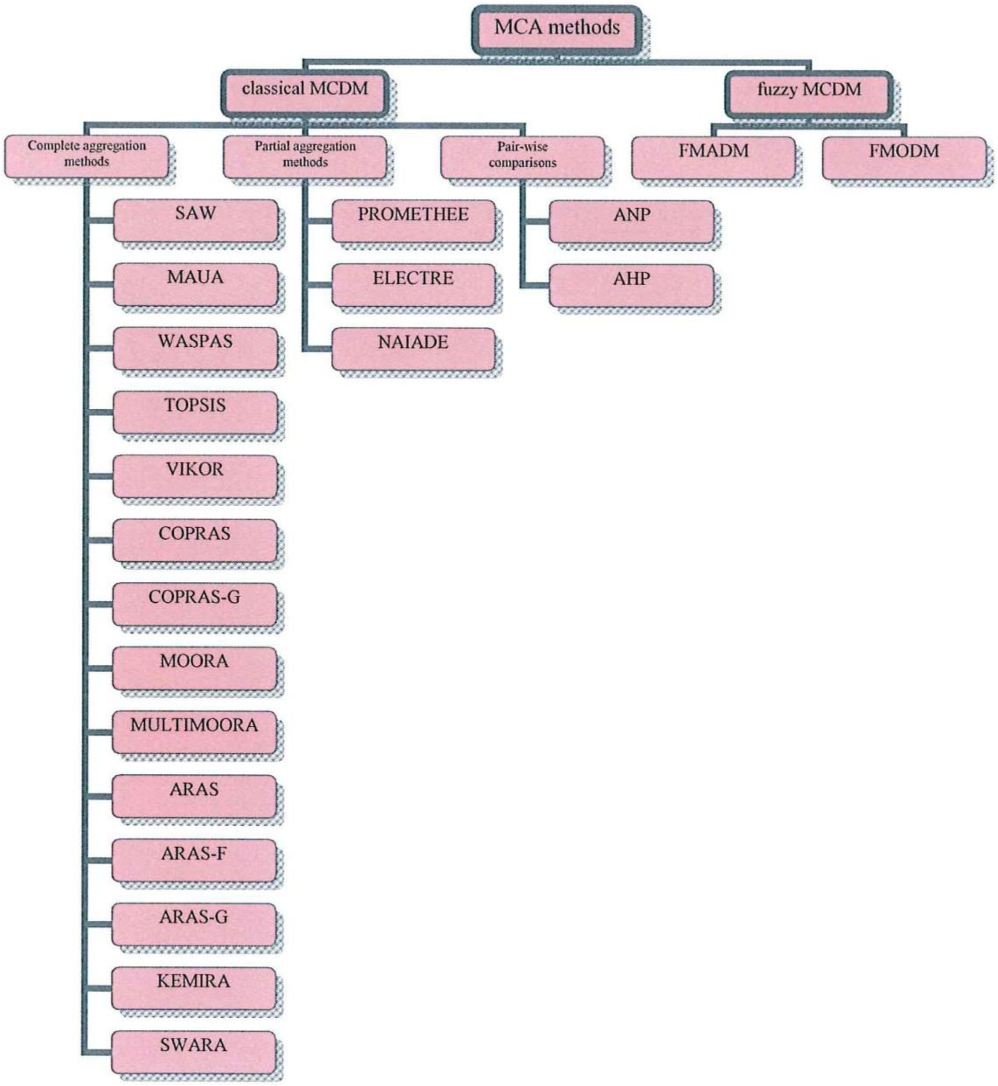

Fig. 1. Different methods for Multi-Criteria Analysis

Source: Created by author

However, two broad categories of MCA can be distinguished – classical MCA and fuzzy MCA [29]. MCDM is considered as a complex decision-making tool involving both quantitative and qualitative factors [43], yet at the same time these several different criteria (qualitative and quantitative) may affect each other mutually when evaluating alternatives, which may make the selection process complex and challenging [44]. In many cases the decision maker has inexact information about alternatives in respect to an attribute. Thus, classical MCDM methods cannot effectively handle problems when information is imprecise, whereas fuzzy set theory is a powerful tool to handle imprecise data. Fuzzy MCDM (FMCDM) was proposed by Zadeh [45], who suggested key elements in human thinking are not numbers but labels of fuzzy sets. Therefore, classical MCDM problems are the ones, among which the ratings and the weights of criteria, are measured in crisp numbers, and FMCDM problems are the ones, among which the ratings and the weights of criteria evaluated on imprecision, subjective and vagueness are usually expressed by linguistic terms and then set into fuzzy numbers [46]. Various classification of MCA methods exists [29], [43], [47–49], however, scientists distinguish these methods as main for MCA:

Three main methods can be distinguished among classical MCDM:

- complete aggregation methods, which include already mentioned TOPSIS and MULTIMOORA and others – Simple Additive Weighting (SAW) [50], Multi-Attribute Utility Analysis (MAUA) [51], Weighted Aggregated Sum Product Assessment (WASPAS) [52], VlseKriterijuska Optimizacija I Komoromisno Resenje (VIKOR) [53, 54], multiple criteria Complex Proportional Assessment (COPRAS) [55], Complex Proportional Assessment of alternatives with Grey criteria (COPRAS-G) [56], Multi-Objective Optimization by Ratio Analysis (MOORA) [57], Additive Ratio Assessment method (ARAS) [58], Fuzzy Additive Ratio Assessment method (ARAS-F) [59], Grey Additive Ratio Assessment method (ARAS-G) [60], Kemeny Median Indicator Ranks Accordance (KEMIRA) [61], Step-wise Weight Assessment Ratio Analysis (SWARA) [62];
- partial aggregation methods, which not only include higher mentioned PROMETHEE but Elimination and Choice Expressing Reality (ELECTRE) [63] and Novel Approach to Imprecise Assessment and Decision Environments (NAIADE) [64] as well;
- pair-wise comparisons – Analytic Network Process (ANP), (AHP).

Whereas, fuzzy MCDM can be cathegorised into fuzzy multi-attribute decision making (FMADM) and fuzzy multi-objective decision making (FMODM). According to Mardani et al. [29], the objective of FMADM is finite and implicit, whereas the objective of FMODM approach is infinite and explicit, thus in FMADM decision maker’s objectives are unified under decision maker’s utility, which is dependent upon the selection criteria, while in FMODM objectives of decision makers (optimal resource utilization and quality) improvement remain explicit and are assigned with fuzzy weights that reflect their relative significance. All in all, these scientists stress, most important benefit of FMCDM methods in general is their capability of considering many selection criteria.

2. CONCLUSIONS

Although MCA approach and its various techniques is suitable for renewable energy systems evaluation, it has some disadvantages as well, especially one in particular – it lacks public input and opinion, which in democratic societies is highly important. And, while taking into account the fact decision makers has a wide options of many different techniques, which more or less has equal weight, one can say it can be compensated by its ability to deal with complex problems, nonetheless, nowadays, it might be not enough to decide between trade-offs alternative sources in order to choose the most beneficial one. It is highly important to know the attitudes of electricity consumers as well, since their attitudes are the foundations of their resulting behavior [65, 66]. Thus a conclusion can be drawn, MCDA method needs to be “backed up”, with additional analysis, revealing the needs and uprights of society.

3. REFERENCES

1. DOMBI, M., KUTI, I., & BALOGH, P. (2014). Sustainability assessment of renewable power and heat generation technologies. *Energy Policy, 67*, 264–271.
2. JACOBSEN, H. K., PADE, L. L., SCHRÖDER, S. T., & KITZING, L. (2014). Cooperation mechanisms to achieve EU renewable targets. *Renewable Energy, 63*, 345–352.
3. EVANS, A., STREZOV, V., & EVANS, T. J. (2009). Assessment of sustainability indicators for renewable energy technologies. *Renewable and Sustainable Energy Reviews, 13*(5), 1082–1088.
4. STIGKA, E. K., PARAVANTIS, J. A., & MIHALAKAKOU, G. K. (2014). Social acceptance of renewable energy sources: A review of contingent valuation applications. *Renewable and Sustainable Energy Reviews, 32*, 100–106.
5. KOSENIUS, A., & OLLIKAINEN, M. (2013). Valuation of environmental and societal trade-offs of renewable energy sources. *Energy Policy, 62*, 1148–1156.
6. HADIAN, S., & MADANI, K. (2015). A system of systems approach to energy sustainability assessment: Are all renewables really green? *Ecological Indicators, 52*, 194–206.
7. LANKOSKI, J., & OLLIKAINEN, M. (2011). Biofuel policies and the environment: Do climate benefits warrant increased production from biofuel feedstocks? *Ecological Economics, 70*(4), 676–687.
8. MEADOWS, D., RANDERS, J., & MEADOWS, D. (2004). *Limits to growth: the 30-year update* Chelsea Green Publishing.
9. YADOO, A., & CRUICKSHANK, H. (2012). The role for low carbon electrification technologies in poverty reduction and climate change strategies: A focus on renewable energy mini-grids with case studies in Nepal, Peru and Kenya. *Energy Policy, 42*, 591–602.
10. Luong, S., Liu, K., & Robey, J. (2012). Sustainability Assessment Framework for Renewable Energy Technology. *Technologies for Sustainable Built Environment Centre.Reading: Informatics Research Centre*, 1–8.
11. CARRERA, D. G., & MACK, A. (2010). Sustainability assessment of energy technologies via social indicators: Results of a survey among European energy experts. *Energy Policy, 38* (2), 1030–1039.
12. DEVUYST, D., HENS, L., & DE LANNOY, W. (2001). *How green is the city? Sustainability assessment and the management of urban environments*. New York: Columbia University Press.
13. GOHARI, A., ESLAMIAN, S., MIRCHI, A., ABEDI-KOUPAEI, J., BAVANI, A. M., & MADANI, K. (2013). Water transfer as a solution to water shortage: a fix that can backfire. *Journal of Hydrology, 491*, 23–39.
14. HJORTH, P., & MADANI, K. (2014). Sustainability monitoring and assessment: new challenges require new thinking. *Journal of Water Resources Planning and Management.*
15. TURKENBURG, W. C., BEURSKENS, J., FAAIJ, A., FRAENKEL, P., FRIDLEIFSSON, I., LYSEN, E., SINKE, W. C. (2000). Renewable energy technologies. In J. Goldemberg (Ed.), *World energy assessment: energy and the challenge of sustainability* (pp. 219–272) United Nations Development Programme.
16. BECCALI, M., CELLURA, M., & MISTRETTA, M. (2003). Decision-making in energy planning. Application of the Electre method at regional level for the diffusion of renewable energy technology. *Renewable Energy, 28*(13), 2063–2087.
17. POHEKAR, S., & RAMACHANDRAN, M. (2004). Application of multi-criteria decision making to sustainable energy planning – a review. *Renewable and Sustainable Energy Reviews, 8*(4), 365–381.

18. QIN, X., HUANG, G. H., CHAKMA, A., NIE, X., & LIN, Q. (2008). A MCDM-based expert system for climate-change impact assessment and adaptation planning – a case study for the Georgia Basin, Canada. *Expert Systems with Applications, 34*(3), 2164–2179.
19. WANG, J., JING, Y., ZHANG, C., & ZHAO, J. (2009). Review on multi-criteria decision analysis aid in sustainable energy decision-making. *Renewable and Sustainable Energy Reviews*, *13*(9), 2263–2278.
20. WIMMLER, C., HEJAZI, G., DE OLIVEIRA FERNANDES, E., MOREIRA, C., & CONNORS, S. (2015). Multi-Criteria Decision Support Methods for Renewable Energy Systems on Islands. *Journal of Clean Energy Technologies,* 3(3).
21. AFGAN, N. H., & CARVALHO, M. G. (2002). Multi-criteria assessment of new and renewable energy power plants. *Energy, 27*(8), 739–755.
22. BELTON, V., & STEWART, T. (2002). *Multiple criteria decision analysis: an integrated approach* Springer Science & Business Media.
23. ROY, B. (2013). *Multicriteria methodology for decision aiding* Springer Science & Business Media.
24. BERGMANN, A., HANLEY, N., & WRIGHT, R. (2006). Valuing the attributes of renewable energy investments. *Energy Policy,* 34(9), 1004–1014.
25. EK, K. (2005). Public and private attitudes towards “green” electricity: the case of Swedish wind power. *Energy Policy,* 33(13), 1677–1689.
26. GASPARATOS, A. (2010). Embedded value systems in sustainability assessment tools and their implications. *Journal of Environmental Management*, 91(8), 1613–1622.
27. MADANI, K., SHEIKHMOHAMMADY, M., MOKHTARI, S., MORADI, M., & XANTHOPOULOS, P. (2014). Social planner’s solution for the Caspian Sea conflict. *Group Decision and Negotiation*, 23(3), 579–596.
28. MENEGAKI, A. (2008). Valuation for renewable energy: a comparative review. *Renewable and Sustainable Energy Reviews*, 12(9), 2422–2437.
29. MARDANI, A., JUSOH, A., ZAVADSKAS, E. K., CAVALLARO, F., & KHALIFAH, Z. (2015). Sustainable and Renewable Energy: An Overview of the Application of Multiple Criteria Decision Making Techniques and Approaches. *Sustainability*, *7*(10), 13947–13984.
30. BASHIRI, M., BADRI, H., & HEJAZI, T. H. (2011). Selecting optimum maintenance strategy by fuzzy interactive linear assignment method. *Applied Mathematical Modelling,* 35(1), 152–164.
31. DOUKAS, H. C., ANDREAS, B. M., & PSARRAS, J. E. (2007). Multi-criteria decision aid for the formulation of sustainable technological energy priorities using linguistic variables. *European Journal of Operational Research*, 182(2), 844–855.
32. ZANGENEH, A., JADID, S., & RAHIMI-KIAN, A. (2009). A hierarchical decision making model for the prioritization of distributed generation technologies: A case study for Iran. *Energy Policy,* 37(12), 5752–5763.
33. OBERSCHMIDT, J., GELDERMANN, J., LUDWIG, J., & SCHMEHL, M. (2010). Modified PROMETHEE approach for assessing energy technologies. *International Journal of Energy Sector Management*, 4(2), 183–212.
34. SHEN, Y., LIN, G. T., LI, K., & YUAN, B. J. (2010). An assessment of exploiting renewable energy sources with concerns of policy and technology. *Energy Policy, 38*(8), 4604-4616.
35. STREIMIKIENE, D., BALEZENTIS, T., KRISCIUKAITIENĖ, I., & BALEZENTIS, A. (2012). Prioritizing sustainable electricity production technologies: MCDM approach. *Renewable and Sustainable Energy Reviews,* 16(5), 3302–3311.

36. BALEZENTIENE, L., STREIMIKIENE, D., & BALEZENTIS, T. (2013). Fuzzy decision support methodology for sustainable energy crop selection. *Renewable and Sustainable Energy Reviews*, *17*, 83–93.
37. STEIN, E. W. (2013). A comprehensive multi-criteria model to rank electric energy production technologies. *Renewable and Sustainable Energy Reviews*, 22, 640–654.
38. REN, J., FEDELE, A., MASON, M., MANZARDO, A., & SCIPIONI, A. (2013). Fuzzy multi-actor multi-criteria decision making for sustainability assessment of biomass-based technologies for hydrogen production. *International Journal of Hydrogen Energy*, 38(22), 9111–9120.
39. VAN DE KAA, G., REZAEI, J., KAMP, L., & de WINTER, A. (2014). Photovoltaic technology selection: A fuzzy MCDM approach. *Renewable and Sustainable Energy Reviews*, 32, 662–670.
40. TROLDBORG, M., HESLOP, S., & HOUGH, R. L. (2014). Assessing the sustainability of renewable energy technologies using multi-criteria analysis: Suitability of approach for national-scale assessments and associated uncertainties. *Renewable and Sustainable Energy Reviews*, *39*, 1173–1184.
41. ZHAO, H., & GUO, S. (2014). Selecting green supplier of thermal power equipment by using a hybrid mcdm method for sustainability. *Sustainability*, 6(1), 217–235.
42. LUTHRA, S., KUMAR, S., GARG, D., & HALEEM, A. (2015). Barriers to renewable/sustainable energy technologies adoption: Indian perspective. *Renewable and Sustainable Energy Reviews*, 41, 762–776.
43. MARDANI, A., JUSOH, A., & ZAVADSKAS, E. K. (2015). Fuzzy multiple criteria decision-making techniques and applications – Two decades review from 1994 to 2014. *Expert Systems with Applications*, 42(8), 4126–4148.
44. VAHDANI, B., HADIPOUR, H., SADAGHIANI, J. S., & AMIRI, M. (2010). Extension of VIKOR method based on interval-valued fuzzy sets. *The International Journal of Advanced Manufacturing Technology*, 47(9–12), 1231–1239.
45. ZADEH, L. A. (1975). The concept of a linguistic variable and its application to approximate reasoning – I. *Information Sciences*, 8(3), 199–249.
46. WANG, Y., & Lee, H. (2007). Generalizing TOPSIS for fuzzy multiple-criteria group decision-making. *Computers & Mathematics with Applications*, 53(11), 1762–1772.
47. LIOU, J. J., TAMOŠAITIENĖ, J., ZAVADSKAS, E. K., & Tzeng, G. (2015). New hybrid COPRAS-G MADM Model for improving and selecting suppliers in green supply chain management. *International Journal of Production Research*, 1–21.
48. MARDANI, A., JUSOH, A., MD NOR, K., KHALIFAH, Z., ZAKWAN, N., & VALIPOUR, A. (2015). Multiple criteria decision-making techniques and their applications – a review of the literature from 2000 to 2014. *Economic Research-Ekonomska Istraživanja,* 28(1), 516–571.
49. ZAVADSKAS, E. K., & TURSKIS, Z. (2011). Multiple criteria decision making (MCDM) methods in economics: an overview. *Technological and Economic Development of Economy*, 17(2), 397–427.
50. MACCRIMMON, K. R. (1968). *Decisionmaking among multiple-attribute alternatives: a survey and consolidated approach* DTIC Document.
51. KEENEY, R. L., & RAIFFA, H. (1976). Decision analysis with multiple conflicting objectives. *Wiley& Sons, New York.*
52. ZAVADSKAS, E., TURSKIS, Z., ANTUCHEVICIENE, J., & ZAKAREVICIUS, A. (2012). Optimization of weighted aggregated sum product assessment. *Elektronika Ir Elektrotechnika*, 122(6), 3–6.
53. MAVI, R., FARID, S., & JALILI, A. (2012). Selecting the construction projects using fuzzy VIKOR approach. *Journal of Basic and Applied Scientific Research*, 2(9), 9474–9480.

54. OPRICOVIC, S., & TZENG, G. (2004). Compromise solution by MCDM methods: A comparative analysis of VIKOR and TOPSIS. *European Journal of Operational Research,* 156(2), 445–455.
55. ZAVADSKAS, E., KAKLAUSKAS, A., & SARKA, V. (1994). The new method of multicriteria complex proportional assessment of projects. *Technological and Economic Development of Economy,* 1(3), 131–139.
56. LIOU, J. J., & TZENG, G. (2012). Comments on “Multiple criteria decision making (MCDM) methods in economics: an overview”. *Technological and Economic Development of Economy, 18*(4), 672–695.
57. BRAUERS, W. K. M., & ZAVADSKAS, E. K. (2006). The MOORA method and its application to privatization in a transition economy. *Control and Cybernetics,* 35(2), 445.
58. ZAVADSKAS, E. K., & TURSKIS, Z. (2010). A new additive ratio assessment (ARAS) method in multicriteria decision-making. *Technological and Economic Development of Economy,* 16(2), 159–172.
59. TURSKIS, Z., & ZAVADSKAS, E. K. (2010a). A new fuzzy additive ratio assessment method (ARAS-F). Case study: The analysis of fuzzy multiple criteria in order to select the logistic centers location. *Transport,* 25(4), 423–432.
60. TURSKIS, Z., & ZAVADSKAS, E. K. (2010b). A novel method for multiple criteria analysis: grey additive ratio assessment (ARAS-G) method. *Informatica,* 21(4), 597–610.
61. KRYLOVAS, A., ZAVADSKAS, E. K., KOSAREVA, N., & DADELO, S. (2014). New KEMIRA method for determining criteria priority and weights in solving MCDM problem. *International Journal of Information Technology & Decision Making,* 13(06), 1119–1133.
62. KERŠULIENE, V., ZAVADSKAS, E. K., & TURSKIS, Z. (2010). Selection of rational dispute resolution method by applying new step-wise weight assessment ratio analysis (SWARA). *Journal of Business Economics and Management,* 11(2), 243–258.
63. FIGUEIRA, J., MOUSSEAU, V., & Roy, B. (2005). ELECTRE methods. *Multiple criteria decision analysis: State of the art surveys* (pp. 133–153) Springer.
64. MUNDA, G. (2005). A NAIADE based approach for sustainability benchmarking. *International Journal of Environmental Technology and Management,* 6(1–2), 65–78.
65. EK, K. (2005). Public and private attitudes towards “green” electricity: the case of Swedish wind power. *Energy Policy,* 33(13), 1677–1689.
66. STIGKA, Eleni, K., PARAVANTIS, John, A., MIHALAKAKOU, Giouli, K. (2014). Social acceptance of renewable energy sources: A review of contingent valuation applications. *Renewable and Sustainable Energy Reviews,* 32, 100–106.

CYSENI 2016, May 26-27, Kaunas, Lithuania
ISSN 1822-7554, www.cyseni.com

GENERATION OF A TEST REFERENCE YEAR FOR DOBELE, LATVIA

M. Ruduks, **A. Lešinskis**
Department of Architecture and Building
Latvia University of Agriculture
Akadēmijas str. 19, LV-3001 Jelgava – Latvia
Email: martins.ruduks@inbox.lv

ABSTRACT

Precise and reliable meteorological data are necessary for building performance analysis. Since meteorological conditions vary significantly from year to year, there is a need to create a test reference year (TRY), to represent the long term weather conditions over a year. In this paper TRY data model was generated by analysing every 3-hour weather data for a 30-year period (1984–2013) in Dobele, Latvia, provided by the Latvian Environment Geology and Meteorology Centre (LEGMC). TRY model was generated according to standard LVS EN ISO 15927-4. The generated TRY contains from typical months that are included in TRY from a number of different years. The data gathered from TRY was compared with the climate data from the Latvian Cabinet of Ministers regulation No. 379, Regulations Regarding Latvian Building Code LBN 003-15. Average monthly temperature values in LBN 003-15 were lower than the TRY values that indicate on climate changes in this location. The results of this study may be used in building energy simulations and heating-cooling load calculations for selected region. TRY selection process should include the most recent meteorological observations and should be periodically renewed to reflect the long term climate change.

Keywords: test reference year; climate analysis, climate change

1. INTRODUCTION

In Latvian legislation long-term climate data is reflected in the Latvian Building Code (LBN) 003-15 „Būvklimatoloģija” (Construction climatology), [1], where various climatic indicators are shown that represent the climatic situation in the territory of Latvia, providing information about the average monthly and yearly meteorological parameters. But this information is not enough to fully describe the region’s climatic conditions, because there is a necessity to define every day and every hour meteorological data values.

The need of such meteorological data worldwide led to the development of methodologies for generating the typical reference year (TRY) in the USA known as a typical meteorological year (TMY) [2]. TRY is a data set that contains a sequence of 8760 hourly values of chosen meteorological quantities. The requirement of TRY is that it has to correspond to an average year [3]. TRY provides every hour climatic parameter values, enabling to use these parameters for heating, ventilation and air conditioning (HVAC) device management and capacity optimization. One of the most important tasks to optimize these devices is to choose correct and precise outdoor air temperature that can be determined with TRY model [4].

Creation of TRY was introduced in 1978 by Hall et al. [2]. For a network of stations in the United States, a representative database consisting of weather data was created. Hall’s method has been used to successfully generate TRYs for a number of locations across the globe [2–3, 5–16].

LBN 003-15 describes climate parameters for ten cities of Latvia. These parameters have been calculated using data from 1961–1990 [1]. The aim of this research was to generate a representative climate database for one of these cities – Dobele, by employing the method according to standard LVS EN ISO 15927-4 [17]. Generation of TRY of Dobele would provide with hourly climate data that LBN 003-15 does not provide.

Geographical data for Dobele: latitude 56º37'11.65" N; longitude 23º19'10.68" E; on relatively flat, open area surface, elevated 42 m above sea level. Located 60 km from capital city of Latvia - Rīga (Fig. 1). Average annual temperature 5.9°C [1].

The TRY is generated using the available weather data obtained from the station of Dobele by the Latvian Environment Geology and Meteorology Centre (LEGMC), covering the period from 1984–2013. LEGMAC database provides with 3-hour weather data values for the temperature and relative humidity. As TRY consists of every hour values, the necessary values are interpolated.

In the region there are only two studies that uses LVS EN ISO 15927-4 standard with 30-year weather data, it is Estonian TRY [8] and TRY for Alūksne [11].

Fig. 1. Location of Dobele

2. METHODOLOGY

In this study, the ISO 15927-4 [17] method was used to construct the TRY. The primary selection was made on the basis of dry-bulb air temperature, cloud coverage (ISO 15927-4 suggest to use direct normal solar irradiance, but this parameter is not available for this station, so it was replaced with cloud coverage), and relative humidity. The wind speed was used for secondary selection. To guarantee that the selected year represents the Dobele climate as completely as possible, 30-year weather data where applied.

Climate data for TRY creation were obtained from LEGMC database from 1984–2013. LEGMC provides climate data with 3 hour interval, but TRY needs hourly climate data. The necessary data for TRY were calculated by linear interpolation.

In February, there may be 28 or 29 days, and it is not possible to compare years with different count of days; thus, 29. February was excluded from TMY creation. The rest of the days where rearranged in ascending order starting with the first hour of January till the last hour of December (8760 values).

For each climatic parameter p (dry-bulb temperature, cloud coverage and relative humidity), daily means $\overline{p}$ are calculated. For each calendar month m, the cumulative distribution function $\Phi_{p,m,i}$ of daily means over all the years in the data set is calculated using equation (1):

$$\Phi_{p,m,i} = \frac{K_i}{N+1}, \tag{1}$$

where K_i –- rank order of the i-th value of the daily means within that calendar month in the whole data set;

N – number of days in any calendar month in the whole data set.

For each year y of the data set, the cumulative distribution function $F_{p,y,m,i}$ of the daily means within each calendar month is calculated using equation (2):

$$F_{p,y,m,i} = \frac{J_i}{n+1}, \tag{2}$$

where J_i – rank order of the i-th value of the daily means within that calendar month and that year;

n – number of days in an individual month.

For each calendar month m the Finkelstein–Schafer statistic for parameter p, $FS_{p,y,m}$ for each year y of the data set is calculated using equation (3):

$$FS_{p,y,m} = \sum_{i=1}^{n} \left| F_{p,y,m,i} - \Phi_{p,m,i} \right|. \tag{3}$$

To normalize $FS_{p,y,m}$ for months of varying lengths, the results of equation (3) are divided by the number of days of the month (28, 30 or 31). For each calendar month individual months are ranked from the multiyear record in order of increasing value of $FS_{p,y,m}$. Monthly average $FS_{p,y,m}$ values of climate parameters dry-bulb air temperature, cloud coverage and relative humidity are added together and the same months of all years are ranked in the order of the increasing value of $FS_{p,y,m}$. From each calendar month, three candidate months with the lowest total ranking are selected. The monthly deviation of the wind speed of the three months is compared with the corresponding multi-year mean of calendar months. The month with the lowest deviation in wind speed is selected as the best month for inclusion in the TRY.

After the selection of the twelve calendar months for TRY, the months should be joined together. The first and the last eight hours of each month are adjusted by interpolation to ensure a smooth transition when months are joined to form a TRY. The adjustment also includes the last eight hours of December and the first eight hours of January, so that the test reference year can be used repeatedly in simulations [17].

2.1. Heating degree days (HDD)

HDD is a parameter used in the HVAC industry to estimate heating and cooling energy requirements. HDD can be calculated using equation (4) [18]:

$$HDD = \sum_{days} (T_b - T_m), \tag{4}$$

where T_b – base temperature (18 °C);

T_m – outdoor temperature (at duration of heating period);

$\sum_{days}$ – duration of heating period.

3. RESULTS AND DISCUSSIONS

TRY was created combining months from different years based on their ability to follow the criteria described in materials and methods. Selected month/year combinations from which the TRY was created are shown in Fig. 2. Two months (February and December) were selected from year 1987, and two months (July and August) from 1985, but other months were selected from different years. That displays that months were selected from all range of the observed period.

After selected months (Fig. 2) were connected and TRY was created, temperature fluctuation (Fig. 3), temperature distribution (Fig. 5), relative humidity fluctuation (Fig. 4) and wind speed distribution (Fig. 6) was displayed. Results show similar tendencies with data from Estonian TRY [8] and TRY for Alūksne [11].

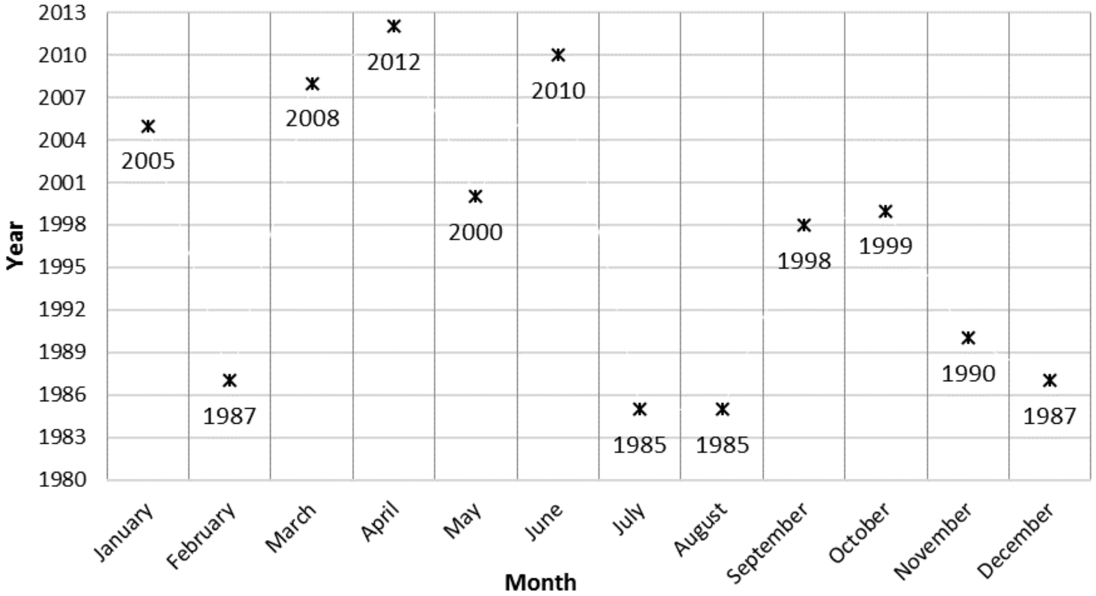

Fig. 2. The Month/Year combinations for the composition of TRY

Figs. 3 and 4 show how temperature and relative humidity values change in TRY model starting from the beginning of January until the end of December.

When TRY model temperature distribution values are compared with 30-year average data (long term data) (Fig. 5), TRY model shows a good agreement with the long-term data. TRY model's maximum temperature value deviation from long-term data is 139 hours per year at 0 °C. The total TRY model's temperature deviation from 30-year average data is 1610 hours. TRY for Alūksne deviation from 30-year average data was 1044 hours [11].

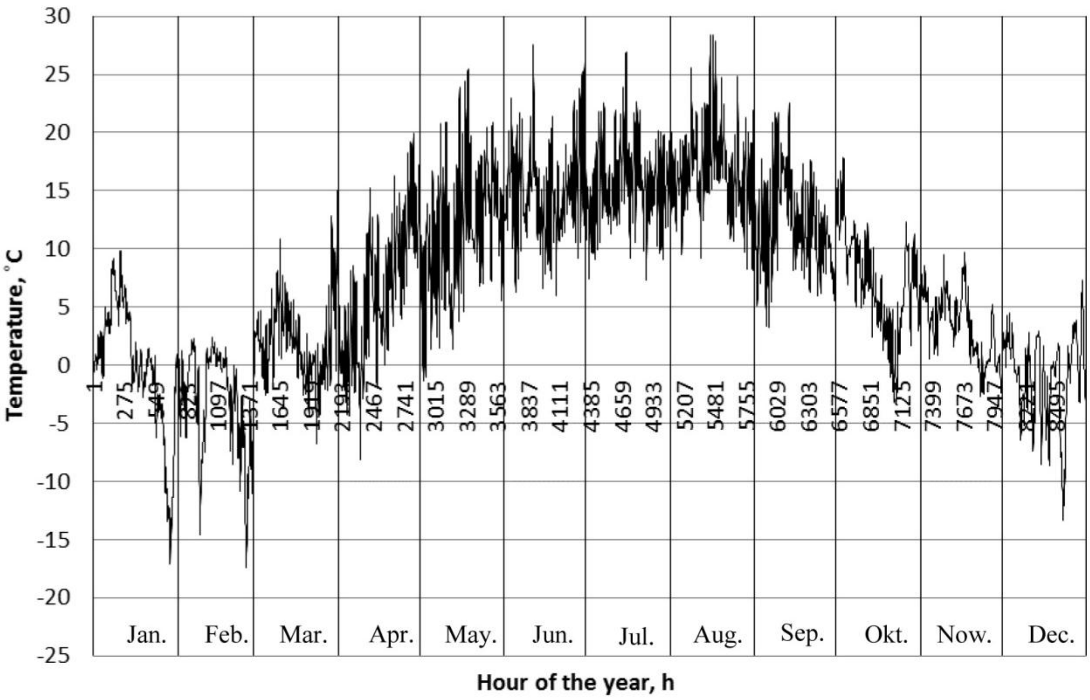

Fig. 3. Temperature fluctuation in TRY

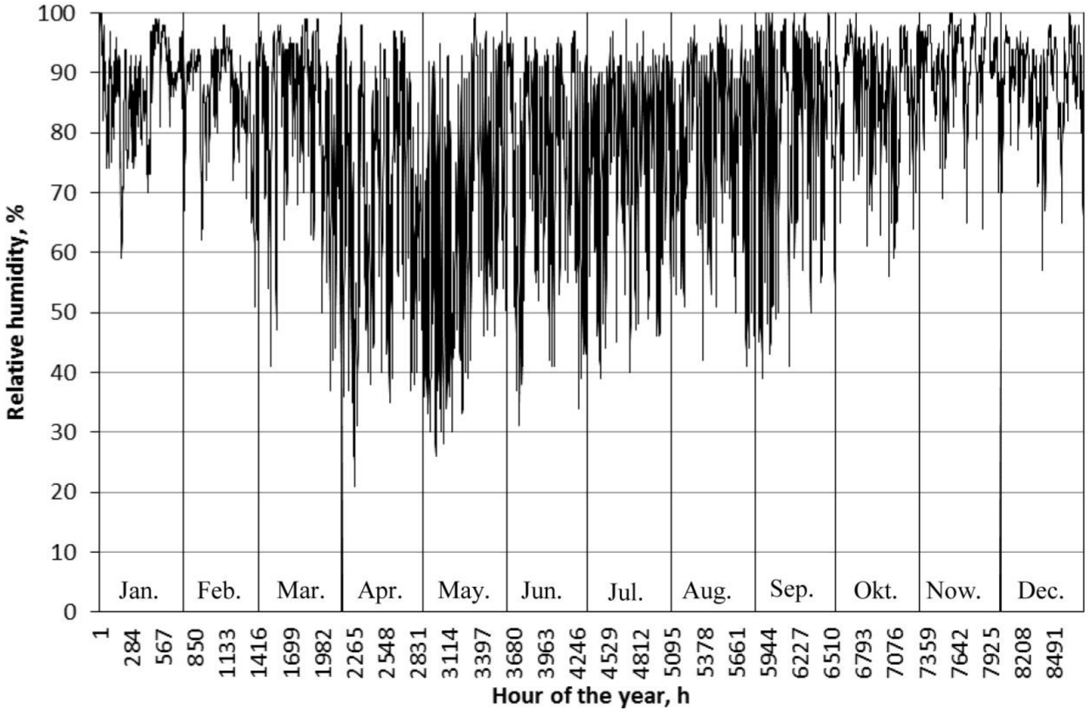

Fig. 4. Relative humidity fluctuation in TRY

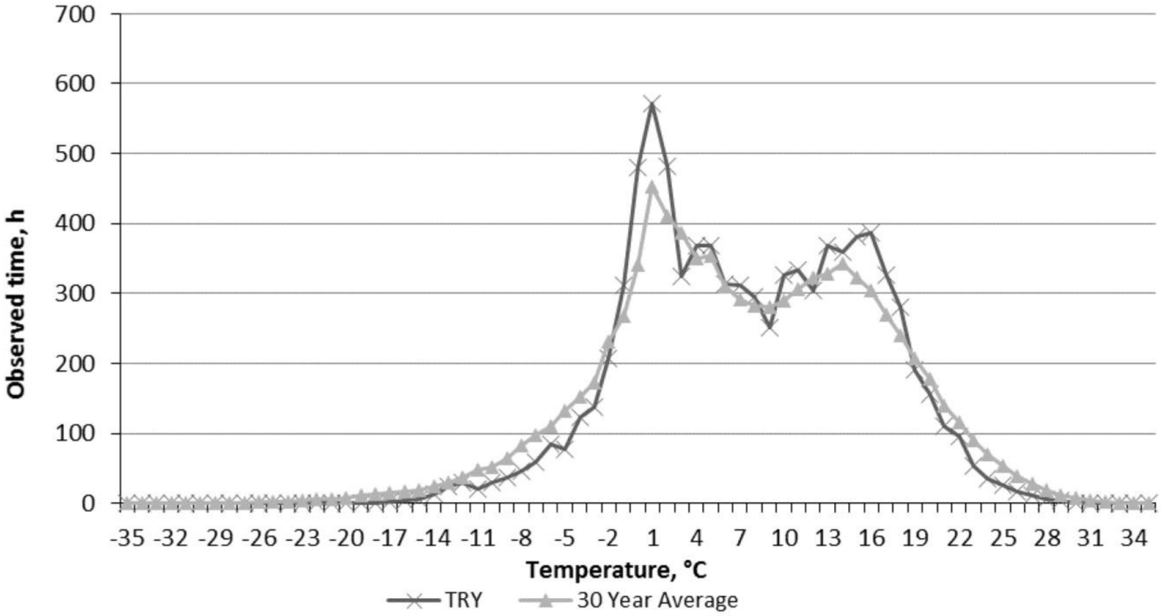

Fig. 5. Hourly temperature distribution for TRY and 30-year average data

Most typical wind speed value in TRY model is 3 m/s, it is observed for 1954 hours. TRY model's maximum wind speed value deviation from long-term data is 149 hours per year at 4 m/s. The total TRY model's wind speed deviation from 30-year average data is 469 hours. (Fig. 6).

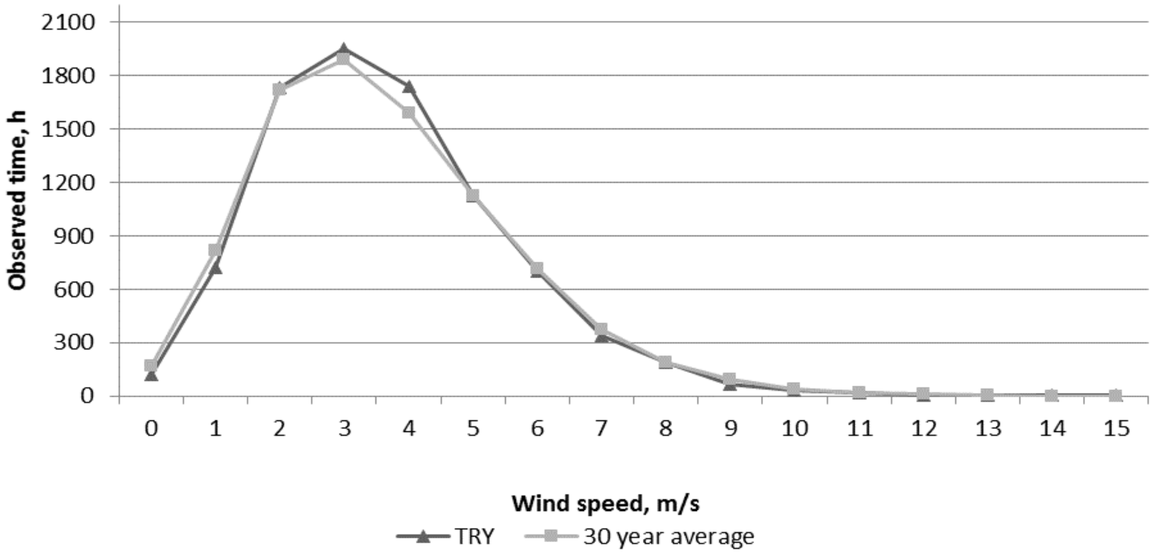

Fig. 6. Wind speed distribution for TRY and 30-year average data

One of the most important results that can be obtained from TRY models is shown in Fig. 7. This figure show how many hours per year each temperature and content of moisture combination can be observed. Most typical content of moisture and temperature combination in TRY model is 4 g/kg at 1 °C. This combination can be observed for 353 hours (Fig. 7). Most typical content of moisture value of TRY for Alūksne is also 4 g/kg, but most typical temperature is 0°C [11]. These results can be used for HVAC system analysis and building energy simulations. Data from Fig. 7 gives an ability to calculate how long it will be necesary to use heating and cooling devices for buildings in this region, and chose optimal capacity for these devices.

Average year temperature value for TRY is 7.2°C, but for 30-year average data it is 7.1°C. Comparing results with LBN 003-15 values the difference is 1.3 and 1.2°C respectively (Table 1). The difference with LBN 003-15 value can be explained by the fact that they have been obtained from 1961–1990, but TRY values were obtained from 1984–2013. The climate change can be the factor for the difference. There is no difference in average relative humidity value for TRY, LBN 003-15 and 30-year average data (Table 2).

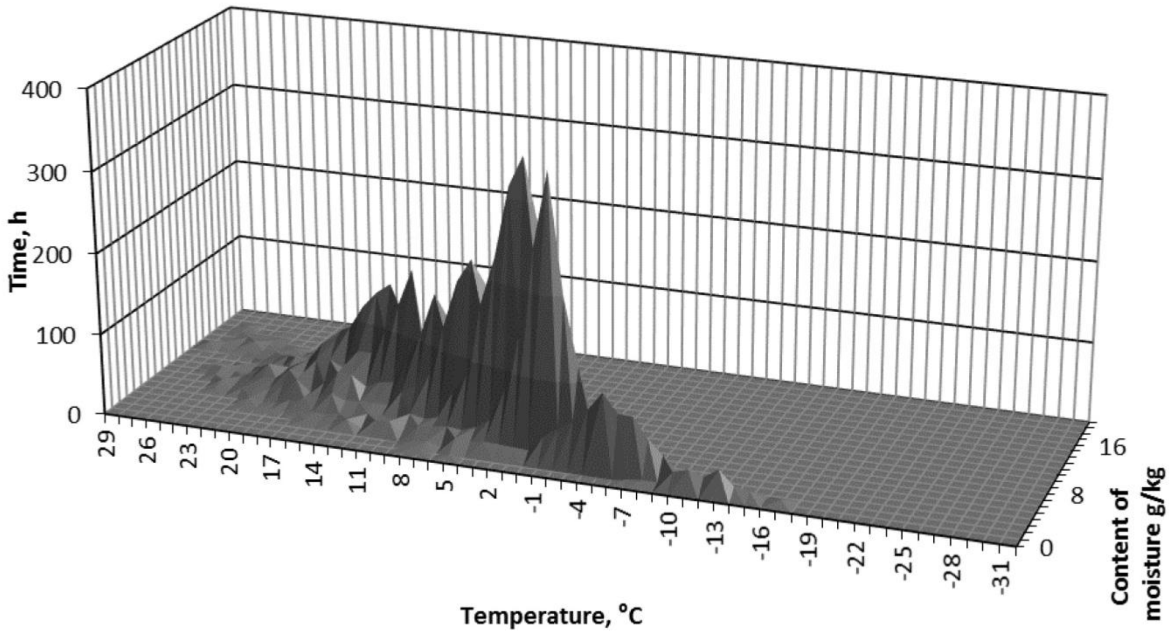

Fig. 7. Combination of temperature and content of moisture for TRY

Table 1. Average monthly temperature values (°C)

Month	Jan	Feb	Mar	Apr	May	Jun	Jul
30 year average	–2.6	–3.2	0.5	6.7	12.4	15.8	18.2
TRY	–0.1	–3.1	2.0	6.2	12.0	15.1	15.7
LBN 003-15	–5.0	–4.7	–1.0	4.9	11.4	15.2	16.5
Month	**Aug**	**Sep**	**Oct**	**Nov**	**Dec**	**Average**	
30 year average	17.2	12.3	7.3	2.2	–1.3	7.1	
TRY	16.8	12.1	7.0	3.2	–1.0	7.2	
LBN 003-15	15.9	11.5	6.8	1.7	–2.6	5.9	

Table 2. Average monthly relative humidity value (%) comparison from January till December

Month	Jan	Feb	Mar	Apr	May	Jun	Jul	Aug	Sep	Oct	Nov	Dec	Average
30 year average	87	85	80	72	69	74	76	78	82	86	89	89	81
TRY	87	86	83	70	66	75	77	79	82	86	92	89	81
LBN 003-15	87	84	81	75	70	73	77	80	83	86	89	89	81

Average year wind speed value for TRY and 30-year average data are the same 3.5 m/s, but difference with LBN 003-01 value is 0.3 m/s (Table 3). The difference can be explained by the fact that LBN 003-01 values have been obtained from 1961–1990, but TRY values were obtained from 1984–2013, and latest studies show that wind speed values decreases [19].

Table 3. Average monthly wind speed values (m/s)

Month	Jan	Feb	Mar	Apr	May	Jun	Jul
30 year average	4.1	3.8	3.7	3.6	3.5	3.2	3.0
TRY	4.4	4.0	3.8	3.7	3.4	3.2	2.9
LBN 003-15	4.2	4.0	4.0	3.9	3.7	3.5	3.2
Month	**Aug**	**Sep**	**Oct**	**Nov**	**Dec**	**Average**	
30 year average	3.0	3.2	3.5	3.7	4.0	3.5	
TRY	2.9	3.2	3.7	3.3	3.9	3.5	
LBN 003-15	3.1	3.4	3.8	4.2	4.3	3.8	

Comparing TRY and LBN 003-15 values (Table 4) LBN 003-15 has the longest duration of heating period, the lowest average temperature in heating period and also it has the greatest number of degree days. All these parameters show the impact of increased average temperature value (Table 1) that can be explained with global changes. This tendency has also been observed in TRY for Alūksne [11].

Table 4. Summary of climate parameters

Parameter	TRY	LBN 003-15
Maximum temperature, °C	28.4	32.8
Minimum temperature, °C	–17.4	–32.5
Duration of heating period, days	194	204
Average temperature in heating period, °C	1.2	–0.4
Number of heating degree days (HDD)	3259	3754

4. CONCLUSIONS

The aim of this research was to generate TRY for Dobele and it was generated based on the most recent 30-year (1984–2013) climate data. The generation of a TRY is very useful for optimal HVAC system design and building energy simulations. With every hour climate data, provided by TRY, it is possible to make building energy simulations and make calculations to determine necessary power for HVAC devices that was not possible with data from LBN 003-15.

Comparing TRY model values with LBN 003-15 ones, they showed deviation of some climate parameters that can be explained with climate changes. These differences show that there is a need for TRY creation and the latest possible climate data should be used. In this paper TRY is created for one city of Latvia, but results suggest that the research needs to be continued, and TRY models need to be generated for all 10 cities that are described in LBN 003-15.

5. REFERENCES

1. LBN 003-15. *Noteikumi par Latvijas būvnormatīvu 003-15 "Būvklimataloģija" (Latvian Building Code 003-15 "Construction climatology")*, 2015- [reffered on 1st of March in 2016 y.]. Link to the internet <http://likumi.lv/ta/id/275013-noteikumi-par-latvijas-buvnormativu-lbn-003-15-buvklimatologija-> (in Latvian).
2. HALL, I.J., PRAIRIE, R.R., ANDERSON, H.E., BOES, E.C. Generation of a typical meteorological year. Denver 1978. Proceedings of the 1978 Annual Meeting of the American Section of the International Solar Energy Society. Denver: Sandia Laboratories. 1978.
3. SKEIKER, K. Generation of a typical meteorological year for Damascus zone using the Filkenstein–Schafer statistical method. *Energy Conversion and Management*, 2004, Vol. 45, p. 99–112.
4. GAUJĒNA, B., BORODIŅECS, A., ZEMĪTIS, J., PROZUMENTS, A. Influence of Building Envelope Thermal Mass on Heating Design Temperature. *IOP Conference Series: Materials Science and Engineering*, 2015, Vol. 96, No. 1, p. 1–8.
5. CHAN, A.L.S., Chow, T.T., Fong, S.K.F., Lin, J.Z. Generation of a typical meteorological year for Hong Kong. *Energy Conversion and Management*, 2006, Vol. 47, p. 87–96.
6. GUGGENBERGER, J.D., ELMORE, A.C., CROW, M.L. Predicting performance of a renewable energy-powered microgrid throughout the United States using typical meteorological year 3 data. *Renewable Energy*, 2013, Vol. 55, p. 189–195.
7. JIANG, Y. Generation of typical meteorological year for different climates of China. *Energy*, 2010, Vol. 35, p. 1946–1953.
8. KALAMEES, T., KURNITSKI, J. Estonian Test Reference Year for Energy Calculations. *In proceedings of the Estonian Academy of Science, Engineering*, 2006, p. 40–58.
9. KALOGIROU, S.A. Generation of typical meteorological year (TMY-2) for Nicosia, Cyprus. *Renewable Energy*, 2003, Vol. 28, p. 2317–2334.
10. LEE, K., YOO, H., LEVERMORE, G.J. Generation of typical weather data using the ISO Test Reference Year (TRY) method for major cities of South Korea. *Building and Environment*, 2010, Vol. 45, p. 956–963.
11. RUDUKS, M., LEŠINSKIS, A. Generation of a Test Reference Year for Alūksne, Latvia. *Proceedings of the Latvia University of Agriculture*, 2015, Vol. 33, No. 1, p. 46–54.
12. SKEIKER, K. Comparison of methodologies for TMY generation using 10 years data for Damascus, Syria. *Energy Conversion and Management*, 2007, Vol. 48, p. 2090–2102.
13. YANG, L., LAM, J.C, LIU, J. Analysis of typical meteorological years in different climates of China. *Energy Conversion and Management*, 2007, Vol. 48, p. 654–668.
14. ZANG, H., XU, Q., BIAN, H. Generation of typical solar radiation data for different climates of China. *Energy*, 2012, Vol. 38, p. 236–248.

15. ZARIŅŠ, M. *Klimata datu izvēle gaisa kondicionēšanas jaudas aprēķinam.* Jelgava: Latvia University of Agriculture, 2001. 59 p.
16. ZHANG, Q. Development of the typical meteorological database for Chinese locations. *Energy and Buildings*, 2006, Vol. 38, p. 1320–1327.
17. LVS EN ISO 15927-4. Latvijas Valsts Standarts. (Latvia State Standard). Ēku hidrotermiskie raksturlielumi. Klimatisko raksturlielumu aprēķināšana un izteikšana. 4. daļa: Ikstundas dati apkures un dzesēšanas ikgadējā enerģijas patēriņa novērtēšanai. (Hygrothermal performance of buildings – Calculation and presentation of climatic – Part 4: Hourly data for assessing the annual energy use for heating and cooling), 2005. (in Latvian).
18. BUYUKALACA, O., BULUT, H., YILMAZ, T. Analysis of variable-base heating and cooling degree-days for Turkey. *Applied Energy*, 2001, Vol. 69, No. 4, p. 269–283.
19. GREEN, J.S., CHATELAIN, M., MORRISSEY, M., STADLER S. Estimated changes in wind speed and wind power density over the western High Plains, 1971–2000. *Theoretical and Applied Climatology*, 2012, Vol. 109, No. 3–4, p. 507–518.

CYSENI 2016, May 26-27, Kaunas, Lithuania
ISSN 1822-7554, www.cyseni.com

WIND ENERGY FOR BUILDING HEATING: CONVERTING MECHANICAL ENERGY IN THE HYDRAULIC SYSTEM

J. Černeckienė, T. Ždankus
Kaunas University of Technology
Studentų str. 48, LT-51367 Kaunas – Lithuania
Email: jurgita.cerneckiene@ktu.edu

ABSTRACT

The world is facing the threat of climate change and the world community is looking for different ways to reduce greenhouse gas emissions. One of the area in Lithuania where it is actively done – the construction sector. Construction sector already implements ambitious plans to reduce greenhouse gas emissions by increasing requirements for building thermal insulation, energy usage effectiveness and renewable energy deployment. The paper presents possibility of heating energy-efficient buildings using wind energy. As a research subject, this topic is relevant because the thermal energy demand dynamics for the heating of buildings over the year correlates to the wind potential distribution (based on Lithuanian climatological data). Wind energy can be converted into heat in a closed hydraulic system with adjustable load. It was determined that for a given wind speed the maximum thermal power generated by hydraulic system is reached only at certain optimal system load regulation valve position, which corresponds to the optimal rotation speed of the hydraulic pump shaft. The paper presents the experimental hydraulic system investigation methodology and results – system potential to generate heat, optimal system load modes, optimal hydraulic pump shaft rotation dependence on wind speed.

Keywords: wind energy conversion, wind energy for heating, hydraulic system for heating, renewable energy sources

1. INTRODUCTION

Analyzing Lithuanian energy sector statistics of the year 2013 [1], it is noted that 52% of the total energy consumption is consumed in the form of thermal energy. Although it is not picked out which part of the thermal energy in Lithuania is consumed for heating buildings, we can rely on the EU data [2] which shows that 40% of the total energy consumption is used in the buildings.

In any case, it is a significant part of the energy balance and this led to why the construction sector has attracted a lot of attention in implementing the EU directive on energy efficiency in Lithuania.

Lithuania raised the ambitious targets for energy saving in buildings, its efficient use and deployment of renewable energy sources. Relevant to the construction technical regulation [3] it is provided that from the end of 2016 all new buildings, regardless of their form of ownership, must attain no lower than “A” energy efficiency class, from the beginning of 2018 – “A+” class and from the beginning of 2021 – “A++” class. The reduction of thermal energy consumption is the most important for sustainable development in the construction sector and we see now that our community accepted these tasks and challenges as well quite quickly. It can be noticed that in public we have more discussion about how to choose the best solutions for the reduction of energy consumption, but not about doing it or not essentially. Since the first steps of sustainable development are made, it is important to pay more attention to energy efficiency and energy production from renewable sources.

According to Lithuanian legislation, implementation of energy usage efficiency is realized by raising the requirements to install automatic control especially for the heating and heat production systems. On the other hand, requirement for the automatic control effectiveness level is not determined. The implementation of renewable sources in the buildings is also emboldened considering, that solar energy can be used for heat and electricity generation and wind-power and hydro-power systems can supply electricity to the building.

Using any of the renewable energy sources, there is a lack of conformity between the energy potential and energy demand and this is the great challenge that scientists and engineers have to cope with. It can be stated that if energy could be "transmitted in time", we could solve all the planet's energy supply issues, as amount of energy received from the Sun to the Earth is well above the Earth's population energy needs, even considering that the technologies we employ can take only a small part of the received energy [4].

Although solar energy is already quite widespread, in colder climates, to which Lithuania is also classified, the thermal energy needs are the highest when the solar power gives us the least. However, the situation changes when we analyze the opportunity to produce heat from wind energy – on the basis of the annual heat demand trends and many years' climatic observations [5], we notice that the wind energy potential and building needs for heating have a close variation trend during the year [6].

While there are lots of pilot plants for heat generation from wind energy [7–9] patented worldwide, also this sphere had attention of the Danish Technical University [10], researchers of the Lithuanian University of Agriculture [11], it didn't turn into commercially successful projects [12]. The sources analyzing fundamentals of mechanical energy conversion into heat declare optimistic efficiency of such process – 100%, but while analyzing the entire energy conversion and transfer system we must estimate thermal losses that surely occur in the completed system.

2. EXPERIMENTAL INVESTIGATION OF WIND DRIVEN HYDRAULIC SYSTEM HEAT GENERATION

The experimental setup was created for simulating the operation of the hydraulic system driven by the wind. Hydraulic system was chosen for the analysis as it has technical implementation using standard hydraulic equipment, the processes of heat generation are well known from the classic mechanics and this system might be relatively cheaper that the system generating electricity from the wind energy. The experimental setup consists of hydraulic system, wind mechanical energy simulation system and measuring equipment.

2.1. Theoretical background

The operation of hydraulic system is based on few processes – mechanical rotor axis movement is transmitted to the axis of the hydraulic pump, hydraulic pump creates an oil flow that circulates in the closed system of pipes and valves and warms up due to the friction.

Hydraulic system energy balance [13] P_{total}, W:

$$P_{total} = P_{heat} + P_{lost}, \tag{1}$$

where P_{heat} – the power of produced thermal energy, W; P_{lost} – energy losses, W.

The produced thermal energy in a closed hydraulic system can be theoretically analyzed as consisting of two components: mechanical energy losses and heat production because of the friction in the straight pipes and in the local obstacles, such as bends, connectors, control valves, reductions, etc.

$$P_{heat} = P_{str} + P_{loc}, \tag{2}$$

where P_{str} – the power of produced thermal energy in the straight pipes, W; P_{loc} – the power of produced thermal energy in the local obstacles, W.

The power of produced thermal energy in the straight pipes can be calculated by determining friction losses according to the Darcy-Weisbach equation, system fluid density and flow:

$$P_{str} = \lambda \cdot \frac{l}{d} \cdot \frac{v^2}{2g} \cdot \rho g \cdot G, \qquad (3)$$

where λ – hydraulic friction factor; l – pipe length, m; d – pipe internal diameter, m; v – flow velocity, m/s; g – gravity acceleration, m/s^2; G – flow, m^3/s; ρ – fluid density, kg/m^3.

In the case of laminar flow, the hydraulic friction coefficient:

$$\lambda = \frac{64}{\mathrm{Re}}, \qquad (4)$$

where Re – Reynolds number.

In the case of turbulent flow, the hydraulic friction coefficient:

$$\frac{1}{\sqrt{\lambda}} = -2\lg\left(\frac{2{,}51}{\mathrm{Re}\sqrt{\lambda}}\right),\ 4000 < \mathrm{Re} < \frac{10}{k}\ \text{or} \qquad (5)$$

$$\frac{1}{\sqrt{\lambda}} = -2\lg\left(\frac{2{,}51}{\mathrm{Re}\sqrt{\lambda}} + \frac{k}{3{,}71}\right), \qquad \frac{10}{k} < \mathrm{Re} < \frac{560}{k}\ \text{or} \qquad (6)$$

$$\frac{1}{\sqrt{\lambda}} = -2\lg\left(\frac{k}{3{,}71}\right),\ \mathrm{Re} > \frac{560}{k}, \qquad (7)$$

where k – relative roughness.

$$\mathrm{Re} = \frac{dv}{\upsilon}, \qquad (8)$$

where υ – fluid kinematic viscosity, mm^2/s.

In all other parts of the hydraulic system, i.e. obstacles – bends, connectors, control valves, resulting thermal energy can be calculated according to the equation:

$$P_{loc} = \varsigma \cdot \frac{v^2}{2g} \cdot \rho g \cdot G, \qquad (9)$$

where ζ – local obstacle coefficient.

Hydraulic systems geometrical parameters are invariable, except regulating control valves, the same oil was used in all experimental tests, therefore, under the equations above we can see that the amount of heat produced in the target hydraulic system depends only on the fluid flow rate and the local obstacle coefficient of control valves.

When we analyze closed hydraulic system that doesn't produce any mechanical work, we can accept that all mechanical energy that system receives can be also expressed by equation:

$$P_{total} = G \cdot \Delta p + P_{lost}, \qquad (10)$$

where Δp is the pressure drop in the system, Pa; G is volumetric flow rate of oil, m^3/s.

According to (1) and (10) equations we can state, that maximal heat output from the hydraulic system can be evaluated according to the equation:

$$P_{heat} = G \cdot \Delta p, \qquad (11)$$

The hydraulic system energy loss P_{lost} is the result of energy that is used to overcome molecular forces between circulating fluid molecules and the hard surfaces molecules that surrounds the flow (tank walls, pipes, different obstacles). These processes influence change of physical properties of the fluid (the fluid viscosity decreases) and the wear on solid surfaces (surface roughness decreases). For these reasons, during the operation of hydraulic systems, it is necessary to change periodically circulating oil and worn out mechanical parts. Flow restricting valves are noticed to wear much faster than the other parts because of the highest velocities in them.

Resuming the process efficiency coefficient evaluating mechanical energy conversion into thermal energy can be calculated:

$$\eta = \frac{G \cdot \Delta p}{P_{total}}. \tag{12}$$

2.2. Experimental Equipment and Methodology

The aim of the experiment – to analyze hydraulic system (Fig. 1) work in different operating modes and to determine operating characteristics that would allow to synchronize its work with the wind rotor.

Equipment and materials used in experimental set are listed in the Table 1 and Table 2.

Table 1. Experimental equipment and materials

Electric frequency converter	Mitsubishi Electric-FR-D740-036SC-EC, three–phase, 1.5 kW, 0.2–400 Hz
Electromotor	BEVI-4AK2 90L-4B14, three-phase asynchronous, four pole, $\cos\varphi = 0.77$, $\eta_{motor} = 0.828$, 1,5 kW
Hydraulic pump (gear)	Vivolo-X2P5702, $V_{pump} = 26.2$ cm^3/rot
Flow (load) regulation valve	VRFB, 90° 3/4″
Oil	Shell, ISO viscosity grade – 32; density 867 kg/m^3, cinematic viscosity 65 cSt; specific heat capacity 1,67 kJ/(kg·K), when t = 20^{o}C; volume – 20 l

Table 2. Measuring equipment and sensors

Temperature sensors	TJ4-Pt100, precision class ⅓ B
Data loggers	Pico logger PT–104, precision at the temperature of 25°C: 0.01°C
Pressure sensors	NAH 25.0 A, 0÷25 bar, 4÷20 mA, measurement precision 0.3%, NAH 2.5 A, 0–2.5 bar, 4÷20 mA, measurement precision 0.3%
Pressure data detectors	LUMEL N20–6112008, 5 digits
Rotation frequency meter	Testo 465, tolerance: 0.01 rpm
Torque sensor	LORENZ MESSTECHNIK DR-2512, accuracy class 0,1
Measuring vessel	2000 ml, A class

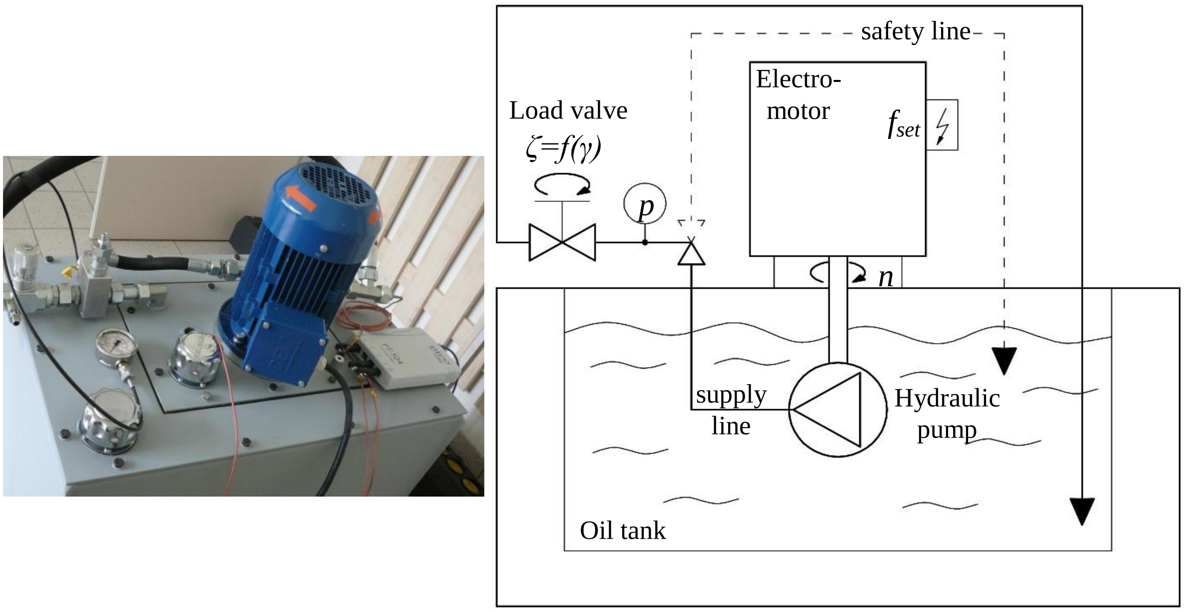

Fig. 1. Photo and schematic view of the experimental hydraulic system

Experimental set is a constructed facility, consisting of the main elements – the electromotor, hydraulic pump, tank, flow regulation valve and piping. The electromotor simulates wind rotor work in laboratory conditions. The engine is connected through electric frequency converter, so it allows setting different speed modes imitating different wind speed on the wind rotor. Electromotor power – 1.5 kW – selected focusing on heating demand of energy efficient individual residential house [6].

The motor is connected in rigid connection to a hydraulic pump, which creates vacuum in the pipes connected to the system. System incorporates a flow regulation valve which controls the load of the hydraulic system given for the electromotor.

First the system flow and rotation frequency were measured on different electric frequencies and peak load positions – the results were mathematically averaged and it was determined that volume on one rotation corresponds the declared 26.2 cm^3/rot and in the later experiments flow can be determined after multiplying rotation frequency and declared hydraulic pump volume per one rotation.

The pressure in the system was measured by sensor installed before the flow (load) regulation valve, where pressure level is maximal.

Temperature measurements in different points were made automatically during all experiments, but not used in further calculations in this research.

Afterwards mechanical characteristics of electromotor were determined during the experiment. It was realized with the help of torque sensor. Electromotor was calibrated separately from the hydraulic system, using the same electric frequency converter. 16 operating modes that imitate wind rotor work in different wind speed were chosen setting electromotor electric frequency f_{set} on 1–8, 10, 12, 14, 16, 20, 30, 40, 50 Hz. The rotation frequency was measured with the rotation frequency meter. Torque was measured with torque sensor and special data converting software. The highest torque and dependant power was reached continuously loading the electromotor and monitoring test results on the computer. The peak points where gathered for further analysis. Total mechanical power was calculated according to the equation:

$$P_{total} = 2\pi n \cdot M \,, \tag{13}$$

where n is the rotation frequency, rpm; M is torque, N·m.

During all experiments the load of the system was regulated with the flow regulation valve, that allowed changing ζ – valve local obstacle coefficient, $\zeta = f(\gamma)$, where γ – valve position from the fully closed fixing ("0") till fully opened ("9.00").

3. RESULTS

In order to check the reproducibility and reliability of the results of the experiment studies, the statistical parameters were calculated for every test series, performed at the same conditions, and it was checked, if the values of the Cochran criteria, variation coefficient and general relative error of the result do not exceed the allowed values [14]. It was determined that the results of the experimental investigation are quite precise, reliable and reproducible.

A few regimes can be distinguished when analyzing hydraulic system work in every f_{set}:

1) zero load, flow control valve is fully opened: $\gamma = 9.00$, $n = n_{max.}$, $\Delta p = \Delta p_{min}$, $P_{heat} = P_{heat\_min}$ – beginning of the experimental series;

2) system loading, flow control valve is being closed gradually: $\gamma \rightarrow \gamma_{opt}$ $(0 < \gamma < 9)$, $n \rightarrow n_{opt}$, $\Delta p \rightarrow \Delta p_{opt}$, $P_{heat} \rightarrow P_{heat\_max}$;

3) peak point – optimal system work: $\gamma = \gamma_{opt}$, $n = n_{opt}$, $\Delta p = \Delta p_{opt}$, $P_{heat} = P_{heat\_max}$;

4) system overloading, flow control valve is being closed gradually: $\gamma \rightarrow 0$ $(0 < \gamma < 9)$, $n \rightarrow 0$, $\Delta p \rightarrow \Delta p_{max}$, $P_{heat} \rightarrow 0$;

5) overloaded system: $\gamma \approx 0$, $n = 0$, $\Delta p = 0$, $P_{heat} = 0$ – flow control valve is fully closed, there is no flow, electromotor is not able to rotate the pump shaft (wind is not able to rotate the wind rotor) – primary hydraulic brake regime.

Fig. 2 shows the character of hydraulic system work in different regimes and can be used to analyze hydraulic load influence on the completed system "wind rotor-hydraulic heat converter" power.

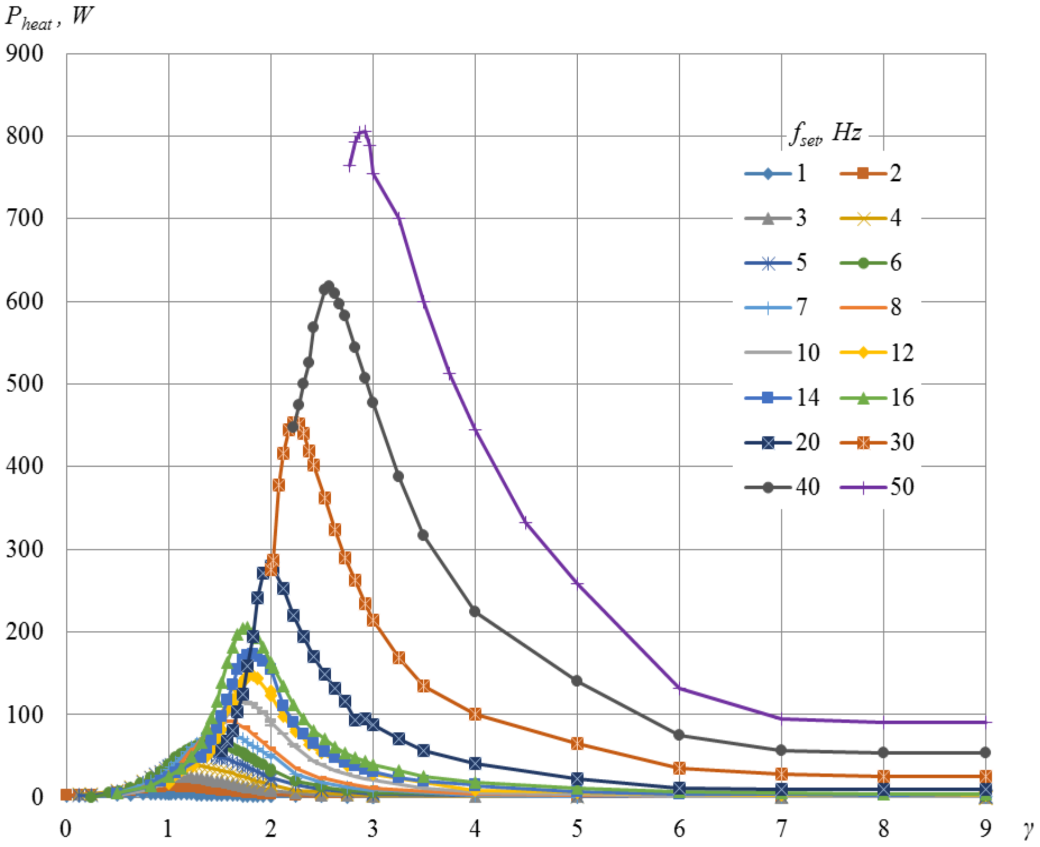

Fig. 2. Dependence of the heat power generated by the hydraulic system P_{heat}, W from the load regulation valve position, $\gamma = 0$ to $\gamma = 9{,}00$, when $1 < f_{set} < 50$ Hz

Fig. 3 shows hydraulic system thermal power dependence on hydraulic pump shaft rotation frequency n. This data can be used for synchronizing hydraulic systems work with chosen wind rotor seeking highest system efficiency.

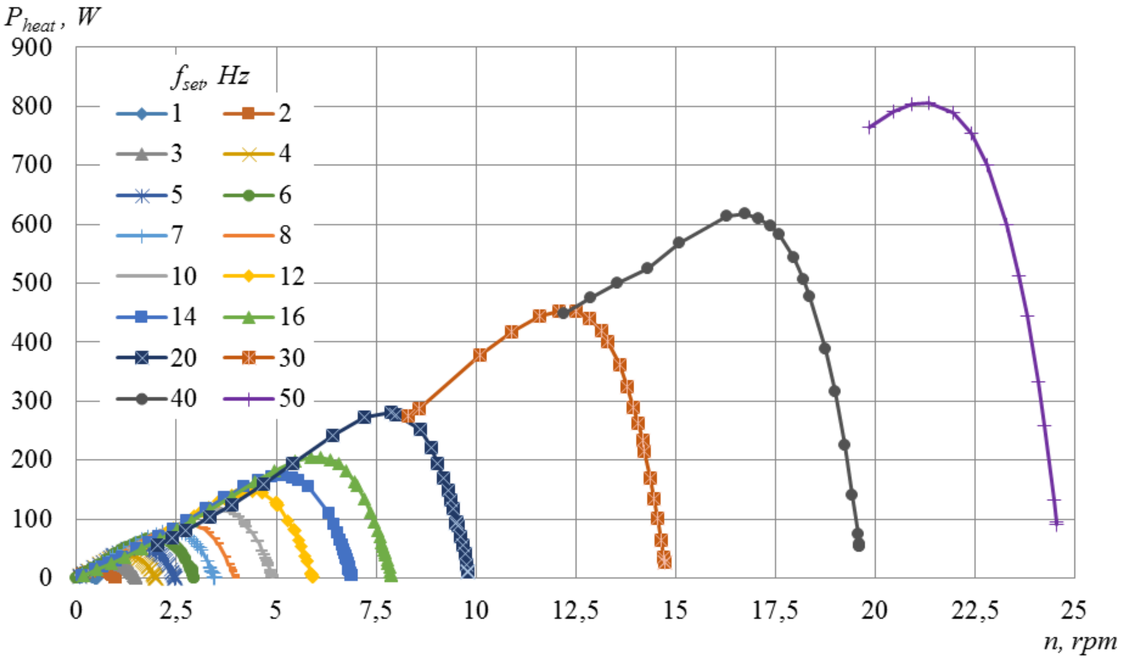

Fig. 3. Dependence of thermal power P_{heat} on the pump shaft rotation frequency n, when $1 < f_{set} < 50$ Hz

It can be noticed by Figs. 2 and 3 that the same P_{heat} can be reached by using different rotation frequency of the pump shaft and loading the hydraulic system more.

After determining optimal (peak) hydraulic system working characteristics, such as hydraulic pump shaft rotation frequency n_{opt} for different f_{set}, electromotor calibration in peak points was made and the inlet mechanical power of the peak point for the hydraulic system $P_{total\_ max}$ was determined. Table 3 shows optimal system working zone mechanical and hydraulic characteristics that allows calculating system energy conversion efficiency η (eq. 12).

Table 3. Optimal hydraulic system working regimes for different simulated wind rotor characteristics

f_{set}, Hz	**1**	**2**	**3**	**4**	**5**	**6**	**7**	**8**
n_{opt}, rpm	0.28	0.568	0.898	1.233	1.563	2.010	2.30	2.79
Δp_{opt}, Pa	5.040	8.980	10.878	12.000	12.837	12.693	13.306	12.612
$P_{heat\_ max}$, W	3.7	13.3	25.4	35.8	52.2	66.3	79.4	91.4
$P_{total\_ max}$, W	4.7	16.3	29.9	44.5	58.1	74.2	89.8	100.7
η	0.787	0.816	0.849	0.800	0.898	0.894	0.884	0.908
f_{set}, Hz	**10**	**12**	**14**	**16**	**20**	**30**	**40**	**50**
n_{opt}, rpm	3.54	4.42	5.17	6.12	7.88	12.07	16.75	21.33
Δp_{opt}, Pa	12.714	12.816	12.877	12.877	13.673	14.448	14.203	14.530
$P_{heat\_ max}$, W	116.9	147.3	173.0	205.0	280.3	453.3	618.5	805.9
$P_{total\_ max}$, W	127.5	162.0	191.2	232.9	309.6	501.4	686.3	841.7
η	0.917	0.909	0.905	0.880	0.905	0.904	0.901	0.957

Every f_{set} corresponds different wind rotor construction work in different wind conditions. Calculated process efficiency coefficient η enables evaluating of economic benefit of wind energy conversion process. It is shown in Table 3 that η can vary from 0.787 to 0.957.

4. DISCUSSIONS

Use of wind energy for building heating can be perspective in cold climate countries. Such type of system can be used directly or combined with thermal energy storage systems (Fig. 4, 5). Combining thermal energy storage system allows implementing heat pump in the system that can be a reserve source of heat energy for building. Also in such case we can extend system working time during the year that could make systems more economically attractive. In any case using renewable energy additional energy source must be planned because of energy demand and source potential variance.

Full wind energy converting systems can be separated and analyzed on the basis of their function: wind rotor, heat generator – subsystems converting energy (energy conversion – EC); the heating networks – subsystems transferring the energy; heat pump – subsystem transforming the energy (energy transformation – ET). All subsystems have their energy performance coefficients that decrease the primary energy capacity, otherwise, they adapt their parameters according to the needs of the building users. One more subsystem that is very important in the usage of the renewable energy resources is the energy accumulation (energy storage – ES), as the energy transfer "in time" is among the most relevant problems, when using the renewable energy resources.

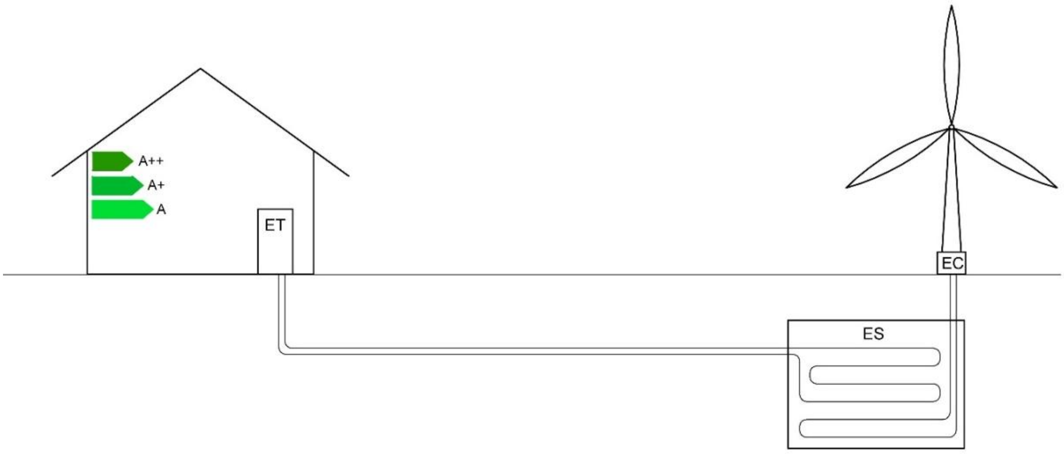

Fig. 4. Local wind energy converting system "Wind rotor (EC) – Heat generator (EC) – Heat accumulator (ES) – Site heat supply network – Heat pump (ET) – Building heating system"

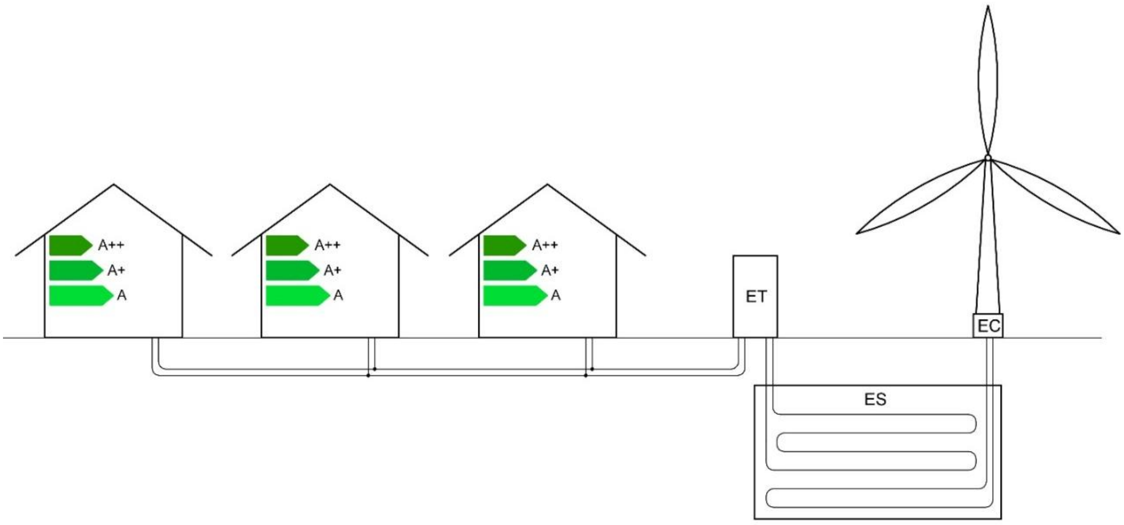

Fig. 5. Settlement wind energy converting system "Wind rotor (EC) – Heat generator (EC) – Heat accumulator (ES) – Heat pump (ET) – Settlement heat supply network – Building heating system"

Using wind energy for building heating through thermal energy storage and heat pump allows implementing additional heat generator units, such as solar water heating collectors, for loading heat accumulator (ES).

5. CONCLUSIONS

The topic of converting wind energy into heat and using it for building heating is relevant because of correlation between wind energy potential and heat power demand during the year.

Wind energy can be used for heat generation by converting mechanical energy in the hydraulic system. The experimental unit of energy conversion imitating wind rotor work was created and researched. Unit has simple construction as it consists only of standard hydraulic elements and can be modified by changing separate parts (pumps, valves) of it.

Analyzed experimental unit shows that in different cases hydraulic system energy conversion efficiency reaches 95.7%.

Optimal hydraulic system-wind rotor work regime can be determined by changing system hydraulic resistance. The same thermal power can be reached by having different rotation frequency of the pump shaft and loading the hydraulic system differently.

The dependence between the optimal rotation frequency of the hydraulic pump shaft and the generated thermal power was determined. Different dependence curves are determined for different wind energy conditions. Such dependence can be used for automatic control of the hydraulic system working as thermal energy generator.

Presented experimental research can be used for studies of hydraulic system with different hydraulic components.

6. REFERENCES

1. MIŠKINIS, V. *Lietuvos energetika / Energy in Lithuania 2013*, Lietuvos energetikos institutas/Lithuanian Energy Institute, Kaunas, 2014. 18 p. ISSN 1822-5268.
2. European Parliament, Directive 2012/27/EU of the European Parliament and of the Council of 25 October 2012 on energy efficiency. *Official Journal of the European Union*, 2012. 56 p.
3. *Statybos techninis reglamentas STR 2.01.09:2012 Pastatų energinis naudingumas. Energinio naudingumo sertifikavimas*., Vilnius, 2015. 153 p.
4. ADOMAVIČIUS, V., KAMINICKAS, M., Analysis of PV power future development possibilities, *Energetika*, 2014, Vol. 60, No. 4, p. 233–248.
5. *Statybinė klimatologija, RSN 156-94*. Vilnius, 1995, 135 p.
6. ČERNECKIENĖ, J., ŽDANKUS, T., Usage of the Wind Energy for Heating of the Energy-Efficient Buildings: Analysis of Possibilities. *Journal of Sustainable Architecture and Civil Engineering*, 2015, Vol. 1, No. 10, p. 58–65.
7. ASHIKLAN, B. Wind motor operated heating system. *United States Patent No. 3752395*, 1973, 5 p.
8. ASHIKLAN, B. Wind operated heating system. *United States Patent No. 3783858*, 1974, 6 p.
9. KNECHT, J. E. Wind driven heating system. *United States Patent No. 4366779*, 1983, 8 p.
10. PAULSEN, U.S. Vindmolleafprovning 5 kW CALORIUS, Roskilde, 1996, 36 p.
11. KAVOLYNAS, A. Application of Solar and Wind Energy. *Summary of the Doctoral Dissertation*, Akademija, 2011, 24 p.
12. MAEGAARD, P., KRENZ, A. *The Rise of Modern Wind Energy – Wind Power for the World*. Pan Stanford Publishing Pte Ltd., 2013, 642 p., ISBN 9789814364935.
13.] YEAPLE, F. *Fluid power design handbook*. CRC Press, 1995.
14. KRUOPIS, J. *Matematinė statistika*. Mokslas, Vilnius, 1993.

CYSENI 2016, May 26-27, Kaunas, Lithuania
ISSN 1822-7554, www.cyseni.com

VERTICAL DISTRIBUTION AND SEASONAL VARIABILITY OF WIND OVER UKRAINE AND ADJACENT TERRITORIES

M. V. Savenets, I. V. Dvoretska
Ukrainian Hydrometeorological Institute
Nauky Av. 37, 03028 Kyiv – Ukraine
Email: mihails@e-mail.ua

G. M. Kruchenitsky
Central Aerological Observatory,
Pervomayskaya Str. 3, 141700 Dolgoprudny – Russia
Email: omd@cao-rhms.ru

ABSTRACT

Nowadays people pay attention to climate change and renewable energy problems. Wind characteristics are one of the most mutable parameters during any climate fluctuations, but these parameters are base for solving numerous energetic problems. Therefore, researches of wind spatiotemporal dynamics are always necessary and actual.

In this research there were analysed climate norms of wind direction, wind speed, zonal and meridional components. Vertical profiles of these parameters and spatial distribution on different isobaric levels allowed forming complete view about spatiotemporal features of wind variability over Ukraine and adjacent territories. This information can be used for solving different problems: from designing of wind power plants to echelon optimization for civil aviation. Critical analysis of raw data and results of seasonal models construction are also present.

Keywords: climate norms, wind direction, wind speed, meridional component, zonal component, vertical profile

1. INTRODUCTION

Wind parameters are very changeable and information always needs rectification, because of using climate normals of wind speed and direction in different applied problems. Defining the meteorological features of aircraft flight levels, modern planning of industrial zones with high point-source pollution, numerical energetic problems – all of them needs regular rectification of wind characteristics [1–4]. Average values are often used for modelling of chemical's total column, when wind is a predictor; while analyzing zonal circulation and air mass interchange. Wind information, when wind used as alternative energy source, shoud be usually updated including upper air data, because wind results from large-scale processes [3, 5]. For the largest wind energy estimation, it is necessary to use wind climate data above the boundary layer [3, 6, 7]. However, the last generalizations for vertical distribution of wind characteristics over Ukraine, which covers a large area, were made more than 30 years ago [8, 9]. Therefore, such research is exceedingly relevant during current climate change. Research contains results of seasonal models calculations and features of wind distribution on different isobaric levels that gives precise idea about it short-term dynamics.

2. METHODOLOGY

Research involved daily upper air soundings data [10] that are present in Wyoming University databases. For analysis there were selected information on 13 standart isobaric levels from 1000 to 30 hPa (approximetely to 23–25 km). The observation time is 1200UTC. To avoid undesirable marginal effects during meteorological field's description there were taken also initial data from the stations situated on adjacent territories. Thus, there were selected 13 stations that help to create network and cover all the territory of Ukraine.

Observations are present for approximately 35 years from 1979 till 2015, but the real period is less because of gaps in data. Soundings data contain information only about wind speed and direction. That's why, for adequate and accurate analysis, there were calculated zonal (Vz) and meridional (Vm) wind components:

$$Vz = v \cdot \sin \alpha , \tag{1}$$

$$Vm = v \cdot \cos \alpha , \tag{2}$$

where v – wind speed; α – wind direction.

The sign of zonal and meridional components not determines by the trigonometric rules, but regarding wind direction, that is azimuth whence wind blows. Therefore, zonal component is negative for wind direction from 0° to 180° and indicates easterlies. Positive sign for wind direction from 180° to 360° indicates westerlies. Meridional component is negative for wind direction from 0° to 90° and from 270° to 360° that indicates wind from north. Positive sign for wind direction 90–270° indicates wind from south.

There was created critical analysis for segregation and removal possible errors in data. The main idea was to define anomalies that weren't present on nearby stations. All suspicious data were checked with residuals of seasonal variations, because it was possibility to remove real anomalies. After climate normals rectification the segregation process started again until all suspicious data either confirmed or removed. Calculation of seasonal models implemented with harmonic analysis using linear regression method on harmonics. Significance tested with Student's function.

3. RESULTS

3.1. Seasonal models of wind characteristics

Significance of 4–5 harmonics almost on all altitudes shows that short-term wind variations form under just as global factors so also regional features. However, seasonality is more legibly observed from tropopause level (Fig. 1). Determination coefficient of seasonal models do not exceed $R^2 = 0.1$, but from tropopause level R^2 increases to significant values. Such changes in determination associated primarily with increasing of fluctuation's amplitudes (Fig. 2), because wind in lower stratosphere changes its direction with alternation of warm and cold seasons and wind speed greatly reduced in warm periods. Meridional circulation is not defining over Ukraine territory and seasonal fluctuations aren't expressed.

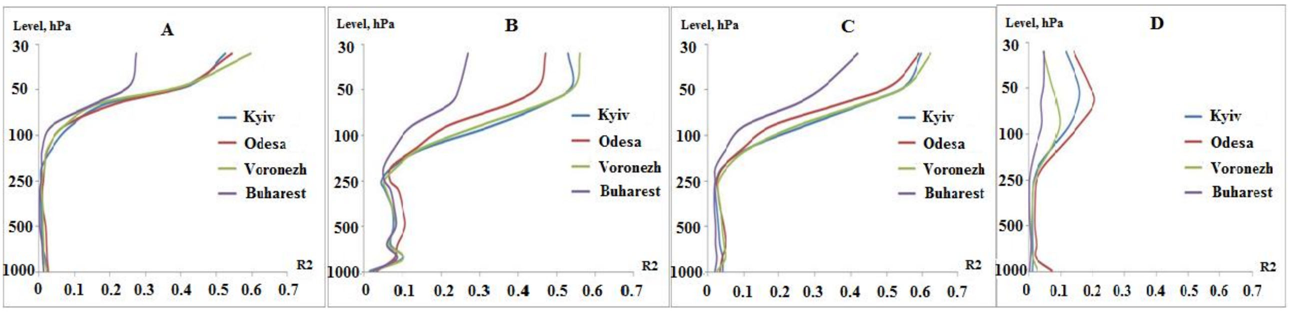

Fig. 1. Vertical distribution of determination coefficient in seasonal models of wind direction (A), wind speed (B), zonal (C) and meridional (D) components

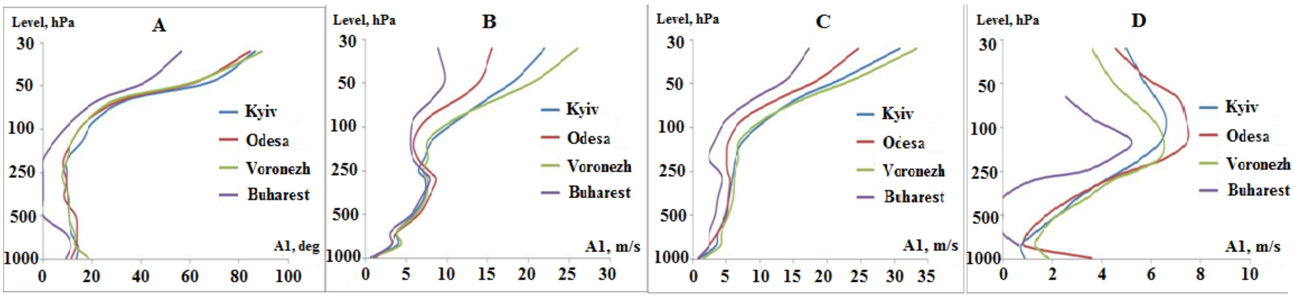

Fig. 2. Vertical distribution of first harmonic amplitude in seasonal models of wind direction (A), wind speed (B), zonal (C) and meridional (D) components

3.2. Wind direction

Location of Ukraine and adjacent territories in 44–54° N lane determine the features of wind distribution over these regions. Average values in troposphere vary from south-east to west directions depend on season. In lower stratosphere direction changes from east to west while warm and cold seasons alternate.

It's possible to define separate vertical layers depends on homogeneity of wind direction fields. 1000 hPa isobaric level is characterized by the most heterogeneous conditions and distinctions from other altitudes. Wind dynamics on this level sufficiently differ through the surface influence. The next layer is from 850 hPa to tropopause inclusively, but the boundary level is less homogeneous and particular seasons are characterized by the stronger latitudinal features. Lower stratosphere is the most heterogeneous layer with alternate wind direction.

Average values of wind direction at 1000 hPa level are within 140–275°. Voeikov axis, where should be observed the changes from the west to the south-east direction, is blurred. We can distinguish three regions by the prevailing of wind directions (Fig. 3). The first region, with south-west component prevailing (Fig. 3A), covers northern and western part of Ukraine and is limited by the 31° E and 47° N in the south. The second region, where considerable frequency, besides south-west component, has also south and south-east components (Fig. 3B), covers southern and eastern part of Ukraine. The third region, with south-east component prevailing, is typical for Rostov and Bucharest stations. Seasonal variations at 1000 hPa isobaric level within all regions (Fig. 4) have insignificant fluctuations of prevailing winds that don't exceed 40° during a year.

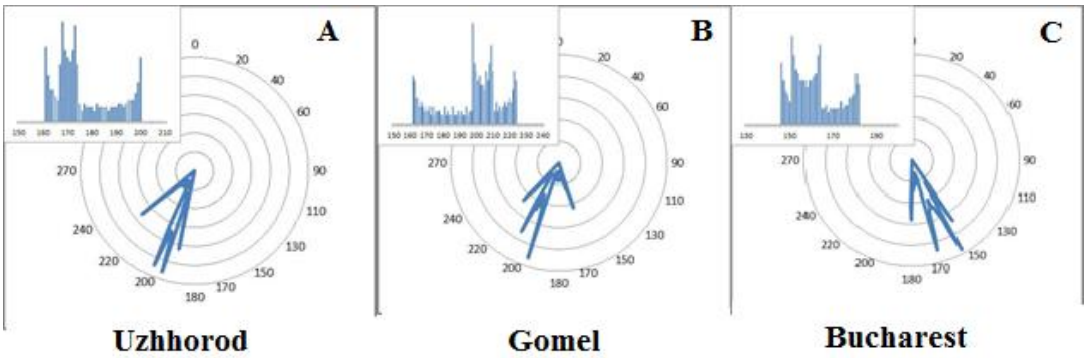

Uzhhorod Gomel Bucharest

Fig. 3. Three types of stations according to prevailing wind directions

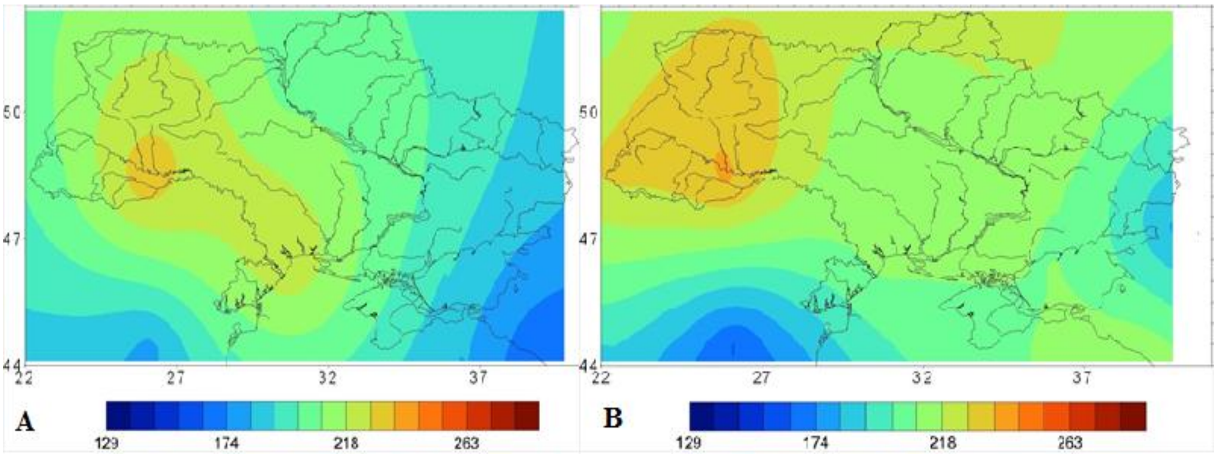

Fig. 4. Spatial distribution of wind direction average values on January, 15th (A) and July, 15th (B) at 1000 hPa isobaric level

Wind direction climate normals at 850–700 hPa levels are within 130–260°. South-west component is prevailing almost on all territory and gradually change to south direction from 45° N to the south. The largest range of values (to 70°) in seasonal variations observes on Tuapse, Chernivtsi and Uzhhorod. The smallest range is on Bucharest and Voronezh stations (30–40°).

Spatial distribution of wind direction at 500–150 hPa levels does not have essential differences and is similar on all altitudes. Westerlies are prevailing here on all territories. West component observes from August to February (6 months a year), south-west component – from February to April and from June to July (4.5 months a year). Only during the second part of spring there are sharp changes to south and south-east components (1.5 month a year).

Alternate wind in lower stratosphere depends on warm or cold periods. In cold period westerlies are present over Ukraine territory with little deviations in the north and south. Westerlies prevail from October to February. South and south-east directions prevail in warm period and observe in May–August. Other months are characterized by wind rearrangement from one period to another.

Vertical distribution of wind direction has several features (Fig. 5). Firstly, distinction in wind direction between stations decreases with altitude; even they are situated on different latitudes and longitudes. Basically, the difference between stations is less than 10° on levels less than 700 hPa. Secondly, there are layers, where wind direction is identical within each layer. The most stable during all year is the layer from 500 hPa to tropopause level, where all variations are synchronous. Another layer is lower stratosphere, but timing of wind direction in spring – summer contradicts within layer. Vertical profiles have significant seasonal variations with amplitude increasing on highest altitudes.

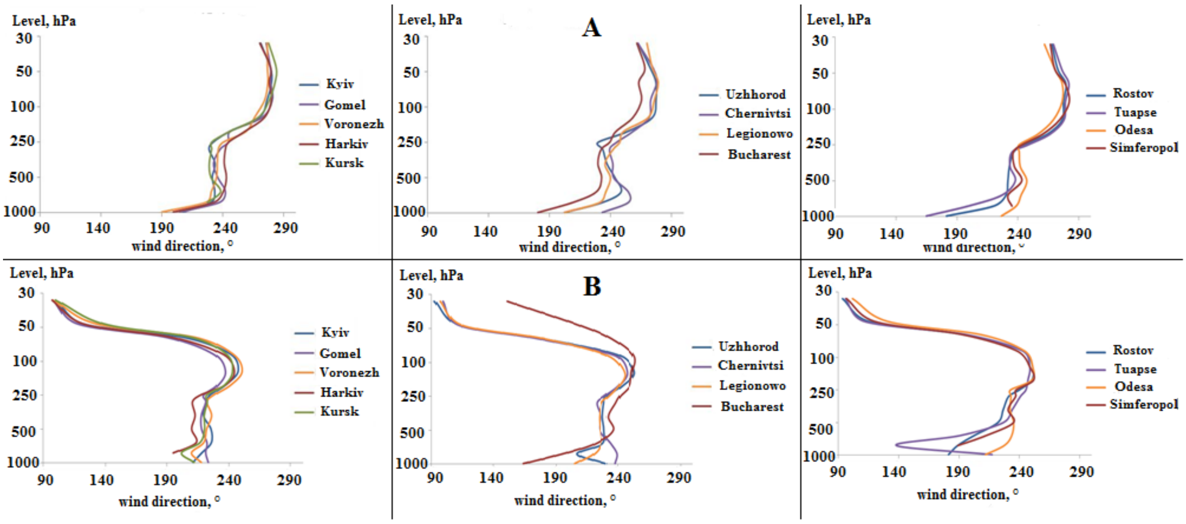

Fig. 5. Wind direction vertical profiles on January, 15th (A) and July, 15th (B)

3.3. Wind speed

Consideration of wind speed spatial distribution allowed defining 5 layers, where dynamics vary from adjacent levels. The most heterogeneous is 1000 hPa level because of friction influence. Wind speed increases from the north-west to the south-east territories on this level. In general average values vary from 2–3 m/s (Uzhhorod) to 6–8 m/s (Rostov). Wind speed increases over Ukraine in cold period and decreases in warm.

Similar spatiotemporal distribution present at 850–250 hPa levels. The main otherness dedicated to the largest amplitudes of seasonal variations on the highest altitudes. Especially strong winds are at tropopause level. Maximum lies over the south-east regions in the second part of summer. Also minimal wind speed shift in time from the summer period to the late spring.

Two layers are distinguished in lower stratosphere: 100–70 hPa and 50–30 hPa. Lower altitudes don't have summer maximum of wind speed in contradiction to 50–30 hPa levels, where in July observes moderate increasing to 10 m/s. The highest values at 100 hPa level observe in January–February. Wind speed sufficiently higher over south stations almost the all months. Range of seasonal variations decreases in the south direction from 15.4 m/s (Gomel) to 10.8 m/s (Tuapse). Range of wind speed seasonality on 50–30 hPa is the largest with two minimums: in May and August.

Analysis of vertical profiles showed main features (Fig. 6): wind speed increases to tropopause level and decreases from 250 to 100 hPa. On lower levels wind speed either constant, or slightly increases with altitude.

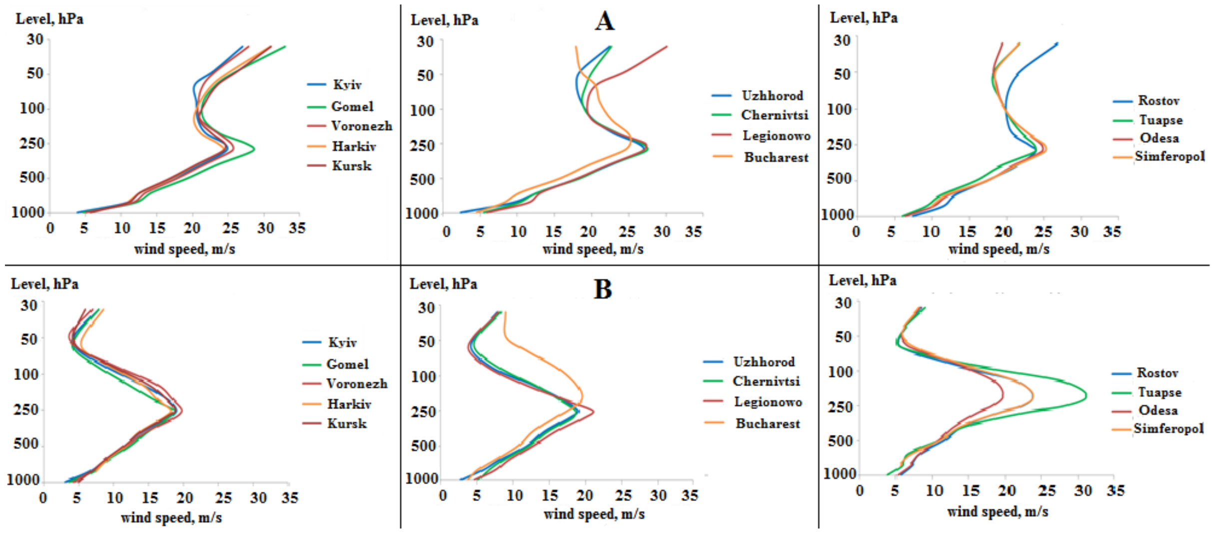

Fig. 6. Vertical profiles of wind speed on January, 15th (A) and July, 15th (B)

3.4. Zonal and meridional components

Boundary level is the most heterogeneous according to the zonal and meridional components. Starting from 850 hPa heterogeneous disappeared and above 700 hPa seasonal dynamics become similar. However, some differences between southern and northern region take place in all troposphere. Smoothing of territorial differences begins at tropopause and in lower stratosphere scheme of zonal and meridional changes become clear.

In winter zonal component always increases with altitude (Fig. 7A) and accomplish maximum values in lower stratosphere. There no significant differences in zonal component between stations in troposphere and tropopause, but in stratosphere on levels less than 150 km, such differences take place between south and north. For example, zonal component in Legionovo equal about 60 m/s, when values in Simferopol and Bucharest are about 30 m/s. Vertical profiles of meridional component vary from 0 m/s to -15 m/s in troposphere, but significant variations in stratosphere aren’t present. So, majority of stations are characterized by profiles with north component.

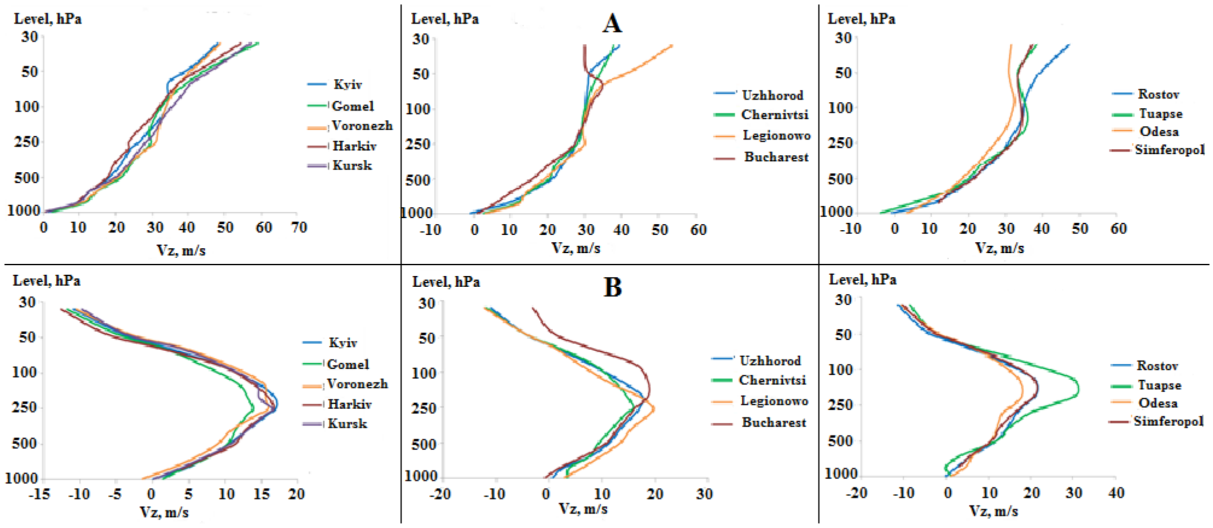

Fig. 7. Vertical profiles of zonal component on January, 15th (A) and July, 15th (B)

In summer profiles of zonal component almost identical in stratosphere (Fig. 7B). Increasing of west component is present from the surface to tropopause level. The strongest easterlies are in stratosphere at 30 hPa (zonal component is about -15 m/s). South direction is typical for meridional component, but in stratosphere values sharply decreases to 0 m/s.

4. CONCLUSIONS

Short-term wind variations over Ukraine adjacent territories are formed under just as global factors so also regional features. Seasonality is significant above tropopause level. Average values of wind direction vary from south-east to west directions. Wind speed increases with altitudes to tropopause level, where maximum values are present. On this level latitudinal differences of zonal and meridional components are smoothed. Wind direction changes in stratosphere with cold and warm period alternation. Variations in wind speed, zonal and meridional components go according to this alternation.

5. REFERENCES

1. БОГАТКИН, О.Г. *Авиационная метеорология*. СПб: Изд. РГГМУ, 2005. 328 с.
2. MARK, J., JACOBSON. *Atmospheric pollution: history, science and regulation*. New York: Cambridge University Press, 2002. 412 p.
3. D.J. DE RENZO. *Wind power: recent developments*. Front Cover D.J. De Renzo. William Andrew, Inc., 1979. 347 p.
4. ВНУКОВ, А.К. *Защита атмосферы от выбросов энергообъектов*. Москва: Энергоатомиздат, 1992. 176 с.
5. EMEIS, S. *Wind energy meteorology: atmospheric physics for wind power generation*. Springer-Verlag Berlin Heidelberg, 2013. 201 p.
6. LORENZ, E. Available potential energy and the maintenance of the general circulation. Tellus 7, 1955. 271–278 pp.
7. MILLER, L.M., GANS, F., KLEIDON A.: Estimating maximum global land surface wind power extractability and associated climatic consequences. Earth Syst. Dynam. 2, 1–12 (2011).

8. СТЕХНЕВСКИЙ, Д.И., ЧУЧКАЛОВ, Б.С. *Атлас климатических характеристик температуры, плотности и давления воздуха, ветра и геопотенциала в тропосфере и нижней стратосферы северного полушария*. Москва: Гидрометеоиздат, 1974. 125 с.
9. КРУЧЕНИЦКИЙ, Г.М., ДВОРЕЦКАЯ, И.В., САВЕНЕЦ, М.В. Климат термобарических полей над территорией Украины. Оптика атмосферы и океана. Физика атмосферы: тезисы докладов XX международного симпозиума. Новосибирск: ИХКГ СО РАН. 2014, 23–27 июня.
10. *Atmospheric soundings*. University of Wyoming, College of Engineering. Link to the internet < http://weather.uwyo.edu/upperair/sounding.html >.

CYSENI 2016, May 26-27, Kaunas, Lithuania
ISSN 1822-7554, www.cyseni.com

SHORT-TERM WIND SPEED FORECASTING USING ARIMA MODEL

Ernesta Grigonytė
Lithuanian Energy Institute
Breslaujos str. 3, LT-44403 Kaunas – Lithuania
Email: ernesta.grigonyte@lei.lt

Eglė Butkevičiūtė
Energetikos sprendimų grupė, MB
Rytmečio str. 7, LT-47491 Kaunas – Lithuania
Email: egle.butkeviciute@groupesg.eu

ABSTRACT

The massive integration of wind power into power system increasingly calls for better short-term wind speed forecasting which helps transmission system operators to balance the power systems with less reserve capacities. The paper addresses the short-term wind speed forecasting using ARIMA (Autoregressive Integrated Moving Average) model. It is a classical time-series methodology but with well-known limitations in wind speed forecasting applications, mainly due to insufficient accuracies of the hourly forecasts for the second half of the day-ahead forecasting period. The authors attempt to find the maximum effectiveness of the model aiming to find 1) how the identification of optimal model structure improves the forecasting results and 2) what accuracy increase can be gained by reidentification of the structure for a new wind weather season. The model structure is defined by rows p, d, q and length of retrospective data period. Both historical and synthetical wind speed data representing the sample locality in Baltic region's were used to run the model. The quantitative study revealed that identification of optimal model structure gives significant accuracy improvement against casual structures and less but appreciable improvement due to by the change of model structure for a new annual season.

Keywords: ARIMA, power system, wind speed, short-term forecasting

CYSENI 2016, May 26-27, Kaunas, Lithuania
ISSN 1822-7554, www.cyseni.com

ON-LINE, INTERACTIVE TOOLS AND ALGORITHMS FOR THERMAL CALCULATIONS OF HEAT PUMPS

V. A. Voloshchuk
National Technical University of Ukraine "Kyiv Polytechnic Institute"
Politehnichna str. 56, 03056 Kyiv – Ukraine
Email: Volodya-28@yandex.ru

ABSTRACT

The work proposes on-line, interactive tools and algorithms for designing, optimizing and analyzing thermal processes in heat pumps. It gives a possibility to perform a wide variety of simulation tasks (both standart and non-standard) in refrigeration systems in a quick and efficient manner without the need to resort to the aid of third-party programmers or specialists. The technique is based on application and integration of Internet-resourses and modern software programs.

Tools for investigation of thermal processes in heat pump systems are implemented and analysed in the work. A new technology for "cloud" computing of vapour compression systems is developed which is based on three options: online calculation, download and reference. Online resources give a possibility to do "cloud" simulations in an interactive mode with the option for each user to enter his own input data. Downloading enables to download ready-made templates for developing further calculations on the own computer. The reference procedure gives a possibility to do a reference to the different functions of refrigeration processes stored on the Internet or in "clouds" for developing further simulations. The tools were successfully tested using various case studies: thermodynamic analysis of vapour compression cycles, thermal processes in heat pump components, techno-economic evaluation of heat pump application in heating systems.

Keywords: "cloud" calculations, heat pumps, templates, Internet resources

1. INTRODUCTION

Computer simulation programs are widely and extensively used for analyzing heat pump systems [1]. However, most of these programs do not publish documentation about the detailed algorithms. As a rule "black box approach" is used for them. Few of them allow users to customize the source code.

Thermophysical properties of working fluids pose a particular challenge for heat pump simulation. A wide range of computer programs (REFPROP, FLUIDS, CHEMCAD, etc.) have been created for calculating properties of working substances in refrigeration systems depending on such parameters as temperature, pressure, specific enthalpy, specific entropy, density, etc. One problem is that these programs have quite narrow possibilities of their further application in computer simulation. Moreover, it is not possible and/or unreasonable to save in one program or one computer data about all existing working substances. In addition, errors and inaccuracies in the existing computer programs take place, which have to be fixed by an update, their application domains are extended and their performance is improved (speed of operation, volume of computer memory, etc.).

In mathematical packages such as Mathcad, Maple, Matlab, Mathematica and others the users can find some amount of ready-made templates. It substantially simplifies and speeds the process of creating calculation methods and mathematical models. But these packages don't have templates which can be directly used for computing refrigeration systems.

One of the most important "IT-revolutions" belongs to the development of so called "cloud computing" – providing remote computing ability, footprint ("clouds") and communication channels for customers. The reason, which promotes using of "cloud" computing, are the high costs for program licenses for stationary workstations, rent of space, electricity and control of software piracy. By "clouds" computing centers are meant, which are significantly more powerful than user's stationary equipment. Instead of physical servers, customers use virtual servers, which are spread in allocated net of computers with industrial ability [2].

2. METHODOLOGY

It is proposed to develop the compuational tools on the basis of Mathcad and Maple.

Mathcad originally designed as a package of numerical mathematics, which later was extended with symbolic kernel of the Maple, which then (in the 13th version) has been replaced by the kernel of the symbolic mathematics of the MuPAD software. Maple is rather a symbolic computing and mathematical software package. Maple is very useful in the theoretical analysis.

A significant benefit of using Mathcad and Maple is their handling of units. Engineering and technical problems are mostly solved with units and dimensional quantities. Mathcad allows investigators and engineers to assign units to their variables and to convert between units simply by reassigning them.

In March 2nd 2016 new version of Maple was released [3]. The Maple 2016 provides new data, computation, and visualization tools for working with thermophysical properties of working fluids applied in thermal engoneering.

Today both MathCad and Maple provide cloud service technologies [4, 5]. Such strategy enables a user to run worksheets via the internet with his/her own parameters online. This outstanding feature gives a possibility and flexibility to analyse and share mathematical computations and solutions among different teams, located in different places, without having to invest in new software. Moreover such technologies can be completely open implying that principles of calculations, algorithms and intermediate results of calculations are visible.

A specific technology developed in [6] was used where a number of tools for the creation of the open and interactive algorithms were applied (Fig. 1). The algorithms 1 contain the following components: part 2 associated with the formulas for the calculation of parameters of a heat pump (thermophysical properties, performance characteristics, etc.) and the corresponding Mathcad code 7; text part 3 that includes support information on formulas, notes to mathematical formulas and the description of the calculations, etc; part 4 related to computer and Internet technologies. The resource 1 provides a client with a number of options, including calculation of characteristics when manipulating data, reading of the text information and copying mathematical formulas or code in general. These options are executed on a remote server not on a personal computer of a user. The packages Mathcad Calculation Server 8 and Microsoft Expression Web 3 9 play an important role in the formation of the resource 1 (Fig. 1).

Most today’s softwares’ devepopers propose web-based users’ communities where it is possible to discuss projects, create documentation, share applications, ready-made templates, connect with peers and help others get the most out of the products – all these encourage collaboration and facilitate participation and interaction. Such users’ communities exist within Mathcad and Maple softwares which was also used in the proposed tools.

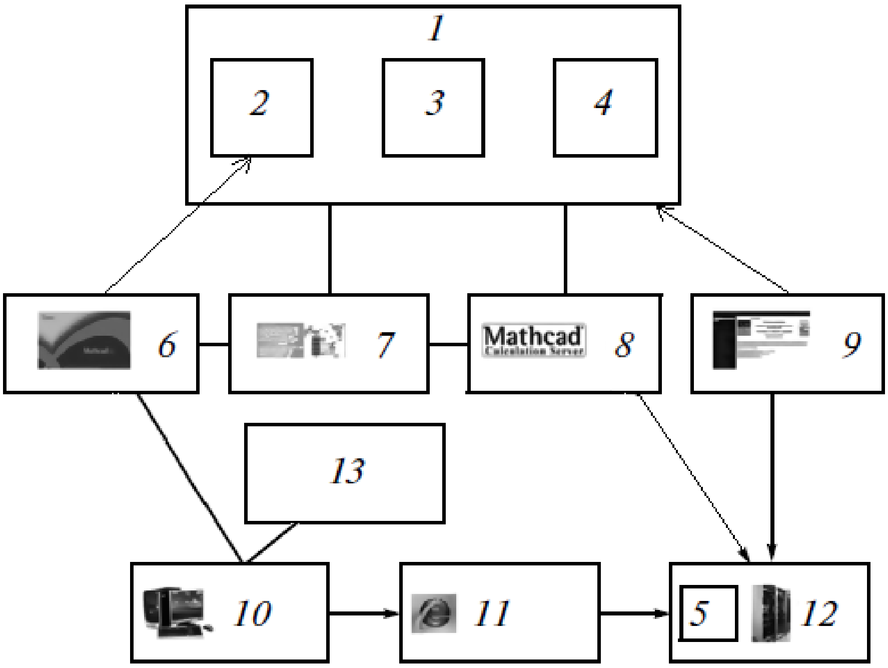

Fig. 1. Sources of information and tools used to create an open interactive algorithm: the open interactive algorithm (*1*), Mathcad field of the algorithm (*2*), text (*3*), part associated with Computer Science and Internet technologies (*4*), the template (*5*), Mathcad-tools (*6*), Mathcad-program (*7*), Mathcad Calculation Server (*8*), package Microsoft Expression Web 3 (*9*), PC user (*10*), Internet (*11*), the remote server (*12*), the individual user program (*13*) [6]

3. APPLICATION OF THE PROPOSED TOOLS

3.1. “Cloud” fuctions on thermophysical properties of working fluids

As an example, Fig. 2 shows the web-page http://twt.mpei.ac.ru/TTHB/2/R407c-eng.html with functions for computing thermophysical properties of refrigerant R407, which is prepared on technology from [6] and is a part of the “cloud” calculation server of the Moscow Power Engineering University’s National Research University (www.mpei.ru) and Ltd Trieru (www.trie.ru). Among the functions there are also some for computing properties at the saturation state depending on one argument. Besides the web-page provides functions of thermophysical properties, which depend on two parameters as initial data: pressure and temperature, pressure and enthalpy, pressure and entropy, temperature and entropy, etc.

For convenience the principle for denoting functions is the following. For example, a function for calculation of specific enthalpy, which is dependent on pressure and temperature, is denoted as R407cHPT(p, T). Here the first five letters indicate the type of working substance (R407c). The sixth letter indicates the parameter, which is calculated (enthalpy H). The last two letters indicate arguments on which the specific enthalpy is calculated (pressure p and temperature T). These parameters (arguments of the function) are duplicated in the brackets after the name of the function.

Based on the technology from [6] a wide range of network, open and interactive functions on thermophysical properties of working fluids applied in heat pumps were developed and located at http://twt.mpei.ac.ru/OCHKOV/VPU_Book_New/mas/eng/index.html. Such data on the thermophysical properties of water and steam, substances used as the main working fluid in thermal engineering, are programmed according to the formulations of Association for the Properties of Water and Steam approved in 1997 and refined in 2007 – [7, 8]. The fuctions on properties of ideal gases and their mixtures are provided based on system of equations from [9]. In [10] the author has proposed a methodology for creation of forward and backward functions that return the values of the thermophysical properties of refrigerants on the basis of tabular values in different areas of the state: single-phase region, two phase region, the saturation line. The tabulated data were generated in the NIST program REFPROP (http://www.nist.gov).

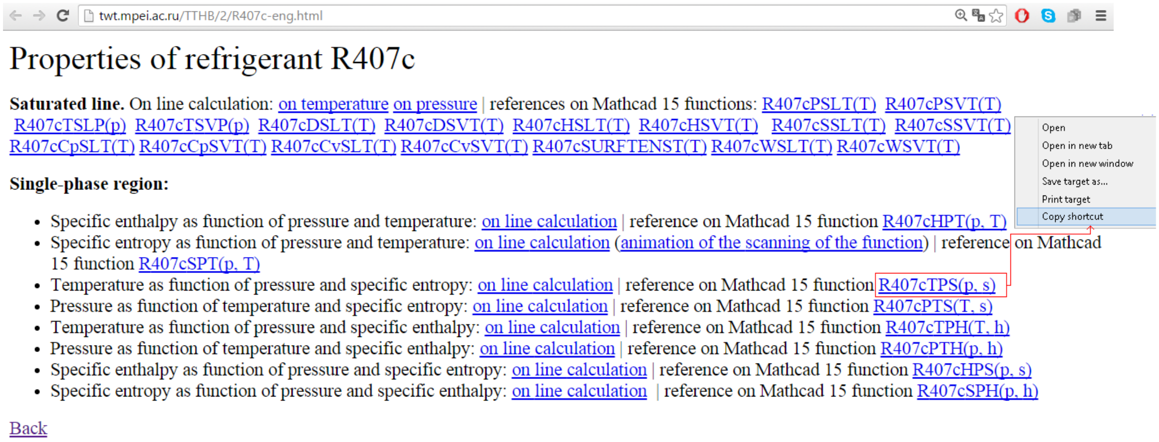
twt.mpei.ac.ru/TTHB/2/R407c-eng.html

Properties of refrigerant R407c

Saturated line. On line calculation: on temperature on pressure | references on Mathcad 15 functions: R407cPSLT(T) R407cPSVT(T) R407cTSLP(p) R407cTSVP(p) R407cDSLT(T) R407cDSVT(T) R407cHSLT(T) R407cHSVT(T) R407cSSLT(T) R407cSSVT(T) R407cCpSLT(T) R407cCpSVT(T) R407cCvSLT(T) R407cCvSVT(T) R407cSURFTENST(T) R407cWSLT(T) R407cWSVT(T)

Single-phase region:

- Specific enthalpy as function of pressure and temperature: on line calculation | reference on Mathcad 15 function R407cHPT(p, T)
- Specific entropy as function of pressure and temperature: on line calculation (animation of the scanning of the function) | reference on Mathcad 15 function R407cSPT(p, T)
- Temperature as function of pressure and specific entropy: on line calculation | reference on Mathcad 15 function R407cTPS(p, s)
- Pressure as function of temperature and specific entropy: on line calculation | reference on Mathcad 15 function R407cPTS(T, s)
- Temperature as function of pressure and specific enthalpy: on line calculation | reference on Mathcad 15 function R407cTPH(T, h)
- Pressure as function of temperature and specific enthalpy: on line calculation | reference on Mathcad 15 function R407cPTH(p, h)
- Specific enthalpy as function of pressure and specific entropy: on line calculation | reference on Mathcad 15 function R407cHPS(p, s)
- Specific entropy as function of pressure and specific enthalpy: on line calculation | reference on Mathcad 15 function R407cSPH(p, h)

Back

Fig. 2. The web-page on “cloud” functions of thermophysical properties of refrigerant R407c with options of online computing, download and reference

3.2. On-line calculations

Fig. 3 shows an example of a web-page where a user can do online calculations of specific enthalpy of ammonia as a function of pressure and temperature (address of the web-page is http://twt.mpei.ac.ru/MCS/Worksheets/Thermal/NH3HPT.xmcd).

The user via his web browser is able to change initial data (in this case pressure and temperature) and to choose required dimensions. After clicking the button “Recalculate” he obtains the results and graphical illustrations of the calculated point in h, p- and h, T-phase diagrams.

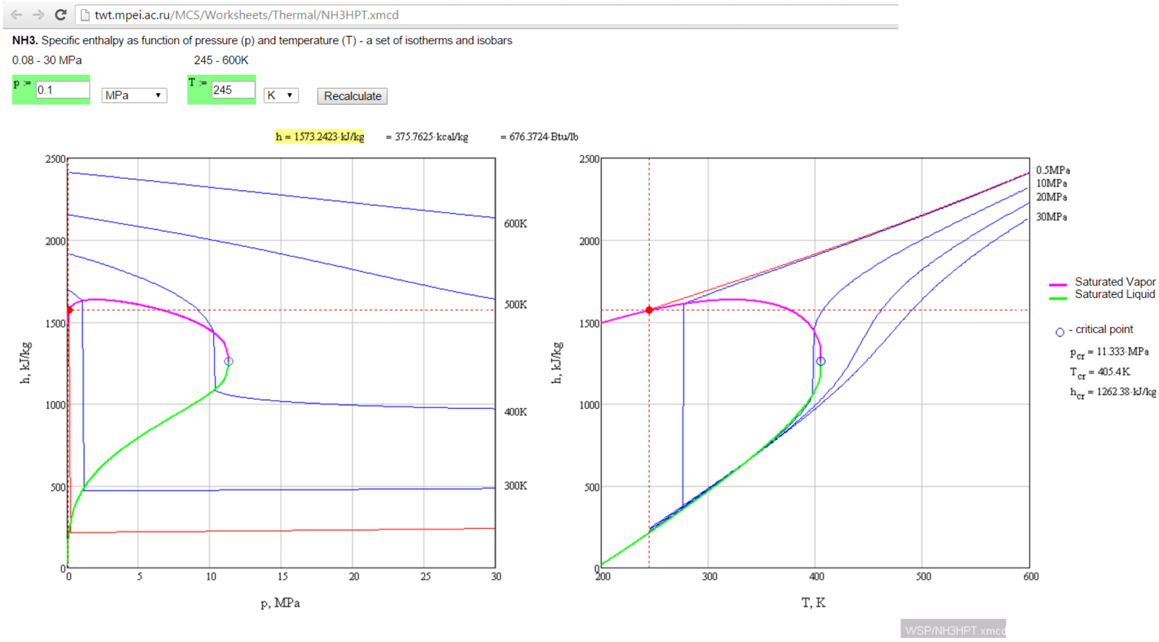
twt.mpei.ac.ru/MCS/Worksheets/Thermal/NH3HPT.xmcd

NH3. Specific enthalpy as function of pressure (p) and temperature (T) - a set of isotherms and isobars

0.08 - 30 MPa

245 - 600K

p := 0.1 MPa

T := 245 K

h = 1573.2423·kJ/kg = 375.7625·kcal/kg = 676.3724·Btu/lb

p_{cr} = 11.333·MPa

T_{cr} = 405.4K

h_{cr} = 1262.38·kJ/kg

Fig. 3. A copy of the internet-page for online calculation of specific enthalpy as a function of pressure and temperature. Illustration of the determined point in h, p- and h, T-phase diagrams

An example of input data block for interactive thermodynamic analysis of cascade vapor-compression heat pump cycle, which is prepared on the technology of Mathcad Calculation Server is shown in Fig. 4. The introduced calculation is located on the “cloud” server of the Moscow Power Engineering University’s National Research University at http://twt.mpei.ac.ru/MCS/Worksheets/PTU/Vv-36.xmcd.

The web-page on this calculation can be found on the server in the interactive reference handbook “Thermodynamic cycles”, Chap. “Heat pumps and refrigerators”. As input data it is proposed: temperature of heat source, temperature of heat consumption, temperature difference in the evaporator, temperature difference in the condenser, isentropic efficiency of the compressor, temperature difference between working fluids in low pressure and high pressure circuits, pressure increase in the compressor of low pressure circuit and types of refrigerants in low pressure and high pressure circuits. For determining of thermodynamic properties of refrigerant references on “cloud” functions were used.

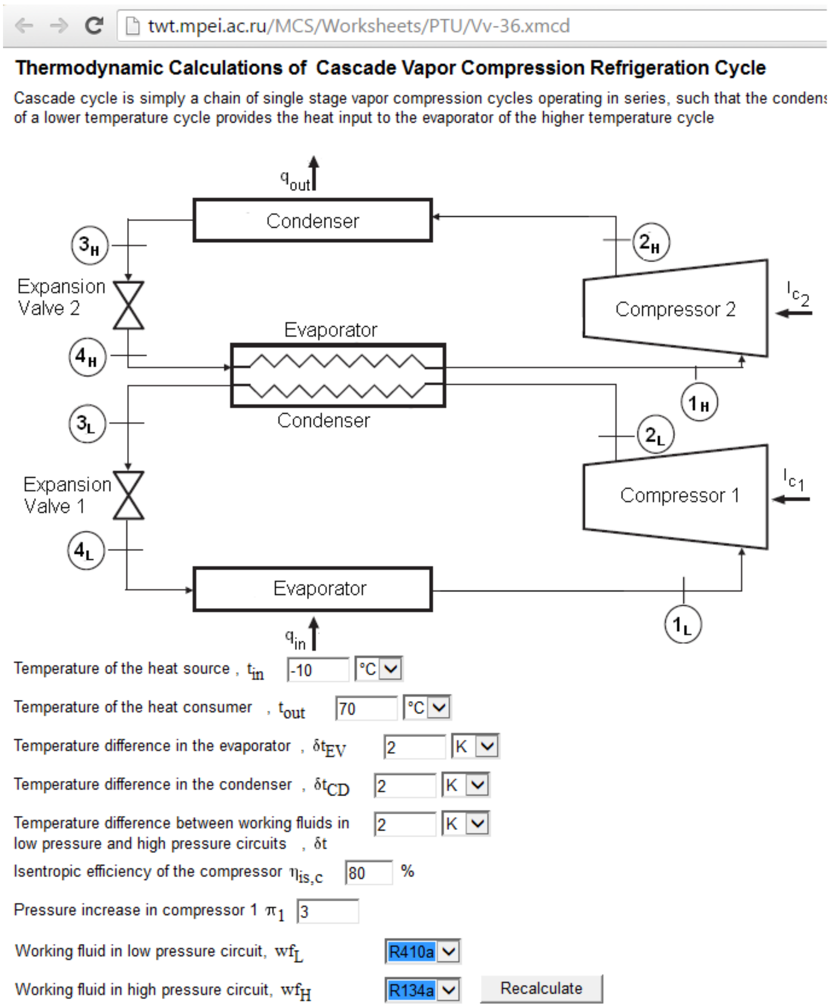

Thermodynamic Calculations of Cascade Vapor Compression Refrigeration Cycle

Cascade cycle is simply a chain of single stage vapor compression cycles operating in series, such that the conden
of a lower temperature cycle provides the heat input to the evaporator of the higher temperature cycle

Temperature of the heat source , t_{in} -10 °C
Temperature of the heat consumer , t_{out} 70 °C
Temperature difference in the evaporator , δt_{EV} 2 K
Temperature difference in the condenser , δt_{CD} 2 K
Temperature difference between working fluids in low pressure and high pressure circuits , δt 2 K
Isentropic efficiency of the compressor $\eta_{is,c}$ 80 %
Pressure increase in compressor 1 π_1 3
Working fluid in low pressure circuit, wf_L R410a
Working fluid in high pressure circuit, wf_H R134a

Fig. 4. Input data block and schematic of cascade vapor-compression refrigeration cycle prepared on technology of Mathcad calculation server

In Fig. 5 an example of numerical simulation results made for the chosen heat pump cycle with help of the given technology is presented. Such technology gives a possibility to see calculations methods which were used for simulation (see Fig. 5).

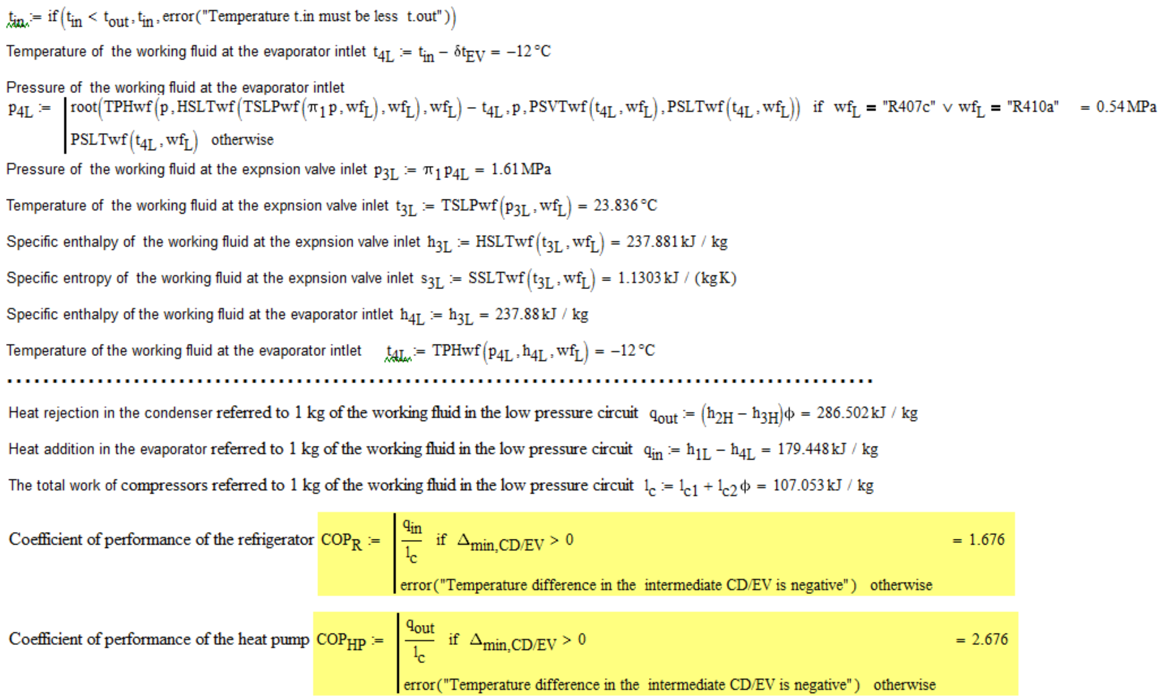

$t_{in} := \text{if}\left(t_{in} < t_{out}, t_{in}, \text{error}(\text{"Temperature t.in must be less t.out"})\right)$

Temperature of the working fluid at the evaporator intlet $t_{4L} := t_{in} - \delta t_{EV} = -12\,°C$

Pressure of the working fluid at the evaporator intlet

$p_{4L} := \begin{cases} \text{root}\left(\text{TPHwf}\left(p, \text{HSLTwf}\left(\text{TSLPwf}(\pi_1 p, wf_L), wf_L\right), wf_L\right) - t_{4L}, p, \text{PSVTwf}(t_{4L}, wf_L), \text{PSLTwf}(t_{4L}, wf_L)\right) & \text{if } wf_L = \text{"R407c"} \vee wf_L = \text{"R410a"} \\ \text{PSLTwf}(t_{4L}, wf_L) & \text{otherwise} \end{cases} = 0.54\,\text{MPa}$

Pressure of the working fluid at the expnsion valve inlet $p_{3L} := \pi_1 p_{4L} = 1.61\,\text{MPa}$

Temperature of the working fluid at the expnsion valve inlet $t_{3L} := \text{TSLPwf}(p_{3L}, wf_L) = 23.836\,°C$

Specific enthalpy of the working fluid at the expnsion valve inlet $h_{3L} := \text{HSLTwf}(t_{3L}, wf_L) = 237.881\,\text{kJ}/\text{kg}$

Specific entropy of the working fluid at the expnsion valve inlet $s_{3L} := \text{SSLTwf}(t_{3L}, wf_L) = 1.1303\,\text{kJ}/(\text{kg K})$

Specific enthalpy of the working fluid at the evaporator intlet $h_{4L} := h_{3L} = 237.88\,\text{kJ}/\text{kg}$

Temperature of the working fluid at the evaporator intlet $t_{4L} := \text{TPHwf}(p_{4L}, h_{4L}, wf_L) = -12\,°C$

……

Heat rejection in the condenser referred to 1 kg of the working fluid in the low pressure circuit $q_{out} := (h_{2H} - h_{3H})\phi = 286.502\,\text{kJ}/\text{kg}$

Heat addition in the evaporator referred to 1 kg of the working fluid in the low pressure circuit $q_{in} := h_{1L} - h_{4L} = 179.448\,\text{kJ}/\text{kg}$

The total work of compressors referred to 1 kg of the working fluid in the low pressure circuit $l_c := l_{c1} + l_{c2}\phi = 107.053\,\text{kJ}/\text{kg}$

Coefficient of performance of the refrigerator $COP_R := \begin{cases} \dfrac{q_{in}}{l_c} & \text{if } \Delta_{min,CD/EV} > 0 \\ \text{error}(\text{"Temperature difference in the intermediate CD/EV is negative"}) & \text{otherwise} \end{cases} = 1.676$

Coefficient of performance of the heat pump $COP_{HP} := \begin{cases} \dfrac{q_{out}}{l_c} & \text{if } \Delta_{min,CD/EV} > 0 \\ \text{error}(\text{"Temperature difference in the intermediate CD/EV is negative"}) & \text{otherwise} \end{cases} = 2.676$

Fig. 5. An example of numerical simulation results made for the cascade vapor-compression refrigeration cycle

Ts-, ph- and hs- property diagrams for the presented vapor-compression cycle of a heat pump, plotted in Mathcad Calculation Server according to user's input data (see Fig. 4) are shown in Fig. 6.

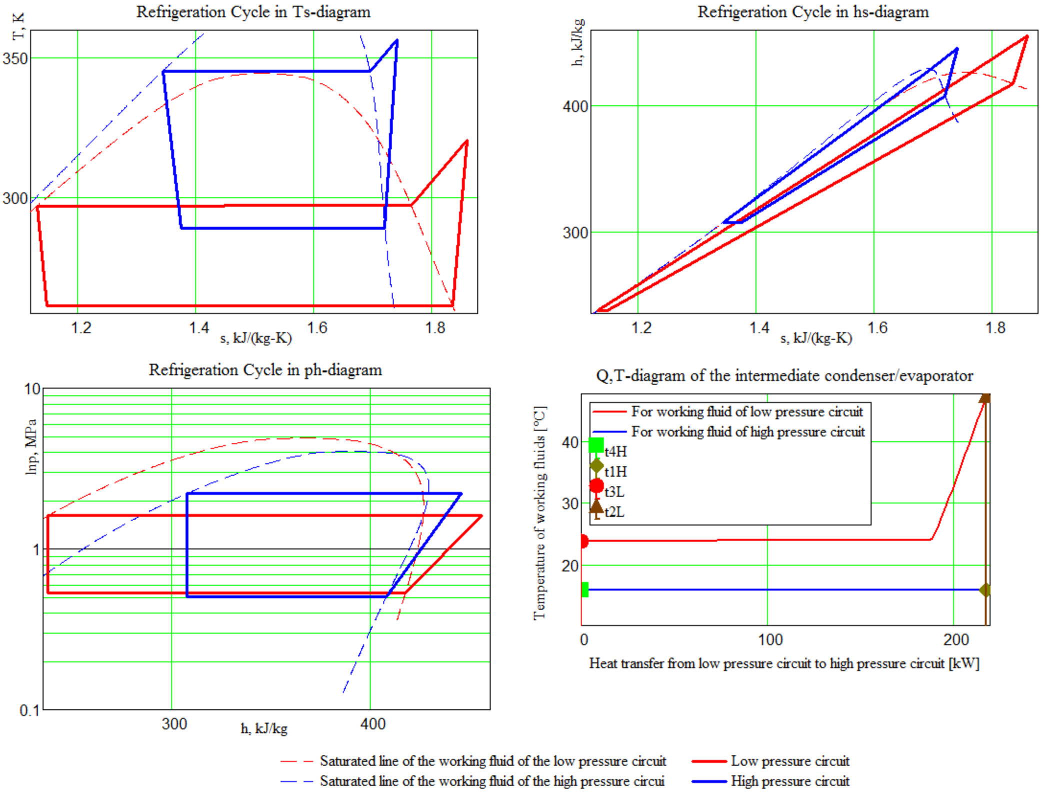

Fig. 6. Ts-, ph- and hs- property diagrams for the cascade vapor-compression refrigeration cycle plotted in Mathcad calculation server

As a rule heat pumps units are not dimensioned for managing the total heating needs. Some part of heating needs, the so-called peak heat load, usually constitutes of alternative solutions (an electrical cartridge, a boiler, and other peak load heaters). The peak load for heating occurs under very cold conditions and only for a limited time of the year – usually during short and very cold spells (see Fig. 7).

A distribution between base or heat pump load and peak load heater must be made for economic reasons. The task to determine heat pump coverage and alternative peak load coverage is an optimization task in which a wide variety of influence factors should be taken into account (climate conditions, technological parameters, prices etc.).

In the Fig. 6 there are two examples of determining rate of heat pump load made on the base of techno-economic optimization with the help of the webpage http://twt.mpei.ac.ru/MCS/Worksheets/PTU/Vv-31.xmcd where a user in his web-browser is able to enter in an interactive mode his own data (climate conditions, technological parameters, prices, tariffs etc.) and receive the procedure of calculations, both intermediate and final results.

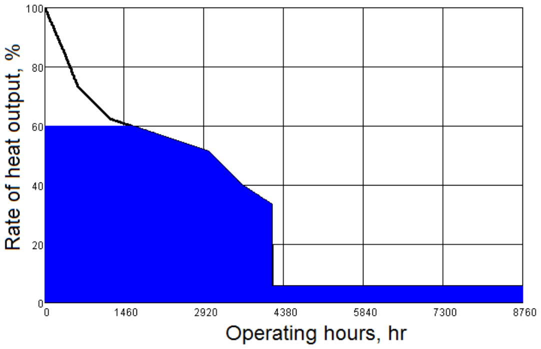

Fig. 7. Example of distribution between base and peak heating load

So, we can see two cases which differ from each other by climate conditions, technological parameters and prices. In case 1 the optimum rate of heat pump load is about 60% because within this rate Net Present Value is the highest and Payback period is the lowest. In case 2 the optimum rate of heat pump load is about 40–50%.

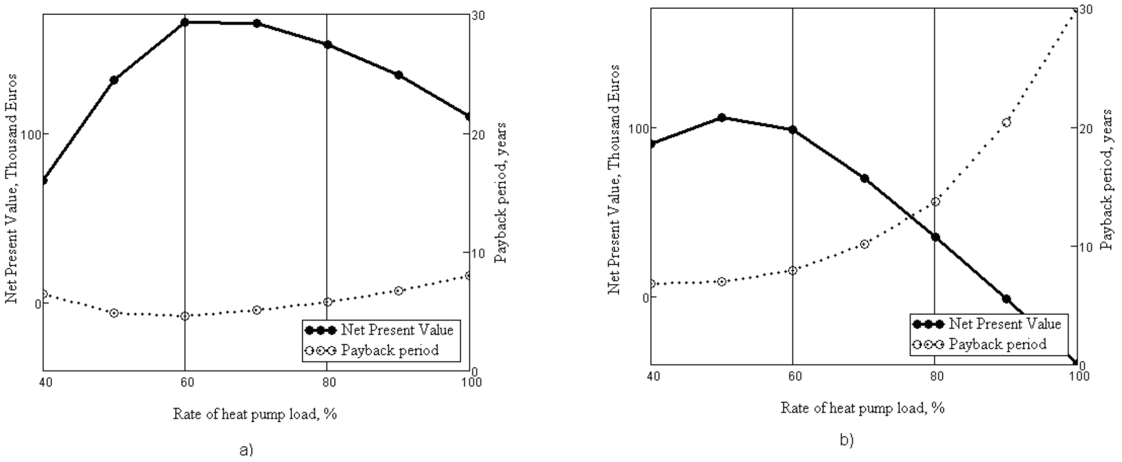

a)

b)

Fig. 8: Dependence of Net Present Value and Payback period on HP rate coverage received with the help of the introduced IT (location at http://twt.mpei.ac.ru/MCS/Worksheets/PTU/Vv-31.xmcd): a) – case 1; b) – case 2

3.3. Technology of reference and downloading

Mathcad offers the possibility to insert a reference to a worksheet from another Mathcad document. The linked document can be located on a personal computer, a local computer network or an internet server. In the calculation, shown in Fig. 9, there are made references to the worksheets, which addresses have been presented in Fig. 2.

Fig. 9 shows an example of using created functions on thermodynamic properties of refrigerant R410a for calculations in MathCad documents the amount of heat $q_{1\text{-}2}$, which is transferred to the working fluid in the isobaric process 1–2. In this case a technology of “cloud” reference, that gives a possibility to refer to functions R410aHPT(p, T) and R410aTPS(p, s), which are located on the internet-server http://twt.mpei.ac.ru/TTHB/2/R410aEng.html, is proposed.

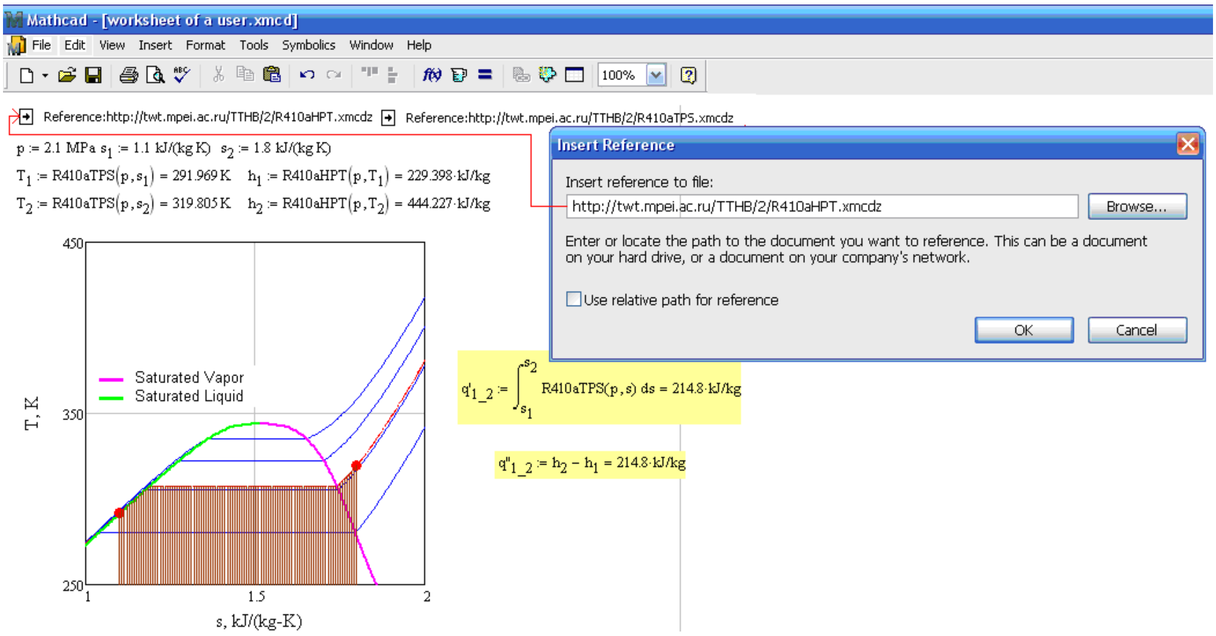

Reference:http://twt.mpei.ac.ru/TTHB/2/R410aHPT.xmcdz Reference:http://twt.mpei.ac.ru/TTHB/2/R410aTPS.xmcdz

$p := 2.1\ \text{MPa}\quad s_1 := 1.1\ \text{kJ/(kg K)}\quad s_2 := 1.8\ \text{kJ/(kg K)}$

$T_1 := \text{R410aTPS}(p, s_1) = 291.969\ \text{K}\quad h_1 := \text{R410aHPT}(p, T_1) = 229.398\cdot\text{kJ/kg}$

$T_2 := \text{R410aTPS}(p, s_2) = 319.805\ \text{K}\quad h_2 := \text{R410aHPT}(p, T_2) = 444.227\cdot\text{kJ/kg}$

$q'_{1\_2} := \int_{s_1}^{s_2} \text{R410aTPS}(p, s)\, ds = 214.8\cdot\text{kJ/kg}$

$q''_{1\_2} := h_2 - h_1 = 214.8\cdot\text{kJ/kg}$

Insert reference to file: http://twt.mpei.ac.ru/TTHB/2/R410aHPT.xmcdz

Enter or locate the path to the document you want to reference. This can be a document on your hard drive, or a document on your company's network.

☐ Use relative path for reference

Fig. 9. Calculation of heat transferred to the refrigerant R410a in isobaric process 1-2 with the help of reference to “cloud” functions

For computing the heat energy $q_{1\text{-}2}$ a well-known formula can be used:

$$q_{1-2} = \int_{s_1}^{s_2} T(p,s)\,ds\,. \tag{1}$$

In order to solve this term, T(p, s) will be replaced by the reverse function R410aTPS(p, s). R410aTPS(p, s) is a function for computing temperature of the refrigerant R410a depending on pressure and specific entropy. The proposed function can be directly used in integration and differentiation operations in Mathcad environment. It substantially simplifies solving tasks of computing refrigerating processes.

In the presented example it is possible to use the first law of thermodynamics – rate of heat transferred to the refrigerant in the isobaric process 1–2 is equal enthalpy change of the refrigerant.

A graphical illustration of the isobaric process 1–2 in T, s-phase diagram is also shown in Fig. 9. The technology of references to “cloud” functions gives the possibility to do more complicated calculations of refrigerating systems.

The following actions should be performed by users for becoming accessible the “cloud” functions in a Mathcad worksheet:

- enter the portal of MPEI’s computation server (www.vpu.ru/mas) and choose “Power & heat engineering” from the interactive handbooks, listed in the table of contents. In the opened handbook choose “Book 2. Theory of heat engineering. Heat engineering experiment” and then “Chapter 2 Thermodynamics”;
- in the opened window, choose the function required for the calculations (see Fig. 1);

- click on the chosen function by the right mouse button;
- in the pop-up menu, choose “Properties,” highlight and copy the corresponding URL address;
- in a MathCad worksheet choose the menu items “Insert”, then “Reference” and insert the previously copied address in the appeared window;
- now, in order to use the required function, it is sufficient to enter its name and the available input data as arguments of this function, e.g. R410aHPT (p, T_1).

All introduced “cloud” functions and calculations as MathCad worksheets can be downloaded as ready-made templates and customized to perform a wider range of modeling tasks in refrigeration systems. In Fig. 10 a screen shot of the web-page of PTC community is shown, where a list of MathCad worksheets for calculations of thermal processes in heat pumps are proposed for downloading.

Maple software also provides a possibility to create on-line, interactive tools and algorithms (MapleNet technology [5]).

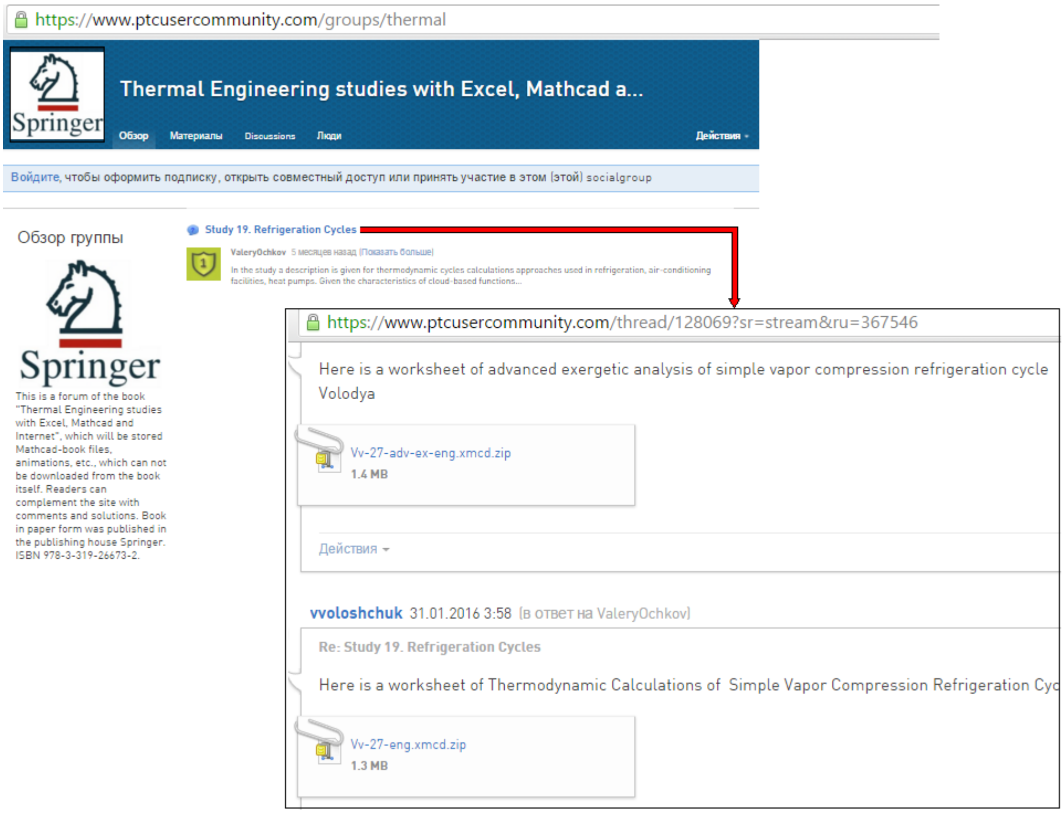

https://www.ptcusercommunity.com/groups/thermal

Thermal Engineering studies with Excel, Mathcad a...

Войдите, чтобы оформить подписку, открыть совместный доступ или принять участие в этом (этой) socialgroup

Обзор группы

This is a forum of the book "Thermal Engineering studies with Excel, Mathcad and Internet", which will be stored Mathcad-book files, animations, etc., which can not be downloaded from the book itself. Readers can complement the site with comments and solutions. Book in paper form was published in the publishing house Springer. ISBN 978-3-319-26673-2.

Study 19. Refrigeration Cycles

ValeryOchkov 5 месяцев назад (Показать больше)

In the study a description is given for thermodynamic cycles calculations approaches used in refrigeration, air-conditioning facilities, heat pumps. Given the characteristics of cloud-based functions...

https://www.ptcusercommunity.com/thread/128069?sr=stream&ru=367546

Here is a worksheet of advanced exergetic analysis of simple vapor compression refrigeration cycle

Volodya

Vv-27-adv-ex-eng.xmcd.zip
1.4 MB

vvoloshchuk 31.01.2016 3:58 (в ответ на ValeryOchkov)

Re: Study 19. Refrigeration Cycles

Here is a worksheet of Thermodynamic Calculations of Simple Vapor Compression Refrigeration Cyc

Vv-27-eng.xmcd.zip
1.3 MB

Fig. 10. Screen shot of the web-page of PTC community where a list of MathCad worksheets for calculations of thermal processes in heat pumps are proposed for downloading

4. CONCLUSIONS

The mathematical package Mathcad with Mathcad Calculation Server (Mathcad Net Publisher) allowed to develop a “cloud” server http://twt.mpei.ac.ru/ochkov/VPU_Book_New/mas/eng/index.html for engineers and scientists, who perform computer simulations and modeling of thermal systems, including refrigeration ones.

The server considers an online service that offers data processing over a web-interface, using a software (in this case Mathcad) that runs remotely within the “cloud”.

The introduced technology provides three options (online calculations, download and reference) of using computing programs, which substantially allows to save users` resources (program licenses, rent of space, electricity etc.).

Maple software also provides such possibilities which will be developed and demonstrated in further papers.

4.1. Abbreviations

q – rate of heat transfer;
T – absolute temperature;
p – absolute pressure;
s – specific entropy;
d – prefix meaning differential.

5. REFERENCES

1. DING, G., Review: Recent Developments in Simulation Techniques for Vapor-Compression Refrigeration Systems. International Journal of Refrigeration, 2007, Vol. 30, pp. 1119–1133.
2. M. ARMBRUST et al. A View of Cloud Computing. Communications of the ACM, 53(4), April 2010, pp. 50–58.
3. Website of Maple [referred on the 6th of March in 2016 y.] Link to the internet < http://www.maplesoft.com/products/maple/new_features/>.
4. Website of PTC MathCad [referred on the 6th of March in 2016 y.] Link to the internet <https://mathcadcalc.ptc.com/MathcadApps/PMG_Splash.html>.
5. Website of Maple [referred on the 6th of March in 2016 y.] Link to the internet <http://www.maplesoft.com/products/maplenet/index_aca.aspx>.
6. OCHKOV V., USTYUZHANIN E., KO Ch. K., SHISHAKOV V. Thermophysical Databases: From Tables to Interactive Internet Resources and Cloud Templates. High Temperature, 2015, Vol. 53, No. 4, pp. 515–520.
7. Revised Release on the IAPWS Industrial Formulation 1997 for the Thermodynamic Properties of Water and Steam (The International Association for the Properties of Water and Steam, Lucerne, Switzerland, August 2007), www.iapws.org.
8. OCHKOV V., ORLOV K., ALEKSANDROV A., OCHKOV A**.** Properties of Water and Steam: Network, Open, and Interactive IT-Resources. Thermal Engineering, 2015, Vol. 62, No. 5, pp. 378–387.
9. ALEKSANDROV A., OCHKOV V., ORLOV K. Equations and Computer Program for Calculating the Properties of Gases and Combustion Products. Thermal Engineering, Vol. 52, No. 3, 2005, pp. 221–229.
10. OCHKOV V., ORLOV K., VOLOSHCHUK V. Thermal Engineering Studies with Excel, Mathcad and Internet. Switzerland: springer international publishing, 2016. 307 p. ISBN 978-3-319-26673-2.

CYSENI 2016, May 26-27, Kaunas, Lithuania
ISSN 1822-7554, www.cyseni.com

ANALYSIS OF WIND POWER PREDICTION ERRORS USING DATA OF HIGH RESOLUTION LOCAL AREA MODEL

Giedrius Gecevičius, Mantas Marčiukaitis, Vaidotas Zimnickas
Lithuanian Energy Institute
Breslaujos str. 3, LT-44403 Kaunas – Lithuania
Email: Giedrius.Gecevicius@lei.lt, Mantas.Marciukaitis@lei.lt, Vaidotas.Zimnickas@lei.lt

ABSTRACT

Installed wind power reached 423 MW in 2015 in Lithuania. The main part of wind farms are located in west of Lithuania and intensive development of wind energy reveals power forecasting inaccuracy. Hub height of wind turbines varies between 78 and 134 metres. As a result of that it is very important to forecast wind speed and wind power for the height close to the hub height. Moreover, power curves of wind turbines are different for various wind directions. This paper presents wind speed forecasting accuracy for different heights – 50, 80, 100, 150 metres and different start time of power prediction every 6 hours using High Resolution Local Area Model (HIRLAM). Investigation of wind power prediction errors reveals influence of wind speed direction and wind speed prediction to different height based on topographical and meteorological conditions.

Keywords: sustainable energy, power generation, wind power prediction, HIRLAM

1. INTRODUCTION

Renewable energy sources (RES) are one of the most rapidly growing energy sectors in the world. For power generation renewable electricity shared 22.8% and 16.6% of them is hydro energy, 3.1% wind energy [1]. To compare, installed power capacity of RES in Europe Union also growing, but there lead modern (wind, solar, etc.) renewable energy technologies.

Installed power capacity of wind energy in EU reached 128.8 GW in 2014. The biggest part of installed power capacity brings Germany with 39.2 GW (30.4%), Spain with 23 GW (17.9%), UK with 12.4 GW (9.7%)[2].

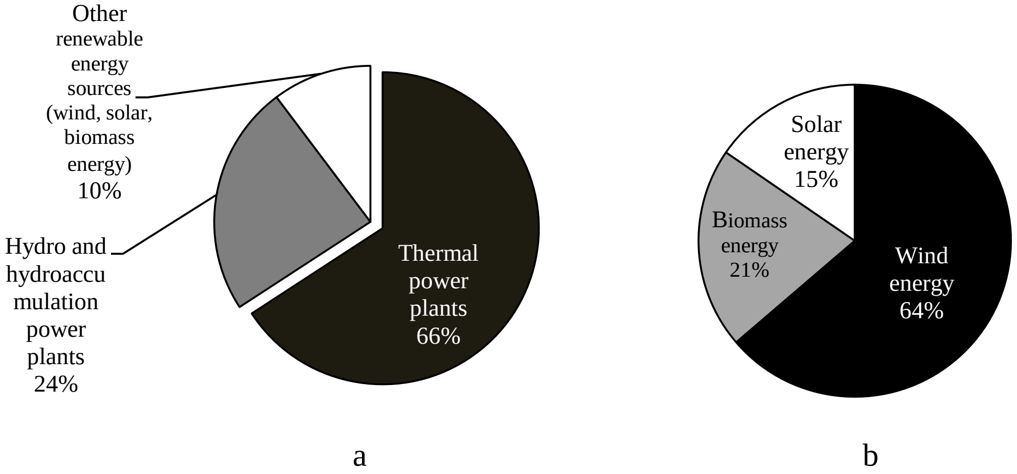

Fig. 1. Distribution of general (a) and renewable energy sources (b) for power generation in Lithuania in 2014 [3]

Despite the fact that Lithuania brings 0.2% of all installed wind power capacity in EU, installed wind power capacity reached 423 MW in the end of 2015 in Lithuania. It brings 64% of other (modern) renewable energy sources in Lithuania (Fig. 1). Rapidly growing wind energy sector makes some problems and issues [4]. One of them is wind power prediction. The main role power forecasting is to predict wind speed and power for a special period. This period consists of short term, midterm and long term forecasting [5]. To predict wind power 3 main types of models are used: statistical, physical and hybrid approach [6, 7]. Statistical models use one or few statistical methods, physical models use atmospheric dynamics process counting principles and hybrid models consist of physical and statistical methods in order to improve forecasting accuracy [8, 9].

Despite improvements of wind power prediction models, annual wind power prediction error reaches 7–8% in Lithuania. To decrease inaccuracy of power prediction it is necessary to analyse power forecasting at different heights, choose optimal suitable parameters, assess the more suitable methods for wind power curves approximation and research adoption of model output statistics for wind power prediction [10–12].

2. OBJECTS OF INVESTIGATION AND METHODOLOGY

To evaluate wind power prediction errors physical approach was used. Wind speed data for power conversion from different heights was taken using High Resolution Local Area Model (HIRLAM) at the point nearest Benaiciai wind farm (Fig. 2). Wind forecasting starts every 6 hours and predict wind speed for 49 hours ahead. Actual data of power output in Benaiciai wind farm is provided by Litgrid (Lithuanian Electricity Transmission System Operator).

Fig. 2. Location of Benaiciai wind farm

Benaiciai wind farm is situated in west of Lithuania and consist of 17 Enercon E82 2MW wind turbines. Hub height of turbines are 98 metres, rotor diameter 82 metres.

In order to compute and compare wind power (from HIRLAM) Enercon E82 2MW power curve was approximated fifth order (equation 1) and sixth order polynomial functions (equation 2):

$$P_A(u) = c_1u^5 + c_2u^4 + c_3u^3 + c_4u^2 + c_5u + c_6\,, \qquad (1)$$

$$P_A(u) = c_1u^6 + c_2u^5 + c_3u^4 + c_4u^3 + c_5u^2 + c_6u + c_7\,, \qquad (2)$$

where:

P_A – predicted wind power (MW),
c_1–c_7 – constants,
u – wind speed (m/s).

Model output statistic (MOS) method was used in order to specify and make more accuracy forecasted power. To do that linear regression was used (equation 3):

$$P_{MOS} = aP + b, \qquad (3)$$

where:

P – power (MW),
a – scaling factor,
b – bias factor.

In order to evaluate inaccuracy of forecasted power, Mean Absolute Error (MAE) was used (equation 4):

$$MAE = \frac{1}{N}\sum_{i=1}^{N}|P_e(i) - P_a(i)|\,, \qquad (4)$$

where:

P_e *– evaluated power (MW),*
P_a *– actual power (MW),*
N – the number of actual power data.

In case of physical power forecasting model wind power prediction consists of three main steps, wind prediction, wind conversion to power and MOS correction [13, 14]. Wind power is predicting by atmospheric model (in this case HIRLAM) in the different heights. Hub height of wind turbines varies between 78 and 134 metres, so it was chosen four wind speed prediction heights – 50, 80, 100, 150 in period 1–9/11/2015.

3. RESULTS AND DISCUSSION

As was mentioned before it is important to describe wind turbine power curve. In order to predict wind power, wind speed was converted to power by approximated power curve on fifth and sixth row polynomials (presented in Fig. 3).

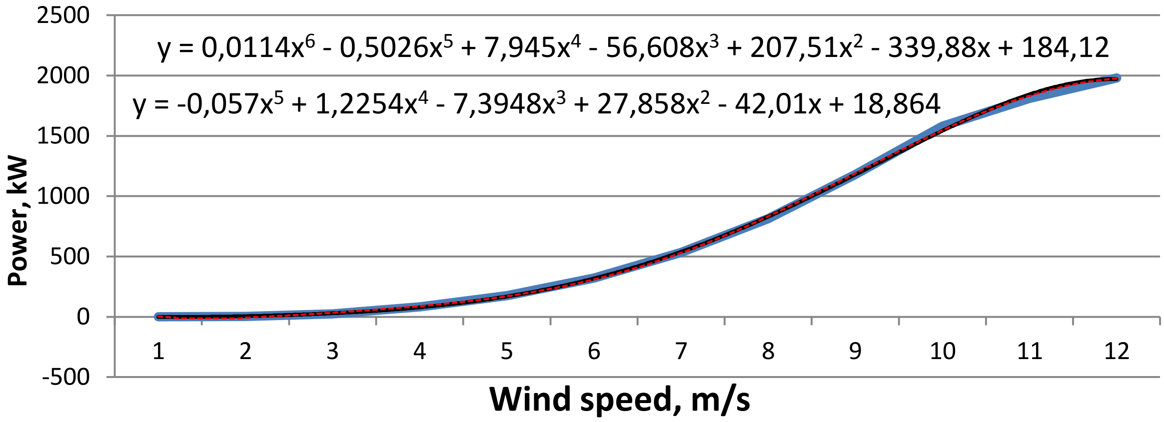

Fig. 3. Approximated power curve of Enercon E82 2MW based on fifth and sixth order polynomial functions (black line – fifth order, red line – sixth order function)

Fifth and sixth order polynomial functions describe part of wind curve, between cut-in and rated power, rated power (12–25 m/s) by maximum power (2000 kW) are described. According to [11, 15] the best results and accuracy of wind speed conversion to power present higher order polynomials.

Model output statistics (MOS) are based by linear regression and reveals relationship between actual and predicted power. Liner function of MOS for 50 m height base on sixth order polynomial in Fig. 4 is presented. Coefficients of linear function make higher accuracy of power prediction.

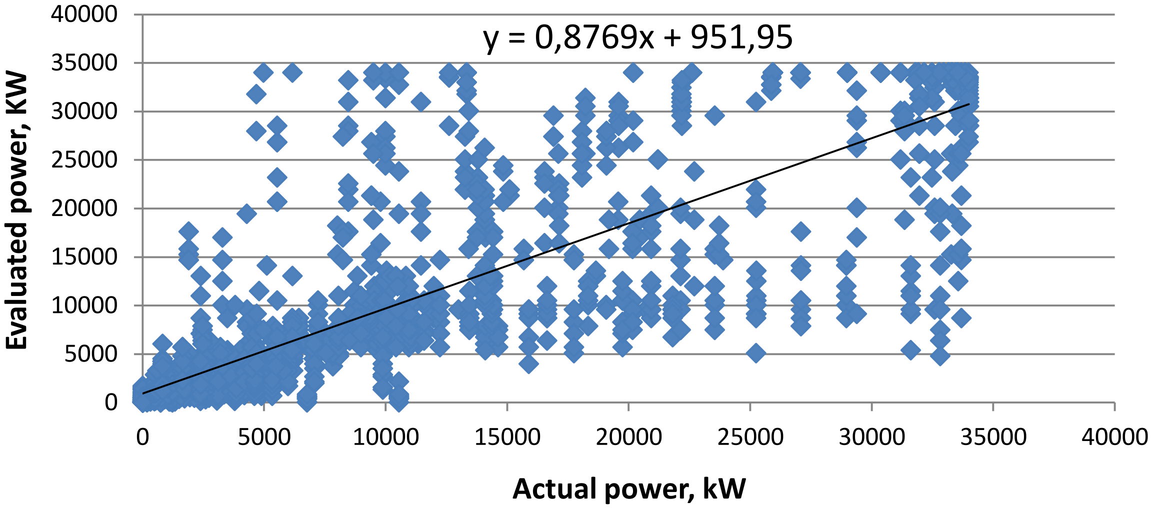

Fig. 4. Relationship between actual and predicted wind power at 50 m height

As was mention before wind power was predicted to the four different heights. Wind power at 50 m height based fifth order polynomial function makes 7.7% mean absolute error (MAE) and lowest error was 5.1% 44 prediction hour, the highest error was 9.8% 12 prediction hour. To compare, the same height with six order polynomial function presented 7.8% MAE, with the lowest error 5.2% 38 prediction hour and the highest 9.5% 12 and 23 prediction hour (Fig. 5). The difference between forecasting errors was 0.1% and that shows, both polynomial functions acceptable for power prediction.

However, both trend lines decrease approximately 2% (Fig. 5) and that indicate inertia of atmospheric dynamic processes in lower height.

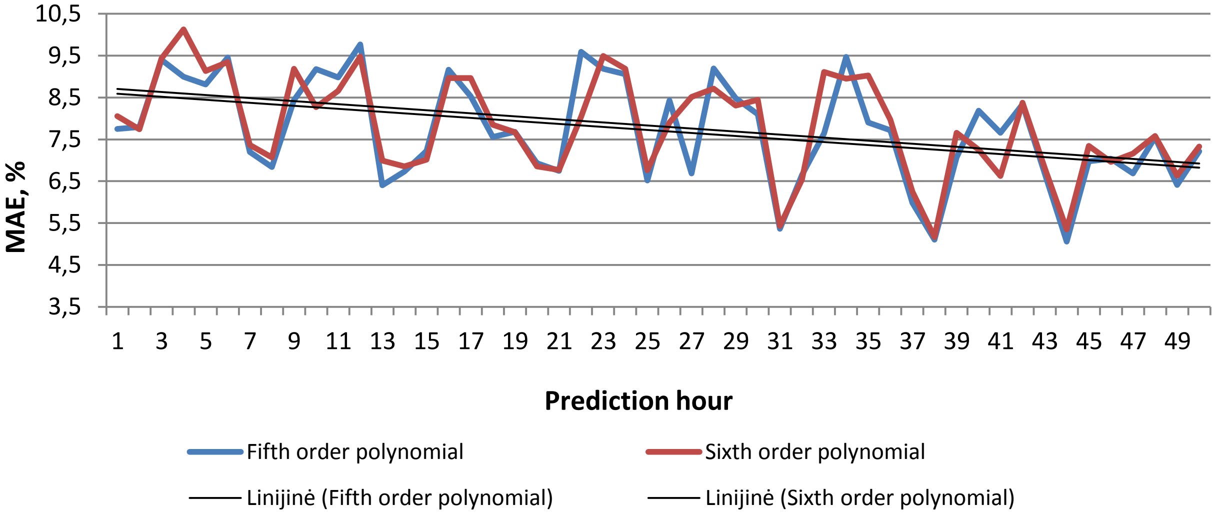

Fig. 5. Wind power prediction at 50 m height based on fifth and sixth order polynomial functions

Wind power prediction at the 80 m height presented in Fig. 6. Average power forecasting MAE based on fifth and sixth order polynomial functions are 6.9% and 7.1% respectively. Maximum values of MAE are 8.5% 10 forecasting hour (fifth order pol.) and 9.7% 10 prediction hour (sixth order pol.). Lowest MAE fixed 5.1% 21 hour and 5.6% 43 forecasting hour based on fifth and sixth polynomial functions respectively. Both trend lines decreases at 80 m height. It was noticed atmospheric processes stability and inertia also.

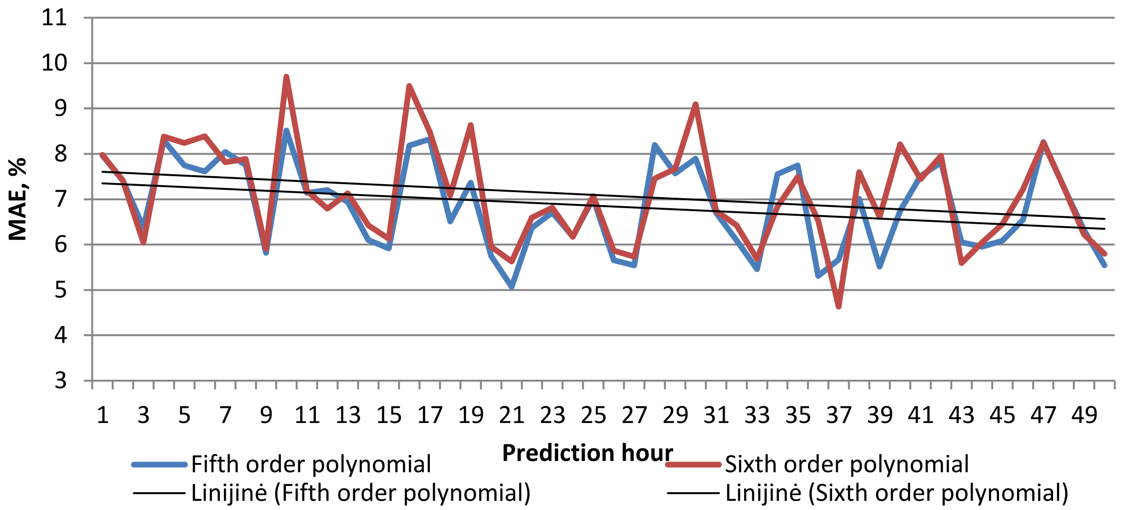

Fig. 6. Wind power prediction at 80 m height based on fifth and sixth order polynomial functions

Wind power prediction height at 100 m is closest hub height of analysed wind turbine 98 m. MAE at the same height based on fifth and sixth order polynomial functions gives 6.8% and 7.1% averages values. Maximum MAE of fifth order polynomial was 9.4% 46 prediction hour and minimum 4.2% 33 prediction hour. Highest value based on sixth order poly was 10% 46 hour and lowest value 3.1% 33 prediction hour (Fig. 7). Despite the fact that average MAE were the lowest at 100 m, but the variations of all errors there are biggest. However, in the contrary at 50 and 80 m, MAE at 100 m increased by 1–2% in analysed period.

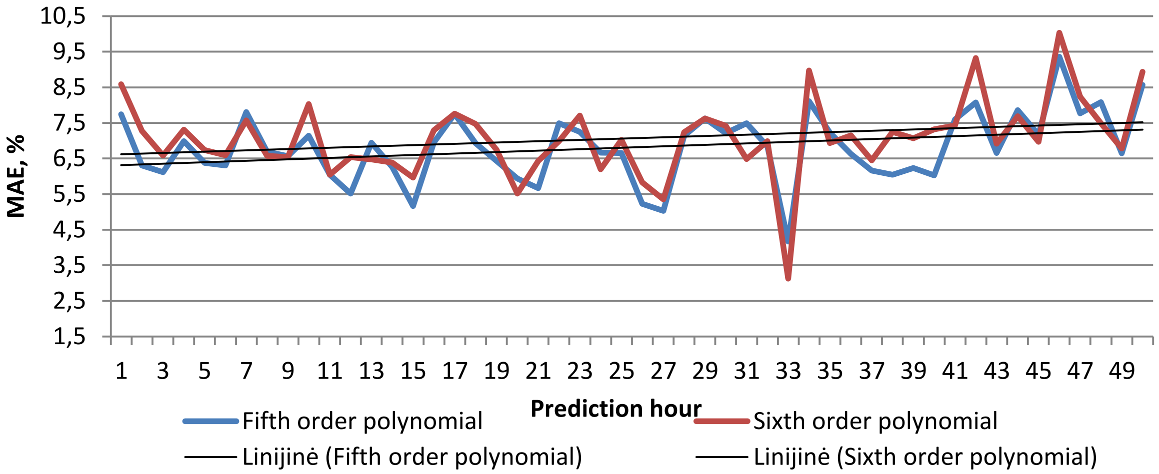

Fig. 7. Wind power prediction at 100 m height based on fifth and sixth order polynomial functions

Wind power at 150 m height was forecasted also. Results indicate that the average MAE based on fifth order poly was 7.3%, highest value 9.9% 34 prediction hour, lowest – 5% 50 prediction hour. To compare MAE based on sixth order pol. average value 8.6%, highest 16.5% 10 prediction hour, lowest 5.8% 11 prediction hour (Fig. 8). MAE between 10–11 hour decreased 3 times. In general, mean absolute error significant increase at this height (app. 2%) in analysed period.

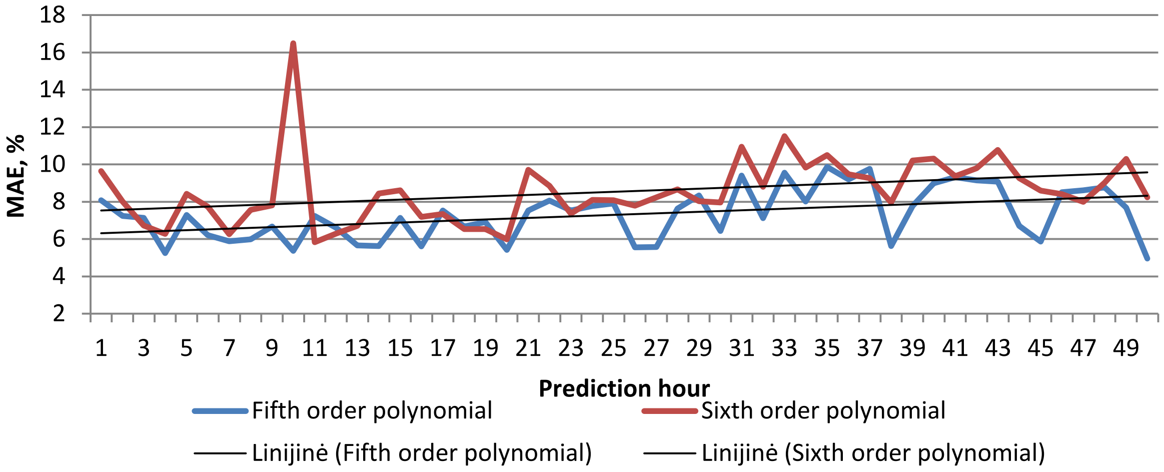

Fig. 8. Wind power prediction at 150 m height based on fifth and sixth order polynomial functions

To compare all heights bias (average of fifth and sixth order polynomials), the best results present power prediction at 100 m with 6.94% error. However, differences between 80 m and 100 m are insignificant – 0.02%. The worst results at 50 and 150 m height were indicated with MAE 7.76% and 7,96% respectively (Table 1).

Table 1. Summarized MAE of wind power prediction

Wind prediction height	Average MAE, %	Average MAE of fifth and sixth pol., %	Average MAE based on fifth order pol., %	Average MAE based on sixth order pol., %
50_5	7.71	7.76	7.17	7.64
50_6	7.81			
80_5	6.85	6.96		
80_6	7.08			
100_5	6.81	6.94		
100_6	7.07			
150_5	7.31	7.96		
150_6	8.60			
Average	7.41			

It was noticed that fifth order polynomial function better approximate analysed power curve than sixth order polynomial function and makes ability to predict wind power more accuracy. To conclude, should be mention that analysed MAE (in period 1–9/11/2015) with the 7.41% is close to annual wind power prediction error in Lithuania.

4. CONCLUSIONS

- The lowest wind power prediction error (MAE) with 6.94% at the height (100 m) is fixed. It is height closest to the wind turbines hub height The worst value was 7.96% at 150 metres height.
- The better performance for wind power prediction was obtained based on fifth order polynomial function than the sixth order polynomial.

- Average wind power forecasting errors decreased in 1–2% limits at 50 and 80 metres height in analysed period, comparing the begin and the end of the prediction horizon. Contrary, MAE of wind power prediction at 100 and 150 metres height increased approximately 1–2% at the same period.
- The smaller variation of power prediction errors could be revealed in longer period of data analysis.

5. REFERENCES

1. REN21. Renewables 2015 Global Status Report. 2015.
2. THE EUROPEAN ENERGY ASSOCIATION (EWEA). Wind in power 2014 European statistics. 2015.
3. Lithuanian Electricity Transmission System Operator Litgrid. 2015. (Available online under: http://www.litgrid.eu/index.php/tinklo-pletra/lietuvos-elektros-perdavimo-tinklo-10-metu-pletros-planas/113. Accesed October 20, 2015).
4. YANG, H., QIU, J., MENG, K., ZHAO, J. H., DONG, Z. Y., & LAI, M. Insurance strategy for mitigating power system operational risk introduced by wind power forecasting uncertainty. *Renewable Energy*, 2016, Vol. 89, p. 606–615.
5. KUSIAK, A., ZHANG, Z., VERMA, A. Prediction, operations, and condition monitoring in wind energy. *Energy*, (2013). Vol. 60, p. 1–12.
6. LAZIĆ, L., PEJANOVIĆ, G., ŽIVKOVIĆ, M., ILIĆ, L. Improved wind forecasts for wind power generation using the ETA model and MOS (model output statistics) method. *Energy*, 2014, Vol. 73, p. 567–574.
7. LEI, M., SHIYAN, L., CHUANWEN, J., HONGLING, L., YAN, Z. A review on the forecasting of wind speed and generated power. *Renewable and Sustainable Energy Reviews*, 2009, Vol. 13, p. 915–920.
8. LYDIA, M., KUMAR, S. S., SELVAKUMAR, A. I., PREM KUMAR, G. E. A comprehensive review on wind turbine power curve modeling techniques. *Renewable and Sustainable Energy Reviews*, 2014, Vol. 30, p. 452–460.
9. MCKENNA, R., HOLLNAICHER, S., OSTMAN, V. D., LEYE, P., FICHTNER, W. Cost-potentials for large onshore wind turbines in europe. *Energy*, 2015, Vol. 83, p. 217–229.
10. OLAOFE, Z. O., & FOLLY, K. A. Wind energy analysis based on turbine and developed site power curves: A case-study of Darling city. *Renewable Energy*, 2013, Vol. 53, p. 306–318.
11. ONER, Y., OZCIRA, S., BEKIROGLU, N., SENOL, I. A comparative analysis of wind power density prediction methods for Canakkale, Intepe region, Turkey. *Renewable and Sustainable Energy Reviews*, 2013, Vol. 23, p. 491–502.
12. PINSON, P., NIELSEN, H. A., MADSEN, H., KARINIOTAKIS, G. Skill forecasting from ensemble predictions of wind power. *Applied Energy*, 2009, Vol. 86(7-8), p. 1326–1334.
13. WANG, X., GUO, P., HUANG, X. A review of wind power forecasting models. *Energy Procedia*, 2011, Vol. 12, p. 770–778.
14. ZHANG, Y., WANG, J., WANG, X. Review on probabilistic forecasting of wind power generation. *Renewable and Sustainable Energy Reviews*, 2014, Vol. 32, p. 255–270.
15. ZHAO, X., WANG, S., LI, T. Review of evaluation criteria and main methods of wind power forecasting. *Energy Procedia*, 2011, Vol. 12, p. 761–769.

CYSENI 2016, May 26-27, Kaunas, Lithuania
ISSN 1822-7554, www.cyseni.com

INVESTIGATION OF SPENT MUSHROOM COMPOST AS AN ALTERNATIVE WASTE-BASED FEEDSTOCK FOR BIOFUEL PRECURSOR PRODUCTION VIA HYDROTHERMAL LIQUEFACTION

L. Jasiūnas
Aalborg University – Department of Energy Technology
Pontoppidanstræde 101, 9220 – Denmark
Email: ljasiu14@student.aau.dk

ABSTRACT

The work investigates a new potential feedstock source in terms of feasibility for hydrothermal liquefaction (HTL) driven bio-crude production. Specifically, the focus is set on utilizing a readily available bio-waste stream from the agricultural sector. Spent mushroom compost (SMC) is a by-product from the mushroom farming industry and is estimated to add up to over 3.4 million metric tonnes globally. It is considered as a feedstock for HTL conversion due to its organic nature (i.e. straw, horse manure and sphagnum) and ample availability. The feedstock has been analysed in terms of current utilization methods and availability. Furthermore, locally acquired samples (from St. Restrup Champignon, Danmark) were analysed chemically and used throughout the experimental phase in a supercritical micro batch HTL setup. The potential of feedstock (SMC and Aspen wood) co-liquefaction is also investigated. The resultant products were evaluated via yield, elemental, FT-IR and GC-MS analyses. Biocrude yields above 50 wt. % on DAF feedstock basis were observed. The study also includes discussions on de-ashing strategies, one of which – co-liquefaction led to ~20 wt. % reduction in post reaction solids.

Keywords: Spent Mushroom Compost, Hydrothermal Liquefaction, biofuel, waste utilization, biocrude

1. INTRODUCTION

Rising climate concerns urge new research and development to pay attention to how new technologies will affect the environment. Such ideology includes considering the whole life cycle of a product/process. One way of identifying global impact is via greenhouse gas (GHG) emission analysis.

In its many forms (i.e. road, air, ship and rail), the transportation sector can be referred to as the intermediate GHG generator due to its large participation in all other carbon dioxide (CO_2), methane (CH_4) and nitrous oxide (N_2O) heavy industries (e.g. electricity and heat production, industrial processes, logistics and agriculture).

The International Energy Agency (IEA) states that the 2015 global road CO_2 emissions were near to 6 billion tonnes of CO_2 equivalent [1]. Humanity must reach a level of 3.9 billion tonnes of road transport emitted CO_2 equivalent to fulfil the demands proposed in the IEA's 2^{o}C scenario (an analogue to the World Energy Outlook's (WEO) 450 scenario). The plan results in an emission reduction of just over 2 billion tonnes of CO_2 equivalent until the year 2050 [1].

Extensive electrification of the energy sector is considered to be a viable solution for effective GHG emission reduction. Besides the already accepted electric resources for both energy generation and land transport needs, bio-energy will undoubtedly play an important role in the future's energy systems worldwide due to the well-developed solid and liquid carbon based fuel infrastructure. Especially when considering heavy transport (e.g. air transport and the shipping industry).

IEA predicts that despite dramatic changes in the energy supply network, the transport sector will still be dominated by crude oil derivatives in 2050 – a corresponding fraction of 62.9%, compared to the current 96.3%. The same analysis expects an estimated growth in biofuel consumption of 21.1 EJ/year. A clear incentive for an active development of renewable biobased fuels [2].

1.1. Biomass resources

The term ’biomass’ envelopes numerous materials, matter which is either living or has recently been. Lignocelluloses derived from well-developed industries such as agriculture and forestry are often regarded as suitable precursors for bio-energy. However, it is not uncommon to include animal and municipal wastes in the definition of renewable biomass [3]. The resource can be further categorized into wet or dry – according to the specific moisture content, and purpose-grown or waste biomasses.

The capacity of biomasses to be converted into multi-phase fuels (i.e. gaseous, liquid and solid) is seen as a key advantage when considering the feasibility of energetic biomass utilization. Furthermore, the fact that neither lignocellulosic nor waste biomasses, specifically, are suitable for dietary human consumption, eliminates the potential issues addressed by the ’food versus fuel’ debate. Additionally, some types of biomass (e.g. micro- and macroalgae) are renown for their ability to grow on non-arable lands. That, combined with the large global abundance of biomasses, serves as a valid basis for investigating whether the resource qualifies for efficient energy production [4].

The Intergovernmental Panel on Climate Change (IPCC) expects that dedicated biomass, despite often being a food competing resource, will generate most material in 2050. The more sustainable dedicated biomass grown on marginal lands, together with forest-derived biomass also will add a significant portion of the overall resource. Whereas agricultural residues will have a lesser influence mainly due to soil amendment strategies that often compete with energy production purposes [5].

The study aims to bring an alternative biomass resource into consideration. One that is rarely included in global estimations but is evidently present. In 2007, the global mushroom production resulted in 3.4 million metric tonnes of the foodstuff worldwide. China held 47% of the worldwide share [6]. It is said that for each kilogram of farm grown button mushrooms (Agaricus bisporus), approximately 5 kg of spent mushroom compost (SMC) are generated. That potentially led to ca. 17 million metric tonnes of the byproduct in 2007. SMC is commonly used as a low cost commercial private scale fertilizer. Its popularity is believed to be a direct result of high availability and low cost. In Denmark, the current bulk price for private use is < 27 EUR/m^3. Spreading SMC on close-by farm fields is often seen as a viable means of disposal for mushroom growers. For instance, 72% of Ireland’s SMC were applied directly on farmlands in the year 2000 [7].

A survey among the three mushroom farms in Denmark was carried out as a part of this work. The corresponding SMC availability is ca. 12 000 tonnes of SMC per year. Whereas in Europe, the number is estimated to be < 47 million tonnes per year, which could potentially lead to < 130 000 tonnes of available feedstock per day (figures adapted from [8]).

1.2. Hydrothermal liquefaction

Hydrothermal liquefaction (HTL) is a thermochemical conversion route where a feedstock, typically biomass, is converted to a bio-crude in the presence of water. As shown in Fig. 1, prior to the conversion, the reactants (i.e. feedstock, catalyst and water) are combined into a *pumpable* slurry. This stream is then subjected to high temperatures and pressures for a predefined reaction time. At such severe conditions water acts as a polar solvent, breaks chemical bonds and reforms the feedstock to a new structure, namely, the high quality biocrude.

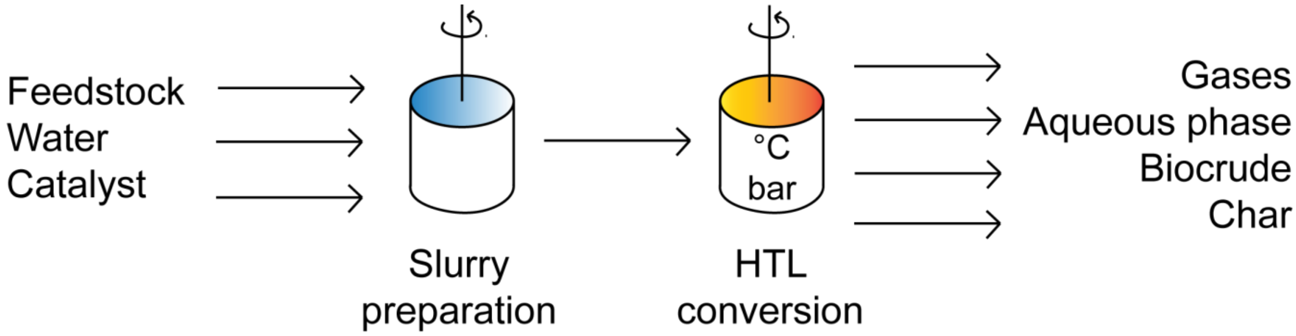

Fig. 1. A simplified process chart to visualize the inputs and outputs involved in HTL conversion

Potential synergy between waste feedstock streams such as SMC and HTL is evident as this study claims that the process is able to convert the low cost feedstock into a high value liquid fuel. Furthermore, the high moisture content of the compost (measured > 50 wt. %) is preferable for the water-assisted conversion, contrary to disadvantageous alternative energetic utilisation methods such as pyrolysis or direct combustion.

1.3. The objective

This study aims to contribute to the positive development of the transportation sector. Herein the main objective is to investigate whether the potential of utilising SMC for HTL derived bio-crude production is indeed promising. This is expressed in terms of biocrude yields and quality, and the characteristically problematic solid by-products. The study explores supercritical catalysed and non-catalysed HTL at 400^{o}C and up to 300 bar with a retention time of 15 min. Co-liquefaction with Aspen wood is analysed. Furthermore, the discussion is expanded to feedstock de-ashing and HTL by-product phase utilization, namely in terms of carbon recovery.

2. MATERIALS AND METHODOLOGY

The spent mushroom compost (SMC, also often defined as spend mushroom substrate (SMS)) used in this study was acquired from a local Danish mushroom farm (St. Restrup Champignon). The compost was gathered shortly after disposal at the facility. Hence it is believed to be highly representative in terms of composition and state. SMC samples were analysed in-house and the characteristics are compiled in Table 1.

Thermogravimetric (TGA), elemental CHN, fibre and inductively coupled plasma (ICP) analyses were carried out in order to clearly define the feedstock at hand. Here, the paper refers mainly to high farm-to-farm composition variance of the waste product SMC. Therefore, the reader is advised not to interpret this analysis as a general composition of SMC but rather as one possible compositional variation. Bomb calorimetry was used to determine the high heating value (HHV). Ash content was determined during the proximate TGA analysis. Finally, elemental sulphur is adapted from literature [9].

The characteristics of the second co-liquefaction feedstock, Scandinavian Aspen wood (Populus tremula, AW), can also be seen in Table 1. Similarly to the SMC characterisation procedure, the fibre composition of AW was measured by the Van Soest method, using a Foss Fibertec^{TM} analyser. Whereas the ash content is measured after combustion at 575^{o}C, as defined in [10].

Table 1. Extensive characterisation of the two used feedstocks: spent mushroom compost (SMC) and Aspen wood (AW)

Parameter [unit]	SMC	AW
As received basis		
Bulk density [kg/m^3]	334.32	277.53
Total moisture [wt. %]	52.14	7.35
Pretreatment	-	Mill, < 1mm
Dry basis		
Proximate analysis:		
Total moisture [wt. %]	3.15	2.75
Volatile matter [wt. %]	42.21	74.92
Fixed carbon [wt. %]	8.84[a]	20.04[a]
Ash [wt. %]	45.8	2.29
HHV [MJ/kg]	11.68[b]	18.64[b]
Pretreatment	Mill, < 3mm	-
Fibre analysis:		
Cellulose [wt. %]	41.18	47.14
Hemicellulose [wt. %]	-[c]	19.64
Lignin [wt. %]	21.24	22.11
Acetone and water extractives [wt. %]	12.76	6.63
Dry ash-free basis		
Elemental analysis:		
Carbon [wt. %]	58.17	50.39
Hydrogen [wt. %]	5.6	6.19
Nitrogen [wt. %]	2.75	0.19
Sulphur [wt. %]	1.96[d]	-
Oxygen [wt. %]	33.49[a]	43.23[a]
Ash analysis: [wt. ‰][e]		
Ca	92.48	148.27
K	26.82	71.97
Mg	4.79	15.49
P	3.77	2.35
Na	3.77	11.99
Fe	3.61	9.18
Al	2.84	11.99
Mn	-	5.66
a – calculated by difference, d – measured via bomb calorimetry, c – unable to determine with the used procedure, d – adapted from [9], e – element concentrations below 2 *‰ are excluded from the table.*		

Finally, the potential of a pretreatment washing step was investigated via vacuum-assisted SMC filtration. FOSS Cold Extraction Unit 1021 was used together with FOSS P2 filtration crucibles (pore size: 40–100 μm). Acetone (Cab-Dan Aps, purity: 95–100%) and de-ionised water were the two used washing liquids.

2.1. Experimental procedure

All experiments were carried out in stainless steel (grade 316) micro reactors, each reactor having an operational volume of 12 mL. In total, 7 independent experiments were conducted in triplicates.

The effects of feedstock composition (SMC to AW mass ratio) variation were investigated. The feedstock composition was ranged from pure SMC to pure AW. Whereas the total feedstock mass loadings of 20% (±3%) were used, and all reactions were carried out at 400^oC ($\pm 5^oC$). Furthermore, the effect of catalyst (10 wt. % Potassium carbonate (K_2CO_3), Sigma-Aldrich, purity: ≥ 99%) addition on HTL of pure SMC was analysed at the same operational conditions.

When the feedstock slurry required mixing, SMC was combined with AW and distilled water to form the predefined feedstock slurry. A total of 5 g (±0.2 g) of slurry was then loaded into each of the reactors. High pressure nitrogen gas was used to simultaneously leak test (80 bar) and purge the reactors to evacuate atmospheric oxygen. The reactors are pre-pressurized to < 20 bar. Hereafter, two reactors were mechanically coupled and, each together with a independent thermocouple, mounted to an agitator providing mechanical mixing of the reagents inside the reactors while being processed. The two reactors were then submerged into a preheated, fluidised sand bath and held for 15 minutes of retention time. Maximal reaction pressures varied within the range of 260 and 300 bar. In this study, retention time is defined as the time that passes between the moment when the reactors have reached the preset temperature of 400^oC ($\pm 3^oC$) and the instance of manually submerging the reactors into the cool ($< 20^oC$) water bath.

As baseline experiments, pure SMC and AW were processed in alkaline aqueous media. For these experiments, the reactants were also mixed in distilled water at a fixed feedstock mass loading of 20% of the total slurry mass. K_2CO_3 was added as the base catalyst to make use of the already well known char formation reducing properties of alkaline liquefaction [11, 12]. The mass of added K_2CO_3 amounted to 10% (±3%) of the total mass of feedstock (i.e. pure SMC and AW, respectively).

After 15 minutes of retention time, the reactors were cooled by quenching in water for minimum half an hour, and the gaseous products were vented via top mounted valves. The remaining products consisted of solid residues, referred to as char or hydrochar, biocrude and an aqueous phase. The reactors were washed with acetone in order to obtain a homogeneous liquid phase mixed with char. The liquid phase was then separated from the solids via vacuum assisted mechanical filtration (VWR filters, particle retention: 5–13 μm). Char, defined as the acetone insoluble solid fraction was then obtained by weighing the solid residue after drying for at least 24 hours at 105^oC. Acetone was evaporated from the homogeneous liquid fraction and the biocrude fraction was manually extracted after centrifuge-aided phase separation. The higher density extracts were defined as biocrude.

Often a secondary, water insoluble, solvent is used throughout the separation procedure when working with micro reactors to reduce the experimental error involved in manual biocrude, aqueous phase separation. Diethyl ether (DEE), a relatively low polarity solvent was used in previous studies [13]. In general, the use of solvents is shown to increase the recorded biocrude yields due to enhanced extraction from the aqueous effluent. However, this in turn leads to a decrease in biocrude quality, hindered by the lower value water soluble compounds [14]. In a continuous setup, a solvent-free separation is always preferable due to economics, not-supporting fossil derivatives and retaining volatile biocrude constituents [15].

Biocrude yields were calculated on a dry, ash-free (DAF) basis according to equation (1). Similarly, char yields were calculated on a dry basis. The experimental error is shown to reside below 10%.

$$Yield_{Biocrude} = \frac{Weight\ of\ biocrude}{Weight\ of\ DAF\ feedstock} \tag{1}$$

Fourrier transform infrared spectroscopy (FT-IR) was used for confirming experimental repeatability both in the resultant aqueous by-products and biocrudes.

Elemental C, H, N and O analysis was carried out on Perkin Elmer 2400 II Series analyzer. For each of the obtained biocrudes, an effective atomic hydrogen-to-carbon ratio (H/C_{eff}) was calculated according to equation (2).

$$H/C_{eff} = \frac{H - 2O}{C} \tag{2}$$

here H, O and C denote elemental amounts in moles.

Volatiles, fixed carbon and ash were determined using a Discovery TGA from TA Instruments at the following ramp profile: room temperature to 600°C at 5 °C/min, then the chamber gas is changed from nitrogen to oxygen and the temperature is raised to 1000°C at 5 °C/min. The reader is advised to note that the auto-sampler is not operating in an oxygen-free environment, hence the evident presence of moisture in the pre-dried (oven, 105°C) samples.

Whereas due to the small amounts of produced biocrude, HHVs were calculated according to the fuel higher heating value determination formula proposed by S.A. Channiwala and P.P. Parikh [16]:

$$HHV = 0.3491 \cdot C + 1.1783 \cdot H + 0.1005 \cdot S - 0.1034 \cdot O + -0.0151 \cdot N - 0.0211 \cdot Ash \tag{3}$$

Finally, gas chromatography - mass spectrometry (GC-MS) analyses of all biocrude samples were carried out on a Thermo Scientific Trace 1300 ISQ GC/MS system. The samples were diluted with 2 ml of DEE and subjected to a fixed predefined temperature ramping profile: 40°C to 300°C at 10 °C/min. 18 largest peaks (by integrated peak area) per sample were identified. Compounds associated with the solvent are excluded from the interpretation.

3. EXPERIMENTAL RESULTS AND DISCUSSION

A total of 7 experiments were conducted to assess processing aspects and synergies when co-liquefying SMC and aspen wood into a biocrude. Table 2 summarises the experimental conditions of the procedure in terms of catalyst usage and feedstock mixing ratio as the two varied parameters throughout the study.

3.1. Biocrude composition

A comparative biocrude GC-MS analysis was carried out. The results show that all products are compositionally dominated by phenolic compounds and straight, and cyclic ketones. All biocrudes were found to primarily consist of light hydrocarbons (C6-C9 carbon range), while AW derived products showed higher occurrences of heavier hydrocarbons (e.g. up to C19-C20 carbon range) on top of the phenolic dominance.

As shown in Table 2, all HTL biocrudes exhibited HHV values within ±1.36 MJ/kg. However, as shown in Fig. 2, SMC dominated products were superior in terms of H/C_{eff} . This is supported by higher hydrogen content. No clear trends were established with regards to oxygen content, where the values averaged out at 14.26 wt. % and never exceeded 17.75 ±0.1 wt. %.

A modified Van Krevelen diagram was used to graphically represent the produced hydrochars, biocrudes, the used raw feedstocks and conventional fossil fuels for reference (Fig. 3). It is clear that HTL is a major processing step towards producing competitive bio-fuels, however, the need for upgrading is obvious. Both in terms of hydrogen addition (low H/C_{eff}) and oxygen elimination (high O/C). Whereas the high O/C ratio of the hydrochar indicate adsorption potential.

Table 2. Experimental summary. Processing conditions, biocrude and hydrochar yields, H/C_{eff} ratios and HHVs of the produced biocrudes are shown

	Experimental runs						
Conditions:	1	2	3	4	5	6	7
SMC:AW ratio	1:0	1:0	2:1	1:1	1:2	1:3	0:1
Catalysed	No	Yes	Yes	Yes	Yes	Yes	Yes
Results:							
Biocrude yield [wt. %][a]	51.80	53.67	24.23	20.16	18.72	15.43	20.66
Hydrochar yield [wt. %][b]	49.15	43.04	42.63	40.48	28.28	23.91	23.36
Biocrude H/C_{eff}	1.13	1.47	1.32	1.02	0.96	0.96	0.96
Biocrude HHV [MJ/kg][c]	34.71	34.33	34.70	34.76	34.59	32.99	34.31
a – based on DAF feedstock, b – based on dry feedstock.							

3.2. Catalytic effect

Catalytic effects of adding K_2CO_3 were investigated in terms of char reduction. 10% of the catalyst (i.e. 0.1 g for every gram of dry feedstock) led to an alkaline slurry and a 5.9% decrease in char. This result indicates that SMC, a pH neutralised feedstock, can benefit from an alkaline HTL reaction medium in terms of enhanced biocrude production, as described in the research group's previous work [13].

3.3. Feedstock washing

The fibre analysis procedure was shown to be incapable of defining the hemicellulose content of SMC. Two hypotheses arise when discussing why this might have happened. Firstly, the procedure was originally created for animal feed determination but is widely used for raw lignocellulosic feedstock analysis as well [17]. Whereas this study deals with a waste material. Fresh mushroom compost (i.e. prior to mycelium inoculation) consists mainly of straw – an agricultural waste, supplemented by horse manure – an animal husbandry waste, and sphagnum as the thin casing layer. Due to the sugar-based composition of holocellulose, its degradation throughout the fruiting period of A. bisporus is much more significant when compared to the aromatic lignin structures. Literature claims that hemicellulose is degraded by as much as < 67%. Meanwhile, cellulose and lignin losses are reported to be < 30% and < 16%, respectively [18].

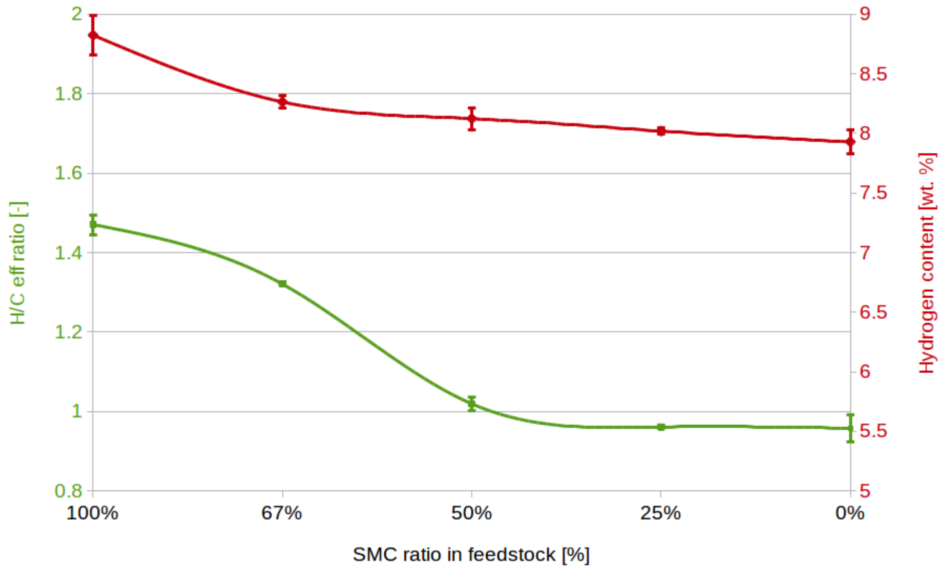

Fig. 2. Calculated H/C$_{eff}$ ratios and corresponding measured hydrogen levels of the produced biocrudes. Results from run 5 are not shown due to high deviations

In the end, besides the expected low hemicellulose content, the large amount of water and acetone extractives (12–14 wt. % of the total sample) might have compromised procedure in terms of hemicellulose determination. Not to mention the significant ash content which would not be encountered in feed materials and raw lignocelluloses. Therefore, the study recommends using a different procedure in order to establish the correct hemicellulose content of SMC.

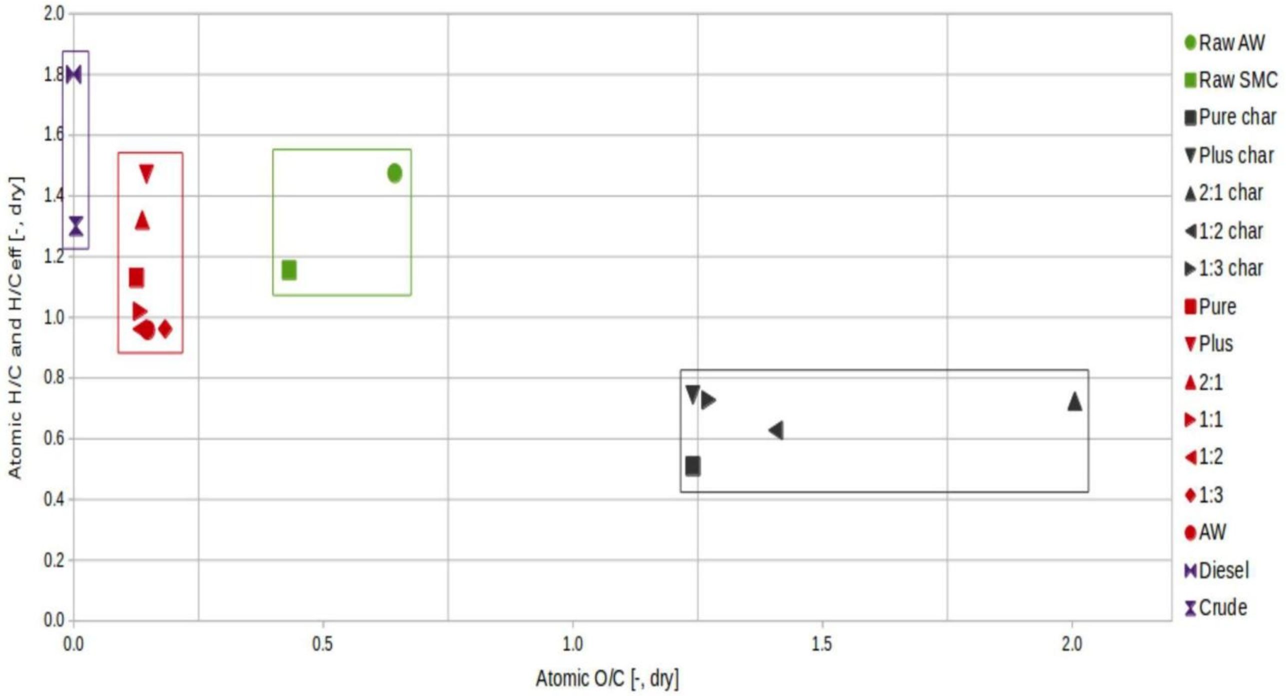

Fig. 3. Material quality characterisation in terms of atomic H/C$_{eff}$ and O/C ratios, using a modified (H/C$_{eff}$ instead of H/C) Van Krevelen diagram. Here, green – dry feedstock, black – produced hydrochar, red – produced biocrude, purple – fossil fuels for reference

Based on the extensive extraction procedure, feedstock washing was considered as a pretreatment step prior to making the reactant slurry. Washing experiments were carried out with two liquids independently: acetone and deionised water. Samples were pre-dried at 105°C before washing with 25 ml of the liquid five times with 5 min of settling time and vacuum filtration (pore size: max.100 µm) in between the runs. The washing was carried out at room temperature. Then, the sample was dried and reweighed. Acetone washing lead to 2.57% mass loss while the identical procedure with water resulted in a decrease of 12.05%. The samples were then ashed at 575°C in order to investigate the de-ashing capabilities of the two procedures. Interestingly, despite the clear differences in mass loss, similar ash reductions were recorded: 1.55% and 1.79% for acetone and water washing, respectively.

3.4. Co-processing SMC and AW

As Table 1 shows and subsection 3.3 emphasizes, raw SMC contains a significant amount of inorganics. The 45.8 wt. % determined by TGA are not accurately representative even for the material used in this study as other ashing methods (775°C and 575°C furnace ashing) carried out in parallel, showed ash content ranging from 35.46 wt. % up to 49.22 wt. %, respectively. Nonetheless such high figures can play an important role when the feedstock is considered for continuous HTL processing. Effective evacuation of the solids is vital in such systems. Operational downtime due to blockages, higher equipment costs and lower biocrude yields are among the major issues with high char operation.

One of the investigated mitigation strategies was co-liquefying SMC with low char yielding lignocellulosic waste materials (i.e. AW sawdust in this study). Table 2 and Figure 4 show that mixing SMC with AW does indeed lead to significantly reduced char formation. Throughout the catalysed co-liquefaction runs, the char decreased from 43.04 wt. % down to 23.36 wt. %. Taking measurement deviations into account (max. standard deviation of 9.46%), char yield development does resemble a linear trend. However, a possible discrepancy is seen in between run 3 and 5, where the linear development is interrupted. This might indicate that the effects of such co-processing are not entirely limited to mixing. Chemical conversion differences, driven by specific feedstock constituent domination are a possibility. The char yields decrease linearly before and after this sudden change, indicating pure mixing effects under these conditions.

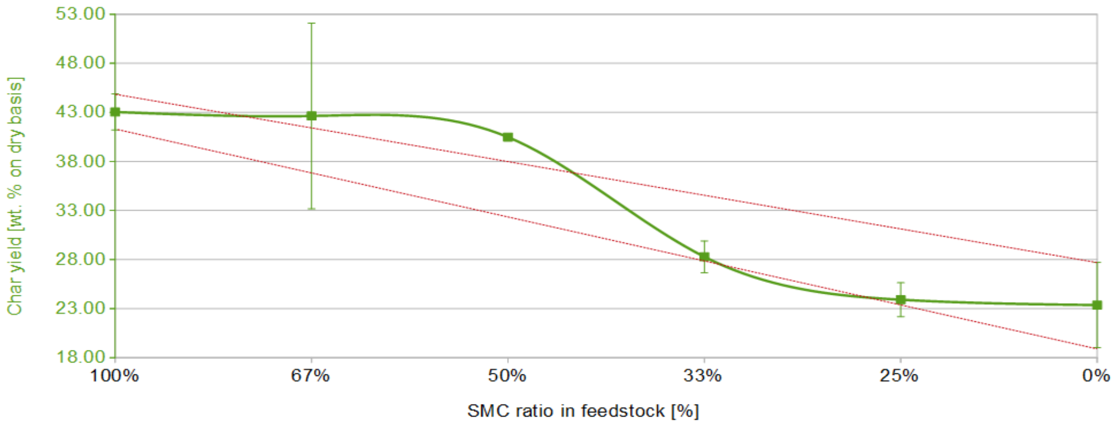

Fig. 4. Char yield measurements throughout the experimental range. Here the dotted red lines visualise the deviation-based expected char formation limits when only linear mixing effects are considered

Furthermore, the baseline pure SMC and AW experiments (runs 2 and 7) show that under these conditions, both feedstocks are compatible with the technology and produce all of the expected four multi-phase products. This is confirmed by checking the product mass balance: all values were within 10% compared to the slurry loading. Repeating the experimental procedure with larger scale batch equipment is seen as a method to minimise this error margin.

As a shown in Fig. 5, biocrude yields decrease with smaller fractions of SMC in the feedstock slurry. These findings imply that the substance could be considered as a full alternative or at least an additive to conventionally accepted forestry residue feedstock for biocrude production.

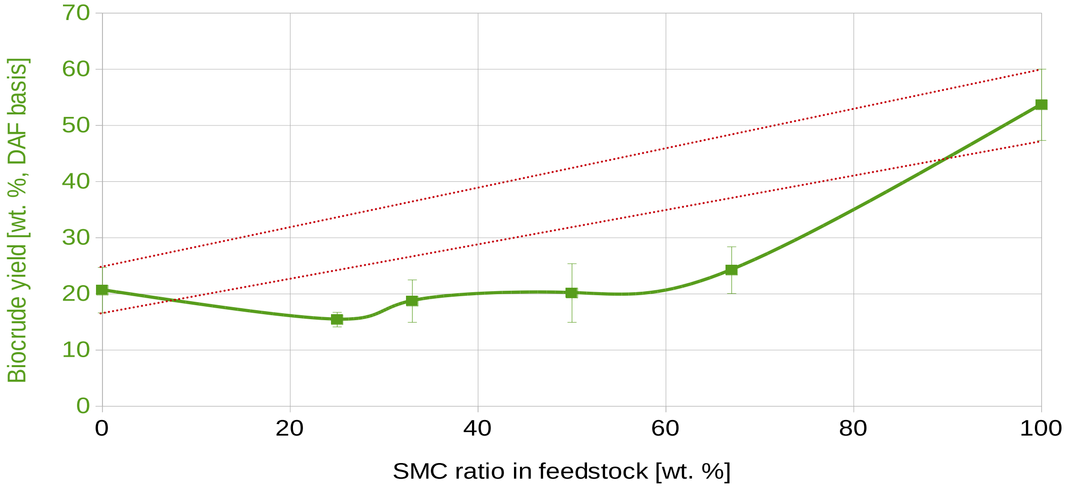

Fig. 5. Biocrude yield development throughout the catalysed experimental runs. Shown at different feedstock mixtures. Here the dotted red lines visualise the deviation-based expected biocrude yield limits when only linear mixing effects are taken into account

The experimental results also show that there are more gases being produced when processing slurries of higher AW concentrations. This is explained by the fact that despite similar cellulose and lignin contents, AW is thought to contain significantly more hemicellulose. These weak polymers readily decompose and produce CO_2 among other gases starting at temperatures as low as 200–300°C in oxygen deprived environments [19].

4. CONCLUSIONS

Despite clear signs of feedstock suitability (i.e. low cost and highly available feedstock, low biocrude O/C, moderate H/C_{eff}, high yield and HHV), the viability of using SMC for continuous liquid biofuel production depends on whether the issue of high inorganics can be overcome.

Catalytic HTL and co-liquefaction are proposed as ash limiting strategies, whereas the study points to the need for HTL processing of de-ashed SMC for further feasibility analysis of the feedstock. A search for a more effective de-ashing method is proposed for future work as neither water nor acetone are suitable agents.

5. ACKNOWLEDGEMENTS

The author would like to thank St. Restrup Champignon for providing the raw feedstock and insight into modern mushroom farming. Saqib S. Toor has been of great help in the laboratories, namely due to his extensive knowledge of the micro HTL experimental setup. Moreover, the collaboration with the chemical and mechanical departments of Aalborg University added extra academic value. Finally, gratitude for support and constructive input is expressed towards the supervisors (Thomas H. Pedersen and Lasse A. Rosendahl) and the remaining HTL research group.

6. REFERENCES

[1] INTERNATIONAL ENERGY AGENCY, *"Energy Technology Perspectives 2015,"* Tech. Rep., 2015.

[2] "ETP 2015 Data Visualisation." [Online]. Available: http://www.iea.org/etp/explore/

[3] A. DEMIRBAS, *"Biomass resource facilities and biomass conversion processing for fuels and chemicals,"* Energy Conversion and Management, Vol. 42, No. 11, pp. 1357–1378, 2001.

[4] R. D. PERLACK, L. L. WRIGHT, A. F. TURHOLLOW, R. L. GRAHAM, B. J. STOKES, D. C. ERBACH, C. DARIN, M. KIMBERLY, AND G. DEEPA, *"Biomass as feedstock for a bioenergy and bioproducts industry: The technical feasibilty of a billionton annual supply,"* Oak Ridge National Laboratory, Tech. Rep., 2005.

[5] INTERGOVERNMENTAL PANEL ON CLIMATE CHANGE, *"Renewable Energy Sources and Climate Change Mitigation"*, 2012.

[6] R. KOOPMAN AND K. LANEY, *"Mushrooms: Industry and Trade Summary"* UNITED STATES INTERNATIONAL TRADE COMMISSION, Tech. Rep. 2010002, 2010.

[7] M. J. MAHER, W. L. MAGETTE, S. SMYTH, J. DUGGAN, V. A. DODD, M. J. HENNERTY, AND T. MCCABE, *"Managing Spent Mushroom Compost,"* No. July 2000, pp. 5,14, 2000.

[8] EUROSTAT, *"Mushrooms, energy crops, GMO: number of farms and areas by size of farm (UAA),"* Tech. Rep., 2015. [Online]. Available: http://appsso.eurostat.ec.europa.eu/nui/show.do?dataset=ef_pomengmo&lang=en

[9] B. C. WILLIAMS, J. T. MCMULLAN, AND S. MCCAHEY, *"An initial assessment of spent mushroom compost as a potential energy feedstock,"* Bioresource Technology, Vol. 79, No. 3, pp. 227–230, 2001.

[10] A. SLUITER, B. HAMES, R. O. RUIZ, C. SCARLATA, J. SLUITER, AND D. TEMPLETON, *"Determination of Ash in Biomass,"* Biomass Analysis Technology Team Laboratory Analytical Procedure, No. January, pp. 1–6, 2004.

[11] S. S. TOOR, L. ROSENDAHL, AND A. RUDOLF, *"Hydrothermal liquefaction of biomass: A review of subcritical water technologies,"* Energy, Vol. 36, No. 5, pp. 2328–2342, 2011.

[12] Z. ZHU, S. S. TOOR, L. ROSENDAHL, D. YU, AND G. CHEN, *"Influence of alkali catalyst on product yield and properties via hydrothermal liquefaction of barley straw,"* Energy, vol. 80, pp. 284–292, 2015.

[13] L. R. T.H. PEDERSEN, L. JASIUNAS, L., CASAMASSIMA, S. SINGH, T. JENSEN, L. ROSENDAHL, *"Synergetic hydrothermal coliquefaction of crude glycerol and aspen wood,"* Energy Conversion and Management, Vol. 106, pp. 886–891, 2015.

[14] D. XU AND P. E. SAVAGE, *"Characterization of biocrudes recovered with and without solvent after hydrothermal liquefaction of algae,"* Algal Research, vol. 6, pp. 1–7, 2014.

[15] D. LOPEZ BARREIRO, W. PRINS, F. RONSSE, AND W. BRIL-MAN, *"Hydrothermal liquefaction (HTL) of microalgae for biofuel production: State of the art review and future prospects,"* Biomass and Bioenergy, Vol. 53, pp. 113–127, 2013.

[16] S. A. CHANNIWALA AND P. P. PARIKH, *"A unified correlation for estimating HHV of solid, liquid and gaseous fuels,"* Fuel, Vol. 81, No. 8, pp. 1051–1063, 2002.

[17] D. J. MOLLER, *"Animal feeding stuff : Global Standard for the Determination of Acid Detergent Fibre (ADF) and Lignin,"* Foss, no. 5, pp. 7–9, 2008.

[18] R. ZHANG, H. WANG, Q. LIU, AND T. NG, *"Chemical and ultrastructural studies of lignocellulose biodegradation during Agaricus bisporus cultivation."* Biotechnology and applied biochemistry, Vol. 61, No. 2, pp. 208–16, 2014.

[19] S. WANG, B. RU, H. LIN, AND Z. LUO, *"Degradation mechanism of monosaccharides and xylan under pyrolytic conditions with theoretic modeling on the energy profiles,"* Bioresource Technology, Vol. 143, pp. 378–383, 2013.

CYSENI 2016, May 26-27, Kaunas, Lithuania
ISSN 1822-7554, www.cyseni.com

A LITERATURE REVIEW OF WIND TURBINES ICING PROBLEMS

V. Zimnickas, G. Gecevičius, A. Markevičius
Lithuanian Energy Institute
Breslaujos str. 3, LT-44403, Kaunas – Lithuania
Email: vaidotas.zimnickas@lei.com

ABSTRACT

In order to accumulate a bigger amount of wind power wind turbines are built in higher altitudes, in more inclement areas. At these areas icing phenomenon occurs. Proves show that wind turbine icing is complicated, because ice grow rate on blades depends on many factors: air temperature, humidity and pressure, wind speed, attack angle of blades, size of water droplets etc. Until now, there are no reliable icing predictions systems. The most commonly used anti – icing method is blade heating which require a lot of energy and is uneconomical. There are many models made until now, which illustrate rime ice formation on the wind turbine blades and only few which shows glaze ice formation.

When wind turbine blades are covered in ice, aerodynamic properties of blades are changed, power generated by wind turbine shrink. More over ice layer on blades creates undesirable load, which can damage wind turbine rotor, shaft and blades. Icing phenomenon has not been understood completely yet. Conditions, which determine icing, are not well known as well as ice growth on wind turbines' blades.

The aim of this article are: to overview, the newest literature related to the icing phenomenon and its' solutions; to compare the most usual anti-icing methods, their advantages and disadvantages; to overview and compare, the newest articles related to the numerical simulation of the icing phenomenon using ANSYS FLUENT and similar software.

Keywords: wind turbines, icing, CDF modelling

1. INTRODUCTION

In order to reduce fossil fuel consumptions and minimize greenhouse gases emission to atmosphere nowadays a lot of attention is paid to renewable resource like wind energy. For example, total accumulation of installed wind power in Europe has reached 134 GW in 2014. It is expected that total installed wind power in Europe will accumulate more than 192 GW by the year 2020. That would be 42% growth and it is expected that it will fulfill about 15% of all EU electrical energy demand [1]. In order to accumulate a bigger amount of wind power wind turbines are built in higher, more inclement and poorly populated areas. Those areas have huge potential because there it is possible to build more powerful wind turbines which do not have big influence on landscape and do not disturb inhabitants. Moreover, 69 GW of wind energy in the world until 2012 was installed in cold climate areas [2]. But unfortunately in these areas wind turbines constructions face other difficulties. For example: in winter, when air temperature drops below 0 ^{0}C icing phenomenon occurs. When wind turbine blades are covered with ice, aerodynamic properties of blades change, power generated by wind turbine shrinks. More over ice layer on blades creates undesirable load which can damage wind turbine rotor, shaft and blades.

2. ATMOSPHERIC ICING CONDITIONS

Cold climate areas are regions, where regular conditions of atmosphere are suitable for icing event. The type of icing depends on weather conditions. Usually three different icing types are distinguished by different weather conditions. The rate of ice accretion depends not only on weather conditions but also on wind turbine parameters such as: angle of attack (AOA), blade length and width, and blades rotation [3].

In cloud icing. This kind of icing occurs when super cooled water drops hit a surface which temperature is below 0 ^{0}C. In this condition water drops temperature could be -30 ^{0}C or lower, they do not freeze in the air because of their size, but they freeze immediately after hitting a surface. Size of the water drops (median volume diameter – MVD), their content in the air (liquid water content – LWC), temperature and wind speed define which type of ice will be formed on the surface: hard rime, soft rime or glaze.

Hard rime appears at higher MVD and LWC which are common at high altitudes and at temperatures below -10 ^{0}C. The most severe rime icing occurs on freely exposed mountains or hilltops where moist air is forced upwards and consequently cooled or where mountain valleys force moist air through passes which also increases the wind speed. Hard rime has higher density 600–900 kg/m^3 and strong adhesion [4].

Soft rime, as well as, hard rime appears at high altitudes, when air temperature is way below 0 ^{0}C and MVD and LWC are quite small. Soft rime has low density 200–600 kg/m^3 and low or medium adhesion [4,5].

Glaze ice occurs when air temperature is between 0 ^{0}C and -10 ^{0}C. Glaze ice can be formed, when not all water drops freeze immediately, after contacting the surface. The part of water which gets on the surface freezes and other part runs back and freezes later. Glaze has high density about 900 kg/m^3 and strong adhesion for that reason it is very difficult to remove it.

Precipitation can be snow or rain. Precipitation has higher percentage of liquid water than clouds and features higher accretion rate which can cause more damage. There are two types of precipitation which can cause icing: freezing rain and wet snow.

Freezing rain occurs when rain drops fall on the surface which temperature is below 0 ^{0}C. Freezing rain has such features as high density and strong adhesion force.

Wet snow is the accretion process when snowflakes partly contain liquid water and therefore are able to adhere to a surface. This process occurs only when ambient temperature is just above freezing point [6].

3. ICING INFLUENCE ON WIND TURBINE

Icing can influence wind turbine in few different ways: disruption of aerodynamics and decrease of generated power, full stop of turbine, decreased turbines and its parts lifetime.

When wind turbine blades are covered by ice, blades lift and drag coefficients change. Ice on the blades increase their airfoil roughness, for this reason air that is leaking over blades surface begins to separate from surface. Process in which air leaking over blades at difference angle of attack (AOA) is showed in Fig. 1.

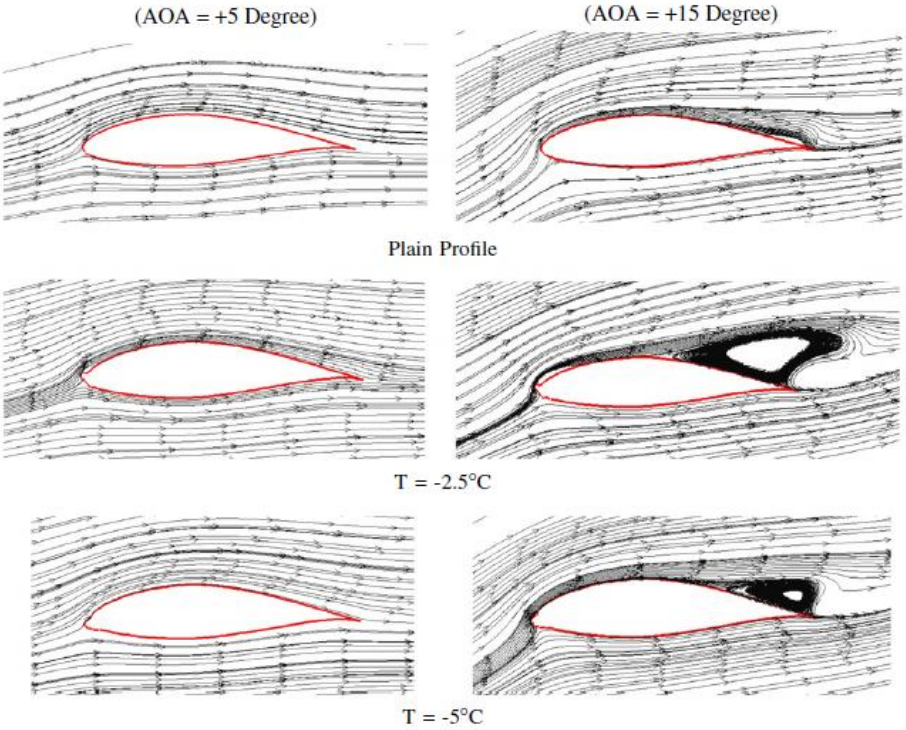

Fig. 1. Air leaking blades stream lines, when AOA is +5 and +15, and air temperature is -2.5 ^{0}C and -5 ^{0}C [7]

From Fig. 1 it is clear that there is no noticeable flow separation at low AOA, and separation increases with increase of AOA. With increasing air flow separation drag coefficient increases while lift coefficient and torque decreases. This process is illustrated in Fig. 2.

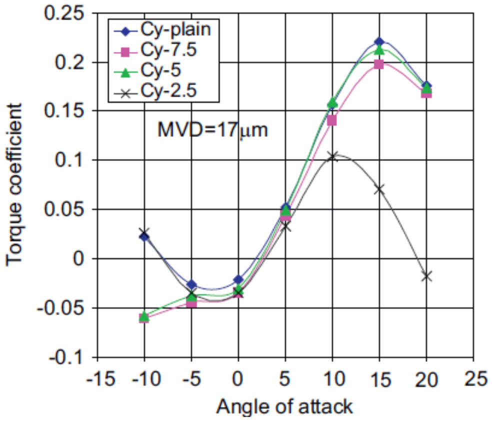

Fig. 2. Torque coefficient at different temperatures [7]

In Fig. 2 it can be clearly seen that the biggest torque decrease is at -2.5 ^{0}C, it can be explained by the fact that at this temperature ice is heavier and more rough.

In heavy icing conditions it is possible that ice mass on the blades reaches critical level. In that case ice accreted on rotor blades causes critical vibrations and aerodynamic imbalance for this reason wind turbine is forced to stop in order to prevent damage. There are reports which show that some wind turbines in Sweden during 2002–2003 winter were forced to stop for 7 weeks. According to Sweden statistics in winter 92% of full stops are caused because of icing [8]. In Germany 85% of full stops of wind turbines in mountains were caused by icing [9].

4. DE – ICING AND ANTI – ICING TECHNIQUES

During recent years a lot of attention was paid to wind turbine icing problems, however almost all de – icing and anti – icing techniques are taken from aviation industry. All de – icing and anti – icing techniques can be classified into two categories: passive and active. Passive techniques are those which change physical features of the surface. Usually physical features change adhesion force or surface roughness, while active techniques rely on external system applied to the blade.

4.1 Passive techniques

4.1.1 Ice-phobic and hydrophobic coatings

Hydrophobic and ice phobic materials repel water or have very low adhesion force.

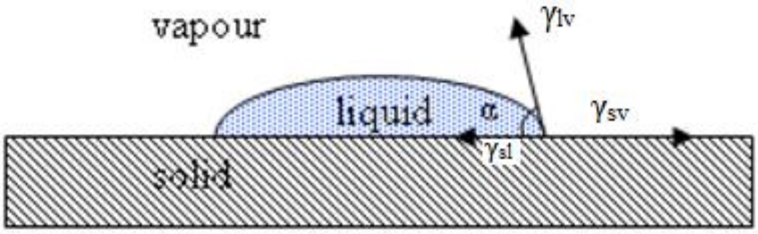

Fig. 3. Liquid on hydrophobic surface [10]

Fig. 3 shows liquid on hydrophobic surface. Liquids act on surface is defined by contact angle.

$$Cos(\alpha) = \frac{\gamma_{sv}-\gamma_{sl}}{\gamma_{lv}}. \quad (1)$$

In this equation α is contact angle, γ_{sv} – angle between surface and vapor, γ_{sl} – angle between surface and liquid, γ_{lv} – angle between liquid and vapor.

Contact angle shows liquid repellent properties. If contact angle is less than 90^0 liquids will wet the surface. If contact angle is 180^0 liquid will form perfect sphere. Materials which have contact angle equal to 150^0 or more are called super hydrophobic.

Nowadays a lot of attention is paid for searching new materials, because some hydrophobic materials, like Teflon, could be easily charged with static electricity. In that case water drops can be easily adhered to blade surface and freeze [10]. Advantages of blades coating with hydrophobic materials are low cost and opportunity to protect whole surface. However special coating is effective only when it is combined with blade heating systems, because most hydrophobic materials are not ice –phobic, also due to contact with ice and insects' hydrophobic layers become more rough [11].

4.1.2 Active techniques

All active techniques are connected to melting ice from the blades. The most widely used technique is electro thermal blade heating. This technique is most popular because of its simplicity and low cost. However, this and all other active techniques like heating with microwaves, warm air heating have same disadvantages: until now there are no reliable icing prognostication and detection systems. For this reason, quiet often blades are heated without any necessity. As a result, energy losses increase and effectiveness of the system decrease.

5. ICE DETECTION SYSTEMS

In order to use an active de-icing and anti-icing techniques effectively, reliable detectors must be available. The most frequently used ice detectors are double anemometer and vibration sensors.

Double anemometer system. It is an ice detection system which consists of two separate anemometers, one of them is heated and the other one is not. When icing begins unheated anemometer shows different wind speed than heated, when the speed values reach 5–10% difference wind turbine blades heating commences. Advantage of this system is its' simplicity and low cost. But it is quite unreliable, because anemometer is much lower than the tip of the blades where the possibility of icing is higher. Also double anemometer could not detect ice when there is no wind. This method could be used only when temperature is around 0 ^{0}C, in lower temperatures unheated anemometer may stay frozen for longer periods.

Vibration sensors. When wind turbine blades are covered with ice, extra vibrations and noise apply when blades turn. Then sensor reacts and heating of the blades starts. This sensor cannot detect ice when there is no wind, same as sensor of the double anemometer. Also there is no investigation what influence has background and varying wind speed noise to data.

Optical sensor. It seems that the best instrument for ice detection should be optical sensor or video cameras. Optical sensor has to be reliable in all weather conditions and also has to be able to detect all types of ice. One of the newest devices which is able to do that is Remote Ice Detection Equipment (RIDE). With this device it is possible to detect glaze and rime ice and measure their layers thickness. Schema of this device is shown in Fig. 4.

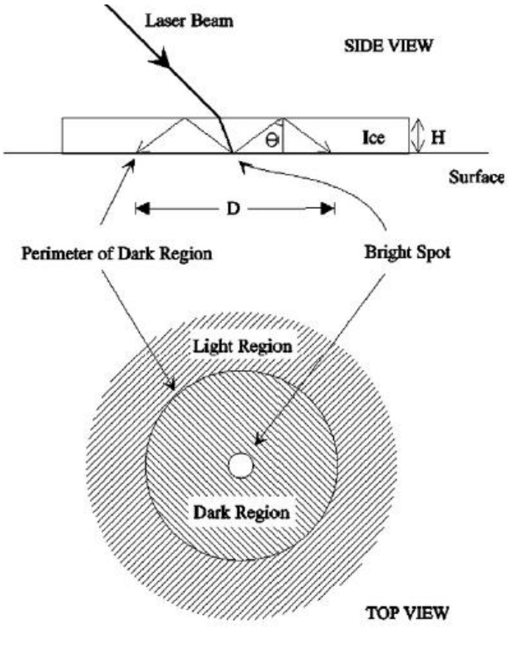

Fig. 4. Principle of RIDE system [12]

A laser of focused light of any visible wavelength outside the region where ice strongly absorbs shoot on a surface is used. The beam traverses the ice layer and impinges on the underlying surface, producing an intense bright spot from which light scatters in all directions. All of the light scattered from the spot and striking the ice interfaces at angle of incidence less than the angle θ passes through the interface. Those rays incident at angles greater than θ get internally reflected from the ice/air interface to strike and illuminate the surface again. As a result, camera shows a bright spot where the laser first strikes the surface: in the center of a dark circular region that is surrounded by a light region that gives the dark region a sharply defined perimeter (diameter *D*). Diameter *D*, marks the distinction between light from the bright spot that was internally reflected inside the layer and light from the bright spot that passed back out through the top ice/air interface [12]. The thickness of the layer could be expressed like this:

$$H = \frac{D}{4 * \tan(\theta)}. \tag{2}$$

6. NUMERICAL SIMULATION OF ICING PHENOMENON

In order to evaluate the impact of ice on wind turbine performance, it is important to understand ice accretion process, how much it affects aerodynamics of blades and how it could be possible to reduce this affect. In order to minimize energy loses of icing it is important to detect place where possibility of icing accretion reaches its maximum.

As mentioned above, there are two types of ice: glaze and rime. In glaze icing situation numerical simulation is quite easy because all water drops freeze at the same place where they hit the surface. In order to calculate ice thickness, it is enough to know water amount captured along the blade. In rime icing situation everything is more complicated because not only ice layer but also water leaking over the blades has to be simulated.

Fernando Villalpando examinated how well standard commercial software simulation fit with experiment data. He divided turbine blades in three sectors as shown in Fig. 5. All sectors have rotation at difference speed and collect different amount of water.

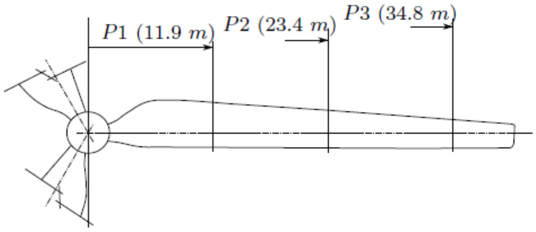

Fig. 5. Radial position of the sections [13]

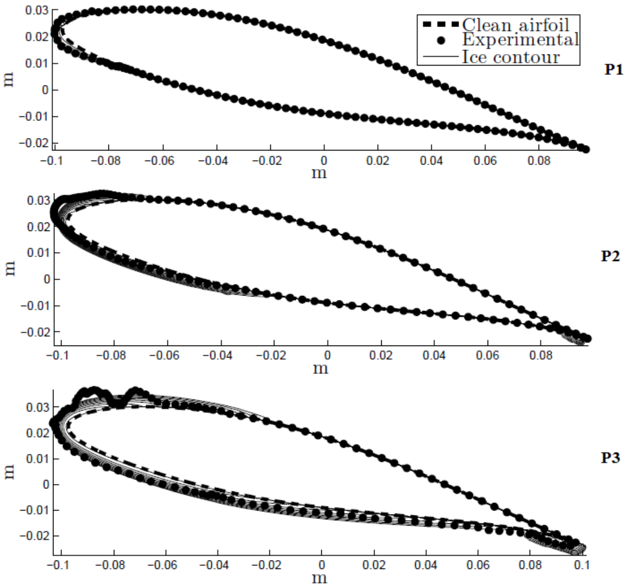

Fig. 6. Ice simulation at different blades place [13]

In Fig. 6 it is clearly visible that simulations of sectors P1 and P2 have good agreement with experiment data. But in simulation P3 ice accretion was overestimated at the trailing edge and under rates at the leading edge. This happened, because numerical model does not take into account effects of gravity and the fact that air shear stress on the water surface has repercussions for the runback water and currently predicts a flattened ice contour.

7. CONCLUSIONS

1. Successful development of wind energy in cold climate areas requests to improve technologies which could detect and measure ice on the wind turbine blades. Most currently used technologies: double anemometer and vibration sensor are not reliable, both of them do not work when there is no wind. Best solution would be to improve video monitoring technologies which can work in all conditions.
2. Until now most reliable protection of icing is blade heating, which require huge amount of energy. In order to reduce this energy loss, it is important to look for new hydrophobic materials, use them together with active de – icing techniques and improve ice detection system.
3. More attention should be paid to rime ice accretion numerical simulation because most widely used ANSYS FLUENT models does not take into account the effects of gravity and the fact that air shear stress on the water surface has repercussions for the runback. Also there should be made 3D icing modeling, because it could help to better evaluate ice distribution on the blades.

8 REFERENCES

1. EUROPEAN WIND ENERGY ASSOCIATION, Wind energy scenarios for 2020.
2. INTERNATIONAL ENERGY AGENCY, 2013 annual report.
3. LI Y., TAGAWA K., FENG F., A wind tunnel experimental study of icing on wind turbine blade airfoil. *Energy Conversion and Management*, Vol. 85, 2014, p. 591–595.
4. TAMMELIN B., CAVALIERE M., Wind energy production in cold climate (WECO), *Finnish meteorological institute.* Publishable report.
5. PARENT O., Adrian ILINICA A., Anti-icing and de-icing techniques for wind turbines: Critical review. *Cold Regions Science and Technology*, Vol. 65, No. 1, January 2011, p. 88–96.
6. HAN Y., PALACIOS J., SCHMITZ S., Scaled ice accretion experiments on a rotating wind turbine blade. *Journal of Wind Engineering and Industrial Aerodynamics*, Vol. 109, October 2012, p. 55–67.
7. HOMOL M., VIRK M., WALLENIUS T., *Journal of Wind Engineering and Industrial Aerodynamics*, Vol. 98, No. 12, December 2010, p. 724–729.
8. LAMRAOUI F., FORTIN G., BENOIT R., Atmospheric icing impact on wind turbine production. *Cold Regions Science and Technology*, Vol. 100, April 2014, p. 36–49.
9. DURSTEWITZ M., A statistical evaluation of icing failures in Germany. Germany, 2004.
10. BOINOVICH L., EMELYANENKO A., Anti-icing potential of super hydrophobic coatings, *Mendeleev Communications*, Vol. 23, No. 1, January–February 2013, p. 3–10.
11. DALILI N., EDRISY A., CARRIVEAU R., A review of surface engineering issues critical to wind turbine performance. *Renewable and Sustainable Energy Reviews*, Vol. 13, No. 2, February 2009, p. 428–438.
12. GAGNON R., GROVES J., PEARSON W., Remote ice detection equipment – RIDE. *Cold Regions Science and Technology*, Vol. 72, March 2012, p. 7–16.
13. VILLALPANDO F., REGGIOA M., ILINICA A., Ice accretion and anti-icing heating power prediction on wind turbines using standard commercial software, Canada, 2015.

CYSENI 2016, May 26-27, Kaunas, Lithuania
ISSN 1822-7554, www.cyseni.com

POSSIBILITIES OF ANAEROBIC DIGESTED SEWAGE SLUDGE THERMAL UTILIZATION IN LITHUANIA

M. Praspaliauskas
Lithuanian Energy Institute
Breslaujos st. 3, LT-44403 Kaunas – Lithuania
Email: marius.praspaliauskas@lei.lt

ABSTRACT

In relation to the growing population in the world, rapid industrial development and environmental pollution increased to a near dangerous level. Wastewater collection and treatment as well as effective utilization of sewage sludge require the increased attention.

Nowadays one of the important tasks is reduction of generated sewage sludge volumes and its effective utilization. However, such utilization of sewage sludge is still considered as subject for investigation, because sewage sludge in most cases contains high content of moisture, high level of ash content, chlorine, sulphur and etc. pollutants.

To obtain such chemical-physical information, 5 sewage sludge samples were randomly taken from sludge storage plants in Vilnius, Kaunas, Klaipėda, Šiauliai, Panevėžys, Alytus and Šilutė cities. There were also some differences of waste water treatment technologies as well as industrial activity in the selected places.

Performed investigations show that composition of sewage sludge and concentrations of main elements are only slightly different from the EU countries' average value. The main element concentrations vary: carbon – from 34.31% to 46.56%, hydrogen 4.49% – 6.52%, nitrogen 4.35% – 7.24%, sulphur 0.99% – 1.83%. It is important to notice that sewage sludge has relatively large amount of sulphur. Directive 2001/80/EC on the limitation of emissions of certain pollutants into the air from large combustion plants maintains that the use of oil containing more than 1% of sulphur is prohibited. The analysis showed that ash content in sewage sludge wary between 41.02% and 21.60%.

Keywords: wastewater treatment quality, sewage sludge disposal, co-incineration, gasification

1. INTRODUCTION

According to EU and other countries' demographic predictions (UN DESA. United Nations Department of Economic and Social Affairs/Population Division World Population to 2030), future amounts of non-processed sewage sludge will be significantly higher. This will be the result of increasing population and more stringent requirements for water treatment quality.

Solving this problem, EU countries in one way or another implement primary, secondary and tertiary wastewater treatment and intensively develop sludge processing and use technologies. Complying with the requirements, more and more EU countries start applying the full cycle of wastewater treatment.

Analysis of the existing experience in sewage sludge use [1, 2] clearly shows several important directions: use of sludge as fertilizer and accumulation in storage plants and landfills (an option which is currently neither acceptable nor desirable in Member States) [3] as well as incineration or alternative thermal utilization processes (anaerobic digestion, pyrolysis, etc.).

Naturally, besides use of sewage sludge in agriculture, there are other sludge treatment technologies, one of which is thermal treatment. Applying thermo-chemical processes amounts of sewage sludge are reduced and additional product – energy – is obtained.

Thermal treatment of sludge partly solves the sewage sludge storage problem since after incineration 15–40% of former sludge volume becomes ashes. Depending on used technologies, energy or other useful products are obtained during incineration of sludge. Amount of organic materials in sludge directly results in heating value [4]. Incineration of sludge or its mixtures with other fuel is more useful concerning the recovery of energy, as well as is alternative thermal utilization processes, such as pyrolysis, gasification and mixed methods [2]. This process also destroys pathogenic and toxic organic materials.

However, heavy metals in the sewage sludge remain within the bottom ashes after incineration or are discharged into the environment together with exhaust gas as fly ashes. This limits use of the ashes and results in implementation of special exhaust gas treatment measures. In case of incineration, discharges into the atmosphere must meet very strict requirements [5–7], however, public dissatisfaction over increased air pollution because of sludge incineration plants still exists. The worrying factor is the influence of toxic heavy metals and volatile organic compounds on the environment and human health.

1.1. Amount of wastewater and its treatment

In Lithuania 2002–2003, approx. 12% of wastewater was discharged into the environment untreated and approx. 30% underwent primary treatment (Fig. 1). Primary and secondary treatments made 6% and 18% respectively [8] and were used in the major cities of Lithuania – Vilnius, Kaunas, Klaipėda and Šiauliai. Since 2004 Lithuania has started a rapid development of wastewater treatment. Minimum amount of untreated wastewater is discharged to surface waters, and secondary wastewater treatment made more than 50% already in 2009. Today primary and secondary wastewater treatments make 98% and 85% respectively.

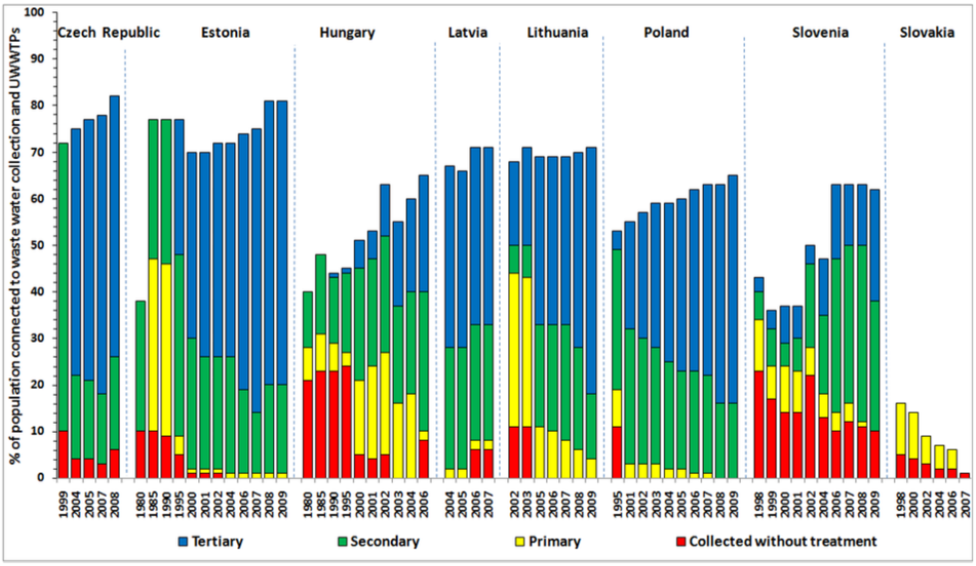

Fig. 1. Wastewater treatment quality in east EU [8]

Approximately 67% of Lithuanian citizens use centralised wastewater collection system, although the numbers differ in urban and rural areas. In urban areas, 90–96% of citizens use the system, while in rural areas the number is only 20–30%. Objectives of the wastewater treatment Directive are planned to be accomplished till 2018, thus then approx. 95% of the citizens will be connected to the wastewater collection network regardless of the area.

1.2. Amount of sewage sludge and its utilization

While evaluating sludge accumulation according to statistical data, it is assumed that currently and in the future at least till 2025, amounts of the accumulated sewage sludge will be the same as forecasted for 2016, i. e. approx. 82,000 t/year of dry sludge (Fig. 2). The assumption is based on the prediction that new industrial companies established in Lithuania till 2025 with innovative modern technologies will not significantly increase pollution discharged into centralised wastewater networks, and according to prognosis of Statistics Lithuania, the number of dwellers will not increase till 2025 compared to number of dwellers census data for 2001 [9].

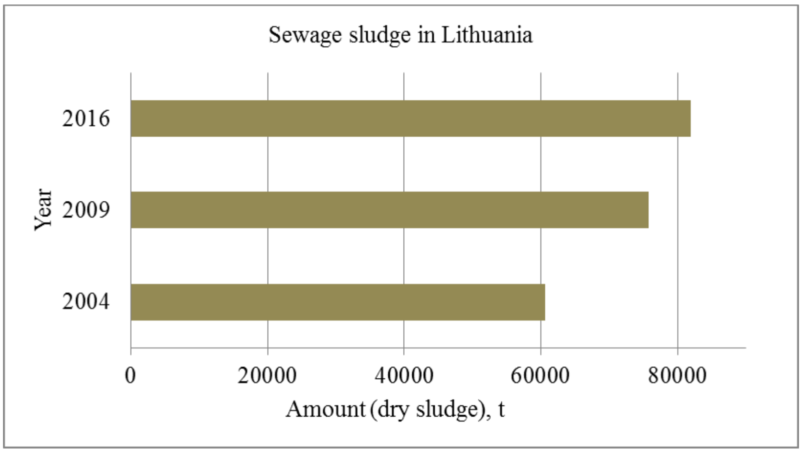

Fig. 2. Sewage sludge amounts in Lithuania

During the recent period, wastewater treatment has been developing, amounts of sewage sludge have been increasing and treatment technologies have changed significantly. Wider application of anaerobic treatment of sewage sludge with additional biogas recovery has been started; centrifuges and belt filter presses have been used for dewatering. Since 2013 sewage sludge has been undergoing drying process in the major cities of Lithuania. Therefore, the current situation on sewage sludge in Lithuania is not very favourable either from environmental or economic point of view. Huge amounts, approx. 60%, are stored in storage plants which require additional expenses for safety.

Since 2013, Lithuanian wastewater treatment companies have been drying sewage sludge and its moisture now ranges from 2% to 10% and, hence, it becomes possible and necessary primarily to implement sewage sludge incineration technologies. Simultaneously, possibilities of implementation of other advanced technologies (gasification, pyrolysis) must be considered, because nowadays most common sewage sludge utilization ways are: agricultural use and composting or other applications.

2. MATERIALS AND METHODS

2.1. Sampling and analysis methodology

5 sewage sludge samples were randomly taken from sludge storage plants in Vilnius, Kaunas, Klaipėda, Šiauliai, Panevėžys, Alytus and Šilutė cities. The investigation strived to cover various systems used in different Lithuanian regions and cities with different number of dwellers and industrial intensity. It should be noted that treatment of the sludge also differs in different cities: Vilnius (S1), Šiauliai (S2) and Šilute (S3) systems treat sewage sludge using anaerobically digestion and drying; Kaunas (S4), Klaipėda (S5) and Panevėžys (S6) systems treat sewage sludge using only anaerobically digestion and dewatering; Alytus (S7) system uses only dewatering.

From the collected sludge samples, moisture and ash content were identified according to specification CEN/TS 15414-1:2010 and standard LST EN 15403:2011, respectively. Proximate analysis to determine the weight percentage of volatile solids was conducted using a TGA 4000 simultaneous TGA/DTA analysis method. Fixed carbon content was calculated as: *Fixed carbon (%) = 100 (%) – Moisture content (%) – Volatile content (%) – Ash content (%)*. Analysis of the elements C, H, S, N and O present in the sludge was performed using a Flash 2000 analyser. Carbon, hydrogen and nitrogen content were determined according to standard LST EN 15407:2011. Sulphur content was also determined according to standard LST EN 15407:2011.

Oxygen content was calculated as follows: *Oxygen content (%) = 100 (%) – Carbon content (%) – Hydrogen content (%) – Nitrogen content (%) – Sulphur content (%) – Ash content*. Chlorine content was estimated using an ISC-5000 DC ion chromatographic system according to standard LST EN 15408:2011. The high heat value (HHV) of sewage sludge was determined using an IKA C5000 calorimeter according to standard LST EN 15400:2011 for automated bomb calorimeters. Characteristic sludge ash melting temperatures were determined using a Carbolite CAF digital furnace according to technical report LST CEN/TR 15404:2010.

3. RESULT AND DISCUSSION

3.1. Thermochemical properties of sewage sludge

Table 1 presents typical characteristics of dried and anaerobically digested, dewatered and anaerobically digested and only dewatered sewage sludge in the investigated wastewater treatment plants.

Table 1. Sewage sludge characteristics in Lithuania’s wastewater treatment plants

Parameter	**Dried and anaerobically digested sludge**			**Dewatered and anaerobically digested sludge**			**Dewatered raw sludge**
	S1	S2	S3	S4	S5	S6	S7
Moisture, %	2.23 ±0.07	9.20 ±0.07	2.91 ±0.07	80.42 ±0.07	74.00 ±0.07	88.37 ±0.07	88.47 ±0.07
Ash content, %	41.02 ±0.21	38.49 ±0.41	30.27 ±0.32	38.27 ±0.21	37.97 ±0.34	22.12 ±0.08	21.60 ±0.19
Volatile solids, %	47.00 ±0.94	49.51 ±0.79	51.02 ±1.07	49.51 ±0.40	48.86 ±0.44	64.00 ±0.36	67.30 ±1.88
Fixed carbon, %	11.98 ±0.98	12.00 ±0.81	18.71 ±0.39	12.22 ±0.36	13.17 ±0.33	13.18 ±0.33	11.10 ±1.56
Carbon, %	36.97 ±1.47	37.04 ±1.10	39.76 ±1.11	34.31 ±1.32	35.39 ±3.21	43.57 ±2.11	46.56 ±1.09
Hydrogen, %	4.59 ±0.46	4.49 ±0.56	5.11 ±0.42	4.59 ±0.51	4.82 ±0.64	6.00 ±0.44	6.52 ±0.42
Oxygen, %	11.65 ±0.25	12.72 ±0.61	17.36 ±1.00	16.51 ±0.36	15.99 ±0.81	19.53 ±0.66	18.49 ±0.78
Nitrogen, %	4.74 ±0.32	5.36 ±1.53	5.83 ±0.30	4.98 ±0.38	4.35 ±0.34	7.24 ±0.33	5.65 ±0.30
Sulphur, %	0.99 ±0.28	1.83 ±0.27	1.53 ±0.26	1.33 ±0.28	1.43 ±0.28	1.38 ±0.27	1.09 ±0.26
Chlorine, %	0.04 ±0.48	0.07 ±0.14	0.14 ±0.10	0.07 ±0.21	0.05 ±0.09	0.16 ±0.12	0.09 0.15±
HHV, MJ/kg	15.66 ±0.87	16.01 ±0.75	17.28 ±1.10	14.81 ±0.55	15.27 ±0.40	19.64 ±0.33	21.55 ±1.79

As data in the table demonstrates, when anaerobic digestion is applied, certain differences between sludge characteristics in various plants have been determined not only by wastewater composition in the plant but also by the treatment technology. Sludge ash content is higher in those cities where the number of dwellers is bigger and which have more industry, e. g., S1, S2, S4 and S5. Regardless of whether additional drying or dewatering was used, the parameter values of these cities are very similar. The biggest deviations from average values 38.94% for ash content, 48.72% for volatile matter and 35.93% for carbon make less than ±5%. Sludge of a small city, e. g. S3, contains significantly larger amount of carbon and volatile matter and less ashes.

Without anaerobic digestion (S7) amounts of carbon and volatile matter increase significantly while ash content reduces. Sludge parameters from S6 wastewater treatment plant show very little difference, which means that the performed anaerobic digestion lacks efficiency. Thus, based on average values of these two cases, it can be summarised that compared to the major cities, amount of carbon in the sludge increases from 35.93% to 45.06%, i. e. by 25%; volatile matter from 48.72% to 65.65%, % i. e. by 35%. Ash content in sewage sludge can reach more than 50% and from the energetic viewpoint it is not a good indicator of fuel [10]. Ash content decreases from 41.02% to 21.60%. These changes fully correspond to the changes in content of hydrogen and oxygen as well as heating values of the sludge.

3.2. Ash melting temperatures

Another important factor for energy generation is ash melting temperature. Low fuel ash melting temperatures is one of the main problems that prevent some fuel types from use in thermochemical processes. Ash melting causes interruptions in technological processes, damages plants and shortens their operation period [11]. Sewage sludge ashes contain great amounts of CaO. Investigation results showed that ash melting temperatures were affected by concentrations of certain elements, for instance, coal ash melting temperature were affected by SiO_2/Al_2O_3 concentrations, while initial deformation temperature is mostly affected by K_2O [12]. Some articles propose that for bigger amount of P_2O_5, temperatures of melting points in the ashes also decrease. Synergetic effect of phosphates and Fe_2O_3 and SiO_2 captured during sewage sludge incineration also reduces melting temperatures [13].

During investigation of sewage sludge ashes from Lithuania's wastewater treatment plants, characteristic ash melting temperatures whose methodology and criteria for determination are regulated by normative documents have been identified (Fig. 3): shrinkage temperature (SST) for which dimensions of the prepared ash sample decrease and area of the sample does not reach 95% of the sample area under 550 °C; initial deformation temperature (DT) for which the sample takes an oval shape and its height equals to half base diameter; flow temperature (FT) for which melting ashes become liquid and spread over the plate in such a manner that the height of the layer equals to half sample height under HT [14].

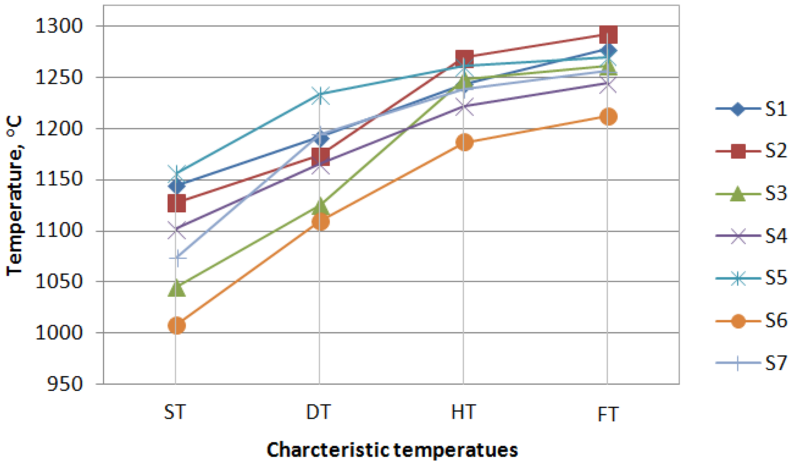

Fig. 3. Characteristic ash melting temperatures of sewage sludge

The shrinkage temperature is more interesting, since one ash starts to melt and become sticky, causing ash related operational problems. As Fig. 3 shows, the S5 ash has the highest initial melting temperature, indicating the lowest sintering tendency. During the ash melting test, the ash shrinkage temperature was identified at about 1150 °C. On the contrary, the ash from S6 has the lowest ash shrinkage temperature about 1010 °C that is considerably lower than those of the other six ashes.

It shows that S1, S2, S4 and S5 have evidently higher ash shrinkage characteristic temperatures than S3, S6 and S7. For that S1, S2, S4 and S5, larger temperature intervals from 1100 °C to 1150 °C were identified than for S3, S6 and S7. For S3, S6 and S7 temperature intervals were from 1010 °C to 1060 °C. As the temperature rises, differences between characteristic temperature values decrease: DT – from 1110 °C to 1236 °C, HT – from 1190 °C to 1270 °C and FT – from 1212 °C to 1290 °C.

3.3. Perspectives for thermal treatment of sewage sludge

Analysis of wastewater treatment technologies applied in Lithuania shows their oncoming to those applied in other EU countries (Fig. 1). Differences of sludge amount, content and its properties are not also substantial if the size of wastewater source and level of its industrialization as well as wastewater treatment technology would be properly evaluated. Thus it is reasonable to solve sludge use problems in Lithuania based on experience of other European countries.

The newest possibilities of sewage sludge use that attract attention are the following: incineration, wet oxidation, pyrolysis, gasification, co-incineration with other fuel (e.g., biofuel). Commercial application of these technologies in Europe is currently are widen. The most rapidly developed technology of sewage sludge treatment is incineration that is widely used in Germany, the United Kingdom and Denmark. Co-incineration is common in the Netherlands, France, Belgium and Chech Republic [15]. Highly strict requirements are applied to the emissions of the incinerated sewage sludge [5, 6].

Major problems related to thermal treatment of sewage sludge are as follows [16]:

- installation of the system requires large investments;
- thermal processes require energy;
- wide range equipment is necessary to reduce air pollution.

The main advantages of these technologies are:

- large reduction of sewage sludge volume. Amount of ash accumulated after incineration can be up to 30% of the initial amount of the dried sludge used as fuel;
- thermal decomposition of toxic compounds into less toxic compounds;
- high energetic efficiency of the technological process because of the sufficiently high heating value of the sludge as a fuel;
- recovery of renewable energy [17].

In Lithuania, steps forward are taken to use the sewage sludge for energy production and valuable products extraction. In this field clear tendencies to apply thermal treatment technologies are observed; the following should be considered more closely: incineration and gasification.

4. CONCLUSIONS

The major Lithuanian wastewater treatment plants universally apply modern wastewater treatment systems analogous to the EU treatment systems. Anaerobic sewage sludge treatment while extracting biogas is widely used. Centrifuges and belt presses are used for sludge dewatering, then the sludge undergoes drying process.

According to statistical data, currently and in the near future at least until 2025, amount of dry sludge will be up to 82,000 t/year. The assumption is based on the prediction that new industrial companies constructed in Lithuania till 2025 with innovative modern technologies will not significantly increase pollution discharged into centralised wastewater networks, and according to prognosis of Statistics Lithuania, the number of dwellers will not increase till 2025.

Performed investigations show that composition of sewage sludge and concentrations of main elements are only slightly different from the EU countries' average value. The main element concentrations vary: carbon – from 34.31% to 46.56%, hydrogen 4.49% – 6.52%, nitrogen 4.35% – 7.24%, sulphur 0.99% – 1.83%. It is important to notice that sewage sludge has relatively large amount of sulphur. Directive 2001/80/EC on the limitation of emissions of certain pollutants into the air from large combustion plants maintains that the use of oil containing more than 1% of sulphur is prohibited. In this case, sewage sludge contains 1.83% of sulphur. Ash content in sewage sludge can reach more than 50% and from the energetic viewpoint it is not a good indicator of fuel. The analysis showed that ash content in sewage sludge wary between 41.02% and 21.60%.

5. REFERENCES

1. WETLE S., WILK R.K. A review of methods for the thermal utilization of sewage sludge: The Polish perspective. *Renewable Energy* 35 (2010), p. 1914–1919.
2. FYTILI D., ZABANIOTOU A. Utilization of sewage sludge in EU application of old and new methods-a review. *Renewable and Sustainable Energy Reviews* 12 (2008), p. 116–40.
3. FONTS I., GEA G., AZUARA M., ÁBREGO J., ARAUZO J. Sewage sludge pyrolysis for liquid production: A review. *Renewable and Sustainable Energy Reviews* 16 (2012), p. 2781–2805.
4. STASTA P., BORAN J., BEBAR L., STEHLIK P., ORAL J. Thermal processing of sewage sludge. *Applied Thermal Engineering* 26 (2006), p. 1420–1426.
5. CEC (Council of the European Communities), 2001. Commission decision of 16 January 2001 amending Decision 2000/532/EC as regards the list of wastes (2001/118/EC). *Official Journal of the European Communities*. 47, 1–31.
6. EC (European Commission), 2008. Directive 2008/98/EC of the European parliament and the council of 19 November 2008 on waste and repealing certain Directives. *Official Journal of the European Union*. 312, 3.
7. POKORNA E., POSTELMANS N., JENICEK P., SCHREURS S., CARLEER R., YPERMAN J. Study of bio-oils and solids from flash pyrolysis of sewage sludges. *Fuel* 88 (2000), p. 1344–1350.
8. European Environmental Agency http://www.eea.europa.eu
9. Feasibility Study. An investment program for sludge treatment in Lithuania. Environmental Projects Management Agency under the Ministry of Environment of the Republic of Lithuania 2006. Contract Nr. 2005/6/ND/P/LT. 04. 2006.
10. M. OTERO, X. GOMEZ, A.I. GARCIA, A. MORAN. 2008. Non-isothermal thermogravimetric analysis of the combustion of two different carbonaceous materials, *Journal of Thermal Analysis and Calorimetry* 93:619–626.
11. XIAO R.R., CHEN X.L., WANG F.C., YU G. The physicochemical properties of different biomass ashes at different ashing temperature. Renew. Energy 36 (2011), p. 244–249.
12. GUPTA S.K, GUPTA R.P, BRYANT G.W, WALL T.F. The effect of potassium on thefusibility of coal ashes with high silica and alumina levels. *Fuel* 77 (1998), p. 1195–1201.
13. ZHANG Q., LIU H., QIAN Y., XU M., LI W., XU J. The influence of phosphorus on ash fusion temperature of sludge and coal. *Fuel Processing Technology* 110 (2013), p. 218–226.
14. DUNNU G., MAIER J., SCHEFFKNECHT G. Ash fusibility and compositional data of solid recovered fuels. *Fuel* 89 (2010), p. 1534–1540.
15. KELESSIDIS A., STASINAKIS A.S. Comparative study of the methods used for treatment and final disposal of sewage sludge in European countries. *Waste Management* 32 (2012), p. 1186–1195.
16. KHIARI B, MARIAS F, ZAGROUBA F, VAXELAIRE J. Analytical study of the pyrolysis process in a wastewater treatment pilot station. *Desalination* 167 (2004), p. 39–47.
17. KELESSIDIS A., STASINAKIS A.S. Comparative study of the methods used for treatment and final disposal of sewage sludge in European countries. *Waste Management* (32) 2012), p. 1186–1195.

CYSENI 2016, May 26-27, Kaunas, Lithuania
ISSN 1822-7554, www.cyseni.com

STATISTICAL ANALYSIS OF MEASUREMENT DATA OF WIND ENERGY PARAMETERS

G. Kondratavičienė
Lithuanian Energy Institute
Breslaujos str. 3, LT-44403 Kaunas – Lithuania
Email: gabija.kondrataviciene@lei.lt

ABSTRACT

Usually, the potential of renewable energy resources for major entities of energy production – such as biomass or biogas processing objects – is calculated. However, the potential of the sun and wind is largely neglected in Lithuanian cities. City environment is only discussed in the present paper due to the peculiarities of wind and turbulence developments caused by the location and territorial distribution of high-rise buildings. The integration of these energy resources within the city territory would largely contribute to the decrease of environmental pollution. Successful technological equipment adaptation to climatic conditions directly affects the efficiency of the equipment. Consequently, the extent of equipment integration is affected as well. Frequently, the pre-planned energy needs are not satisfied after the installation of the equipment as the project design fails to adequately consider the natural meteorological conditions.

The evaluation of wind energy potential in cities is heavily affected by wind gusts and air turbulence stemming from differences of edifice height and their arrangement. Seasonality and the time of the day also affect the amount of wind power.

In order to assess the available potential of solar and wind energy in the urban environment, solar and wind energy parameter measurement data analysis is initially conducted. That is why the present paper conducts analysis of meteorological parameters of three different locations: Kalotė (Klaipėda District Municipality), the roof of one of the buildings of Klaipėda University and a meteorological station located in the outskirts of Kaunas City. Methodology for the evaluation of the impact of wind speed, direction, wind stream turbulence and other wind parameters energy characteristics has been developed.

Keywords: wind speed, wind direction, meteorological parameters

1. INTRODUCTION

Statistical analysis reveals various interdependencies of phenomena even in such cases which do not allow performing academically grounded testing. Statistical analysis is essentially applicable across the entirety of branches of science, its results are based on the laws of mathematics and are applicable to a large extent across a broad range of fields of academic research. As statistical methods are universal, the same tools may apply for vastly different sciences, yet the way of dealing with a statistical problem, the choice of the criteria as well as the establishment of interrelationships must be adapted specifically to the objective of the research and its expected outcome.

The extent of the data of meteorological analysis is defined by the period of gathering of the analyzed data. It may be divided into three levels: the meteorological data for 1 year, for 10 years and for 30 years. Analysis of the data partially depends on the duration of the discussed period, hence modeling may be performed at different levels as well as in various ways depending on the objective of the research and the likely results.

Meterological data is dynamic and non-stationary; it also largely depends on the location of the sampling. Taken simultaneously, the meteorological data for open spaces and city zones will be prominently different. Even more, the parameters of different areas within the territory of the same city will not be the same, either. As urban territories are denoted by the development of peculiar cyclones, the wind speed and direction depends on the exact location; the speed and direction values are likely to differ in the centre and in the suburbs. The city wind system produces the tunnel effect. The meteorological conditions of the city and open spaces are to some extent also defined by seasonality and daytime. Consequently, metyeorological forecasts for urban areas are extremely complex, and statistical analysis is usually involved in dealing with this task.

2. METHODOLOGY OF STATISTICAL ANALYSIS

Calculation methods applied in the framework of mathematical statistics allow establishing the generalized patterns with minor error margins of the relationship between the wind speed and other meteorological parameters as well as the wind angle (direction) and other meteorological parameters. Analysis of key statistical parameters requires outlining two tasks: (1) what is the relationship between the climatic data system and the wind speed and (2) what is the relationship between the climatic data system and the wind direction? In order to deal with the two challenges, *Microsoft Excel*-based calculations [10] were performed in the framework of potential solutions offered by the methodology of statistical analysis. The *Microsoft Excel* package features specific tools aimed at dealing with statistical tasks. The fundamental steps of discovering analytically-based dependencies in the field of mathematical statistics were as follows:

1) grouping of statistical data;
2) discovery of dot and interval values distributed across some unknown theoretical pattern;
3) verification of hypotheses on the theoretical distribution and its parameters;
4) regression and correlation analysis allowing to investigate the type and extent of relationships among random values.

Whenever data is observed to be prominently incongruous, the following criteria are used for its rejection: *Smirnov* test based on the known arithmetic average x of the sample and medium square deviation s; *Dixon* test with the application of special tables ($n < 25$); Student t (as defined by V. S. Gosset); *Winsor* test as a method of replacing a rejected value with the nearest one.

The following criteria were used for the statistical verification of the randomness and independence of the obtained results: the *series* criterion derived from the median of the sample (the alteration of pluses and minuses must be random), the rise and fall of the criterion series (in a sequence of signs, the number of series does not serve as a way of measurement, and the length of a series is substantial), and the criterion of consecutive difference squares which is usually more precise than the other above listed criteria.

The distribution of the hypothesis validation results according to the regular law leads to the average absolute deviation ($n < 120$) (it serves to decrease the impact of the extreme values), the approximate normality criterion when asymmetry and excess indices are calculated, *Variation amplitude* R ($3 < n < 1000$), for rapid verification of a hypothesis; Shapiro and Wilk compatibility criterion W ($n \leq 50$) producing a higher possibility of rejection of false hypotheses, Pearson compatibility criterion 2 χ and others.

Correlation analysis presumes the establishment of statistical relationship among features (in this particular situation, we mean meteorological data with the primary focus on the wind speed and direction. Correlation analysis defines the linear relationship of random values. The values of the correlation coefficient belong to the interval [- 1; 1]. When there is no normal distribution or when the distribution law is not known, when the relationship is not linear and $n < 30$, the interrelationship of random values is established with non-parameter methods, specifically, *Spearman* $S\ r$ or *Kendall* τ. Yet if the distribution is close to normal distribution, the use of parameter methods is preferable as they are more precise.

Regression analysis is a statistical method allowing the research of the functional dependence of a variable Y (the dependent variable or the criterion variable) on one or multiple variables Xi (independent variables). Regression analysis is usually treated as a specific facet of correlation analysis. The difference lies in the point that correlation models mutual statistical relationship between features whereas regression analysis models a single direction functional relationship. One of the correlating features is necessarily defined as the determining factor (the independent variable) and, by eliminating random factors, our objective is to characterize not statistical but rather functional relationship between the criteria of interest for the researcher [8, 9].

The following model of linear regression was applied: $y = a + bx + e$. Where *y* and *x* are variables; *a* and *b* are constants; *a* is the free member (*intercept*), *b* is the factor of the line direction (*slope*) and *e* is the random error.

Regression analysis allows writing the regression equation and evaluating its parameters. The measure of the reliability of the regression straight line is the standard evaluation error $S^2_{y/x}$. These errors of valuations are used to define the reliability intervals $\left[Y - S^2_{y/x} t_{a,n-2}; Y + S^2_{y/x} t_{a,n-2}\right]$ into which the values under observation may fall within some reliability levels[2].

Verification of the adequacy of the regression model. When the regression equation has been established and its parameters have been evaluated, verification of the precision of the result description achieved with this equation takes place, i.e. the adequacy of the regression equation is verified with the use of *F* – Fisher's criterion [4,5]. When the adequacy hypothesis is not verified, transition to a higher power regression equation has to take place.

3. RESULTS OF METEOROLOGICAL MEASUREMENTS AND THEIR ANALYSIS

The present research primarily used the one-year data obtained in Klaipėda District (Kalotė settlement). The data was sourced by a meteorological station which was set on the roof of Klaipėda University. This station was registering the average air temperature hourly as well as the minimum average value and time, the maximum average value and time, the average air humidity, the average pressure, the average precipitation, the average sunlight, the average speed of wind, the time of the maximum wind speed and its value, and the wind direction.

Methods of statistical analysis allowed obtaining correlation and regression analysis of the data for each month, the results were generalized, and conclusions were drawn. Table 1 shows correlation data for the impact of meteorological parameters on the formation of wind of a specific direction. The results presented in Table 1 show that the impact of various meteorological criteria on the formation of wind of a specific direction ranges from 0.414 to 0.802 with the approximate value of 0.569 during the year. In this aspect, January is evidently singled out as its correlation coefficient *R* equals 0.802. Hypothesis values H_0: $b = 0$, H_A were obtained for all the cases: at least one $b \neq 0$; the result of the research $p < 0.05$, which shows that the interrelationship is statistically important. Analysis of errors: deviations (from the graph or standard errors), deviation error averages equal zero or deviations equal the normal distribution of random values, and the dispersion is consistent (homoscedastic).

Table 1. Key statistical indices: impact of metrological parameters on the formation of a specific wind direction

	JAN.	**FEB.**	**MAR.**	**APR.**	**MAY**	**JUN.**
Regression Statistics						
Multiple *R*	0.802	0.568	0.414	0.508	0.435	0.500
R Square	0.643	0.322	0.172	0.258	0.189	0.250
Adjusted *R* Square	0.638	0.313	0.161	0.249	0.179	0.240
Standard Error	45.276	35.314	89.222	89.844	97.293	81.736
No. of observations	743	672	744	720	744	744

Table 1. Key statistical indices: impact of metrological parameters on the formation of a specific wind direction. Continued

	JUL.	**AUG.**	**SEPT.**	**OCT.**	**NOV.**	**DEC.**
Regression Statistics						
Multiple *R*	0.441	0.533	0.672	0.609	0.591	0.754
R Square	0.195	0.284	0.451	0.370	0.349	0.568
Adjusted *R* Square	0.185	0.276	0.444	0.363	0.341	0.563
Standard Error	84.605	77.034	69.147	58.388	32.183	44.938
No. of observations	744	750	728	757	725	761

Table 1. Key statistical indices: impact of metrological parameters on the formation of a specific wind direction. Continued

	AVG	**MAX.**	**MIN.**
Multiple *R*	0.569	0.802	0.414
R Square	0.338	0.643	0.172
Adjusted *R* Square	0.329	0.638	0.161
Standard Error	67.082	97.293	32.183
No. of observations	736	761	672

Table 2 shows indices for the regression formula during various months of the year ranging from -4830.377 to 5305.815 with the yearly average of 631.390. As differences between regression coefficients for specific months are prominent, more extensive research is required in order to establish the annual regression formula.

Table 2. Statistical indices: impact of metrological parameters on the formation of a specific wind direction

Intercept	
1	-637.842
2	140.012
3	-450.770
4	5305.816
5	2309.779
6	-1931.497
7	-2214.132
8	3937.722
9	4482.189
10	-4830.377
11	2170.941
12	-705.153
AVG	631.390
MAX	5305.816
MIN	-4830.377

Table 3 shows correlation data for the impact of meteorological parameters on the formation of wind of a specific speed. The results presented in Table 3 show that the impact of various meteorological criteria on the formation of wind of a specific speed ranges from 0.898 to 0.971 with the approximate value of 0.946 during the year. In this aspect, December is evidently singled out as its correlation coefficient *R* equals 0.898. Hypothesis values H_0: b = 0, H_A were obtained for all the cases: at least one b $\neq$ 0; the result of the research $p < 0.05$, which shows that the interrelationship is statistically important. Analysis of errors: deviations (from the graph or standard errors), deviation error averages equal zero or deviations equal the normal distribution of random values, and the dispersion is consistent (homoscedastic).

Table 3. Key statistical indices: impact of metrological parameters on the formation of a specific wind speed

	JAN.	**FEB.**	**MAR.**	**APR.**	**MAY**	**JUN.**
Regression Statistics						
Multiple *R*	0.964	0.955	0.960	0.952	0.952	0.932
R Square	0.930	0.912	0.921	0.906	0.907	0.869
Adjusted *R* Square	0.929	0.911	0.920	0.905	0.906	0.867
Standard Error	0.997	0.905	1.026	0.863	0.890	0.978
No. of observations	743	672	744	720	744	744

Table 3. Key statistical indices: impact of metrological parameters on the formation of a specific wind speed. Continued

	JUL.	**AUG.**	**SEPT.**	**OCT.**	**NOV.**	**DEC.**
Regression Statistics						
Multiple *R*	0.931	0.948	0.933	0.971	0.960	0.898
R Square	0.866	0.899	0.870	0.944	0.921	0.807
Adjusted *R* Square	0.865	0.898	0.868	0.943	0.920	0.805
Standard Error	0.910	0.991	0.996	0.870	0.798	1.393
No. of observations	744	750	728	757	725	761

Table 3. Key statistical indices: impact of metrological parameters on the formation of a specific wind speed. Continued

	AVG	**MAX**	**MIN**
Regression Statistics			
Multiple *R*	0.946	0.971	0.898
R Square	0.896	0.944	0.807
Adjusted *R* Square	0.895	0.943	0.805
Standard Error	0.968	1.393	0.798
No. of observations	736	761	672

Table 4 shows indices for the regression formula during various months of the year ranging from -32.112 to 18.245 with the yearly average of -1.939. As differences between regression coefficients for specific months are prominent, more extensive research is required in order to establish the annual regression formula.

Table 4. Statistical indices: impact of metrological parameters on the formation of a specific wind speed

Intercept	
1	-32.112
2	8.549
3	-19.986
4	-26.743
5	9.730
6	13.382
7	18.245
8	12.891
9	7.085
10	-22.967
11	16.862
12	-8.201
AVG	-1.939
MAX	18.245
MIN	-32.112

Preliminary data for yearly regression statistics concerning the impact of meteorological parameters on the development of a specific force of wind is shown in Table 5. The yearly correlation coefficient equals 0.952 which means that very strong linear relationship is observed between the researched variables, the result of the research is within $p < 0.05$ which means that the relationship is statistically important. In this case, the direct regression formula is derived as follows:

$$y = 0.375 - 0{,}5467 \cdot t_{avg} + 0.7212 \cdot t_{\min} - 0{,}195 \cdot t_{\max} - 0.005 \cdot w - 4{,}245 \cdot p - 0.0001 \cdot r_y +$$
$$+ 0.001 \cdot s_y + 0.555 v_{\max} - 0.003 \cdot d.$$

Table 5. Regression statistics of yearly data

Regression Statistics		
Multiple *R*	0.952	
R Square	0.907	
Adjusted *R* Square	0.907	
Standard Error	1.015	
No. of observations	8832	
	Coefficients	***Standard Error***
Intercept	0.375	0.148
Air temp avg., avg. h. temp. ^{0}C	-0.547	0.066
Air temp min., avg. h. temp. ^{0}C	0.721	0.043
Air temp max, ^{0}C	-0.195	0.030
Humidity, %	-0.005	0.001
Barometer, mm Hg	-0.000	0.000
Rain yearly, mm/h	-0.000	0.000
Solar avg., W/m^2	0.001	0.000
Wind speed max, m/s	0.555	0.002
Wind direction, 0	-0.003	0.000

Preliminary annual regression for Klaipėda and Kaunas cities in terms of wind direction and speed when the impact of the wind direction on the development of wind of specific speed is presented in Table 6.

Table 6. Comparison of statistical data

Regression Statistics	**Data for Klaipėda**	**Data for Kaunas**
Multiple R	0.052	0.243
R Square	0.003	0.059
Adjusted R Square	0.002	0.059
Standard Error	3.316	1.886
Observations	8832	8759

The table shows that the value of the correlation coefficient may be substantially different; the data for Klaipėda City produces the coefficient 0.052 which denotes linear very weak relationship between the researched variables whereas the value of 0.243 produced in Kaunas City represents linear weak relationship between the researched data points. In both cases, the relationship is statistically significant; yet, more extensive academic research is required in both cases in order to establish a more precise regression formula.

4. CONCLUSIONS

1. Analysis of statistical regression showed that in all the cases the relationship between the researched variables is correlation linear relationship; this relationship is statistically significant. In order to produce a precise regression formula, more extensive academic research is required.
2. In all the cases analysis of errors showed that deviations from the graph or standard errors are equal to zero whereas errors are normally distributed random values; the dispersion is consistent (homoscedastic).
3. Statistical analysis of each month taken separately develops a correlation coefficient based on the impact of meteorological parameters on the formation of specific directions of wind ranging from 0.414 to 0.802 with the average value of 0.569 during the year.
4. Statistical analysis of each month taken separately develops a correlation coefficient based on the impact of meteorological parameters on the formation of specific speeds of wind ranging from 0.898 to 0.971 with the average value of 0.946 during the year.

5 REFERENCES

1. KOPUSTINAS, V., ALZBUTAS, R., AUGUTIS. J. Matematinių modelių parametrų jautrumo ir rezultatų neapibrėžtumo statistiniai tyrimo metodai *ENERGETIKA*. 2007. Vol. 53. No. 3. p. 10–15.
2. DARGIS. E. Statistinių metodų taikymas tyrimo rezultatams apdoroti. Šiaulių Universitetas 2011 [referred on the 3th of Febrary in 2016 y.]. <http://vddb.laba.lt/fedora/get/LT-eLABa-0001:E.02~2011~D_20110804_094737-09571/DS.005.0.01.ETD.>.
3. JASILIONIS, A., NAGURNAS, S., MELAIKA, M., Use of mathematical methods of statitics for analyzing engine characteristics. The Free Library By Farlex 2012 [referred on the 3th of Febrary in 2016 y.]. <http://www.thefreelibrary.com/Use+of+mathematical+methods+of+statistics+for+analyzing+engine...-a0310866689>.

4. MIŠKINIS, V., KONSTANTINAVIČIŪTĖ, I., UŠPURAS, E., KALIATKA, A., KOPUSTINSKAS, V. Neapibrėžtumo analizės taikymas energetikos ekonomikos vienmačių modelių uždaviniams *ENERGETIKA*. 2006. No. 2. p. 1–9.
5. KONTAUTAS, A.; URBONAVIČIUS, E. Preliminary analysis of aerosol deposition and distribution in PHEBUS containment under FPT–3 experiment conditions // 6th Annual Conference of Young Scientists on Energy Issues CYSENI 2009, Kaunas, Lithuania, May 28–29, 2009. Kaunas: LEI, 2009. ISSN 1822–7554, p. 475–482 (INSPEC).
6. WILKS S. S. Statistical prediction with special reference to the problem of tolerance limits // Annals of Mathematical Statistics.1942. Vol. 13. p. 400–409.
7. HOFER E. Sensitivity analysis in the context of uncertainty analysis for computationally intensive models // Computer Physics Communications. 1999. Vol. 117. P. 21–34.
8. KAMINSKIENĖ, B. Matematinės statistikos elementai, I dalis . Vilnius, 1976, 278 p.
9. SVETULEVIČIENĖ, V. Matematinės statistikos elementai, II dalis . Vilnius, 1976, 142 p.
10. ŠAKNYS, V. Skaičiuoklė Microsoft Excel. Vilnius Baltic Amadeus, 1995. 336 p. ISBN 9986-484-03-0.

CYSENI 2016, May 26-27, Kaunas, Lithuania
ISSN 1822-7554, www.cyseni.com

FREQUENCY REGULATION WITH VEHICLE TO GRID (V2G) OPTION IN MULTI GENERATION POWER NETWORK

H. D. Mathur, Y. K. Bhateshvar
Birla Institute of Technology and Science, Pilani
Vidhya Vihar, Pilani, 333031 – India
Email: mathurhd@pilani.bits-pilani.ac.in

ABSTRACT

In smart grid scenario, penetration of large scale renewable energy sources are increasing rapidly. Even at global level, different authorities and governments are looking for solutions to reduce carbon emission. In order to achieve this goal of cleaner and greener environment for newer generations, fossil fuel based vehicles are being replaced with electric vehicles. Apart from encouragement from these authorities for replacing fossil fuel based vehicles, electric vehicles also becoming popular due to advancement in battery and electric motor technologies. Rise in number of electric vehicles will not only solve the emission problem but also accumulatively sources of power that can further supply back to grid during peak demand. It is going to be a win-win situation for both consumers and grid. This concept is termed as Vehicle to Grid (V2G), is explored for frequency regulation aspect in multi generation power network in this work. When in interconnected power system, automatic generation control (AGC) is not sufficient to manage balance between demand and supply, accumulative vehicle energy storage is considered a viable option for short term active power support in order to bring frequency back to normal. In energy storage possibilities, super conducting magnetic energy storage, ultra-capacitor etc. are primarily discussed. This paper focuses on integrated model of vehicle to grid (V2G) and wind power generating system (WPGS) as alternatives to supply instant power to regulate frequency when system is subjected to sudden perturbation. APSO (Adaptive particle swarm optimization) optimized fuzzy logic controller is used to intelligently suppress frequency and tie-line power oscillations. Effects of V2G and WPGS are examined for step load and continuously varying demand. To evaluate the performance of the system, differernt performance indices have been obtained, these are peak undershoot, peak overshoot and settling time at step load, but these performance indices are not applicable for varing load profile. Error based function are only suitable as performance indices for varying load profile over a time period, thus integral of absolute error (IAE) is choosen in this work. Results obtained are comprehensively presented and discussed in achieving power-frequency balance. MATLAB/Simulink is used for the simulation purpose.

Keywords: Automatic Generation Control, Adaptive particle swarm optimization, Vehicle to Grid; Short term active power, Wind power, Fuzzy Logic Controller.

CYSENI 2016, May 26-27, Kaunas, Lithuania
ISSN 1822-7554, www.cyseni.com

COMPARISON OF COMMONLY USED MATHEMATICAL MODELS FOR LIGHTNING RETURN STROKE CURRENT WAVEFORM

V. Zimackis
Riga Technical University
Āzenes 12/1, LV-1048 Riga – Latvia
Email: viesturs.zimackis@edu.rtu.lv

ABSTRACT

In electrical engineering the return stroke is the most important event in lightning flash, because return stroke current causes most of the damage and disturbance in electrical network. Return stroke mathematical models help engineers to predict transient voltages and currents induced in electrical networks by return stroke electromagnetic fields. Return stroke models can be divided into three groups: the electro-thermodynamic models, the transmission line models and engineering models. This paper compares the most commonly used engineering return stroke models, including Heidler model which is used in International Electrotechnical Commission (IEC) standard and return stroke current model recommended by the International Council on Large Electric Systems (CIGRE).

Over-voltages induced by direct or indirect lightning strike in the electrical network are the main cause of damage in households, according to statistics of European insurer companies. In this paper Alternative Transient Program/Electromagnetic Transient Program (ATP/EMTP) is used to create model of the electric power distribution network and to perform simulations of the transient process during lightning discharge in network. Various lightning return stroke current peak values and waveforms in electrical network with or without surge arresters were simulated. Aim of the research is to compare lightning current models offered in ATP/EMTP by entering identical input parameters for different scenarios.

Keywords: lightning, return stroke, mathematical models, current waveform

1. INTRODUCTION

Latvian distribution network consists of underground cable lines and overhead lines, both bare conductors and covered conductors. Despite the installed surge arresters, spark gaps and arc protection devices Latvian main distribution network operator JSC "Sadales tīkls" continues to face electric power interruptions, caused by lightning, as well as overvoltages and insulation damages of covered conductor. It is planned to find effective lightning protection for distribution network through ATP/EMTP simulations.

ATP/EMTP offers a choice of four exponential surge function sources: double exponential, Heidler, CIGRE and Standler. Standler source will not be discussed in this paper, because it is not applicable to power lines [1]. All types offer different lightning current waveform based on input parameters. In the case study all three ATP/EMTP offered surge function sources will be simulated on 20 kV branch line with and without surge arresters, with different waveforms and return stroke current amplitudes. The aim of this study is to compare all three surge functions by entering identical input parameters in various situations and analyzing amplitude values of lightning current and overvoltage in different points of power line in order to find source where it is easy to see how input parameters affect lightning return stroke current waveform and one that gives comparable results for various input parameters.

2. LIGHTNING RETURN STROKE CURRENT MODELS

2.1. Double exponential model

Double exponential expression was proposed in 1941 by Bruce and Golde and it is the first return stroke model that tried to integrate the experimental observations available at the time into a following mathematical expression of a current function i(t) [2], [3]:

$$i(t) = I_0(e^{-\alpha t} - e^{-\beta t})\,, \tag{1}$$

where I_0, α and β are constants that can be obtained from lightning characteristics. Double exponential expression has following drawbacks. Constants in equation (1) are not directly related to lightning main parameters such as peak current value, front time and time to half value [2]. With this function it is impossible to produce short stroke currents, because it increases maximum current steepness [4].

2.2. Heidler model

Heidler function is used in the IEC lightning protection standard to represent first and subsequent return stroke current waveform. According to Heidler current waveform can be described using following formula [2], [5]:

$$i(t) = \frac{I_0}{k}\cdot\frac{(t/\tau_1)^n}{1+(t/\tau_1)^n}e^{-\frac{t}{\tau_2}}\,, \tag{2}$$

where I_0 – peak current value, k – correcting coefficient of the peak value, τ_1 – front time constant, τ_2 – wave tail time constant and n – current steepness factor (IEC fixed value to 10).

IEC for first and subsequent return stroke current uses parameters given in Table 1, which vary for different lightning protection levels (LPL).

Table 1. Parameters for equation (2) according to IEC-62305-1

Parameter	**First stroke current**			**Subsequent stroke current**		
	LPL			**LPL**		
	I	**II**	**III-IV**	**I**	**II**	**III-IV**
I_0, kA	200	150	100	50	37.5	25
k	0.93	0.93	0.93	0.993	0.993	0.993
τ_1, μs	19	19	19	0.454	0.454	0.454
τ_2, μs	485	485	485	143	143	143

2.3. CIGRE model

According to CIGRE [6] rising front part of first return stoke current waveform can be described by

$$i(t) = At + Bt^n\,. \tag{3}$$

The basic assumption is that the current shape reaches the maximum steepness which is 90% of amplitude at a time t_n dependent on the exponent n. Both variables have to be evaluated by an iterative solution of the generalized equation:

$$\left(\frac{1-3x}{2S_N}\right)(1-x)^n = \frac{x(n-1)}{2S_N} + \left(\frac{1-3xn}{2S_N}\right)(1-x) \tag{4}$$

with

$$S_N = s_m \frac{t_f}{I}, \tag{5}$$

where I – current amplitude, s_m – maximum steepness (and t_f – front time. Sufficiently accurate solutions can be obtained using following equations:

$$n = 1 + 2(S_N - 1)\left(2 + \frac{1}{S_N}\right), \tag{6}$$

$$t_n = 0.6 t_f \left[\frac{3S_N^2}{\left(1 + S_N^2\right)}\right]. \tag{7}$$

The constants A and B are given by

$$A = \frac{1}{n-1}\left[0.9\frac{I}{t_n} \cdot n - s_m\right], \tag{8}$$

$$B = \frac{1}{t_n^n (n-1)}\left[s_m \cdot t_n - 0.9I\right]. \tag{9}$$

The front part of subsequent return stroke current is represented by

$$i(t) = s_m \cdot t_f. \tag{10}$$

The tail of the current waveform is represented by

$$I = I_1 e^{-\frac{(t-t_n)}{t_1}} - I_2 e^{-\frac{(t-t_n)}{t_2}}, \tag{11}$$

where time constants t_1 and t_2 are given by

$$t_1 = \frac{(t_h - t_n)}{\ln 2}, \tag{12}$$

$$t_2 = 0.1\frac{I}{s_m}, \tag{13}$$

where t_h is the time to half value. The constants I_1 and I_2 are given by

$$I_1 = \frac{t_1 \cdot t_2}{t_1 - t_2}\left[s_m + 0.9\frac{I}{t_2}\right], \tag{14}$$

$$I_2 = \frac{t_1 \cdot t_2}{t_1 - t_2}\left[s_m + 0.9\frac{I}{t_1}\right]. \tag{15}$$

The average values of a first stroke are $I = 31$ kA, $s_m = 26$ kA/µs, $t_f = 3$ µs and $t_h = 75$ µs [6]. Main disadvantages of this model are many additional calculations which may lead to mistakes in resulting waveform and the current front and the current tail are described by two different equations. Equation (3) describes the front up to 90% of the amplitude, but expression (11) describes the amplitude range on the tail.

3. ATP/EMTP MODEL FOR 20 KV BRANCH LINE

A schema of existing medium voltage branch line simulated in this study is given in Fig. 1. Network consists of a three phase infinite 20 kV source, an aluminium steel reinforced AS 70 bare conductor overhead line of total length of 1274 m, underground cable line AHXAMK-W 12/20 kV 3 × 240 + 35 Cu with total length of 1744 m, two 20/0.42 kV compact transformer substations and one 20/0.42 kV H-pole transformer substation.

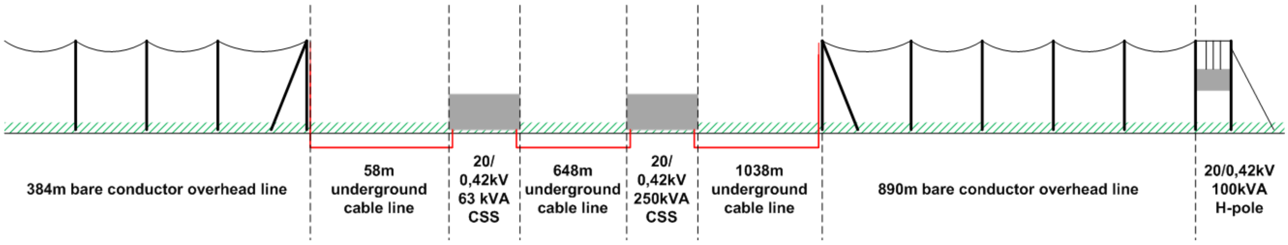

Fig. 1. A scheme of 20 kV branch line

Graphical preprocessor ATPDraw of the ATP/EMTP is used for simulation of the network. ATPDraw model of schema in Fig. 1 is shown in Fig. 2. Network source was simulated with a three phase (20 kV, 50 Hz) AC source (1). Aluminium steal reinforced bare conductor overhead lines were simulated with RL branch (2), where R and L are calculated according to the length of section. Resistance and inductance of conductor are 0.7774 Ω/km and 0.4 Ω/km respectively [7]. Underground cable lines with RL branch with parallel capacitor (3), where R, L and C are calculated according to the length of section. Resistance for given cable is 0.11 Ω/km, inductance is 0.35 mH/km and capacitance is 0.29 μF/km [7]. 20/0.42 kV substations were simulated with ideal three phase transformer with RL load (4), where resistance R and inductance L are calculated according to power of each transformer.

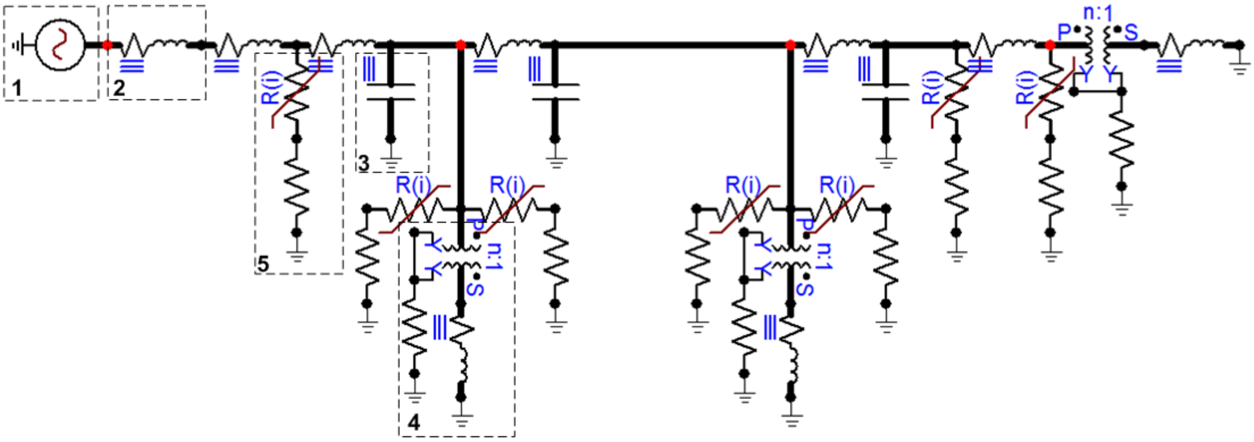

Fig. 2. A three phase of a 20 kV branch line in ATPDraw

Surge arresters are installed according to Latvian energy standard LEK 042-1 [8]. For cable lines 60 m < L < 1500 m metal oxide surge arresters are installed at both ends of cable line. H-pole substations S < 630 kVA should be protected with one set of metal oxide surge arrester. ABB POLIM-D 24 kV surge arresters are used in Latvian distribution network, which are simulated with nonlinear current-dependent resistor (5). Surge arrester characteristics are obtained from manufacturers datasheet [9]. The characteristic curve of the arrester used for the simulation is shown in Fig. 3. The grounding resistance was taken as 10 Ω [10].

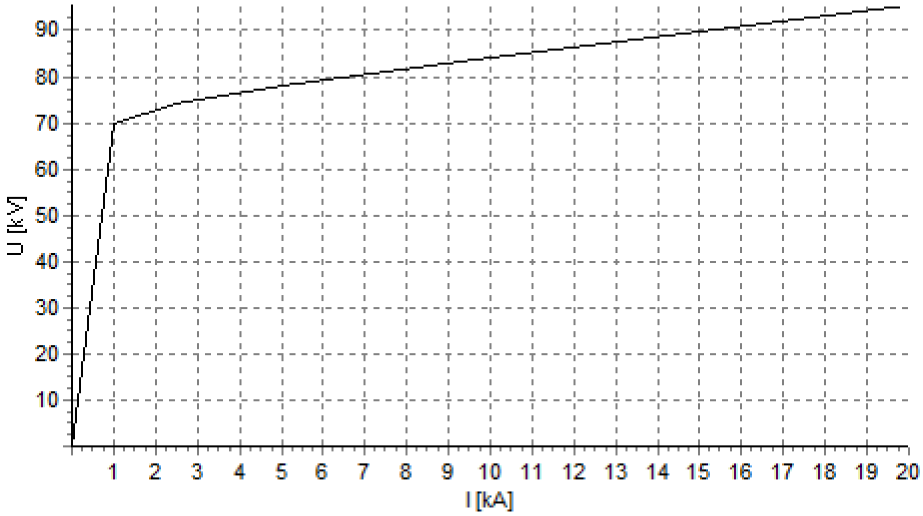

Fig. 3. Characteristic curve of the ABB POLIM-D 24 kV metal oxide arrester (8/20 μs)

4. CASE STUDY

Given 20 kV branch line was simulated with lightning strike in the middle of first bare conductor overhead line as shown in Fig. 4. For comparison three ATP/EMTP exponential surge functions (1) were used. The impedance of a lightning channel is represented as a parallel 400 Ω resistance (2) [11]. To compare all three sources and to measure lightning current and its induced over-voltages in 20 kV branch line current (3) and voltage (4) probes were used. Voltage was measured at each transformer substation.

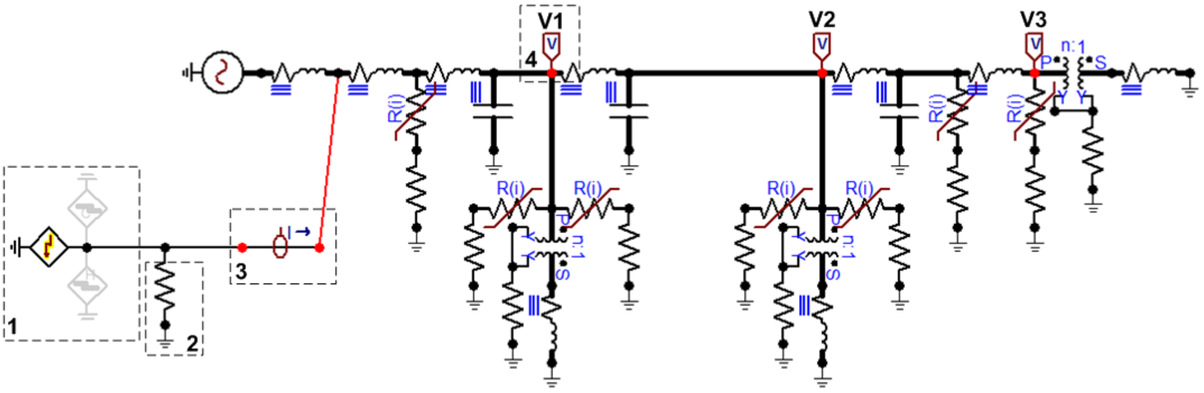

Fig. 4. Lightning strike simulation in ATPDraw

For more complete comparison measurements were made with two different lightning peak currents, 100 kA and typical peak current in Baltic countries and northern Europe which is 30 kA [12]. Three different lightning current wave forms were simulated (T_1/T_2): 10/350 μs, 0.25/100 μs and 8/20 μs which represents first direct lightning stroke, subsequent direct lightning stroke and indirect lightning stoke respectively. All simulations were made for two scenarios when there are no surge arresters installed and when they are installed according to LEK 042-1 [8] as shown in Fig. 2. For Heidler model current steepness factor n in all scenarios was fixed to 10 as recommended in IEC standard. For CIGRE model maximum steepness s_m in all scenarios was fixed to average value 26 kA/μs [6]. Double exponential model does not have fixed parameters, rising front steepness cannot be adjusted. Simulated peak currents and over-voltages at each substation for 100 kA lightning peak current are given in Table 2 and for 30 kA in Table 3.

Table 2. Modelled values for 100 kA lightning peak current

T_1/T_2	Model	without arresters				with arresters			
		I_{max}, kA	Overvoltage, kV			I_{max}, kA	Overvoltage, kV		
			V1	V2	V3		V1	V2	V3
8 / 20 μs	*Heidler*	95.8	3587.4	1413.8	1305.6	99.2	172.1	65.6	50.4
	CIGRE	97.6	2162.0	1348.1	1312.5	99.8	149.5	67.2	49.6
	Double exponential	32.5	750.9	587.7	567.0	32.4	92.4	42.7	28.6
10 / 350 μs	*Heidler*	101.8	3607.3	1602.0	1608.7	99.7	160.5	99.5	80.0
	CIGRE	99.9	2055.2	1385.3	1500.2	100.0	151.6	100.2	81.1
	Double exponential	87.2	1202.0	1093.1	1235.1	87.3	129.7	98.5	79.3
0.25 / 100 μs	*Heidler*	104.8	4063.3	1570.7	1464.1	106.4	804.6	93.7	76.1
	CIGRE	105.3	4086.5	1574.9	1515.6	106.9	807.0	97.1	77.3
	Double exponential	-	-	-	-	-	-	-	-

Table 3. Modelled values for 30 kA lightning peak current

T_1/T_2	Model	without arresters				with arresters			
		I_{max}, kA	Overvoltage, kV			I_{max}, kA	Overvoltage, kV		
			V1	V2	V3		V1	V2	V3
8 / 20 μs	*Heidler*	28.7	1090.2	438.1	405.7	29.7	98.5	28.9	24.5
	CIGRE	27.8	765.9	385.4	384.2	28.5	95.6	27.9	24.5
	Double exponential	9.7	239.3	190.3	184.1	9.7	36.3	25.2	20.8
10 / 350 μs	*Heidler*	30.5	1096.2	494.6	496.6	29.8	98.0	42.6	38.7
	CIGRE	30.3	759.9	413.9	453.7	30.8	103.5	43.1	39.2
	Double exponential	26.1	374.6	341.9	384.5	26.2	65.9	39.5	35.9
0.25 / 100 μs	*Heidler*	31.4	1233.0	485.2	453.2	31.9	255.4	39.0	31.8
	CIGRE	31.6	1239.9	486.5	468.7	32.0	256.1	40.3	34.4
	Double exponential	-	-	-	-	-	-	-	-

Overvoltage peak values differ more when lightning peak current is higher, particularly in scenario without surge arresters, because of the fluctuations which can be seen in Fig. 5. Transient process with surge arresters is shown in Fig. 6. Heidler and CIGRE models shows relatively similar results in all scenarios.

Double exponential functions incapability to produce short stroke currents is clearly visible in Table 2 and Table 3 results. It was not able to simulate direct lightning stroke at all, because ATP/EMTP have limited α and β values to 1000000 which represents 1μs. There is a great difference in indirect lightning stroke waveform as well. Difference in first direct lightning stroke waveform occurs, because I_0 in equation (1) does not represent the peak value of return stroke current.

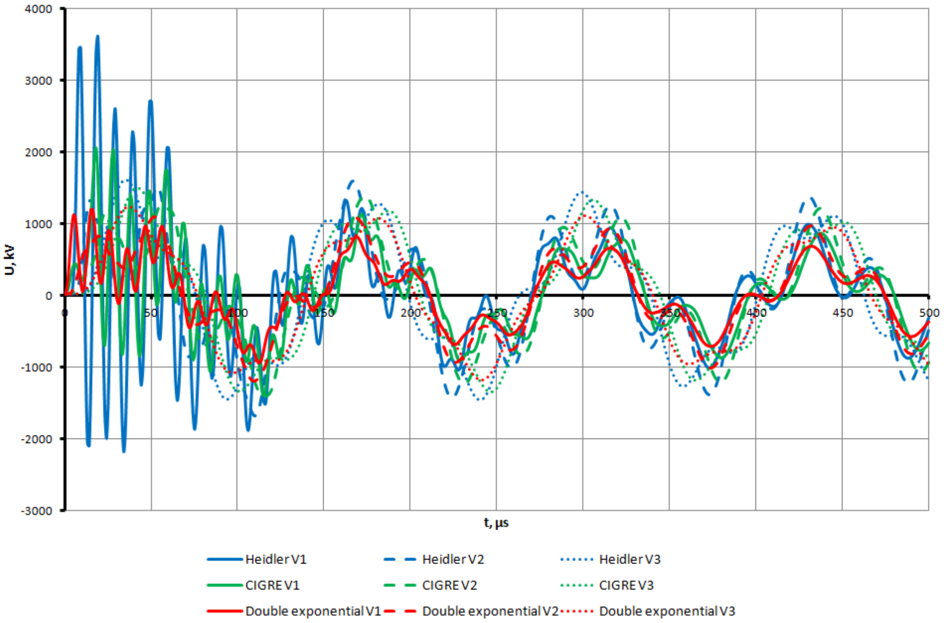

Fig. 5. Induced overvoltage without surge arresters (10/350 µs, 100 kA)

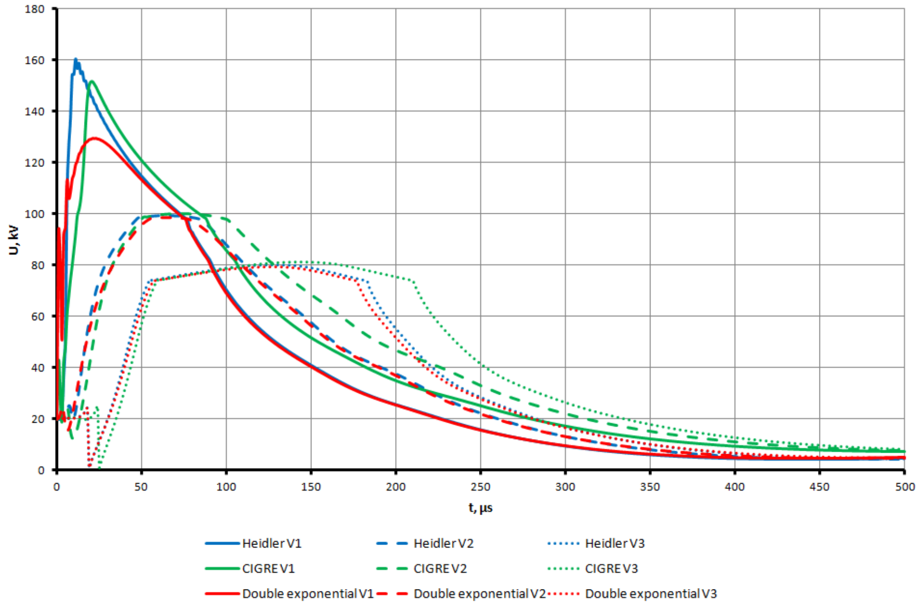

Fig. 6. Induced overvoltage with surge arresters (10/350 µs, 100 kA)

5. CONCLUSIONS

Three different mathematical models for lightning return stroke current simulation were tested using 20 kV branch line model in ATP/EMTP, based on existing Latvian distribution network line. Simulations were made with three different waveforms, two various peak currents and two scenarios without surge arresters and when surge arresters are installed according to Latvian energy standard. From results following conclusions were obtained.

Double exponential model is not able to simulate short stroke currents, for example, subsequent direct lightning stroke, because of ATP/EMTP limitations for function (1). Input parameters are not directly linked with the desired current waveform parameters, which make it difficult to apply for certain lightning current waveform.

CIGRE uses two equations to describe lightning return stroke current and none of them directly uses input parameters.

Heidler model gives higher overvoltages than two other models, differences results from different rising front part of lightning return stroke waveform.

CIGRE and Heidler model shows similar results in mostly all chosen scenarios. Based on results of the research I choose to use Heidler model in ATP/EMTP modelling, because if surge protection conditions are fulfilled in the worst case, they are also satisfied in other cases.

6. REFERENCES

1. STANDLER, Ronald B. *Protection of Electronic Circuits from Overvoltages*, 1st edition. New York: John Wiley & Sons, November 1989, 464 p. ISBN 0-486-42552-5.
2. WEI, H., BA-LIN, X., YOU-GANG, G. Analysis of the lightning waveshape. Radio Science Conference, 2004. Proceedings. Asia-Pacific. 2004 August 24–27.
3. COORAY, Vernon. *The lightning flash*, Power and energy series 34. London: The Institution of Engineering and Technology, 2013, 574 p. ISBN 0-85296-780-2.
4. HEIDLER, F., ZISCHANK, W., FLISOWSKI, Z., BOUQUEGNEAU, Ch., MAZZETTI, C. Parameters of lightning current given in IEC 62305 - background, experience and outlook. 29th International Conference on Lightning Protection. Uppsala, Sweden. 2008 June 23–26.
5. COORAY, Vernon. *Lightning protection*, Power and energy series 58. London: The Institution of Engineering and Technology, 2010, 1036 p. ISBN 978-0-86341-744-3.
6. CIGRE. *Guide to procedures for estimating the lightning performance of transmission lines*. Working Group 01 (Lightning) of Study Committee 33, October 1991.
7. Draka Keila cables. *Product Catalogue.* [referred on the 2nd of March in 2016 y.]. Link to the internet <http://media.drakakeila.ee/2016/01/Draka_Cataloque_EN.pdf>.
8. Latvian energy standard LEK 042-1. *Overvoltage protection of medium-voltage power grids*, first edition, 2005. (in Latvian).
9. ABB Data sheet. *Surge arrester POLIM-D*, 2013. 1HC0075853 E01 AD. [referred on the 2nd of March in 2016 y.]. Link to the internet:
<http://new.abb.com/high-voltage/surge-arresters/medium-voltage-arresters>.
10. Latvian energy standard LEK 048. *Grounding of electrical installations and electrical safety measures. Principal technical requirements*, first edition, 2005. (in Latvian).
11. AMETANI, A. Lightning surge analysis by EMTP and Numerical Electromagnetic Analysis Method. 30th International Conference on Lightning Protection. Cagliari, Italy. 2010 September 13–17.
12. ENNO, Sven-Erik. *Thunderstorm and lightning climatology in the Baltic countries and in northern Europe*. Tartu, Estonia: University of Tartu Press, 2014, 142 p. ISBN 978-9949-32-537-5.

CYSENI 2016, May 26-27, Kaunas, Lithuania
ISSN 1822-7554, www.cyseni.com

CUSTOMER BEHAVIOUR IN ENERGY CONSUMPTION: ENVIRONMENTAL ACTIVITIES

V. Varanavicius
Lithuanian Energy Institute
Breslaujos str. 3, 44403 Kaunas – Lithuania
E-mail: v.varanavicius@gmail.com

ABSTRACT

Entering the millennium age has challenged a great scale of people. But no matter in which sphere company operates customers are always on the center stage. Consumer behavior should be understood as an investment, which does not produce results in the short period. Investigations of released academic papers regarding the customer behavior enhancement via and environmental activities have revealed that this field is highly unexplored. With this in mind, the current paper aims to prove the fact that paying more attention to such elements like environmental activities and adapting them into the business practice would serve as a help to save the financial resources and attain new and retain old customer base. Hence, the current article is initiated on the breath analysis of customer behavior in energy consumption though environmental activities. There are three-fold objectives: 1) briefly analyze the main element of consumer behavior from theoretical point of view; 2) to investigate key energy consumption factors; 3) to make the brief investigation of main environmental activities.. Additionally, this study paper brings in a new approach regarding a great variety of collected understandings of customer behavior and its connections with synergy and environmental activities. The key methods of the study are used: 1) logical and comparative analysis of literature; 2) synthesis and deduction.

Keywords: energy consumption; customer behavior; synergy; environmental activities.

1. INTRODUCTION

Entering the millennium age has challenged a great scale of people. But no matter in which field company operates customers are always on the center stage. A growing body of literature suggests that non-financial performance measures are leading indicators of financial performance [5]. Consumer behavior should be understood as an investment, which does not produce results in the short period.

The novelty of the study: this study shows that environmental activities influence on psychological concept of consumer behavior in energy consumption, therefore, it is recommended to incorporate the idea of uncomplicated information availability for consumers taking into consideration long term habits.

The object of this study is: environmental activities influence on consumer behavior in energy consumption.

The problem of the study is: how environmental activities influence consumer behavior in energy consumption?

The aim of the study is: briefly analyze the key environmental activities influencing consumer behavior in energy consumption.

The objectives of the study are three-fold:

1) Briefly analyze the main element of consumer behavior from theoretical point of view.
2) To investigate key energy consumption factors.
3) To make the brief investigation of main environmental activities.

The method of the study is logical and comparative analysis of literature which is closely related with customer behavior energy consumption and environmental activities.

2. SUSTAINABLE ENVIRONMENT

According to Hofer, Cantor and Dai (2012) [7], companies are using environmental activities to obtain competitive advantage against competitors and adapt consumer behavior for their products consumption, including energy. The managers are analyzing the environment actions of their competitors, because understanding the sustainable environment actions have the same importance as following competitors' financial situation, marketing and development actions. In most of the cases the size of the company becomes a disadvantage for environmental activities. The larger companies become not flexible and slower, which is the big disadvantage against competitors. The growing companies should put a lot of effort to decrease the bureaucracies and allow quick implementations for adequate environmental initiatives.

To hold a position of industry leader in environmental activities is not easy, the company has to recognize and counter the strategic moves of their competitors, also adapt them to customer behavior. Hofer, Cantor and Dai (2012) [7] point put that: "Industry leaders consistently have inferior environmental performance, which puts them at a strategic disadvantage. Closing this performance gap is vital, especially considering the growing emphasis put on the environment. Recognizing the importance of environmental management and following these simple recommendations allows managers to improve their competitive standing and the environment at the same time." The environmental activities are adopted according to customer behavior. Moreover, mentioned activities have both side effect, it forms customer behavior, also these activities are implemented according to already existing ones with a goal to reshape them and gain the competitive advantage.

3. CUSTOMER BEHAVIOR

The traditional economic theory of customer preference is based on four main elements: customer income, market price of goods, customer preferences and behavior assumption about the maximum of achievable benefit. When exist the limited income, the customer is choosing the preferred goods by using the method to ensure getting the maximum benefit, also which is allowed by limited income. [3]

It is important to detail several elements, such as realized customer rationality. The classical users or consumers usually are those who maximizes their benefit from various purchase options. Seeking to get the highest benefit consumer has to have overall information: the group of possible purchase options and the prices of each good. It is admitted that the role of information in very important for the customer behavior when real life situation is analyzed. The rational choice is possible only then the context of perfect information availability exist. [8]

It is worth to mention, that the consumer choices, tastes that have the high impact on the choice is valued. The consumer preference theory has not much information about nature of customer behavior, structure and environment. The individual and collective consumer preferences is known as much as it was analyzed through the rational consumption during the process of consumer decision making. It is said that economy is promoted, that there is no constrains on desire of individual goods or services. The wishes of the consumer is unlimited, this is the constraint for theory which says that customer is willing to get the highest values. However, the main factors that make influence is the individual taste, preferred costs and benefit. So, the role of information is said to have the highest influence that allows to make the rational decisions to the consumer. To sum up, the one constraint is the assurance of needed information to ensure the rational decision making, including the costs and the benefit that correlates with each other [4].

4. ENERGY CONSUMPTION

It can be stated that equalizing energy consumption with behavior is not possible, on the other hand, it can be described as consequences of behavior, such as turning on the lights or thermostat level reduction [2].

It is important to mention that authors divide the two types of energy consumption in households, the table below show the types of energy saving behavior:

Table 1. Energy saving behavior types

Behavior Types	Examples
Productive behavior	Investments with clear nature Ceiling Insulation Walls insulation Double windows installation
The behavior which decrease energy consumption	Recurring operational actions Turning off the light Keeping windows closed Turning off equipment

Source: Abrahamse et. al. (2005). [1]

It is worth mentioning that these behavior types may be considered from the economic perspective, as an example can be taken that the consumption behavior can be related with the monetary aspect. Or on the other hand the energy consumption can be seen as value approach, as an example energy consumption behavior may be influenced by saving the environment that persons are cared about.

According to Geller (2002) [6], there is still not clear which behavior type – the productive behavior or the behavior which decrease energy consumption is more effecting on energy saving. It is also said that behavior that decease energy consumption creates the conditions for developments of behavior changes in the long term perspective. However, the author Abrahamse et. al. (2005) [1] states that productive behavior is more effective when seeking for energy saving and environmental sustainability.

It does not matter, if the behavior is based on clear nature of investments, or it is recurring operational activities, on both sides the behavior of each individual is affected by social or individual factors. Evaluating from the macro level perspective, development of technologies, economic growth, demographical and institutional factors, development of culture make influence on our behavior in long run. On the other hand evaluating from the perspective of micro level the factors such as motivation, opportunities and possibilities influence on the behavior in individual level [1]. Also it is worth to mention that the behavior of individuals is affected by habits and some routine procedures which is made automatically, not thinking and spontaneously. Summing up, influencing factors can be grouped into internal (attitudes, norms, and beliefs) and external (institutions, rules, regulations).

5. CONCLUSIONS

1. The traditional economic theory of customer preference is based on four main elements: customer income, market price of goods, customer preferences and behavior assumption about the maximum of achievable benefit.
2. To ensure the rational decision, the availability of information is important, including the costs and the benefits that customer is going to have.

3. Behavior that decease energy consumption creates the conditions for developments of behavior changes in the long term perspective.
4. Energy consumption behavior is affected by habits and some routine procedures which is made automatically, not thinking and spontaneously. Behavior influencing factors are grouped into internal (attitudes, norms, and beliefs) and external (institutions, rules, regulations).
5. Companies' environmental activities has two sided effect. It is cheated according to customer behavior, also those activities are making the influence on customer behavior.

6. REFERENCES

1. ABRAHAMSE, W., STEG, L., VLEK, C., ROTHENGATTER, T., (2005). A review of intervention studies aimed at household energy conservation. *Journal of Environmental Psychology*, Netherlands, No. 25, p. 273–291.
2. BECKER, L., SELINGMAN, C., FAZIO, R., DARLEY, M., (1981). Relating Attitudes to Residential Energy Use. *Environment and Behavior*, Nr. 13, p. 590–609.
3. BEGG, D. K. H., FISCHER, S., DORNBUSCH, R., DAMIAN WARD, D., (2005). *Economics*, 8th Edition, McGraw-Hill Education, Berkshire.
4. BRENNAN, T., (2007). Consumer preference not to choose: Methodological and policy implications. *Energy Policy*, No. 3, p. 1616–1627.
5. CHEN, X. (2006). Customer satisfaction, customer bargaining power, and financial performance. USA: University of Southern California.
6. GELLER, S., (2002). The Challenge of Increasing Proenvironment Behavior. Handbook of Environmental Psychology. Wiley, New York.
7. HOFER, CHRISTIAN, CANTOR, DAVID E., JING DAI, (2012). The competitive determinants of a firm's environmental management activities: Evidence from US manufacturing industries, *Journal of Operations Management*, 30: 9–84.
8. NUNES, P., (2002). Using factor analysis to identify customer preferences for the protection of a natural area in Portugal. *European Journal of Operational Research*.

CYSENI 2016, May 26-27, Kaunas, Lithuania
ISSN 1822-7554, www.cyseni.com

STUDY OF POWER TRANSFORMER MECHANICAL FAULTS DETECTION BY USING VIBRODIAGNOSTICS

Janis Marks
Riga Technical University
12/1 Azenes Street, LV-1048 Riga – Latvia
Email: janis.marks@rtu.lv

ABSTRACT

Power transformers are important elements of the electrical system and have a high degree of risk since in case of failure the generator connected to the damaged transformer cannot transfer energy to electrical system. Therefore, a generated power deficit may be formed and part of the consumers can be disconnected from power supply.

Power transformers can experience various types of faults that may be potentially dangerous and cause the failure of the device. Various diagnostic methods exist for the detection of these damages. Each of them designed for a specific transformer characteristic. For example, measurement of winding insulation resistance and dissolved gas analysis can be used to detect electrical faults, but thermography is used to identify thermal defects. It should be noted that these widely used methods are not intended to detect mechanical faults. However, one possible approach to detect them is based on analysis of vibration measurements on the surface of transformer tank. This method is discussed in this article.

In order to detect mechanical defects, certain difficulties occur. It is impossible to see what is happening inside the transformer tank without opening it, but vibration analysis can acquire information about transformer windings and core mechanical condition without doing so. This is because vibration sensors are mounted on the transformer tank surface. Consequently, it is possible to analyse the causes of mechanical defects, their location within the transformer's structure and their intensity while transformer is operating.

A case study is provided where data is analysed from a power transformer with increased vibration levels, which is installed in a power plant in Latvia. A method is proposed for graphical analysis of the results of vibration measurements. It allows obtaining more information about vibration amplitudes, their distribution and epicentres, as well as vibration changes within a specified time period caused by the transformer.

Keywords: Power transformers, fault detection, condition monitoring.

1. INTRODUCTION

Alternating current flows in the windings of power transformer while it is working in nominal conditions. This process creates a magnetic field with constantly changing values around the windings. Consequently, this field induces electromotive force in secondary winding of transformer.

This force allows the flow of current if the electric circuit of secondary winding is closed. One of determining conditions to provide the operation of transformer is the position of magnetic field within the construction of the transformer. It is necessary for it to flow through every individual loop of secondary winding since this is the part of the magnetic field that induces electromotive force in the secondary winding. For this purpose, magnetic circuits are made of steel consisting of separate strips. This way the magnetic permeability is much higher than the surrounding air or any other dielectric next to it and the position of magnetic field is located utmost through the secondary winding of power transformer. The magnetic circuit cannot be implemented from monolith steel because eddy currents are generated within it. It should be noted that it is impossible for all magnetic flux to flow through the secondary winding since some portion of the magnetic flux will be linked through insulation and other components of the transformer. This component is called leakage flux and a part of it closes through the construction of primary and secondary windings. Therefore, both current conducting windings are positioned within a magnetic field and are exposed to electrodynamic forces proportional to current squared in the given winding. It should be noted that similar forces are acting upon the core of transformer because its material has a characteristic to change dimensions depending on the value and direction of the magnetic field within it. Therefore, electrodynamic forces act upon the transformer and cause vibrations while it is connected to supply of electric energy [1].

Transformer is subject to relatively intense repeating thermal and electrodynamic processes within long-term operation. The result of this is the degeneration of both the insulation condition between transformers windings and the clamping pressure of windings and magnetic core. Over time, the situation can deteriorate and irreversible faults can occur since transformer degenerates through time. It is necessary to carry out transformer diagnostics to avoid these faults. However, the dimensions and construction of large power transformers are non-homogeneous and are not symmetrical. Therefore, certain difficulties occur in order to check the mechanical condition of windings and magnetic core of transformer [2].

Arising vibrations spread within the surrounding space and this process also occurs inside the construction of transformer. The vibrations from windings and magnetic core propagate through the lairs of insulation, constructive components and the tank of transformer. Therefore, it is possible to measure amplitudes and harmonics of vibrations from the surface of transformer with sensors intended for these measurements. However, it is necessary to take in consideration the altered vibration characteristics due to their propagation through the structure of transformer since these vibrations pass through certain parts of transformer and are damped with their kinetic energy distributed throughout a larger space. Additionally, every component of structure has natural frequencies and influences certain harmonics of vibration differently. This also changes the information of vibrations obtained on the surface of transformer. Furthermore, vibrations have a fundamental property of arising in a certain place when they are suppressed in a different region and their paths of spreading are changed. For example, middle three magnetic core segments of five-leg transformer are covered by the primary and secondary windings and vibrations from both the magnetic and electric circuits of transformer bulge mostly in the side segments of the magnetic core since there is relatively low mechanical resistance in these regions. Therefore, the actual mechanic fault can occur in one place but its effects on vibrations generated emerge in a different location since the given distribution path has less resistance [3–5].

However, it is possible to estimate the mechanical condition of windings and magnetic core of transformer from measurements taken from the surface of transformer by taking in consideration the uncertainties caused by distribution of vibrations. Therefore, certain standards exit defining the levels of all vibration characteristics (displacement, velocity and acceleration). It is considered that transformer has developed a mechanical fault if these levels are exceeded. However, more precise information cannot be obtained [6].

The objective of this article is to show that it is possible to obtain information about the mechanical condition of windings and magnetic core of transformer with the visualization and approximation of surface vibration of transformer.

A case study is provided where the data of surface vibration of transformer installed in Latvia is viewed, visualization and approximation is performed and corresponding conclusions are made.

2. POWER TRANSFORMER DIAGNOSTIC METHODS USED IN LATVIA

Diagnostic methods used for power transformers in Latvian power plants are shown in Table 1, as well as potentially detectable fault types. The “+” indicates detectable fault types and the “*” indicates the potentially detectable fault types of corresponding methods. Every diagnostics method is intended for a specific transformers element or characteristic. The occurring faults within power transformers can be divided in 3 groups [8] depending on their nature – thermal, electrical and mechanical.

Table 1. Summary of diagnostic methods

Diagnostic methods name	**Detectable fault type**		
	Mechanical	**Electrical**	**Thermal**
Physical chemical analysis of oil	*	+	+
Chromatographic analysis of oil		+	+
Thermography testing of transformer			+
Vibrodiagnostics	+		
Termination of partial discharge	*	+	
External visual inspection of transformer	+		
Insulation resistance	+	+	+
Dielectric loses		+	
Winding active resistance measurements with direct current		+	+
Detection of short-circuit resistance	+		
No-load losses		+	

Various diagnostic methods for power transformer are used in practice. They differ in their content, provided information and characteristics. They can be applied both when the power transformer is operating and out of service. Single diagnostic method by itself cannot provide information about all possible power transformer faults. Therefore, the most optimal combination of these methods must be found to acquire the data sufficient to evaluate technical condition. As it is shown in Table 1, the mechanical condition of power transformer windings and magnetic core can be evaluated primarily by using vibrodiagnostics. This method allows to collect data about the source of vibrations within power transformers construction, their nature and amplitude. When either windings or magnetic core gradually delaminates, their created vibrations increase with direct proportion [1, 4].

Table 1 also shows that aside from vibrodiagnostics, there are other diagnostic methods, which can detect defects of mechanical nature in power transformer. Winding resistance measurements are one of these methods that allows detecting such faults as burnout of solid insulation, high moisture and water content, and mechanical deformations. These faults have negative effects on the transformers winding insulation and as a result, the insulation deteriorates. However, it is not possible to determine, which of these defects have actually caused the fault. Therefore, in order to clarify this, additional diagnostic methods are required [1, 4].

Another alternative method exists, which is short-circuit resistance detection. Since transformer winding geometric configuration can change as a result of short-circuit this change affects short-circuit resistance and allows to diagnose mechanical faults [9].

3. VIBRATIONS IN POWER TRANSFORMERS

Vibrations data is acquired with sensors on the surface of power transformer tank during vibrodiagnostics. However, this approach alters the original pattern since vibrations originate within transformers windings and magnetic core but afterwards they spread through the internal structure of transformer, reach tank’s surface through oil and only then are received by sensors. Fig. 1 shows the graphical interpretation of this process [10].

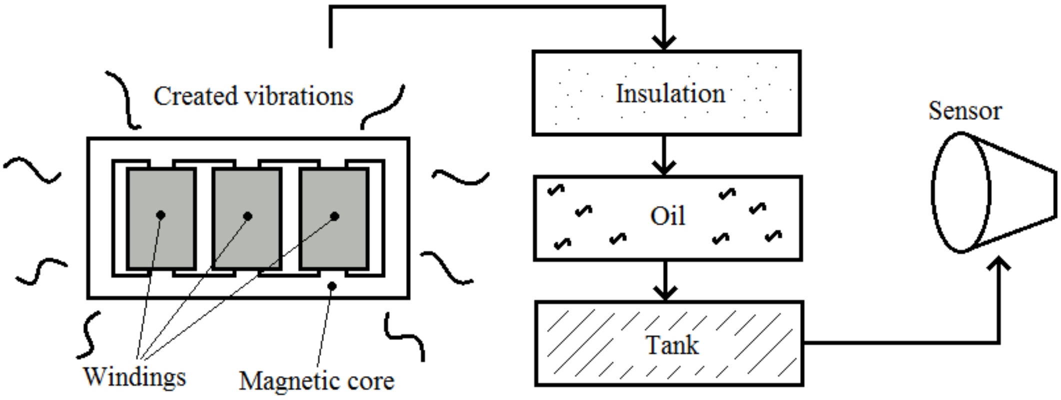

Fig. 1. Transformer vibration distribution

There is a difference between sensor readings on the surface of the tank and originally generated vibrations because their transmission path is relatively long and diverse. This affects both vibration spectrum and combined amplitude. In general vibration data from both inside of transformer or outside of it can be used as input data for detection of mechanical faults since the vibration generation source is the same [3]. But it is difficult to directly acquire information about vibrations of power transformer windings and magnetic core. Therefore, vibrodiagnostic methods use either an expert system (specifically designed software) or rough approximation. Equation 1 shows an example of vibration value change due to transformers structure [11].

$$v_{\tan k,100} = (\alpha + \beta\theta_{to})i^2 + (\gamma + \delta\theta_{to})u^2, \tag{1}$$

where $v_{tank,100}$ is vibration signal amplitude in 100 Hz frequency, i and u respectively current and voltage within transformers winding, θ_{to} is the temperature of transformers tank and α, β, γ, δ are coefficients, which are related to the geometry of each individual transformer [11].

Power transformer has other components that generate vibrations such as oil pumps for forced cooling. These devices generate additional vibrations and further negatively affect diagnosis of mechanical condition. However, these vibrations have defined frequency spectrum and can be differed from the main transformer by filtering them [10].

Additionally, the transformer tank can be nonhomogeneous and asymmetric. For this reason, vibrations are received differently in places with varying distances from vibration generation sources. This negative influence is countered by taking into account the position, geometric parameters and respective configuration of transformer tank and other relatively large components within it [3].

Interpretation of the results of vibrodiagnostic test with modelling of vibrations generated in power transformer has a large advantage since it is possible to input all characteristics of transformer tank and other components in the model and acquire more accurate results. The generated results then are compared to situation in reality.

4. SUMMARY OF GRAPHIC INTERPRETATION METHODS OF VIBRATION MEASURMENT RESULTS

In practice there are a large number of power transformer diagnostic methods [7, 11–13]. A part of these methods use graphic simulations or graphic interpretation of the results and a fraction of them are shown in Table 2. It also displays their comparison, given disparities and the input data l, v, a, (displacement, velocity and acceleration). The methods differ both in the necessary input data and in the obtained information from final results.

Table 2. Comparison of vibrodiagnostic methods

Method	**Input data**					**Necessary software**	**Fault location**
	l	**v**	**a**	**Used harmonics (frequencies)**	**Transformer geometry**		
Vibro-acoustic method	-	-	+	1–10 (100–1000 Hz)	Not needed	Expert system	In transformer windings and magnetic core
Finite element modelling	+	+	+	1–1000 Hz (continuous spectrum)	Is needed	Expert system	In transformer windings and magnetic core
Surface velocity pattern	-	+	-	1 (100 Hz)	Not needed	Expert system	In transformer windings
Vibration sensor network designing	-	+	-	1–20 (100–2000 Hz)	Not needed	Expert system	In transformer windings and magnetic core

Vibro-acoustic method uses specialized software with an expert system and utilizes Fourier transformations to calculate and obtain the necessary results from original vibration data of transformer surface [7].

Both inner and outer structures of a transformer are modelled in finite element method. As the result, natural frequencies are generated and vibrations within the transformer are created. Afterwards, modelled data is compared to vibrations measured in practice, generally approximately 10% difference is obtained [11]. This method is effective since more information is obtained about the processes inside the structure of transformer. However, it can be more complicated to carry out since the method is more complex [11].

The acquisition of velocity pattern on the transformer surface gives information about vibration amplitudes and their changes considering temperature fluctuations within the transformer and around it. The obtained data provides a rough notion about the mechanical condition of the transformer windings, however surface pattern velocity method does not provide information on mechanical condition of other parts of the transformer [12].

The designing of vibration sensor network allows the possibility to adapt it to each individual power transformer. More accurate information can be acquired about vibrations caused by transformer windings and therefore their mechanical condition. It should be noted, that a disadvantage exists since the sensor network is designed for a specific situation and this developed setup will not be as effective and precise if the conditions change. This is explained by the fact that the placement of largest vibration epicentres may change if transformer windings or magnetic core deforms and the configuration of installed sensor network will not correspond optimally to the new situation [13].

5. CASE STUDY

5.1. Problem statement

Results of vibration measurements are analysed for a power transformer installed in a power plant in Latvia as the case study of this article. Increased vibration values have been observed for this transformer during a period of 5 years. The author expresses gratitude to JSC Latvenergo for providing data of vibration measurements for the case study.

Certain difficulties occurred with the processing of the results of vibration measurements with vibrodiagnostic methods analysed in previous chapter of this article because not all necessary information is given within the literature.

- The coefficient for the technical condition using vibro-acoustic method describes the mechanical condition of windings and magnetic core within sectors of transformer. It is calculated by using an expert system [7].
- The software required and mathematical model used for finite element modelling method is not indicated in [11].
- The method of tank surface velocity pattern requires software and a mathematical model to carry out the diagnostic. This software is not specified and model it is not shown in [12].
- The method for vibration sensor network designing selects a specific sensor network for each individual power transformer. It is not possible to do interpretation of data if it is already obtained with a different sensor network [13].

Therefore, there is a necessity for interpretation method of the results of vibration measurements that is freely available and universal enough, and capable of providing the insight about the mechanical faults of transformer windings and magnetic core. Furthermore, the explanations would be available with open code for the operation and expert system of such method.

Table 3 shows the description for proposed method within its current stage of development.

Table 3. Description of the proposed method

Input data					**Necessary software**	**Fault location**
l	**v**	**a**	**Used harmonics (frequencies)**	**Transformer geometry**		
-	+	-	Vibration total value	Sensor relative position on transformers tank	Not needed	In transformer windings and magnetic core

5.2. Proposed method and evaluation of the results

The proposed method uses data of the total values of vibration velocity. It contains all vibration harmonics received from sensors located on the surface of tested power transformer. These sensors can receive frequencies from 10 *Hz* to 1000 *Hz* [14]. Fig. 2 shows the sensor position for this power transformer. Initially, there was only a small amount of sensors but the count was increased due to measured vibrations with high amplitudes. This was carried out in practice. However, this method can be used for different sensor arrangements as well. Measured results are used for data approximation that is carried out with different power polynomials, and approximated values are obtained in places where sensors were not positioned. Then this information is visualized with *Matlab* program and positions with higher vibration values are highlighted. It is possible to analyse vibration characteristics, distribution from main epicentres and intensity by using this method. It should be noted, that the proposed method currently cannot detect whether the cause of higher vibration values in a specific region is the winging or magnetic core within it.

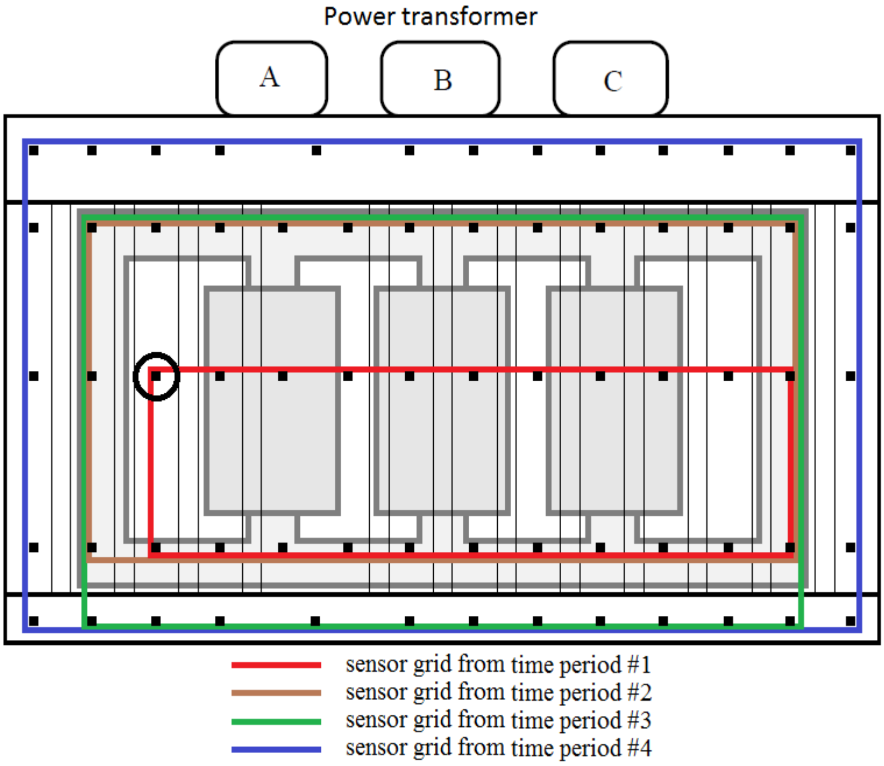

Fig. 2. Sensor grids used vibration measurements in different time periods

Fig. 3 shows with blue colour the results obtained with the proposed graphic interpretation method for one side. Vibration amplitudes with higher values are displayed in red colour. Fig. 3.a shows the approximation results when transformer is operating with no load and Fig. 3.b shows results when transformer is operating with full load. The differences can be explained because there is no current flowing in the secondary winding in no-load operation mode since the secondary electric circuit in not closed. Therefore, electrodynamic forces are not acting upon this winding, and the nature of vibrations caused by the transformer is different.

These results show that vibrations with higher values are generated mostly in phase A winding and the very left side of magnetic core. The highest vibration values overall are in this region of the magnetic core. This can be explained that the tested transformer is five-legged and this construction of magnetic core has this characteristic because the side parts of the magnetic core are not as well fixed in place as the middle sections, which are surrounded by transformers primary and secondary windings.

It should be noted, that there are vibration epicentres with lower values. In most cases they are located respectively against the phases of the transformer. These changes should be taken in consideration because the vibration values are relatively higher.

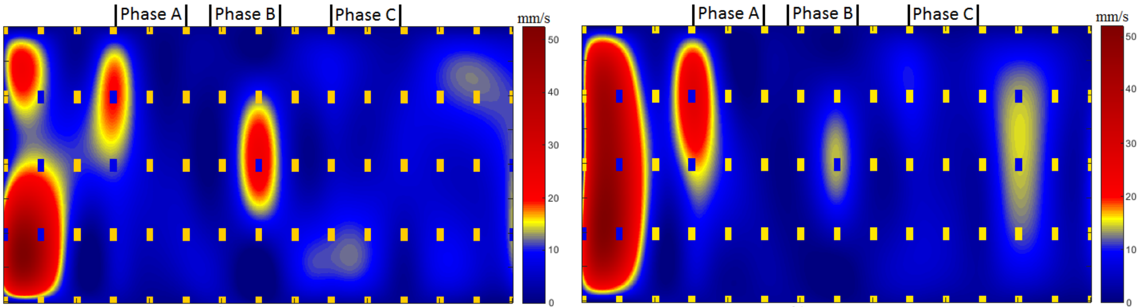

a) No load b) Full load

Fig. 3. Graphical interpretation of vibration velocity

The proposed method allows the possibility to acquire results of vibration change within time if the data is available from multiple measurements. The black circle in Fig. 2 and Fig. 4 displays the point where the values of vibration amplitude have increased the most. Fig. 5 shows the results from this change. Fig. 4 shows and emphasizes the vibration velocity amplitudes growth within period of 5 years. The position and arrangement of sensor networks was different and it was necessary estimate correct relative position. This procedure allowed combining vibration results from different sensor grids and obtaining vibration change within time. Drastic differences are shown at phase A and the segment of magnetic core on the left of it. This could indicate mechanic faults with the windings and magnetic core of power transformer.

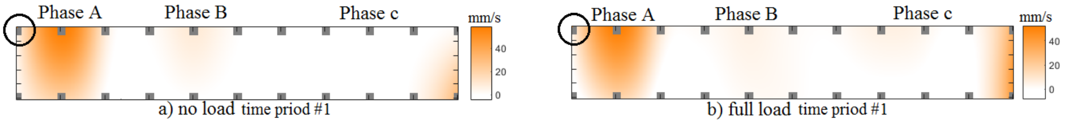

a) no load time priod #1
b) full load time priod #1

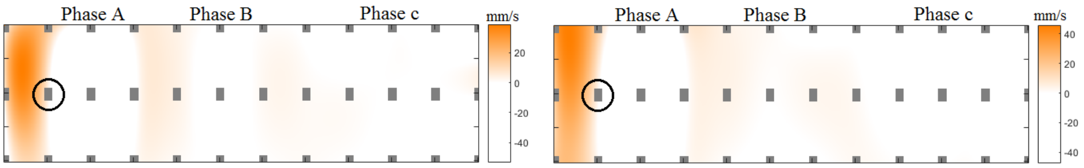

c) no load time priod #2
d) full load time priod #2

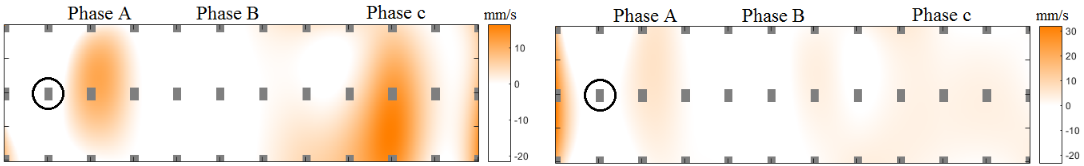

e) no load time priod #3
f) full load time priod #3

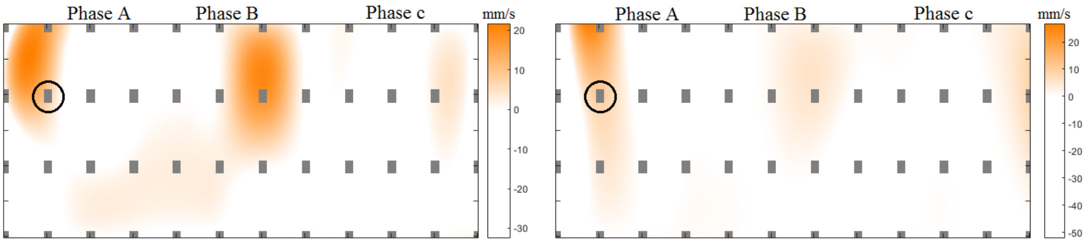

g) no load time priod #4
h) full load time priod #4

Fig. 4. Results of vibration amplitudes change

Fig. 5 shows the tendency for vibration amplitude to increase in this region. Similar situation is displayed in both no-load and full-load conditions. The decrease in one period of time can be explained because the windings were repressed and their clamping pressures increased in that year.

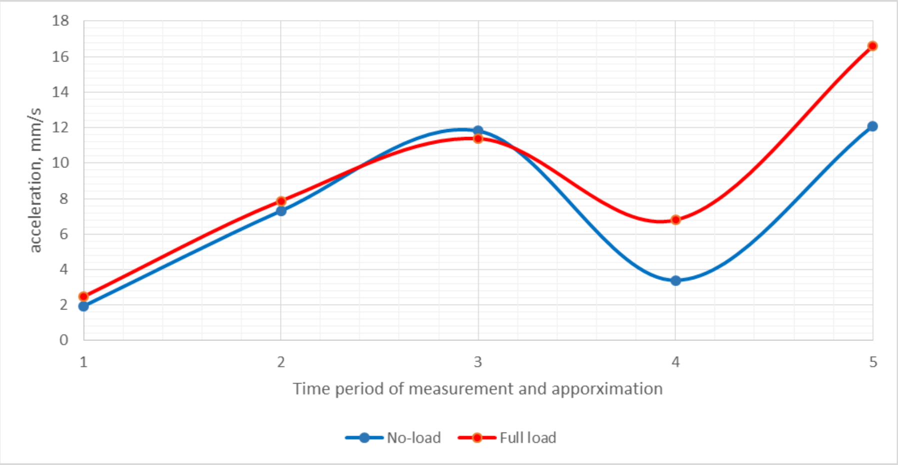

Fig. 5. Vibration change of previously marked point

Acquired results with proposed graphical interpretation method correctly displays maintenance action performed on the tested transformer which allows concluding that evaluation performed with proposed method is technically valid.

6. CONCLUSIONS

The analysis of literature allows concluding that different approaches exist to obtain information about the mechanical condition and possible faults of windings and magnetic core of power transformer. The main approaches are modelling transformer construction considering precise geometric parameters or processing measured vibration data. In both mentioned cases the obtained result has some error from the diagnostic of transformer because it is impossible to carry out approximation or modelling identically to the situation in practice.

The graphic interpretation method of measured vibration data proposed in this paper has the advantage to use data obtained from the surface of transformer tank. It is possible to perform approximation and visualization by using this method. Additionally, this methodology provides the possibility evaluate process for vibration change within time period even if sensor grids are different and to acquire graphic results in positions on the surface of the transformer tank where vibration sensors were not installed.

Improvements are planned for the proposed method by adding information about geometry of the transformer, positions of separate construction elements and their mechanical characteristics when considering vibration transmission.

This is necessary to model vibration distribution from windings and magnetic core to the surface of transformer. That would allow determining the causes of faults within windings or magnetic core.

7. REFERENCES

1. BETLE M.; TENBOHLEN S. Investigations on vibrations of power transformers. Proceedings of XVII International Symposium on High Voltage Engineering. Hannover: Institute of Power Transmission and High Voltage Technology. 2011 August 22–26.
2. Probabilistic vibration models in the diagnosis of power transformers. Instituto de Investigaciones Electricas. 2011 Link to the internet <http://cdn.intechopen.com/>.
3. Study on transformer tank vibration characteristics in the field and its application. Xi′an Jiaotong University. 2011 Link to the internet <http://pe.org.pl/>.
4. JIN M., PAN J., HUANG H., ZHOU J. Transmission of vibration of a power transformer from the internal structures to the tank. Proceedings of Acoustics 2012. Fremantle: School of Mechanical and Chemical Engineering, The University of Western Australia. 2012 November 21–23.
5. CHIESA N., LOTFI A., HOIDALEN H.K., MORK B., RUI O., OHNSTAD T. Five-leg transformer model for GIC studies. International Conference on Power Systems Transients. Vancouver 2013 July 18–20.
6. *International Electrotechnical Commission*. Geneva, Switzerland, 2001. International standart IEC 60076-10. Link to the internet <https://webstore.iec.ch/preview/info_iec60076-10%7Bed1.0%7Den.pdf>.
7. Vibro-Acoustic Method of Transformer Clamping Pressure Monitoring.
8. PREMALATHA V., SRUTHI S.S., VIKASH M., ILAMPOORNAN M.K. Instrument transformer winding fault analysis using frequency response analysis. ICACCCT 2012. Proceedings of International Conference. Ramanathapuram. 2012 August 23-25.
9. KULKARNI S.V., KHAPARDE S.A. *Transformer Engineering Design and Practice*. New York: Marcel Dekker, INC 2005. 452 p. ISBN 0-203-97059-4.

10. LI K., XU H., LI Y., ZHOU Y., MA H., LIU J., GONG J. Simulation test method for vibration monitoring research on winding looseness of power transformer POWERCON 2014. Proceedings of 2014 International Conference on Power System Technology. Chengdu: Hohai University. 2014 October 20–22.
11. WANG Y., PAN J., JIN M. Finite element modelling of the vibration of a power transformer. Proceedings of ACOUSTICS 2011. Gold Coast: The University of Western Australia. 2011 November 2–4. Proceedings of 2010 International Conference on Electrical Machines. Rome.
12. HACKL A., HANBERGER P. Investigation of surface velocity pattern of power transformers tanks. Electrical Machines (ICEM). 2010 September 6–8.
13. Diagnostics of mechanical faults in power transformers - vibration sensor network design under vibration uncertainty. 2014 Link to the internet <https://www.phmsociety.org/>.
14. Vibration sensor data and sensor characteristics. Link to the internet <http://www.vicont.ru/vk-310ru.html>.

CYSENI 2016, May 26-27, Kaunas, Lithuania
ISSN 1822-7554, www.cyseni.com

EXPERIMENTAL ANALYSIS OF VERTICAL AXES WIND TURBINE ACTIVE PITCH CONTROL SYSTEM WITH PERMANENT MAGNET SYNCHRONOUS MOTOR USING MATLAB SIMULINK TOOLS

T. Komass
Institute of Energetic, Latvia University of Agriculture
J. Cakstes bulvaris 5, LV-3001 Jelgava – Latvia
Email: tf11198@llu.lv

ABSTRACT

Efficient vertical axis wind turbine (VAWT) technology is a key topic for the future wind energy market. At the moment VAWTs are seldom used for electricity production. Development of the new technologies for building a new generation of VAWTs, which will be more efficient, user-friendly, with very low noise pollution levels is the target for many researchers. The goal of this research was to analyse an active pitch control system in an experimental setting through construction of an active pitch control system test bench using a Permanent Magnet Synchronous Motor (PMSM), and to develop new testing programmes for analytical system performance tests. Current commercial turbines do not carry an active pitch system for a VAWT, however the concept of an active turbine blade pitching opens new opportunities for boosting the efficiency, safety and user-friendliness of VAWTs. The research consists of the mathematical model and control system operating in a simulation environment in a closed loop with the test bench setup consisting of an active pitch control system. By applying a specially-developed VAWT simulation model implemented in MATLAB Simulink, the active pitch system was tested and analysed under various conditions, which are as close as possible to the real-world operating conditions. The research covers the real experimentation with the pitch system test bench using PMSM and the special servo controller for the system control. To achieve better results of data analysis the simulation was done in MATLAB *Simulink* using real time simulation function synchronised with Kernel real time clock in MATLAB. Within testing the main goal was to research the speed ability of the servo system and to determine what control strategy could be possible required for real pitch system work. Within the test time system tuning analysis was performed, which did show additional critical points for the future control system algorithm to achieve the best performance results. System tuning for servo system in very essential as incorrect tuning can make system unstable and result in ineffective operation. After fine-tuning the process analysis system the test bench was used for real active pitch control tests using real system theoretical work reference points and functions. The pitch system servo motor position reference is a complex function of the wind turbine rotor angle, wind speed, wind direction. In line with the changes of the parameters the control system setpoint reference is changed. Under real-life conditions the wind force perturbation on the blade is variable and that is the one of the points which can be tested only in the wind tunnel conditions. The results of the testing and analysis show that an active pitch system using PMSM can be very efficient and fast-operating. Depending of the wind turbine geometrical parameters the servo system can complete the task with the high speed and efficiency. The active pitch system is able to operate under the necessary conditions by using PMSM. One of the conditions is to use the direct drive or geared mechanism that makes the system very flexible. Experiments show that the pitch system with geared mechanisms ensures higher system stability and the gearbox forks act as a very good force filter, which gives an option to use less powerful control system for the variable force filtering over the direct motor mode. Analysis shows that while using the PMSM for a turbine active pitch system, certain conditions should be taken into account in order to achieve the best results and to reduce costs. Full and effective use of the active pitch system components can improve VAWT performance.

Keywords: VAWT, pitch control, PMSM, wind turbine, MATLAB

CYSENI 2016, May 26-27, Kaunas, Lithuania
ISSN 1822-7554, www.cyseni.com

MULTICRITERION SUPPORT MEASURES EFFECTIVENESS INVESTIGATION FOR RES-E DEVELOPMENT IN LITHUANIA

Modestas Krečius
Lithuanian Energy Institute
Breslaujos str. 3, LT-44403 Kaunas – Lithuania
Fax: +370 (37) 351271

ABSTRACT

There are many strategies for RES penetration in the market, which have been tested and implemented in recent years. Despite of RES strategies diversities, the main ***objective*** remain the same – to stimulate RES-E substitution for fossil fuel energy. Many microeconomic researches have been conducted based on support schemes. Notwithstanding, there is no obvious decisions which system of support schemes for RES-E should be focused on whether ***price – driven*** (e.g. Feed in tariffs (FIT)) or ***capacity – driven*** (e.g. Tradable Green Certificate-based quotas (TGC)) that may influence society results. Different support policy options have direct influence on evolution of electricity system, where companies are driven to maximize their profit by investing a huge amount of money. Renewable energy sources (solar, wind) installation require relatively high investments cost, whereas payback takes quite a long time. Therefore, scholars have started to pay considerable attention on effectiveness and efficiency for developing RES-E promotion strategies. Thereby, various policy strategies by promoting RES-E can be assessed based on several indicators: *Average annual growth rate*, *Absolute annual growth rate*, *Effectiveness indicator*, *Total cost indicator (TCI)*.
This paper analyse main support measures indicators for RES-E development that leads to positive effect for end-consumers, investors, RES-E demand or even attractiveness of investments.

Keywords: Indicators, efficiency, renewable energy

1. INTRODUCTION

The number of installations and usage of RES is quite fast growing in recent years. However, the expansion is based on strict European Union rules: European Parliament and the Council of the European Union accepted new directive by promoting renewable energy sources in December 2008. Nevertheless, new renewable energy sources directive was fully confirmed on April 23 (2009/28/EC), where each EU member state have to reach individual mandatory target resulting 20% gross final energy consumption in EU by 2020 from renewable energy sources (EC, 2009).

Each country use different promotions instruments that would help to reach successfully European Parliament and the Council defined targets. However, there is no specific "natural" exceptional instrument for successful practice by expanding RES, since each EU state have distinctive strategic framework that leads to different promotions models as well (Reiche, 2004). In general, there are a few elements that increase success of RES deployment:

- *Security for investors in a long time period;*
- *Strong integration of power supply system (grid expansion & fair access to the grid);*
- *Measures that enable to reduce local resistance against RES.*

Hence, renewable energy market penetration is largely depends on the government, since it is necessary specific support policies in order to meet economic, social and environment objectives. Additionally, it fosters competitiveness with conventional energy sources without distorting energy prices. In order to enlarge renewable energy consumption, subsidies for investment or preferential tariff were significant across all EU28 countries, that estimated about 40 billion (EUR) in 2012, where solar and onshore wind respectively accounted for 14.7 billion (EUR) and 10.1 billion (EUR).

Green energy deployment is important not only for reaching 2020 targets by each country, but it is critical element by stimulating economy (Ellen McArthur Foundation, 2012). Additionally, policymakers believe that support measures for renewable energy may eliminate economic (*limited access to finance, high capital cost because of high risk*) and market barriers (*limited access to power market*). It should be noted that risk elimination is one of the most important elements for investors, as it reduces capital costs. Moreover, risk reduction is a basic economic principle for RES deployment (Mitchell et al., 2006).

Currently renewable energy deployment is successfully applied in EU-28 promoted by national policies, where stakeholders such as households and business may active participate in energy market – consumers turn to energy producers by selling and buying electricity from the grid. On the other hand, there are no many articles at least for Lithuania energy sector that analyse renewable energy policy success that is critical for consumers and business. Therefore, this paper analyse renewable energy policy multicriterion elements based on ***effectiveness*** and ***efficiency***.

The aim of this paper to overview Lithuanian electricity from RES deployment support policies performance based on multicraterion effectiveness and efficiency parameters: *Average annual growth rate, Absolute annual growth, Effectiveness indicator, Total cost indicator, Policy impact indicator*. The main objectives of the following information analysis are:

- to assess the most applied RES-E support strategies;
- to calculate Lithuanian RES-E support effectiveness indicators with regard to 2020 targets;
- to suggest the most applied RES-E support effectiveness indicators for Lithuanian market.

Data collection of this study will be used in accordance with the following method:

- Statistical data analysis.

It should be mentioned that this paper status − objectives and methodology adjustment, information analysis that leads to dissertation status.

2. RES-E SUPPORT STRATEGIES

A recent data shows that electricity generation from renewable energy sources (*Solar, Wind turbines, Hydropower, Biomass & renewable waste*) have increased around 50% in EU countries rising from 420 TWh in 2003 to reach level of 890 TWh in 2013 (Eurostat, 2015). Overall, it is assumed that RES electricity consumption will reach 35% in 2020 or 60–80% in 2050 by comparing 17% in 2008 (Hirth, 2013). There are many strategies how to improve renewable energy expansion in the market, which have been tested and implemented in recent years. Despite of RES strategies diversities, the main ***objective*** remain the same – to stimulate electricity produced from renewable energy sources (RES-E) substituting fossil fuel energy. RES-E benefits compared to conventional electricity are these: *social*, *environmental* and *economic*.

There were conducted many RES-E researches based on support schemes. Notwithstanding, there is no obvious conclusions which support policies should be focused on whether ***price – driven*** (e.g. Feed in tariffs (FIT)) or ***Quantity – driven*** (e.g. Tradable Green Certificate-based quotas (TGC)) that may influence society results (Fagiani R., 2013). Yet, these two different systems works as follow:

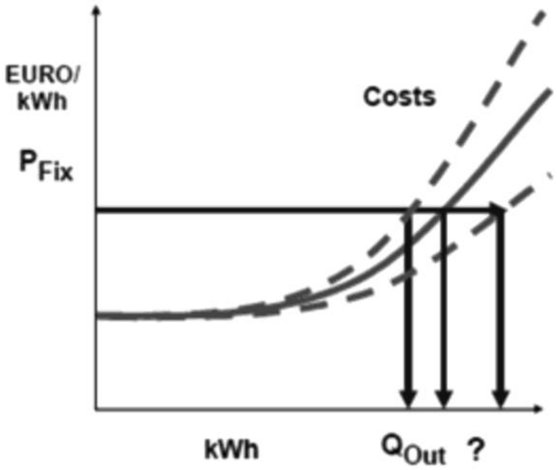

Fig. 1. Price driven mechanism
(Haas, et al., 2004)

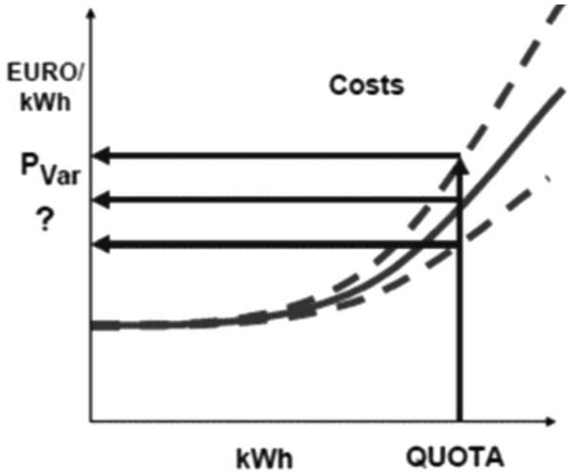

Fig. 2. Quantity driven mechanism
(Haas, et al., 2004)

Price driven mechanism (Fig. 1) is based on fixed price, where quantity is defined by the market. Quantity driven mechanism (Fig. 2) is based on fixed quantity, where the price is defined by the market.

Table 1. RES-E support policies (Haas et al., 2008)

	Price driven	**Quantity driven**
Investment	- Investments subsidies - Tax credits	- Tendering systems for investment grants
Generation	- Fixed price feed-in tariffs - Premium feed-in tariffs	- Tendering systems for long term contracts - Renewable energy portfolio standards (i.e. quotas)

As can be seen from Table 1 there are different policy types for stimulating RES-E generation. Yet, the main support types for RES-E generation in EU-28 is based on Feed-in tariff and TGC based quotas obligations. All in all, FIT‘s & TGC can be structured in more detail, that helps to understand why it is successfully applied in Europe. Initially, FITs mechanism can be characterized by the following statements:

1) Commitment for grid operator to purchase all electricity from RES-E producers that are connected to grid system;
2) A Feed-in tariff make sure that all RES-E producers will get above market price that is defined per kWh for a number years;

Fripp & Poputoaia (2008) argue that above mentioned statements are link with **positive** benefits:

- Low transaction costs;
- Policy elasticity/flexibility *(such policy can be adapted and constantly improved, since technology and market change over time);*
- Easy entry for small and medium-sized enterprises (**SMEs**) to the market;
- Diminished risk for business people by developing RES-E projects due to easier access to capital with smaller costs;
- Ability to provide higher subsidies for immature technologies that are able to provide more benefit in a long term.

Unfortunately, FITs mechanism have **negative** features as well:

- FITs mechanism is used for generating RES-E in domestic market, therefore cost saving may be lost via international trade of RES-E;

- FITs mechanism do not change automatically, when costs of RES-E goes down, therefore consumers will pay more than necessary;

Quota system is a quantity-driven instrument based on **TGC** (tradable green certificates). It should be mentioned that quota is determined and set by the government. In general, quota is designed for electricity providers, who have to show that they get a particular quantity electricity from RES-E. Nevertheless, electricity providers may show this by purchasing green certificates or RES-E itself. Quota system based on **TGC** works well for „market oriented" government, where the main benefits are the following:

- Quota system do not require additional money channel through government for developing RES-E projects
- Market developers of any sources for RES-E generation can contribute to quotas obligation by minimizing costs for society (Fripp et. all 2008).

TGC as FITs mechanism also have drawbacks. These concerns are linked to increased project risks for RES-E developers:

- Policy environment is critical for RES-E stability. As have been showed previous lessons learned from Sweden and Belgium, it caused financial (investments) instability in 2002;

- Capital scarcity may affect the smaller participants elimination in the market, that involves innovation reduction as well;

- TGC quota mechanism are able to serve RES-E development under defined target. There are no additional incentive systems by exceeding defined targets in order to install additional quantities of RES-E.

- The value of TGC could be unstable, when system is close to target. If target even slightly is exceeded there is possibility that value of TGC could crash.

3. MULTICRITERION SUPPORT MEASURES EFFECTIVENESS

Theoretical review of support measures effectiveness indicators have been discussed in greater detail by Krečius (2015) in an international conference CYSENI 2015. Despite of such fact, it is necessary practical calculations based on support measures indicators that would allow to assess RES-E different technologies development in Lithuania. There are a variety of indicators that can be used to measure policy effectiveness that support renewable energy. Hence, the main support measures effectiveness indicator are as follows:

- Average annual growth rate;
- Absolute annual growth rate;
- Effectiveness indicator;
- Total cost indicator (TCI).

3.1. Average annual growth rate

Average annual growth rate is one of the alternative indicator of support policies. The following indicator is important for small countries which deploying status of RES is low.

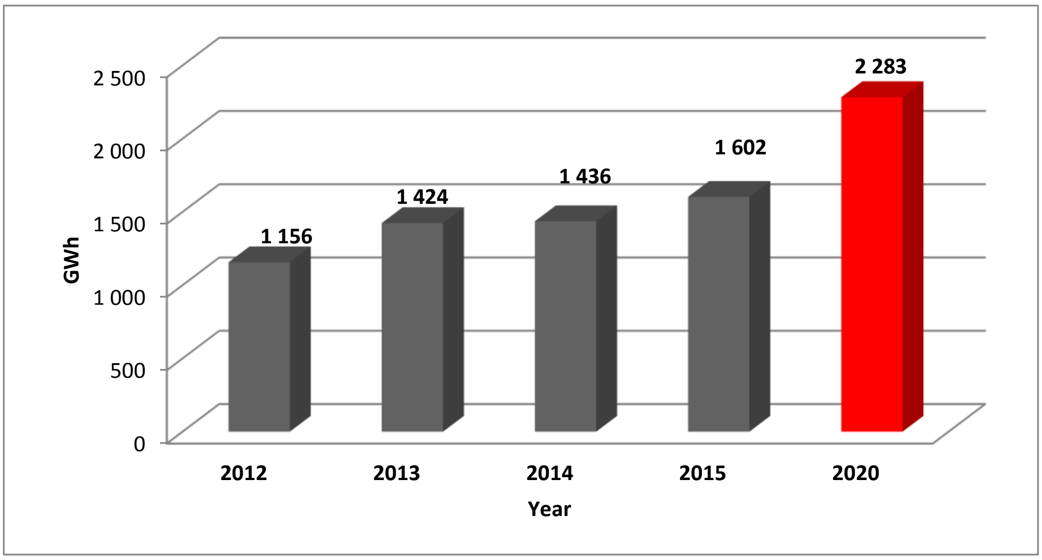

Fig. 3. RES-E supply to grid system in Lithuania (Litgrid AB, 2016)

As can be seen from Fig. 3 electricity supply to grid system from renewable energy sources is constantly growing which amounted to 1156 GWh in 2012 and reached 1602 GWh in 2015. It is expected that growth rate of RES-E will reach 2283 GWh by 2020 considering the growth rate period of 2012–2015. In addition, it has been calculated effectiveness indicator – ***Average annual growth rate*** based on equation (1).

$$g_n^i = \left(\frac{G_n^i}{G_{n-t}^i}\right)^{\frac{1}{t}} - 1 \tag{1}$$

g_n^i = Average annual growth rates,
G_n^i = Electricity generation by RES technology i in year n.

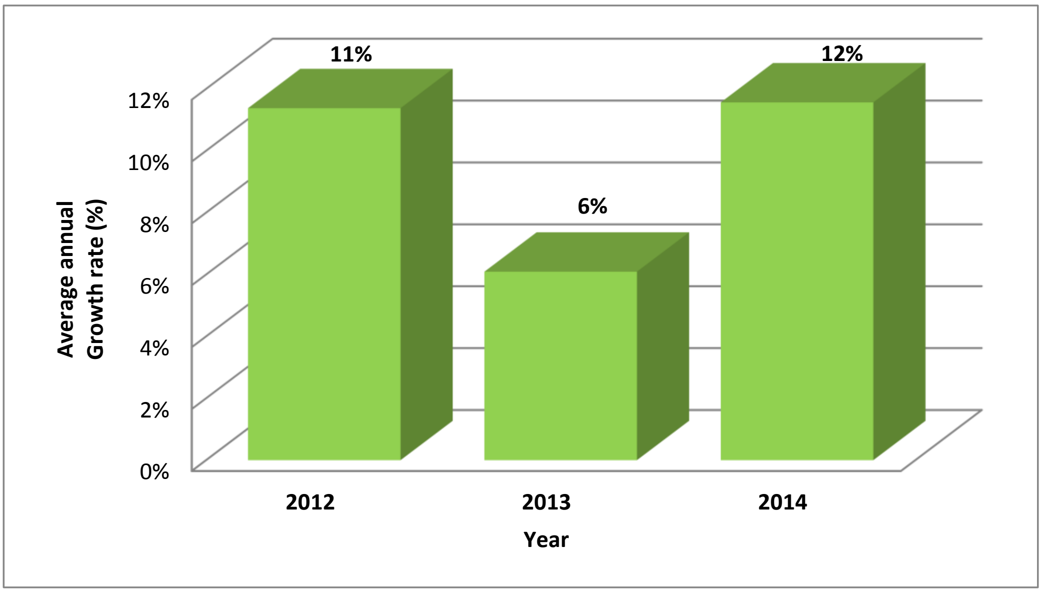

Fig. 4. Average annual growth rate in Lithuania

Hence, Lithuanian ***average annual growth rate*** in a period of 2012–2015 are the following (see Fig. 4):

$$g_{2015-2014}^{All\ RES-E\ technologies} = 12\%;$$

$$g_{2015-2013}^{All\ RES-E\ technologies} = 6\% ;$$

$$g_{2015-2012}^{All\ RES-E\ technologies} = 11\%.$$

To sum up, the higher average growth rate is the better policy success on market growth. For instance, China in a period of 2000–2005 average annual growth rate has even accounted for 30%.

3.2. Absolute annual growth

Another policy effectiveness indicator that shows market growth – ***absolute annual growth rate***. In order to see more comprehensive view of *absolute annual growth* by different technologies of RES-E in Lithuania, the data were analysed from 2012 to 2015.

Table 2. RES-E supply (kWh) to grid system in Lithuania by different technologies from 2012 till 2015(Litgrid AB, 2016)

RES-E technology	**2012 vs 2013**	**2013 vs 2014**	**2014 vs 2015**
Hydro	95.325.865	-122.426.506	-48.333.621
Wind onshore	62.317.769	36.241.849	170.065.206
Solar	42.482.179	28.186.306	358.153
Bio	67.498.664	70.635.905	43.998.895

Table 2 shows that *wind onshore* electricity supply to grid system increased since 62.317.769 kWh for the period 2012–2013 to 170.065.206 kWh in 2014–2015. On the other hand, hydro electricity supply to grid system declines for several years: electricity during 2014 was supplied 122.426.506 kWh less than 2013, whilst in 2015 it was supplied even less than 2014 that accounted for 48.333.621 kWh reduction. However, these changes are not linked with support policies but to inflow of surface water, therefore it should be excluded from policy analysis.

Bio and solar development has also been impressive growth during 2012–2015 (see Fig. 5). High FIT rate inflated solar bubble 2011, since National regulator sets the FiT for 47 EUR ct/kWh and 2012 were reduced till 42 EUR ct/kWh regardless the type and capacity of instalations. Therefore, solar absolute annual growth rate was quite high in 2012–2013 and 2013–2014. However, in order to avoid significant market distortion the prices has been reduced even by 46–62% (solar PV building integrated – 20 EUR ct/kWh, not integrated 16 EUR ct/kWh) from 2012 till 2015. Moreover, some regulations have been changed that allowed to defend public interest within the Law on Energy from Renewable Sources:

1) FiT and capacity quotas for installations exceeding 10 kW allocated by auction *(30 kW previously;*
2) Review of FiT levels for each technology on a quarterly basis;
3) 100% discount for electrical connection to the grid for installations up to 30 kW is abolished.

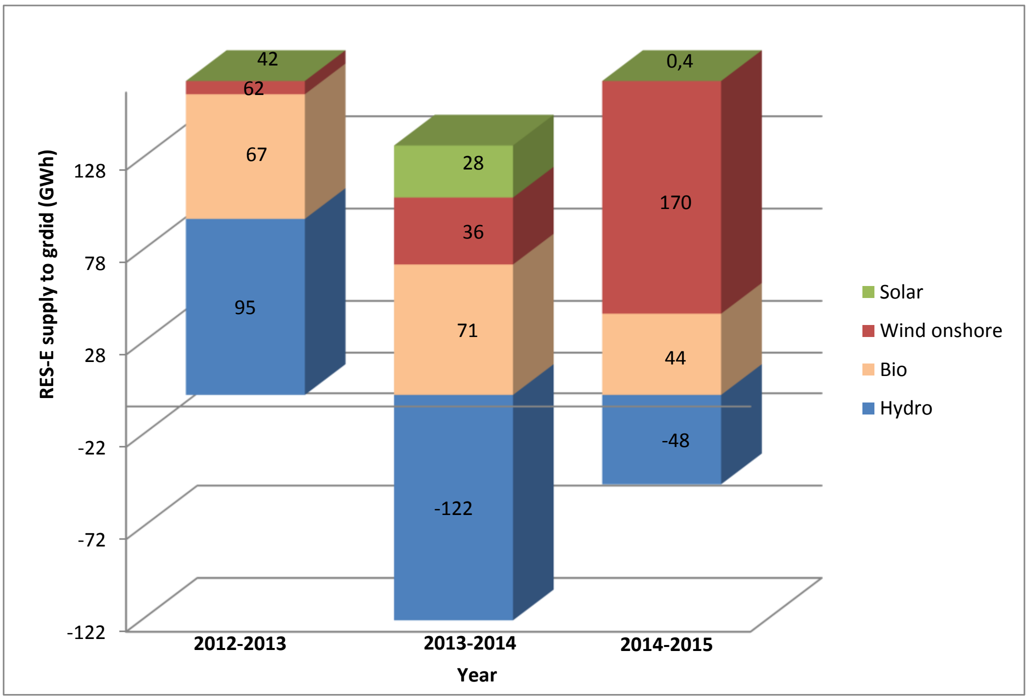

Fig. 5. Absolute annual growth by different technologies from 2012 till 2015 (Litgrid AB, 2016)

3.3. Effectiveness indicator

The final indicator that shows policy success in the market is ***effectiveness indicator***. In order to calculate effectiveness indicator there were made some corrections link to equation (2), since there is no a particular data such as additional generation potential ($ADDPOT_{2020}$). For this reason, variable G (generation) has been changed to C (capacity).

$$E_n^i = \frac{(G_n^i - G_{n-1}^i)}{ADDPOT_n^i} \Rightarrow E_n^i = \frac{(C_n^i - C_{n-1}^i)}{ACIPOT_n^i} \tag{2}$$

E_n^i = Effectiveness indicator for RES technology i for the year n,
C_n^i = Capacity installation of RES technology i in year n,
$ACIPOT_n^i$ = Additional capacity installation of RES technology i in year n until 2020.

According to Ministry of Energy of the Republic of Lithuania (2016) RES capacity development from 2009 till 2014 have substentially increased (see Fig. 6). A huge growth was solar capacity installation that accounted for (+70 MW) in a period of 2009–2014. Despite of low solar and hydro capacity installations during 2015, meanwhile the rest technologies such as bio & wind onshore installations were growing by comparing with 2014. It is expected that capacity of installations will reach the following results till 2020 by considering capacity growth in a period of 2009–2015: solar – 137.5 MW, wind onshore – 521.8 MW, Bio – 119.9 MW, hydro – 133.7 MW. It is seen that solar and wind onshore technologies will reach defined target till 2020, however bio and hydro technologies will not achieve it (Fig. 6).

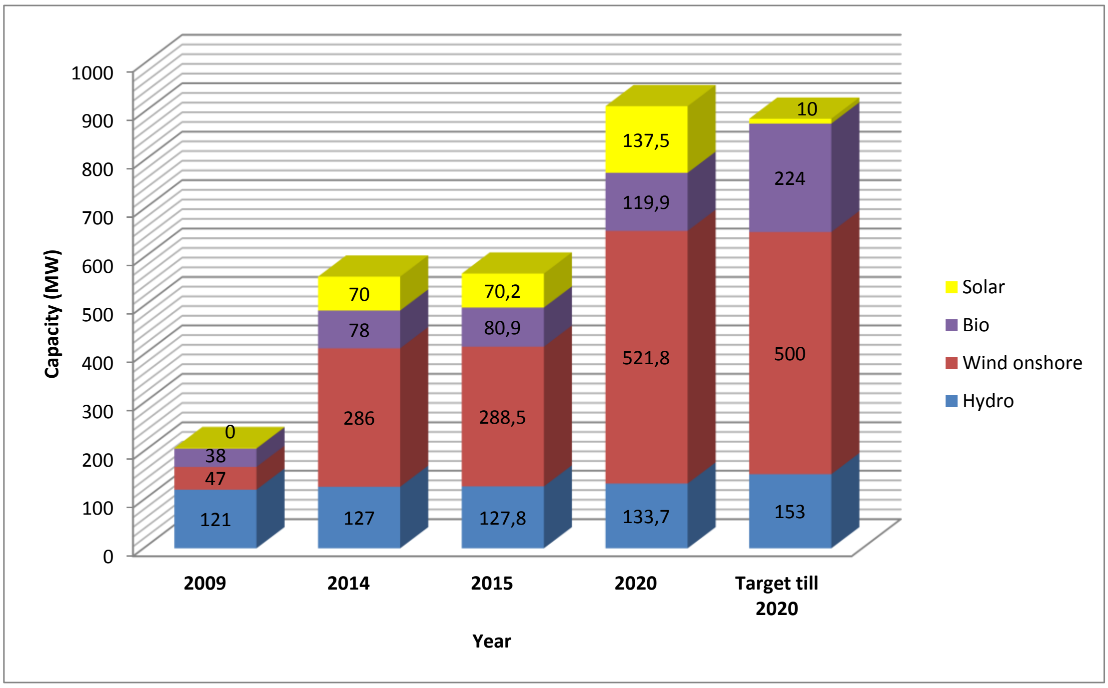

Fig. 6. RES different technologies capacity installations (MW) vs target 2020 (Ministry of Energy of the Republic of Lithuania, 2016)

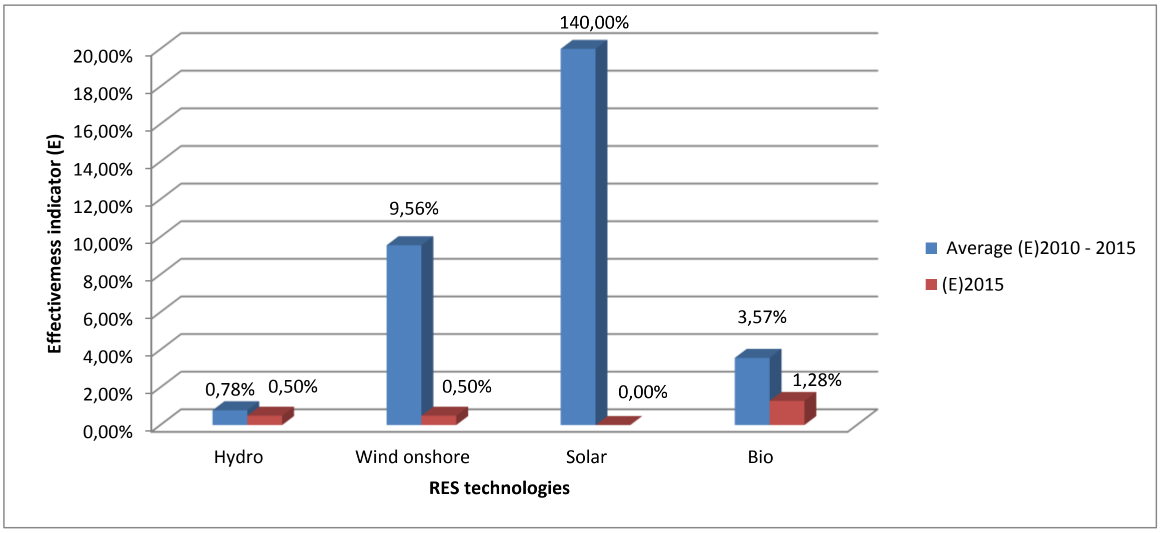

Fig. 7. Effectiveness indicator (E) by different RES-E technologies (2010–2015)

Effectiveness indicator (E) is important, as it helps to see all RES-E technologies development rate during a certain of period. As can be seen from Fig. 7, solar technologies have the highest average effectiveness indicator (E) – 140% over the past 5 years. Nonetheless, solar effectiveness indicator of 2015 is equal 0%. Wind onshore has the second highest results of average effectiveness indicator (E) over the past 5 year period of 2010–2015 that accounts for 9.56%. Meanwhile, bio average effectiveness indicator (E) is 3.57% respectively. It should be noted, that the higher indicator is the better policy effectiveness.

3.4 Total cost indicator (TCI)

Total cost indicator shows how much money country spends in addition to the market price for energy to get x amount of additional generation from renewable technology.

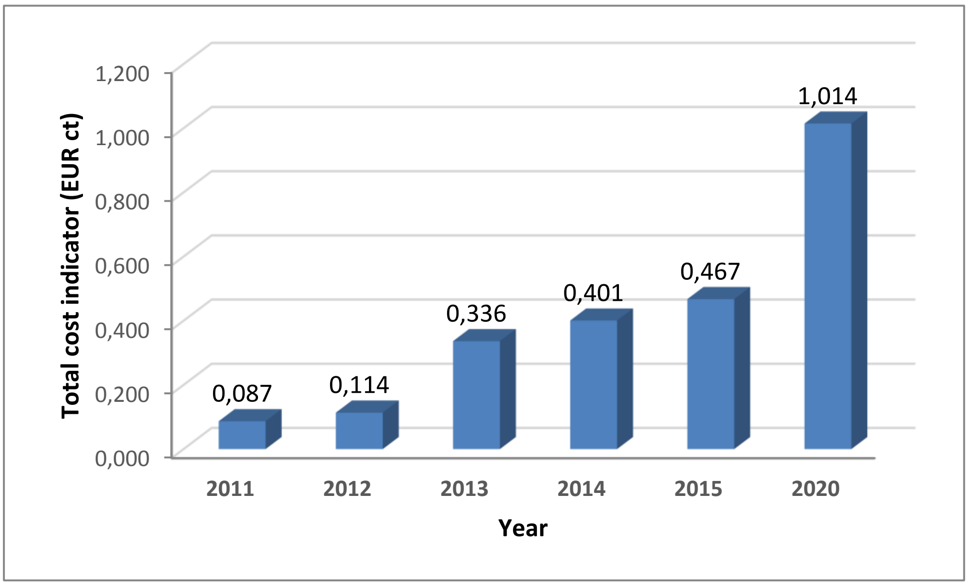

Fig. 8. Total cost indicator 2011–2015

It is seen that electricity price is additionally growing from 0.087 EUR ct/kWh in 2011 to 0.467 EUR ct/kWh in 2015 due to support for RES development in the market. It is expected that electricity price will reach 1 EUR ct/kWh in 2020 if support policies will remain the same. Despite of such assumption, there is a low likelihood that it will happen, due to rapidly evolving RES-E technologies.

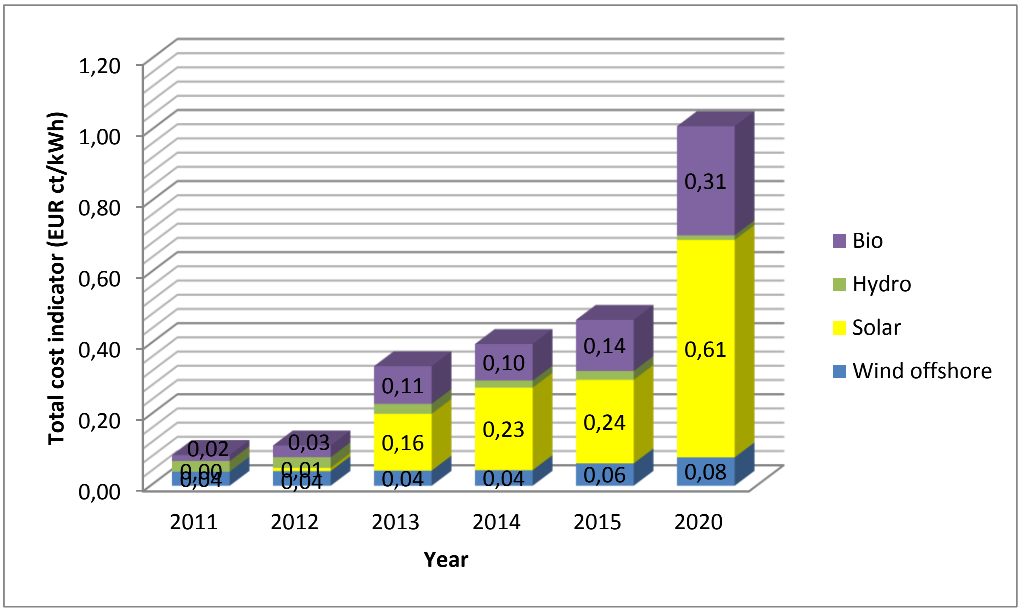

Fig. 9. Total cost indicator by different RES-E technologies 2011–2015

Fig. 9 indicates total cost indicator by different RES-E technologies during 2011–2015. Yet, support for solar development is a major contributor for higher electricity prices which constitute 0.16 EUR ct/kWh in 2013 and increase 0.24 EUR ct/kWh in 2014. By 2020 price would be 0.61 EUR ct/kWh, if price rate will keep the same as previous 5 years. In contrast, support for wind offshore is a lowest contributor for higher electricity prices that range from 0.04 EUR ct/kWh in 2011–2014 till 0.06 EUR ct/kWh.

4. CONCLUSIONS

Renewable energy policies effectiveness indicators have showed that Lithuania has implemented effective support policies for some kind of RES-E technologies, i.e. solar average effectiveness indicator in a period of 2010–2015 reached 140%. The consequences of such support policy were obvious – “solar bubble” formation that damaged solar energy reputation. In order to avoid “solar bubble” once again, it has been launched new net metering system for generating facilities that are smaller than 10 MW. On the other hand, a huge support by government to solar development shows the highest total cost indicator, that directly influence higher prices of electricity. It should be stressed that wind offshore average effectiveness indicator by 2010–2015 is quite high rate that accounts for 9.56%. Moreover, wind offshore total cost indicator is one of the lowest 0.06 EUR ct/kWh that influence at lowest possible electricity higher prices. Lithuania has a huge potential for improvement of bio development. It is expected that there will be installed additional capacity 100 MW till the end of 2019 by generating electricity out of waste incineration plants in Vilnius and Kaunas. Current data shows that bio total capacity installation reach just 80.5 MW by 2015, where the target is around 224 MW till 2020. Negative trend is seen by hydro technologies, where electricity supply to grid system is declining for several years -122.426.506 kWh by 2013–2014 and -48.333.621 kWh in a period of 2014–2015. It is predicted, that low rainfall in a summer period has direct affect for electricity generation.

To sum up, all above mentioned support policy effectiveness indicators (*Average annual growth rate*, *Absolute annual growth rate*, *Effectiveness indicator*, *Total cost indicator (TCI)*, *Policy impact indicator (PII)*) are critical, therefore, it is recommended to apply all of them for analyzing RES-E different technologies growth in the market.

5. REFERENCES

1. ALBERICI, S., BOEVE, S. (2014) Subsidies and costs of EU energy; an interim report. *Ecofys*. October 2014.
2. EC, 2009. Directive of the European Parliament and of the Council on the promotion of the use of energy from renewable sources and amending and subsequently repealing Directives 2001/77/EC and 2003/30/EC. *Official Journal of the European Union* (5.6.2009).
3. EDENHOFER, O., HIRTH, L., KNOPF, B., PAHLE, M., SCHLÖMER, S., SCHMID, E., UECKERD F., On the economics of renewable energy sources. *Energy Economics* 40 (2013) S12–S23.
4. ELLEN McARTHUR FOUNDATION. Towards the Circular Economy: Economic and business rationale for an accelerated transition, (2012) Cowes.
5. EUROSTAT. Renewable energy statistics. 2015 [referred on the 22th of February in 2016y.].Link to the internet <http://ec.europa.eu/eurostat/statistics explained/index.php/Renewable_energy_statistics>
6. FAGIANI, R., BARQUI´N, J., HAKVOORT, R. Risk-based assessment of the cost-efficiency and the effectivity of renewable energy support schemes: Certificate markets versus feed-in tariffs. *Energy Policy* 55 (2013) 648–661.
7. FRIPP, M., POPUTOAIA, D. *European experience with tradable green certificates and Feed in tariffs for renewable electricity support*. (2008) Environmental Change Institute, University of Oxford.
8. HAAS, R., EICHHAMMER, W. 2004 How to promote renewable energy systems successfully and Effectively. *Energy Policy* 32 (2004) 833–839.
9. HAAS, R., MEYER, N.I. *Promoting electricity from renewable energy sources – lessons learned from the EU, United States, and Japan.* In: Sioshansi, Fereidoon P.(Ed.). 2008. Competitive Electricity Markets. Elsevier, Oxford.

10. HIRTH, L. The market value of variable renewables. The effect of solar wind power variability on their relative price. *Energy Economics* 38 (2013) 218–236.
11. IEA (International Energy Agency). World energy outlook. 2014 [referred on the 26th of February in 2016 y.] Link to the internet. http://www.worldenergyoutlook.org/weo2014/>.
12. KREČIUS, M. Support measures for renewable energy assessing the development effectiveness // 12th Annual international conference of young scientists on energy issues (CYSENI 2015), Kaunas, Lithuania, May 27–28, 2015. Kaunas: LEI, 2015. ISSN 1822-7554. p. 61–72.
13. LITGRID AB., 2016. [referred on the 28th of February in 2016 y.] Link to the internet. <http://www.litgrid.eu/index.php/paslaugos/kilmes-garantiju-suteikimas/ataskaitos/563>.
14. MARTINOT, E., CHAUREY, A., LEW, D. Renewable energy markets in developing countries. Ann. Rev. *Energy Environ*. 2002. 27:309–48 doi: 10.1146/annurev.energy.27.122001.083444.
15. MINISTRY OF ENERGY OF THE REPUBLIC OF LITHUANIA. Renewable energy sources [referred on the 28th of February in 2016 y.] Link to the internet <https://enmin.lrv.lt/en/sectoral-policy/renewable-energy-sources>.
16. MITCHELL C., BAUKNECHT, D., CONNOR, P.M., Effectiveness through risk reduction: a comparison of the renewable obligation in England and Wales and the feed-in system in Germany, (2006). *Energy Policy* 34, 297–305.
17. MELLINO C. Renewables Saw More Money Invested and More Capacity Added in 2015 Than Ever Before. [referred on the 28th of February in 2016 y.] Link to the internet. <http://ecowatch.com/2016/01/14/renewables-record-investment/>.
18. REICHE D., BECHBERGER M. Policy differences in the promotion of renewable energies in the EU member states. *Energy Policy* 32 (2004) 843–849.

CYSENI 2016, May 26-27, Kaunas, Lithuania
ISSN 1822-7554, www.cyseni.com

A NOVEL APPROACH TO OFFSHORE GRIDS TRANSMISSION EXPANSION AND MODELLING

J. G. Dedecca, R. A. Hakvoort
Faculty of Technology, Policy and Management, Delft University of Technology
Jaffalaan 5, 2628BX Delft – The Netherlands
Email: j.dedecca@tudelft.nl

ABSTRACT

The European Northern Seas offshore grid is an important building block for the Energy Union. This grid faces technical, economic, regulatory and governance barriers for its integration, barriers which have so far been studied qualitatively or through optimization models. Since actual transmission expansion pathways will be non-optimal, we propose a novel offshore grid exploratory model to simulate power transmission investments. These investments are the main constraints in order for policymakers to shape expansion pathways. Different expansion topologies are considered for investment, leading to non-optimal expansion pathways. The single and multi-period case studies demonstrate that internationality, asset characteristics and dependence on geography and project timing all influence the pathways, leading to different degrees of offshore grid integration. To shape the grid to more integrated pathways, policy and governance frameworks for the offshore grid must coherently address anticipatory investments, the distribution of costs and benefits, and the costs and standardization of direct-current transmission technology. Also, Energy Union cooperation for the Northern Seas must be aware of the specific characteristics of this grid.

Keywords: Offshore grid; offshore wind; simulation; myopic optimization; transmission expansion

1. EXPLORATION OF THE OFFSHORE GRID

The Northern Seas offshore grid is the most prominent example of an offshore grid. The offshore grid concept refers to a future grid with substantial integration of two functions, interconnection of onshore systems through interconnectors (ICs) and connection of offshore generation technologies, usually wind power [1]. The Northern Seas offshore grid is thus related to the supergrid concept of von Hirschhausen [2], but with a minimum of function integration as an additional and necessary feature.

Several drivers push the development of this offshore grid, and hence many grid developments related to governance and support initiatives, projects and research are ongoing [1, 3–10]. Despite these advances, the Northern Seas offshore grid still faces barriers, which increase with more integration, due to differences in project risk, energy policy preferences, market, renewables and permitting regulation, and the distribution of benefits and costs that result in winners and losers at the national and actor levels.

Rivier et al. [15] define transmission planning (TEP) as the “recursive process of generation and evaluation of potential transmission expansion plans in search for a preferred solution that best meets the prescribed set of criteria”. New developments such as the integration of renewable energy and decentralized markets bring increased challenges to traditional transmission expansion planning approaches using optimization or heuristics [17].

In summary, an integrated grid provides benefits but its development is delayed by various barriers. Given its importance, it has received the attention of numerous research projects using mostly qualitative or conventional TEP approaches. As section 2 discusses, simulation models are another possible approach to TEP, but are not frequently employed. When they are, the most common one is game theory, with system dynamics or agent-based modelling (ABM) being rarer [18–22].

We aim to explore the expansion of the offshore grid by simulating investment pathways in transmission links. Our novel exploratory model applies a myopic investment optimization which has a restricted investment horizon of one period, leading to a non-optimal simulation of the grid expansion. In this way, the exploratory model contributes to transmission systems simulation. More specifically, it studies the influence of offshore grid characteristics on transmission expansion pathways, and the policy consequences for the Northern Seas offshore grid in Europe. By using a non-optimal approach we explore what could happen, instead of what should, and how to shape pathways. As such, this article provides policy support for planners and decision makers. Also, to the authors' best knowledge simulation has not been applied to offshore grids transmission expansion [1]. Hence, the study provides researchers with an alternative methodology to the ones frequently applied to study grid pathways, and transmission infrastructures in general.

The rest of this article is organized as follows. Section 2 presents the simulation approach to energy systems modelling, and its advantages and disadvantages against other approaches. Then, a theory on the constraints to infrastructure change arising from investments is presented, along with the characteristics of infrastructures, power systems and offshore grids. Section 3 presents the proposed offshore grid exploratory model, the modelling assumptions and the case studies for the offshore grid pathways. The results and a discussion in relation to current developments are presented in section 4. Section 5 then concludes with the consequences to policy making for the Northern Seas offshore grid.

2. TRANSMISSION EXPANSION PLANNING, SIMULATION AND PATHWAYS

Energy system models can be classified as top-down or bottom-up models, following Jägemann [23], where the author opposes the macroeconomic, aggregated top-down approach to the technological, sector-specific one of bottom-up models. Bottom-up models can be further sub-divided in optimization and simulation [23]. A particular optimization approach is myopic optimization, where the horizon is limited, i.e. the optimization considers only a part of the whole problem (e.g. a limited area or time period). Myopic optimization does not provide global optima, and thus applications employing it can be classified in simulation.

Both optimization and simulation are relevant to study energy systems, but address different research questions. On the one hand, optimization provides a desirable state. Simulation models, on the other hand, are more capable of modelling complex system features [24]. This can be done in a fast manner, allowing the rapid exploration of multiple, unrealized futures [25].

To this exploratory model investments in the offshore grid constrain its expansion pathways. First of all, systems and their subsystems exhibit characteristics which may differ, and these characteristics constrain technical change (of assets) more than the social change (of institutions). The combined system change occurs through two management types: operational, which acts through institutional change, and strategic management, which acts through investments and divestments of assets. A given system state performance is a result of the interaction of both the technical and social subsystems elements, but strategic management is costlier and slower than operational management, so investments and divestments shape system pathways, as illustrated by Fig. 1.

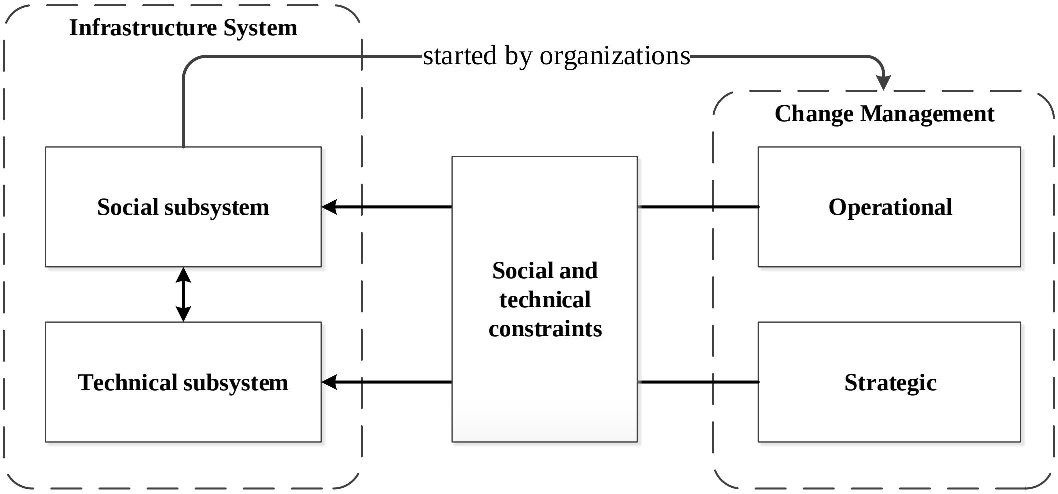

Fig. 1. Infrastructure change argumentation

Given this argumentation simulation can help study pathways of infrastructures. Furthermore, by modelling asset investment and divestment the pathway behaviors of path dependence, critical masses and tipping can be simulated. Thus, simulation with the strategic management of assets is an appropriate approach to compare infrastructure pathways.

3. METHODOLOGY

As argued in section 1 usual transmission expansion approaches use an optimization model. Moreover, section 2 indicates a non-optimal myopic optimization approach is adequate to explore transmission expansion pathways of offshore grids. For this, our model simulates sequential periods composing an expansion pathway, with three steps per period iteration: creation of an expansion portfolio, system operation, and investment decision, as indicated in Fig. 2.

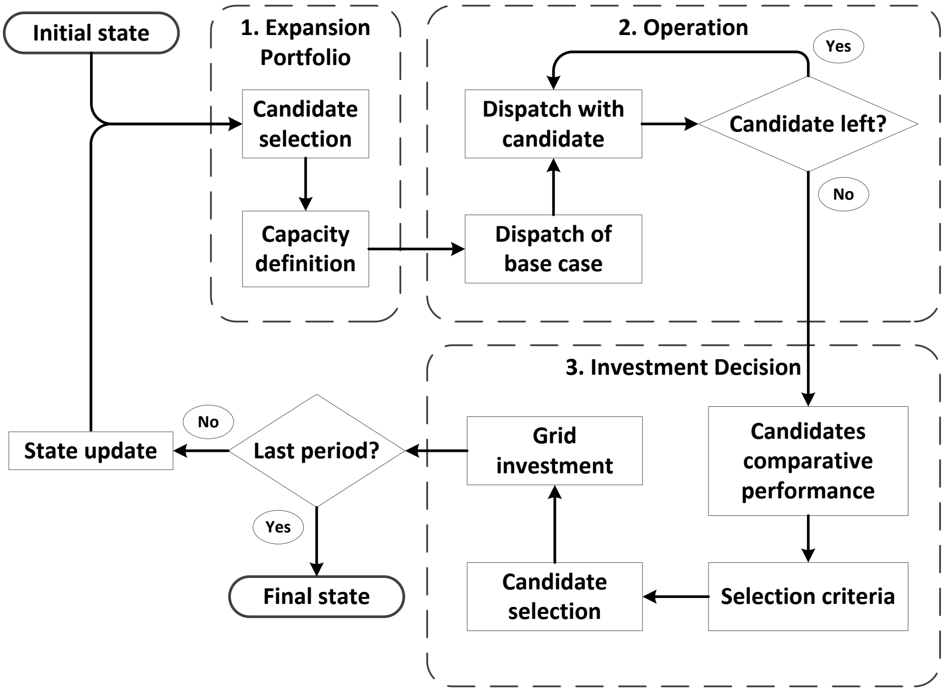

Fig. 2. The offshore grid exploratory model

The expansion portfolio step defines all expansion candidates to be considered, with five expansion topologies possible. In the following step of system operation, the economic dispatch for the base case and for each expansion candidate is calculated individually. Finally, the investment step calculates the comparative expansion candidate benefit, defined as total welfare changes from the starting system for the period to the expanded one. Welfare is composed of consumer and producer surplus and congestion rents [26]. The investment step also calculates the expansion candidate investment cost and the cost and benefit indicator NPV. Then, the expansion candidate with the highest cost and benefit indicator is selected and implemented. The three simulation steps are iterated until the final simulation period.

3.1. Power system modelling

The exploratory model is implemented entirely in the python programming language, making use of the PYPOWER python port for the load flow modelling and NumPy for scientific computing [30, 31, 42]. The model has nodes representing offshore wind farms, offshore hubs, and onshore power systems. Onshore generation mixes may be comparatively cheaper (exporters) or more expensive (importers) as in Figure 3, and six technologies are modelled (Appendix A). Each node power demand and generation capacities is characterized per period and representative hour. Representative hours consider variable renewable generation capacity with availability factors, as in the guidelines of the European Network of System Operators for Electricity [27], while only onshore nodes have demand, which is inelastic. Per period the offshore grid is the same and its performance is given by the probability-weighted average of the representative hours indicated in Appendix B.

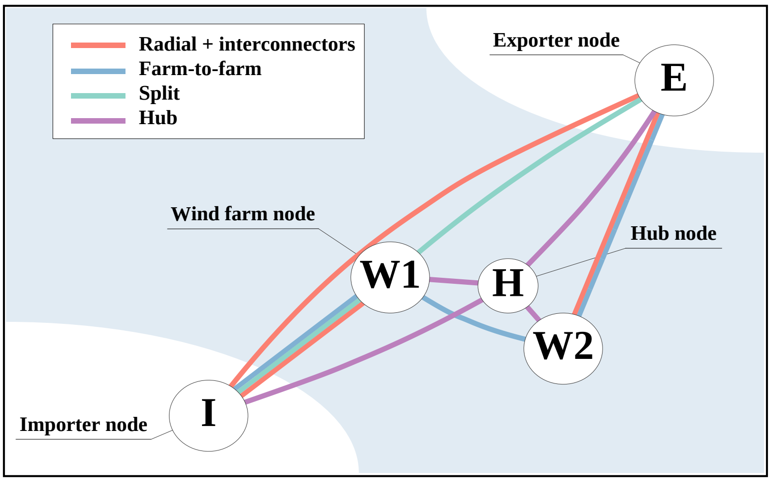

Fig. 3. Model transmission topologies and node types

3.1.1. Cost and benefit indicator

The exploration model selects in each period the expansion candidate with the highest positive cost and benefit indicator. This indicator guarantees that the expansion benefits exceed the investment costs, with two indicators possible, the absolute net present value NPV_a and the net present value ratio NPV_r:

$$NPV_a = (B_e - CI_e)\,, \tag{1}$$

$$NPV_r = (B_e - CI_e)/CI_e \tag{2}$$

where B_e and CI_e are the benefits and costs of investment of expansion candidate *e*.

3.1.2. *Transmission candidates portfolio*

A single expansion candidate is composed of multiple transmission links, with several transmission capacities combinations per topology possible. The expansion candidate types and capacities rules of the portfolio are presented in Table 1, and the standard expansion and initial transmission capacity are indicated in Table 2 and Appendix C. For each topology, capacities are sequentially accumulated in the path from the exporting to importing nodes to determine final candidate link capacities, to channel the potential generation of nodes in the path.

Table 1. Expansion topologies

Expansion candidate	**Link composition**	**Adjusted link capacities?**
Radial + ICs	Independent farm links and interconnectors	For all farm links
Radial + exporting ICs	Independent farm links and interconnectors from exporter	For all farm links
Farm-to-farm	Farms to closest onshore nodes and between farms	Accumulated and adjusted after 1st farm
Hub	All nodes to offshore hubs	For links from farms to hub
Split	Exporter to importer through a farm	For links to importer node

Links connecting to wind farms are adjusted in two ways. First, a variation of ±20% in 10% increments of the link capacities is considered to allow for over- or underplanting of the wind farms [28]. Then, the central capacity value is reduced by the wind link multiplier to account for the average availability of wind in *rh* representative hours, given by:

$$\text{wind link multipler} = \frac{\sum \text{wind availability factor}}{rh} \tag{3}$$

3.1.3. *Benefits and Costs*

The distribution of NPV among nodes is not equal, and thus certain node may object a certain expansion candidate. Thus, in this study the social, regional and developer veto benefits and costs scopes are considered, addressing partially the social constraints indicated in Fig. 1. Give a system with *n* nodes and an expansion candidate involving n_{ec} nodes, where $n_{ec} \leq n$, the scopes are given by:

$$\mathrm{B_e} - \mathrm{CI_e} = \sum_i^n (\Delta CS_i + \Delta PS_i + \Delta CR_i) - \mathrm{CI_e}, \tag{4}$$

$$\mathrm{B_e} - \mathrm{CI_e} = \sum_i^{n_{ec}} (\Delta CS_i + \Delta PS_i + \Delta CR_i) - \mathrm{CI_e}, \tag{5}$$

$$\mathrm{B_e} - \mathrm{CI_e} = \begin{array}{c} \sum_i^{n_{ec}} (\Delta CS_i + \Delta PS_i + \Delta CR_i) - \mathrm{CI_e} \\ if \;\; \Delta CS_i + \Delta PS_i + \Delta CR_i \geq 0 \;\; \forall i \\ 0, otherwise \end{array} \tag{6}$$

where ΔCS, ΔPS, ΔCR and $\mathrm{CI_e}$ are the consumer surplus, producer surplus, congestion rent changes and allocated nodal investment cost for node *i*. Hence, the social benefit accounts for benefit changes and costs for all *n* nodes, while the regional considers only nodes $\mathrm{n_{ec}}$ involved in the expansion candidate. For the developer veto a project costs and benefits are null if any participating node is a net loser. Finally, to have comparable costs and benefits the model considers a net present value of the total benefits B_e using 20 years with 8790 hours and a 15% discount rate.

The CI_e of a candidate *e* with L links and T terminals is the sum of its total link CL and terminal CT costs:

$$CI_e = \sum_i^T CL_i + \sum_j^T CT_j , \tag{7}$$

$$CL_i = c_{kl} * K_l * l , \tag{8}$$

$$CT_j = c_k * K_t . \tag{9}$$

The link unit cost c_{kl} depends on the link transmission capacity *k*, and length *l*, while the terminal unit cost c_t varies by terminal type (values are in Appendix E). K_t is the terminal capacity, and for all terminal types depends on connected links and their capacity as follows. First, for exporting onshore terminals K_t is the maximum capacity among all terminal links. Then, for onshore importing terminals K_t is the maximum capacity of incoming links times the number of links. Finally, a multi-terminal HVDC grid as the one of Akhmatov et al. [29] needs converters only for points injecting or withdrawing power, thus reducing the converter requirements. Therefore, to model these multiterminal economies two different capacities K_t are considered for offshore wind farms, hubs and exporter onshore terminals. When these economies exist, K_t equals the maximum capacity among all terminal's links. With no multiterminal economies K_t is calculated as for onshore importing terminals, i.e. multiplied by the number of terminal links.

3.1.4. Power market modelling

Revenues and costs of producers, consumers and transmission links are determined by optimal power flow simulations for each period and representative hour with the MATPOWER package through its PYPOWER python port [30, 31]. All links are simulated as HVDC parallel (point-to-point) links.

The system operation benefits and costs calculation uses the nodal prices provided by the optimal power flow simulation. The model assumes generation technologies bid their marginal variable cost in a competitive central market, as in Hogan [26]. However, in the model, offshore wind farm and hub nodes do not represent price zones, but rather belong to one of the onshore price zones. Thus offshore nodal prices are equalized to the minimum accessible onshore nodal price, when congested interconnector and wind farm-to-wind farm links are disregarded.

3.1.5. Data Sources

The marginal generation costs of Appendix D include fuel and operation and maintenance costs of EIA [33], while link and terminal costs are obtained from [34]. The case studies use 3 equiprobable representative hours with an offshore availability factor of 0.7, 0.4 and 0.1, leading to an average wind availability factor of 0.4. According to DECC [35] the capacity factor for offshore wind farms in the UK in 2014 was 37.3%, while the 2014 capacity factor of Danish offshore wind farms commissioned since 2009 it amounted to 48% [36]. For onshore renewables, the availability factors are 0.4, 0.25 and 0.1, for an average availability factor of 0.25. For the UK, Germany and Denmark IEA [37] indicates capacity factors of 28–34% for onshore wind and 10–13% for solar photovoltaics, while ECF [38] consider 25–40% and around 12%, respectively.

3.2. Case studies and offshore grid features

We explore three case studies as presented in Table 2 with the 3-onshore node system of Fig. 4. It has one offshore hub and two wind farms, with nodal generation capacities and demand of

Fig. 5 (details on Appendix A and Appendix C). The case studies analyze the effect of the investment costs, benefit types, cost and benefit indicators, and multiterminal economies.

Table 2. Case studies presentation

Case	**Single-period**	**Simultaneous multi-period**	**Sequential multi-period**
Target characteristics and behavior	Cost structure Multiterminal economies NPV scope	Path dependency Benefit types	
Expansion periods	1	2	2
Standard expansion capacity (GW)	8	4	8
Wind farm capacity addition	W1 and W2 with 8 GW on the single period	W1 and W2 with 4 GW in each period	W1 in period 1 and W2 in period 2, both 8 GW

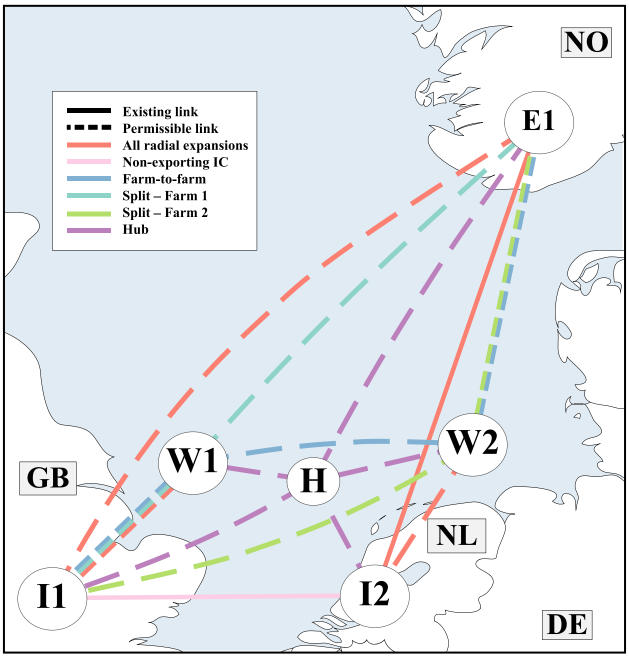

Fig. 4. 3-onshore nodes system for case studies

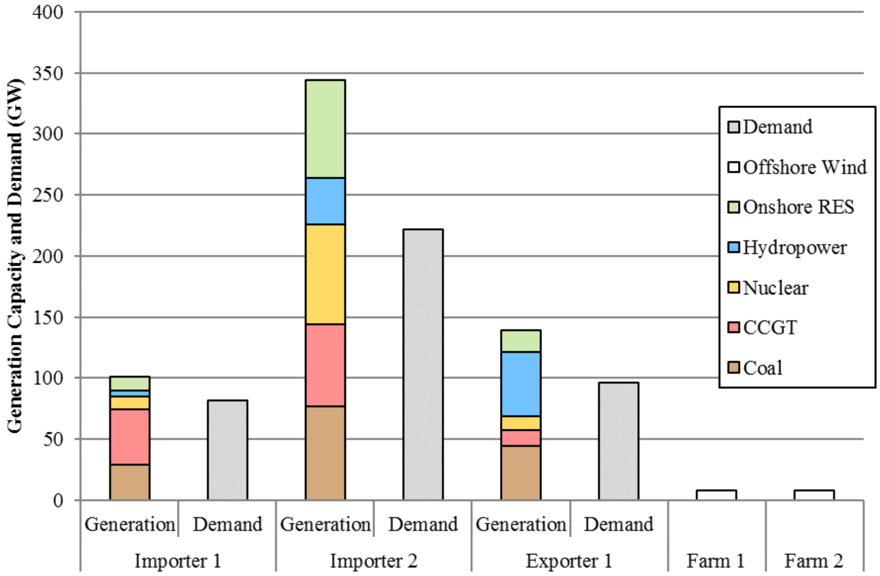

Fig. 5. Total nodal generation capacities and demand

Although the case studies represent abstract systems, for increased comprehension data values are scaled to ones comparable to Northern European power systems. Thus, the exporter node E1 represents Scandinavian and Baltic countries, the first importer node I1 stands for Great Britain, and the second importer node I2 is central western Europe.

The first feature of the exploratory model addressed is the influence of cost parameters per length, capacity and nodes. While benefits are constant, expansion candidates cost changes with cost parameters, and thus influences the NPV. The second feature addressed are the NPV scopes. While several transmission expansion business models exist, in Europe the most common is the centralized planning with regulated remuneration [15]. For the Northern Seas grid, planning is predominantly national, and thus demands the cooperation of national TSOs. The NPV scopes represent this variety of actors. Thus, while a system-level decision maker would use the social benefit, actual planners would ignore positive or negative externalities. Moreover, they not support a candidate if it resulted in a net loss to any of them, a preference represented by the developer veto scope. The 2nd case study uses the same system topology, but introduces multiple periods to allow the study of expansion pathways.

4. RESULTS

The first subsection presents the first expansion period results, for all case studies. Then, the results of the multi-period cases studies for the second period are presented.

4.1. First period expansion

Table 3 presents the maximum social NPV_a value and the corresponding selected topology for various combinations of parameters. For the single-period case, in most combinations the split topology connecting wind farm 1 and the importer node 1 is the preferred expansion. It connects a low-cost exporter node and a wind farm to a node with a deficit of low cost generation. Simultaneously it presents lower investment costs by integrating the connection and interconnection functions, which leads to a higher NPV_a.

However, the radial + ICs expansion is preferred in certain cases. Hence, high wind farm terminal costs make the split topology comparatively more expensive and the radial expansion is chosen. Moreover, since wind power generation does not constrain power flows between onshore systems in the radial expansion, this topology is preferred with the a NPV_a. However, both exceptions are valid only for social and regional NPV scopes, for in this topology comprising all nodes there is always at least one net loser node. Finally, for very specific conditions the hub topology may have a higher NPV_a, when multiterminal economies and comparatively low offshore costs favor it.

For the simultaneous multi-period case the radial expansions are almost exclusively the chosen ones, for the reduced standard expansion capacity of 4GW increases the benefits of separating the connection and interconnection functions of transmission. Thus, for a NPV_a the radial + ICs expansion is preferred, while since the radial + exporting ICs is more efficient it the selected topology under a NPV_r.

The sequential multi-period case has the same standard transmission capacity as the single-period case, and thus more similar expansion selections. Hence the split topology is most frequent, with the radial topology in second place. However, here wind farm 2 is not available in the first period, and thus the radial + exporting ICs is more efficient than the alternative radial expansion for a NPV_r, and even for a NPV_a under high wind farm and onshore terminal costs.

Table 3. First period expansion maximum NPV_a and selected topology

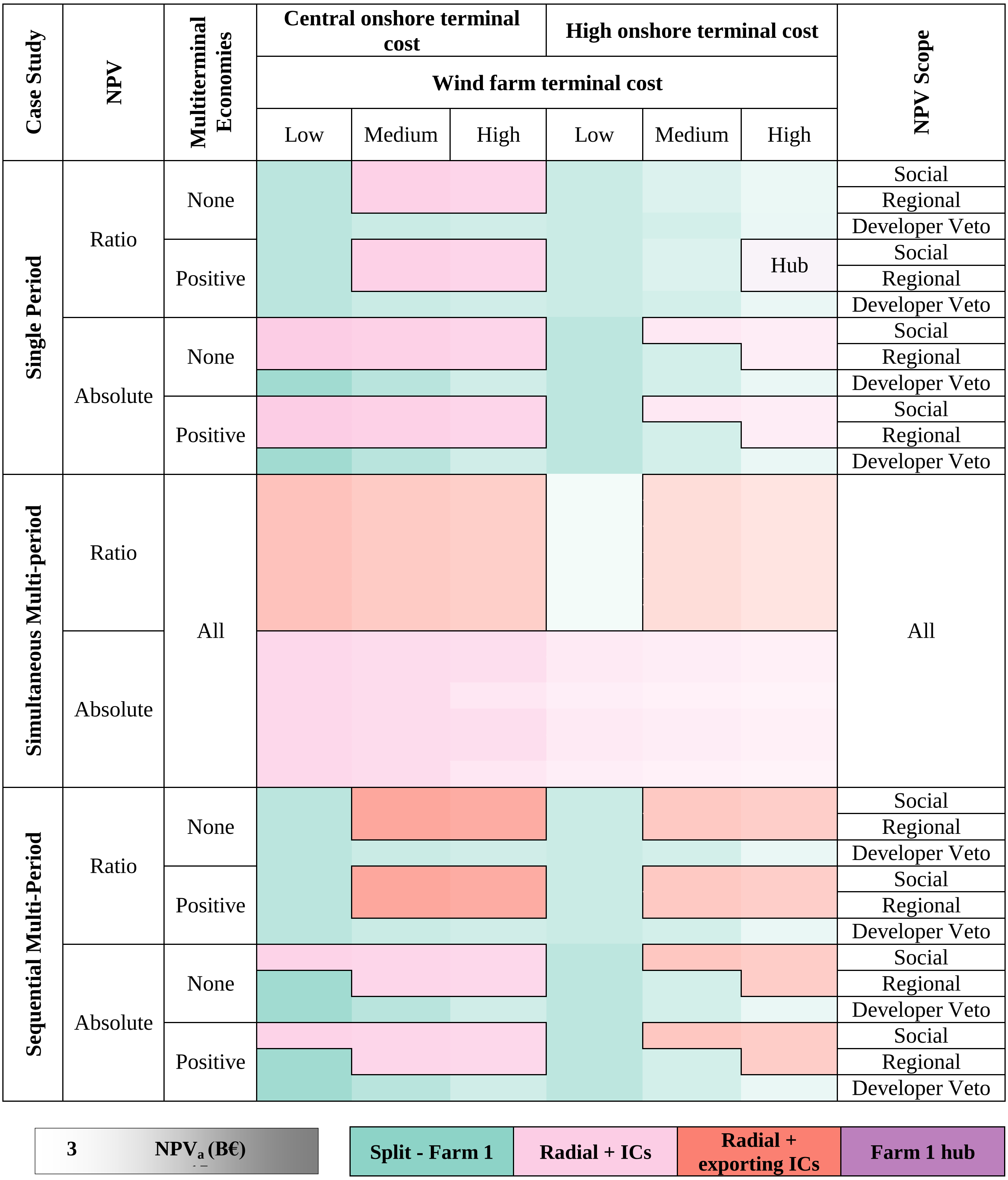

Case Study	**NPV**	**Multiterminal Economies**	**Central onshore terminal cost**			**High onshore terminal cost**			**NPV Scope**
			Wind farm terminal cost						
			Low	Medium	High	Low	Medium	High	
Single Period	Ratio	None	🟩	🟪	🟪	🟩	🟩	🟩	Social
			🟩	🟪	🟪	🟩	🟩	🟩	Regional
			🟩	🟩	🟩	🟩	🟩	🟩	Developer Veto
		Positive	🟩	🟪	🟪	🟩	🟩	Hub	Social
			🟩	🟪	🟪	🟩	🟩	Hub	Regional
			🟩	🟩	🟩	🟩	🟩	🟩	Developer Veto
	Absolute	None	🟪	🟪	🟪	🟩	🟪	🟪	Social
			🟪	🟪	🟪	🟩	🟩	🟪	Regional
			🟩	🟩	🟩	🟩	🟩	🟩	Developer Veto
		Positive	🟪	🟪	🟪	🟩	🟪	🟪	Social
			🟪	🟪	🟪	🟩	🟩	🟪	Regional
			🟩	🟩	🟩	🟩	🟩	🟩	Developer Veto
Simultaneous Multi-period	Ratio	All	🟥	🟥	🟥	🟩	🟥	🟥	All
	Absolute		🟪	🟪	🟪	🟪	🟪	🟪	
Sequential Multi-Period	Ratio	None	🟩	🟥	🟥	🟩	🟥	🟥	Social
			🟩	🟥	🟥	🟩	🟥	🟥	Regional
			🟩	🟩	🟩	🟩	🟩	🟩	Developer Veto
		Positive	🟩	🟥	🟥	🟩	🟥	🟥	Social
			🟩	🟥	🟥	🟩	🟥	🟥	Regional
			🟩	🟩	🟩	🟩	🟩	🟩	Developer Veto
	Absolute	None	🟪	🟪	🟪	🟩	🟥	🟥	Social
			🟩	🟪	🟪	🟩	🟩	🟥	Regional
			🟩	🟩	🟩	🟩	🟩	🟩	Developer Veto
		Positive	🟪	🟪	🟪	🟩	🟥	🟥	Social
			🟩	🟪	🟪	🟩	🟩	🟥	Regional
			🟩	🟩	🟩	🟩	🟩	🟩	Developer Veto

3 NPV_a (B€)	🟩 **Split - Farm 1**	🟪 **Radial + ICs**	🟥 **Radial + exporting ICs**	**Farm 1 hub**

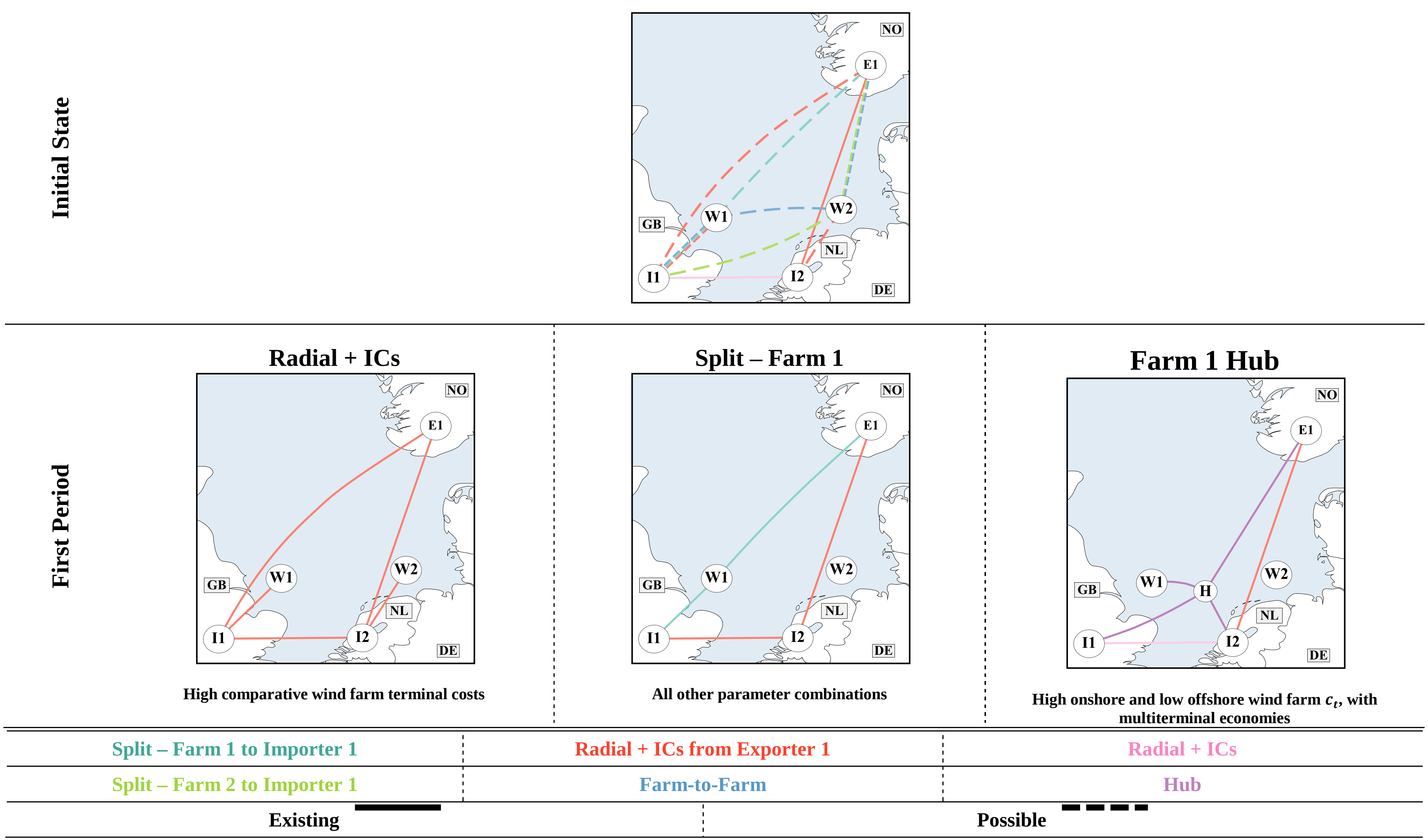

Fig. 6. 1st period expansion

Multiterminal economies represent the reduced number of HVDC converters required by a multiterminal technology, in comparison to a point-to-point HVDC, and improve the NPV of multiterminal topologies relative to other expansion candidates. Multiterminal economies strongly improve the indicator for hub and farm-to-farm topologies (Fig. 7). The increase on the NPV_r for the farm-to-farm topology makes it almost the preferred one for low offshore wind farm terminal costs.

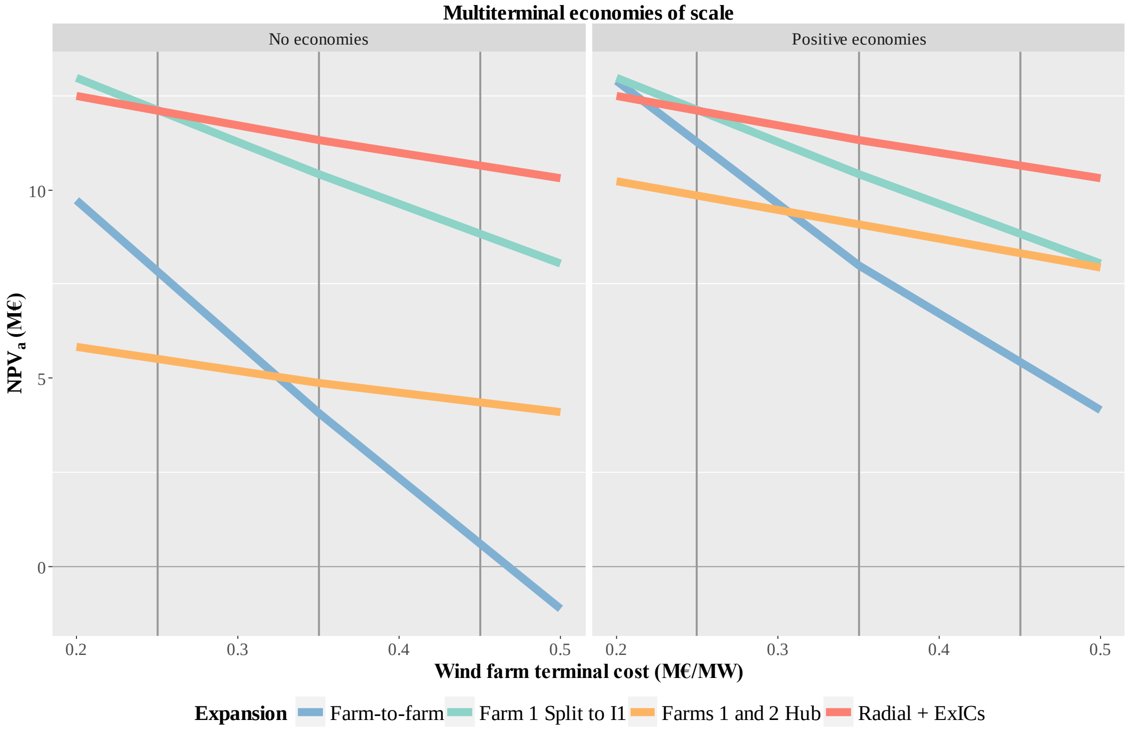

Fig. 7. Influence of multiterminal economies

4.2. Second period expansion

In the multiple period case study the offshore wind farm capacities are introduced simultaneously or sequentially as in Table 2, and here the expansion pathways with a NPV_r and no multiterminal economies are analyzed. As Table 3 present in the first period the preferred topologies are the radial + exporting ICs (due to the separation of connection and interconnection) or the farm 1 split topology (due to efficient link use in a high onshore terminal cost scenario). In the multi-period expansion figures points represent the expansion selected in the previous period, and the lines the NPV_r of the current period.

The second-period expansion is affected by the previous one, as exemplified by the simultaneous case. Thus, an initial split expansion leads to a second-period split expansion of the wind farm 2, for the benefits of this yet-to-connect wind farm are higher than any expansion alternative. On the other hand, if the exporting radial expansion is selected in the 1st period, a number of options are preferred. Hence, whether a split connection with one of the wind farms or the alternative radial expansion is chosen depends on terminal costs, NPV scope and sequence of wind farm additions. In general the farm 2 split connection is preferred, except for a simultaneous addition and central onshore terminal costs. Then, the exporting radial expansion is preferred under a social scope. However, the farm 1 split topology is preferred under a regional scope, for it causes negative externalities on importer node 2 which is not internalized then.

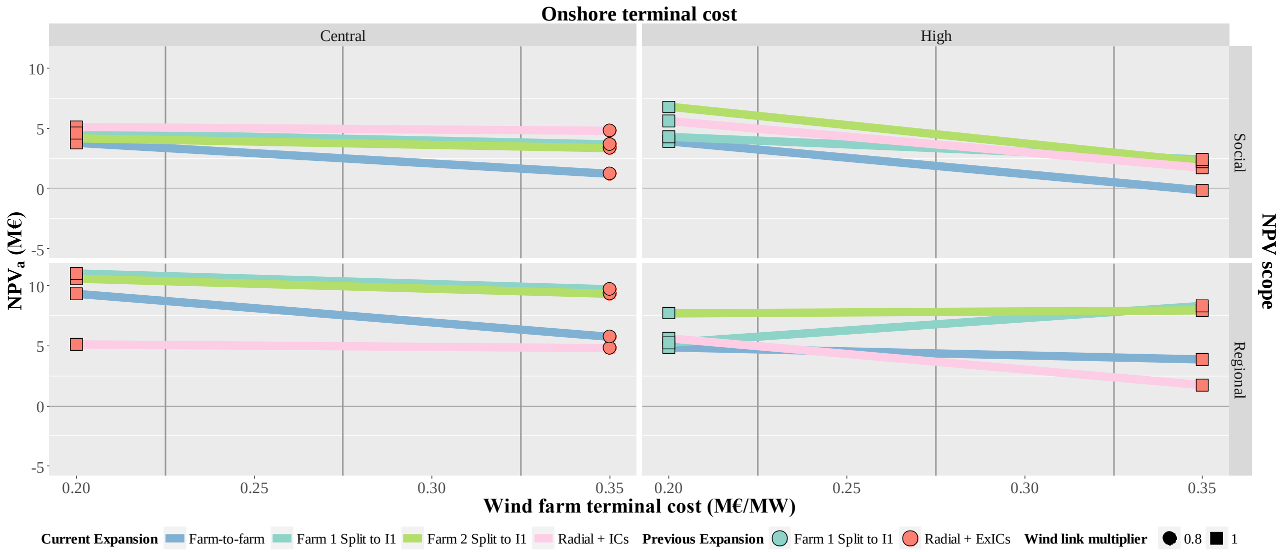

Fig. 8. Multi-period simultaneous expansion

Fig. 9 exemplifies the sequential expansion case for no multiterminal economies, where it can be noted that in contrast to the simultaneous addition of wind farms, a radial expansion is less frequently preferred.

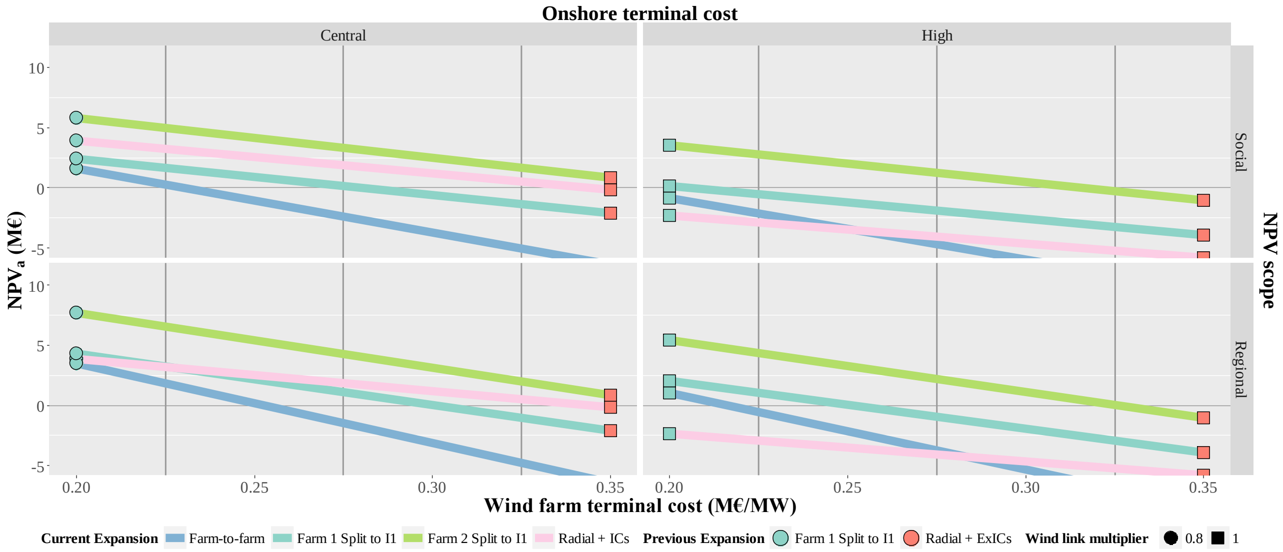

Fig. 9. Multi-period sequential expansion

Figs. 8 and 9 also indicate that the standard size and wind link capacity adjustment interact with the terminal units costs and selected expansion. In this way, higher wind farm terminal costs or a split topology may lead to lower wind link multipliers.

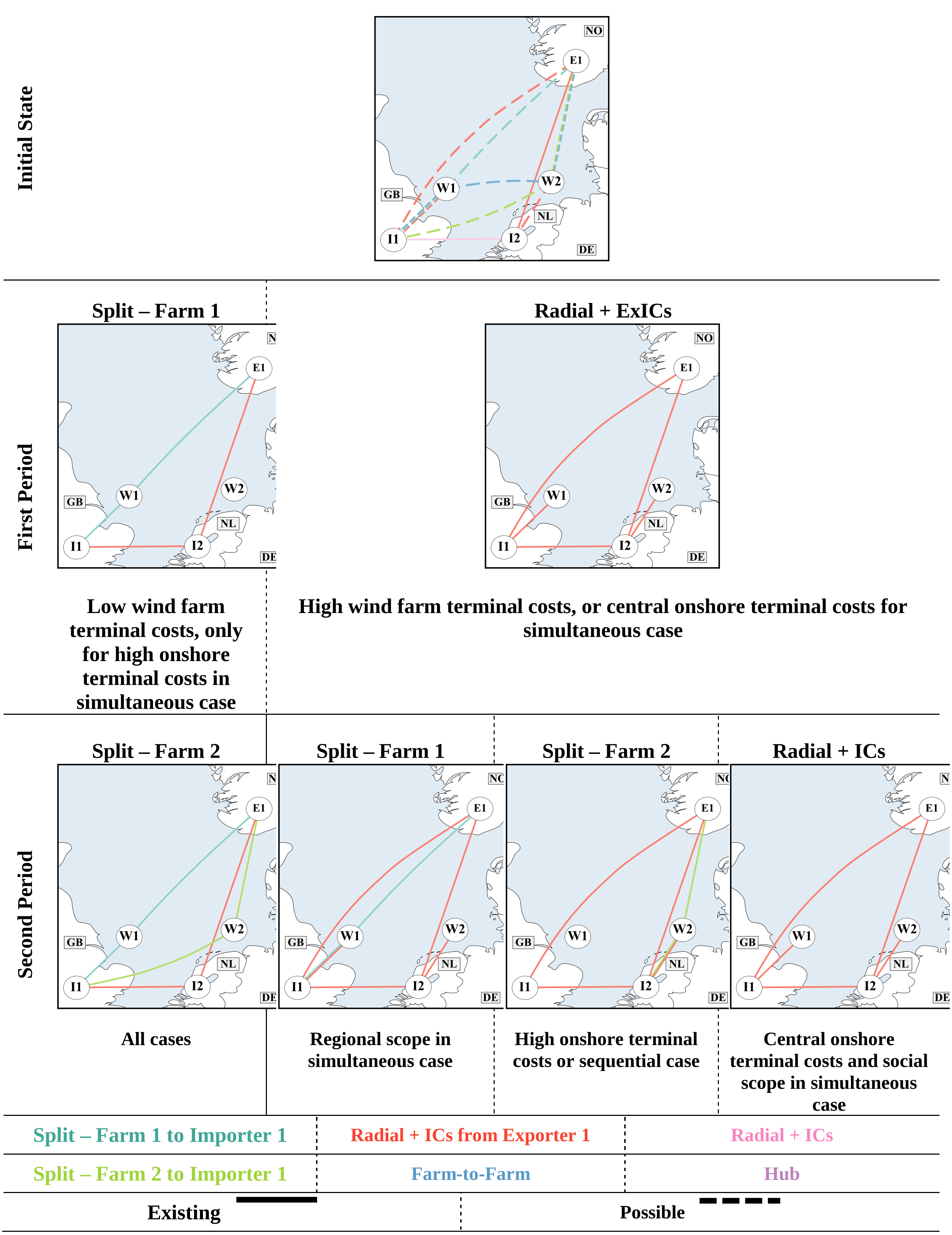

Fig. 10. Multi-period expansion topologies

4.3. Relation of results to the current developments

The case studies analyze static and dynamic problems. Even in the static case the most adequate topologies are few, and which is preferred is affected by terminal unit costs, especially their relation (i.e., between onshore, wind farms and hub terminal costs), by NVP scope, and by multiterminal economies.

The myopic expansion using two periods demonstrates a strong path dependency for this study. Thus, different topologies expansions and wind farm additions in the 1st period influence the 2nd period expansion and results in different offshore grid final states. Moreover, it is possible for no expansion candidate to have a positive NPV, for previous expansions exhaust benefit opportunities. This means that expansion opportunities in subsequent periods are restricted both by previous expansions and by the expansion of the rest of the power system.

Regarding the scope, while the developer veto scope is restrictive, it is nonetheless realistic, for it models the interest of net losers. In situations where this impedes certain topologies, it may be adequate to implement redistribution mechanisms. Moreover, in this study nodes often lost congestion rent, which has implications for the incentives of the transmission systems operators, central actors in developing the offshore grid.

High wind farm terminal costs lead to less integrated expansions being preferred, so cost reductions for HVDC converters and circuit breakers are important for an integrated grid. Moreover, the need for DC/DC converters arising from the lack of anticipatory investments and standardization in HVDC technology also leads to higher terminal costs. Additionally, it is not only the relation between offshore and onshore terminal costs that matter. Indeed, both wind farm and hub nodes in a future offshore grid will use HVDC technology [41]. However, the need for DC breakers, DC/DC converters and multiterminal control will likely be higher for hub than wind farm nodes. Since different development and cost reduction rates can be expected for the different components of HVDC transmission, the attractiveness of the different topologies will also be affected.

The case studies presented some of the characteristics of offshore grid as infrastructure systems. Thus, the internationality and component interaction of the grid is decisive to the distributions of costs and benefits and investment decisions. Moreover, project timing and geography affect the expansion pathways. Finally, asset characteristics (lumpiness, specificity and capital intensiveness) determine costs and capacities, which are crucial for expansion selection.

5. CONCLUSIONS

The aim of this study was to present an exploratory model of offshore grids, simulating transmission expansion pathways. The novelty of the exploratory model is to consider the interaction of the two grid functions using a simulation modelling approach. The studied modelling features lead to different expansion pathways, with each candidate expansion providing net benefits up to around 13 M€. Previous optimization studies of the Northern Seas offshore grid did indicate the importance of technology, costs and benefits distribution and the timing of offshore wind development. However, they do not focus all these aspects. The present exploratory model is capable of representing these simultaneously to derive expansion pathways to support policies and governance of this grid. Also, this is the first application of a simulation approach to the offshore grid, conducting hence descriptive analyses of what could be, instead of prescriptive ones of what should. Moreover, though it addresses features characteristic of offshore grids, the model could be applied to onshore transmission expansion planning.

The current debate on the Energy Union covers several topics, but despite the constellation of proposals, one factor is common to all: The need to coherently integrate the factors shaping the European climate and energy challenges. The presented exploratory model confirms this interdependency between technology, investment and governance. Governance frameworks need to address these interdependencies but also the characteristics particular to the offshore grid. Thus, Energy Union regional cooperation framework guidelines may be general, but the resulting group for the Northern Seas should consider these particular characteristics.

Given the points above, further simulation research on the grid requires developing the exploratory model to include other grid characteristics and to represent pathway behaviors. The focus should therefore be on including costs and benefits redistribution mechanisms, energy policies and regulation for investment and operation of transmission and offshore wind, multiterminal HVDC and (in)compatibility between transmission technologies, energy storage, and finally investment in offshore wind.

6. APPENDICES: CASE STUDIES PARAMETERS AND RESULTS

		I1	I2	E1	W1	W2
	(GW)	**All periods**			**First Period / Final**	
Generation capacity	Offshore wind				4 / 8	4 / 8
	Hydropower	5	38	52	0	0
	CCGT	45	67	13	0	0
	Coal	29	77	44	0	0
	Nuclear	11	82	12	0	0
	Onshore Renewables	11	80	18	0	0
Demand		82	222	96	0	0

Appendix A: Terminal generation capacities and demand

Representative hour	**Unit**	**1**	**2**	**3**
Probability	-	1/3	1/3	1/3
Offshore wind availability factor	(% of installed capacity)	70	40	10
Onshore renewables availability factor		40	25	10

Appendix B: Representative hours

Link	**From**	**To**	**Initial Transmission Capacity (GW)**	**Length (km)**	**Reactance (p.u)**
0	I1	E1		910.48	9.10
1	I1	W1		190.93	1.91
2	I1	H1		293.34	2.93
3	I1	I2	5	324.49	3.24
4	I1	W2		520.87	5.21
5	E1	W1		724.00	7.24
6	E1	H1		657.29	6.57
7	E1	I2	5	797.10	7.97
8	E1	W2		543.40	5.43
9	W1	H1		179.57	1.80
10	W1	I2		317.29	3.17
11	W1	W2		402.73	4.03
12	H1	I2		184.73	1.85
13	H1	W2		231.99	2.32
14	I2	W2		277.97	2.78

Appendix C: Transmission link parameters

	Offshore wind	**Hydropower**	**CCGT**	**Coal**	**Nuclear**	**Onshore Renewables**
Generation cost (€/MWh)	22.5	10.9	59.5	33.6	24.0	11.4

Appendix D: Generation marginal cost parameters

	Link Cost	**Terminal Cost ct**		
Parameter	cl_{kl}	Onshore c_{on}	Wind Farm c_{owf}	Offshore Hub c_{hub}
	M€/MW.km	M€/MW		
Low	0.00015		0.20	
Central	0.00025	0.10	0.35	0.20
High	0.00035	0.20	0.50	

Appendix E: Infrastructure cost parameters

7. REFERENCES

1. GORENSTEIN DEDECCA, J., HAKVOORT, R.A., A review of the North Seas offshore grid modeling: Current and future research. *Renewable and Sustainable Energy Reviews*. 2016, *60*, p. 129–143.
2. VON HIRSCHHAUSEN, C., Developing a Supergrid, in: Moselle, B., Padilla, J., Schmalensee, R. (Eds.), *Harnessing Renewable Energy in Electric Power Systems: Theory, Practice, Policy*, 2010.
3. ADEUYI, O.D., WU, J., Briefing: The North Sea grid. *Proc. ICE - Energy* 2015.
4. ANDOURA, S., VINOIS, J.-A., From the European Energy Community to the Energy Union - A Policy Proposal for the Short and the Long Term, 2015.
5. EC, European Commission. Launching the public consultation process on a new energy market design - COM(2015) 340 final. 2015.
6. GLACHANT, J.-M., VASCONCELOS, J., RIOUS, V., A Conceptual Framework for the Evolution of the Operation and Regulation of Electricity Transmission Systems Towards a Decarbonised and Increasingly Integrated Electricity System in the EU, 2015.
7. EC, EUROPEAN COMMISSION, Energy Union Package - A Framework Strategy for a Resilient Energy Union with a Forward-Looking Climate Change Policy, 2015.
8. DONNELLY, M., A Meshed Offshore Grid for the North Seas - Why We Need to Look Beyond Boundaries. 2014.
9. RODRIGUES, S., RESTREPO, C., KONTOS, E., TEIXEIRA PINTO, R., et al., Trends of offshore wind projects. *Renewable and Sustainable Energy Reviews*. 2015, *49*, p. 1114–1135.
10. E3G, North Seas Grid Project Pipeline Analysis, E3G, 2013.
11. JAY, S.A., TOONEN, H.M., The power of the offshore (super-) grid in advancing marine regionalization. *Ocean & Coastal Management*. 2015.
12. FITCH-ROY, O., An offshore wind union? Diversity and convergence in European offshore wind governance. 2015.
13. FLYNN, B., Brussels Offshore? Explaining the Largely National Politics of Europe’s Experiment with Marine Renewables, in: 2015.
14. PUKA, L., SZULECKI, K., The politics and economics of cross-border electricity infrastructure: A framework for analysis. *Energy Research & Social Science*. 2014, *4*, p. 124–134.
15. RIVIER, M., PÉREZ-ARRIAGA, I., OLMOS, L., Electricity Transmission, in: Pérez-Arriaga, I.J. (Ed.), *Regulation of the Power Sector*, Springer London, 2013, p. 251–340.
16. LATORRE, G., CRUZ, R.D., AREIZA, J.M., VILLEGAS, A., Classification of publications and models on transmission expansion planning. *IEEE Transactions on Power Systems. On* 2003, *18*, p. 938–946.
17. LUMBRERAS, S., RAMOS, A., The new challenges to transmission expansion planning. Survey of recent practice and literature review. *Electric Power Systems Research*. 2016, *134*, p. 19–29.
18. YEN, J., YAN, Y., CONTRERAS, J., MA, P.-C., ET AL., Multi-agent approach to the planning of power transmission expansion. *Decision Support Systems*. 2000, *28*, p. 279–290.
19. CONTRERAS, J., GROSS, G., ARROYO, J.M., MUÑOZ, J.I., An incentive-based mechanism for transmission asset investment. *Decision Support Systems*. 2009, *47*, p. 22–31.
20. VAN BLIJSWIJK, M.J., DE VRIES, L.J., Modeling transmission investment under different regulatory regimes, in: 2014.
21. OJEDA, O.A., OLSINA, F., GARCÉS, F., Simulation of the long-term dynamic of a market-based transmission interconnection. *Energy Policy* 2009, *37*, p. 2889–2899.

22. OCHOA, C., DYNER, I., FRANCO, C.J., Simulating power integration in Latin America to assess challenges, opportunities, and threats. *Energy Policy* 2013, *61*, p. 267–273.
23. JÄGEMANN, C., FÜRSCH, M., HAGSPIEL, S., NAGL, S., Decarbonizing Europe's power sector by 2050 – Analyzing the economic implications of alternative decarbonization pathways. *Energy Economics.* 2013, *40,* p. 622–636.
24. HERBST, A., TORO, F., REITZE, F., JOCHEM, E., Introduction to energy systems modelling, 2012.
25. PAPACHRISTOS, G., Towards multi-system sociotechnical transitions: why simulate. *Technology Analysis and Strategic Management.* 2014, *26*, p. 1037–1055.
26. HOGAN, W.W., Transmission Benefits and Cost Allocation. 2011.
27. ENTSO-E, EUROPEAN NETWORK OF TRANSMISSION SYSTEM OPERATORS FOR ELECTRICITY., ENTSO-E Guideline for Cost Benefit Analysis of Grid Development Projects, 2015.
28. THE CROWN ESTATE, Sharing lessons learned and good practice in offshore transmission: Summary report, 2014.
29. AKHMATOV, V., CALLAVIK, M., FRANCK, C.M., RYE, S.E., ET AL., Technical Guidelines and Prestandardization Work for First HVDC Grids. *IEEE Transactions on Power Delivery*. 2014, *29,* p. 327–335.
30. LINCOLN, R.W., Learning to Trade Power, University of Strathclyde, 2011.
31. ZIMMERMAN, R.D., MURILLO-SÁNCHEZ, C.E., THOMAS, R.J., MATPOWER: Steady-State Operations, Planning, and Analysis Tools for Power Systems Research and Education. *IEEE Transactions on Power Systems.* 2011, *26*, p. 12–19.
32. MILANO, F., Power System Modelling and Scripting, Springer Berlin Heidelberg, Berlin, Heidelberg 2010.
33. EIA, UNITED STATES ENERGY INFORMATION ADMINISTRATION., Levelized Cost and Levelized Avoided Cost of New Generation Resources in the Annual Energy Outlook 2015, 2015.
34. E3G, DWG, DNV GL, ECN, ET AL., NorthSeaGrid - Offshore Electricity Grid Implementation in the North Sea. Annexes to the Final Report, 2015.
35. DECC, DEPARTMENT OF ENERGY AND CLIMATE CHANGE, Digest of United Kingdom Energy Statistics 2015, 2015.
36. DEA, DANISH ENERGY ADMINISTRATION, Master Data Register of Wind Turbines - Data on operating and decommisioned wind turbines (as at end of September 2015), 2015.
37. IEA, INTERNATIONAL ENERGY AGENCY, Projected Costs of Generating Electricity 2015, 2015.
38. ECF, EUROPEAN CLIMATE FOUNDATION, Roadmap 2050: a practical guide to a prosperous, low-carbon Europe, 2010.
39. E3G, DWG, DNV GL, ECN, ET AL., NorthSeaGrid - Offshore Electricity Grid Implementation in the North Sea, 2015.
40. WOOLLEY, O., Governing a North Sea Grid Development: The Need for a Regional Framework Treaty. *Competition and Regulation in Network Industries*. 2013, p. *14*.
41. YARAMASU, V., WU, B., SEN, P.C., KOURO, S., ET AL., High-power wind energy conversion systems: State-of-the-art and emerging technologies. *Proceedings of the IEEE.* 2015, *103*, p. 740–788.
42. S. VAN DER WALT, S. C. COLBERT, and G. VAROQUAUX. The NumPy Array: A Structure for Efficient Numerical Computation. *Computing in Science & Engineering*, Volume *13*, 2. 2011, p. 22–30.

CYSENI 2016, May 26-27, Kaunas, Lithuania
ISSN 1822-7554, www.cyseni.com

ANALYSIS OF THE APPLICATION OF FINANCIAL INSTRUMENTS TO RENEWABLE ENERGY TECHNOLOGY

P. Mačiulis
Lithuanian Energy Institute
Breslaujos str. 3, LT-44403 Kaunas – Lithuania
Email: povilas.maciulis@gmail.com

ABSTRACT

Renewable energy has made significant achievement on the world stage in recent years. In 2014, global investments in renewable energy increased by 17 percent. This was the first increase in investment for three years. This sector still does not realise its full potential and at these stage faces a host of barriers, which are formed by underdeveloped financial markets, technology and regulatory risks, policy makers decisions. Examples of barriers include lack of long-term loans, high financing costs, high transaction costs. The aim of this paper is to analyse the application of financial instruments that could reduce barriers. The paper considers how well different financing instruments address different barriers and risks. The list of instruments covered includes equity, debt, grants, guarantees, and insurance as well as more targeted categories such as small-scale project financing or carbon financing. Policy makers tend to go straight to the use of a particular financing instrument without necessarily analyzing which measures would be most effective for a given valuable package of conditions. The use of financing instruments (publicly funded) requires that government agencies have the institutional capacity to manage such instruments in an effective and transparent way. Institutions must be able to effectively prepare and plan renewable energy technology projects and programs for support, to implement instruments in a timely manner, and to follow all necessary procedures and regulations. Furthermore, public finance instruments have to pursue to minimise investment risk and maximise leverage for additional financing through private and public partnerships.

Keywords: financing instruments, renewable energy technology

CYSENI 2016, May 26-27, Kaunas, Lithuania
ISSN 1822-7554, www.cyseni.com

EXPERIMENTAL EQUIPMENT DESIGN FOR INVESTIGATING CONDENSATION PHENOMENA AT HORIZONTAL WATER-VAPOR INTERFACE

Mindaugas Drūlia
Lithuanian Energy Institute
Laboratory of Nuclear Installation Safety
Breslaujos str. 3, LT-44403 Kaunas – Lithuania
Email: Mindaugas.Drulia@lei.lt

ABSTRACT

A short literature review on the issue of condensation at water – vapor interface is presented. There exists a disagreement between experimental results of condensation coefficients, as these results scatter in a range of several orders of magnitude, depending on the application field. Thus, the fundamental understanding about physical mechanisms of condensation as the ongoing process requires deeper knowledge level, compared to the results achieved so far. The hydrogen bond between water molecules is one of the unique water properties that play an important role in condensation processes. Therefore this work is concentrated in examining the influence of water properties to the overall condensation process. The calculations of the similar experiments done by other researchers were made, where instantaneous condensation bursts have been measured. According to the assessments made, the design of experimental stand is being projected so that the conditions would be sufficient in causing rapid condensation intensities. The chosen geometry were a vertical cylinder with water and vapor inlets and outlets at bottom and top of the cylinder. The results are discussed and further objectives are determined.

Keywords: condensation coefficient, condensation rate, condensation burst, hydrogen bonding, water-vapor interface

1. INTRODUCTION

Water is the most abundant and most common natural compound on Earth. However it has a series of properties that are unusual compared to analogous materials. Due to the water's unique physical properties, it is widely used in technological installations. For example, one of the characteristics of water is high heat capacity (4.19 kJ/kgK); water for this reason is practical to use in nuclear reactors and thermal circuits as heat carrier. Pure water is a very good solvent, which is why it constantly has enough amount of solute salts to influence water features and condensation processes; that is why there are relatively few experiments made with pure water. The phase reversibility of water is used in vapor turbines to generate electric power, etc. The question arises, what factors determine all the properties for what the water is so widely applied? Or, in other case, how it would be possible to evaluate the influence of water properties to the water's behavior by changing the ambient conditions?

The aim of this paper is to present the design of the experimental stand for investigating condensation phenomena at water-vapor interface that is being constructed, according to the assessments made in similar condensation experiments.

2. LITERATURE REVIEW

2.1. Unique water physical properties

Considering the point of the molecular level, water molecules are made of one oxygen and two hydrogen atoms that are joined together by covalent bonds. When a liquid system is made of more water molecules they interact by weaker Van der Waals bonds and hydrogen bonds [1]. The latter ones are responsible for many unique and anomalous water physical properties. All in all, one H_2O molecule may form 6 bonds with neighbouring molecules. By maximum, four of them may be based on hydrogen bonding; other bonds may be based on Van der Waals or other forces. Due to hydrogen bonds water molecules can be formed to polymeric units called clusters (see Fig. 1). A single H_2O molecule has a polarity, and when it forms into a cluster, it has a resultant polarity. The clusters are formed near one another, and the amount of them is characterized by the cluster density. It is calculated that clusters that are near the water-vapor interface are of a lower cluster density than those in the bulk of the liquid [10].

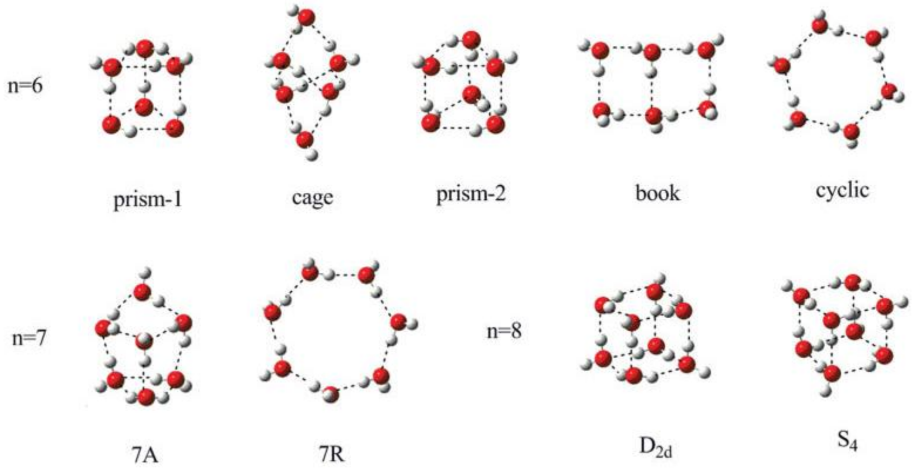

Fig. 1. Various types of low energy water clusters simulated. Adapted from [12]

Also, using computational techniques it is calculated that by average one H_2O molecule composes 3 hydrogen based bonds with other H_2O molecules [1]. A single cluster exists for 10^{-12}–10^{-9} seconds period by average [2]. It is a short duration, which depends on the electron moving rate around hydrogen nucleus and on rapid thermal vibrations [2]. But the formed bonds are quite strong, compared to the thermal energy (k_B*T) (k_B – Boltzmann constant) of water molecules. For example, under conditions of standard temperature and pressure, the strength energy of hydrogen bonding is is 0.24 eV (i.e. 23.3 kJ/mol, [9]), while the thermal energy equals 0.023 eV, i.e. about 10 times less than hydrogen bond. Besides, under ambient conditions, water hydrogen bonding energy is still about 5 times greater than the average thermal collision fluctuation. When the cluster is broken, a new one is formed almost instantaneously. In 2006, Smith and co-workers wrote an article, based on a work about water cluster simulations [3]. They state that hydrogen bonds between molecules break every 10^{-12}–10^{-9} seconds and re-establish in a range of 2×10^{-13} seconds, i.e. so rapidly that all the liquid system can be considered as continuous network of hydrogen bonds. It is important to perceive that hydrogen bonds cannot be neglected in taking part at condensation occurrence, and we need to understand the influence or concrete fraction of these bonds playing during the process, i.e. not only qualitative, but also quantitative approach.

2.2. Water models

In order to define the behaviour of water molecules, the theoretical water models are composed and established [4]. They are operated under such conditions, when H_2O molecules are moving in liquid and in vapor, during the condensation or evaporation processes, or in other cases. Water models are used both for simplifying transitional processes calculations and making water structure view as close as possible to the physical reality (see Fig. 2). While creating the specific water model based on the needs, various parameters are related with a hypothetical molecule. It is done with a purpose to characterize a single H_2O molecule and to apply it for computational simulations between the groups of molecules. The parameters usually have an equivalent in physical reality, e.g. the length between bonds and their strength, the polarity of a molecule, attractive and repulsive forces with respect to other water molecules, the number of molecules, etc. The more precisely such a model predicts the physical properties of the material; the more precise structural view of this material is achieved. In fact, however, theoretical water models are not successful in recreating the real water properties, even though these models give some useful information about the behaviour of water, e.g. the rotation or vibration of molecules and clusters [5] [11].

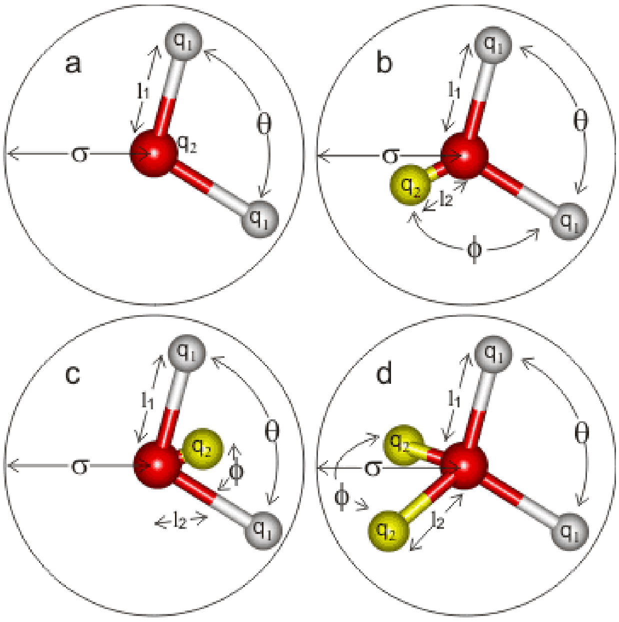

Fig. 2. Various water molecular models [5]

2.3. Experimental observations

Water evaporation and condensation processes are being widely investigated for around a century, both creating theoretical models [4] and experimentally, for measuring the speed of processes. Marek & Straub [6] evaluated condensation coefficients used by various researchers in their experiments (see Fig. 3). The coefficients ranged by several orders of magnitude under the same pressure in different investigations. The errors may be neglected if results differed by few percent. In this case the blinking of the fact is inadequate. The scattering of the results presuppose an idea that the used condensations coefficients may not correspond to the physical reality. It may happen either due to experimental results inaccuracy or due to misconstruction of assumptions done before the coefficients were accepted as the right ones. The same hypothesis was stated by Almenas [17] in his monograph.

At the beginning of the development of classical theory, based on Maxwell-Boltzmann distribution and applied to water, one of the logical assumptions were that the liquid water molecules can change into vapor phase, in a case when the average temperature of liquid molecules exceeded the average temperature of vapor molecules. Water molecule was assumed as a hard ball, and the event of condensation or evaporation were assumed to be caused by two particles interaction. However, the results in the experimental works of researchers Ward et al [7], and Badam et al [8] were contradicting to this theory. The phase-change temperature jumps across the water-vapor interface were detected both in cases of condensation and evaporation, while the temperature of vapor were higher than that of water surface by several degrees Celsius. And also, the same results were achieved under the special heating of vapor phase. In Badam et al experiment a lot of attention was paid to the improvement of measurements accuracy, so the results are reliable. Also Badam et al observed increasing temperature jumps by increased heating of wire placed at vapor phase. Ward et al and Badam et al experiments support and strengthen the position that while solving the tasks of condensation, the coefficients used in the classical methodology are introduced because of the initial Maxwell-Boltzmann theory assumption for water is unsuitable.

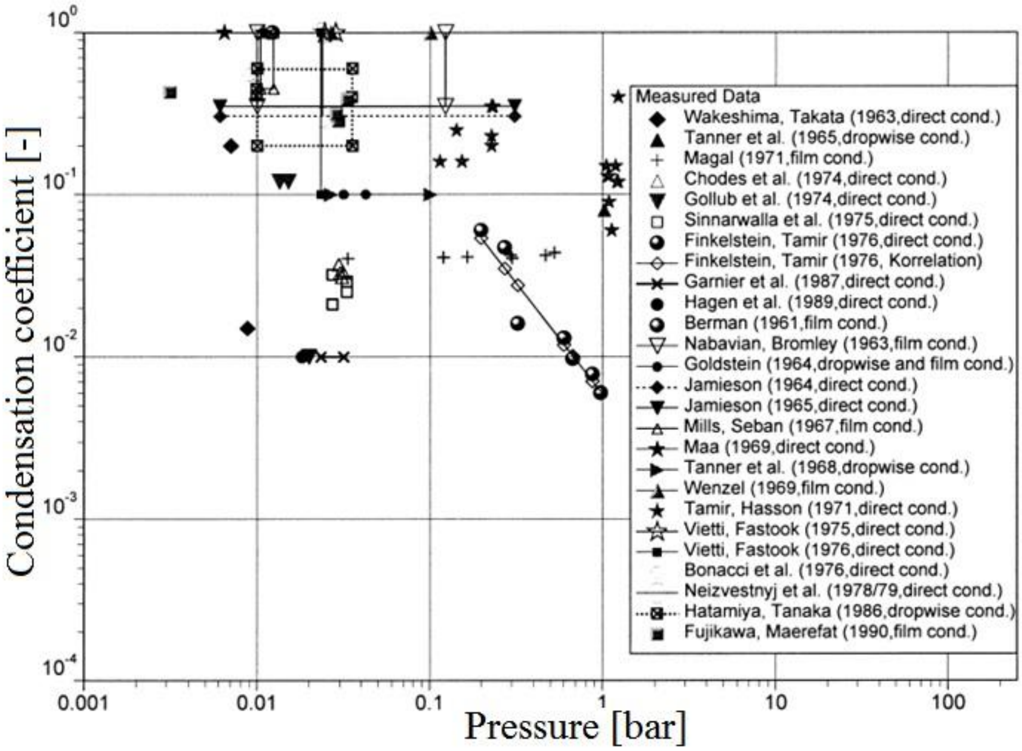

Fig. 3. Condensation coefficient of water as a function of pressure. Adapted from [6]

The fundamental of classical theory is that the event of H_2O molecule evaporation and condensation is caused by the interaction of two molecules. The theory is in good agreement with the experimental results, when the particles are assumed to be hard balls. The analytic techniques, used to measure the condensation fluxes and rates through the water-vapor interface, are often deduced from so-called Hertz-Knudsen-Schrage equation:

$$J = \left(\frac{2}{2-\alpha e}\right)\sqrt{\frac{M}{2\pi R}}\cdot\left(\frac{\alpha c\cdot P_{fi}}{\sqrt{T_{fi}}}-\frac{\alpha e\cdot P_{gi}}{\sqrt{T_{gi}}}\right), \qquad (1)$$

where J is the flux of condensation or evaporation; α_c and α_e are the condensation coefficient and evaporation coefficient; M is the molar mass of H_2O; R is the universal gas constant; P_{fi} and P_{gi} are pressures near interface from liquid side and from vapor side, respectively; T_{fi} and T_{gi} are the corresponding temperatures.

Since the water molecule is strongly polar and quite non-spherical, and the molecules are tied by hydrogen-bond attractions, the analysis of water molecules as hard balls becomes complicated, and some correction factors must be set, in order to make results closer to the physical measurements. Under the development of calculations, the correction coefficients sometimes differ even though the experimental conditions are quite the same, as written by Marek & Straub [6]. The appropriate theoretical model for operating without correction factors or minimizing their influence in condensation rate calculations is still lacking or under development.

Sonin et al [13], Jackson et al [14] and Celata et al [15] investigated condensation phenomena. For Celata and Sonin rapid condensation bursts were undesirable conditions, so they continued experiments at lower rates so as not to cause condensation shocks. But before that it were observed disruption of interface, either intermittently or continuously [14]. In Lithuanian Energy Institute (LEI) a series of experiments were made concerning the issue of initiating and controlling continuous rapid condensation bursts, and investigating condensation implosion event [16].

However, the conditions of just-beginning of condensation implosion phenomena were not investigated purposely. It is important to pay an attention to the initiation conditions and investigate condensation phenomena, and get more knowledge about fundamental physics of condensation at molecular level.

3. METHODOLOGY

3.1. Experimental stand design

The test stand is being designed and constructed for testing and evaluating the rapid condensation bursts at the beginning of their initial phase. The geometry of the stand were chosen a vertical fused quartz cylinder. Test section is shown in Fig. 4. The decision of vertical cylinder was the following due to experiments made by other researchers, who managed to reach the conditions that are necessary to start rapid condensation intensities [13–15]. Cylinder has diameter $D = 0.15$ m, it is transparent to visible light and having proper thermal resistance and thermal expansion characteristics. Cylinder length is equal to 0.90 m, and it should be partially filled with water. Steam height calculated in the test section cannot be lower than 3 cylinder diameters or exceed 4 cylinder diameters, i.e. $3 \leq z_s/D \leq 4$. Another important characteristic is nozzle for water inlet into the test section, whose diameter d must be 24 times smaller than cylinder diameter D, or $d = 0.00625$ m. The maximum water inlet flow rate to the test section is up to 5.83×10^{-4} m^3/s or 0.582 kg/s. Maximum steam flow rate could reach up to 0.0035 kg/s, and normally it would be strongly turbulent. We needed to achieve laminar steam inlet conditions, therefore two flange system were designed (top and middle flanges in Fig. 4). Top flange is serving as a wall for the steam not to pass

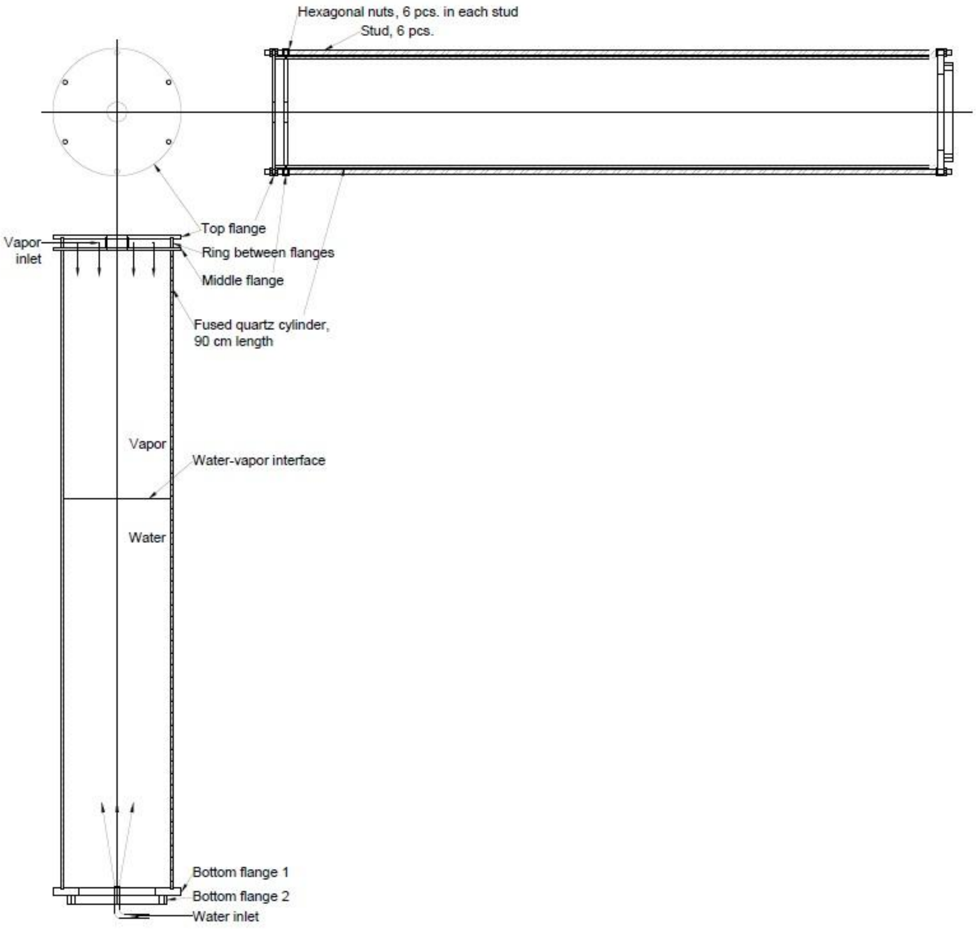

Fig. 4. Experimental stand test section

into atmosphere. The middle flange is designed so that the turbulent flow of steam would be reduced to laminar flow. This is achieved through 192 small holes that are drilled through flange in a chequerboard way. The flow is calculated to be laminar, with Reynolds numbers $Re \leq 1200$. Bottom flange system is made of two flanges. First bottom flange (BF1) is connected with the cylinder, and the second bottom flange (BF2) is intended for water inlet and outlet holes. BF2 can be changed if we notice that water inlet and outlet geometry makes asymmetric influence for condensation at water-vapor interface.

4. DISCUSSION

According to the comparison of intermolecular bonds strength (0.24 eV) vs water thermal energy amount (0.023 eV), the assumption can be made: for a single H_2O molecule, in order to condense, the momentum impact of another single H_2O molecule is insufficient for being inserted between three hydrogen bonds. The moment, when a water molecule is not formed into hydrogen-bond based clusters, is very short and rare event. On the other part, the average kinetic energy of water vapor molecule (about 0.03 eV) is usually lower than water surface tension forces (binding energy being about 0.045 eV for surface liquid molecule) [17]. In order for a molecule to be inserted in between those bondings and to be condensed, there is possibly existing another mechanism than just two-molecules interaction. The verification of such hypothesis requires additional experiments shall be done. For the verification of hypothesis the experimental stand is being constructed, according to calculations and experimental observations made from other experimental works [13–16], and now there is a test section made, that is designed in a way that rapid condensation bursts could occur. Further development of the system is being done, and there will be examined condensation implosion initiation characteristics.

5. CONCLUSIONS

Unique water physical properties are caused by intermolecular hydrogen bonds between H_2O molecules. These properties make an influence for condensation process intensities.

The strength of hydrogen bond is about 10 times higher compared to the thermal energy of water under normal conditions.

Experimental stand test section was chosen and is being designed, according to calculations done by other researchers with similar experiments, who noticed and observed rapid condensation bursts. The system design fits the requirements for initial condensation implosion conditions.

6. REFERENCES

1. LENZ A., OJAMÄE L. Theoretical IR spectra for water clusters $(H_2O)n$ (n = 6-22, 28, 30) and identification of spectral contributions from different H-bond conformations in gaseous and liquid water. *J. Phys. Chem. A*, 110, (2006) p. 13388–13393.
2. LOWER S. A gentle introduction to water and its structure. Vancouver, Canada (2014) [referred on the 22nd of April, 2016 y.]. Link to the internet <http://www.chem1.com/acad/sci/aboutwater.html>.
3. SMITH J. D., CAPPA CH. D., WILSON K. R., COHEN R. C., GEISSLER P. L., SAYKALLY R. J. Unified description of temperature-dependent hydrogen bond rearrangements in liquid water. *Proceedings of the National Academy of Sciences* (2005).
4. WALLQVIST A., MOUNTAIN R. D.. Molecular models of water: Derivation and description. *Reviews in Computational Chemistry* 13 (1999) p. 183–247.
5. CHAPLIN M. Water structure and science. London South Bank University, UK (2015) [referred on the 22nd of April, 2016 y.]. Link to the internet <http://www1.lsbu.ac.uk/water/water_structure_science.html>.

6. MAREK R., STRAUB J. Analysis of the evaporation coefficient and the condensation coefficient of water. *Int. J. Heat Mass Transfer* (2001) Vol. 44, p. 39–53.
7. WARD C. A., STANGA D. Interfacial conditions during evaporation or condensation of water. *Phys. Rev. E*, (2001) Vol. 64, p. 05159091–05159099.
8. BADAM V.K, KUMAR V., DURST F., DANOV K. Experimental and theoretical investigation of interfacial temperature jumps during evaporation. *Experimental Thermal and Fluid Science*, (2007) Vol. 32, p. 276–292.
9. SURESH S. J., NAIK V. M. Hydrogen bond thermodynamic properties of water from dielectric constant data. *J. Chem. Phys.*, 2000 Vol. 113, p. 9727–9732.
10. CHAPLIN M. Theory vs Experiment: What is the Surface Charge of Water? *Water Journal* (2009) Vol. 1, p. 1–28.
11. GUILLOT B.. A reappraisal of what we have learnt during three decades of computer simulations on water, *Journal of Molecular Liquids* (2002) Vol. 101, p. 219–260.
12. QIAN P., SONG W., LU L., YANG Z. Ab Initio Investigation of Water Clusters $(H_2O)_n$ ($n = 2–34$). *International Journal of Quantum Chemistry*, 2009, Vol. 110, No 10, p. 1923–1937.
13. SONIN A. A., SHIMKO M. A., CHUN J. H. Vapor condensation onto a turbulent liquid. I. The steady condensation rate as a function of liquid-side turbulence. *Int. J. Heat Mass Transfer*, 1986, Vol. 29, No. 9, p. 1319–1332.
14. JACKSON J.D., ZHAO C.L., DOERFFER S., BYRNE J.E., FALAKI H. Effect of pool turbulence on direct contact condensation at a steam/water interface. *International Atomic Energy* Agency, 2000, IAEA-TECDOC–1149, p. 13–19.
15. CELATA G. P., CUMO M., FARELLO G. E., FOCARDI G. Direct contact condensation of steam on a horizontal surface of water. *Heat and Mass Transfer*, 1987, Vol. 21, No. 2, p. 169–180.
16. ŠEPORAITIS M., Pabarčius R., Almenas K. Kondensacijos pliūpsnio tyrimai: konstrukcinis pulserio kriterijus. *Energetika*, 2006, No. 3, p. 77–85.
17. ALMENAS K. *Evaporation/condensation of water. Unresolved issues. I. Phase change at low pressures, laminar conditions*. Kaunas: Vytautas Magnus University, 2015. 72 p. ISBN 978-609-467-097-8.

CYSENI 2016, May 26-27, Kaunas, Lithuania
ISSN 1822-7554, www.cyseni.com

THE NEW STRUCTURED PACKING CUB FOR REALIZATION HEAT AND MASS TRANSFER PROCESSES

I. V. Novikova, A. S. Pushnov
Moscow State University of Mechanical Engineering
Bolshaya Semenovskaya str. 38, 107023 Moscow – Russia
Email: irrrinochka93@mail.ru

ABSTRACT

The main idea of our work is the new structured packing for heat and mass transfer processes such as evaporation cooling, fractionation and absorption in column apparatuses. As experimental data shown the new packing is more effective than the most used type of structured packing. This type of structured packing represents some corrugated sheets turned through 90 degrees in horizontal plan relatively to each other. The main disadvantage of this type of packing is the absence of side to side mixing of reacting flows between adjacent corrugated sheets in the packing block volume. We found out the way for removing this disadvantage. Namely, traditional cross section packing geometry was changed so as to achieve side-to-side mixing. The first check of our approach was the test paper models of the new and the most used packings. Data of pressure drop in packing bed were detected within gas velocity number from 0.53 to 1.2 m/s. Results of these experiments showed that in fact the new structured packing increased side to side mixing due to additional flow turbulence. The same results were obtained for metal models. In this work we present the second part of our research. We tested the new and based packing at laboratory stand in our university. Obtained results show that the new packing is more effective than the most used one. We found out optimal geometry of cross section of the new packing, namely, number of elements and parameters of one element. The new construction of structured packing is applicable for both type of column cross-section round and square.

Keywords: cooling towers, heat and mass transfer, structured packing

1. INTRODUCTION

It is known that the most effective method to increase effectiveness and productivity of power equipment is an impact on heat and mass transfer processes at microscopic scale and the impact accumulation with transport it to macro scale.

Fig. 1. Example of structured packing [2]

Packings are used for realization heat and mass transfer processes in column apparatuses for creation highly developed surface of interacting fluid and gas streams. Use of structured packings becomes more and more popular now. They have an essential advantage over random packings – low pressure drop under highly-developed contact surface. It is very important factor for realization heat and mass transfer processes which pressure drop is limitative in. For example, chemical technology processes that are realized under vacuum. [1]

The feature of random packings is more intensive frequent disruption of liquid film which works toward intensification heat and mass transfer processes. The disruption fluid film frequency is dictated by size element: the less packing elements size is, the more packing effectiveness increases.

Fig. 2. Some types of metal random packings [3]

Structured packing has two principal disadvantages:

1) lesser intensity of fluid film renewal that is conditioned by the height of packing storey;
2) low side-to-side mixing.

2. LITERATURE REVIEW

Researches of ntensification heat and mass transfer in structured packing columns have being carried out in our university for several years now.

In doctoral dissertation [4] vertical separation of adjacent corrugated packing blocks by inserts to create turbulation was proposed. This approach was developed in dissertation [5]. Author presented creating turbulisation way in the form of vertically alternated blocks of corrugated sheets with lattice prisms layers.

Fig. 3. Structured packing block made in form of particular short layers [6]

Successful effort to eliminate the first of mentioned above disadvantages, namely lesser intensity of fluid film renewal, is undertaken in dissertation [6]. Intensification of heat and mass transfer process was achieved by entered hydrodynamic effects use in this work. Structured packing block was made in form of particular short layers. These layers are interruptedly disposed height along and are turned 90 degrees relatively to each other in horizontal plan as it is shown in Fig. 3. As test data shown, such packing construction increased mass transfer coefficient comparison with traditional structured packing. Optimal height of SLP was found out. It was approximately 3–6 d_h, where d_h – hydraulical diameter of packing.

In all these works intensification increment had been gained but the problem of side to side mixing hadn't been solved. That's why further increasing of exist structured packings effectiveness is connected with eliminating mentioned above problem, namely, creating of side to side mixing of interacting streams.

3. THE CONCEPTION

Proposed approach to increase side to side mixing in structured packing is as follows:

1) the division packing block into particular short layers (storeys) equally-spaced height along (Fig. 4);
2) the changing cross section geometry of each layer of the packing block (Fig. 5).

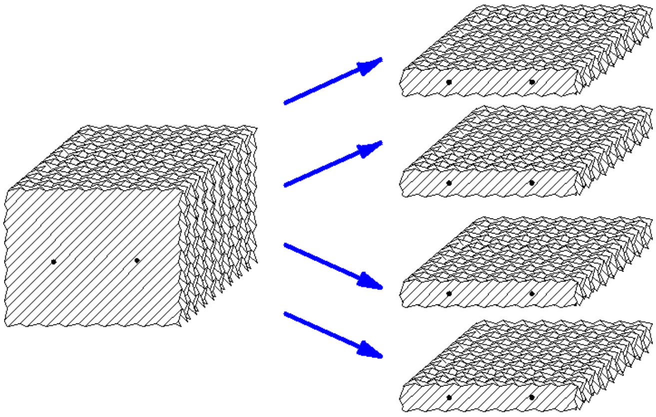

Fig. 4. Packing block division into short layers

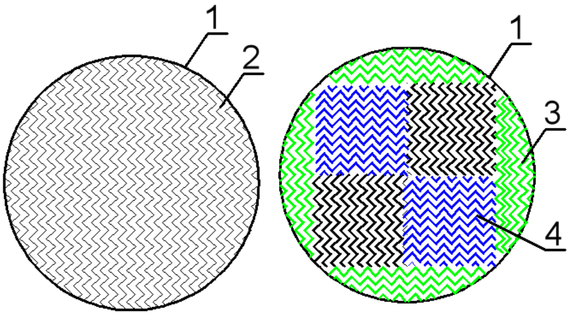

Fig. 5. The changing of packing block cross-section geometry. (1) – column apparatus, (2) – standard structured packing, (3) – segmented elements, (4) – cubical elements

As it is shown in the Fig. 5, the proposed packing cross section is some cubical elements turned 90 degrees relatively to each other in horizontal plan and four segmented elements. Overall dimensions of one element are dictated by the height of short layer and column diameter.

The effect of side-to-side mixing of proposed packing is directly proportional to increasing number of cubical elements that are fitted in the column apparatus cross section. In other words, the smaller cubical elements are, the more intensive side to side mixing is. It can be explained that the formation takes place just between adjacent cube faces (Fig. 6). The vortex-like flows lead to increase side-to-side mixing.

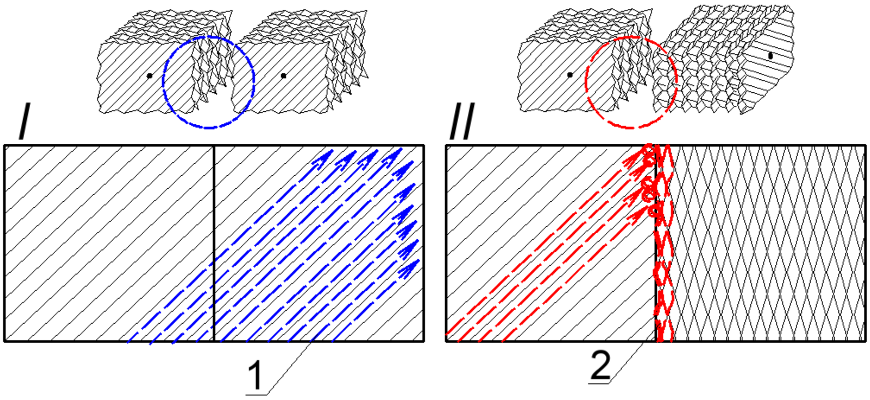

Fig. 6. Gas flow behavior at the junction of adjacent cubical elements (I) – gas flow in the structured packing, (II) – gas flow in packing CUB, (1) – gas flow motion trajectory, (2) – vortex activity (turbulence)

In a word side-to-side mixing effect is achieved due to aerodynamic change by new packing structure without surface increasing.

As a result the multi-structured packing is obtained. It comprises advantages of random and structured packings. The proposed packing construction allows decreasing side-to-side mixing problem and establishes necessary conditions for intensification heat and mass transfer process in the apparatus volume.

4. TEST RESULTS

4.1. Experimental stand and experimental procedure

Comparative tests of base packing and packing CUB prototypes were carried out. Traditional structured packing was taken as a base. These packings are presented on the Figs. 7, 8.

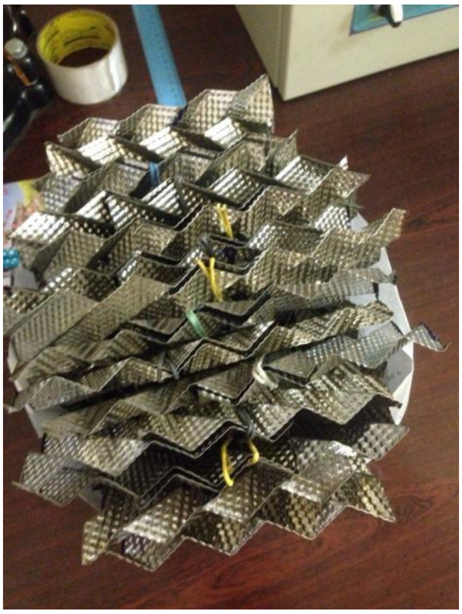

Fig. 7. The prototype of base packing

Fig. 8. The prototype of packing CUB

Geometrical characteristics are listed in the Table 1. Specific surface and void fraction were found out experimentally (by weighting method). Hydraulic diameter of channel was calculated by formula 1:

$$d_h = \frac{4 \cdot \varepsilon}{a}, \tag{1}$$

where: a – is specific surface (m^2/m^3); ε – is void fraction of a packing (m^3/m^3).

Table 1. Geometrical characteristics of tested packings prototypes

	CUB	**Base packing**
Specific surface, m^2/m^3	159.1	169.4
Void fraction, %	76	69.9
Hydraulic diameter, m	0.0192	0.016
Packing bed height, m	0.23	0.24

The experimental stand (Fig. 9) consists of packed column (1), fan (2), airflow measuring device (3), liquid flowmeter (rotameter) (4), faucets a and b, differential manometers (5a) and (5b), computer (6), spray separator (7), humidity meters (8) and thermal couples (9). The air is conducted to the column (1) by the fan (2) through the airflow measuring device (3). The air is removed in the athmospere by spray separator (7). When testing spray column selected flow quantity is carried through the rotameter (4). Differential manometers (5a) and (5b) detect pressure drop in the column and air flow rate.

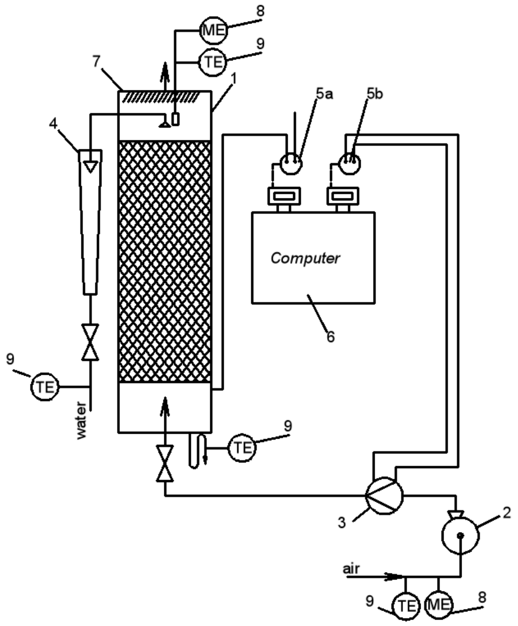

Fig. 9. The experimental stand

Packings testing was carried out in the water-air system. Dry and spray packings were tested and water heating process under direct interaction with air in counter-current flow was carried out. Liquid spray rate was 190 $m^3/(m^2 \cdot s)$ in hydraulic and heat and mass transfer testings. Superficial gas velocity varied from 0.21 m/s to 1.19 m/s. Airflow rate, water rate, pressure drop of dry and spray packing beds were detected when hydraulic testing. Airflow rate, water rate, temperatures at input of the air and water, temperatures at output of the air and water, humidity of the air at input and output were detected when heat and mass transfer testing.

4.2. Test results

4.2.1. Hydrodynamic of dry packings

Pressure drop data of dry and spryed packings are necessary for equpment calculation – determining the height of packing bed, apparatus diameter, process gas speed.

Pressure drop of dry packing is calculating by formula (2):

$$\Delta P_{dry} = \xi_0 \cdot \frac{H}{d_h} \cdot \frac{\rho_g \cdot w_0^2}{2}, \qquad (2)$$

where ξ_0 – dry packing coefficient of resistance; H – the height of packing bed, (m); w_0 – gas velocity (m/s); ρ_g – gas density (kg/m^3).

Experimental dependents dry specific pressure drop ΔP/H of superficial gas velocity w_0 for both types of tested packings are presented in the Fig. 10. Testing of based packing and proposed packing (CUB) were carried out in the laboratory stand under the same conditions.

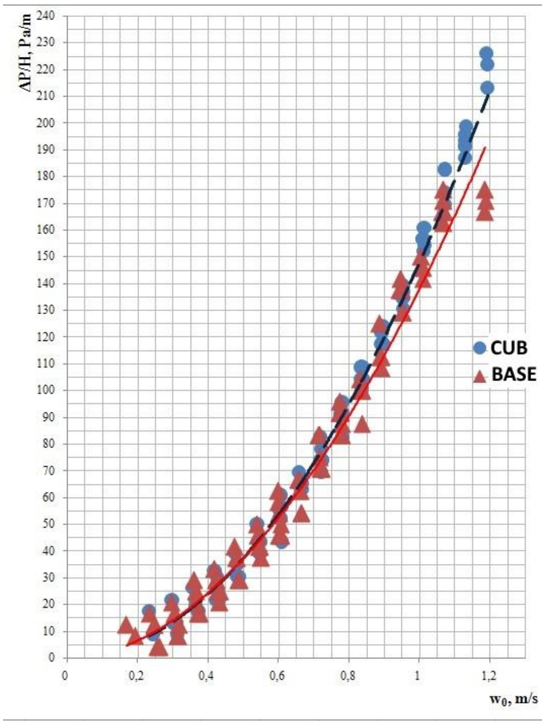

Fig. 10. Experimental dependents dry specific pressure drop of superficial gas velocity for both types of tested packings

4.2.2. Hydrodynamic of sprayed packings

Pressure drop of spryed packing is calculating by formula (3):

$$\Delta P_{spryed} = \xi_{spryed} \cdot \frac{H}{d_h} \cdot \frac{\rho_g \cdot w_{relative}^2}{2}, \qquad (3)$$

where ξ_{spryed} – spryed packing coefficient of resistance, $w_{relative}$ – relative gas velocity, (m/s).

Results of sprayed packings testing are presented in the Fig. 11 in the shape of characteristic curves.

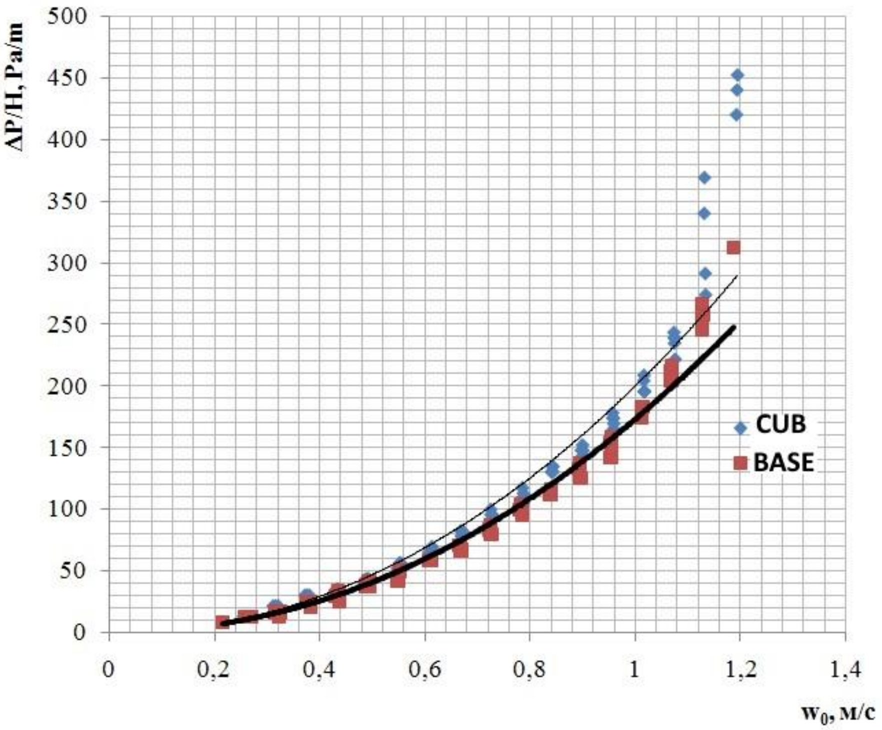

Fig. 11. Experimental dependents sprayed specific pressure drop of superficial gas velocity for both types of tested packings

4.2.3. *Heat and mass transfer*

Mass transfer coefficient K_m is calculated by formula:

$$K_m = \frac{M}{\Delta\bar{y} \cdot F}, \left[\frac{kg}{m^2 \cdot h \cdot \left({kg_{wet}}/{kg_{dry\ air}}\right)}\right], \tag{4}$$

where M – wet component rate, (kg_{wet}/h); $\Delta\bar{y}$ – average moving force, ($kg_{\ wet}/kg_{\ dry\ air}$); F – contact surface, (m^2).

Heat transfer coefficient K_t is calculated by formula:

$$K_t = \frac{Q}{\Delta\bar{t} \cdot F}, \left[\frac{kJ}{m^2 \cdot h \cdot {}^{o}C}\right], \tag{5}$$

where Q – quantity of transmitted heat, (kJ/h); $\Delta\bar{t}$ – average moving force, (^{o}C); F – contact surface, (m^2).

Dependents mass transfer coefficient K_m and heat transfer K_t coefficient of Reynolds number Re for both types of tested packings are presented in the Figs. 12 and 13.

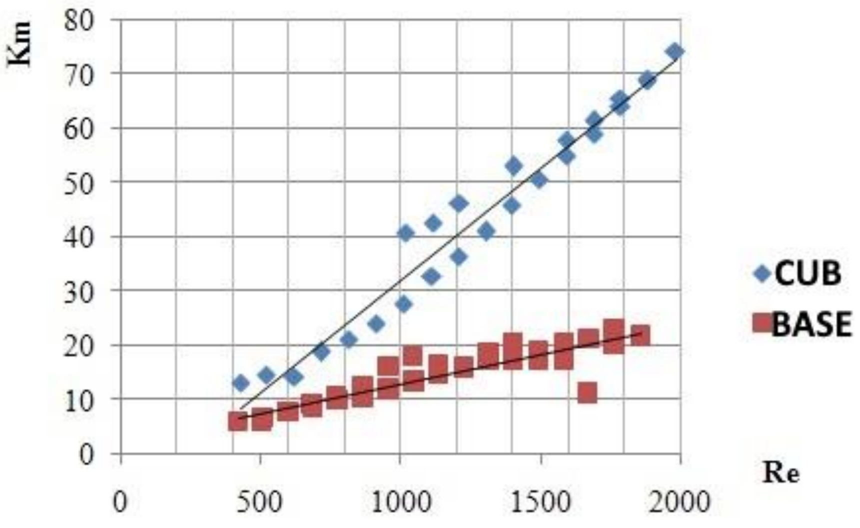

Fig. 12. Experimental dependents mass transfer coefficient of Reynolds number for both types of tested packings

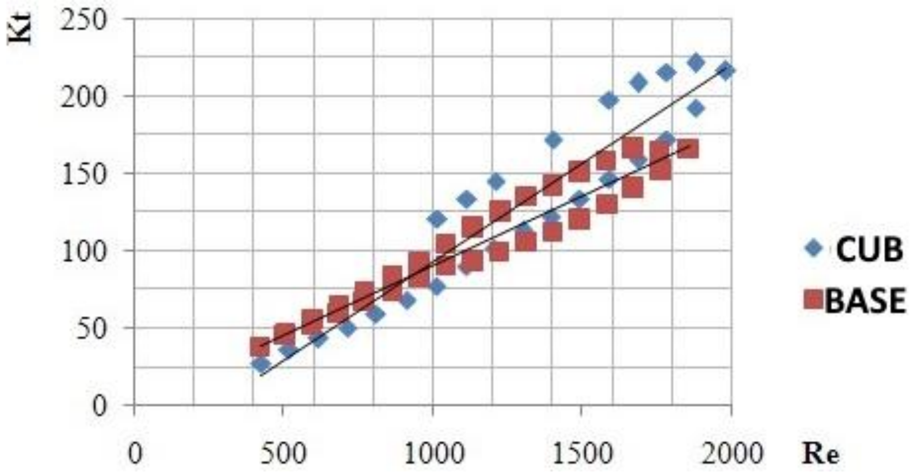

Fig. 13. Experimental dependents heat transfer coefficient of Reynolds number for both types of tested packings

5. DISCUSSION OBTAINED RESULTS

Common criterion of effectiveness packings is absent in literature today. But in work [7] energetical complexes E to estimate hydrodinamic and mass transfer characteristics of packings was published.

$$E = \frac{\Delta p_{spryed} \cdot h_{sp}}{H} \qquad (6)$$

where Δp_{spryed} – pressure drop of spryed packing; h_{sp} – height of transfer unit; H – the height of packing bed.

Than lesser E is, than more packing effectiveness is.

It is shown in the Fig. 10, the dependents $\Delta P/H = f(w_0)$ of based and proposed packings diverge within number of gas velocity from 0.8 to 1.2 m/s. The divergence increases with gas velocity increasing. When gas velocity is 1.15 m/s pressure drop of CUB is higher by 7.1% than pressure drop of SLP is.

The same tendency, but more clearly expressed is observable for sprayed packings (Fig. 11). The divergency of curves starts when gas velocity is 0.5 m/s. Pressure drop of CUB is higher by 15.9% when gas velocity is 1.15 m/s.

Pressure drop increasing means that proposed packing creates local vortex flows in the packing volume due to changing gas flow aerodynamic.

As it is seen from Figs. 12, 13 proposed construction allows to increase mass transfer and heat transfer coefficients. Mass transfer coeffiicent of CUB is higher by 58.77% than mass transfer coeffiicent of base when Reynolds number is 1855 (gas velocity is about 1,18 m/s). Heat transfer coeffiicent of CUB is higher by 20.4% in comparison with based packing under the same gas velocity.

The following task of our research is the correlation pressure drop ΔP and the growth of heat and mass transfer process effectiveness. Everything depends on limitative stage of process – namely, liquid or gas phase. For example, if limitative stage is liquid then this phase should be tirbulized to increase effectiveness of process.

6. CONCLUSIONS

1. The use of proposed structured packing allows to increase side-to-side mixing gas phase between adjacent corrugated sheets in the block packing volume by additory flow turbulence. Proposed laying adjacent elements of packing CUB that are turned by 90 degrees relatively to each other in horizontal plan creates side to side mixing gas phase by vortex-like flow. It admits to eliminate the mentioned disadvantage of structured packing.

2. Comparative investigations of proposed and based packings were carried out. The investigations proved the increasing of heat and mass transfer effectiveness due to proposed construction of the new packing CUB.

3. It was showed that using packing CUB allows to increase heat transfer coefficent by 20.4% and mass transfer coefficent by 58.77% under gas velocity 1,18 m/s.

7. REFERENCES

1. PUSHNOV, Alexander S.; KAGAN, Alexander M. *Structure and hydrodynamic of packing apparatuses. Introduction to chemical engineering*. Saint Petersburg: Publishing office of Polytechnic University, 2011. 135 p. ISBN 978-574223080-9.
2. *Website of Russian scientific centre "Applied chemistry"*. Link to the internet <http://www.giph.su>.
3. *Website of Y&G International Trading Company Limited*. Link to the internet <http:// http://www.yugie.com.cn>.
4. DMITRIEVA, Galina B., *Hydrodynamics and mass transfer in structured packing of corrugated sheets*. Doctoral dissertation: 05.17.08/ Dmitrieva Galina Borisovna [Ivanovo State University of Chemistry and Technology]. Ivanovo. 2007. 255p.
5. KHARITONOV, Anton A., *Evaporation cooling in structured combination contact devices of cooling tower*. Doctoral dissertation: 05.17.08/ Kharitonov Anton Alexandrovich [Ivanovo State University of Chemistry and Technology]. Ivanovo. 2013. 160 p.
6. TSURIKOVA, Natalya.P. *Influence high of block on structured packing to evaporation cooling in mechanical-draft cooling tower*. Doctoral dissertation: 05.17.08/ Tsurikova Natalya Petrovna [Moscow State University of Fine Chemical Technologies named after M.V. Lomonosov]. Moscow. 2013. 131p.
7. LAPTEV, Anatoly G., NIKOLAEV N. A., BASHAROV., M.M. *Methods of intensification and modeling heat and mass transfer processes*. Moscow: "Heating engineer", 2011. 288. ISBN 978-5-98457-104-3.

CYSENI 2016, May 26-27, Kaunas, Lithuania
ISSN 1822-7554, www.cyseni.com

PRELIMINARY RESULTS ON CONDENSATION MODELLING IN VERTICAL FLAT CHANNEL

Andrius Gediminskas
Lithuanian Energy Institute
Breslaujos str. 3, LT-44403, Kaunas – Lithuania
Email: andrius.gediminskas@lei.lt

ABSTRACT

It is necessary to analyse two-phase flows in order to simulate the condensation phenomenon, which plays an important role in heat transfer mechanisms. Condensation is a common phenomenon in various heat exchangers where the cold wall and steam interact; hence, numerous papers have been released on numerical and experimental researches of condensation. Several different software products can be used in order to carry out numerical modelling of condensation. In this paper, analysis of different software and methods is presented. Also a still-under-development mathematical model for condensation modelling and heat transfer in a 2D vertical flat channel is described. In it, hot gas which consists only of steam enters a vertical channel from above and a liquid film of condensate starts forming on the cold wall. This model uses the ANSYS Fluent software and the Volume of Fluid method. A self-written module is implemented in the ANSYS Fluent software as a User Defined Function to extend ANSYS Fluent capabilities. Detailed information about the geometry, mesh, governing equations and Volume of Fluid equations are described in this paper. Some preliminary modelling data are also presented and analysed.

Keywords: condensation, vertical channel, numerical modelling, Volume of Fluid method, ANSYS Fluent

1. INTRODUCTION

Condensation is a very common phenomenon in various heat exchangers. A complete knowledge of two phase flows including phase change is required in order to model a condensation phenomenon. Condensation performance depends on number of factors: fluid properties, pressure, geometry of a heat exchanger, mass flow rate, etc. Many different authors use many different software products and approaches, because this problem is very important and actual right now, however, condensation phenomenon is still not fully understood.

In this paper a review of software's and model's used by other author's for condensation modelling is performed. Based on this review, the software and method to develop the mathematical model is selected. Some preliminary results are also presented and compared to other author's results.

2. LITERATURE REVIEW

There are many different ways to perform condensation modelling. While some authors choose commercial software, others decide to write their own software for two phase modelling. In [1] paper a computational study about heat and mass transfer in a heated vertical tube with water film cooling is reported. The authors used their own written code for turbulence modelling and an elliptical scheme for computation. They modelled the condensation and evaporation processes. Paper [2] analyses the condensing downward flow of steam-air mixtures in vertical tubes with a constant wall temperature. Non-condensing gas (air) is present in the mixture. The in-house code solves parabolic governing equations for steady, axi-symmetric laminar flow. The detailed results are presented for both the water film region and the mixture region.

Table 1. Nomenclature

Nomenclature

c_p – specific heat, J/(kg K)
f – body force, N
F – volume fraction factor (VOF)
g – gravitational acceleration, m/s^2
k – thermal conductivity, W/(m * K)
L – length, m
L_H – latent heat, J/kg
m_c – mass source term for condensation, kg/(m^3 * s)
p – pressure, N/m^2
Q_T – energy source term for condensation, W/m^3
t – time, s
T – temperature, K
u – x velocity, m/s
v – y velocity, m/s
$\vec{V}$ –velocity vector, m/s
W – width of the channel, m
x, y – Cartesian coordinates

Greek symbols

μ – dynamic viscosity, kg/(m * s)
ρ – density, kg/m^3

Subscripts

l – liquid
sat – saturated
v – vapor
x – x direction
y – y direction

There are many papers in which commercial code is used for modelling of condensation. The literature review covers those papers where commercial software products which are accessible to Lithuanian Energy Institute are used: ANSYS Fluent, ANSYS CFX, Comsol Multiphysics and Matlab. In [3] authors used Matlab to solve a set of differential and algebraic equations for heat and mass transfer in condensers with a present water vapour and non-condensing gas mixture. Detailed information on surface temperatures on the condenser's walls was given. Zschaeck et al. [4] published a paper on a mathematical model implemented in ANSYS CFX for simulation of wall condensation in the presence of non-condensing gases.

For condensation modelling, ANSYS Fluent can provide three different methods: Species Transport model, Wall Film model, and Volume of Fluid (VOF) method. Vyskocil et al. [5] presented a condensation model for ANSYS Fluent software. The authors used the Species transport model and performed modelling of condensation from a vapour and non-condensing gases mixture. Diffusion was also simulated. In [6], [7] and [8], the authors presented modelling cases which were performed with ANSYS Fluent. However, they did not specify what methods they had used, only that User Defined Functions had been involved. In all three articles a rather good agreement between the experimental data and the modelling was found.

Special attention was paid to authors who use ANSYS Fluent software and the Volume of Fluid (VOF) method in their investigations. Fadhl et al. [9] were modelling two phase flow in a heat pipe of thermosyphon. Water was used as the working fluid. The authors used the VOF method for a CFD modelling. Phase change processes, such as evaporation and condensation, were performed by adding a user defined functions (UDFs) to the ANSYS Fluent code. Later, the simulation results were compared with the experimental results and a satisfactory agreement was observed. Chen et al. [10] describe an investigation of condensation flow in a 1- mm rectangular microchannel of a refrigerator. The authors were also using the VOF method. The modelling showed that the vapour phase in the microchannel forms a wall film. The numerical study was validated using experimental studies from literature. Ganapathy et al. [11] proposed a numerical model for simulation of condensation and fluid flow in a microchannel. The VOF method was also used for the modelling. The standard governing equations for conservation of the volume fraction and energy were modified to include the source terms which were incorporated in the programme as a UDF. Alizadehdakhel et al. [12] performed a study of gas/liquid two-phase flow modelling including the evaporation and condensation phenomenon in thermosyphon. The authors used the VOF method and a UDF. The simulation-predicted temperature profile was compared with the experimental measurements, and a rather good agreement was observed. Liu et al. presented a paper [13] where a two-fluid CFD model was proposed to simulate the vertical upward two-phase annular flow. The VOF method and a UDF were used in this modelling. The proposed model solved basic mass and momentum equations for gas region flow and liquid film flow. Kouhikamali [14] published a paper about condensation in circular cylindrical channels. The author investigated the effects of hydraulic diameter, velocity, Reynolds number, and temperature difference variation on heat transfer in a circular cylindrical channel. A UDF and the VOF were used in this paper. Liu et al. [15][16] published two papers about condensation modelling using a UDF and the VOF. In [15] the authors proposed different source terms that could be used in a UDF.

Based on the literature review and ANSYS tutorials, all three methods provided by ANSYS have advantages and disadvantages.

Table 2. Pros and Cons of ANSYS Fluent methods

Method	Pros	Cons
Species Transport	2D and 3D geometries	No multiphase flows modelled
	Fast computational time	Require UDF for phase-change
	Cartesian and cylindrical coordinates	
Wall Film	ANSYS recommended	Very little research available
		Only 3D geometries
		Require UDF for phase-change
Volume of Fluid	2D and 3D geometries	Longer computational time (double precision solver required)
	Cartesian and cylindrical coordinates	Require UDF for phase-change
	Most versatile	
	Most popular	

According to [15], the VOF method is a simple and powerful approach to condensation modelling. This method proved to be more flexible and efficient that other methods for treating free boundary configurations. Based on the literature review, the ANSYS Fluent software and the VOF method were chosen for modelling of condensation in this paper.

3. METHODOLOGY

3.1. Channel description

Hot water vapour enters the channel from the top and flows downward. There is a thick layer of water liquid on the walls which are colder than the vapour. The hot vapour starts cooling down and condensing on the wall.

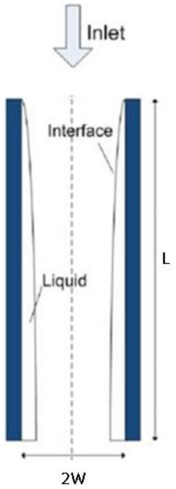

Fig. 1. Channel description

The following are the governing equations for 2D laminar modelling for conservation of mass, momentum and energy:

$$\frac{\partial(\rho u)}{\partial t} + div(\rho\, \vec{V}) = 0, \tag{1}$$

$$\frac{\partial(\rho u)}{\partial t} + div\left(\rho u\vec{V}\right) = -\frac{\partial p}{\partial x} + div(\mu gradu) + f_x, \tag{2}$$

$$\frac{\partial(\rho v)}{\partial t} + div\left(\rho v\vec{V}\right) = -\frac{\partial p}{\partial y} + div(\mu gradv) + f_y, \tag{3}$$

$$\frac{\partial(\rho c_p T)}{\partial t} + div\left(\rho c_p T\vec{V}\right) = div(kgradT) + Q_T. \tag{4}$$

The mesh consists of 100 × 1000 cells. The mesh is coarser near the walls with a ratio of 1:10 comparing to the centre of the channel. The vapour inlet temperature T_{sat} = 373 K; the wall temperature is constant and equal T = 363 K. The vapour inlet velocity is $1\frac{m}{s}$. The channel dimensions are: channel length L = 30 cm, width W = 2 cm.

3.2. Volume of Fluid method

The VOF method relies on the fact that two different fluids (vapour and liquid) are not interpenetrating each other. In other words, the VOF method is used to track the interface between the phases. The picture below illustrates the interface tracking if liquid is a primary phase, and vapour is a secondary phase.

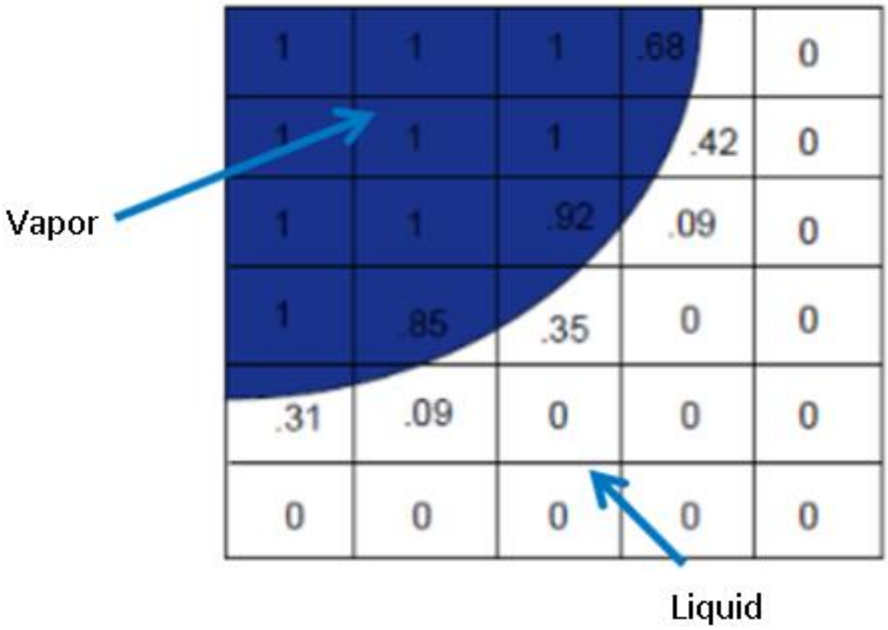

Fig. 2. Volume of Fluid scheme

The VOF equation can be written in the following way:

$$\frac{\partial F_v}{\partial t} + div\left(F_v\vec{V}\right) = -\frac{m_c}{\rho_v} \tag{5}$$

Where m_c is a mass production rate of condensation and F_v is a volume fraction factor of the vapour. If $F_v = 1$, that region is pure vapour. If $F_v = 0$, that region is pure liquid. If $0 < F_v < 1$, that regions is the mixture or the interface between the liquid and the vapour. The physical properties are evaluated as a mixture of both phases. Thermal conductivity, density, dynamic viscosity, and specific heat are calculated as stated in [15].

3.3. User defined functions

ANSYS Fluent does not have the ability to simulate the phase change process, such as evaporation or condensation, but an additional code can be used for that purpose. A UDF can integrate additional source terms into the VOF equation, thus enabling ANSYS Fluent to simulate the phase-change process. Different authors provide different source terms.

Table 3. Mass and energy source terms found in literature

Reference	Thermal energy	Phase change process	Temp. Condition	Phase	Source term
[9]	Mass transfer	Evaporation	$T > T_{sat}$	Liquid	$m_c = -0.1F_l\rho_l\frac{T - T_{sat}}{T_{sat}}$
				Vapour	$m_c = 0.1F_l\rho_l\frac{T - T_{sat}}{T_{sat}}$
		Condensation	$T < T_{sat}$	Liquid	$m_c = 0.1F_v\rho_v\frac{T_{sat} - T}{T_{sat}}$
				Vapour	$m_c = -0.1F_v\rho_v\frac{T_{sat} - T}{T_{sat}}$
	Heat transfer	Evaporation	$T > T_{sat}$	Liquid	$Q_T = -0.1F_l\rho_l\frac{T - T_{sat}}{T_{sat}}L_H$
		Condensation	$T < T_{sat}$	Vapour	$Q_T = 0.1F_v\rho_v\frac{T_{sat} - T}{T_{sat}}L_H$
[10]	Mass transfer	Evaporation	$T > T_{sat}$	Liquid	$m_c = f_0F_l\rho_l(T_{sat} - T)$
		Condensation	$T < T_{sat}$	Liquid	$m_c = f_0F_v\rho_v(T_{sat} - T)$
		Evaporation	$T > T_{sat}$	Vapor	$m_c = -f_0F_l\rho_l(T_{sat} - T)$
		Condensation	$T < T_{sat}$	Vapor	$m_c = -f_0F_v\rho_v(T_{sat} - T)$
[12]	Mass transfer	Condensation	$T < T_{sat}$	Liquid	$m_c = -0.1F_l\rho_l\lvert\frac{T - T_{sat}}{T_{sat}}\rvert$
	Mass transfer			Vapor	$m_c = 0.1F_l\rho_l\lvert\frac{T - T_{sat}}{T_{sat}}\rvert$
	Heat transfer			Liquid	$Q_T = -0.1F_l\rho_l\lvert\frac{T - T_{sat}}{T_{sat}}\rvert L_H$
	Mass transfer			Liquid with non-condensing gas	$m_c = 0.1x_vF_v\rho_v\lvert\frac{T - T_{sat}}{T_{sat}}\rvert$
	Mass transfer			Vapor with non-condensing gas	$m_c = -0.1x_vF_v\rho_v\lvert\frac{T - T_{sat}}{T_{sat}}\rvert$
	Heat transfer			Liquid with non-condensing gas	$Q_T = 0.1x_vF_v\rho_v\lvert\frac{T - T_{sat}}{T_{sat}}\rvert L_H$
[15][16]	Mass transfer	Evaporation	$T \geq T_{sat}$	Liquid	$m_c = -\beta F_l\rho_l\frac{T - T_{sat}}{T_{sat}}$
		Condensation	$T < T_{sat}$	Gas	$m_c = \beta F_v\rho_v\frac{T_{sat} - T}{T_{sat}}$

where f_0 is an adjustable parameter, x_v is the volume fraction of water vapor in the gas phase and β is positive numerical coefficient.

It is obvious that many authors decide to use the same source terms. In this paper, formulas from [15] and [16] are used. The author-estimated value of β by a trial-and-error procedure is $5 \cdot 10^3$ s^{-1}.

4. RESULTS

Hot vapour at the saturation temperature 373 K enters the channel from above. The wall temperature is 363 K and when the vapour temperature drops down below the saturation temperature, condensation process starts. Fig. 3 shows the volume fraction factor fields in the channel. Fig. 3 illustrates the situation at the inlet of the channel. Blue colour represents the vapour (Phase 0) and red colour represents the water (Phase 1). As the condensation process proceeds, more condensate forms on the wall surface. This condensate wall film is pulled downwards due to gravity, and waves begin to appear. The experiments in [15] show that even laminar film flow can become wavy. As the condensation process continues, the wall film begins to break (Fig. 4), and some separate liquid patches of the condensate begin to appear near the wall. With increasing distance, bigger patches start to appear further from the wall (Fig. 5).

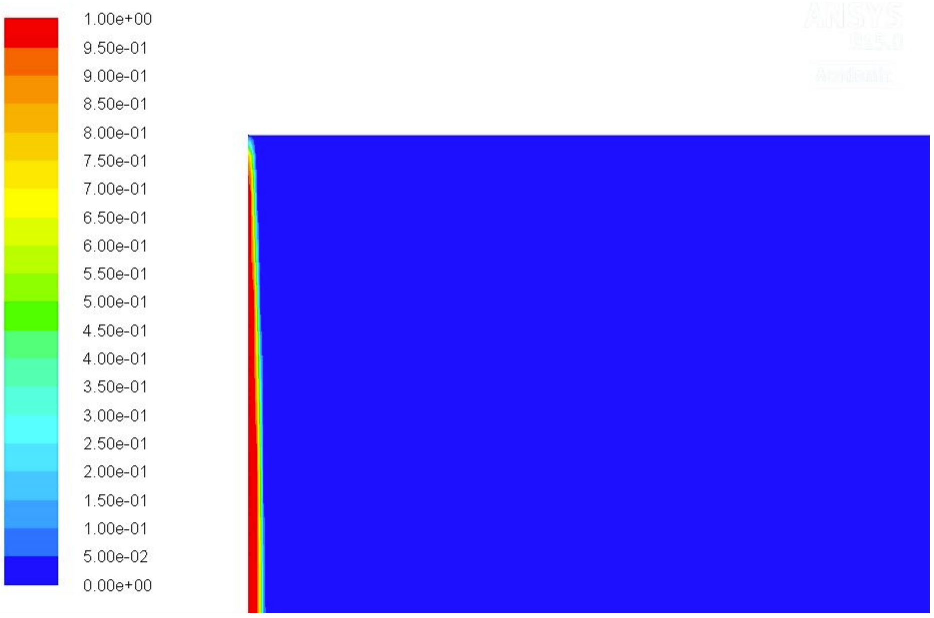

Fig. 3. Contours of Volume fraction 1

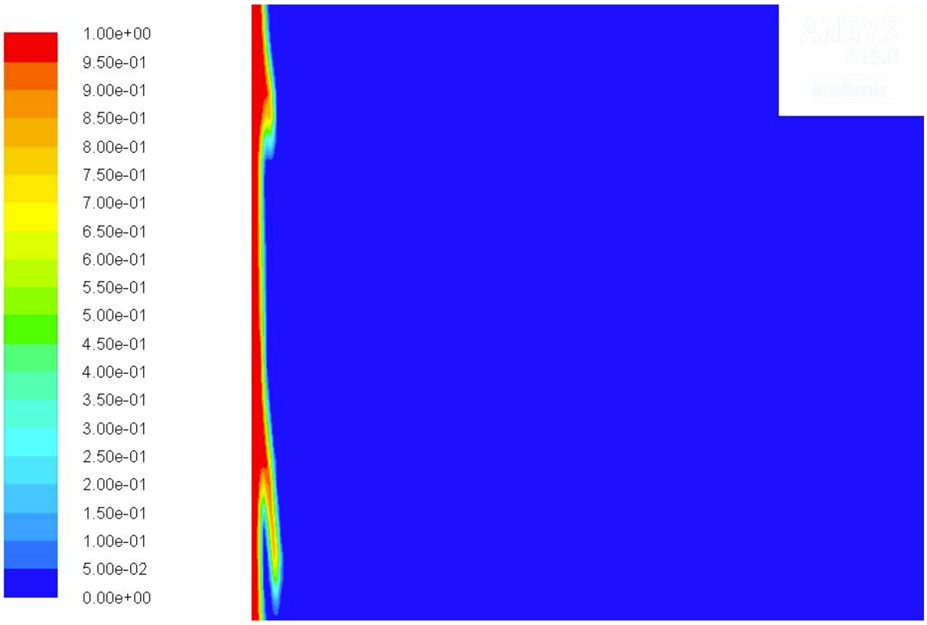

Fig. 4. Contours of Volume fraction 2

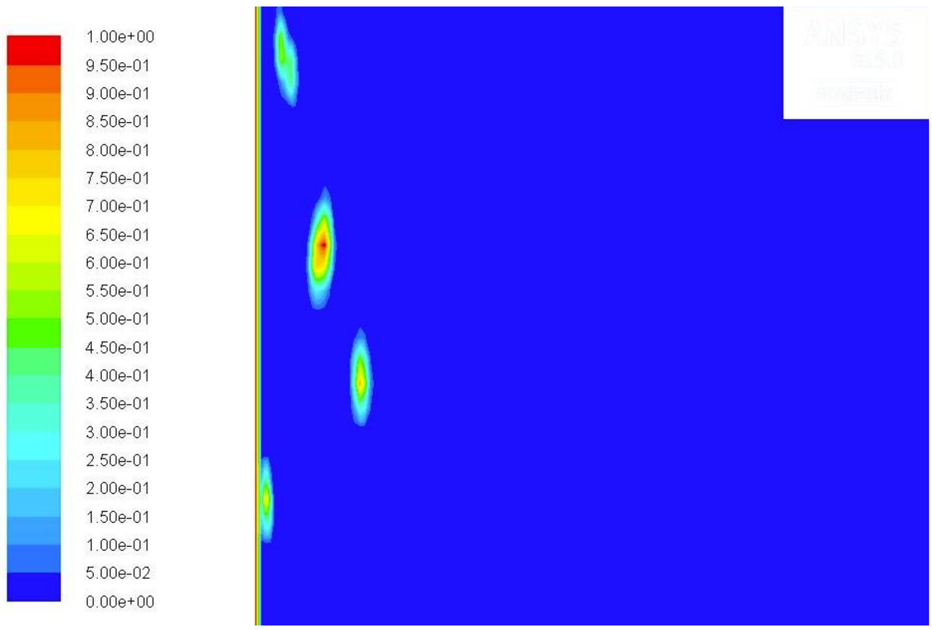

Fig. 5. Contours of Volume fraction 3

These preliminary results correlate with the modelling data presented in [15], where near the inlet of the channel the liquid wall film was laminar, no waves were detected. As the condensation process continues, waves start to appear and later transform into separate liquid patches. The pattern of flow downstream presented in [15] has all the same stages, as results presented in this paper.

5. CONCLUSIONS

In this paper an in-depth literature review has been presented. Based on this review, ANSYS Fluent software and VOF method were chosen for future modelling of condensation. The review of the source terms used in literature is performed and justification is made for selection of the source term for this study. Computer model with UDF for selected source term of the flat channel is developed for the ANSYS Fluent code and some preliminary modelling results are presented and compared with other author’s results. This is the first step of the wider study oriented to comparison of different source term for modelling adequately of condensation processes in the vertical channels.

6. REFERENCES

1. HE, S., AN, P., LI, J., JACKSON, J.D. Combined heat and mass transfer in a uniformly heated vertical tube with water film cooling. *International Journal of Heat and Fluid Flow*, 1998, 19, p. 401–417.
2. HASSANINEJADFARAHANI, F., GUYOT, M.K., ORMISTON, S.J. Numerical analysis of mixed-convection laminar film condensation from high air mass fraction steam-air mixtures in vertical tubes. *International Journal of Heat and Mass Transfer*, 2014, 78, p. 170–180.
3. LI, J.D., SAIRAIREH, M., THORPE, G. Condensation of vapour in the presence of non-condensable gas in condensers. *International Journal of Heat and Mass* Transfer, 2011, 54, p. 4078–4089.
4. ZSCHAECK, G., FRANK, T., BURNS, A.D. CFD modelling and validation of wall condensation in the presence of non-condensable gases. *Nuclear Engineering and Design*, 2014, 279, p. 137–146.
5. VYSKOCIL, L., SCHMID, J., MACEK, J. CFD simulation of air-steam flow with condensation. *Nuclear Engineering and Design*, 2014, 279, p. 147–157.

6. DEHBI, A., JANASZ, F., BELL, B. Prediction of steam condensation in the presence of noncondensable gases using a CFD-based approach. *Nuclear Engineering and Design*, 2013, 258, p. 199–210.
7. LI, J.D. CFD simulation of water vapour condensation in the presence of non-condensable gas in vertical cylindrical condensers. *International Journal of Heat and Mass Transfer*, 2013, 57, p. 708–721.
8. WU, T., VIEROW, K. Local heat transfer measurements of steam/air mixtures in horizontal condenser tubes. *International Journal of Heat and Mass Transfer*, 2006, 49, p. 2491–2501.
9. FADHL, B., WROBEL, L.C., JOUHARA, H. Numerical modelling of the temperature distribution in a two-phase closed thermosyphon. *Applied Thermal Engineering*, 2013, 60, p. 122–131.
10. CHEN, S., YANG, Z., DUAN, Y. CHEN, Y. WU, D. Simulation of condensation flow in a rectangular microchannel. *Chemical Engineering and Processing: Process Intensification*, 2014, 79, p. 60–69.
11. GANAPATHY, H., SHOOSHTARI, A., CHOO, K., DESSIATOUN, S., ALSHEHHI, M., OHADI, M. Volume of fluid-based numerical modelling of condensation heat transfer and fluid flow characteristics in microchannels. *International Journal of Heat and Mass Transfer*, 2013, 65, p. 62–72.
12. ALIZADEHDAKHEL, A., RAHIMI, M., ALSAIRAFI, A.A. CFD modelling of flow and heat transfer in a thermosyphon. *International Communications in the Heat and Mass Transfer*, 2010, 37, p. 312–318.
13. LIU, Y., LI, W.Z., QUAN, S.L. A self-standing two-fluid CFD model for vertical upward two-phase annular flow. *Nuclear Engineering and Design*, 2011, 241, p. 1636–1642.
14. KOUHIKAMALI, R. Numerical simulation and parametric study of forced convective condensation in cylindrical vertical channels in multiple effect desalination systems. *Desalination*, 2010, 254, p. 49–57.
15. LIU, Z., SUNDEN, B., YUAN, J. VOF modelling and analysis of filmwise condensation between vertical parallel plates. *Heat Transfer Research*, 2012, 43, p. 47–68.
16. LIU, Z., SUNDEN, B., YUAN, J. Numerical simulation of condensation in a rectangular minichannel using VOF model. Proceedings of the ASME 2012 International Mechanical Engineering Congress & Exposition. Houston, Texas, USA. 2012 November 9–15.

CYSENI 2016, May 26-27, Kaunas, Lithuania
ISSN 1822-7554, www.cyseni.com

INVESTIGATION OF FLUID FLOW STRUCTURE IN OPEN TYPE CAVITY UNDER STATIONARY AND PULSATILE FLOW CONDITIONS

P. Vilkinis, M. Valantinavičius, N. Pedišius
Lithuanian Energy Institute
Breslaujos str. 3, LT-44403 Kaunas – Lithuania
Email: paulius.vilkinis@lei.lt

ABSTRACT

Fluid flow in structured channels plays an important role in most fluid dynamics problems. Flow in cavity is used to increase mixing in microreactors and microelectrochemical systems (MEMS), also to increase heat transfer intensity in heat sinks. Knowledge about fluid flow in micro cavity could be useful to mitigate the symptoms of aneurysms. In this work micro particle image velocimetry (μPIV) system was used to investigate water flow in straight, square cross section (0.5 × 0.5 mm^2) microchannel with two oppositely located micro cavities with same cross section as main channel, and depth of 1 mm. Because of symmetry, flow structure of primary vortex was investigated in only one cavity. Measurements were made in different planes over the entire height of the cavity under flow conditions of Reynolds number in range 100–3000. Change of vortex structure and location of maximum and minimum velocities of vortex was observed at different measurement planes. Vortex structure and velocity distribution across the cavity highly depends on Reynolds number. At laminar flow regime only one vortex above lid of cavity is formatted. At large Reynolds number in cavity forms two (primary and secondary) counter rotating vortices and whole structure obtains form of eight at, which is most evident around middle plane of cavity. Velocity profiles along the cavity obtained from two-dimensional measurements indicate that velocity differences between flow entering the cavity near forward-facing wall and leaving the cavity near backward-facing wall are registered. In conjunction with change of location of primary and secondary vortices over the height of cavity it can be concluded that cross-section overflows exists across the vortex and flow is three-dimensional in the cavity. Three-dimensional velocity vortices were created from many two-dimensional profiles measured in different planes. The flow in the cavity was under stationary and pulsating conditions. Three-dimensional profiles confirmed that flow in cavity is three-dimensional with transversal flow vortex structure. This is indicated by change of velocity profile shape over the height of cavity. In addition, vortex system depends on flow regime and pulsation conditions. When pulsatile flow conditions are applied, structure of primary vortex is divided into two parts at low Reynolds number and velocity profile is smoother at higher Reynolds number with significant maximum near backward-facing wall.

Keywords: microfluidics, flow in microchannel, micro particle image velocimetry, micro cavity, flow in open-type cavity, transverse flow, vortex structure

CYSENI 2016, May 26-27, Kaunas, Lithuania
ISSN 1822-7554, www.cyseni.com

EFFECTS OF HEMP FIBRES PRE-PROCESSING ON LINEAR LOW DENSITY POLYETHYLENE MATRIX COMPOSITE MECHANICAL PROPERTIES

Zane Zelca, Silvija Kukle, Sandra Jegina
Riga Technical University, Faculty of Material Science and Applied Chemistry,
Institute of Design Technologies,
Kipsalas Street 6, LV-1048 Riga – Latvia
Email: gusare@inbox.lv

Janis Kajaks
Riga Technical University, Faculty of Material Science and Applied Chemistry,
Institute of Polymer Materials, P. Valdena Street 3/7, LV-1048 Riga – Latvia

ABSTRACT

The influence of sol-gel modified fibres content on tensile strength, modulus of elasticity, elongation at break and surface microhardness (by Vickers) of a linear low density polyethylene composite was investigated. The fibres were modified with silica xerogel prepared by the sol-gel polymerization of tetraethylorthosilicate (TEOS) under hydrolytic conditions using acid catalists. Alkali pre-treatment was used for some variants and some composite samples were prepared by adding maleic anhydride grafted polyethylene (MA-g-PE).

Keywords: linear low density polyethylene, hemp fibres, composite mechanical properties, sol-gel method.

1. INTRODUCTION

The tensile properties of the composites are improved by adding fibres to the polymer matrix since fibres have much higher strength and stiffness values. If the fibres weight ratio increases till optimum value, load is distributed to more fibres, which are well bonded with matrix resulting in better tensile properties [1].

On the fibre surfaces, there are waxes and other non-cellulosic substances such as hemicellulose and pectins, lignin, which create poor adhesion between the matrix and the fibres. Alkali treatment is one of the most popular chemical pre-treatments of natural fibres [2, 3]. It is necessary to increase fibres hydrophobicity by surface chemical modification. The chemical coupling is also one of well known methods to improve the interfacial adhesion. Among different coupling agents, maleic anhydride (MA-g-PE) is the most commonly used for polyolefins natural fibre composites [4].

Vihodceva and co-authors reported about sol-gel technology for improving of such properties as water resistance and UV protection [5]. In this investigation the sol-gel method was utilized for improving adhesion interaction between the fibres and the polymer matrix and increasing of mechanical properties of the composite. The method also insures good protection against water absorption and maintains sufficient good fluidity of the composite melts (fibre content 50 wt%).

In this article the tensile properties (σ_{max}, E_t and ε_t) of composites and surface microhardness (HV) are improved by hemp fibres mercerization and sol-gel treatment before composite formation. MA-g-PE was added during mixing process. Zink acetate dihydrate 5 wt% (ZAD) was used as a modifier of the sol-gel system for some variants to improve the composite mechanical properties.

2. MATERIALS AND METHODS

The hemp fibres were obtained from hemp stems harvested from a trial plot at the Agriculture Science Centre of Latgale in the Vilani district, Latvia, in 2013 (Sample 2a-7b). Hemp fibres of the variety ’Bialobrzeskie’ in growing process were cultivated with active nitrogen fertilizer (N30). The harvested hemp stems were left for dew-retting on the field for 4 weeks.

Table 1. LLDPE mechanical properties of tensile

Sample	**E_t, MPa**	**σ_{max}, MPa**	**ε_t, %**	**HV, MPa**
0	75.71	12.87	59	5-8 [6]
	Relative error, %	**Relative error, %**		
	5	2		

Linear Low Density Polyethylene (LLDPE) grade LL 6201 was used as polymer matrix, with melting temperature T_{melt} =123^{0}C, and mechanical properties are presented in Table 1. Eleven composite samples and LLDPE control sample (Sample 0) were prepared with different hemp fibres pre-treatment and LLDPE matrix (see Table 2). Samples marked with (a) were treated with xerogel, but samples marked with (b) have a MA-g-PE additive. Fibres content 40 wt% are 2a-5b, but 50 wt% 6-7b. Before mixing, the fibres were dried in an air chamber at +105^{0}C for 24 h.

Table 2. Samples of pre-treatment methods and compositions

Sample	**Hemp fibres pre-treatment methods and additives**	**Fibres content, wt%**
0	LLDPE	0
2a	Fibres pre-treated with Silica sol	40
2b	Fibres pre-treated with Silica sol; MA-g-PE 5 wt% aditive	40
3a	Fibres pre-treated with Silica sol modyfied with ZAD 5 wt%	40
3b	Fibres pre-treated with Silica sol modyfied with ZAD 5 wt%; MA-g-PE 5 wt% aditive	40
4a	Fibres pre-treated with NaOH 2 w% and Silica sol	40
4b	Fibres pre-treated with NaOH 2 wt% and Silica sol; MA-g-PE 5 wt% aditive	40
5a	Fibres pre-treated with NaOH 2 wt% and Silica sol modyfied by ZAD 5 wt%	40
5b	Fibres pre-treated with NaOH 2 wt% and Silica sol modyfied by ZAD 5 wt%; MA-g-PE 5 wt% aditive	40
6	Without fibres pre-treatment	50
7a	Fibres pre-treated with Silica sol	50
7b	Fibres pre-treated with Silica sol modyfied with ZAD 5 wt%; MA-g-PE 5 wt% aditive	50

The content of hemp fibres (length up to 1 mm) in composites was 40 and 50 wt% with pre-treatment of NaOH (SIA “Enola”, ES) 2 wt% solution (4h +23C^0) and sol-gel method. Materials used for sol synthesis: $C_8H_{20}O_4Si$ (Alfa Aesar, German), C_2H_5OH and HF (SIA “Enola”, ES), deionized water, $Zn(CH_3COO)_2{\cdot}2H_2O$ (Scharlau, Spain). The sol synthesis method reported by Vihodceva et.al [5]. MA-g-PE (Licocene fine grain TP 4351) was used as a coupling agent (5 wt%).

Composites were prepared by mixing components on two rolls mill (T = 150^{0}C, t = 10min), then cooled and pressed in 1 mm thick sheets. The tensile tests were conducted on the universal material testing machine UTS-100 (standard ASTM D 638 M – 93). Vicker microhardness (HV) was examined by Vickers M41 at the load 200 g.

The tensile strength, modulus of elasticity and surface microhardness values were proportionally postponed on axes to create radar charts, Fig. 1–6.

3. RESULTS AND DISCUSSION

Adding ZAD 5 wt% modifier to the sol-gel treated hemp fibres increases E_t by 76% and σ_{max} results by 40%, but decreases HV by 48% of 40 wt% hemp fibre composite (graphs 2a and 3a), Fig. 1.

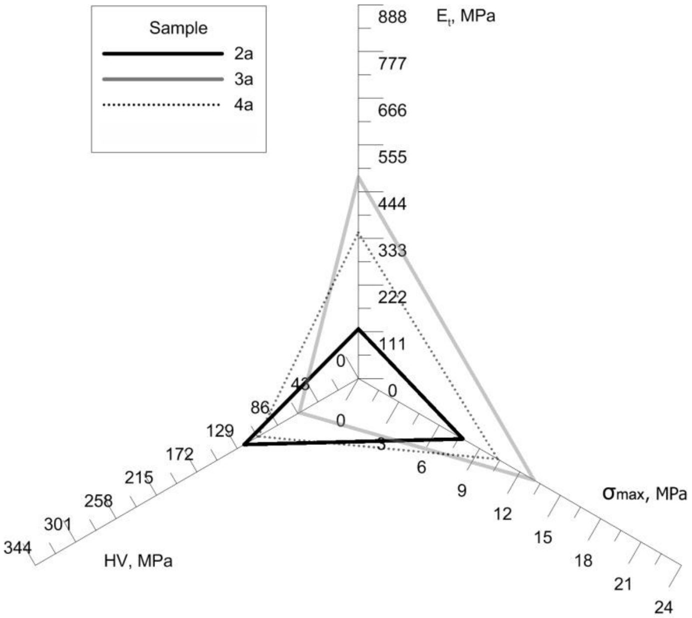

Fig.1. Effect of hemp fibres pre-tretment with Silica sol (2a), Silica sol modyfied with ZAD 5 wt% (3a) and combined NaOH 2 wt% and Silica sol pre-treatment (4a) on 40 wt% composite E_t, σ_{max} and HV

To obtain an even layer of xerogel on the fibre surface, the pre-treatment with NaOH was used, as well as to remove surface impurities and dust. In the previous tests after fibres pre-treatment with the alkali 2 wt% microhardness of 30 wt% composites decreased, E_t and elongation at break increased, but decreases the σ_{max} [7]. The experimental results reported by Li X. et. al. show that modification of flax fibres with NaOH 2 wt% could remove surface impurities, increase surface roughness and reduce diameter of natural fibres, that increase composites tensile strength and modulus, but decrease elongation at break [8]; it partly does not coincide with the results of experiments under discussion.

Graph 4a from Fig. 1 shows that combined NaOH 2 wt% and Silica sol fibres pre-treatment allows to improve composite E_t by 200 % and σ_{max} by 40% to compare with Silica sol modified samples (2a) and HV value does not decrease substantially.

Graphs (3a) and (5a) of Fig. 2 (left) show that combined fibres pre-treatment does not influences composite E_t, σ_{max} and HV substantially. It means that alkali 2 wt% pre-treatment of fibres before treatment with ZAD 5 wt% sol is not needed. At the same time alkali 2 wt% pre-treatment could improve Silica sol modified fibres composite E_t by 195 % and σ_{max} by 33%, but HV decreases by 12% (Fig. 2, right).

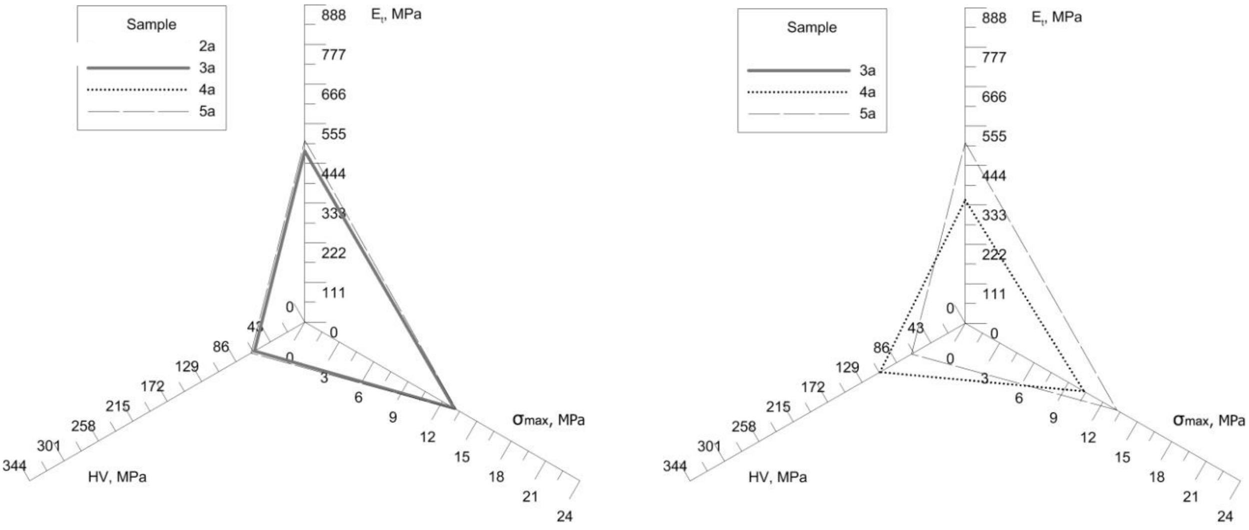

Fig. 2. Influence of combined pre-treatment of hemp fibres by NaOH 2 wt% and ZAD 5 wt% sol on mechanical properties of 40 wt% fibres composite

Comparision of the graph 4a from Fig. 2 with the graph 4b from Fig. 3 show, that MA-g-PE additive 5 wt% could improve by 8% E_t and by 21% σ_{max} of composite with 40 wt% alkali and Silica sol treated fibres filling without decrease of HV.

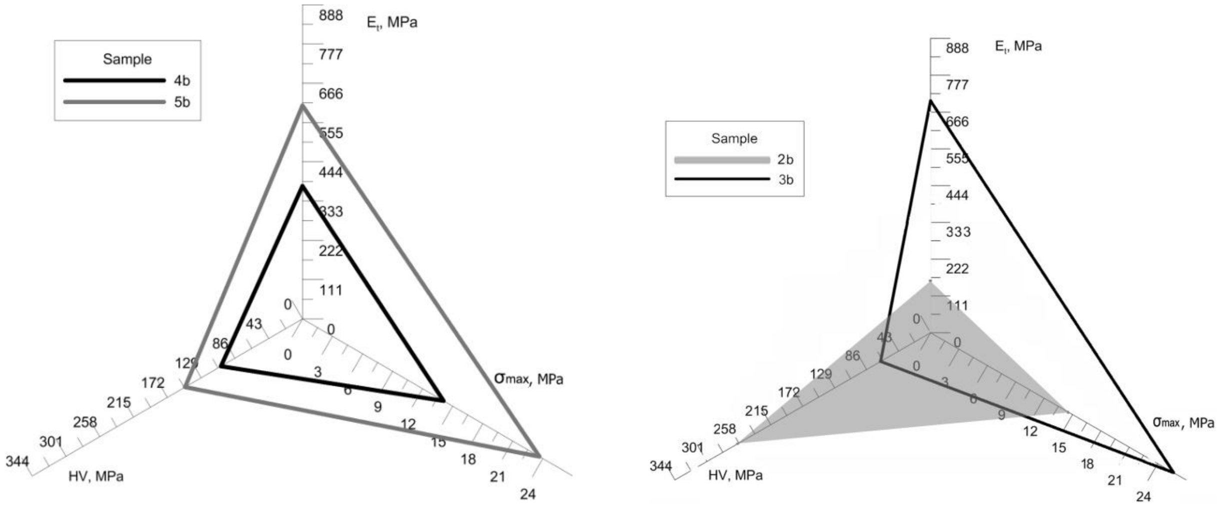

Fig. 3. Effect of hemp fibres treatment with Silica sol or ZAD 5 wt% on E_t, σ_{max} and HV of 40 wt% composite with MA-g-PE 5 wt% aditive (with NaOH pre-treatment 4b, 5b and without 2b, 3b)

Hemp fibres pre-processing by ZAD 5 wt% modified Silica sol makes the increase of mechanical properties of 40 wt% composite with the MA-g-PE 5 wt% aditive proportional and readable, as sides of both triangles are almost paralel (Fig. 3 left). It is seen from graphs 4b and 5b that all three parametres under discussion substantially increase of composite with ZAD 5 wt% sol pre- processed fibres compare to the same composition composite with Silica sol pre-processed fibres: E_t by 61%, σ_{max} by 68% and HV by 44%.

As seen from Fig. 3 (right) composites without NaOH pre-treatment and with MA-g-PE 5 wt% aditive all three parametres under discussion changes unproportionaly (sample 2b and 3b).

From the results it can be concluded that using the NaOH pre-treatment in combination with MA-g-PE additive, sol-gel method provides homogeneous composite.

Young’s modulus of natural fibre reinforced polymer composites increases with the fibres content increasing [9]. As seen from Fig.4 σ_{max} increases by 55%, HV increases by 155% and Et decreases by 32% of LLDPE composite with the 50 wt% pre-treated with ZAD 5 wt% sol fibres and MA-g-PE 5 wt% aditive (graph 7b of Fig.4) compare to the composite with untreated fibres and without MA-g-PE 5 wt% aditive (graph 6 of Fig.4).

In comparision σ_{max} increases by 18% and HV by 175% and E_t decreases 61% of composite with Silica sol pre-treated fibres (graph 7a of Fig.4,) to compare with the corresponding properties of composite with untreated fibres (graph 6).

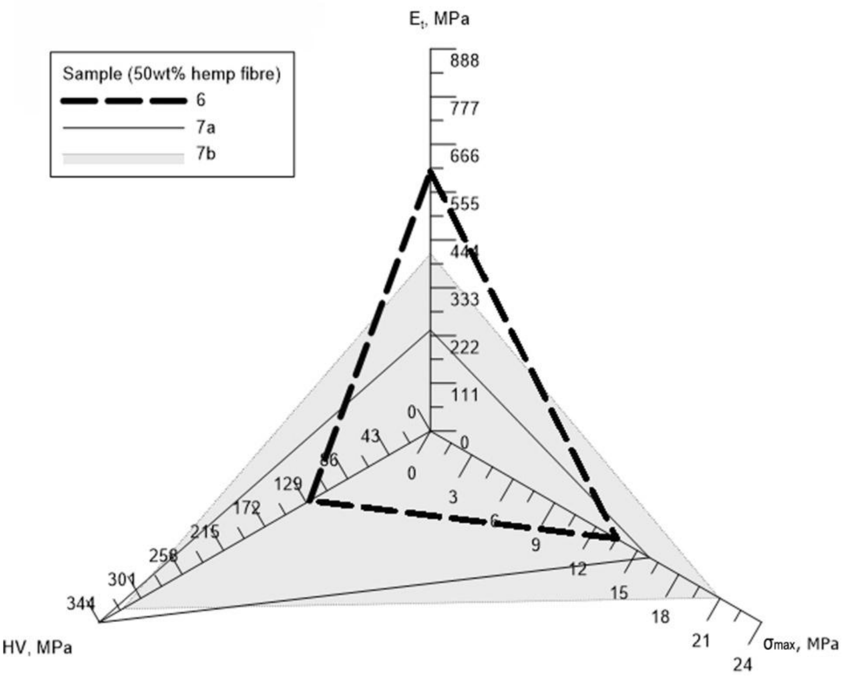

Fig. 4. Hemp fibres 50 wt% composite E_t, σ_{max}, HV

As the pre-treatment of fibres with Silica sol makes their surface harder, the fibre diameter increases and consequently the composite HV increases for both variants (7a and 7b).

Sol pre-treatment increases fibres possibility to blend into the composite 50 wt% and as a result proportionaly increases rates of all three composite mechanical properties (Fig. 5). HV increases by 183%, and the values of E_t, σ_{max} increase respectively by 99% and 104% increasing the fibre content from 40 to 50 wt%.

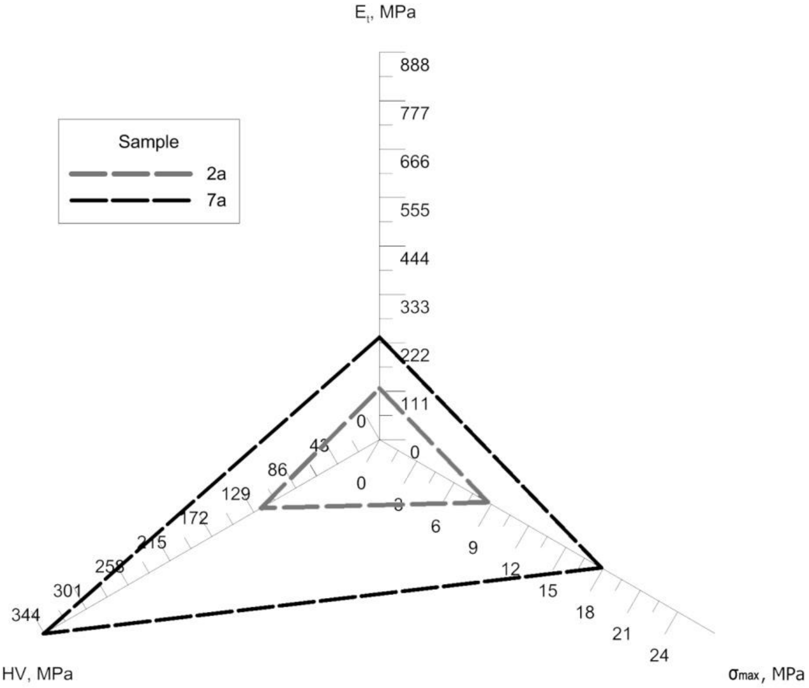

Fig. 5. Influence of pre-treated with Silica sol hemp fibres content increase on composite E_t, σ_{max} and HV

The elasticity module of sol treated fibres composite decrease to compare with the untreated fibres composite, but HV and σ_{max} increase. Therefore Silica sol pre-treatment is promising for blending a greater amount of fibres into the polymer, simultaneously improving HV and σ_{max}, and fluidity as well (24.4 g/10 min sample 2a) [10].

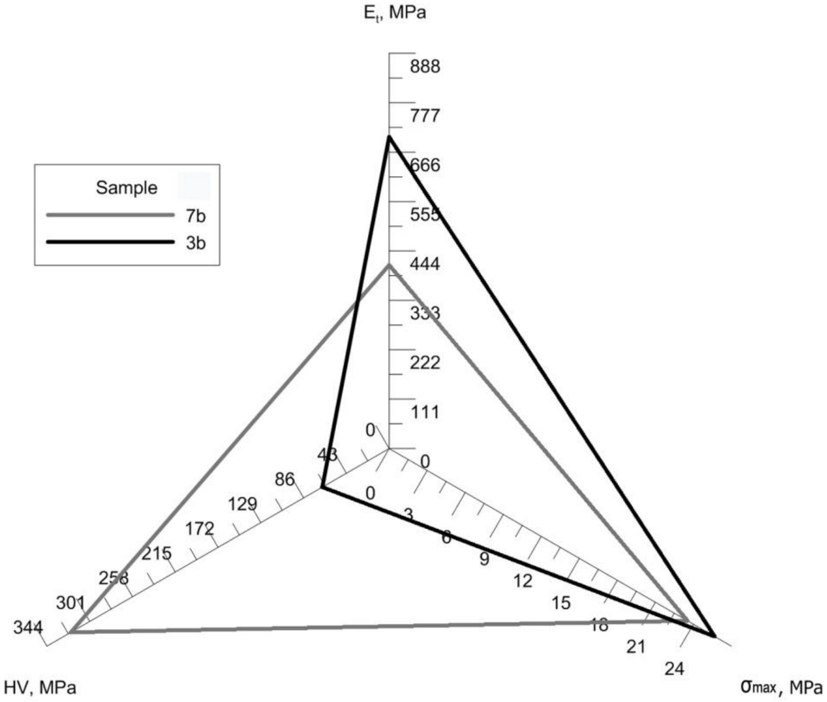

Fig. 6. Influence of pre-treated with ZAD 5 wt% sol hemp fibres content increase on E_t, σ_{max} and HV of composite with MA-g-PE additive

Increasing the ZAD 5 wt% sol pre-treated fibres content from 40 to 50 wt% in composite with MA-g-PE additive, the values of HV increase by 377%, but the values of E_t and σ_{max} decrease by 41% and 8%. It can be explained by the unsufficient mutual adhesion of the matrix and the fibres that can increase the fragility of the material if the fibre content is increased. Therefore, the optimum fibre content if emphasis in application is on higher Yung's modulus preferable is composite 40 wt% (Fig. 6). If more important property is hardness combined with the good strength at break, composite 50 wt% with ZAD 5 wt% pre-treated fibres and MA-g-PE additive 5 wt% is preferable over composite 40 wt% of the same technology.

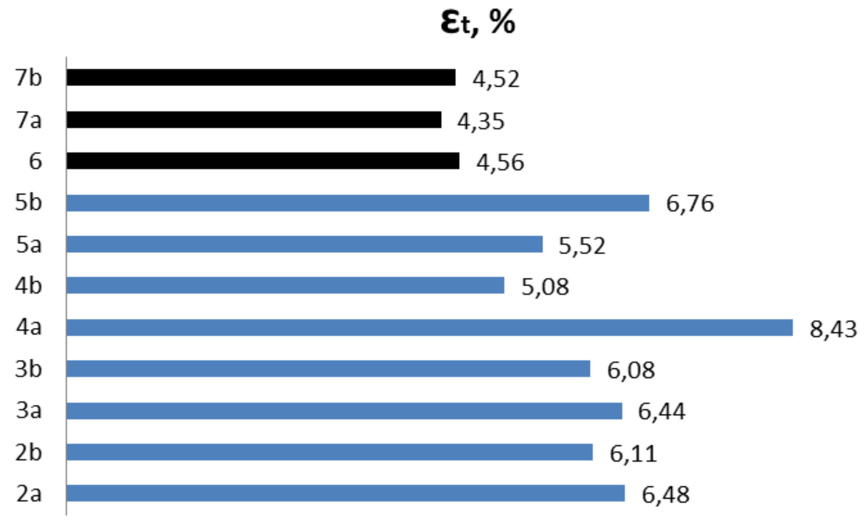

	2a	2b	3a	3b	4a	4b	5a	5b	6	7a	7b
Relative error, %	6	6	6	13	10	7	7	6	8	9	8

Fig. 7. Elongation at break of composite variants

As show Fig. 7 elongation at break mainly depends on hemp fibres content in composite diminishing elongation from 59% of LLDPE matrix to average 4.5% of composite 50 wt%. Impacts of other factors under investigation do not create regular framework.

4. CONCLUSIONS

Hemp fibres pre-treatment with NaOH 2 wt% decrease mechanical properties of composite variants as the concentration of solution used for pre-treatment seems too high.

Pre-treatment of hemp fibres with ZAD 5 wt% modyfied sol improves the modulus of elasticity and tensile strength of composite with 40 wt% fibres, but decreases microhardness to compare with Silica sol pre-treated fibres composite. With the MA-g-PE additive 5 wt% mechanical properties of all variants improve, except sample 4b, value of HV decrease by 3% in contrast of sample 4a.

Fibres share enlargement to 50 wt% allow to get composites with comparable low elongation at break, high enough elasticity modulus and strength, especially with ZAD 5 wt% modified sol pre-procession, and excellent surface hardness of modified fibres composite.

5. REFERENCES

1. KU, H., WANG, H. PATTARACHAIYAKOOP, N. and TRADA, M. A review on the tensile properties of natural fiber reinforced polymer composites. *Composites Part B Engineering*, 2011, Vol. 42, No. 4, p. 856–873.

2. LEE, B. H., KIM, H. J., YU, W. R. Fabrication of long and discontinuous natural fibre reinforced polypropylene biocomposites and their mechanical properties. *Fiber Polym*ers, 2009, Vol. 10, p. 83–90.
3. ZHANG, J., ZHANG, H., ZHANG, J. Effect of Alkali Treatment on the Quality of Hemp Fiber. *Journal of Engineered Fibres and Fabrics*, Vol. 9, Iss. 2, 2014, p. 24.
4. ROUMELi, E., TERZOPOULOU, Z., PAVLIDDOU, E. CHRISSAFIS, K., PAPADOPOULOU E., ATHANASIADOU E., TRIANTAFYLLIDIS, K., BIKIARIS D., N. Effect of maleic anhydride on the mechanical and thermal properties of hemp/high-density polyethylene green composites. *Journal of Thermal Analysis and Calorimetry*, Vol. 121, Iss. 1, 2015, pp. 93–105.
5. VIHODCEVA, S., KUKLE, S. Cotton Fabric Surface Modification by Sol-Gel Deposition of ZnO Thin Films. *IOP Conference Series: Materials Science and Engineering*, Vol. 38, Iss. 1, 2012, p. 012022.-012022. ISSN 1757-8981. e-ISSN 1757-899X doi:10.1088/1757-899X/38/1/012022.
6. ASHBY, M., JOHNSON K., *Materials and Design: The Art and Science of Material Selection in Product design*, Oxford: Elsevier, 2002. 188 p. ISBN 978-1-85167-497-8.
7. KAJAKS, J., ZELČA, Z., KUKLE, S. The Effect of Modification Methods on Performance Characteristics of Composites based on Linear Low Density Polyethylene (LLDPE) and Natural - Hemp Fibres. *Mechanics of Composite Materials*, Vol. 51, Iss. 5, 2015, pp. 955.-964. ISSN 0191-5665. e-ISSN 1573-8922.
8. LI, X., PANIGRAHI, S, TABIL L., G. A study on flax fiber-reinforced polyethylene biocomposites. *Applied Engineering in Agriculture*, Vol. 25, 2009, pp. 525–31.
9. KHOATHANE, M., C., VOSTER, O., C., SADIKU, E., R. Hemp fiber-reinforced 1-pentene/polypropylene copolymer: the effect of fiber loading on the mechanical and thermal characteristics of the composites. *Journal of Reinforced Plastics and Composites*, 2008, 27:1533–44.
10. ZELČA, Z. KUKLE, S. KAJAKS, J. Effects of Hemp Fibres Pre-Processing and Content on Linear Low Density Polyethylene Matrix Composite Properties. Baltic Polymer Symposium 2015. Programme and Proceedings, Latvia, Sigulda, 2015 16–18. September. Riga: RTU Press, 2015 117 p.

CYSENI 2016, May 26-27, Kaunas, Lithuania
ISSN 1822-7554, www.cyseni.com

COMPARATIVE STUDY ON SELECTION OF SUBSTRATE MATERIAL FOR HYBRID MICROWAVE INTEGRATED CIRCUITS (HMICs) USING ASHBY'S AND TOPSIS'S TECHNIQUES

N. Gupta, A. Mishra
Birla Institute of Technology and Science, Pilani
Vidhya Vihar, 333031 Pilani – India
Email: ngupta@pilani.bits-pilani.ac.in

ABSTRACT

This paper presents systematic approach of material selection for substrate material in hybrid microwave integrated circuits (HMICs). The performance of HMICs starts detroriating at microwave frequncies because the circuit dimensions become comparable to the wavelength. So it is important to design HMICs in such a way that its performance remains unaffected even at high frequencies. One way to fulfill this requirement is to fabricate a proper device. For this, substrate material in HMICs plays an important role. But there are different types of materials available which can be used as substrate material of HMICs. The commonly reported materials are; Silicon (Si), Gallium Arsenide (GaAs), Indium Phosphide (InP), Alumina (Al_2O_3), Beryllia, Fused Silica, Sapphire, Woven PTFF/Glass, PTFE/Glass, Polyolefin and Ferrite/Granite. As each material is having its own advantages and limitations therefore it is important to choose the best possible material out of all possible materials. For this purpose two decision making techniques are used. Firstly, Ashby's approach as Multi Objective Decision Making (MODM) technique is used and then Technique for Order Preference by Similarity to Ideal Solution (TOPSIS) as Multiple Attribute Decision Making (MADM) technique is used. Ashby's approach provides effective material selection technique to select the best material based on their material and performance indices for better device performance. While TOPSIS approach is the decision making approach which is basically used to determine the best alternative which should have shortest Euclidean distance (S *) from the ideal solution (A*) and largest Euclidean distance (S-) from negative ideal solution (A-). For MICs, the material indices considered and evaluated are surface roughness, relative dielectric constant, loss tangent, thermal conductivity and dielectric strength. It is observed that Sapphire followed by high-purity alumina (99.5 percent pure or better) are good candidates for substrate material in hybrid MICs. The surface roughness of sapphire is better than alumina, though the dielectric strength of both these materials are same. Comparision between two different methods for material selection shows consistency between the two methods of material selection. Both the methodologies show that Sapphire is the most suitable substrate material for hybrid MICs.

Keywords: Material selection, Microwave integrated circuits (MICs), TOPSIS, Ashby's Approach, MADM, MODM

CYSENI 2016, May 26-27, Kaunas, Lithuania
ISSN 1822-7554, www.cyseni.com

CHARACTERISATION OF ZIRCONIUM DOPED TITANIUM DIOXIDE THIN FILMS DEPOSITED BY CHEMICAL SPRAY PYROLYSIS

Abayomi Oluwabi, Ilona Oja Acik, Malle Krunks
Laboratory of Thin Film Chemical Technologies, Department of Materials Science,
Tallinn University of Technology,
Ehitajate tee 5, 19086 Tallinn – Estonia.
Email: abayomioluwabi@gmail.com

Valdek Mikli
Chair of Semiconductor Material Technology, Department of Material Science,
Tallinn University of Technology,
Ehitajate tee 5, 19086 Tallinn – Estonia.,

Albert Juma
Department of Physics and Astronomy, Botswana International University of Science and
Technology, Private bag 16, Palapye, Botswana.

ABSTRACT

The importance of TiO_2 has attracted its use has an energy material despite its large band gap (3.2–3.5 eV). Zr doping has been reported to be effective to enhance its use for solar cells, photo-catalytic and transparent transistor applications. To our knowledge, chemical spray pyrolysis (CSP) has not been reported for deposition of Zr doped TiO_2 films. Zr-doped TiO_2 thin films were prepared by CSP and the morphological, structural and optical properties of the deposited film investigated. A set of samples were successfully deposited from titanium isopropoxide and zirconium acetylacetate dissolved in ethanol as precursor solution with acetylacetone as a stabilizer. Different concentrations of the precursor solutions were prepared by varying Zr/Ti molar ratios (0, 5, 10, 20 and 40 mol %) and were sprayed onto heated substrates at 450 ^{o}C. The SEM images showed that the Zr-TiO_2 films were homogeneous with smaller grain sizes compared to the pure-TiO_2 films. As-deposited Zr-TiO_2 films were amorphous while the pure-TiO_2 films were crystalline with anatase structure as revealed by X-ray diffraction and Raman spectroscopy. Upon annealing at 500 ^{o}C, Zr-TiO_2 films became crystalline with crystallite size decreasing from 50 nm to 30 nm with increasing Zr content from 5% to 20% respectively. Subsequent annealing in steps of 100 ^{o}C led to the formation of mixture of anatase and rutile phase at 700 ^{o}C for pure-TiO_2 film and at 800 ^{o}C for Zr-doped TiO_2 films. Optical band gap of as-deposited Zr-TiO_2 film was higher (3.26 eV) than the as-deposited pure-TiO_2 films (3.14 eV) showing a strong dependence on phase composition. Zr/Ti ratio in the film increased from 0.014 to 0.13 as doping concentration in the solution increases from 5% to 40 mol%, as revealed by EDX analysis.

Keywords: Chemical Spray Pyrolysis; Thin films; Doping; Zr-TiO_2

1. INTRODUCTION

The study of TiO_2 as a semiconductor material have been an area of interest for most researchers due to its unique properties ranging from optical to electronic properties hence it have gained use in a wide range of applications such as photocatalysis, memory devices, solar cells, transistors among many others [1- 6]. Many routes have been adopted to enhance its properties, but the doping of TiO_2 with different metallic or non-metallic elements has been revealed to be most effective [7, 8] owing to the fact that doping affect the phase transition temperature [9].

ZrO_2 is an insulating material with good optical and dielectric properties [10, 11]. Zr-doped TiO_2 thin film, nano-rods, micro sphere have been reported for photo-catalytic application [1, 12]. Chang and Doong [13] have reported a series of Zr doped TiO_2 which was prepared by sol-gel process. Venkatachalam *et al*. [14] reported an enhanced photo-catalytic activity of Zr-doped TiO_2.

Lukac *et al.* [15] also reported the effect of annealing temperature on the photo-catalytic performance of Zr-doped TiO_2 films. The behaviour of Zr^{4+} dopant ion in Zr-doped TiO_2 nanoparticles was investigated by Wang research group [16].

Several methods have been used for the deposition of TiO_2 such as chemical vapour deposition [17], sol-gel method [18, 19], reactive sputtering [20–23] and spray pyrolysis [24]. Among these methods, the chemical spray pyrolysis (CSP) method is a solution based method that allows for free mixing of precursor solution prior to deposition. It is relatively simple and the most economical method of deposition for mass production.

CSP is an attractive technique for the preparation of thin films for reasons like: it's simple to use, film thickness and deposition parameters are easy to control, it can be operated at moderate temperature and it is not selective in the choice of substrate [25]. CSP offers the opportunity to deposit uniform and compact films. The properties of the films strongly depended on the precursor reagent and on the deposition conditions [25]. Castaneda *et al.* have reported deposition of TiO_2 thin films by spray pyrolysis in the substrate temperature range of 300–500 ^{o}C [26]. Okuya *et al.* [27] equally reported the role of additives in precursor solution on the mechanism of crystallisation of TiO_2. Oja *et al.* [28] have studied the properties of TiO_2 films prepared by spray pyrolysis method. To the best of our knowledge, Zr-doped TiO_2 thin film has not been reported using CSP.

In this paper, Zr-doped TiO_2 thin films were deposited using CSP by varying Zr/Ti mole ratio in the solution and the structural, morphological and optical properties of the deposited films investigated.

2. EXPERIMENTAL DETAILS

Zr-doped TiO_2 films were deposited using an analytical graded Titanium (IV) isopropoxide (TTIP) and Zirconium acetylacetate [$Zr(AcacH)_4$] reagents bought from MERCK and ALDRICH respectively as precursor solution. The synthesis of TiO_2 precursor was as follows: TTIP (1.8 ml) was first stabilized with acetylacetone (1.2 ml) in the ratio 1:2 which was maintained all through the experiment. To this solution 13.5 ml of ethanol was added and stirred to ensure homogeneity. The prepared solution was sprayed using a pneumatic spray set-up onto pre-heated quartz and silicon substrates.

Zr-doped TiO_2 solution was prepared by adding quantitative amount of $Zr(AcacH)_4$ corresponding to Zr/Ti mole ratio into an already stabilized TTIP and the above procedure was repeated. Precursor solutions with varying concentrations of Zr-dopant were prepared by varying the Zr/Ti mole ratio (5, 10, 20, 40 mol %). The substrates were placed on a tin bath maintained at 450 ^{o}C and the precursors sprayed at the rate of 2.5 ml/min with compressed air as the carrier gas. The flow rate of the carrier gas was 8 l/min. One spray cycle consisted of 60 s spraying plus 60 s pause and ten spray cycles were made from each solution. The samples were then annealed in air for one hour at temperatures from 500 to 900 ^{o}C using Nabertherm L5/11/06D furnace. The as-deposited and annealed films were labelled 'Pure-TiO_2 and x-Zr-TiO_2' for the un-doped and doped samples respectively, where x corresponds to the mol% concentration of Zr in sprayed solution.

Optical measurements were performed by measuring total transmittance and total reflectance spectra using Jasco-V670 spectrophotometer in the wavelength range 300–800 nm. X-ray diffraction (XRD) patterns were obtained using ULTIMA IV Rigaku D/max 2500 diffractometer having a Cu K_{α} radiation source operated at 40 kV and 40 mA. Surface morphology and elemental composition were studied using ZEISS HR FESEM Ultra 55 scanning electron microscope (SEM) with Bruker EDS system ESPRIT 1.8. The acceleration voltage for SEM measurements was 4.0 kV and for EDS was 7.0 kV. Raman spectra were acquired using a micro-Raman spectrometer HORIBA Jobin Yvon Model HR800 with 532 nm laser line which delivers 5 mW of power at 10 μm laser spot size during measurement. The Raman peak analysis was based on Lorenzian-fitting.

3. RESULTS AND DISCUSSIONS

3.1. Surface Morphology and Composition

Fig. 1 shows the SEM images of the as-deposited (450 ^{o}C) samples and annealed samples at 600 ^{o}C and 800 ^{o}C. The pure-TiO_2 and Zr-doped TiO_2 films are homogenous and compacted. Smaller grains start to develop in the film after annealing at 600 ^{o}C (Fig. 1 b, e, h). After annealing at 800 ^{o}C the surface of the pure TiO_2 film consist of small and larger grains which are up to about 500 nm in size (Fig. 1 c), however, the surface of 20-Zr-TiO_2 film (Fig. 1 i) consist of grains with a size up to about 50 nm. The thickness of the film was determined from the SEM cross-sectional image which shows that the pure-TiO_2 film is 330 nm thick, which is slightly higher than the 5-Zr-TiO_2 film (310 nm). The presence of Zr in the as-deposited Zr-doped TiO_2 film was confirmed by EDX analysis and Zr content in the film calculated from the atomic unit reveals that the Zr/Ti atomic ratio increased from 0 to 0.13 as doping concentration increases from 0 to 40 mol% (Table 1).

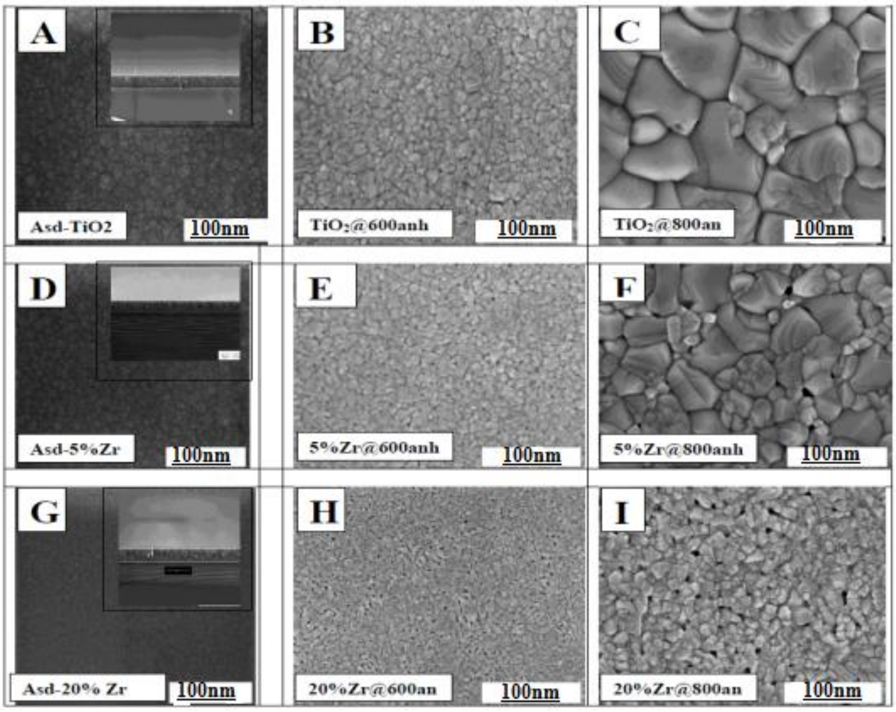

Fig. 1. SEM images of pure-TiO_2 (A – C), 5-Zr-TiO_2 (D – F), 20-Zr-TiO_2 (G – I) films; as-deposited (A, D, G) and after annealing at 600 ^{o}C (B, E, H) and 800 ^{o}C (C, F, I)

Table 1. Zr/Ti ratio in the film depending on Zr concentration in the solution (0–40% Zr)

Sample	**0 mol%**	**5 mol%**	**10 mol%**	**20 mol%**	**40mol%**
Zr/Ti atomic ratio	0	0.014	0.025	0.044	0.13

3.2. Structural Characterisation

The XRD diffraction pattern of pure-TiO_2 and Zr-doped TiO_2 are shown in Fig. 2. For the As-deposited samples (Fig. 2 a), pure-TiO_2 film shows a sharp peak and 5-Zr-TiO_2 film a weak peak at $2\theta = 25.40^{o}$ belonging to the anatase (101) phase (PDF-01-075-1573) [29]. The (10–40)-Zr-TiO_2 films are amorphous. This demonstrated the amorphisation effect of incorporating a larger amount of Zr into the TiO_2 lattice structure. Gao *et.al.*, also reported that Zr-doping delays the transition of amorphous to anatase phase of TiO_2 deposited by sol-gel method [30]. The (5–40)-Zr-TiO_2 samples showed amorphous to anatase phase transition after 500 ^{o}C annealing which was sustained up to

700 °C. After annealing at 700 °C and 800 °C (Fig. 2 b and c), the pure-TiO_2 film showed a mixture of both rutile and anatase phases with the anatase (101) peak at $2\theta = 25.40^o$ and the rutile (110) main peak at $2\theta = 27.43^o$ (PDF01-071-4808) [29] while the doped films remains anatase. However, anatase and rutile mixed phases appear in 10-Zr-TiO_2 film after 800 °C annealing which was an indication of the stabilisation the anatase phase thereby delaying rutile phase formation.

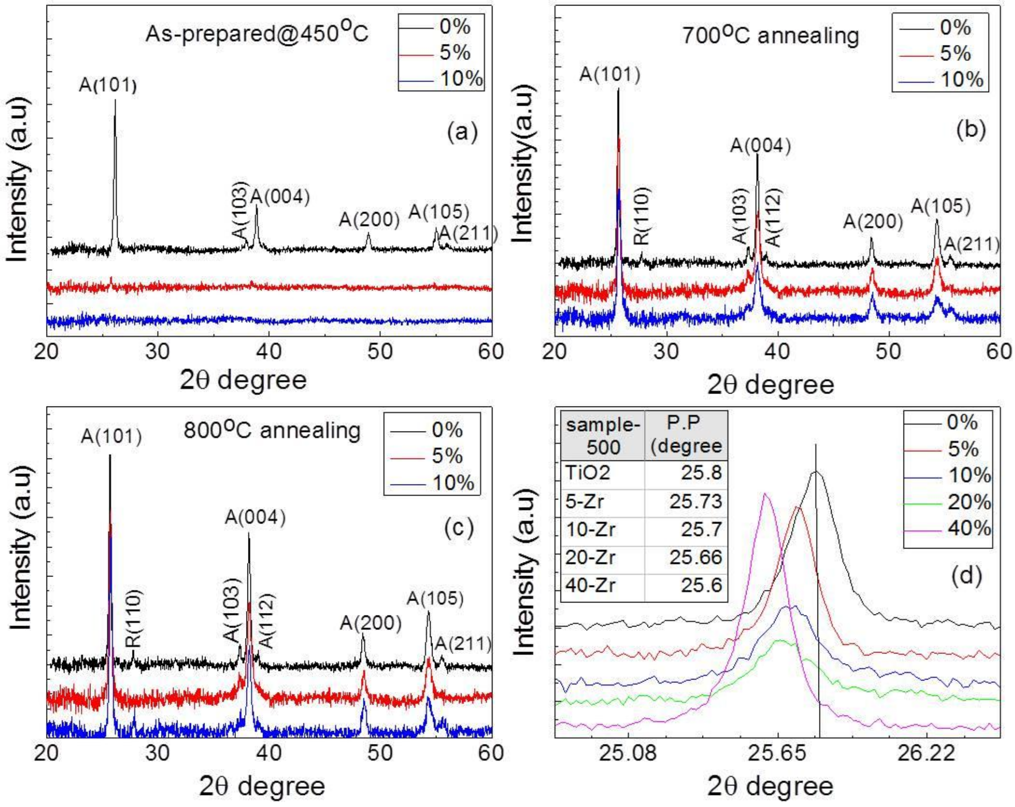

Fig. 2. XRD plot of pure and Zr-doped TiO_2 thin films (a) As-deposited at 450 °C (b) after annealing at 700 °C, and (c) 800 °C temperature. The shift in the anatase (101) main diffraction peak is presented in (d)

Fig. 2 d reveals the shift in the position of the anatase (101) main peak as a function of the Zr concentration in the film after annealing at 500 °C. The position of the (101) diffraction peak shifted to lower values of diffraction angle 2θ in the diffraction pattern with increasing Zr in the film, which confirms the incorporation of Zr^{4+} in the TiO_2 lattice structure. The presence of Zr^{+4} which has a larger ionic radius of 0.072 nm compare to Ti^{+4} (0.061 nm) in the TiO_2 matrix causes an increase in the unit cell parameters, which causes a decrease in the value of 2θ where their diffraction peak appears as explained by the Bragg's law [1, 31].

The mean crystallite size of the pure and Zr-doped TiO_2 films annealed at different temperatures was calculated by applying the Scherrer's formula on the (101) anatase peak and the values obtained are presented in Table 2. The 20-Zr-TiO_2 film have a relatively smaller crystallites compared to 5-Zr-TiO_2 film.

Table 2. Average crystallite size of pure, 5-Zr and 20-Zr-TiO_2 at different temperature of annealing

Annealing Temp. (° C)	**Pure TiO_2 (nm)**	**5-Zr-TiO_2 (nm)**	**20-Zr-TiO_2 (nm)**
500	40	50	30
600	30	30	20
700	35	30	25
800	40	35	30

Raman spectra for the pure and Zr-doped TiO_2 are given in Fig. 3. From Fig. 3 a, the as-deposited pure-TiO_2 spectrum reveals a Raman band at 141 cm^{-1} belonging to TiO_2 anatase phase while the doped film are amorphous, concurring to the XRD data. After annealing at 800 ^oC (Fig. 3 b) all the TiO_2, 10-Zr-TiO_2 and 20-Zr-TiO_2 films revealed Raman peaks at 141, 191, 398, 513 and 639 cm^{-1}, which are characteristics of crystalline TiO_2 anatase phase [32]. The peaks at 141, 191 and 639 cm^{-1} corresponds to the E_g vibration modes, while 398 and 513 cm^{-1} peaks correspond to B_{1g} and A_{1g} + B_{1g} modes, respectively [33]. It can be observed that the intensity of the Raman peaks decreased upon introduction of Zr.

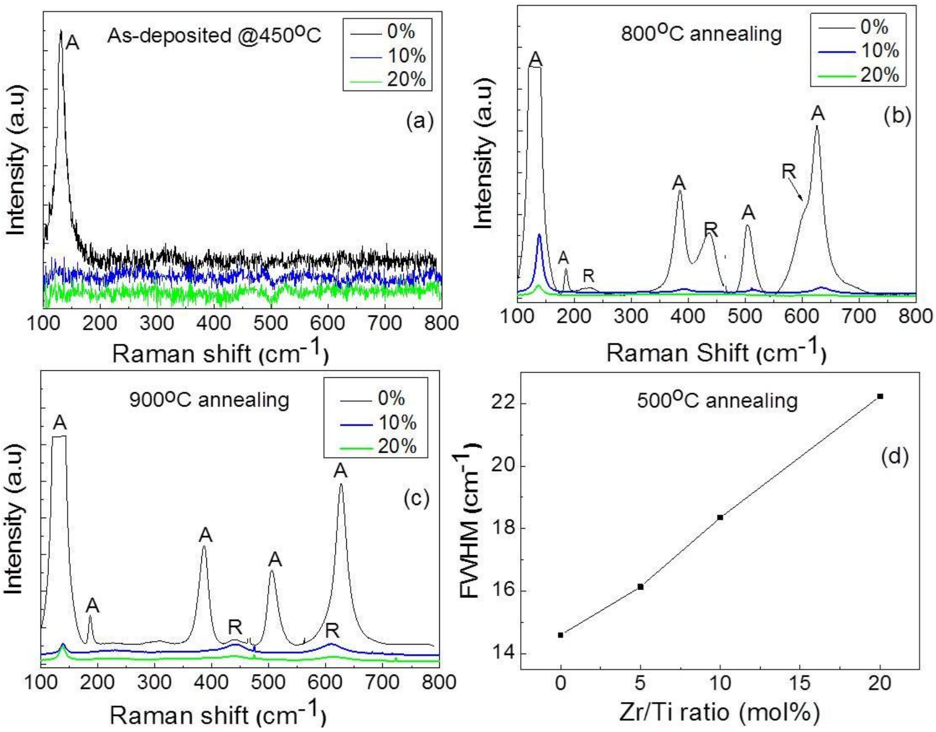

Fig. 3. Raman spectral for the pure and Zr-doped TiO_2 film (a) as-deposited, after annealing at (b) 800 ^oC and (c) 900 ^oC. The FWHM as a function of Zr/Ti mol ratio in the spray solution after annealing at 500 ^oC is presented in 3(d)

This indicates an increase in lattice imperfections due to the incorporation of Zr [34]. The undoped TiO_2 film shows additional peaks at 232 and 449 cm^{-1} which belong to the TiO_2 rutile phase. Also after annealing at 900 ^oC, the 10-Zr-TiO_2 and 20-Zr-TiO_2 films show mixed anatase and rutile phases (Fig. 3 c). The FWHM values of the anatase main peak at 141 cm^{-1} as a function of doping concentration after annealing at 500 ^oC are presented in Fig. 3 d. The value increases with concentration of Zr^{+4} indicating a reduction in the size of the crystallite as the Zr^{+4} is being incorporated into the TiO_2 matrix.

3.3. Optical Properties

Fig. 4 shows the total transmittance spectra for the as-deposited TiO_2 thin film at different Zr-doping concentrations in the wave length range between 300–800 nm. All the thin films shows interference pattern with high optical transparency above 60% in the visible region (from 400 to 800 nm). The interference patterns are a result of multiple reflections at the air/film and film/substrate interfaces due to the difference in the refractive index between the air, TiO_2 film and the substrate. This confirms that the films were transparent in the visible region, homogenous and uniformly coated on the substrates [35, 36] as seen in the SEM images. The interference occurs when the film surface is reflective with less scattering or absorption in the bulk. If the film surface is rough, the incident light will be scattered in all direction without reflection [36]. The total transmittance increases as the concentration of Zr in the film was increased. A blue shift in the transmittance spectra of the Zr-doped TiO_2 films compared with the pure-TiO_2 spectra denotes an increase in the optical band gap with increasing Zr dopant.

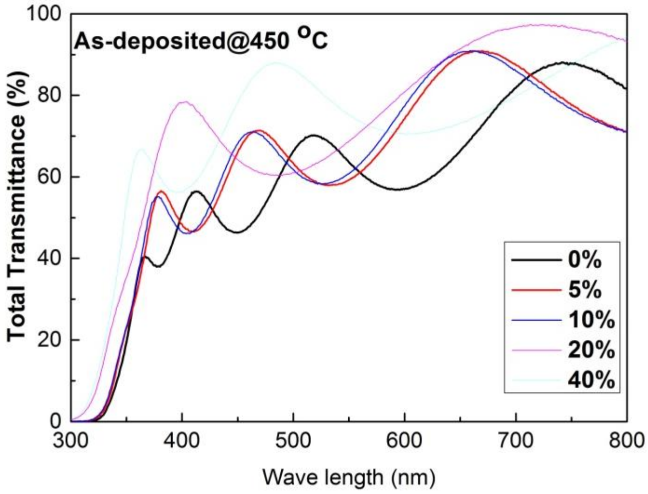

Fig. 4. Total transmittance spectra of the as-deposited films with different Zr-doping concentrations

Optical direct band gap energy of the deposited films was calculated after taking into consideration the reflectivity, absorption coefficient, and thickness of the film; as these strongly affect the transparency of the film. The interference peaks was eliminated by relating transmittance (T) to absorption coefficient ($\boldsymbol{\alpha}$) in equation (1)

$$T \cong (1-R)^{-\alpha d}\,, \tag{1}$$

where R is the reflectance and d is the thickness of the film. Therefore expression (2) can be applied to a Tauc plot [37].

$$(\alpha h v) = A\left(h v - E_g\right)^n\,, \tag{2}$$

where hν is the photon energy, A is a constant called critical absorption, n value varies depending on the band transition whether it is direct transition or indirect and E_g is the optical band gap. The value of E_g for undoped and Zr-doped TiO_2 films were obtained by plotting $(\boldsymbol{\alpha} h\nu)^2$ against the photon energy and extrapolating the linear part of the curve to photon axis as shown in Fig. 5 a for (0-10)-Zr-TiO_2 films [38, 39]. The band gap energy of the 10-Zr-TiO_2 thin film (3.20 eV) is higher than the pure-TiO_2 film (3.14 eV). The as presented in Fig. 5 b, the value of E_g increased slightly with annealing temperature up to 600–700 ^{o}C and then decreased as the film started transforming into the rutile phase.

Theoretical calculation on the electronic properties of Zr-TiO_2 has shown no change in the band gap [40, 41] while experimental results give mixed results depending on the method of preparation and the nature of doping. An increase in the band gap has been reported for nanocrystalline samples and this is due to quantum confinement effect because of the small particle sizes [14]. The increase in the band gap with Zr-doping was also reported for sol-gel deposited samples [26, 36], which resulted from a decrease in the crystallite sizes. The slight change in the band gap values observed in this work can therefore be due to structural changes caused by Zr-doping and also due to annealing [15].

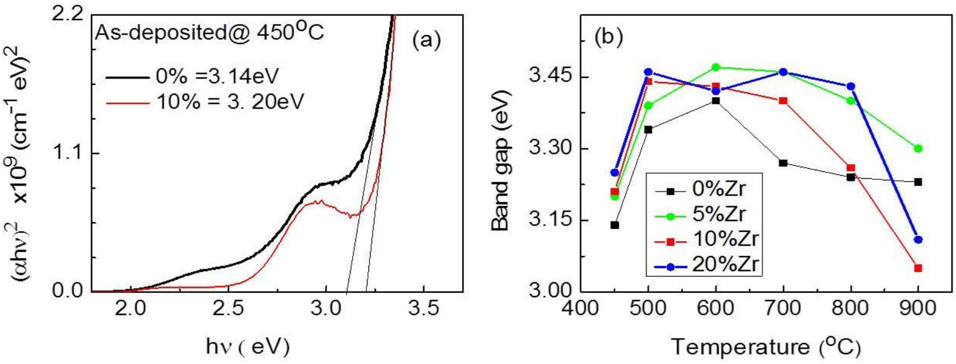

Fig. 5. (a) Determination of the optical band gap of undoped and Zr-doped TiO_2 films and (b) the variation of the band gap of undoped and Zr-doped TiO_2 with annealing temperature

4. CONCLUSION

CSP method was used to deposit a uniform and homogenous Zr-doped TiO_2 film and the influence of Zr concentration in the solution studied. The XRD data reveals that the as-deposited Zr-doped samples are amorphous and became crystalline with anatase crystal structure oriented along (101) plane after 500 ^{o}C temperatures of annealing with average crystallite size between 20 nm to 50 nm. A mixture of anatase and rutile phases was observed after annealing at 800 ^{o}C for the Zr-doped TiO_2. Raman analysis which complements the XRD results shows that the FWHM value of the anatase main peak at 141 cm^{-1} increases with Zr/Ti mole ratio in the precursor solution confirming the decrease in the crystallite sizes with enhanced Zr-doping. CSP is therefore a suitable method for the deposition of highly homogeneous and uniform thin films for various applications especially thin film transistors.

5. ACKNOWLEDGEMENT

This study was financially supported by the Estonian Ministry of Education and Research project IUT19-4, Tallinn University of Technology based financing project B24 and by the European Union through the European Regional Development Fund project TK141 “Advanced materials and high-technology devices for energy recuperation systems”.

6. REFERENCES

1. HERNANDEZ-ALONSO M.D., CORONADO J.M., BACHILLER-BAEZA B., FERNANDEZ-GARCIA M., SORIA J. Influence of structural and surface characteristics of $Ti_{1-x}Zr_xO_2$ nanoparticles on the photocatalytic degradation of methylcyclohexane in the gas phase. Chem. Mater., 2007, Vol. 19, p. 4283–4291.
2. ZHAO C., ZHAO C. Z., WERNER M., TAYLOR S., CHALKER P. Dielectric relaxation of high-k oxides. Nano. Res. Lett., 2013, Vol. 8, p. 456.
3. LEE M.-K., YEN C.-F., FAN C.-H. High dielectric constant nickel-doped titanium oxide films prepared by liquid-phase deposition. Appl. Phys. A, 2014, Vol. 116, pp. 2007–2010.
4. FRANK A. J., KOPIDAKIS N., VAN DE LAGEMAAT J. Electrons in nanostructured TiO_2 solar cells: transport, recombination and photovoltaic properties. Coord. Chem. Rev., 2004, Vol. 248, pp. 1165–1179.
5. KIM S.K., Kim K.M., JEONG D.S., JEON W., YOON K. J., HWANG C. S. Titanium dioxide thin films for next-generation memory devices. J. Mater. Res., 2013, Vol. 28, pp. 313–325.

6. ES-SOUNI M., OJA I., KRUNKS M. Chemical solution deposition of thin TiO_2-anatase films for dielectric applications. J. Mater. Sci.: Mater. in Electr., 2004, Vol. 15, pp. 341–344.
7. LIU G., YANG H. G., WANG X., CHENG L., PAN J., LU G. Q., CHENG H. M. Nano sized anatase TiO_2 single crystals for enhanced photocatalytic activity. J. Am. Chem. Soc., 2009, Vol. 131, p. 12868.
8. LU X., HUANG F., MOU X., WANG Y., and XU F. A General Preparation Strategy for Hybrid TiO_2 Hierarchical Spheres and Their Enhanced Solar Energy Utilization Efficiency. Adv. Mater., 2010, Vol. 22, Iss. 33, p. 3719–3722.
9. REIDY D.J., HOLMES J.D., MORRIS M.A. The critical size mechanism for the anatase to rutile transformation in TiO2 and doped-TiO_2. J. Eur. Ceram. Soc., 2006, Vol. 26, pp. 1527–1534.
10. ZELNER M., MINTI H., REISFELD R., Cohen H., TENNE R. Preparation and characterization of CdS films synthesized in situ in zirconia sol-gel matrix, Chem. Mater. J., 1997, Vol. 9, pp. 2541.
11. SASHCHIUK A., LIFSHITZ E., REISFELD R., SARAIDAROV T., ZELNER M., WILLENZ A. Optical and conductivity properties of PbS nanocrystals in amorphous Zirconia sol-gel films. J. sol-gel science and technology. 2001. Vol. 24, p. 31.
12. HUANG Y., ZHENG Z., AI Z., ZHANG L., FAN X., ZOU Z. Core-shell microspherical $Ti_{1-x}Zr_xO_2$ solid solution photocatalysts directly from ultrasonic spray pyrolysis. J. Phys. Chem. B, 2006, Vol.110, pp.19323–19328.
13. CHANG S. M., DOONG R. A. Characterisation of Zr-doped TiO_2 nano crystals prepared by a nonhydrolytic sol-gel method at high temperatures. J. Phys. Chem. B, 2006, Vol. 110, No. 42, pp. 20808–20814.
14. VENKATACHALAM N., PALANICHAMY M., ARABINDOO B., MURUGESAN V. Enhanced photocatalytic degradation of 4-chlorophenol by Zr^{4+} doped nano TiO_2. J. Mol. Catal. A: Chem., 2007, Vol. 266, No. 1, pp. 158–165.
15. LUKAC J., KLEMENTOVA M., BEZDICKA P., BAKARDJIEVA S., SUBRT J., SZTMARY L., BASTL Z., JIRKOVSKY J. Influence of Zr as TiO_2 doping on photocatalytic degradation of 4-chlorophenol. Appl. Catal. B: environ., 2007, Vol. 74, No. 1, pp. 83–91.
16. WANG J., YU Y., LI S., GUO L., WANG E., CAO Y. Doping behaviour of Zr^{4+} ion Zr^{4+}-doped TiO_2 Nanoparticles. J. Phy. Chem. C, 2013, Vol. 117, pp. 27120–27126.
17. YEUNG K. S., LAM Y.W. Variable Optical Band gap for TiO_2 Thin films deposited in a D. C. Magnetron Sputtering System. Thin Solid Films, 1983, Vol. 109, p. 405.
18. VOROTILOV K. A., ORLOVA E. V., PETROVSKY V. I. Solgel TiO_2 film of silicon substrate.Thin Solid films,1992, Vol. 207, No. 1–2, pp. 180–184.
19. GARTNER M., PARLOG C. OSICEANU P. Spectroellipsometric characterisation of lanthanide-doped TiO_2 films obtained via the sol-gel technique. Thin Solid films, 1993, Vol. 234, No. 1–2, pp. 561–565.
20. SUHAIL M. H., MOHAN RAO G., MOHAN S. Dc Reactive Magnetron Sputtering of Titanium-Structural and Optical Characterization of TiO_2 Films. J. Appl. Phys., 1992, Vol. 71, No. 3, pp. 1421–1427.
21. MARIUS D. S. On the dielectric properties of dc magnetron TiO_2 thin films. J. Appl. Sur. Sci., 2003, Vol. 218, pp. 317–322.
22. LAZAR G., VASCAN I. Influence of the bias voltage on the optical properties of sputtered a-C:H thin films. Rom. J. Phys. 1998, Vol. 43, p. 571.
23. TANG H., PRASAD K., SANJINES R., SCHMID P. E., LEVY F. Electrical and optical properties of TiO_2 anatase thin film. J. Appl. Phys., 1994, Vol. 75, No. 4, pp. 2042–2047.
24. OJA I., MERE A., KRUNKS M., SOLTERBECK C-H., ES-SOUNI M. Properties of TiO_2 films prepared by the spray pyrolysis method. Solid State Phenomena. 2004, Vol. 99, pp. 259–262.

25. PRAMOD S. P. Versatilityy of Chemical Spray Pyrolysis technique. J. Mat. Chem. & Phys., 1999, Vol. 59, No. 3, pp. 185–198.
26. CASTANEDA L., ALONSO J. C., ORTIZ A., ANDRADE E., SANIGER J. M., BANUELOS J. G. Spray pyrolysis deposition and characterisation of TiO_2 thin films. Mater. Chem. Phys. 2002, Vol. 77, pp. 938–944.
27. OKUYA M., PROKUDINA N. A., MUSHIKA K., KANEKO S. TiO_2 thin film synthesised by spray pyrolysis deposition technique. J. Eur. Ceram. Soc., 1999, Vol. 19, No. 6–7, pp. 903–906.
28. OJA I., MERE A., KRUNKS M., SOLTERBECK C-H., ES-SOUNI M. Properties of TiO_2 films prepared by the spray pyrolysis method. Solid State Phenomena. 2004, 99/100, pp. 259–262.
29. Powder Diffraction File (PDF), PDF-2 Release 2008.
30. GAO B., LIM T.M., SUBAGIO D.P., TEIK-THYE L. Zr-doped TiO_2 for enhanced photocatalytic degradation of bisphenol A. J. Appl. Catal. A-Gen., 2010, Vol. 375, pp. 107–115.
31. YU J.C., LIN J., KWOK R.W.M., $Ti_{1-x}Zr_xO_2$ solid solutions for the photocatalytic degradation of acetone in air. J. Phys. Chem. B 1998, Vol. 102, pp. 5094–5098.
32. OHSAKA T., IZUMI F., FUJIKI Y. Raman spectrum of anatase TiO_2. Journal of Raman Spectroscopy, 1978, Vol. 7, pp. 321–324.
33. ZHANG W. F., HE. Y. L., ZHANG M. S., YIN Z., and CHEN Q. Raman scattering study on anatase TiO_2 nanocrystals. J. Phys. D: App. Phys., 2000, Vol. 33, pp. 912–916.
34. BINEESH K. V., KIM D.-K, and PARK D.-W. Synthesis and characterisation of Zirconium-doped mesoporous nano-crystalline TiO_2. J. Nanoscale, 2010, Vol. 2, pp. 1222–1228.
35. KIM S. S, YUM J. H., SUNG Y. E. Electrophoretically deposited TiO_2 photo-electrodes for use in flexible dye-sensitized solar cells. Photochem. Photobio. A. Chem J., 2005, Vol. 173, No. 1, p. 269.
36. BENSAHA R., BENSOUYAD H. Synthesis, Characterisation and properties of Zirconium oxide doped Titanium oxide thin films obtained via Sol-gel process. Intech- open Sci., 2012, Vol. 10, pp. 207–234.
37. PANKOVE Jacque.I. Optical Process in Semiconductors. Prentice Hall: Englewood Cliffs N.J., 1971.422 p. ISBN 0-136-38023-9.
38. ZHAO X. K, FENDLER J. H. Size quantization in semiconductor particulate film. Phys. Chem. J. 1991, Vol. 95, pp. 3716–3721.
39. TANG H., PRASAD K., SANJINES R., SCHIMID P.E, LEVY F. Electrical and optical properties of TiO_2 anatase thin film. App. Phys. J., 1994. Vol. 75, No. 4, pp. 2042–2047.
40. YAO X., WANG X., SU L., YAN H., and YAO M. “Band structure and photocatalytic properties of N/Zr co-doped anatase TiO2 from frist-principle study.” J. Mol. Catal. A: Chem., 2011, Vol. 351, pp. 11–16.
41. LIPPENS P. E., CHADWICK A. V., WEIBEL A., BOUCHET R., and KNAUTH P. “Structure and chemical bonding in Zr-Doped Anatase TiO_2 Nanocrystals,” J. Phys. Chem. C, 2008, Vol. 112, pp. 43–47.

CYSENI 2016, May 26-27, Kaunas, Lithuania
ISSN 1822-7554, www.cyseni.com

INCORPORATION OF NANOPARTICLES INTO THE BULK OF EPS FOAM USING PVD SYSTEM

Š. Varnagiris, D. Milčius
Lithuanian Energy Institute
Breslaujos str. 3, LT-44403 Kaunas – Lithuania
Email: sarunas.varnagiris@lei.lt

ABSTRACT

Expanded polystyrene foam (EPS) is used for various applications because of its significant properties (low weight, low cost, good thermal insulation, etc.). However requirements for polystyrene are increasing with the growing of global demand for polystyrene. In order to increase some of polystyrene characteristics, additional materials are incorporated into polystyrene. This article presents the results of nanoparticles incorporation into EPS bulk using physical vapour deposition (PVD) system. TiO_2 was used as an additional material, which was incorporated into EPS foam. This compound was chosen in order to increase antibacterial characteristics of EPS. Pre-expanded polystyrene beads were used as a substrate. These beads were treated with argon plasma in order to achieve better surface adhesion. Plasma was generated in 1×10^{-1} mbar pressure using pulsed DC power source (frequency – 20 kHz, voltage – 400 V). Nanoparticles were deposited on the surface of pre-expanded polystyrene beads. Titanium cathode was used as a primary material. Formation of nanoparticles was done using magnetron sputtering in reactive atmosphere. Mixture of argon and oxygen gas was used in order to form TiO_2 nanoparticles (argon – 82%, oxygen – 18%). Vacuum pressure was 6×10^{-3} mbar during nanoparticles formation process (power during deposition – 240 W). Plasma treatment and TiO_2 nanoparticles deposition were done without polystyrene beads extraction to atmospheric pressure. TiO_2 nanoparticles were formed on the surface of non expanded polystyrene beads. Polystyrene beads were expanded and compounded into one-peace foam after TiO_2 deposition. XPS results showed that TiO_2 particles do not form any other compound and do not separated from polystyrene beads surfaces during expansion and moulding processes. SEM results and EDS views of mapping showed that TiO_2 particles distributed uniformly in all bulk of EPS. Cracking of TiO_2 pieces into smaller parts were observed after pre-expansion of polystyrene beads. These results showed that such type of additional particles incorporation into EPS bulk could lead to achieve desirable characteristics. Economic and energetic assessment showed that PVD (KJLC, PVD 75) system is not suitable for industry application because of price and time consumption. However similar industrial applied system with some modifications could reduce price about 400 times compared to PVD (KJLC, PVD 75).

Keywords: Expanded polystyrene foam, deposition, nanoparticles

CYSENI 2016, May 26-27, Kaunas, Lithuania
ISSN 1822-7554, www.cyseni.com

INFLUENCE OF THE SECONDARY THERMAL ANNEALING ON THE PROPERTIES OF $CdTe/CdS:CdCl_2:O_2$ STRUCTURE

W. Yang, N. Spalatu, N. Maticiuc, M. Krunks, J. Hiie
Tallinn University of Technology
Ehitajate tee 5, 19086 Tallinn – Estonia
Email: wangjun1yang@gmail.com

ABSTRACT

Fabrication of superstrate CdTe/CdS solar cells deposited by close spaced sublimation includes $CdCl_2:O_2$ activation at 420 °C. This process results in a deep recrystallization and sintering of both CdS and CdTe layers, substantially improving the optoelectronic properties of the solar cells. However, high concentration of chloride residuals ($CdO{\cdot}CdCl_2$) and solid solution of CdS in $CdCl_2$, as precipitates on grain boundaries, limits the hole density in CdTe ($< 10^{15}$ cm^{-3}) and causes hygroscopicity of the cells. We use a controlled thermal treatment of $CdTe/CdS:CdCl_2:O_2$ structures in $N_2 + H_2$ ambient at 200–400 °C in order to remove the chloride residuals – the so-called gettering of impurities, which can improve the optoelectronic properties of the cells. In addition, the possible mechanisms behind the post-activation treatment and its influence on the solar cell performance are discussed. The CdTe/CdS thin films and devices were characterized by scanning electron microscopy, energy dispersive spectroscopy, photoluminescence, and current-voltage measurements.

Keywords: Cadmium telluride, thin films, cadmium chloride, thermal treatment, optoelectronic properties, solar cells efficiency.

1. INTRODUCTION

The CdTe based solar cell is a very competitive photovoltaic (PV) product in the solar cell market, reaching recently a conversion efficiency of 21.5% [1]. Despite the high photovoltaic performance of these solar cells, there are still several aspects such as technology related issues, back contact strategy, and/or junction activation that require more optimization and better understanding [2].

$CdCl_2:O_2$ activation step is a standard and vital process for CdTe/CdS structure that results in deep recrystallization and sintering of both CdS and CdTe layers substantially improving the optoelectronic properties of the solar cell. However, during this step some residual $CdCl_2$ may segregate and after washing the water-insoluble oxychlorides can stick to the CdTe surface [3]. The chloride in the lattice together with residual phases of $CdO{\cdot}CdCl_2$ and the solid solution of CdS in $CdCl_2$ on grain boundaries limit the concentration of holes in CdTe and to cause hygroscopicity of the cells [4]. As a solution for gettering of impurities from CdTe/CdS structure is applied a secondary thermal annealing after the $CdCl_2:O_2$ activation step. By changing the temperature and environment of the annealing process one can remove the residues and improve the optoelectronic properties of the CdTe/CdS solar cells.

In our previous [5] work we showed that morphology and polycrystalline structure of CSS CdTe film is affected by $CdCl_2$ activation and by condensation temperature of CdTe on the substrate. Here we report a systematic investigation of influence of post-activation treatment in N_2+H_2 ambient at temperatures from 200 °C to 400 °C on the properties of $CdCl_2:O_2$ heat treated CdTe/CdS structures. In addition, we discuss the mechanisms responsible for the changes in structural and optoelectronic properties of the solar cells.

2. EXPERIMENTAL DETAILS

CdS/CdTe solar cells were fabricated in a superstrate configuration by close spaced sublimation (CSS) on glass substrates coated with a 200 nm thick fluorine doped tin oxide (FTO) layer. Films of CdS, 100–150 nm thick, were deposited at 400 °C from 5N CdS powder. CdTe films with a thickness of 3 μm were deposited onto CdS layers from 3N purity CdTe powder. The substrate was fixed at a distance of 7 mm from the source material, while the source and substrate temperatures were kept at 600 and 450 ^{o}C respectively.

Every sample passes two post-deposition steps: heat-treatment primary oxychloride activation and secondary thermal treatment procedure. After deposition the CdTe/CdS/FTO/glass samples were soaked in a saturated $CdCl_2$ methanol solution for 1 h followed by a 30 min heat treatment in air at 420 ^{o}C in a two-zone tube furnace ($CdCl_2$:O_2 activation step). These activated samples were rinsed in deionized water and etched in standard H_3PO_4:HNO_3:H_2O (NP) solution to remove chloride and oxide residues. After $CdCl_2$:O_2 activation a secondary thermal annealing was carried out in a quartz process tube in stationary atmosphere of N_2 + 10 vol. % H_2 gas at 200, 250, 300, 350 and 400 ^{o}C. The furnace was slowly heated up to the set temperature allowing the residual precipitates to out-diffuse to the CdTe surface.

Finally, a Te/Ni back contact was applied by thermal evaporation. The tellurium prior to back contact formation represents a heavily doped (p+) film at the back surface of CdTe absorber which aim is to reduce or to moderate the width of Schottky barrier adjacent to the contact.

Morphology of the CdTe film and CdS/CdTe cross-section was investigated by scanning electron microscopy (SEM) ZeissEVO-MA15 at an operating voltage of 10 kV, while the elemental composition was analyzed by energy-dispersive X-ray spectroscopy (EDX) with the Röntec EDX XFlash 3001 detector and Oxford Instruments INCA Energy system. Photoluminesence (PL) was measured at room temperature by excitation with a green laser (532 nm) at 10 mW density of excitation. Spectra were measured on a Renishaw-type device from the glass (CdS) side and from the back (CdTe) side of the CdTe/CdS structures. Solar cells were characterized by current–voltage measurements under AM1.5 simulated standard test conditions. The dispersed light from the Xe lamp, incident on the solar cell as monochromatic light was optically chopped at 30 Hz.

3. RESULTS AND DISCUSSION

When excitation and PL measurement are performed from the back contact side, near-bandgap PL emission spectra (Fig. 1a) demonstrate a maximum at 1.50 eV. The main defects which form the 1.5 eV PL band here are substitutional chlorine Cl_{Te} (donor) and complex V_{Cd}-Cl_{Te} (acceptor) [6]. PL emission spectra are similar to those observed by others for CdTe films [7]. The shape of PL emission lines is rather complex but are the same for samples 1–4, suggesting that the dominant recombination mechanism does not change with increasing temperature of thermal annealing in $N_2 + H_2$. However, the intensity of 1.5 eV peak systematically decreases with the increase of treatment temperature up to 400 ^{o}C. This indicates that the chlorine impurities are removed from the CdTe films [6] at increasing temperature of treatment in $N_2 + H_2$. An out-of-trend behavior is observed for PL spectrum of the sample treated at 200 ^{o}C in $N_2 + H_2$. Moreover, the same CdS/CdTe structure is described by a darkened color of the Ni back contact.

When excitation and PL measurement were performed from the glass side of the CdS/CdTe structure yield a much higher signal in comparison to the back contact side while the PL spectra look different (Fig. 1b). In addition to 1.50 eV CdTe peak, there is a stronger peak at 1.44–1.45 eV attributed to CdS_xTe_{1-x} [7]. The intensity of 1.44 eV peak increases with temperature of treatment which confirms the well-known fact of sulfur diffusion into CdTe film at increasing temperatures [8]. The third wide peak at ~1.7 eV in the Fig. 1b corresponds to the neutral complex $(V_{Cd}2Cl_S)^o$ in CdS and serves as an analytical tool for the chlorine detection in CdS films [9]. In accordance to the 1.5 eV PL peak, the 1.7 eV peak confirms the removal of chlorine impurities from CdTe in the process of thermal treatment in $N_2 + H_2$ ambient. However, too low intensity of the 1.7 eV PL peak for the sample treated at 200 ^{o}C may correspond to the “concentration quenching” – a typical phenomenon in PL for CdS at high concentrations of dopant when donor-acceptor pairs create neutral complexes [10].

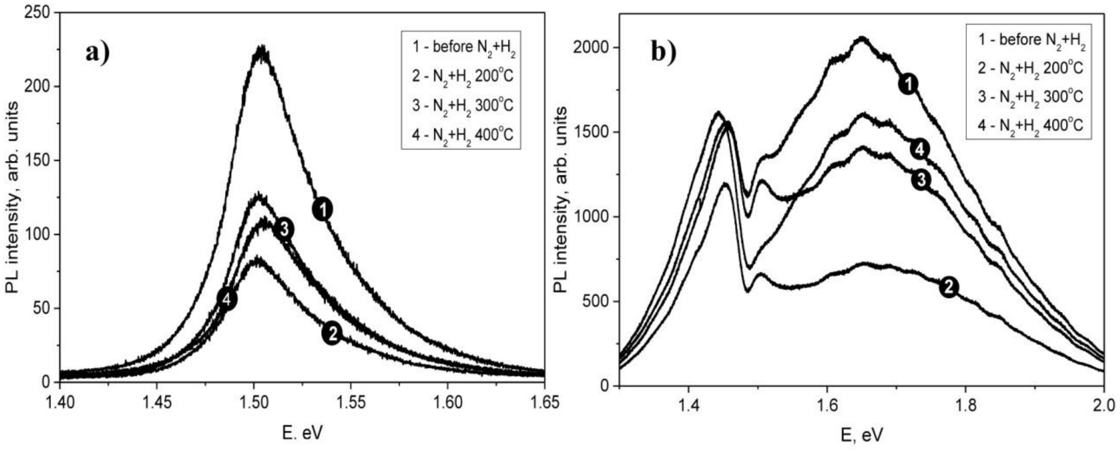

Fig. 1. Photoluminescence spectra of glass/FTO/CdS/CdTe structures thermally treated in N_2+H_2 ambient at different temperatures. The measurements were made from CdTe side (a) and from glass side (b)

In order to clarify the darkened back contact of the CdS/CdTe structure we analyzed the surface microstructure by means of SEM (Fig. 2). The $CdCl_2$:O_2 activation promoted the crystallization of CdTe grains and smoothed the film surface (Fig. 2a, 2b). During the NP etching, which is applied to enrich the CdTe surface with Te, a uniform Te film is formed on the CdTe surface and also at grain boundaries. This Te-rich surface of CdTe contributes to lower signals in comparison to the measurement from CdS side (Fig. 1a, 1b). After etching and N_2 + H_2 thermal treatment at 200 °C (Fig. 2c) the CdTe surface is covered by needle-shaped particles of Te (Table 1).

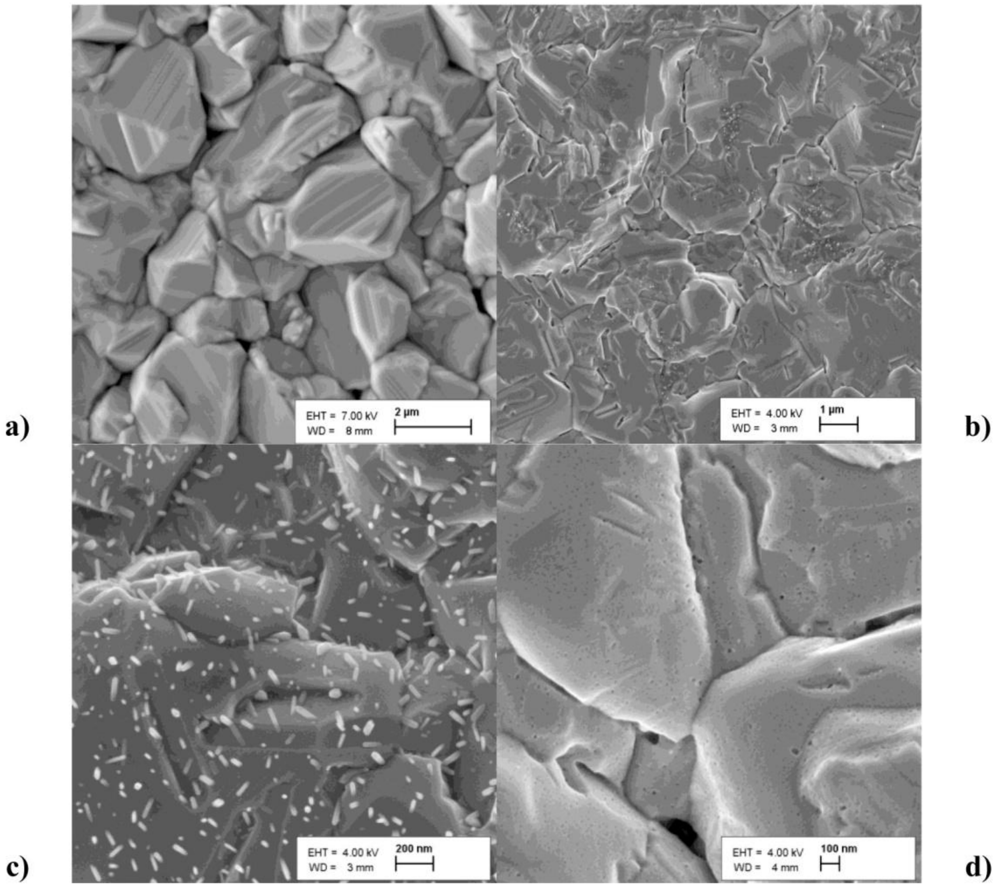

Fig. 2. SEM top view pictures of CdTe surface: after CdTe deposition (a), after $CdCl_2$:O activation (b), after N_2 + H_2 treatment at 200 °C (c) and 300 °C (d)

Table 1. Relative atomic concentrations of elements in CdS/CdTe structures

Samples	Cd (Atomic concentrations %)	Te (Atomic concentrations %)
As-deposited	51.85	48.15
After $CdCl_2$ heat treatment	50.46	49.48
Annealed at 200°C in $N_2 + H_2$	41.27	55.73
Annealed at 300°C in $N_2 + H_2$	52.64	47.36

We assume that during the heating at 200 °C Te on the surface and from grain boundaries starts to diffuse and agglomerate the extended line dislocation defects. The extended defect on CdTe surface represent the nucleation centers where the needle grow. The increased concentration of Te at the back side of CdTe acts as a blocking wall for the excitation beam during PL measurement and drastically decreases the intensity of 1.50 eV PL peak for 200 °C treated sample (Fig. 1a). At increased temperature (from 300 °C) the Te needles (20 nm diameter and 100 nm length) evaporate from CdTe surface, leaving behind a surface with dimples (Fig. 2d). Appearance of dimples with about~20 nm diameter might be due to the solubility of CdTe in solid phase of Te.

At high concentration of chlorine the concentration of $V_{Cd}2Cl_{Te}$ complexes increases and the excess of Cl_{Te} abruptly decreases the p-type conductivity of CdTe [11]. PL analysis demonstrated that we can decrease the concentration of chlorine impurities by means of thermal treatment of CdS/CdTe structures in N_2 + H_2 ambient (Fig. 1). In result the photovoltaic parameters of CdS/CdTe solar cells should be improved. However, the current-voltage characteristics of CdS/CdTe solar cell demonstrate the opposite (Fig. 3).

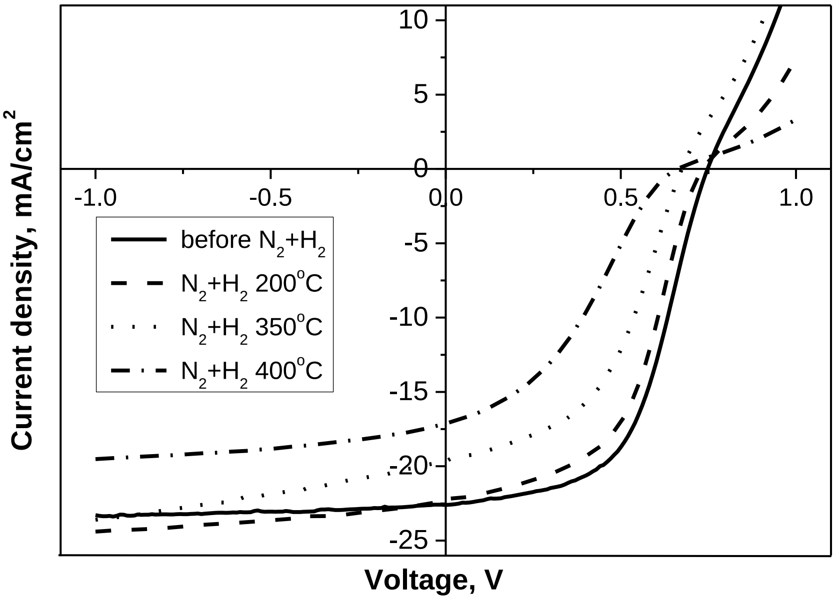

Fig. 3. Current-voltage characteristics of CdS/CdTe solar cells thermally treated in N_2 + H_2 ambient at different temperatures

The solar cell that did not pass any thermal treatment after the oxychlorine activation show high performance (Table 2). Although the concentration of chlorine impurities was decreased, additional processes, such as intermixing at CdS/CdTe interface (Fig. 1b) and formation of Te needles at the back side of the CdTe (Fig. 2c), seem to be responsible for the worsening of solar cells characteristics. Additionally, we should take into account the presence of cadmium oxychloride residuals ($CdO{\cdot}CdCl_2$) appeared at the grain boundaries as a result of reaction between $CdCl_2$, O_2 and CdTe [4].

Table 2: Photovoltaic parameters of CdS/CdTe solar cells treated in $N_2 + H_2$ ambient at different temperatures

$T_{treatm.}$, (°C)	V_{oc} (mV)	**J_{sc} (mA/cm^2)**	**FF (%)**	**Eff (%)**
–	750.0	22.2	55.0	9.1
200.0	740.0	21.9	51.0	8.3
250.0	730.0	22.4	56.0	9.2
300.0	730.0	22.6	58.0	9.6
350.0	680.0	19.0	48.0	6.3
400.0	660.0	16.0	35.0	3.7

We apply the thermal treatment in the presence of hydrogen gas in order to remove the oxygen which tend to retain an excess chlorine in the crystalline lattice of both CdS and CdTe. Reaction between hydrogen and $CdO{\cdot}CdCl_2$ on grain boundaries results in removal of oxygen by water evaporation, but also in formation of metallic Cd (1). This metallic Cd decreases the concentration of V_{Cd} thereby reducing CdTe conductivity and the intensity of 1.5 eV PL band (Fig. 1a). With increasing annealing temperature this process occur deeper in the CdTe film and the increased resistance of CdTe worsen all photovoltaic parameters (Table 2). Due to the fluctuation of the Te-rich layer on the CdTe surface (Fig. 2) the roll-over of the current-voltage characteristics becomes more acute (Fig. 3) with increasing temperature of treatment.

$$CdO{\cdot}CdCl_{2(s)} + H_{2(g)} \rightarrow CdCl_{2(s)} + H_2O_{(g)} + Cd_{(s)}. \quad (1)$$

4. CONCLUSIONS

In this work we studied the effect of thermal treatment in N_2+H_2 ambient on structural and optoelectronic properties of $CdCl_2$:O_2 activated CdTe/CdS thin film solar cells. The $CdCl_2$:O_2 activation promotes the crystallization of CdTe grains whereas the post-activation treatment in N_2 + H_2 at 200 °C covers the CdTe surface by needle-shaped particles of Te. We assume that during the heating Te agglomerates on the CdTe surface. When the process temperature reaches 300 °C ,these Te needles evaporate leaving a dimpled CdTe surface.

The photoluminescence measurements demonstrate that the goal of removing chlorine impurities from the CdTe films by means of thermal treatment in N_2+H_2 ambient was achieved. However the current-voltage characteristics of CdS/CdTe solar cell demonstrate worsened performance. We assume that processes such as interdiffusion at CdS/CdTe interface and formation of Te needles at the back side of CdTe could be responsible for the decrease of solar cell parameters. Moreover, the hydrogen from treatment ambient reacts with $CdO{\cdot}CdCl_2$ on grain boundaries removing the oxygen by water evaporation and forming a metallic Cd. This Cd precipitate decreases the concentration of V_{Cd} thereby reducing CdTe P-type conductivity and the intensity of 1.5 eV PL band.

Although the removal of chlorine impurities from the CdTe films did not improve the solar cell performance, we managed to understand the processes going on during the N_2 + H_2 treatment from 200 °C to 400 °C. As a further work, we plan to optimize the post-activation treatment of CdTe solar cell.

5. REFERENCES

1. M.A. Green, K. Emery, Y. Hishikawa, W. Warta, E.D. Dunlop, Solar cell efficiency tables (version 46), Prog. Photovolt: Res. Appl. 23 (2015) 805–812.
2. S. Girish Kumar, K.S.R. Koteswara Rao, Physics and chemistry of CdTe/CdS thin film heterojunction photovoltaic devices: fundamental and critical aspects, Energy Environ. Sci. 7 (2014) 45–102.
3. D. W. Niles, D. Waters and D. Rose, Chemical reactivity of $CdCl_2$ wet-deposited on CdTe films studied by X-ray photoelectron spectroscopy, Appl. Surf. Sci. 136 (1998) 221–229.
4. T.A. Gessert, M.J. Romero, C.L. Perkins, S.E. Asher, R. Matson, H. Moutinho, D. Rose, Microscopic analysis of residuals on polycrystalline CdTe following wet $CdCl_2$ treatment, Mat. Res. Soc. Symp. Proc. 668 (2001) H1.10.1–6.
5. N. Spalatu, J. Hiie, V. Valdna, M. Caraman, N. Maticiuc, V. Mikli, T. Potlog, M. Krunks, V. Lughi, Properties of the $CdCl_2$ air-annealed CSS CdTe thin films, Energy Procedia 44 (2014) 85–95.
6. V. Valdna, p-Type doping of CdTe, Solid State Phenom. 67-68 (1999) 309-314.
7. D. Kuciauskas, A. Kanevce, J.N. Duenow, P. Dippo, M. Young, J.V. Li, D.H. Levi, T.A. Gessert, Spectrally and time resolved photoluminescence analysis of the CdS/CdTe interface in thin-film photovoltaic solar cells, Appl. Phys. Lett. 102 (2013) 173902.
8. B.E. McCandless, M.G. Engelmann, R.W. Birkmire, Interdiffusion of CdS/CdTe thin films: Modeling x-ray diffraction line profiles, J. Appl. Phys. 89 (2001) 988–994.
9. M. Weber, J. Krauser, A. Weidinger, J. Bruns, C.-H. Fischer, W. Bohne, J. Röhroch, R. Scheer, Hydrogen impurities in chemical bath deposited CdS, J. Electrochem. Soc. 146 (1999) 2131–2138.
10. W.M. Yen, S. Shionoya, H. Yamamoto, Phosphor Handbook (2nd edition), CRC Press, Boca Raton FL, p. 247–282.
11. V. Valdna, Optoelectronic properties of chlorine- and oxygen-doped CdTe thin films, Sol. Energy Mater. Sol. Cells 87 (2005) 369–373.

CYSENI 2016, May 26-27, Kaunas, Lithuania
ISSN 1822-7554, www.cyseni.com

NUMERICAL INVESTIGATION OF CRITICAL STRESS INTENSITY FACTOR

R. Janulionis, G. Dundulis, A. Grybėnas
Lithuanian Energy Institute
Breslaujos str. 3, LT-44403 Kaunas – Lithuania
Email: remigijus.janulionis@lei.lt

ABSTRACT

The main task of fracture mechanics is to evaluate constructions resistance to fracture. The resistance to fracture can be reduced by the change of material properties or by developing cracks. When the metal is ageing under certain conditions the crack can appear what finally could lead to the failure of construction. To evaluate the resistance to fracture of the constructions with cracks usually the fracture criterions are used. One of such criterion used to evaluate brittle fracture is stress intensity factor. Calculated value of failure criteria in construction with crack is compared with its critical value for the material the construction is made of. The critical values of stress intensity factor for the materials are usually experimentally determined. This article presents the methodology for the calculation of critical stress intensity factor using numerical methods. For this purpose, the Finite Element (FE) method was used as numerical method and ABAQUS as FE code.

In this investigation the critical stress intensity factor of steel P91 was calculated and the results were compared with experiment. Numerically determined critical stress intensity factor has good coincidence with experiment results. Therefore, the presented methodology can be used for estimation of critical stress intensity factor.

Keywords: finite element method, critical stress intensity factor

Acknowledgments. This research was funded by a grant (No. MIP-023/2014) from the Research Council of Lithuania.

1. INTRODUCTION

Traditional approach in structural design and material selection is when design stress is compared to mechanical properties such as yield or tensile strength of candidate material. The material is assumed to be adequate if its strength is greater than the applied stress. Such approach together with imposed safety factor is widely used in construction designing. The approach is good for the constructions and materials with minor imperfections. However, if the construction has a flaw fracture mechanic approach has to be used. It has three important variables such as applied stress, flaw size and fracture toughness. Fracture mechanics quantifies the critical combinations of these three variables [1].

There are two types of fracture. The first is when large residual stresses are produced and the second when residual stresses are small or none. According to this the fracture is called ductile or brittle. Depending on what fracture type is analysed one of two corresponding fracture theories are used [1]:

- linear elastic fracture mechanics (LEFM);
- elastic-plastic fracture mechanics (EPFM).

LEFM refers to linear elastic material behaviour when plastic strain is possible in small areas and close to crack tip. The stress intensity factor (SIF) is the parameter used in LEFM. SIF depends on construction shape and sizes and place of crack. SIF can be calculated by the following expression:

$$K = \sigma\sqrt{\pi a} \cdot f\,, \qquad (1)$$

where:

σ – nominal stress, Pa;
a – crack size, m;
f – non-dimensional function of load and geometry of construction and crack.

EPFM is not limited by plastic strain and it can be produced in whole section of analysed construction. Crack tip opening displacement (CTOD) and J-integral are the parameters used to describe the conditions of crack tip in elastic-plastic materials and each can be used as fracture criterion.

To use SIF, CTOD or J-integral as a criterion it is necessary to determine their critical values. Usually it is done by experiment and the procedures are described in standards such as ASTM, ISO and etc. However it is not always possible to conduct an experiment. Sometimes it is required to test the specimen in certain environment which cannot be achieved in the laboratory, the material can be irradiated or even the volume of the sample material can be an issue because the machined specimens should be of certain size. Therefore alternative methods for determination of critical values of fracture parameter are necessary. Usually finite element method (FEM) is used as alternative method. A number of papers can be found on fracture parameters calculation using FEM [2-3]. However these papers do not present the methodology of determination of critical fracture parameter and only limited amount of papers can be found which discuss the current issue. For example, Nazmus Sakib A.R. and Ashfaq Adnan [4] investigate the critical stress intensity factor dependency on size. However the authors investigate nanofilm using nanoscale models. This article presents the methodology for the calculation of critical stress intensity factor using FEM and standard Compact Tension (C(T)) specimen size models.

2. METHODOLOGY

The idea of numerical investigation of critical stress intensity factor is numerically simulate the experiment according to actual procedures/instructions used for experiment conduction. For this purpose instructions described in ASTM E399 standard [5] were used and computer code ABAQUS v6.11 [6] which uses finite element method (FEM) has been chosen for numerical simulation. ASTM E399 instructions for critical stress intensity factor determination are presented in the following section.

2.1. Instructions for critical stress intensity factor determination

According ASTM E399, to determine critical stress intensity factor K_{IC} in the first place it is necessary to determine so called conditional stress intensity factor K_Q. After K_Q is determined and if yield strength, specimen size and K_Q meet ASTM E399 conditions it is possible to state that $K_Q = K_{IC}$. To determine K_Q the tension load vs. crack opening displacement (COD) curve has to be constructed. This curve is used for load P_Q determination at which stress intensity factor reach K_Q value. For this purpose in the tension load vs. COD curve (see Fig. 1) the line OP_5 through the origin of the test record with slope $(P/v)_5$ $K = \sigma\sqrt{\pi a} \cdot f = K = \sigma\sqrt{\pi a} \cdot f$ $0.95(P/v)_O$, where $(P/v)_O$ is the slope of the tangent OA to the initial linear part of the curve has to be drawn. The load P_Q is then defined at intersection point between curve and line $(P/v)_5$ for the curve TYPE I. For the other curve types the load P_Q is determined at the first vertex of the curve.

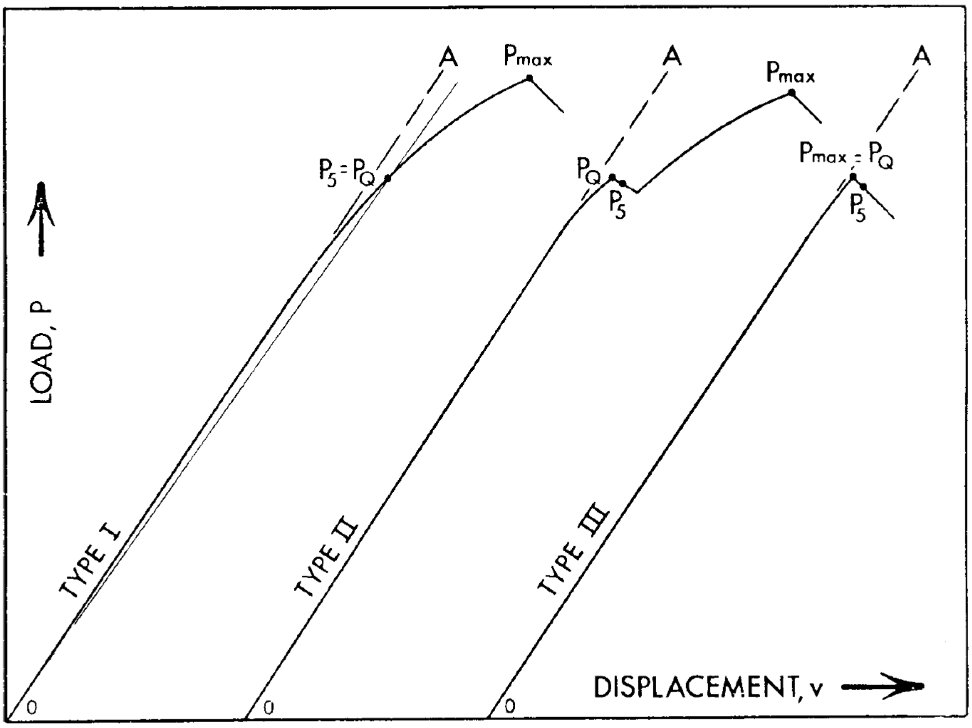

Fig. 1. Principal types of load vs. crack opening displacements curves and determination of P_Q according to ASTM E399

When the load P_Q is determined the conditional stress intensity factor K_Q for C(T) type specimen can be analytically calculated using the following equation:

$$K_Q = \left(P_Q / BW^{1/2}\right) \cdot f\left(a/W\right), \tag{2}$$

where:

$$f\left(a/W\right) = \frac{\left(2+\frac{a}{W}\right)}{\left(1-\frac{a}{W}\right)^{3/2}} \cdot \left[0.886 + 4.64\left(\frac{a}{W}\right) - 13.32\left(\frac{a}{W}\right)^2 + 14.72\left(\frac{a}{W}\right)^3 - 5.6\left(\frac{a}{W}\right)^4\right], \tag{3}$$

where:

P_Q – load at which conditional stress intensity factor KQ is reached, N,
B – specimen thickness, m,
W – specimen width (see Fig. 2), m,
a – crack length (see Fig. 2), m.

2.2. Numerical model

Finite element model of compact tension specimen was prepared for modelling of stress intensity factor. The mesh of the model is shown in Fig. 2. The dimensions of 2D FE model are the same as dimension of C(T) specimen used in the experimental testing. 2D FE model can be meshed with two type elements: CPE8R and CPS8R [6]. Both are 2D plane biquadratic 8 nodes elements; however one is evaluating plane strain and other plane stress state. Plane strain state means that strains are evaluated in 2 directions and stresses are evaluated in three directions while plane stress state is in opposite. This article present numerical SIF calculation using both, plane strain and plane stress states. The length of fatigue crack in FE model was the same as in C(T) specimen used in experiment and it was equal to a_1 = 1.8 mm (see Fig. 2).

Boundary conditions in the model were added to the Reference Points (RP) placed at the centres of the holes used for pins in experiment. The displacements of one RP were restricted in two directions, i.e. along the X and Y axes, and the other RP displacements were restricted only in X axis direction. The displacement along Y axis added to the last mentioned RP was used as load. As calculation results the following parameters were received: reaction force at the RP where displacement was added, crack opening displacement Δ*v* between points were extensometer was attached in experiment and SIF at crack tip.

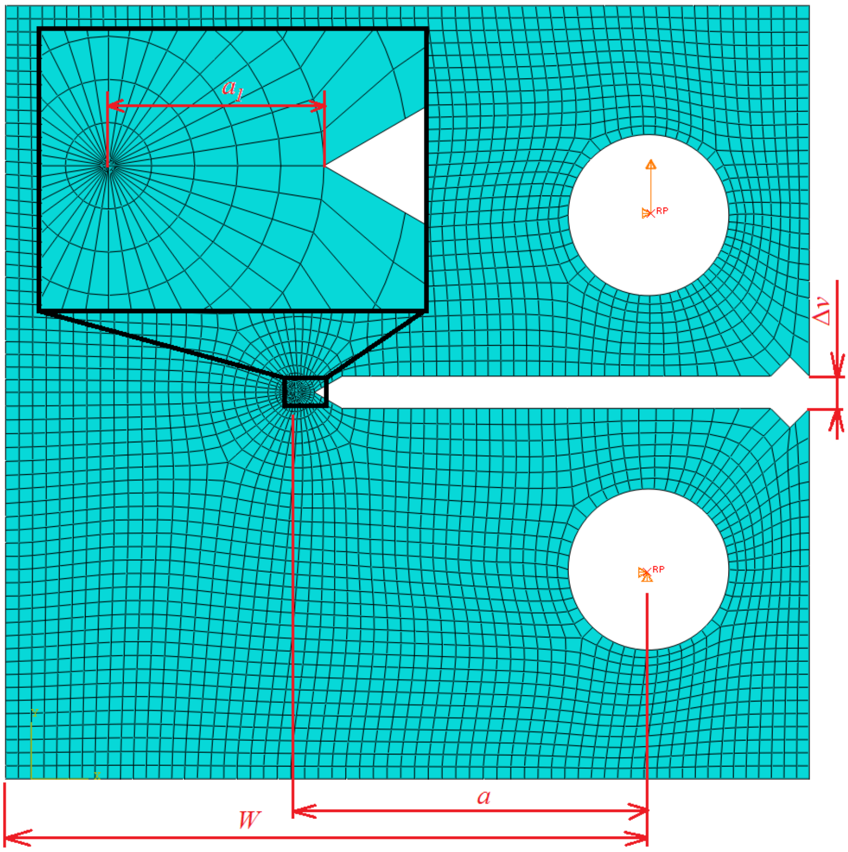

Fig. 2. Finite element mesh of C(T) specimen

It is very important to mesh the crack tip correctly for modelling of fracture parameters. It is recommended [6] to perform the analysis using rectangular shape elements created in circular pattern around crack tip. To create such mesh the nodes of one edge of elements closest to the crack tip have to be collapsed to a single node. Collapsing the nodes of one edge to the sing node we are getting the elements which still have 8 nodes but have triangle shape (see Fig. 2).

Experimentally and numerically investigated material was steel P91. Steel P91 is a ferritic-martensitic class steel. It has higher thermal conductivity, lower thermal expansion, high resistance to swelling and high thermal resistance comparing to austenitic stainless steels [7].

To describe the elastic part of the mechanical properties of material the following parameters have been entered:

- Young’s modulus E = 215 GPa;
- Poisson’s ratio υ = 0.3.

The plastic behaviour of the material was described by entering stress-strain curve shown in the Fig. 3.

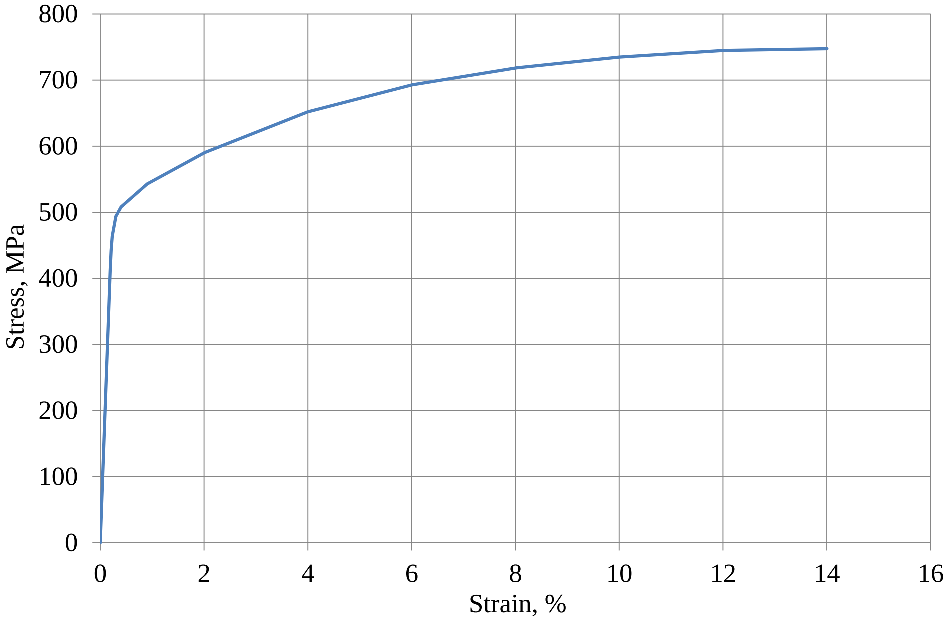

Fig. 3. Stress-strain curve of steel P91

To determine critical stress intensity factor using FEM the tension simulation of C(T) specimen is carried out twice:

- the first tension of CT specimen is carried out for construction of tension load vs. COD curve and load P_Q is determined;
- the second calculation is used for stress intensity factor vs. tension load curve construction and determination of K_Q value.

Running the first tension simulation, elastic-plastic material properties has to be used. However to construct stress intensity factor vs. tension load curve the simulation has to be carried out using only elastic properties of the material. It is due to the fact that SIF is the linear fracture mechanics parameter as it was described in section 1 and it can be calculated running linear FE analysis only.

3. CALCULATION RESULTS

When first calculation step was completed tension load vs. COD curve was obtained. The calculations were done for both plane strain and plane stress states. Calculation results were compared with experiment and presented in Fig. 4. This figure presents experiment results of three different specimens. The experiment results are very close to each other. As it is seen in the figure, compared to experiment results plane strain state overestimates and plane stress state underestimates the value of reaction force, meanwhile experiment curve lies almost in the middle of numerically constructed curves. So it was decided to draw a fourth curve which is an arithmetic average of plane strain and plane stress curves. According to the figure the average curve match the experiment quite well. The calculated values do not deviate from experimental results more than 4%.

The next step was to determine P_Q load. As the average curve had the best match with experimental curves this curve was chosen for determination of P_Q load. P_Q load was determined using the ASTM E399 procedure described in section 2.1 and determination itself is shown in Fig. 5.

Fig. 6 presents stress intensity factor vs. load lines. The lines were constructed for plane strain and plane stress states. These lines have overlapped ideally what means that SIF values for both states are the same. Therefore only one line for numerical simulations is presented. It was also analytically calculated stress intensity factor vs. load line and presented in Fig. 6. To calculate SIF analytically previously presented equations (1) and (2) were used. Comparing numerically constructed and analytically calculates lines it can be seen that lines do match very well. Analytically calculated SIF values deviate from numerically calculated just up to 0.55% at load value of 50 kN.

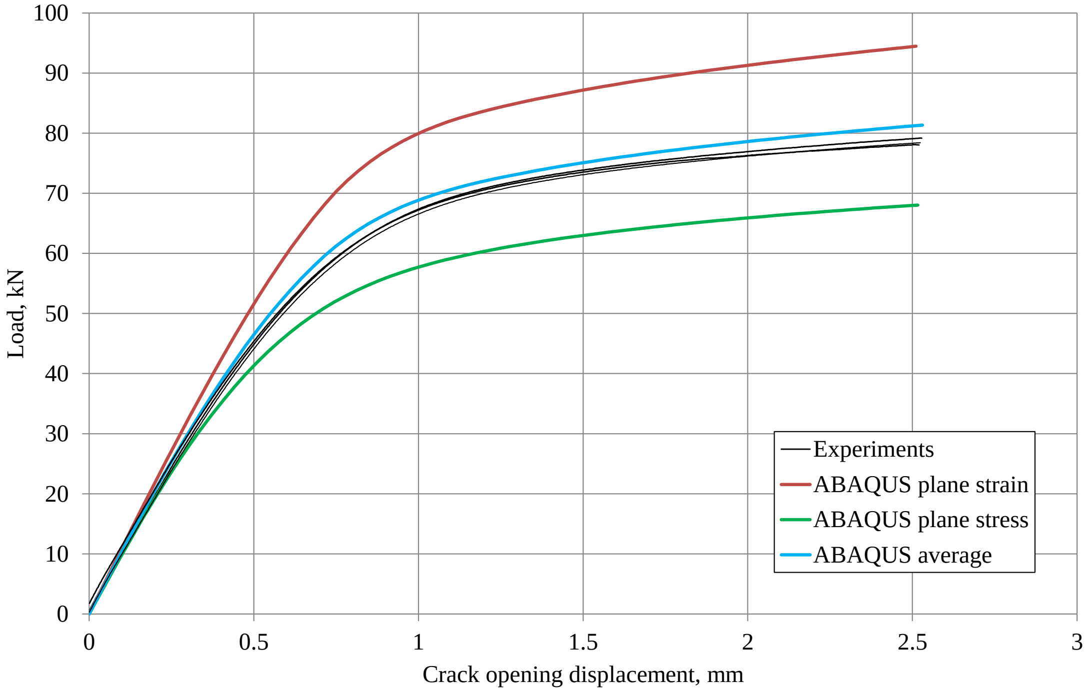

Fig. 4. Tension load vs. crack opening displacement curves for P91 steel C(T) (W = 50 mm) specimen

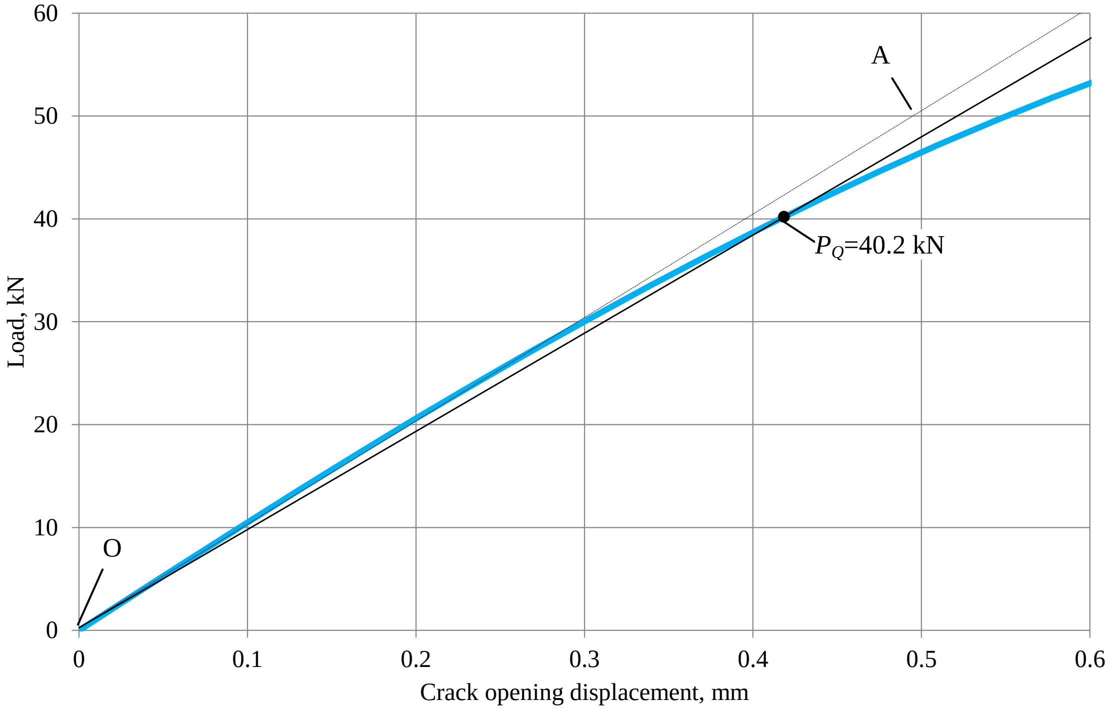

Fig. 5. Determination of P_Q load for average curve

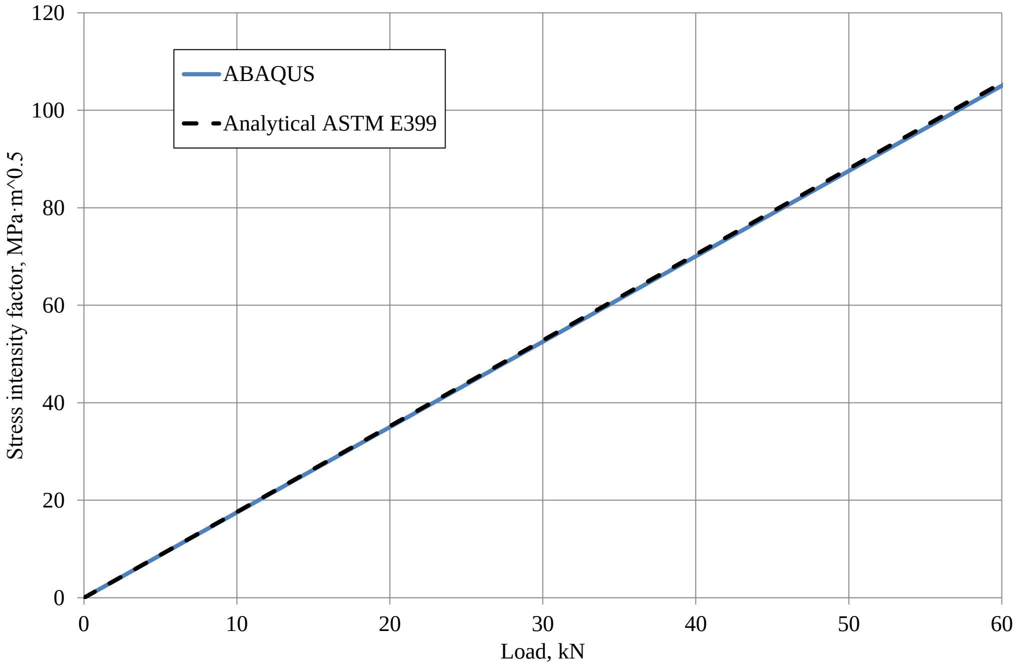

Fig. 6. Stress intensity factor vs. load

The comparison of results of numerically and experimentally determined P_Q and K_Q values are presented in Table 1. K_Q values for numerical simulation case were determined in two ways: analytically using equations (2) and (3) and using numerically constructed stress intensity factor vs. load line presented in Fig. 6.

Table 1. Numerical simulation and experimental results of P_Q and K_Q determination

Analysis case	**P_Q, kN**	**K_Q, MPa√m**	**Deviation from experiment, %**
ABAQUS, numerical K_Q	40.2	70.38	4.1–6.8
ABAQUS, analytical K_Q	40.2	70.76	3.6–6.3
Experiment	40.6–42.8	73.4–75.5	–

According to the results presented in the Table 1 the closer numerical prediction was obtained when K_Q was calculated analytically. It is because experimentally SIF was calculated using the same equations as in ABAQUS, analytical K_Q case while in ABAQUS, numerical K_Q case it was determined using numerically constructed SIF vs. load line which values are slightly lower. However the actual difference between numerically and analytically calculated K_Q is only 0.5%.

4. CONCLUSIONS

This article presents the methodology for numerical determination of critical stress intensity factor. As an example the determination of stress intensity factor K_Q of steel P91 was presented and obtained results were compared with experiment.

Numerical simulation and experimental results show that to predict tension load vs. crack opening displacement of C(T) specimen by 2D FE model, an arithmetic average of curves obtained by running plane strain and plane stress state analysis can be used. The calculated values of average curve do not deviate from experimental results more than 4 %.

Predicted stress intensity factor K_Q results compared with experiment deviate from 4.1% to 6.8% for the numerically calculated case and from 3.6% to 6.3% for the case when SIF is calculated analytically. As the difference between these calculation cases is only 0.5 percentage point the both ways to calculate K_Q are good to be used.

5. REFERENCES

1. ANDERSEN, T.L. *Fracture Mechanics. Fundamentals and Applications*. Boca Raton, Ann Arbor, Boston: CRC Press Inc, 1991. 793 p. ISBN 0-8493-4277-5.
2. ZARE, A., KOSARI, E. S. M., ASADI, I., BIGHAM, A., BIGHAM, Y. Finite Element Method Analysis of Stress Intensity Factor in Different Edge Crack Positions, and Predicting their Correlation using Neural Network method. *Research Journal of Recent Sciences*, 2014, Vol. 3(2), p. 69–73.
3. LIKEB, A., GUBELJAK, N., MATVIENKO, Y. Stress Intensity Factor and Limit Load Solutions for New Pipe–Ring Specimen with Axial Cracks. *Procedia Material Science*, 2014, Vol. 3, p. 1941–1946.
4. NAZMUS SAKIB, A.R., ASHFAQ ADNAN. On the size-dependent critical stress intensity factor of confined brittle nanofilms. *Engineering Fracture Mechanics*, 2012, Vol. 86, p. 13–22.
5. Annual book of ASTM standards. *Section 3: Metals Test Methods and Analytical Procedures*. West Conshohocken, PA, 1997. Vol. 03.01. 1116 p. ISBN 0-8031-2372-8.
6. ABAQUS/Standard User's Manual, Version 6.11.
7. IAEA. *Structural materials for liquid metal cooled fast reactor fuel assemblies — operational behaviour*. IAEA nuclear energy series No. NF-T-4.3, Vienna, 2012. 87 p. ISBN 978-92-0-131610-3.

CYSENI 2016, May 26-27, Kaunas, Lithuania
ISSN 1822-7554, www.cyseni.com

THE EFFECT OF SODIUM CHLOROPHYLLIN ON POLYVINYL ALCOHOL ELECTROSPUN NANOFIBER DIAMETERS

S. Jegina, A. Sutka, S. Kukle, Z. Zelca
Institute of Design Technologies, Riga Technical University
Kipsalas str. 6, LV-1048 Riga – Latvia
Email: sandra.jegina@edu.rtu.lv

ABSTRACT

The fiber diameter is the most important structural characteristic of electrospun nonwoven web and is crucial in the drug release process in medical applications. In order to make an electrospinnable solution using plant extracts, biocompatible polymers are used. Polyvinyl alcohol (PVA) is known as non-toxic biodegradable polymer, which is compatible with human tissues and widely used in biomedical applications. Sodium chlorophyllin (SChl) contains derivatives of "a" and "b" chlorophyll (chlorines, sodium salts of chlorophylline acids etc.), sodium salts of resinous acids (pimaric-, isopimaric-, abietic- and labdane types), sodium salts of fatty acids (mainly oleic-, stearic- and linoleic). Due to such composition SChl has bacteriostatic, regenerative and deodorant properties, which could be useful in biomedical applications. Several compositions of PVA solution in water (8 wt%) and different concentrations (1 – 5 wt%) of sodium chlorophyllin derived from spruce greenery were prepared. The viscosity and conductivity measurements of PVA/SChl solutions were performed before spinning. The diameters of electrospun fibers were evaluated quantitatively from atomic force microscope (AFM) images. PVA/SChl nanofiber composites with different concentrations of sodium chlorophyllin (1wt%, 3 wt% and 5 wt%) were analyzed in the research. Also pure PVA solution and nanofiber web were tested in order to evaluate the effects of added sodium chlorophyllin.

Keywords: needleless electrospinning, nanofibers, sodium chlorophyllin, polyvinyl alcohol

1. INTRODUCTION

Needleless electrospinning is a simple, yet versatile method of creating polymer-based non-woven nanofiber web [1]. Needleless or nozzle-less electrospinning is characterized by high productivity and scalability, high fiber diameter and web uniformity, economical operation and easy maintenance, as well as flexibility in used polymers and substrates [2].

The quality of the nanofiber web depends on the viscosity, electrical conductivity, molecular weight, concentration, and surface tension of the polymer solution, as well as on the applied voltage, the distance between electrodes and the rotation speed of the electrode [3].

In electrospun nonwoven webs fiber diameter is the most important structural characteristic. In medical application fiber diameter is crucial in the drug release process [4]. In order to substitute chemical drugs with natural alternatives, the possibility of using plant extracts in electrospinning researched continually all over the world. Biocompatible polymers are used for making the electrospinnable solutions with integrated plant extracts [5] [6]. There are numerous studies showing promising results of using PVA in wound dressing applications [7]. PVA has biodegrable, biocompatible and noncarcinogenic characteristics, it is blendable with natural and synthetic polymers and improves physicochemical and mechanical properties of obtained polymeric materials [8]. The aim of combining nanotechnology and herbal extracts is to improve bioavailability of the active ingredients and to decrease toxicity [9], as well as to reach the level of large scale production of the final product. Scientists have discovered a long time ago the similarities in human organism and the living parts of plants such as blood haemoglobin haem and plants chlorophyll (Fig. 1). Positive results have been shown in preventing deficit of these compounds with herbal products [10].

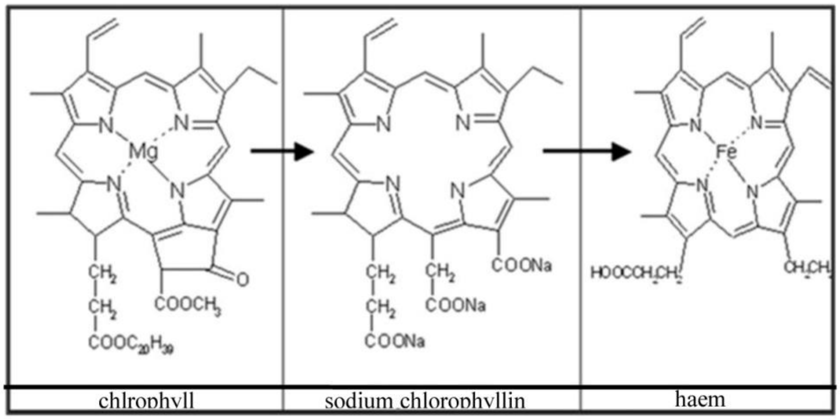

Fig. 1. Similarity in chlorophyll, sodium chlorophyllin and haemoglobin haem [11]

One of the ways to achieve sustainability of the manufacturing process is to utilize locally grown plants. In this paper the effect of locally harvested spruce greenery derived sodium chlorophyllin on polyvinyl alcohol electrospun nanofiber diameter parameters is analyzed.

2. MATERIALS AND METHODS

2.1. Preparation of spinning solution

PVA (10849 Aldrich Mowiol® 28–99 Mw ~145,000) was dissolved in distilled water (concentration 8 wt%). The solution was made using heating magnetic stirrer AREC, Velp Scientifica. For obtaining homogenous solution, applied temperature was 120–135 °C at 1000 rpm. Stirring time – 2 hours.

Sodium chlorophyllin ($C_{32}H_2CN_4Na$ or SChl; manufacturer – Joint Stock Company “Biolat”, Latvia; lot No. 6, year 2014; obtained from spruce greenery of locally grown *Picea abies (L.) H.Karst.*) was also dissolved in distilled water (concentrations 1 wt%, 3 wt% and 5 wt%) using the magnetic stirrer. In order to avoid any possible loss of the active ingredients, no heating was applied. Stirring time – 30 minutes at 1000 rpm.

As shown in Table 1, four samples of spinning solution were prepared.

Table 1. Samples of prepared PVA and sodium chlorophyllin spinning solutions

Sample	**Composition**	**$C_{32}H_2CN_4Na$ content wt%**
1	PVA (8 wt%)	0
2	PVA (8 wt%) and SCh	1
3	PVA (8 wt%) and SCh	3
4	PVA (8 wt%) and SChl	5

2.2. Viscosity and conductivity measurements of the solution

Viscosity and conductivity measurements of PVA and SChl solutions were performed before subjection to electrospinning process.

For the solution to be spinnable, viscosity of the solution should be within 100–2000 millipascal-seconds (mPa-s). Viscosity was measured using HAAKE Viscotester 6 plus thermo with following parameters – 12 rpm, measurement range up to 2500 mPa-s, temperature 20 ±0.5 °C.

Conductivity was measured by WinLab® Data Line Conductivity meter as a solution electroconductivity is a precondition of the spinning process stability and fibres web structure quality.

2.3. Electrospinning

Electrospinning was performed on Nanospider™ LAB 200 (Elmarco, Czech Republic). The scheme of electrospinning setup is shown in Fig. 2. The cylindrical electrode has to be fully covered with the solution before applying voltage. It is achieved by starting rotation process first. The roller speed plays important role in electrospinning. If the speed is too low, Taylor cones don‘t form due to insufficient amount of solution on the electrode surface. If the speed is too high, Taylor cones can‘t form due to short time. Both cases affect spinning performance, therefore to ensure higher production rate correct roller speed has to be considered [3].

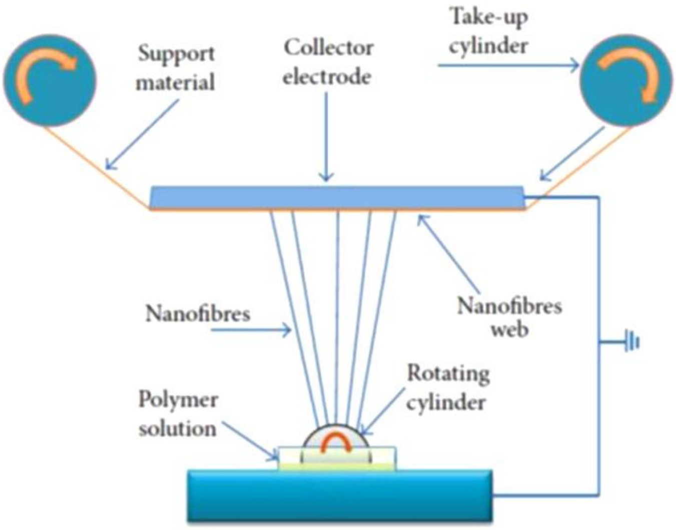

Fig. 2. The scheme of electrospinning setup [12]

When the electrode is evenly covered with the solution, appropriate voltage is applied and the electrospinning process begins. For the solvent to evaporate and for the nanofibers to solidify on substrate material, the distance between electrodes has to be set properly [12].

Electrospinning parameters of all prepared polymer solutions is shown in Table 2.

Table 2. Parameters of electrospinning

Distance between electrodes (cm)	**Applied voltage (kV)**	**Roller speed (rpm)**	**Temperature (Cº)**
16	65	4	19

The benefits of electrospinning in production of wound-dressing materials are protection of wound from infection and dehydration oxygen permeation and scaffold with more homogeneity [14].

2.4. Atomic force microscopy (AFM)

Atomic force microscope Dimension Edge Veeco (Bruker, USA) with silicone cantiliver OTESPA-R3, f0 = 300 kHz, k = 26 N/m in tapping mode was used for evaluation of the PVA/SChl nanocomposite nanofiber mat and measuring fiber diameters.

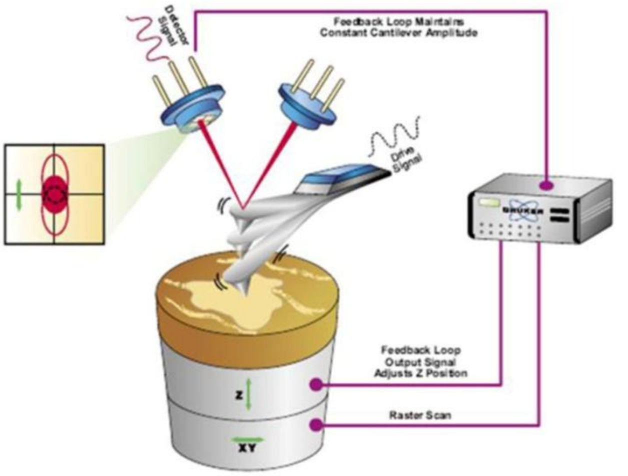

Fig. 3. AFM tapping mode [14]

3. RESULTS AND DISCUSSION

Measurements of solution properties (Table 3) show that with increase of concentration of SChl viscosity decreases due to interaction of PVA and SChl, but conductivity increases due to sodium salts of resinous acids and sodium salts of fatty acids of SCh [15].

Table 3. PVA and sodium chlorophyllin solution properties

Sample	Viscosity (mPa-s)	Conductivity (µS/cm)
PVA (8 wt%)	673	324
PVA (8 wt%) and SCh (1 wt%)	645	1163
PVA (8 wt%) and SCh (3 wt%)	593	2710
PVA (8 wt%) and SCh (5 wt%)	562	3868

The average fiber diameter was determined by measuring their diameters in AFM images at 100 places using Dimension Edge Vecco in-built software. As shown in Fig. 4, diameters of electrospun nanofibers tend to decrease non-linear when concentration of SChl is increased. As shown in Fig. 4, PVA 8 wt% electrospun nanofibers have the biggest diameter compared to other samples, while PVA/SChl 5 wt% nanocomposite nanofibers have the smallest diameter.

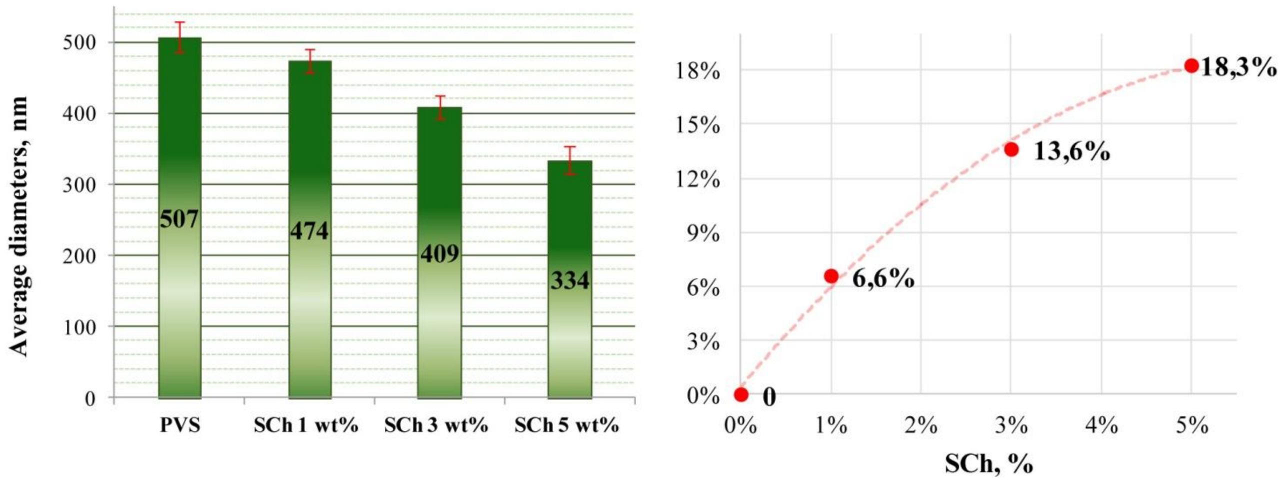

(a) (b)

Fig. 4. Average diameters of the electrospun nanofibers (a) and % rate of diameters decrease (b)

The rate of diameter decrease with the growth of sodium chlorophyllin concentration could be characterized by equation(1):

$$D = 0{,}0035 + 6{,}091x - 50{,}597\,x^2, \qquad (1)$$

where x – SCh concentration in spinning solution.

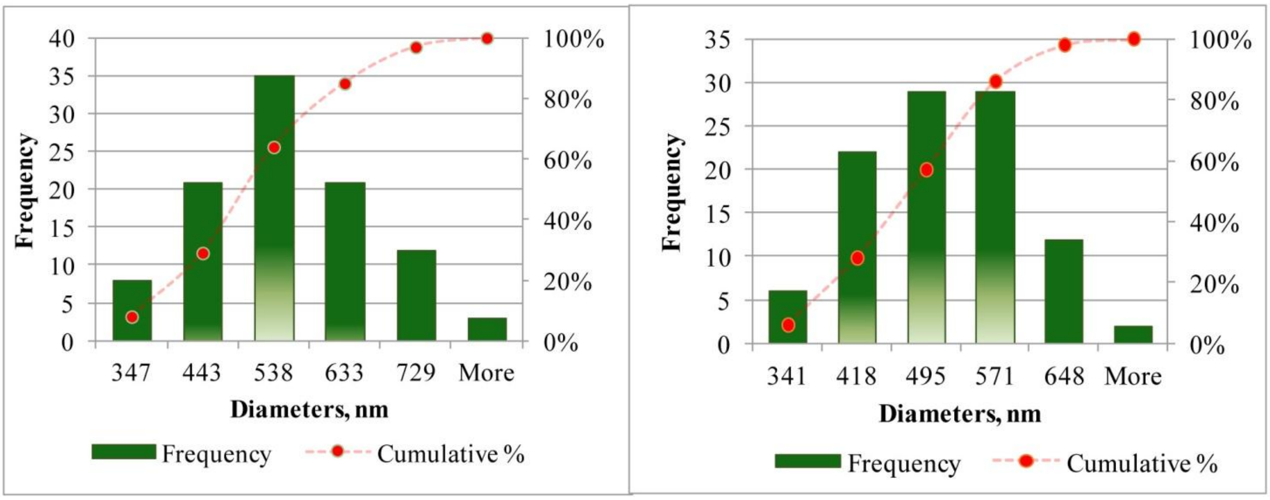

(a) (b)

Fig. 5. Nanofiber diameters of (a) PVA 8 wt% and (b) PVA+ SChl 1 wt%

Evaluation of pure PVA 8 wt% nanofibers shows that the most frequent diameter sizes are found in a range from 490 to 586 nm, with the mode 538 and average 507 nm; 64 % fibers diameters do not exceed 538 nm (Fig. 5 a).

Diameters distribution of composite PVA 8 wt%/SCh 1 wt% fibers is slightly moved to the smaller diameters, show wide modal diameters interval from 456 to 609 nm vith the average 474 nm and 58% fibers included (Fig. 5 b).

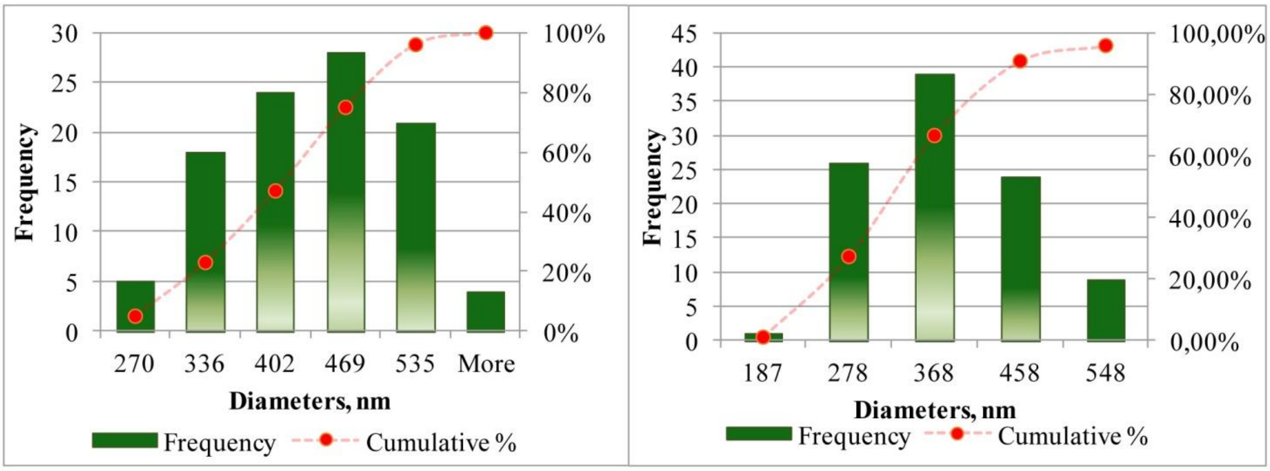

(c) (d)

Fig. 6. Nanofiber diameters of (c) PVA+ SChl 3 wt% and (d) PVA+ SChl 5 wt%

It is seen from PVA 8 %wt/SChl 3 wt% diameters distribution graph (Fig. 6 c) that modal diameter 469 nm differs from average value 409 nm by 15% and median 479 nm by 17% witnessed about distribution left asymmetry. Compare to the both previous variant diameters distribution range is shifted to the smaller diameters.

Distribution of PVA 8 wt%/SCh 5 wt% composite (Fig. 6 d) diameters had became almost symmetrical as seen from graph and average diameter 334 nm placement between median (320 nm) and modal (368 nm) diameters testify about symmetry as well. The average diameter of PVA 8 wt% /SCh 5 wt% composite fibers decreases by 34% compared to average diameter of PVA fibers.

4. CONCLUSIONS

The studies have shown that from PVA/sodium chlorophyllin solutions in proper concentrations nanofiber webs could be produced.

Concentrations of SChl in the range from 1 wt% to 5 wt% have the ability to influence the viscosity and especially conductivity of the PVA based spinning solution.

Diameters of electrospun composite nanofibers decrease with the increase of sodium chlorophyllin concentration and become more symmetrical with larger concentrations as with added SChl decreases viscosity and increases conductivity of spinning solution.

The smallest diameter (187 nm) was obtained from tested solution with 5 wt% SChl concentration.

5. REFERENCES

1. LI, D.; XIA, Y.; Electrospinning of Nanofibers: Reinventing the Wheel? *Advanced Materials*, 2004, Vol. 16, No. 14, p. 1151–1170.
2. *Nanospider™ Electrospinning Technology*. Liberec (Czech Republic): ELMARCO s.r.o. [referred on the 15th of February in 2016 y.]. Link to the internet <http://www.elmarco.com/electrospinning/electrospinning-technology/>
3. YENER, F.; New methods in the study of roller electrospinning mechanism. Summary of the thesis. Liberec: Technical University of Liberec. 2014. [referred on the 15th of February in 2016 y.]. Link to the internet <http://www.ft.tul.cz/document/240>.
4. HRIB, J.; SIRC, J.; HOBZOVA, R. et al. Nanofibers for drug delivery – incorporation and release of model molecules, influence of molecular weight and polymer structure. *Beilstein Journal of Nanotechnology*, 2015, Vol. 6, p. 1939–1945.
5. VENUGOPAL, J.; SREEPATHY, S.; RAMAKRISHNA, S. Electrospun plant-derived natural biomaterials for Tissue engineering. *Plant Science Today*, 2014, Vol. 1, No. 3, pp. 151–154.
6. RAMAKRISHNA, S. Polymer Nanofibers in Medicine, Biotechnology & Engineering. International Congress of Nanotechnology 2004. San Francisco (CA). 2004 November 7–10. [referred on the 15th of February in 2016 y.]. Link to the internet <http://www.ianano.org/Presentation/Ramakrishna-NUS-11-10-GW3.pdf>.
7. ABRIGO, M.; McARTHUR, S. L.; KINGSHOTT, P. Electrospun Nanofibers as Dressings for Chronic Wound Care: Advances, Challenges, and Future Prospects. *Macromolecular Bioscience*, 2014, Vol. 14, No. 6, pp. 772–792.
8. KAMOUN, ELBADAWY, A.; CHEN, X.; MOHY ELDIN, M.S.; KENAWY, El-Refaie S. Crosslinked poly(vinyl alcohol) hydrogels for wound dressing applications: A review of remarkably blended polymers. *Arabian Journal of Chemistry*, 2015, Vol. 8, No. 1, pp. 1–14.
9. SAHU, A.N. Nanotechnology in herbal medicines and cosmetics. *International Journal of Research in Ayurveda & Pharmacy*, 2013, Vol. 4, No. 3, p. 472–474.
10. SIKSNA, S.; DABERTE, I.; BARENE, I.; IRISTE, V. Coniferous greenery – valuable natural raw material of biologically active substances. *Medicinos teorija ir praktika (Theory and Practice in Medicine)*, 2012, Vol.18, No. 2, pp. 146–148.
11. JEGINA, S. Innovative and Biologically Active Nanostructured Nonwovens for Medical Applications. Master Thesis. Riga: RTU Institute of Design Technologies, 2015.

12. SUTKA, A.; KUKLE, S.; GRAVITIS, J. et al. Nanofibre Electrospinning Poly (vinyl alcohol) and Cellulose Composite Mats Obtained by Use of a Cylindrical Electrode. *Advances in Materials Science and Engineering*, 2013, Vol. 2013, Article ID 932636, 6 pages.
13. AGARWAL, S.; WENDORFF, J. H.; GREINER, A. Use of electrospinning technique for biomedical applications. *Polymer*, 2008, Vol. 49, pp. 5603–5621.
14. Bruker. AFM Probes TappingMode™ AFM. Camarillo, USA. [referred on the 16th of February in 2016 y.]. Link to the internet http://blog.brukerafmprobes.com/guide-to-spm-and-afm-modes/tapping-mode-afm/
15. BIOLAT, JSC. Sodium chlorophyllin. Salaspils, Latvia. [referred on the 16th of February in 2016 y.]. Link to the internet <http://biolat.lv/85/section.aspx/59>.

CYSENI 2016, May 26-27, Kaunas, Lithuania
ISSN 1822-7554, www.cyseni.com

NIOBIUM DOPED TiO_2 LAYERS BY CHEMICAL SPRAY PYROLYSIS

I. Dündar, I. Oja Acik, A. Mere, A. Katerski, M. Krunks
Laboratory of Thin Film Chemical Technologies
Department of Materials Science
Tallinn University of Technology
Ehitajate tee 5, EE-19086 Tallinn – Estonia
Email: ibrahimdundar@ymail.com

V. Mikli
Chair of Semiconductor Materials Technology
Department of Materials Science
Tallinn University of Technology
Ehitajate tee 5, EE-19086 Tallinn – Estonia

ABSTRACT

Nb-doped TiO_2 layers were fabricated by chemical spray pyrolysis and characterized their morphology, structural and optical properties as a function of the Nb content in the spray solution. The films were sprayed from the solution containing titanium (IV) isopropoxide (0.2 $molL^{-1}$) and acetylacetone in molar ratio of 1:2 in ethanol. Niobium (V) ethoxide was used as the Nb- source, Nb content was varied between 0 and 40 at% in the spray solution. The resulting TiO_2 and Nb-doped TiO_2 layers were annealed at 500 °C and 700 °C for 30 min in air. According to SEM, the TiO_2 film is uniform with the thickness of 260 nm. Nb-doped TiO_2 samples consist of a film covered with particles. The number of particles increases, however, the thickness of the films decreases from 245 nm to 130 nm with increasing the Nb content from 10 to 40 at% in the spray solution. The EDX studies confirm the presence of Nb in the layers. Although the Nb/Ti ratio for film is decreasing from 0.05 to 0.02 with increasing the [Nb] in the spray solution, it is conversely increasing for nanoparticles from 0.3 to 0.6. Raman and XRD analysis show that the as-deposited samples are amorphous. The samples annealed at 500 °C consist of anatase phase irrespective of the [Nb] in the solution.

Keywords: Nb-doped TiO_2, Chemical spray pyrolysis, thin films

1. INTRODUCTION

Besides its ease to fabrication and relatively low cost, titanium dioxide (TiO_2) has excellent chemical and physical properties such as chemical durability, high transmittance, and low resistivity, making it remarkable in both energy and environmental applications. It has been intensively employed for gas sensors, transistors, photocatalytic and photovoltaic applications [1–4].

At room temperature and atmospheric pressure, TiO_2 occurs in three widely known polymorphic crystal forms: anatase (tetragonal), rutile (tetragonal) and brookite (orthorhombic) [5]. Formation of phase transitions depends mainly on the nature of the starting material, dopant element, preparation method, and annealing temperature. Thermally, the most stable phase is rutile, while anatase and brookite are metastable [6–7]. The obtained films with different phases exhibit different physical and chemical properties. The indirect band gap of anatase phase is slightly larger than that of rutile, 3.20 eV and 3.00 eV, respectively [7]. Moreover, in terms of electrical conductivity, the most desirable phase of TiO_2 is anatase, because it has a higher mobility than rutile, which is more suitable for transparent contact applications [8].

It has been reported that doping TiO_2 lattice with metal ions (Ta, Cr, Zr and Nb etc.) affect the structural, optical and electrical properties of thin films [9]. Nb doped TiO_2, investigated by many researchers applying both physical and chemical deposition techniques show retarded anatase to rutile phase transformation, inhibition of the crystallite growth, high transparency in visible light and lower resistivity compared to that of undoped TiO_2 [4–8–10]. Lately, chemical deposition techniques such as atomic layer deposition [24], chemical vapor deposition [19], sol-gel-spin coating [22], and dip coating [9] have been extensively applied to deposite Nb-doped TiO_2 films. Despite of that there is a very few papers on Nb-doped TiO_2 films deposited by spray pyrolysis method [11]. According the literature, the commonly used Nb and Ti sources are niobium (V) ethoxide [6] and titanium (IV) isopropoxide[12], respectively, yet it is sometimes encountered that the preferences of niobium chloride [3] as a niobium source and tetrabutyl titanate [10] for Ti-source.

Chemical spray pyrolysis is a simple and cost-effective wet-chemical technique for preparation of thin films. In this paper, Nb-doped TiO_2 layers are deposited on Si and quartz substrates by using chemical spray pyrolysis method. The aim of this study is to deposit Nb-doped TiO_2 films by chemical spray pyrolysis method and to characterize the morphology, structural and optical properties of the formed layers.

2. METHODOLOGY

Undoped and Nb doped TiO_2 thin films were deposited onto c-Si and glass substrates using pneumatic chemical spray pyrolysis (CSP) method. The spray solution was composed of titanium (IV) isopropoxide (0.2 molL^{-1}) and acetylacetone in a molar ratio of 1:2 in ethanol.

Nb-doped TiO_2 films were obtained by mixing to the previous precursor with a proper amount of niobium ethoxide ($Nb_2(OC_2H_5)_{10}$; $Nb(OEt)_5$), as a Nb source, into the TiO_2 spray solution. The Nb concentration in TiO_2 solution [Nb/]/[Ti] was 0, 10, 20 and 40 at%. Compressed air with a flow rate of 8 l/min was used as the carrier gas while the spraying rate was adjusted to 3.5 ml/min. The nozzle to substrate distance fixed at 19 cm in front of the tin bath on which the substrates were placed. The tin bath temperature was adjusted to 260 °C. The number of spray cycles was set to nine, each consisting of a spray for 60s and a pause of 60s. One of the each sample was excluded to serve as a reference, yet the rest of the samples were subjected to heat treatment. The samples were annealed at 500 °C and 700 °C for 30 min in air in a furnace Nabertherm L5/11/06D.

The structure of the samples was investigated by X-ray diffraction (XRD) and Raman spectroscopy methods. XRD patterns were recorded by a Rigaku Ultima IV diffractometer with Cu Kα radiation (λ = 1.5406 Å, 40 kV at 40 mA). The measurements were performed in 2 theta configurations with scan range of 20–60°, with a step of 0.02° and a scanning speed of 2°/min. The mean crystallite size was calculated by the Scherrer method from the FHWM (full width at half maximum) of the (101) reflection of TiO_2 anatase phase. Raman spectra were acquired on a micro-Raman spectrometer HORIBA Jobin Yvon Model HR800 in the spectral range of 100–1200 cm^{-1} using 532 nm laserline for excitation.

The surface morphology, cross-section and elemental composition of the layers was studied with the help of a scanning electron microscopy (SEM) and energy dispersive X-ray analysis (EDX) using a Zeiss HR FESEM Ultra 55 with Bruker EDS system ESPRIT 1.8. An acceleration voltage for SEM measurements was 4.0 kV and for EDS analysis 7.0 kV. Furthermore, the mean grain size determination is obtained by using imageJ software applied SEM microphotos.

The total transmittance and reflectance spectra of the films were obtained by Jasco V-670 spectrophotometer set up with spectral range between 200 and 1200 nm.

3. RESULTS AND DISCUSSIONS

3.1. Surface Morphology

Fig. 1 shows SEM surface images of as-deposited TiO_2 and Nb-doped TiO_2 layers deposited with various Nb concentrations of 10, 20 and 40 at% in the spray solution. The films were deposited by chemical spray pyrolysis method onto the Si substrate at deposition temperature of 260 °C. As seen from SEM images, the layers morphology changes with Nb doping. Undoped TiO_2 sample

(Fig. 1 a) is relatively uniform and homogeneous. However, the Nb-doped TiO_2 layers are inhomogeneous, as observed from SEM images (Fig. 1 b–d). The surface of the Nb-doped TiO_2 layers consists of uniform layer with plane surface structure, similar to that of undoped TiO_2 film; which is covered by several spherical islands (e.g. inset Fig. 1 c) and particles (e.g. inset Fig. 1 d). The spherical islands with a size of ca 10 µm on the surface could originate from the spray droplets. The mean grain size, visible in the spherical islands on the Nb-doped TiO_2 layer surface (Fig. 1 b–d), were measured from SEM microphotos by using imageJ particle analysis software. The obtained values show that the mean grain size of Nb-doped TiO_2 layers increases from 100 to 300 nm with increasing Nb concentration in the spray solution. The number and the size of the particles (e.g. inset of Fig. 1 d) on the surface of Nb-doped TiO_2 layers is increasing with [Nb] in the spray solution. The size of the particles increases from ca 500 nm to ca 10 µm by increasing the Nb concentration in the spray solution from 10 to 40 at%.

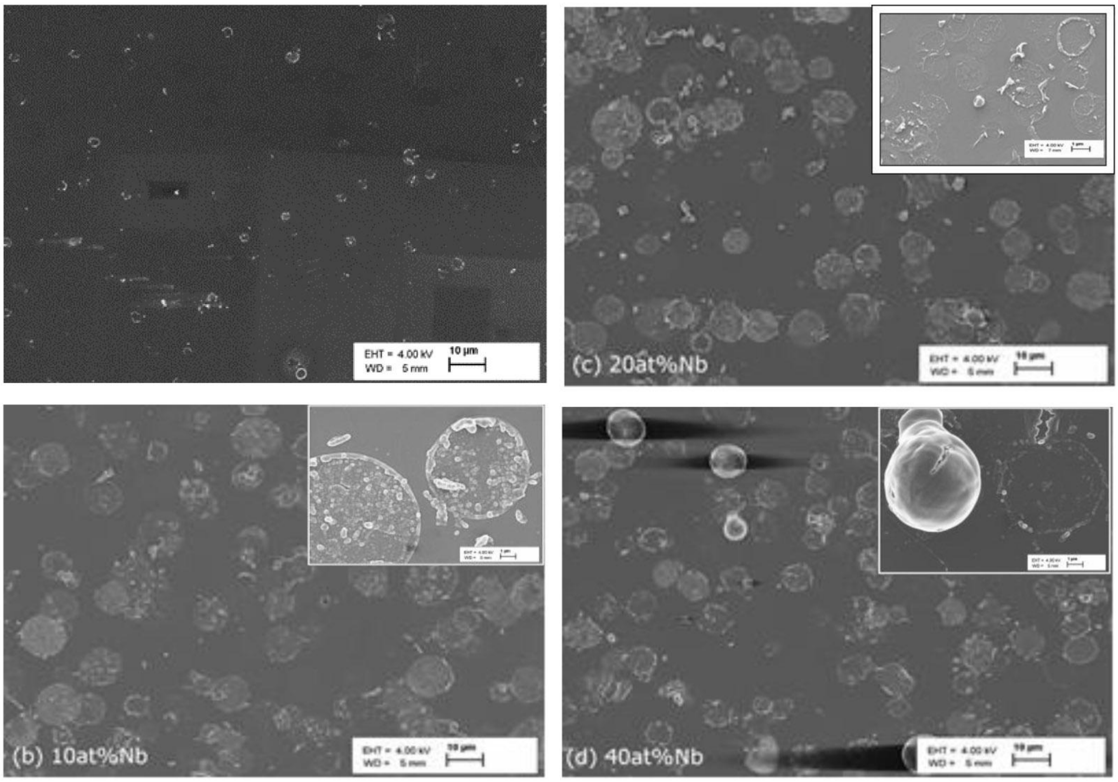

Fig. 1. SEM surface images of as-deposited: (a) TiO_2; and Nb doped TiO_2 layers with various Nb concentrations in the spray solution; (b) [Nb] = 10 at%; (c) [Nb] = 20 at% and (d) [Nb] = 40 at%. TiO_2 and Nb-doped TiO_2 layers were deposited onto c-Si substrates. Inset in figures (b), (c) and (d) shows the specific surface characteristics of the corresponding samples

The formation of the specific surface characters, such as spherical islands and particles, could be attributed to the relatively low deposition temperature, high spraying rate and high solution concentration. However, according to the thermal analysis study, the thermal decomposition of $Nb(OEt)_5$ takes place in the temperature region of 140–250 °C with a total mass loss of 95% [13]. Also high solution spraying rate could favour the dopant incorporation into the matrix material, as observed in the case of In-doped ZnO films deposited by chemical spray pyrolysis method [14]. Thus, taking into account the thermal decomposition data and the knowledge on sprayed In-doped ZnO films these deposition parameters are seemed to be essential in order to prevent loss of Nb during the deposition.

The effective thickness of TiO_2 film and Nb-doped TiO_2 layers ([Nb] = 10, 20 and 40 at%) deposited on Si substrate is determined from their cross-sections by SEM. Fig. 2 compares the

SEM cross-sectional images of undoped TiO_2 film (Fig. 2 a) and Nb-doped TiO_2 film deposited from the solution with [Nb] of 40 at% (Fig. 2 b). According to SEM cross-sectional images the TiO_2 films thickness is ca 260 nm. The thickness of the Nb- doped films is decreasing from 245 to 130 nm with increasing the [Nb] in the spray solution from 10 to 40 at%. The decrease in the TiO_2 film thickness with increasing the [Nb] in the solution has been observed also in case of the aerosol assisted chemical vapour deposition of Nb-doped TiO_2 films [15].

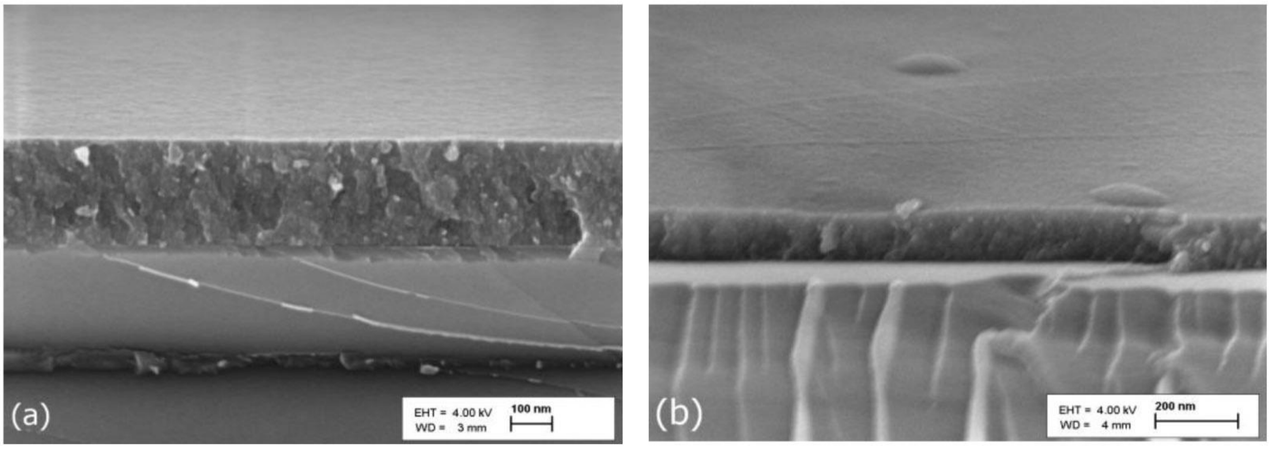

Fig. 2. SEM cross-sectional images of the (a) undoped TiO_2 film and (b) Nb-doped TiO_2 film deposited from the solution with [Nb] = 40 at% onto the Si-substrate at deposition temperature of 260 °C

3.2. Elemental Composition

According to EDX studies (Table 1), all as-deposited layers still contain organic residues, which are originated form the un-decomposed precursors. Previous studies have shown that annealing at temperatures above 500 °C is enough to remove the organic residues from the film [16]. The signal of Si is originated from Si substrate. EDX study indicates that Nb is incorporated into the film, island and particles of the Nb-doped layers.

Table 1. Elemental composition of the TiO_2 and Nb-doped TiO_2 samples (Nb-TiO_2) by varying the [Nb] in the spray solution as obtained from EDX analysis

Surface feature from SEM image	**Sample**	**[Nb] in solution, at%**	**Content of elements at%**					
			Ti	O	Nb	C	Si	Nb/Ti
FILM 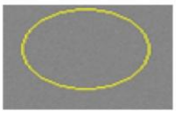	TiO_2	0	29.5	39.5	0.0	6.3	24.7	0.00
	Nb-TiO_2	10	26.4	40.1	1.0	3.8	28.7	0.04
	Nb-TiO_2	20	17.8	43.4	0.5	4.8	33.5	0.03
	Nb-TiO_2	40	16.4	36.5	0.1	3.6	43.4	0.01
ISLAND 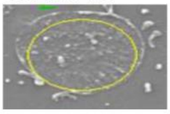	Nb-TiO_2	20	25.5	41.1	1.1	3.6	28.7	0.04
PARTICLE 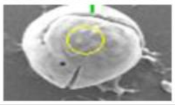	Nb-TiO_2	10	21.1	65.1	5.8	7.4	0.6	0.27
	Nb-TiO_2	20	18.3	66.5	7.1	7.3	0.8	0.39
	Nb-TiO_2	40	25.6	58.0	16.4	0.0	0.0	0.64

varying the [Nb] in the spray solution as obtained from EDX analysis.

The film part of the Nb-doped TiO_2 layers indicate relatively low Nb doping as the [Nb]/[Ti] ratio is decreasing from 0.04 to 0.01 with increasing the [Nb] in the solution from 10 to 40 at%. However, as seen from EDX results, the Nb concentration is higher in particles than in film part of the same Nb-TiO_2 sample. The Nb amount in particle ranges from 5.8 up to 16.1 at% and also the [Nb]/[Ti] ratio is increasing from 0.27 to 0.64 with increasing the [Nb] in the solution. Thus, showing that the particles on the surface of Nb-doped TiO_2 films are highly Nb-doped. It should be noted that the [Nb]/[Ti] is slightly higher in island compared to that of the film, viz. 0.04 and 0.03 for the Nb-doped TiO_2 film deposited from the solution with [Nb] = 20 at%.

According to SEM study, the increasing the [Nb] in the spray solution favours the formation of particles and islands on the surface of Nb- doped TiO_2 layer with a decrease of the film thickness underneath. EDX shows that Nb is incorporated into Nb-doped TiO_2 layer containing of Nb-poor film part and Nb-rich particles on the surface.

3.3. Structural Properties

3.3.1. X-Ray Diffraction

Fig. 3 a shows the XRD patterns of TiO_2 and Nb-doped TiO_2 films deposited from spray solution with [Nb] = 10, 20 and 40 at% onto Si substrate. The XRD measurement was performed after the samples were annealed at 700 °C for 30 min.

The XRD patterns of TiO_2 film and Nb-doped TiO_2 samples, irrespective of the [Nb] in the solution, exhibited diffraction peaks at 2 theta of 25.5°, 37,8°, 48,2°, 53,9° and 55° that all films mostly obey the anatase structure of TiO_2 [17]. No diffraction peaks corresponding to rutile or niobium oxide was found on the XRD patterns. An additional diffraction peak appearing at 2 theta of 31,5° could belong to another TiO_2 phase, according to ICDD card number 01-074-9520 (PDF-2).

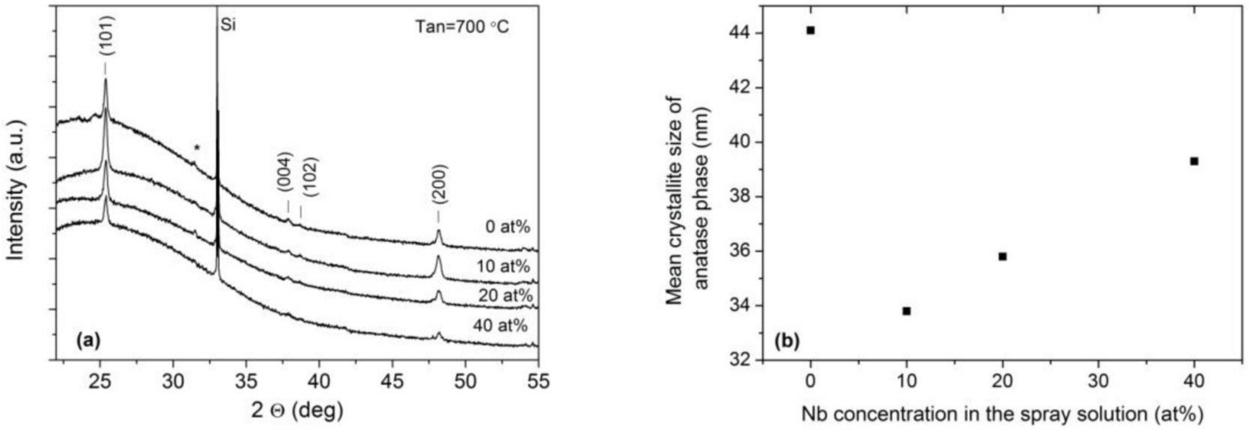

Fig. 3. (a) XRD patterns of TiO_2 and Nb-doped TiO_2 layers deposited from solution with [Nb] = 10, 20 and 40 at% onto Si substrates; (b) The mean crystallite size of the anatase phase as a function of the [Nb] concentration in the spray solution. The samples were annealed at 700 °C for 30 min in air

The (101) peak of anatase phase in the XRD pattern was used to calculate the mean crystallite size of the TiO_2 by the Scherrer formula (Fig. 3 b). As seen from Fig. 3 b, the undoped TiO_2 films exhibit the mean crystallite size of 44 nm and that Nb-doped TiO_2 layers show a lower mean crystallite size in the range of 34 to 40 nm. Interestingly the Nb-doped TiO_2 film deposited from solution with [Nb] = 10 at% indicate the lowest mean crystallite size of 34 nm. This is in correspondence of EDX data (Table 1), showing the highest [Nb]/[Ti] ratio among in Nb-doped TiO_2 layers. As XRD takes into account the whole sample, then most probably the number of particles on top of film is relatively low and gives no impact on the XRD data.

It has been found also in literature that the crystallite size of Nb-doped TiO_2 films is smaller than that in pure TiO_2 [9]. The reason behind this has been explained by the fact that the Nb^{+5} radius is slightly bigger than the Ti^{+4} which means that the Nb atoms causes slight stress in TiO_2 lattice, which may hinder the growth of the TiO_2 crystallites [6,18].

3.3.2. Raman Spectroscopy

Raman spectra of TiO_2 and Nb-doped TiO_2 layers deposited with various [Nb] in the spray solution onto Si substrate and annealed at 700 °C are presented in Fig. 4. The different areas of the Nb-doped TiO_2 samples, like film (Fig. 4 a) and particles (Fig. 4 b), were investigated separately. Fig. 4 a shows the Raman spectra of TiO_2 film and the film part of the Nb-doped TiO_2 layers. As seen, all Raman spectra, irrespective of [Nb] in the solution, exhibit the bands at 142 (Eg) cm^{-1}, 197 (Eg) cm^{-1}, 395 (B1g) cm^{-1} and 639 (Eg) cm^{-1} which are characteristic of TiO_2 anatase phase [20]. In addition, the peaks at 302 and 520 cm^{-1}, belonging to the Si substrate, are visible.

Fig. 4 b shows the Raman spectra of the particles on top of Nb-doped TiO_2 layers deposited with various [Nb] in the spray solution. The spectra of particles on top of Nb-doped TiO_2 layers with [Nb] = 10 at% in the solution shows anatase structure. The observed broad band in the range of 940–990 cm^{-1} is due to the formation of Si-O-Ti bands [27]. The spectra of particles on top of Nb-doped TiO_2 layers with [Nb] = 20 and 40 at% in the solution reveal anatase structure and several new Raman bands.

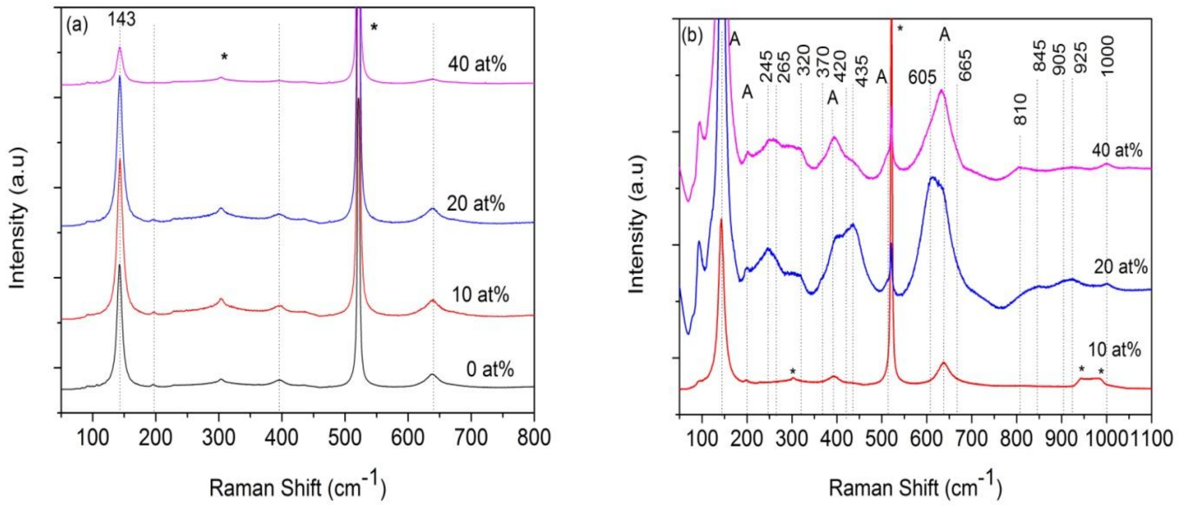

Fig. 4. (a) Raman spectra of the TiO_2 film and from the film part of the Nb-doped TiO_2 layers deposited from the solution with [Nb] = 10, 20 and 40 at%; (b) Raman spectra of the particles on top of the Nb-doped TiO_2 layers deposited from the solution with [Nb] = 10, 20 and 40 at%. The films were deposited onto Si substrate at 260 °C and annealed at 700 °C for 30 min. The Raman bands assigned to anatase phase are marked by dotted line, the peaks corresponding to Si substrate are marked by *

According to literature the Nb ions occupy the Ti site in the anatase TiO_2 lattice. The ionic radius of Nb^{5+} is only a bit larger than Ti^{4+} ($r(Ti^{4+}) = 0.605$ Å versus $r(Nb^{5+}) = 0.64$ Å) [29]. Therefore, Nb can be easily incorporate into the lattice of TiO_2 at high concentration. The amount of Nb that can be accommodated in the anatase has been reported to have a saturation point over 10 at. %. [1]. Morover, it has been reported in the literature that the titania lattice can incorporate up to 20% of Nb ions and within that range forms a solid solution with anatase TiO_2 [19].

According to literature the formation of Nb_xO_y and Ti_2O_3 phases have been observed in Nb-doped TiO_2 materials [19–20]. The Raman spectra of the Nb_2O_5 reveals strong bands at 235, 261, 324, 632, 846 and 992 cm^{-1} [21] and the spectra of NbO_2 show strong Raman bands at 415, 434, 580 cm^{-1} [22]. The Ti_2O_3 show strong Raman bands at 238, 279, 350, 465 cm^{-1} [21]. Thus, taking into account the literature data we could assume the formation of Nb_xO_y phases in addition to Nb-doped TiO_2 phase in the particles (Fig. 4 b) on top of Nb-doped TiO_2 layers. According to XRD and Raman studies, the TiO_2 and Nb- doped TiO_2 samples irrespective of the [Nb] in the spray solution consists of anatase phase. Raman studies showed that the particles formed on top of Nb-doped TiO_2 layer show the presence of Nb-doped TiO_2 anastase and Nb_xO_y phases.

3.4. Optical Properties

The optical transmittance spectra of undoped and Nb-doped TiO_2 thin layers sprayed on quartz substrate at 260 °C and annealed at 500 °C and 700 °C are measured in the wavelength between 200 and 1200 nm (Fig. 6 a). The transmitance is approximately 80% for TiO_2 films in the spectral region of 500–1200 nm, and transmittance decreases with the increase of Nb concentration in the solution. (Fig. 6 a). The decrease in transmittance with increasing the [Nb] in solution has been observed also in case of sol-gel spin coating and ultrasonic spray pyrolysis depositions of Nb-doped TiO_2 films [22, 23].

The transmittance of the thin films is affected by both reflectivity and combination of absorption coefficient and film thickness. The equation (1) is used in order to eliminate the effect of the interference fringes on the transmittance (T) (Fig. 5 b) [25].

$$T/(1-R) = e^{\alpha d}. \qquad (1)$$

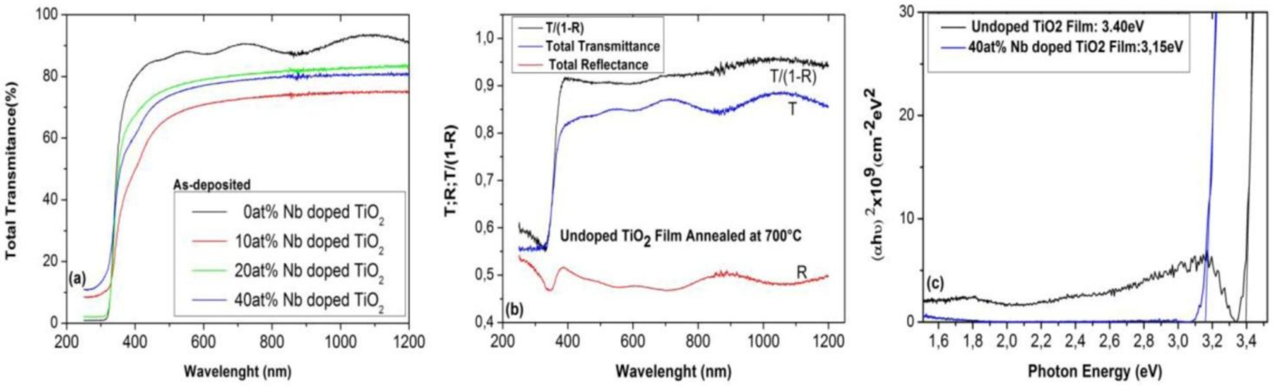

Fig. 5. (a) Total transmittance spectra for as deposited TiO_2 and Nb-doped TiO_2 sample with a various Nb concentrations on solution; (b) Transmission T, reflection R, T/ (1-R) = $e^{\alpha d}$ spectra of 500–1200 nm; (c) Determination of band gap by ploting of $(\alpha h\nu)^2$against photon energy

The equation (2) is employed to obtain absorption coefficient (α) which is necesarry to find the optical band gap. The optical band gap was determined using Tauc expression [26]:

$$\alpha = Ah\nu(h\upsilon - Eg)^n, \qquad (2)$$

where A is constant, hυ is the photon energy, Eg is band gap and n = 1/2 for direct or n = 2 for indirect transitions. The values of Eg were obtained by extrapolating the linear region of the plot of $(ah\upsilon)^2$ against the photon energy by assuming indirect band gap shown in Fig. 5 c. As shown also in Fig. 5 c, the band gaps for TiO_2 and 40% Nb-doped TiO_2 layers deposited from solution with [Nb] = 40 at% layers annealed at 700°C are 3.4 eV and 3,15eV, respectively. As deposited TiO_2 and Nb-doped TiO_2 samples deposited from solution with [Nb] = 10 and 40 at% show the Eg values of 3.55 eV, 3.40 eV and 3.45 eV, respectively. The decrease in optical band gap of TiO_2 films with increasing Nb content in the solution is observed also in Nb-doped TiO_2 films deposited spin coating and ultrasonic spray pyrolysis methods [22, 23, 28].

4. CONCLUSION

Nb doped TiO_2 thin layers were perepared by chemical spray spray pyrolysis with different Nb concentrations.The effect of Nb concent on morphological, structural, and optical properties was investigated. SEM images showed the formation of particles on surface with Nb doping. The number of particles increases, however, the thickness of the films decreases from 245 nm to 130 nm with increaasing the Nb content from 10 to 40 at% in the spray solution. The EDX studies confirm the presence of Nb in the samples. Although the [Nb]/[Ti] ratio for film is decreasing from 0.05 to 0.02 with increasing the [Nb] in spray solution, it is conversly increasing for particles from 0.3 to 0.6. XRD measurments confirmed the presence of anatase phase in both TiO_2 and Nb doped TiO_2 layers. Moreover, it revealed that the crystallite size decreases with increased Nb content in the film part of the sample. Raman spectroscopy was performed for film areas and particles. It shows that film parts were consisted of anatase TiO_2 whereas the spectra of particles revealed peaks probably belonging to Nb_xO_y. Nb-doped TiO_2 layers showed lower transmittance than TiO_2 film in the spectral region of 500–1200 nm. The band gap of TiO_2 and Nb-doped TiO_2 layers deposited from the solution with [Nb] = 40 at% are 3.55 eV–3.45 eV, respectively.

5. ACKNOWLEDGEMENT

This study was financially supported by the Estonian Ministry of Education and Rseach project IUT19-4, Tallinn University of Technology based financing project B24 and by the European Union through the European Regional Development Fund project TK141 “Advanced materials and high-technology devices for energy recuperation systems”.

6. REFERENCES

1. RUIZ, Ana M., DEZANNEAU, G., J. ARBIOL, A. CORNET, MORANTE, Joan R., Insights into the structural and chemical modifications of Nb additive on TiO_2 nanoparticles. Chemistry of Materials, Vol. 16, p. 862–871.
2. OK, Kyung C., PARK, Y., Kwun-Bum CHUNG, Jin-Seongg PARK, The effect of Nb doping on the performance and stability of TiOx devices. Applied Physics, Vol. 46, No. 295102, p. 1–5.
3. ZHAO, L., ZHAO, X., LIU, J., ZHANG, A., WANG, D.,WEI, B. Fabrications of Nb-doped TiO2 transparent conductive oxide polycrystalline films on glass substrates by sol-gel method. Journal of Sol-Gel Science and Technology. Vol. 53, p. 475–479.
4. POTLOG, T., DUMITRIU, P., DOBROMIR, M., MANOLE, A., LUCA D., Nb-doped TiO_2 thin films for photovoltaic applications. Materials and Design, Vol. 85, p. 558–563.
5. HU, Y., TSAI, H., HUANG C. Effect of Brookite phase on the anatase-Rutile transition titania nanoparticles. Journal of the European Ceramics Society, Vol. 23, p. 691–696.
6. WANG, G.Q., LAN, W., YU, M.L., HAN, G.J., WANG, Y., SU, Q., LIU, X.Q. Optical and structural properties of TiO2 films as a function of Nb doping concentration, Journal of Material Science Vol. 22, 2011, p. 463–466.
7. DORIAN, A., HANAOR, H., SORREL, Charles C. Review of the anatase to rutile phase transformation. Journal of Material Science, Vol. 46, p. 855–874.
8. HITOSUGI, T., TiO_2-based Transparent Conducting Oxide. Advance Institute for Materials Research Tohuku University, p. 1–10.
9. Koozegar KALEJI, B., MAMOORY, Sarraf R. FUJISHIMA, A. Influence of Nb dopant on the structural and optical properties of nanocrystalline TiO_2 thin film. Materials Chemistry and Physics Vol. 132, p. 210–215.
10. LU, Y., KHAN, S., SONG, C.L.,WANG KK., YUAN, G.Z., LI, W., HAN, G.R. Doping concentration effects upon column structured Nb:TiO2 for transparent conductive thin films

prepared by a sol-gel method. Journal of Alloys and Compounds, Vol. 663, No. 206, p. 413–418.

11. ADOMNITEI, C., LUCA, D., GRIRTAN, M., SANDU, I., NICA, V., SANDU, A.V., MARDARE, D. Nb-doped TiO_2 Thin films deposited by spray pyrolysis method. Journal of Optoelectronics and Advanced Materials, Vol. 15, p. 519–522.
12. MANOLE, A.V., DOBROMIR, M., GIRTAN, M., MALLET, R., RUSU, G., RUSU, D., LUCA, D., Optical properties of Nb-doped TiO_2 thin films prepared by sol- gel method. Ceramics International, Vol. 39, p. 4771–4776.
13. CAI, Y., YANG, S., JIN, S., YANG, H., HOU, G., Electrochemical synthesis, characterization and thermal properties of niobium ethoxide. Journal Central South University Technolgy, Vol. 18, p. 73–77.
14. KRIISA, M., KRUNKS, M., KÄRBER, E., KUKK, M., MIKLI, V., MERE A., Effect of Solution Spray Rate on the Properties of Chemically Sprayed ZnO: In Thin Films. Journal of Nanomaterials ArticleID 423632.
15. BHACHU, Davinder S., SATHASIVAM, S., SANKAR, G., SCANLON, David O., CIBIN, G., CARMALT, Claire J., PARKIN, Ivan P., WATSON, Graeme W., BAWAKED, Salem M.,OBAID, Abdullah Y., AL-THABAITI, S., BASAHEL, Sulaiman N. Solution Processing Route to Multifunctional Titania Thin Films: Highly Conductive and Photcatalytically Active Nb:TiO_2. Advance Functional Materials, Vol. 24, p. 5075–5085.
16. ACIK, Ilona O., MERE, A., KRUNKS, M., SOLTERBECK, C., ES-SOUNI, M. Properties of TiO_2 Films Prepared by the Spray Pyrolysis Method. Solid State Phenomena, Vol. 99–100, p. 259–264.
17. Powder Diffraction File (PDF), (01-070-7348) , PDF-2 Release 2013.
18. ARBIOL, J., CERDA, J., DEZANNEAU, G., CIRERA, A., PEIRO, F., CORNET, A., MORANTE, J. R., Effects of Nb doping on the TiO_2 anatase-to-rutile phase transition. Journal of Applied Physics, Vol. 92, p. 853–861.
19. GARDECKA, A. J., GOH, G. K. L., SANKAR, G., PARKIN, I. P., On the nature of niobium substitution in niobium doped titania thin films by AACVD and its impact on electrical and optical properties. Journal Material Chemistry, Vol. 3, p. 17755–17762.
20. NEUMANN, B., BIERAU, F., JOHNSON, B., KAUFMANN, Christian A., ELLMER, K., TRIBUTSCH, H. Niobium doped TiO_2 films as window layer for chalcopyrite solar cells. Physics State Solution, Vol. 245, No. 9, p. 1849–1857.
21. DASH, J.K., CHEN, L., TOPKA, Michael R., DINOLFO, Peter H., ZHANG, L. H., KISSLINGER, K., LU, T.M., WANG, G.C., A simple growth method for Nb_2O_5 films and their optical properties. Vol. 5, p. 36129–36139.
22. LEE, Deuk Y., PARK, Ju H., KIM, Young H., LEE, Myung H., CHO, Nam I. Effect of Nb doping on morhology, crystal structure, optical band gap energy of TiO_2 thin films, Current Applied Physics, Vol. 14, p. 421–427.
23. BHAVANA, N., HYUN, J., MAIKEL Y., HEST, van F. A. M.,YOON, Sam S. Niobium doped Titania Photocatalyst Film Prepared via a Nanaqueous Sol-Gel Method. Journal American Ceramic Society, Vol. 96, p. 2623–2627.
24. NIEMELÄ, Janne P., HIROSE, Y., HASEGAWA, T., KARPPNEN M., Transition in electron scatteering mechanism in atomic layer deposited Nb:TiO_2 thin films. Applied Physics Letters, Vol. 106, No. 042101.
25. KYKYNESHI, R., McINTYRE, D.H., TATE, J., PARK, C.H., KESZLER, D.A. Electrical and optical properties of epitaxial transparent conductive BaCuTeF thin films deposited by pulsed laser deposition. Solid State Sciences, Vol. 10, p. 921–927.

26. TAUC, J., Optical properties and electronic structure of amorphous Ge and Si. Materials Research Bulletin, Vol. 3, p. 37.
27. STEM, N., DE SOUZA, Le M., DE FARIA, L. A. Dalva, DOS SANTOS FILHO, Sebastiao G., Formation of Ti(III) and Ti(IV) states in Ti_3O_5 nano- and microfibers obtained from hydrothermal annealing of C-doped TiO_2 on Si. Thin Solid Films, Vol. 558, p. 67–74.
29. YANG, J., ZHANG X., WANG, C., WANG L., XIA B., LIU Y. Solar photocatalytic activities of porous Nb-doped TiO_2 microspheres prepared by ultrasonic spray pyrolysis. Solid State Sciences, Vol. 14, p. 139–144.

THE INFLUENCE OF GAS TYPE ON THE PLASMA TORCH ELECTRICAL AND THERMAL CHARACTERISTICS

D. Gimžauskaitė, A. Tamošiūnas, P. Valatkevičius, V. Valinčius
Lithuanian Energy Institute
Plasma Processing Laboratory
Breslaujos str. 3, LT-44403 Kaunas – Lithuania
Email: Dovile.Gimzauskaite@lei.lt

ABSTRACT

The article focuses on the impact of different type of gases on the electrical and thermal characteristics of the plasma torch. Four experimental options were created using several types of gases (air, carbon dioxide, air/water vapour and carbon dioxide/water vapour) for plasma formation and cathode protection. In the case of air, the power of plasma torch was 38–90 kW, the arc current in the range of 120–220 A, and the voltage was 294–430 V. In the next case (carbon dioxide), the power of plasma torch ranged from 52 to 95 kW, arc current 160–220 A, and arc voltage was 320–440 V, respectively. Using a mixture of air/water vapour, the power of plasma torch was 46–71 kW, arc current was 160–220 A, and arc voltage was 243–343 V. Finally, using carbon dioxide/water vapour mixture as cathode protective gas, the power of plasma torch was 44–77 kW, arc current was 160–220 A, and arc voltage was 274–364 V. The results of the research reveal the regularity of behaviour of plasma torch electrical characteristics depending on gas composition. The obtained experimental results were also compared between the observed groups by providing more comprehensive results of the study. The received information has contributed to the development of novel water vapour plasma technology as one of the most promising solutions to environmental problems and sustainable development in the near future (e.g. the technology could be used for neutralization of hazardous waste, recycling of organic, municipal waste).

Keywords: thermal plasma, carbon dioxide, air, water vapor, plasma torch

1. INTRODUCTION

Increasing the efficiency of energy usage and reducing the emissions have recently become the worldwide focus because of environmental protection demands and energy shortage [1]. Sustainable development – one of the main criteria and the evaluation scale for the adoption of individual decision and formation of country policies. The main task of sustainable development strategy is an appropriate and reliable supply of energy at the affordable price in a safe and environmentally friendly manner and in compliance with a social and economic development needs. Therefore, energy plays the main role in all of the aspects of Sustainable development and is one of the most essential factors influencing the social development and the economic growth. However, the production of energy and its use influences the quality of environment on all levels: the local, the regional and the global [2].

Moreover, energy and waste are two key elements in the management of urban areas (especially in megacities). High energy consumption and greenhouse gases (GHG) emissions are among the concerns. At the same time, cities produce municipal and industrial waste at a high rate, which require appropriate management to avoid pollution, high landfill demand, social repulsion and other issues [3]. All these factors are exigent to develop alternative, environmentally-benign energy sources, technologies which can provide energy and at the same time are able to solve the problem of miscellaneous waste utilization.

Nowadays there is growing interest in syngas (H_2 + CO_2), because it could be generated from various carbon sources (coal, biomass, municipal solid waste, and even coke oven gas) [4, 5] and is suitable for further synthesis of chemicals, fuel cell applications [6, 7].

The necessity of the production of clean syngas with controlled composition has led to the technologies based on allothermal processes with external energy supply for materials gasification

[8]. Among these is gasification using a plasma torch. In general, plasma contains active radicals, ions, and high-energy electrons which can catalyze chemical reactions and reduce reaction time [9, 10]. The plasma capability, as well as its high energy density, ensures the compactness of the material-modifying system [11]. It means that substantially lower plasma flow rates are needed to supply sufficient energy for gasification compared with other media used for this purpose. This results in minimum contamination and dilution of produced syngas by plasma gas and easy control of syngas composition [12].

Furthermore, the plasma system can be adapted for reforming of various hydrocarbons, such as natural gas, heavy oils, and biofuels. When steam is used as a plasma-forming gas, the reductive and oxidative radicals are produced in the plasma stream enabling to effectively reform different hydrocarbons [13–16]. The experimental study on the characteristics of steam added gasification [17, 18] showed that the addition of steam favored the formation of H_2 and CO_2 (syngas), and restrained the CO formation by water–gas shift reaction [19].

This article presents the development of a new plasma technology, as one of the most promising solutions for environmental and sustainable development problems in the near future (e.g. the technology could be used for syngas production from waste/biomass and at the same time for neutralization of hazardous pollutants, recycling of organic, municipal and industrial waste). During the development of this technology it is essential to determine the parametric characteristics of the plasma torch enabling a stable operation within the reforming/gasification process [20]. This work aims at analyzing the impact of the different types of gases (air, carbon dioxide, air/water vapor and carbon dioxide/water vapor) on the electrical and thermal characteristics of the plasma torch.

2. EXPERIMENTAL SETUP AND METHODOLOGY

The experimental plasma system used in this work consists of a linear (direct current) DC plasma torch with copper cathode junction containing a tungsten button-type emitter (used in the presence of water vapor) or with hafnium emitter (used in the presence of oxygen-containing gas) and a step-formed copper anode (Fig. 1). A cylindrical anode is positioned along the axis in one line with the cathode and it is used to fix the mean arc length. Sudden expansion of the anode channel leads to the prevention and minimization of a large-scale shunting of the electric arc [21]. Electrodes of the plasma torch are separated by the neutral section and the insulation rings. The rings have an inlet holes for the tangential supply of shielding and plasma-forming gas. The experimental setup also contains the sub-systems, such as an electrical power source, measurement and cooling systems, as well as a gas supply and overheating. The plasma system is operating under atmospheric pressure. In addition, water vapor is generated using 5 bar of pressure water steam generator GAK-50 [22].

The electrical and thermal characteristics of the linear plasma generator with step-formed anode were generalized using theory of similarity [23].

The electric arc in the discharge channel of the plasma torch, which is flown past by gas in general terms may be described analytically by very complicated equations. Solution of these equations is complex and is not exact enough. Therefore, application of methods of similarity theory for this case is of great importance. So, the main equation for electrical characteristics may be presented according to equation:

$$\frac{Ud}{I} = A\left(\frac{I^2}{Gd}\right)^m \left(\frac{G}{d}\right)^n (pd)^k \left(\frac{l}{d}\right)^r \tag{1}$$

where U – arc voltage (V), d – anode diameter (m), I – arc current (A), G – total gas flow rate ($kg \cdot s^{-1}$), p – pressure in the arc chamber (Pa), l – length of the anode (m), A, m, n, k, r – constant values depending on plasma torch construction and operating regime [24].

Generalization of the thermal characteristics of plasma torch is similar to the generalization of electrical characteristics [24]:

$$\tilde{\eta} = \frac{1-\eta}{\eta} = B\left(\frac{I^2}{Gd}\right)^m \left(\frac{G}{d}\right)^n (pd)^k \left(\frac{l}{d}\right)^r \tag{2}$$

where B – constant established from the dependence of efficiency from arc current, η – thermal efficiency of the plasma torch $\tilde{\eta}$ – integral coefficient of heat transfer.

It is worth pointing out that thermal efficiency of the plasma torch (η) is the ratio of the heat, carried by the gas from the plasma torch per unit time, to the arc power. Meanwhile, integral coefficient of heat transfer ($\tilde{\eta}$) determines the ratio of the heat losses in the plasma torch to the heat content of the plasma jet [21].

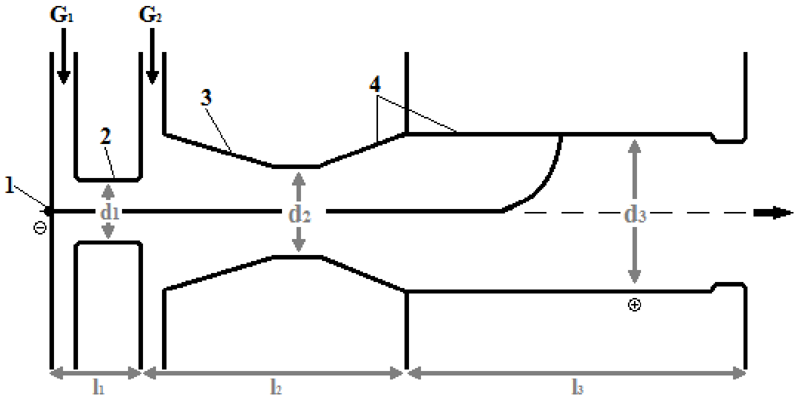

Fig. 1. A scheme of plasma torch. 1 – cathode, 2 – neutral section, 3 – intermediate anode, 4 – step-formed anode. G_1, G_2 – shielding and plasma-forming gas, respectively

3. RESULTS AND DISCUSSION

Four experimental conditions were investigated using several types of gases and their mixtures (air, carbon dioxide, air/water vapor and carbon dioxide/water vapor) for plasma formation and cathode protection. The main operational characteristics of plasma torch are given in Table 1.

Table 1. The experimental parameters of plasma torch

	Air	**CO_2**	**Air/water vapor**	**CO_2/water vapor**
Arc current (A)	120–220	160–220	160–220	160–220
Arc voltage (V)	294–430	320–440	243–343	274–364
Arc power (kW)	38–90	52–95	46–71	44–77
Gas flow rate (cathode), G_1 ($\times 10^{-3}$ kg/s)*	1	1	1	1.04
Gas flow rate (anode), G_2 ($\times 10^{-3}$ kg/s)*	3–11	3–11	2.4–4.65	2.4–4.65
Total gas flow rate,G ($\times 10^{-3}$ kg/s)	4–12	4–12	3.4–5.65	3.44–5.69
Plasma torch efficiency, η	0.76–0.88	0.78–0.89	0.6–0.75	0.61–0.77

* In the cases of air/water vapor and CO_2/water vapor G_2 corresponds to water vapor.

The electric arc at atmospheric pressure usually appears as a constricted area of electrical and mechanical forces which causes plasma fluid to move away from the arc column. The plasma fluid in that case is replaced by the cold gases injected into the arc reacting zone from outside. So, the processes in the electric arc zone include: turbulent mixing, chemical reactions, ionization processes, transfer of electric energy to conducting particles, transformation of electric energy into thermal energy and radiation. Investigation of the influence of mentioned factors requires simultaneous characterization of the arc and its characteristics in the association with gas and plasma flow parameters.

3.1. Electrical characteristics of plasma torch

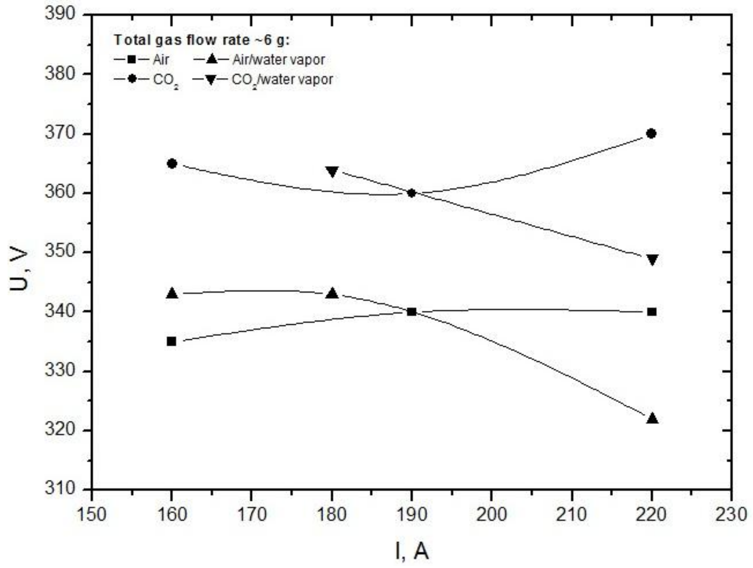

Fig. 2. The voltage-current characteristics (VCC) of the air, carbon dioxide, air/water vapor and carbon dioxide/water vapor plasma torches than total gas flow rate ~ $6{\cdot}10^{-3}$ kg·s^{-1}

The gas is injected at the cathode and anode side and is dissociated and ionised in the arc channel. In the present study the radial injection was applied and VCC observed as slightly increasing or decreasing in dependence of arc current in the range of 160–220 A. Fig. 2 illustrates voltage-current characteristics of four different types of plasma forming gases at total gas flow rate equal to ~ $6{\cdot}10^{-3}$ kg·s^{-1}. It is evident that in the case of CO_2 the characteristic is parabolic shaped. The VCC in air plasma are rising in the range of current intensity of the electric arc between 160 and 190 A. However, it can be assumed that in the range of 195–220 A VCC becomes as constant. The VCC of air/water vapor are also steady when current intensity varies from 160 to 180 A. Besides higher current levels the arc shunting takes place, and the voltage become as decreasing. Therefore, in the range of 180–220 A it begins progressively to decrease. In the case of CO_2/water vapor the characteristics are dropping and the main reason of this process could be also shunting of the electric arc. In order to guarantee a stable work of plasma torch, the curve of VCC must rise or remain constant.

It is important to notice, that changes in the morphology of electrodes due to material lose by erosion during operation of plasma torch or the motion of cathode spot didn't take into account.

After analysis of the primary experimental results, the VCC were generalized. The generalized VCC of the plasma torch operating on the different types of gases are shown in Fig. 3 and Fig. 4. The general equations of VCC were determined by the theory of similarity and are provided below.

Plasma forming gas is air:

$$\frac{Ud_2}{I} = 3.2 \times 10^2 \left(\frac{I^2}{Gd_2}\right)^{-0.48} \times \left(\frac{G}{d_2}\right)^{-0.22} \tag{3}$$

Plasma forming gas is CO_2:

$$\frac{Ud_2}{I} = 1.6\times10^3 \left(\frac{I^2}{Gd_2}\right)^{-0.56} \times \left(\frac{G}{d_2}\right)^{-0.3} \quad (4)$$

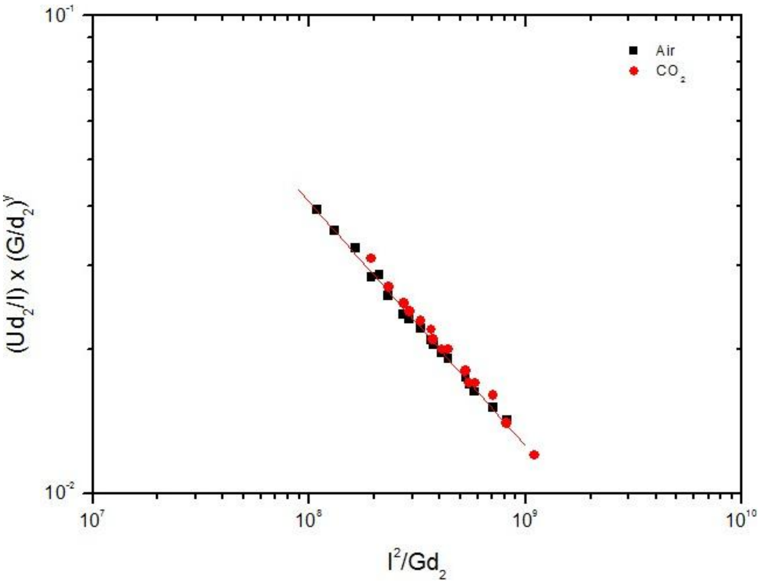

Fig. 3. The generalized VCC characteristics of the air and CO_2 plasma torch. In the case of air: $(Ud_2/I) \times (G/d_2)^{0.21}$ and in the case of CO_2: $(Ud_2/I) \times (G/d_2)^{0.3}$

Air/water vapor:

$$\frac{Ud_2}{I} = 2.8\times10^3 \left(\frac{I^2}{Gd_2}\right)^{-0.59} \quad (5)$$

CO_2/water vapor:

$$\frac{Ud_2}{I} = 6.8\times10^3 \left(\frac{I^2}{Gd_2}\right)^{-0.63} \quad (6)$$

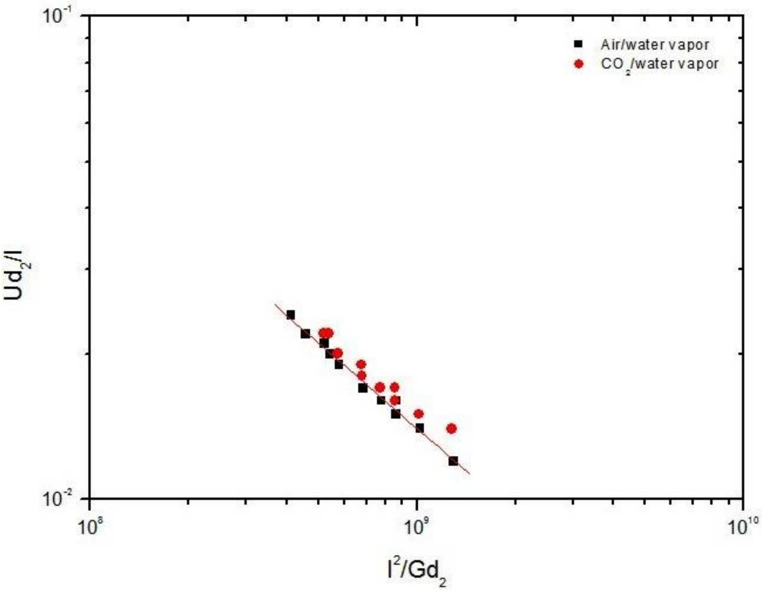

Fig. 4. The generalized VCC characteristics of the air/water vapor and CO_2/water vapor plasma torch

As is visible, generalized VCC always became as dropping. Generalized VCC helps to determine and select working parameters to which plasma system will operate more stable and cost-effectively.

3.2. Thermal characteristics of plasma torch

Fig. 5 and Fig. 6 shows the generalized thermal characteristics of the plasma torche operating on air, CO_2, air/water vapor and CO_2/water vapor, respectively. The general equations of the plasma torche thermal efficiency were determined by the theory of similarity and are given below.

Air:

$$\tilde{\eta} = 2.7 \times 10^2 \left(\frac{I^2}{Gd_2}\right)^{0.34} \tag{7}$$

CO_2:

$$\tilde{\eta} = 1.1 \times 10^3 \left(\frac{I^2}{Gd_2}\right)^{0.42} \tag{8}$$

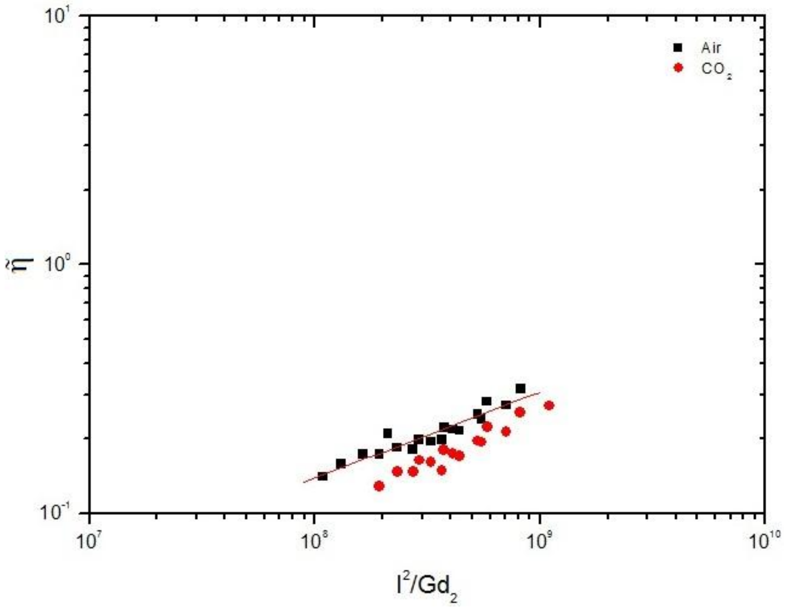

Fig. 5. The generalized thermal characteristics of the air and CO_2 plasma torch

Air/water vapor:

$$\tilde{\eta} = 2.3 \times 10^{-5} \left(\frac{I^2}{Gd_2}\right)^{0.43} \times \left(\frac{G}{d_2}\right)^{-1.36} \tag{9}$$

CO_2/water vapor:

$$\tilde{\eta} = 1.2 \times 10^{-4} \left(\frac{I^2}{Gd_2}\right)^{0.36} \times \left(\frac{G}{d_2}\right)^{-0.96} \tag{10}$$

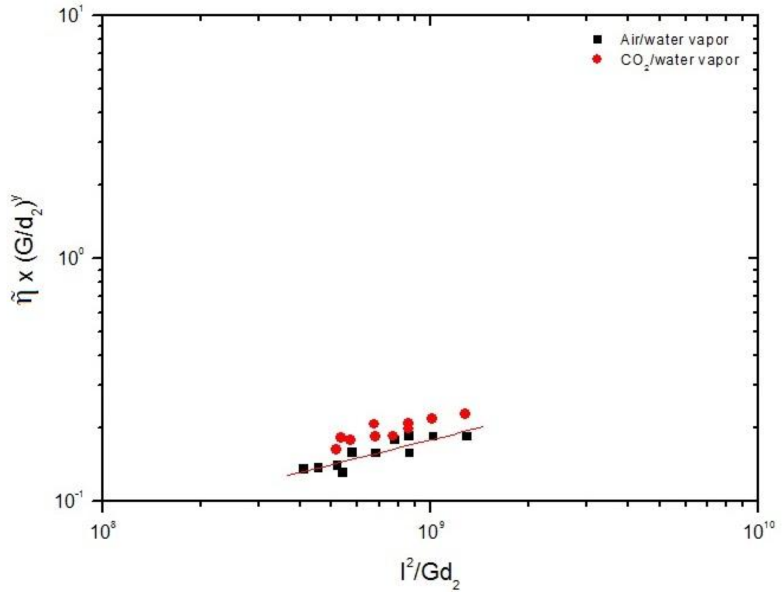

Fig. 6. The generalized thermal characteristics of the air/water vapor and CO_2/water vapor plasma torch. In the case of air/water vapor: $\tilde{\eta} \times \left(\frac{G}{d_2}\right)^{1.36}$ and in the case of CO_2/water vapor: $\tilde{\eta} \times \left(\frac{G}{d_2}\right)^{0.96}$

Experimental dates are given for the same of voltage, current and radial flow rate. The following results were obtained:

The maximum thermal efficiency of the air plasma torch, $\eta = 0.88$ was reached at the current $I = 120$ A, voltage $U = 420$ V and the mass flow rate of working gas 12×10^{-3} kg·s^{-1}.

The maximum thermal efficiency of the CO_2 plasma torch, $\eta = 0.89$ was at the current $I = 160$ A, voltage $U = 440$ V and the mass flow rate of working gas 12×10^{-3} kg·s^{-1}.

The maximum thermal efficiency of the air/water vapor plasma torch, $\eta = 0.75$ was at the current $I = 160$ A, voltage $U = 343$ V and the mass flow rate of working gas 5.65×10^{-3} kg·s^{-1}.

The maximum thermal efficiency of the CO_2/water vapor plasma torch, $\eta = 0.77$ was at the current $I = 180$ A, voltage $U = 364$ V and the mass flow rate of working gas 5.69×10^{-3} kg·s^{-1}.

On one hand, the obtained results revealed that the greatest thermal efficiency of the plasma torch was achieved using air or CO_2 as plasma-forming gases. Slightly the inferior efficiency was achieved using mixtures of air/water vapor and CO_2/water vapor. Therefore, on the other hand, the mixtures of air/water vapor and CO_2/water vapor required a smaller amount of working gases.

4. CONCLUSIONS

Generalization of the plasma torch thermal and electrical characteristics based on the principles of dynamic similarity theory was found to be reasonable successful. During the process under the tangential injection of the plasma-forming gas, the arc inside the plasma torch was reduced and stabilized, and therefore the generalized VCC became dropping.

The gas injection location and composition has an important influence on the arc shape, dimensions and VCC. Under the adjustment of the arc voltage and current, using various plasma forming gas mixtures, it was possible to significantly increase the power of the plasma torch and change the VCC character.

The influence of gas composition and injection location (into the reaction arc zone or cathode area) was evaluated by the factor $(G/d_2)^{0.136}$ for air/water vapor and $(G/d_2)^{0.96}$ in the case of CO_2/water vapor.

The performed generalization allows improve the plasma torch parameters and efficiency.

5. REFERENCES

1. LAI W.H., LAI M.P., HORNG R.F. Study on hydrogen-rich syngas production by dry autothermal reforming from biomass derived gas. *International journal of hydrogen energy*, 2012, 37, p. 9619–9629.
2. STREIMIKIENE D., SIKSNELYTE I. Sustainability assessment of electricity market models in selected developed world countries. *Renewable and Sustainable Energy Reviews*, 2016, 57, p. 72–82.
3. SALVI B.L., SUBRAMANIAN K.A. Sustainable development of road transportation sector using hydrogen energy system. *Renewable and Sustainable Energy Reviews*, 2015, 51, p. 1132–1155.
4. LEBARBIER V.M., DAGLEA R.A., KOVARIKA L., ALBRECHT K.O., LI X., LI L., TAYLOR C.E., BAO X. WANG Y. Sorption-enhanced synthetic natural gas (SNG) production from syngas: A novel process combining CO methanation, water-gas shift, and CO_2 capture. *Applied Catalysis B: Environmental*, 2014, 144, p. 223–232.
5. LIUA Q., GUA F., LUA X., LIUA Y., LI H., ZHONG Z., XUA G., SUA F. Enhanced catalytic performances of Ni/Al_2O_3 catalyst via addition of V_2O_3 for CO methanation. *Applied Catalysis A: General*, 2014, 488, p. 37–47.
6. SAJJADI S.M., HAGHIGHI M., RAHMANI F. Dry reforming of greenhouse gases CH_4/CO_2 over MgO-promoted $Ni–Co/Al_2O_3–ZrO_2$ nanocatalyst: effect of MgO addition via sol–gel method on catalytic properties and hydrogen yield. *Journal of Sol-Gel Science and Technology*, 2014, 70, p. 111–24.
7. CHOI J.S., MOON K.I., KIM Y., LEE J., KIM C.H., TRIMM D. Stable carbon dioxide reforming of methane over modified Ni/Al_2O_3 catalysts. *Catalysis Letters*, 1998, 52, p. 43–7.
8. HLINA M., HRABOVSKY M., KAVKA T., KONRAD M. Production of high quality syngas from argon/water plasma gasification of biomass and waste. *Waste Management*, 2014, 34, p. 63–66.
9. YOON S.J., LEE J.G. Hydrogen-rich syngas production through coal and charcoal gasification using microwave steam and air plasma torch. *International journal of hydrogen energy*, 2012, 37, p. 17093–17100.
10. JASIŃSKI M., DORS M., NOWAKOWSKA H., MIZERACZYK J. Hydrogen production via methane reforming using various microwave plasma sources. Chemicke Listy, 2008, 102, s4, p. s1332−s1337.
11. CHOI D.H., CHUN S.M., MA S.H., HONG Y.C. Production of hydrogen-rich syngas from methane reforming by steam microwave plasma. *Journal of Industrial and Engineering Chemistry*, 2016, 34, p. 286–291.
12. HLINA, HRABOVSKY M., KONRAD, M., KOPECKY M., KAVKA V., LORCET, H. Properties of synthetic gas produced by plasma gasification of biomass. In: Proceedings of the XVIII International Conference on Gas Discharges and their Applications, INP Greifswald, p. 452–455. ISBN 0-9539105-4-7.
13. SEKIGUCHI H., MORI Y. Steam plasma reforming using microwave discharge. *Thin Solid Films*, 2003, 435, p. 44–48.
14. JASINSKI M., DORS M., MIZERACZYK J. Production of Hydrogen via Methane Reforming using Atmospheric Pressure Microwave Plasma Source with CO_2 swirl. *International Journal of Plasma Environmental Science & Technology*, 2008, Vol. 2, No. 2, p. 134–139.
15. YOON S.J., LEE J.G. Hydrogen-rich syngas production through coal and charcoal gasification using microwave steam and air plasma torch. *International journal of hydrogen energy*, 2012, 37, p. 17093–17100.
16. UHM H.S., NA Y.H., HONG Y.C., SHIN D.H., CHO C.H. Production of hydrogen-rich synthetic gas from low-grade coals by microwave steam-plasmas. *International journal of hydrogen energy*, 2014, 39, p. 4351–4355.

17. LUCAS C., SZEWCZYKA D., BLASIAKA W., MOCHIDAB S. High-temperature air and steam gasification of densified biofuels. *Biomass Bioenergy*, 2004, 27(6), p. 563–75.
18. BLASIAK W., SZEWCZYK D., LUCAS C. Reforming of biomass wastes into fuel gas with high temperature air and steam. In: Pyrolysis and gasification of biomass and waste conference, Strasbourg, France; 2002, 15 p.
19. ZHANG Q., DOR L., ZHANG L., YANG W., BLASIAK W. Performance analysis of municipal solid waste gasification with steam in a Plasma Gasification Melting reactor. *Applied Energy*, 2012, 98, p. 219–229.
20. TAMOŠIŪNAS A., VALATKEVIČIUS P., GRIGAITIENĖ V., VALINČIUS V. Electrical and thermal characteristics of water vapor plasma torch used for thermal plasma reforming. CYSENI 2013, May 29–31, Kaunas, Lithuania, ISSN 1822-7554.
21. ZHUKOV M. F., ZASYPKIN I. M., TIMOSHEWSKII A. N., MIKHAILOV B. I., DESYATKOV G. A. *Thermal Plasma Torches.* Novosibirsk, Nauka, 1999, p. 288.
22. TAMOŠIŪNAS A., VALATKEVIČIUS P., GRIGAITIENĖ V., VALINČIUS V. Water Vapor Plasma Torch: Design, Characteristics and Applications. World Academy of Science, Engineering and Technology, 2012, 6, p. 10–13.
23. ZHUKOV, M. F., ZASYPKIN, I. M. Thermal Plasma Torches: Design, Characteristics, Applications. Cambridge International Science Publishing Ltd, 2007. 600 p. ISBN-13: 978-1-904602-02-6.
24. GRIGAITIENĖ V., SNAPKAUSKIENĖ V., VALATKEVIČIUS P., TAMOŠIŪNAS A., VALINČIUS V. Water vapor plasma technology for biomass conversion to synthetic gas. *Catalysis Today*, 2011, 167, p. 135–140.

CYSENI 2016, May 26-27, Kaunas, Lithuania
ISSN 1822-7554, www.cyseni.com

THE CAUSE AND MECHANISM OF PELLETIZED BIOMASS SWELLING UPPON PYROLYSIS

Rolandas Paulauskas, Algis Džiugys, Nerijus Striūgas
Lithuanian Energy Institute
Breslaujos str. 3, LT-44403 Kaunas – Lithuania
Email: paulauskas.r@mail.lei.lt

ABSTRACT

Gasification process is a fairly complicated matter and using pelletized biomass for the gasification mostly results in fuel agglomeration. The pelletized biomass moving from the pyrolysis zone to the oxidation zone sticks together in lumps due to the initial expansion of pellets and disrupts entire process. In order to investigate the cause and mechanism of biomass expansion, thermal analysis and experimental research of pelletized biomass thermal deformations during pyrolysis were performed.

Experimental investigations were performed in a horizontal pyrolysis reactor from 400 °C to 1000 °C temperature capturing wood particle, wheat straw and wood pellet size changes by a digital camera. The observed changes of the biomass samples and the center temperature variations reveal that when increasing the pyrolysis temperature from 400 °C to 800 °C, the wheat straw and wood pellets expands at the beginning of pyrolysis process and after it start to shrink, while wood particle is only affected by shrinkage. It is caused due to more intensive wood particle decomposition than pelletized samples when faster devolitilization and surface charring bypass particle expansion by accumulated water vapors and volatiles eruption. The swelling phenomenon of pelletized samples starts decreasing over 600 °C heating temperature and disappears when the temperature is higher than 800 °C due to more intensive thermochemical processes which cause full release of volatiles and char formation.

According to microscopic images of samples and experimental results pelletized biomass expands when accumulated water vapour and volatile compounds inside pellet fail to evaporate from the pellet center due to chemical processes ongoing on the surface and influence the pellet porosity decrease. Due to the same reasons, pelletized fuel conglutinate in pyrolysis zone between 400 and 900 °C temperatures in the gasifier and stops further process.

Keywords: pyrolysis, pelletized biomass, decomposition, shrinking, swelling

1. INTRODUCTION

Biomass usage for electricity and heat production is increasing over years. The growing demand for these stocks and their price results in aiming to use not only the high-quality biomass, but also and low-quality. One of the option to use lower quality biomass for heat or electricity production to make biomass pellets and use for gasification process where solid fuel is converted into valuable producer gas. However gasifying pelletized fuel, sometimes bridging of fuel occurs in hoppers [1], in oxidation zone due to a high ash continent in fuel [2]. Also one more problem was observed during pelletized biomass gasification tests where moving pellets from the pyrolysis zone to the oxidation zone due to initial expansion pellets stuck together and stopped the entire process. In order to determine the cause of the cohesion of biomass pellets and find tendency of thermal deformations, it is necessary to understand processes which influences the swelling of pelletized biomass upon pyrolysis.

When biomass is inserted into a high temperature environment, a number of chemical and physical processes take place: dehydration, preheating, devolitilization and charring. Due to these processes, thermal conversion of biomass occurs resulting in shrinkage. Mostly shrinking of wood particle has been investigated for few decades and was found that birch particle shrinks till 80% at 700 °C [3], cubic wood particle – from 45% to 70% respectively at 350–900 °C [4]. Pelletized fuel changes are not so well investigated during thermal conversion and only scientist group from Sweden [5] researched swelling of recovered solid waste pellets (8 mm diameter) during pyrolysis in 500–900 ºC temperature range. The sample was pyrolysed at the constant temperature in an inert environment. During tests change of pellet mass was recorded and the pellet surface and center temperature was measured by K-type thermocouples. Also the change in the size of the pellet was captured by the CCD camera. Obtained results revealed that the recovered solid waste pellets expanded to 54% of the initial volume at 550 ºC heating temperature and after that the particle started to shrink. At higher heating temperature (660 ºC) swelling of the sample reached 58% of the initial volume. For comparison purposes, the authors repeated the experimental investigation with the straw pellets. The tendency of the straw pellet swelling and shrinking was different: the pellet expanded to 18% of the initial volume at 660 ºC heating temperature [5].

The reviewed works mostly analyse the shrinking phenomenon of biomass particles and only swelling effect of recycled solid waste pellets is researched at high temperatures, what shows that pelletized biomass thermal deformations are not fully clarified.

2. RESEARCH METHODOLOGY

Experimental research of wood particle, wood and straw pellets thermal deformations was carried out using the electrically heated horizontal tubular furnace Nabertherm RS 80/500/13. A scheme of this experimental rig is shown in Fig. 1.

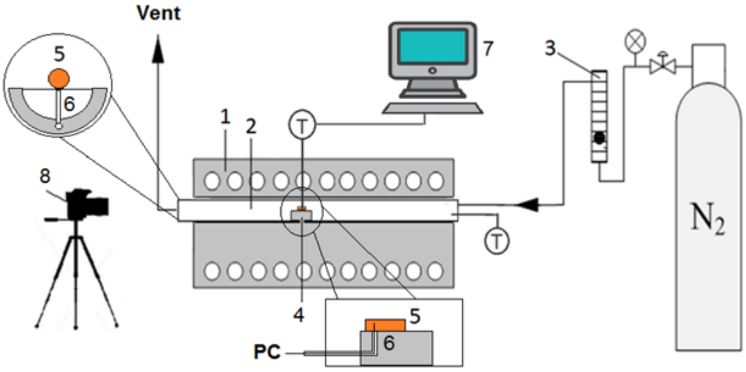

Fig. 1. Scheme of the experimental rig: 1 – electrical furnace RS 80/500/13; 2 – heating tube; 3 – nitrogen flow meter; 4 – sample holder with thermocouple; 5 – wood pellet; 6 – K-type thermocouple; 7 – computer; 8 – digital camera Fuji HS25 EXR

A heating tube (2) with outer diameter of 80 mm and length of 850 mm was mounted inside the furnace (1) and heated on both sides. One end of the tube was supplied by a nitrogen flow, which temperature was measured by an installed K-type thermocouple. The other end of the tube was left open for placement of a special pad with pelletized fuel particle and for capturing the sample size changes. The nitrogen flow of 8 l/min controlled by the flow meter (3) was fed into the furnace when the temperature reached the desired level. The special pad (4) with the sample (5) was inserted in the middle of the working tube through the open end. K-type thermocouple (6) was installed in the pad for sample centre temperature measurement during the pyrolysis process. The measured center temperature values were collected by data logger PICO TC-08 and sent to the computer (7). The pelletized fuel particle was captured with the digital camera Fuji HS25 EXR (8) through the open end of the tube during the pyrolysis process until the pellet stopped shrinking. The initial diameter of the sample was measured with a varnier caliper, which provided precision to 0.05 mm before the sample load. The measurements were performed with wood particle, wood and straw pellets at constant heating temperature from 400 °C to 1000 °C by 50 °C step repeating 5 times. The high-resolution (1920 × 1080 pixels) recorded videos of pelletized fuel particles changes were analysed using GIMP software. Each 150th recorded video frame was converted into a photo and the pelletized fuel particle diameter was measured with a digital ruler in pixels with 0.5 pixel accuracy. Obtained data in pixels was expressed as the relative units.

3. RESULTS AND DISCUSSIONS

Biomass samples swelling and shrinking and profile of center temperature at 400 °C, 600 °C, 800 °C and 1000 °C heating temperature are presented in Fig. 2. As it can be seen from Fig. 2 swelling effect occurs only for pelletized biomass. At low heating temperature (400 °C) only water evaporation and partial decomposition of samples dominates. Dehydration process takes place after 20 s from the beginning of experiment and lasts till center temperature of samples reaches 130 °C. With the end of water evaporation starts partial hemicellulose, lignin and cellulose decomposition causing swelling effect for pellets – diameter expands around 1% (Fig. 2 A) – and shrinking for wood particle. Wood particle center overheats faster than pelletized samples causing intensive thermal degradation with result of final shrinkage by 16.5% of initial diameter. After pellets swelling stabilizes, expanded samples starts to shrink and wheat straw pellet loses 8.5% of initial diameter, wood pellet ~ 6.7% of initial diameter. With growing heating temperature (600 °C), thermal conversion of samples is more intensive: water evaporation process shifts towards higher center temperatures till 140 °C and swelling effect of pelletized samples take place earlier (after 40 s from the beginning of experiment). At this temperature point, swelling of pelletized biomass is most intensive: wood pellet expands by 2.93% and wheat straw pellet – 3.93% of initial diameter (Fig. 2 B). Pelletized samples start to shrink immediately after swelling stabilizes: wood pellet loses 24.4% of initial diameter, wheat straw pellet – to 14.2%. Wood particle is affected only by shrinkage and loses 34.3% of initial diameter. At higher heating temperature (800 °C) trend of thermal conversion in biomass samples remains the same as at 600 °C temperature (see Fig. 2 B, C), though the decomposition is 1.65 time faster due to received higher amount of heat. Wood particle starts to shrink after 10 s from the placement to the reactor and loses 35.2% of initial diameter (see Fig. 2 C), while wood and wheat straw pellet is affected by swelling. Wood pellet expands less (1.13% of initial diameter) than wheat straw pellet (3.1% of initial diameter). After expansion, both pellets starts to shrink and wood pellet and wheat straw pellet loses respectively 25.4% and 14.9% of initial diameter (see Fig. 2 C). Swelling effect of pelletized samples is no more observed at 1000 °C heating temperature and only shrinkage dominates for all samples (Fig. 2 D). The shrinking of wood particle is most intensive and particle starts to shrink immediately after placement into heated tube. Measured shrinkage values respectively are 35.8% for wood particle, 26.4% for wood pellet and 16.8% of initial diameter for wheat straw pellet.

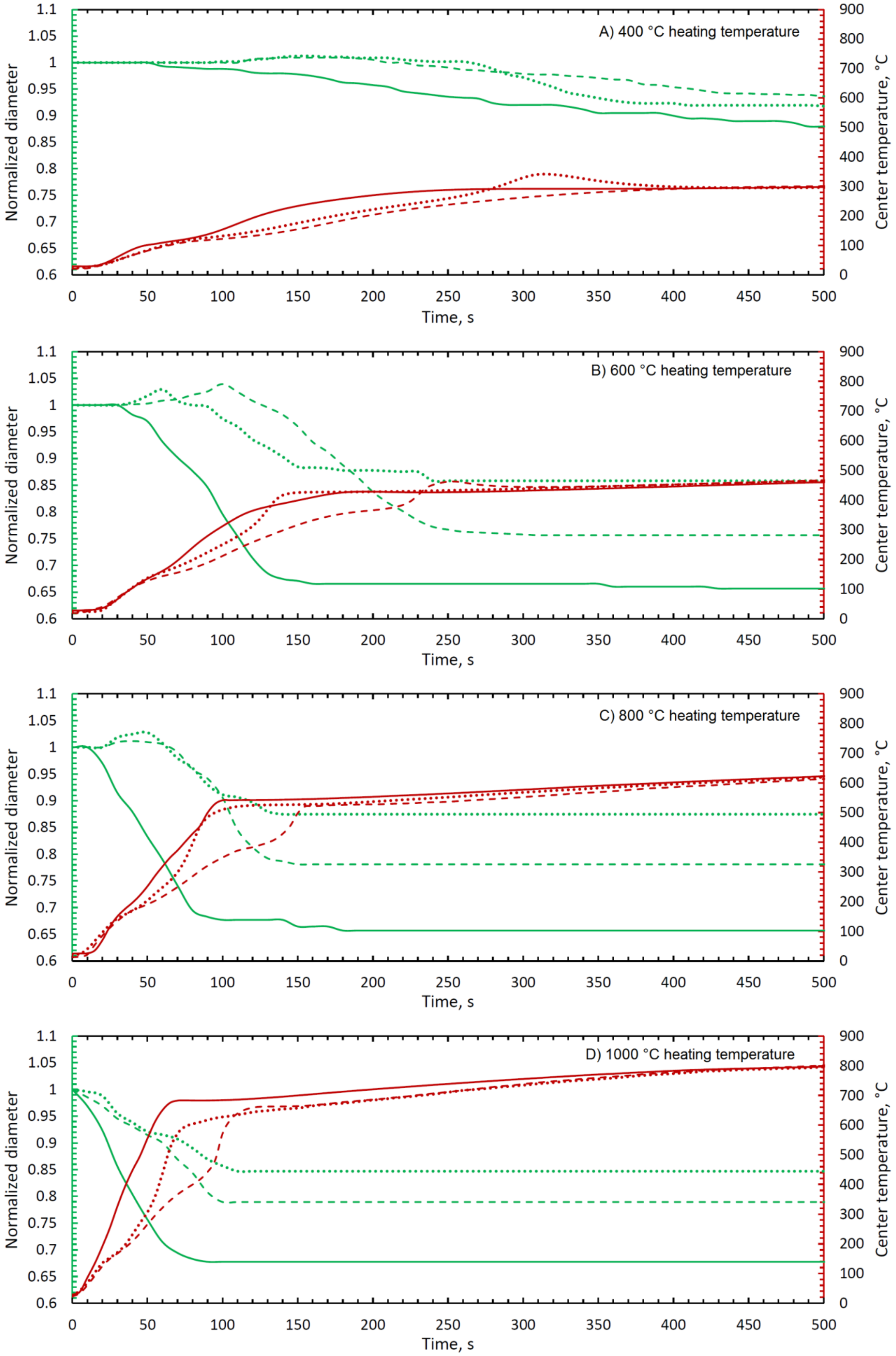

Fig. 2. Wood particle (solid line), wood pellet (dash line) and wheat straw pellet (round dot line) diameter and center temperature changes at different heating temperature

Analysed results reveals that thermal deformations of biomass samples are related to pyrolysis temperature and heat transfer inside the particles. Microscopy analysis of pyrolysed samples at various temperatures was performed using optical Olympus BX51 microscope with high-resolution digital color camera Go-21 controlled by QCapture software to identify swelling mechanism. Acquired pictures with 10X optical magnification is presented in Fig. 3.

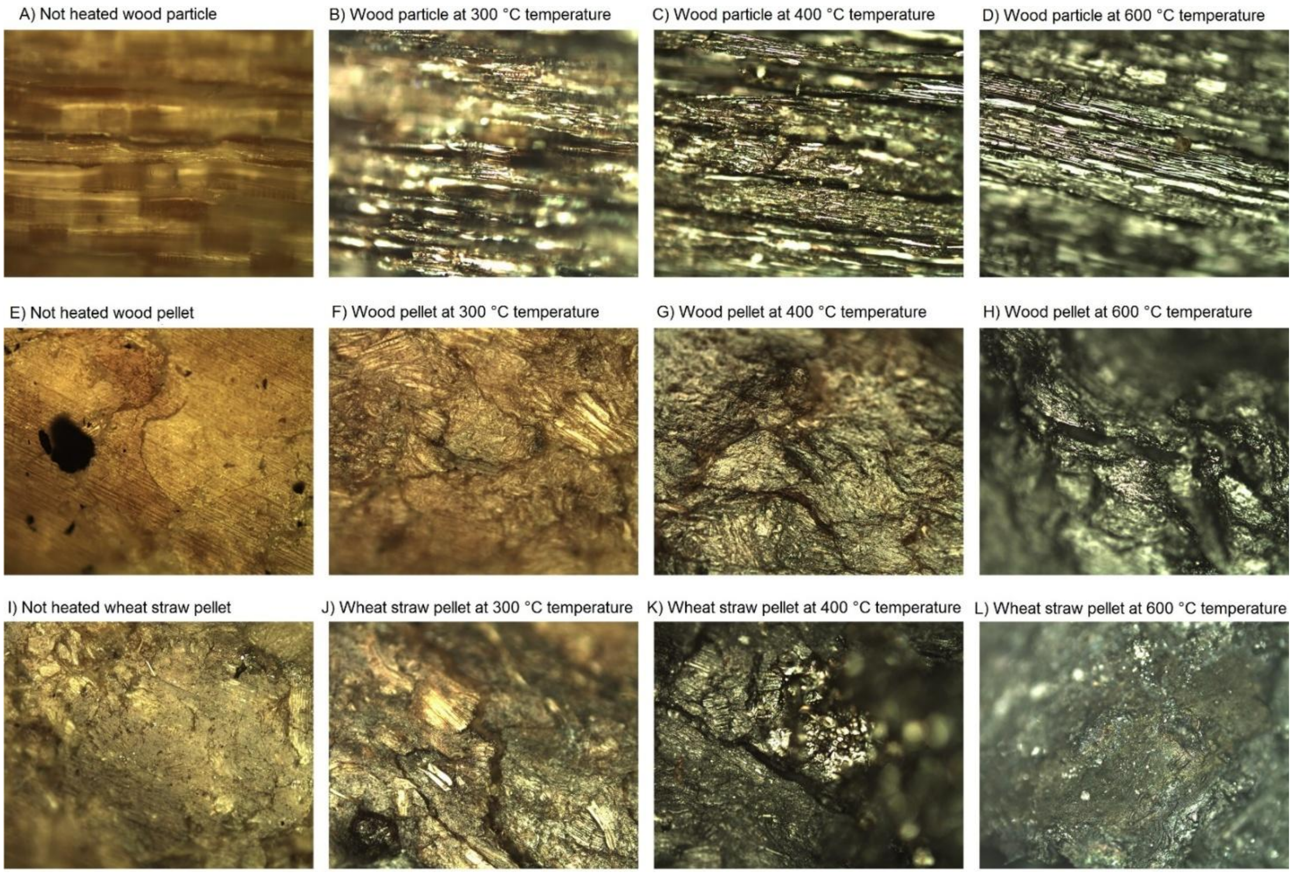

Fig. 3. Images of wood particle, wood and wheat straw pellets surface at different heating temperature acquired by optical microscope at 10× magnification

As it is seen from Fig. 3, surface of unheated wood particle is uniform structure where mostly cells are directed in one line without vessels (Fig. 3 A) while surfaces of pelletized samples consists of chaotically located pressurized sawdust or straw scobs with occurred vessels (Fig. 3 E, I). Surface of wood particle affected by 300 °C heating temperature starts charring (Fig. 3 B), what indicates intensive thermochemical processes. With growing heating temperature (400–600 °C) these processes cause wide cracks on surface and volatiles are emitted easily without any structure expansion resulting in fast shrinking (Fig. 2 and Fig. 3 C, D). Pelletized biomass surface is less affected by thermochemical processes at 300 °C temperature and only micro cracks and neglible tar melting occurs on surface (Fig. 3 F). Besides previous work [6] showed that pellets are not affected by swelling at 300 °C temperature. On the surface, affected by 400 °C heating temperature, tar melting is more intensive (Fig. 3 G, K) causing wider cracks. Besides vessels are formed on melted surface zones. Vessels occurs due to complicated devolatization process where formed water vapour and volatile compounds inside pellet fail to evaporate from the pellet center due to the chemical processes such as tar condensation ongoing on the surface which influence the pellet porosity decrease – melted surface in Fig. 3 F, G, J, K. In this way, water and volatile substances accumulate inside the pellet and internal pressure is becomes critical near the pellet’s surface, which destroys the surface structure of the pellet (swelling occurs) and spreads cracks on surface (Fig. 3) by freeing accumulated water vapour and volatiles. Shrinkage of pellets starts after drastic evaporation. The swelling phenomenon is no longer observed when the heating temperature is over 800 °C. The pellets overheats so quickly that the compounds emitted from the surface layer are decomposed by high amount of heat and the evaporation of volatiles becomes uncomplicated from the deeper layers without eruption.

4. CONCLUSIONS

Experimental research of wood particle, wood and straw pellet shrinkage and swelling during pyrolysis process can be summarized in few statements. The observed changes of biomass pellets diameter and the center temperature variation reveal that when increasing the heating temperature from 400 ºC to 1000 ºC, shrinkage intensifies exponentially from 16.5 to 35.8% for wood particle, from 6.7 to 26.4% for wood pellet and from 8.51 to 16.8% for wheat straw pellet. At low temperatures (up to 400 ºC), only water evaporation and negligible fuel decomposition occurs causing neglible swelling effect of pelletized biomass by 1% of initial diameter. Meanwhile the wood particle is only affected by shrinkage, what is due to more intensive decomposition than pelletized samples when faster devolitilization and surface charring bypass particle expansion by accumulated water vapors and volatiles eruption. The swelling phenomenon intensifies with the heating temperature increase up to 600 ºC causing maximum expansion: wood pellet by 2.93%, straw pellet 3.93% of the initial diameter. When the heating temperature is higher than 600 ºC, expansion of pellets starts decreasing and disappears when the temperature is higher than 800 ºC due to the intensive biomass decomposition which causes full release of volatiles and char formation. The expansion phenomenon is no longer observed at 1000 °C temperature.

According to obtained results pelletized biomass expands when accumulated water vapour and volatiles inside pellet fail to evaporate from the pellet center due to the chemical processes such as tar condensation on the surface which influence the pellet porosity decrease.

5. REFERENCES

1. STRIŪGAS, N., ZAKARAUSKAS, K., DŽIUGYS, A., NAVAKAS, R., PAULAUSKAS, R. An evaluation of performance of automatically operated multi-fuel downdraft gasifier for energy production. *Applied Thermal Engineering*, 2014, Vol. 73, Iss. 1, p. 1149–1157.
2. HAMEL, S., HASSELBACH, H., WEIL, S., KRUMM, W. Autothermal two stage gasification of low density waste derived fuels. *Energy*, 2007, Vol. 32, p. 95–107.
3. LARFELDT, J.; LECKNER, B.; MALAAEN, M., C. Modelling and measurements of the pyrolysis of large wood particles. *Fuel*, 2000, 79, 1637–43.
4. DAVIDSSON, K. O.; PETTERSSON, J. B. C. Birch wood particle shrinkage during rapid pyrolysis. *Fuel*, 2002, 81, 263–70.
5. ZHOU, C., ZHANG, Q., ARNOLD, L., YANG, W., BLASIAK, W. A study of the pyrolysis behaviors of pelletized recovered municipal solid waste fuels. *Appl Energy*, 2013, Vol. 107, p. 173–82.
6. PAULAUSKAS R., DŽIUGYS A., STRIŪGAS N. Experimental investigation of wood pellet swelling and shrinking during pyrolysis. *Fuel*, 2015, Vol. 142, p. 145–151.

CYSENI 2016, May 26-27, Kaunas, Lithuania
ISSN 1822-7554, www.cyseni.com

THE EXPERIMENTAL STUDY OF AUTO-IGNITION OF HYBRID METHANE/AIR/COAL DUST MIXTURE UNDER TEMPERATURE 950–1200 K

V. V. Leschevich, O. G. Penyazkov, S. Yu. Shimchenko
Heat and Mass Transfer Institute
P. Brovki str. 15, 220072 Minsk – Belarus
Email: sergey.shimchenko@gmail.com

ABSTRACT

This paper represents experimental investigation of ignition of combustible gaseous mixture with reactive particles in the rapid compression machine. It provokes interest because there is always some quantity of solid particles in gas media. At laboratory conditions in contrast to real combustion it is possible to reduce or to control amount and size of the particles in the test volume. For real applications it's necessary to take into account that reactive gas mixture contains solid combustible particles. In several cases effect of the particles presence can become significant.

The experiments were carried out with stoichiometric methane/air mixture in the presence of coal particles at size under 32 μm. The compression ratio was 39/1, resulting in compression pressure of 1.5–2.0 MPa and temperature of 950–1200 K. It was found that the presence of these particles not only reduces ignition time but influences on the ignition temperature of mixture. It is ascertained that ignition time of methane in pure air is longer than with same mixture with addition coal dust. This difference is explained to preignition of methane oxidation near burning particles. It is shown that ignition of coal dust originates at the temperature of oxidant higher 850 K. Temperature of particles burning in methane/air and air environment heated by compression was measured. The mean temperature is 2500 K. It indicates possibility of premature ignition of gas mixture heated by compression to temperature 1000–1100 K by addition of coal particles.

Keywords: auto-ignition, coal dust, methane, rapid compression machine

1. INTRODUCTION

Ignition investigation of dispersed systems consisting of reactive particles, gaseous fuel and oxidizer is topical from explosion and fire safety terms, for example in the coal mining industry. There are suspended solids in an atmosphere of coal mines, where methane may contain too. A lot of works have been directed in order to predict ignition conditions, ignition and flame propagation. A lot of attention is given to formation of dust cloud and initiation of its combustion because of local ignition and propagation of methane combustion wave. Development of this process leads to calamitous consequences. It is known that hybrid mixtures (methane/air/coal dust) are ignited at lower energy of external influence (for example electric spark) than is necessary for ignition of particular suspension of coal particles in the air [1, 2]. Research of this phenomenon is no less interesting from the point of view of process control of the gas mixture ignition. It can become scientific basis to create new modes of traditional fuels combustion. Thereby main purpose of this research is establishment of the possibility to control ignition of gas mixture by addition of known reactive particles to the test mixture.

2. EXPERIMENTAL RESULTS AND DISSCUTION

In the study of the reasons of gas mixtures premature self-ignition in the rapid compression machine (RCM) was found that this process is initiated in the separate sites that are formed mainly in the around the burning extraneous particles [3]. It has been very problematic to get rid of these particles and to carried out experimental measure of delay ignition of reactive gas mixture. The Fig. 1 shows the pressure change signals in the combustion chamber RCM and photomultiplier

(PMT) signals that registed the natural light. These signals were obtained in three experiments with a stoichiometric methane/air mixture at the similar conditions (1.6–1.8 MPa, 1050 ±10 K). Methane ignition was observed in only one case (the experiment *a*). The photomultiplier signal of this experiment shows that the relatively low intensity peak with width of 0.5 ms precedes to the main growth light which corresponds to methane ignition. This light is likely caused by the burning of foreign particle in the test volume.

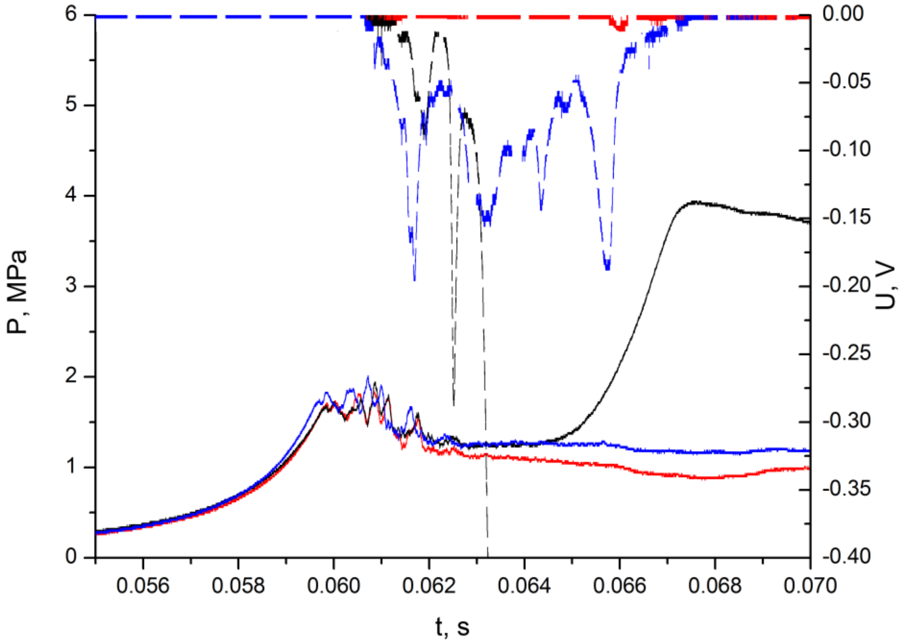

Fig. 1. Pressure (solid lines) and natural light (dashed lines) registered in three experiments (*a* – black line, *b* – red line, *c* – blue line) for methane/air mixture

The PMT signal amplitude from experiment *b* does not exceed the noise level. In the experiment *c*, the PMT has registered more intense glow, however, the ignition of the mixture was not observed. The obtained video frames showed the presence of several burning particles. It was found that test mixture does not ignite in all experiments provided thorough cleaning the inner surface of the rapid compression machine and use of piston rings lubrication at decreasing the temperature to 1000 K.

In this way, there was a need to establish a range of conditions, where accelerate of ignition of the gas mixture is possible, i.e. ignition of a mixture by burning particles. In this paper, coal dust at size no more than 32 μm was used as such particles. The sample with mass about 5 mg was evenly sprayed on the inner surface of the combustion chamber and on the front plane of the piston. Stoichiometric methane/air mixture was used as the gas component of the hybrid mixture. Ignition of the coal particles in the synthetic air (20.9% O_2 and 78.1% N_2) was investigated separately. Experiments were conducted in the RCM. During the combustion stroke, gas mixture temperature reached 800–1200 K at pressure 1.5–2.0 MPa. The initial pressure was chosen so to obtain approximately the same molar concentration of oxygen at the end of the compression stroke ($4\cdot10^{-5}$ mol/m^3) at different temperatures. Development of the ignition process was recorded by a high speed camera “LaVision HighSpeed Star X” with a frequency of 12,500 frames per second and a resolution of 1024 × 1024 pixels. Observation was carried out through a quartz window in the end wall of the combustion chamber. The window diameter (50 mm) was equal to the diameter of compression cylinder of the RCM. Pressure measurement carried out by the high temperature piezoelectric sensor Kistler 6031U18. Light emission from the test volume was transferred to the two photomultipliers on dual fiber optic cable; the common end of the cable was connected to the quartz window (5 mm dia) in the cylindrical wall of the combustion chamber from the top.

Emission of excited CH radicals was separated from the natural light by two narrow-band interference filters (430.4 nm and 430.8 nm, $\Delta\lambda_{0.5}$ = 2.6 nm) that were established in front of one of the PMT photocathode. The natural light of the flame during the combustion of methane or coal dust were recorded by the second photomultiplier with spectral sensitivity range is 300–600 nm.

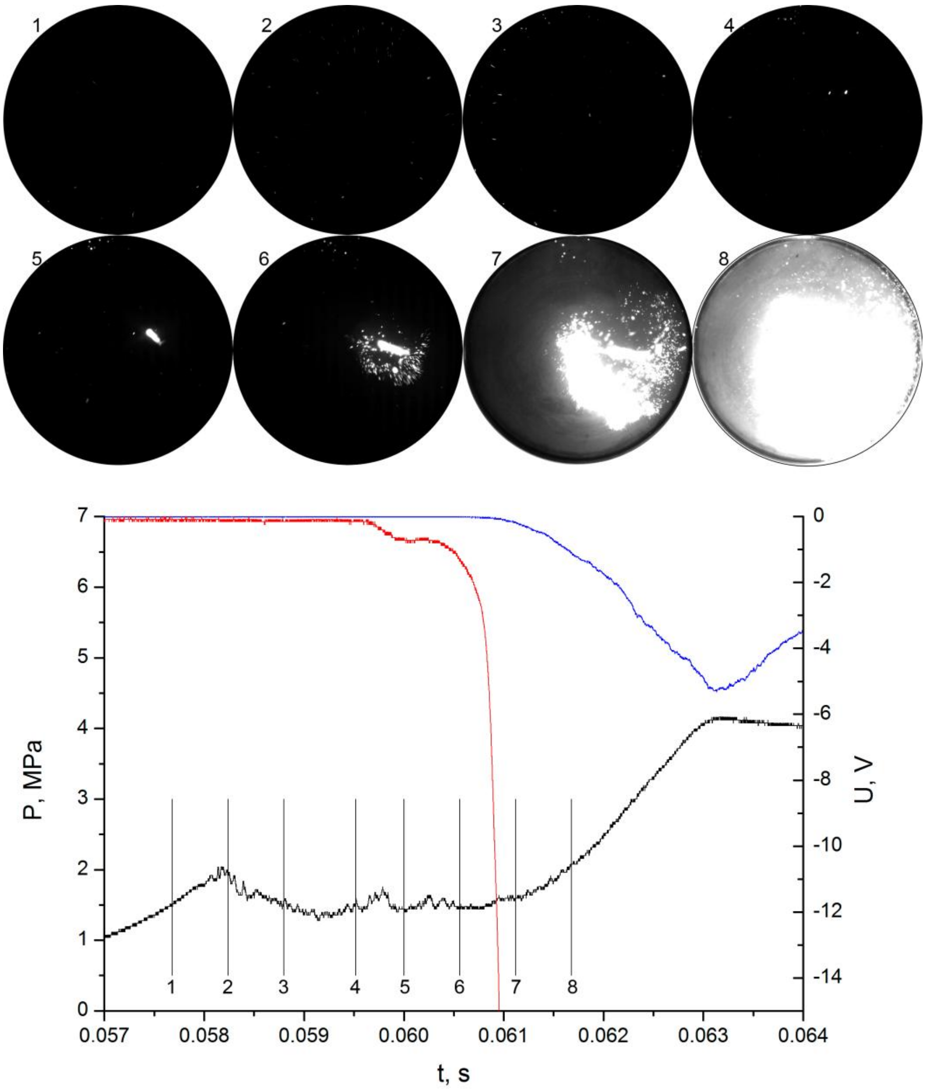

Fig. 2. Pressure (black line), natural light (red line), and emission of CH radicals (blue line) registered at methane/air/coal dust ignition together with frames from high-speed video

Signals of the pressure sensor and photomultiplier and eight frames (time of each is marked by lines on the chart) registered in the experiment with the methane mixture that contains coal dust particles in size of 20–32 µm, are shown on the Fig. 2. It was found that, ignition of certain particles ignition occurs in the compression process at the temperature about 880 K. During further compression, and increasing the temperature to 1010 K the number of burning particles increases and their combustion continues until the ignition of the methane/air mixture. It is clearly visible on the frames № 4 and № 5 that ignition of methane is initiated around of one of the particles.

At lower temperatures in the end of compression stroke the number of experiments with methane ignition, consisting of the hybrid mixture, decreased. The experiments with coal particles in the synthetic air heated by the compression showed that its ignition occurs at temperatures from 850 K. Herewith, the single burning particles that burn much faster than at more higher temperatures were obtained on the frames. Probably, size of these particles is far less than the size of the main parts of the sample that have not been separated by sieving used powder. Generalization of the results of all experiments is shown in the Fig. 3.

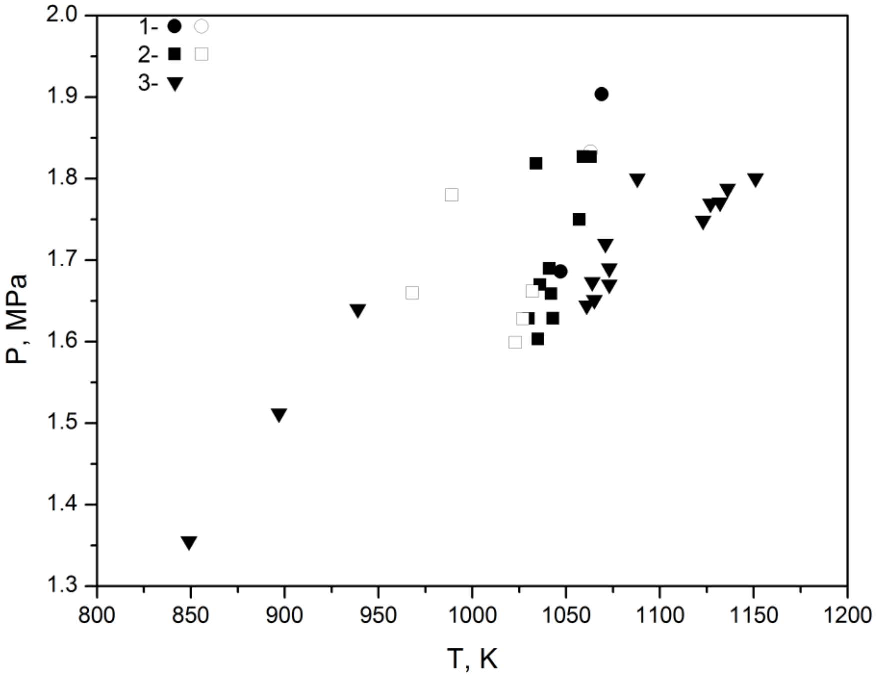

Fig. 3. The conditions of the test mixtures for the study of ignition: methane/air (1), methane/air/coal dust (2), and air/coal dust (3)

Blacken symbols correspond to conditions (temperature and pressure), in which methane/air and hybrid mixtures ignite and individual particles of coal dust in the air begin to burn. It is seen that the limited temperature is about 1060 K for ignition of stoichiometric methane/air mixture in the RCM. The ignition of hybrid mixture occurs at temperatures above 1030 K. Thereby, addition of coal particles (20–32 μm) slightly decreases limit temperature of methane ignition in the air. But this difference is within the error estimate of the temperature at the end of compression stroke (less than 5%). It indicates that in experiments without the addition of coal particles, methane ignition was probably initiated by foreign particles. This assumption is based on the video frames obtained in the previous experiments without included coal dust in test volume. Burning particles were found on these frames too.

The possibility of ignition of methane/air mixture by burning coal dust was confirmed by temperature measurement using photoemissive pyrometer. It was installed instead of a highspeed video camera. The luminous flux from the combustion chamber was focused on the photocathode by a collimator. Temperature measurement of burning coal particles (20–32 μm) was carried out with a frequency – 200 kHz under temperatures: in synthetic air – 800–1200 K and methane/air mixture – 950–1100 K. The results of these measurements are presented in the Fig. 4 at equal temperature of gaseous medium in the end of the compression stroke (1060 K) and molar concentration of oxygen. The temperature of coal particles have been marked by symbols at different time moments in the Fig. 4. together with the pressure signals (lines in the Fig. 4). These temperature values are enclosed in the shaded region for clearness. The equilibrium temperature of the products of the reaction of methane with oxygen at a constant pressure is 2700 K. It's theoretically calculated on the basis composition and initial conditions (the temperature and the pressure) mixture without loss heat by using known kinetic mechanism of chemical reaction GRI-mech 3.0. It possesses the lower value than certain values of coal dust temperature. It is seen that the particles temperature is higher than the gas mixture temperature measured at time interval corresponding to the induction period of methane/air mixture. It should be noted that the values of the measured temperatures of the particles in methane/air mixture are in the same range with burning particles temperatures in air. The average value of measured temperature is 2500 K. A similar value was obtained in paper [4] in which larger porous carbon particles were used. These measurements indicate that the burning particles may cause nonuniform temperature distribution in the combustion chamber.

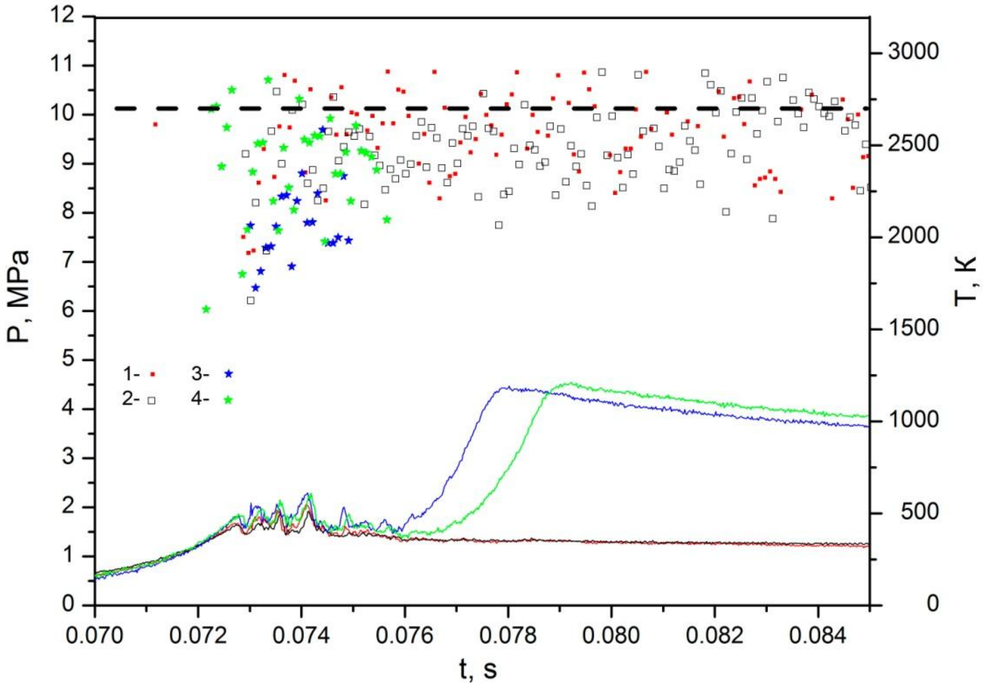

Fig. 4. Pressure (red and black lines – air, green and blue lines – methane/air) and results of a temperature measurement of coal dust: in air (1 and 2) and in methane/air medium (3 and 4). Dashed line is equilibrium temperature of the products of the reaction of methane with oxygen

3. CONCLUSIONS

In the result of this work, it is shown that the combustion of individual particles of coal dust occurs earlier than the ignition of a stoichiometric methane/air mixture at temperature range from 850 K to 1100 K. Burning particles reduce time and the limit temperature of methane/air mixture ignition at temperatures higher 1000 K. The temperature of burning coal particles in methane/air and air environments heated by compression was measured. The mean temperature is 2500 K. As a result, there is the possibility of methane–air mixture ignition by burning coal particles with size 20–32 μm under the temperature 1000–1100 K.

4. REFERENCES

1. NAGY, J., MITCHELL, D. W. Experimental coal-dust and gas explosions (No. BM-RI-6344). Bureau of Mines, 1963, Washington, DC (USA).
2. AMYOTTE, P. R., MINTZ, K. J., PEGG, M. J., SUN, Y. H. The ignitability of coal dust-air and methane-coal dust-air mixtures. *Fuel*, 1993, Vol. 72, No. 5, p. 671–679.
3. KRIVOSHEYEV, P. N., LESCHEVICH, V. V., PENYAZKOV, O. G., SHIMCHENKO, S. Yu. High-speed imaging of premature ignition in rapid compression machine. *Advances in Nonequilibrium Processes: Plasma, Combustion, and Atmosphere*, 2014. p. 137–147.
4. CHELLIAH, H. K., MILLER, F. J., KELLEY, A., MERCADO, A., WARFIELD, B. Heterogeneous Combustion of Porous Carbon Particles Under Normal and Reduced Gravity. In Fourth Joint Meeting of the US Sections of the Combustine Institute, 2005, Philadelphia.

CYSENI 2016, May 26-27, Kaunas, Lithuania
ISSN 1822-7554, www.cyseni.com

RESEARCH OF OH* CHEMILUMINESCENCE INTENSITY DEPENDENCE ON EXECESS AIR RAITIO IN PREMIXED NATURAL AND PRODUCER GAS FLAME

A. Saliamonas, R. Navakas, N. Striūgas A. Džiugys, K. Zakarauskas
Lithuanian Energy Institute
Breslaujos str. 3, LT-44403 Kaunas – Lithuania
Email: andrius.saliamonas@gmail.com

ABSTRACT

This article presents results of flame analysis by the emission spectroscopy method for registering chemiluminescent radical species of OH* from different angles at same time. The aim of this research is to investigate how OH* chemiluminescence intensity distributes along flame from various angles at same time and how this information can be used to determine air equivalence ratio. Also this is a continuation of experiments in order to investigate how mixing producer gas (PG) (a product of a biomass gasification process) in to the natural gas (NG) flow affects spectral characteristics of flame at specific wavelengths representing formation reactions of OH* radical species. The experiments were carried out when air equivalence ratio (ER) ranged from 1.04 to 1.20. All air, natural gas and producer gas flows were premixed before entering combustion chamber. The producer gas was generated from wood pellets in a lab scale gasification reactor. For flame emission spectroscopy a combination of spectrograph and five optic fiber setup was used to achieve data from 5 different angles and in various heights from burner outlet. After analyzing the distribution of chemiluminescent species intensity along the burner vertical axis, it was determined zones in flame, where OH* generation is at maximum and the effect of addition producer gas to natural gas and the OH* chemiluminescese dependence on air equivalence ratio was observed.

Keywords: Chemiluminesence, spectroscopy, producer gas, renewable energy, OH*

1. INTRODUCTION

Since 2014 biomass provides more than 10% of the primary energy resources in the world. Processing of biomass (for example gasification) is able to produce producer gas with high hydrogen content and its use is considered environmentally friendly due to the use of fuels coming from natural carbon dioxide consumers, having very low sulfur content and assented as CO_2 neutral.[1]. Producing biomass-based producer gas directly can be economically competitive with natural gas for price projections based on current policies [2]. However, for future policies associated with major greenhouse gas emission constraints, no direct economic incentive for switching to biomass-based producer gas production is achieved.

Despite that producer gas generation from biomass has the potential to displace petroleum and other fossil fuels. However, the presence of deleterious contaminant species is a big challenge to commercial deployment of biomass gasification at large scale [3]. Therefore exists a limited time challenge to research and develop better combustion techniques for producer gas combustion optimization. One of most promising non intrusive combustion process optimization technique is flame chemiluminescence monitoring. According to [4] ratios between various signals (for example, the ratio OH^*/CH^*) corresponding to light collected at different wavelength are commonly proposed as a reliable parameter to monitor a wide range of practical flames.

In a chemiluminescent reaction a released portion of energy turns in to a excited electronic state. The created energy state is short-lived and relaxes through a number of mechanisms, including collisional deactivation which is non-radiative and spontaneous photon emission. In the case of photon emission, species emits a characteristic wavelength, signaling presence of the species [5].

OH^*, CH^* and C_2^* radical chemiluminescence intensities show monotonously increasing trends with the air–fuel equivalence ratio [6]. In addition if light is collected from more than one direction at same time it is possible to do a computed tomography of chemiluminescence and use it to obtain the 3D, instantaneous, visible chemiluminescence profile of a flame [7].

The aim of this work is to apply 3D flame chemiluminescence scanning technique to compare OH^*, CH^* and C_2^* chemiluminescence intensity values along flame when using conventional fuel and with producer gas addition. This article presents comparison of chemiluminescence along flame from five different angles registered at same time with optical fiber ant spectrograph system. The experiments cover two fuels: natural gas and mixture of natural gas and producer gas. Experiments where performed for air equivalence ratio ranging from 1.04 to 1.20.

2. METHODOLOGY

The experiments were performed using the experimental setup consisting of an air/gas supply system, a lab scale gasification reactor system for producer gas supply, a combustion chamber, and a flame optical analysis system. All supply systems (air, producer gas and natural gas) were connected to combustion chamber. For each measurement of flame chemiluminescence, an initial volumetric gas flow was set with calibrated flow meters (Fig. 1).

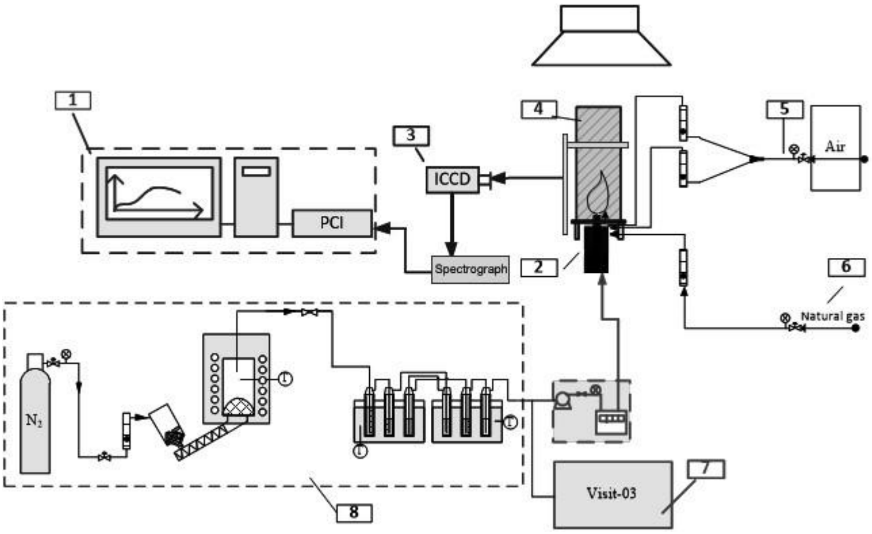

Fig. 1. Experimental setup: 1) Computer with spectroscopic data analysis software; 2) Gas premixing chamber; 3) ICCD camera with optical fibers; 4) Combustion chamber; 5) Air supply system; 6) Natural gas supply system; 7) Producer gas composition analyzer; 8) Producer gas generation system

3. ICCD CAMERA AND SPECTROGRAPH SETUP

The entire combustion process was observed by an optical system, which produced the output data for analysis of OH∗ spatial distribution in flame at atmospheric pressure. For capturing images, the ICCD (Intensified Charge Coupled Device) camera was used. The 18 mm-sized sensor consisted of 1024 × 1024 pixels sensitive to 200–800 nm wavelength light. The sensor was digitally divided in to 5 equal areas to collect light from each of 5 optical fibers. The ICCD camera was operated with “Solis” software. Single frame exposure was set to 5 s, and 10 frames were accumulated into a single image for each flame condition at 20 measurement planes along flame height. Multiple frames were recorded for each combustion and imaging regime (fuel mixture composition, fuel and air flow rates, selected measurement plane) in order to minimize the effect of possible flame instability.

For registering a combustion process, five optical fibers were used. Fibers where placed in parallel to horizontal plane around the flame. Each fiber was mounted on a metal ring and targeted to flame center. Angle between fibers was 72°. Each fiber has a 10° field of view. Metal ring with fibers was mounted to a vertical ruler for measurements at different height (Fig. 2).

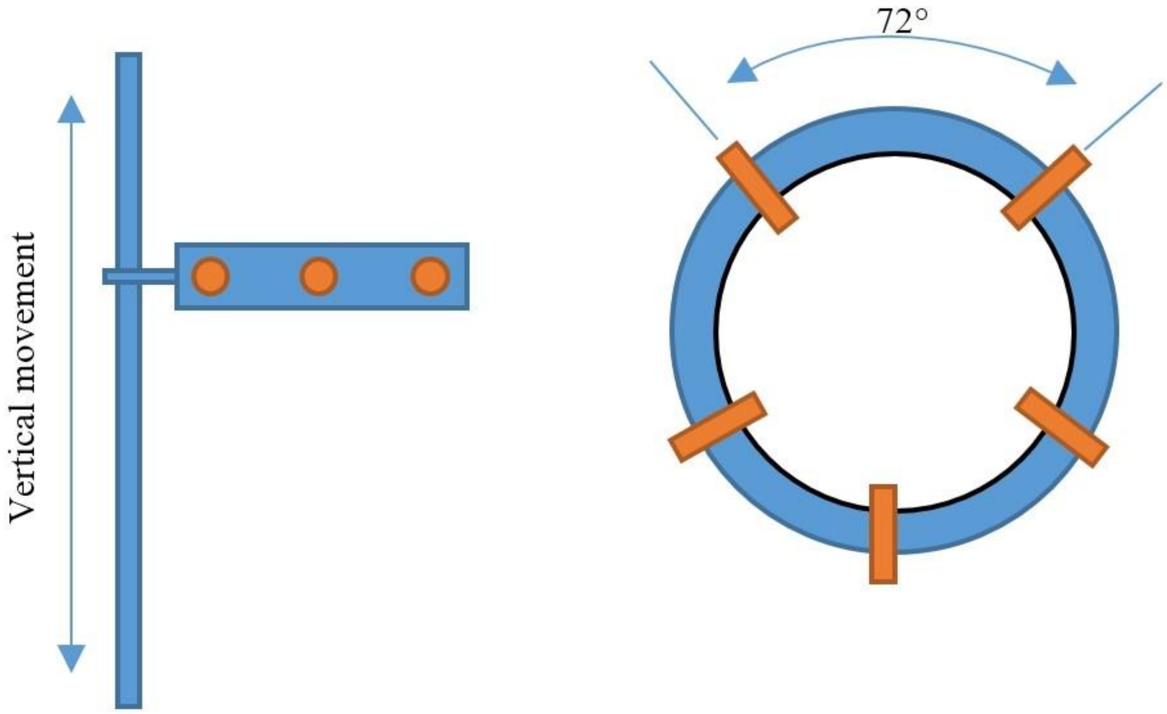

Fig. 2. Optic fiber placement

Optical system working principle is following: light from 5 flame areas was collected with optic fibers at same time. Optic fibers where connected to Andor Shamrock 303i spectrograph side input. Inside of spectrograph light was dispersed in to spectrum lines. ICCD camera was connected to spectrograph at direct output port. Dispersed light was projected on ICCD camera sensor. Sensor was digitally divided in to 5 areas for each optic fiber signal readout. Five spectrum charts where acquired for further analysis.

4. COMBUSTION RIG

The combustion chamber was made of 56 cm height and 6 cm diameter transparent quartz glass pipe. The pipe was mounted on a gas mixing chamber. Natural gas, producer gas and primary air flows were connected to the mixing chamber via steel pipes. Secondary air was connected direct to combustion chamber, bypassing the mixing chamber. Mixing of fuel/oxidant flows occurred inside the mixing chamber. Secondary air flow was installed to be used for flame stability on low excess air ratios, but in current work it was not used (Fig. 3). All gas flows were controlled by flow meters (Operating range 0.5–20 l/min).

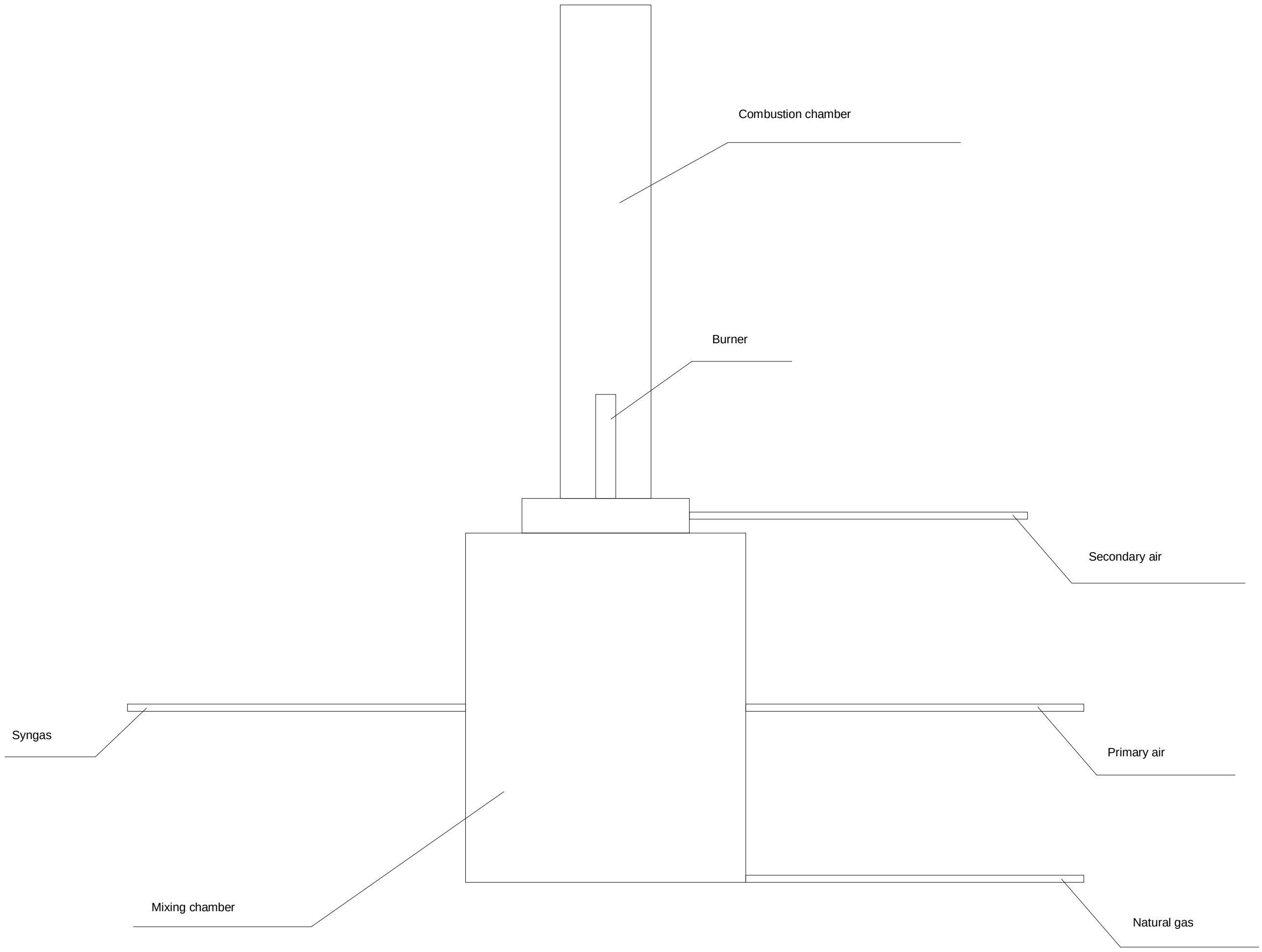

Fig. 3. Combustion chamber scheme

Producer gas was generated by using lab scale gasification reactor, which was described in detail elsewhere [8]. Producer gas was generated by the following procedures: Nitrogen flow (1.8 l/min) for pyrolysis gas transportation was supplied into a container filled with fuel pellets. Pellets made from a mix of pine and spruce wood were used for experiments. The pellet properties are given in Table 1.

Table 1. Properties of wood pellets used in experiment

Ash, wt.%	Moisture content, wt.%	Lower calorific value, MJ/kg	Wood composition, wt.% dry				
			C	H	O	N	S
0.35	5.20	19.00	49.20	6.20	44.46	0.08	0.06

5. RESULTS AND DISCUSSION

Flame spectra was collected from five different angles to reconstruct intensity spatial distribution (Fig. 4). Each optical fiber signal presented intensity values in 200–600 nm wavelength range. 6 bands for OH∗ chemiluminescence intensity determination were picked out from all data and compared for different flame conditions.

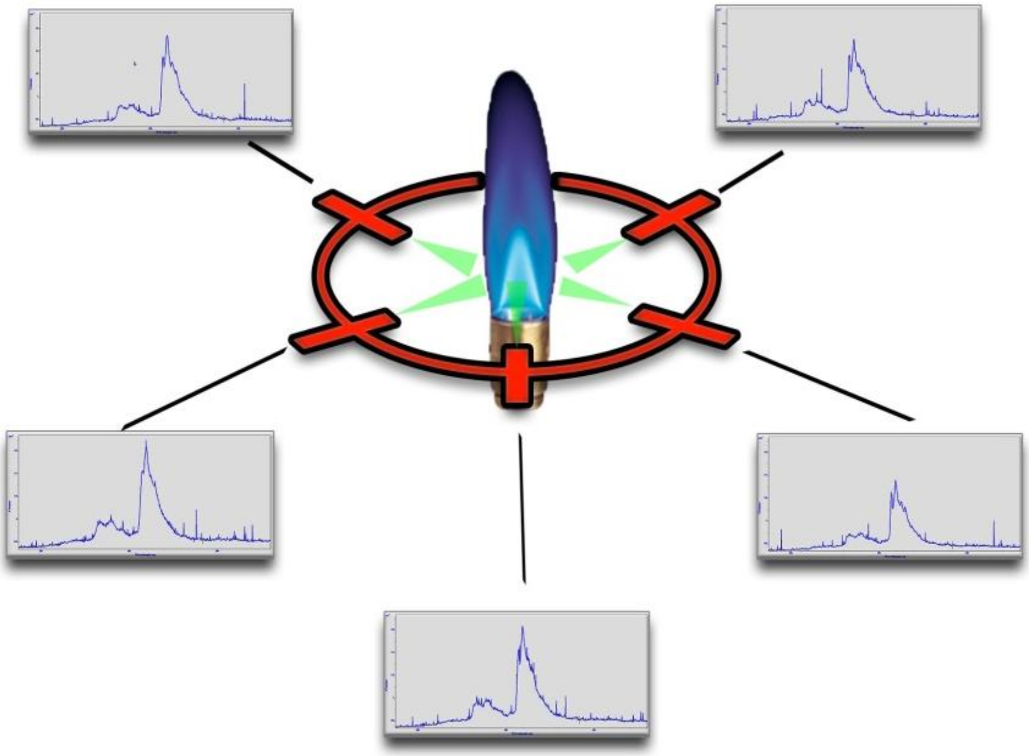

Fig. 4. Data accuisition scheme

The chemiluminescence intensity along flame height distributed unevenly, meaning that there was significant zone-dependent amount of chemical reactions that emitted light in UV spectral range in combustion zone. Main chemiluminescent species of interest were OH^* radicals as they are known to show strongest intensity [9, 10] and tend to have relation to excess air ratio. Main reactions of these radicals formation are given in Table 2 [11].

Table 2. Chemiluminescence reaction mechanism to model OH^* formation and quenching

Reactions of OH^* fomation and quenching
$H+O+M \longleftrightarrow OH^*+M$
$CH+O_2 \longleftrightarrow OH^*+CO$
$OH^*+H_2O \longrightarrow OH+H_2O$
$OH^*+CO_2 \longrightarrow OH+CO_2$
$OH^*+CO \longrightarrow OH+CO$
$OH^*+H_2 \longrightarrow OH+H_2$
$OH^*+OH \longrightarrow OH+OH$
$OH^*+H \longrightarrow OH+H$
$OH^*+N_2 \longrightarrow OH+N_2$
$OH^*+CH_4 \longrightarrow OH+CH_4$

Results, gathered from different angles for various flame conditions show that chemiluminescence was strongest and 288 degree angle. In our case this was combined result of non-uniform distribution of chemical reactions in flame, flame instability and possible burner alignment asymmetry (Figs. 5–7). This result also confirm meaningfulness of using multi-spot flame monitoring, because intensity distribution variations can be significant for accurate local excess ratio and other parameters determination. In OH^* chemiluminescence intensity range at 289.9 nm and 309.8 nm it was determined that 309.8 nm wavelength signal is stronger yet showing similar behavior like 289.9 nm. Also addition of producer gas increased overall intensity values, but the relations to excess air ratio remained unchanged (Figs. 5 a and b).

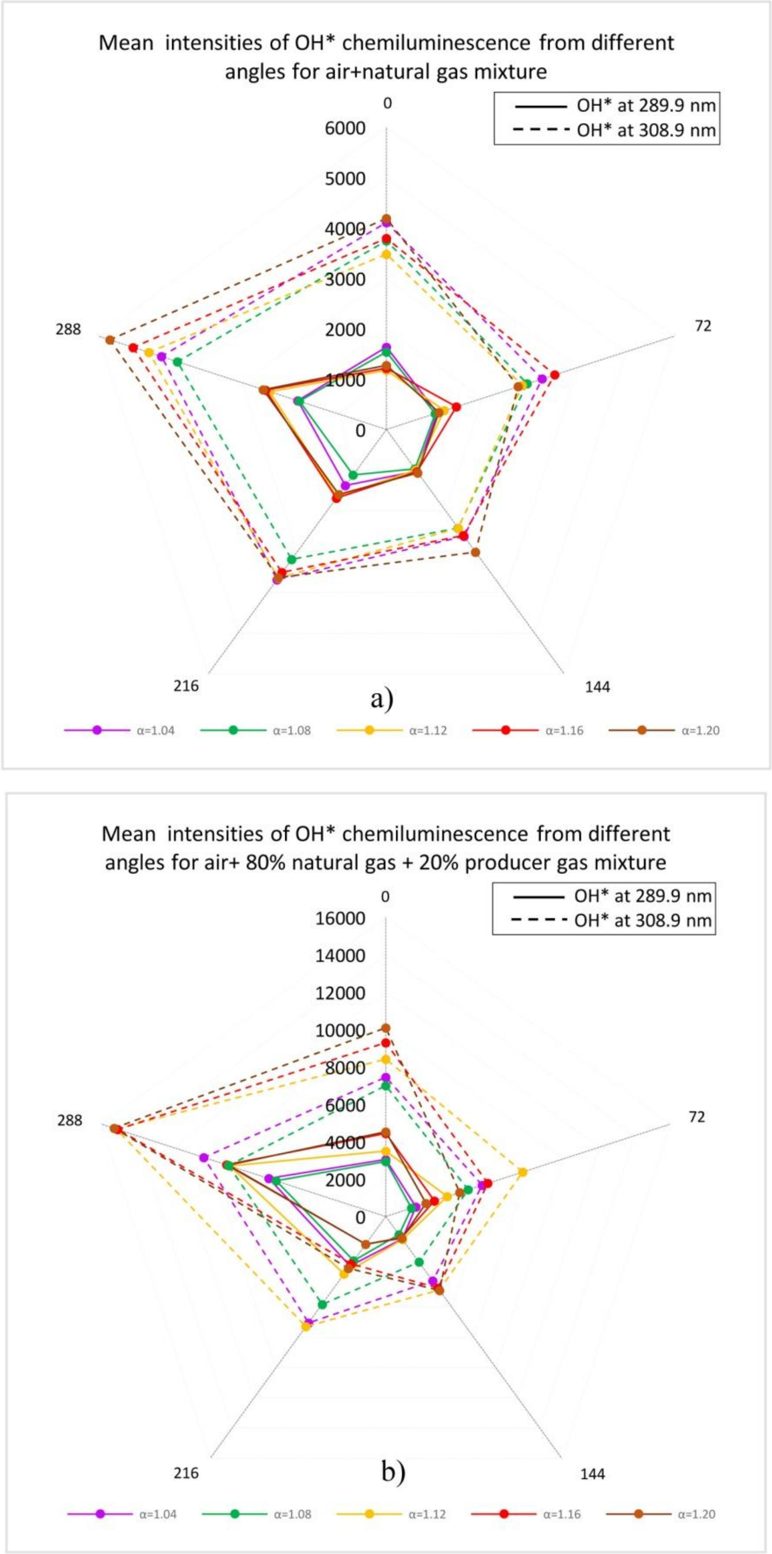

Fig. 5. Mean intensities of OH* chemiluminescence from different angles for a) air + natural gas b) air + natural gas + producer gas mixture

All registered intensities maximum values were allocated between 0.5 and 1.5 cm distance from burner outlet. According to Hardalupas et al. [12] only the maximum intensity values are important when deciding about chemical reaction at a defined point in space and the areas before and after the peaks are considered as reaction beginning and ending zones. It means that most of chemical reactions related to OH* radical transitions from excited state to ground state [10] occurred near burner outlet Also it can be seen that with addition of producer gas (PG) due to hydrogen presence in the mixture, the reaction zone tends to be even shorter, leaving no recordable signal of chemiluminescence nearly at 4 cm distance from outlet (Figs. 8–10). Hydrogen reacts faster with oxidant than methane and increases temperature in reaction zone so the combustion reactions complete faster and closer to the burner's nozzle. The chemiluminescence intensity shift toward burner's nozzle can be seen in the results [13]. The producer gas composition analysis confirmed hydrogen presence in mixture for combustion.

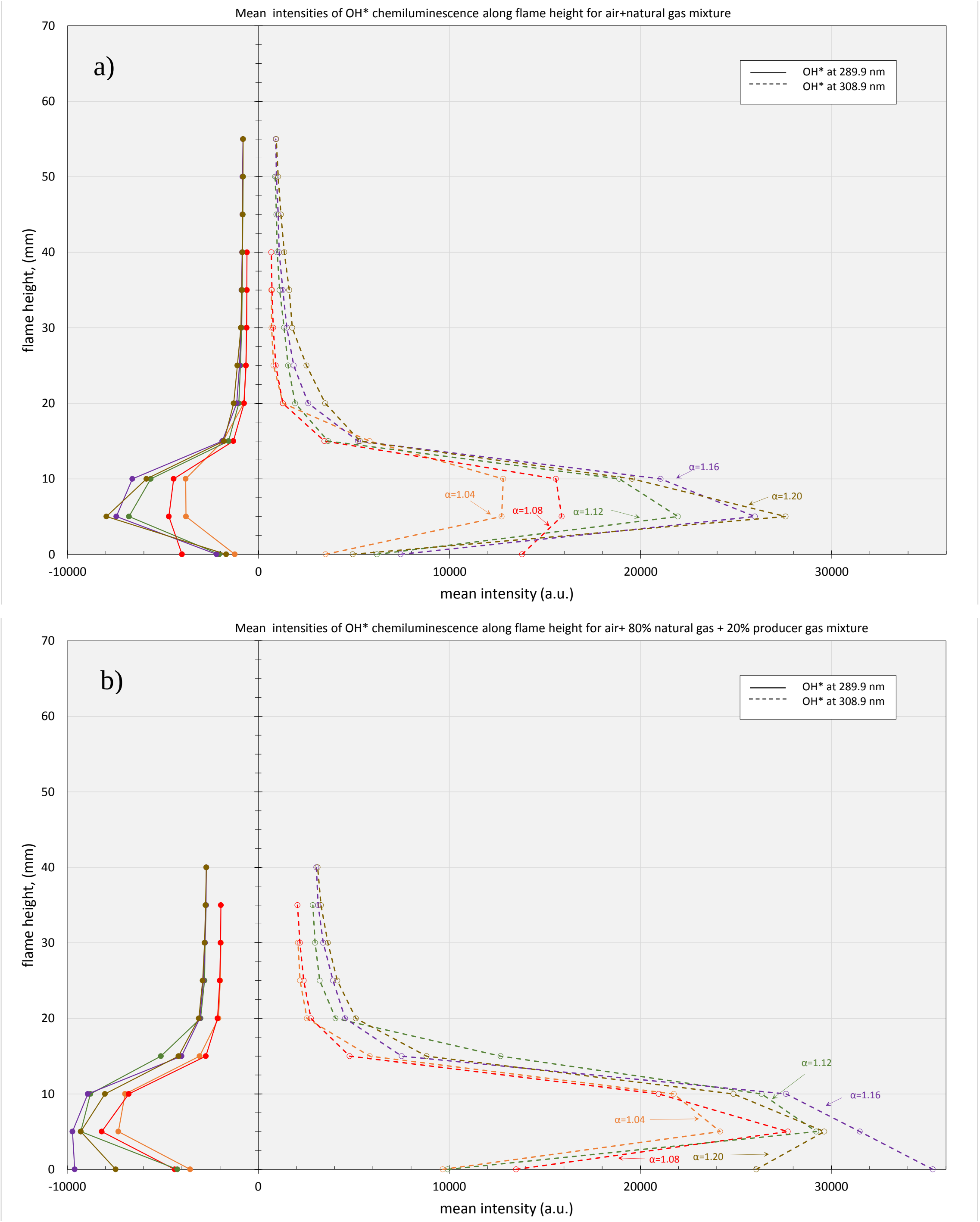

Fig. 6. Mean intensities of OH* chemiluminescence along flame height for: a) air + natural gas; b) air + natural gas + producer gas mixture

For comparing chemiluminescence intensity distribution of OH*, all 5 point angular intensity data was merged in to single flame front chemiluminescent intensity curve. The differences between intensities from different angles where taken into account by applying a correction coefficient based on maximum intensity values. A single curve for every excess air ratio, gas mixture and wavelength was created and representing chemiluminescence intensity distribution along flame height. The tendention of shorter flame can be seen in all images, approving the effect of hydrogen presence in producer gas (Fig. 6).

To show excess air ratio relation with chemiluminescent species the experimental points at heights from 0 to 1,5 cm were taken into account. This was the zone, where intensity was registered at maximum values. Results were obtained by interpolating experiment data points with a cubic polynomial. Results show that OH∗ tends to show strongest relation between intensity and excess air ratio but more experimental point and a moredetailed model needs to be applied in order to have well defined and numerically expressed correlation. In case when produced gas was used the OH* vs excess air ratio produced a steeper curve. This result gives suggestion of possible increase of adiabatic temperature [14].Other radical species chemiluminescence are also related to temperature fields [15] (Fig. 7).

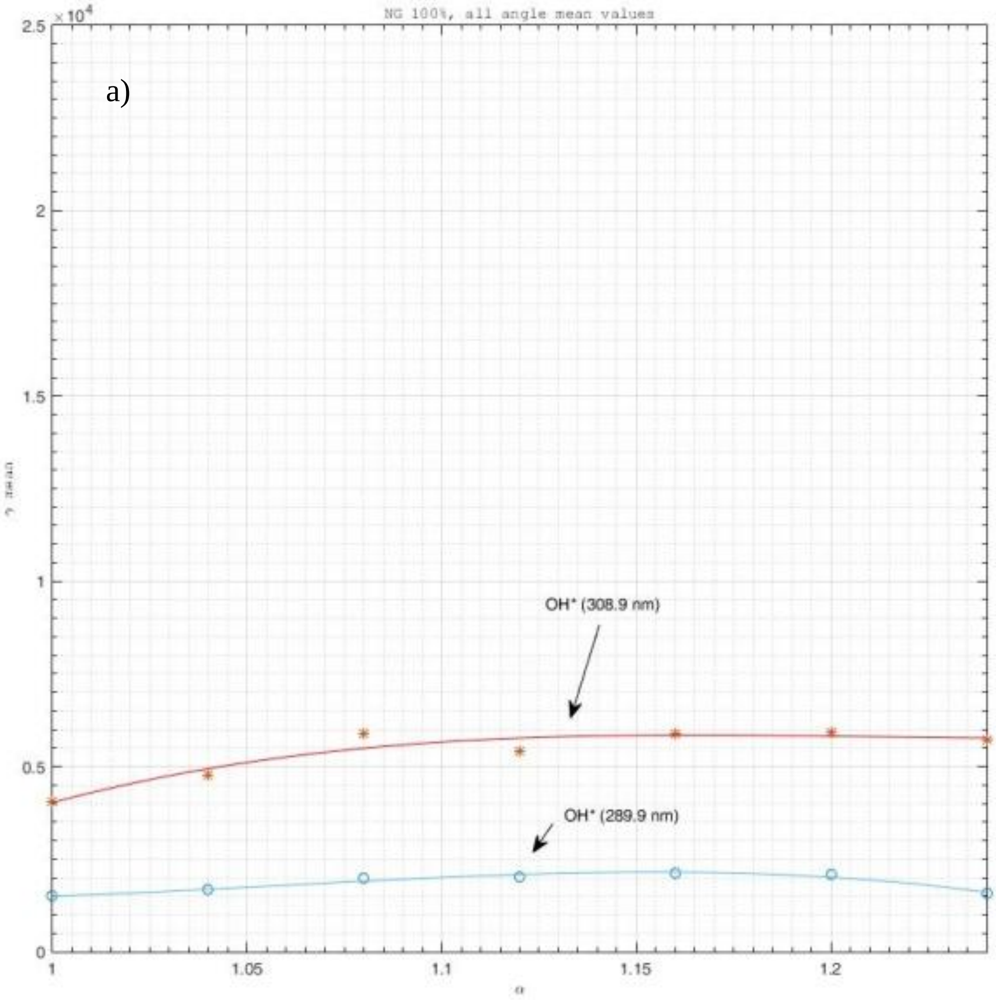

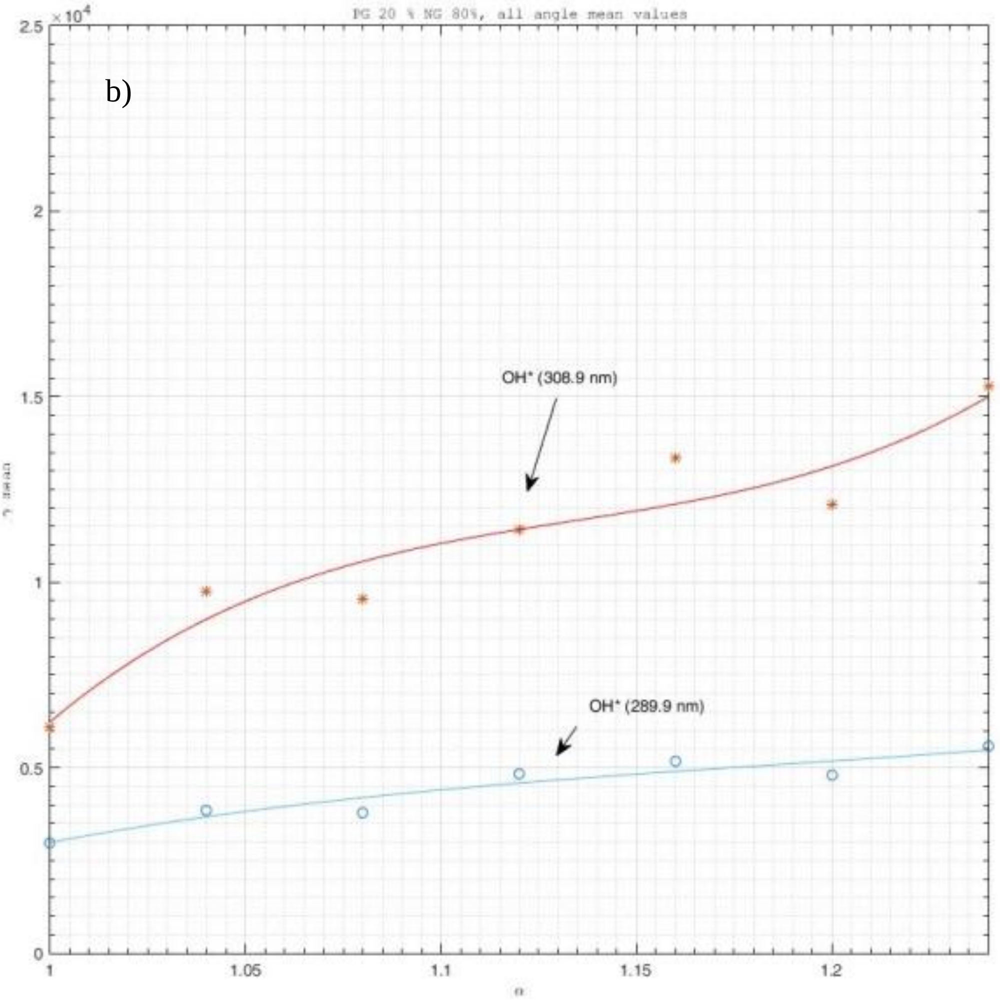

Fig. 7. Excess air rati dependence on chemiluminescence intensity for *OH** in: a) air + natural gas; b) air + natural gas + producer gas mixture.

6. CONCLUSIONS

The multi-point imaging of chemiluminescence intensity has been implemented with ICCD camera, and used to obtain the 3D, instantaneous, visible chemiluminescence profile of a premixed natural gas and natural gas + producer gas flames. A total of five optical filters and a system acquisition plane elevation provided multiple views along flame. Measurements have been performed at excess air ratios between 1.04 and 1.20, and were processed using Matlab. Processing included signal noise filtering, rejection of unnecesarry data (leaving only 6 wavelengths), curve fitting operations and graphical output generation.

Chemiluminescent intensity in flame distributed non uniformly due to different chemical reactions occurring at different flame locations. The locations of known excited state radical species were determined by maximum intensity values at specific wavelengths. In all cases the maximum intensity was between 0 and 1.5 cm from burner outlet. It was assumed that at these locations the reactions from described chemical kinetics mechanism are mostly expected.

It was found that OH* intensity at 309.8 nm has strongest intensity in all experiment result. After determination of highest intensity zones in flame a relation to local excess air ratio and OH* intensity was found by interpolating experimental points with a cubic polynomial. The addition of producer gas to mixture makes chemiluminescence intensity values higher and more concentrated at distances near burner outlet. This effect is due to hydrogen presence in mixture. OH* dependence on excess air ratio in mixture of producer gas and natural gas is more sensitive to changes in air/fuel ratio. This effect might have a relation between OH* intensity ant flame adiabatic temperature, but to confirm this assumption it is important to expand experiments by adding more excess air ratio values in experiments and to implement a reliable temperature field measurements in combustion chamber. Five different measuring angles gives enough information for further analysis, by using computed flame tomography algorithms.

7. REFERENCES

1. SEBASTIAN CARO, DANIEL TORRES, AND MARIO TOLEDO. Syngas production from residual biomass of forestry and cereal plantations using hybrid filtration combustion. *International journal o f hydrogen energy*, 40:2568–2577, 2015.
2. MARIA ARVIDSSON, MATTEO MORANDIN, AND SIMON HARVEY. Biomass gasification-based syngas production for a conventional oxosynthesis plantgreenhouse gas emission balances and economic evaluation. *Journal of Cleaner Production*, 99:192–205, 2015.
3. NOURREDINE ABDOULMOUMINE, SUSHIL ADHIKARI, AVANTI KULKARNI, AND SHYAMSUNDAR CHATTANATHAN. A review on biomass gasification syngas cleanup. *Applied Energy*, 155:294–307, 2015.
4. TATIANA GARCIA-ARMINGOL, YANNIS HARDALUPAS, A.M.K.P. TAYLOR, AND JAVIER BALLESTER. Effect of local flame properties on chemiluminescence-based stoichiometry measurement. *Experimental Thermal and Fluid Science*, 53:93–103, 2014.
5. SUNNY KARNANI AND DEREK DUNN-RANKIN. Visualizing ch* chemiluminescence in sooting flames. *Combustion and Flame*, 160:2275–2278, 2013.
6. VIKTOR JOZSA AND ATTILA KUN-BALOG. Spectroscopic analysis of crude rapeseed oil flame. *Fuel Processing Technology*, 139:61–66, 2015.
7. J. FLOYD, P. GEIPEL, AND A.M. KEMPF. Computed tomography of chemiluminescence (ctc): Instantaneous 3d measurements and phantom studies of a turbulent opposed jet flame. *Combustion and Flame*, 158:376–391, 2011.
8. N. STRIŪGAS, K. ZAKARAUSKAS, G. STRAVINSKAS, AND V. GRIGAITIENĖ. Comparison of steam reforming and partial oxidation of biomass pyrolysis tars over activated carbon derived from waste tire. *Catalysis today*, 196(1):67–74, 2012
9. F. FERRO, J. SANCHES, AND E. C. FERNANDES. Spectrum analysis of flames chemiluminescence. *Combustion and Flame*, 1–40, 2013.
10. TRUPTI KATHROTIA. *Reaction Kinetics Modeling of OH*,CH*, and C2* Chemiluminescence*. PhD thesis, 2011.
11. VENKATA NORI AND JERRY SEITZMAN. Evaluation of chemiluminescence as a combustion diagnostic under varying operating conditions. *46th AIAA Aerospace Sciences Meeting and Exhibit*, pages 1–14, 2008.
12. Y. HARDALUPAS, M. ORAIN, C. S. PANOUTSOS, M. K. TAYLOR, J. OLOFSSON, H. SEYFRIED, M. RICHTER, J. HULT, M. ALDÉN, F. HERMANN, AND J. KLINGMANN. Chemiluminescence sensor for local equivalence ratio of reacting mixtures of fuel and air (flameseek). *Appl. Therm. Eng*, 24(11):1619–1632, 2004.
13. B.K. SLIM, H. DARMEVEIL, G.H.J. VAN DIJK, D. LAST, G. T. PIETERS, M. H. ROTINK, J. J. OVERDIEP, AND H.B LEVINSKY. Should we add hydrogen to the natural gas grid to reduce CO2-emissions. consequences for gas utilization equipment. *Proceedings of 23rd World Gas Conference*, 2006.
14. J.J. HERNANDEZ, J. BARBA, AND G. ARANDA. Combustion characterization of producer gas from biomass gasification. *Global NEST Journal*, 14(2):125– 132, 2012.
15. C. A. MARTINS, A. P. PIMENTA, J. A. CARVALHO JR., M. A. FERREIRA, AND A. A. CALDEIRA-PIRES. Ch and C2 radicals characterization in natural gas turbulent diffusion flames. *Journal of the Brazilian Society of Mechanical Sciences and Engineering*, 27(2):110–118, 2005.

CYSENI 2016, May 26-27, Kaunas, Lithuania
ISSN 1822-7554, www.cyseni.com

EFFECT OF BIOMASS SETTLING IN THE FIXED BED GASIFICATION REACTOR

J. Kluska, P. Kazimierski, D. Kardaś
Institute of Fluid-Flow Machinery, Polish Academy of Sciences,
Fiszera str. 14, 80-231 Gdańsk – Poland

P. Kazimierski
Gdańsk Univeristy of Technology, Faculty of Mechanical Engineering
Siedliscka str. 4, 80-223 Gdańsk – Poland
E-mail: pkazimierski@imp.gda.pl

ABSTRACT

Typical processing of biomass in a fixed bed gasifier starts from drying, where moisture is released from biomass, then followed by pyrolysis in which gases and char are produced from biomass .In the next phase of gasification process gases are mixed with air and burned to CO_2 and H_2O, whereas charcoal combines with CO_2 and H_2O forming a combustible gas. The most important factors in the gasification process are the temperature and the amount of air supplied to the gasification process. These parameters have a significant impact on the quality of the produced syngas. However in terms of entire process of gasification important role plays fuel particle velocity. This paper presents the problem of fuel settling during gasification process, which means the movement of solid phase in a fixed bed reactor. The aim of the research is to understand the process in terms of its kinetics and describe the motion of the biomass particles as a result of change in their volume. The loss of that volume is caused by pyrolysis and chemical reactions. Experimental studies were carried out in a small scale downdraft reactor with a height of 100 cm and the 20 cm diameter. Researches were carried out in the reactor operating in a continuous mode for different amounts of air supplied to the gasifier. The rate of fuel settling was determined by means of radiography, wherein change of position of the radiographic indicator was recorded during gasification process.

Keywords: gasification, settling velocity, pine wood, fixed bed, pyrolysis

1. INTRODUCTION

During the gasification process in a fixed bed reactor operating in a batch mode, fuel is delivered from the top and moves down. Typical processing of biomass in a fixed bed gasifier starts from drying, where moisture is released from biomass, then followed by pyrolysis in which gases and char are produced from biomass [1]. In the next phase of gasification process gases are mixed with air and combusted to CO_2 and H_2O, whereas charcoal combines with CO_2 and H_2O forming a combustible gas. The most important factors in the gasification process are the temperature and the amount of air supplied to the gasification process [2], [3]. These parameters have a significant impact on the quality of the produced syngas. However in terms of entire process of gasification important role plays fuel particle velocity. This work presents experimental investigation of fuel settling velocity during gasification of pine wood in the small scale batch reactor. The average speed is known, it is results of fuel consumption and reactor dimensions. However, this speed is not constant over the entire height of the reactor and varies in the different zones.

2. WOOD SAMPLE

In order to determine the properties of the tested biomass, pine wood was minced first in a knife mill and then in a centrifugal mill equipped with a sieve with the mesh diameter of 0.2 mm. The results of the proximate and ultimate analysis are shown in the Table 1.

Table 1. Proximate and ultimate analysis of the biomass

LHV [MJ/kg]	19.59
Technical analysis [%]	
Moisture content	15
Volatile	67.9
Char	21.4
Ash	2.3
Elementary analysis [%]	
C	45
H	6.4
O	47.3
N	1.3

Analysis of pyrolytic decomposition of biomass was performed for experiments. The tests were performed using analytical termograwimetry (Fig. 1).

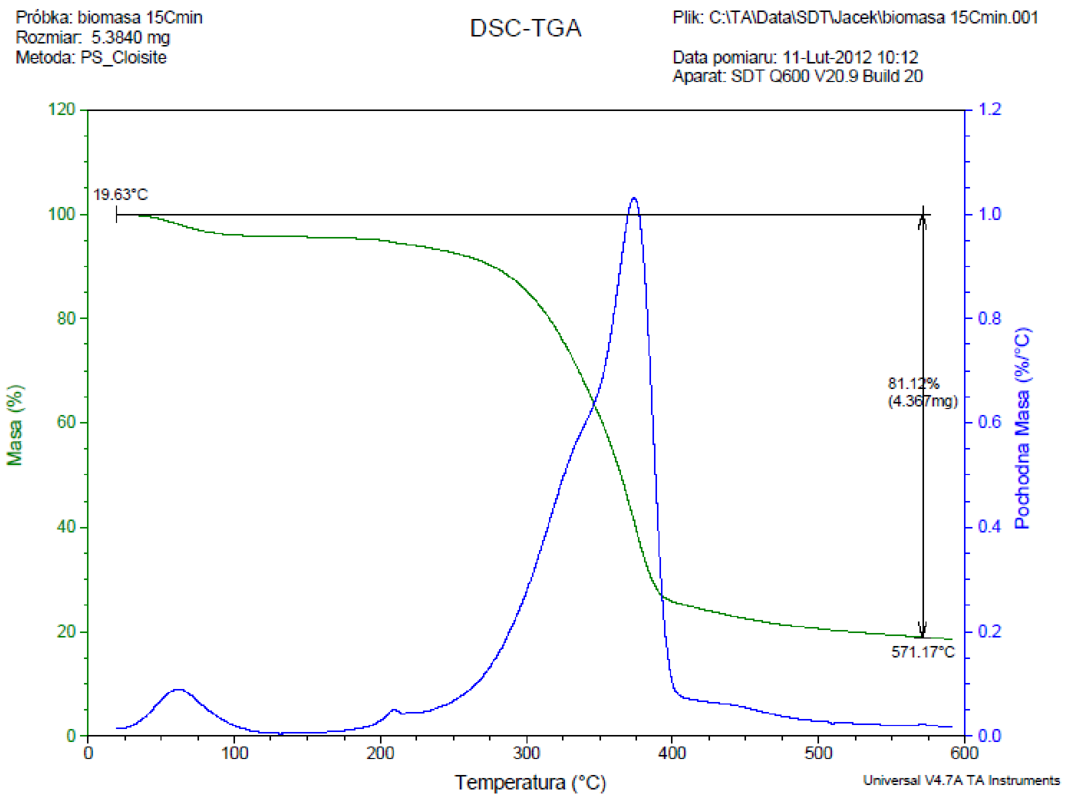

Fig. 1. Pyrolytic decomposition of biomass using TGA

3. GASIFICATION PROCESS

Gasification is process of the conversion solid or liquid feedstock into gaseous fuel or chemical feedstock that can be burned to release energyor used for production of value-added chemicals. Gasification and combustion are two closely related thermochemical processes. Sometimes gasification is first step of combusion in industrial solutions. Important difference between this two process is about in gasification chemical energy of fuel come into chemical bonds in the product gas, less to thermal energy; combustion breaks chemical bonds in fuel and transforms energy to heat. A typical biomass gasification process may include the following steps:

- Preheating and drying

- Thermal decomposition or pyrolysis
- Partial combustion of some gases, vapors, and char
- Gasification of decomposition products

Process is schematically illustrated in Fig. 2.

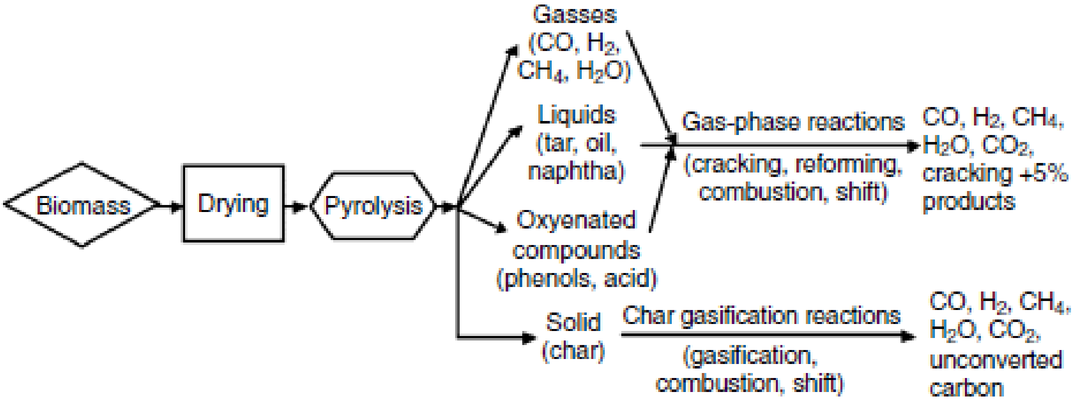

Fig. 2. Steps of gasification process [3]

Gasification process can be guided on many types of reactors. This paper show results obtained in cocurrent fixed bed reactor Fig. 3. In this type of gasifier air and biomass is supplied in upper part of reactor. This arrangement results is obtainment four areas: drying zone at the top, zone of pyrolysis, combustion zone and the zone of char oxidation on the bottom.

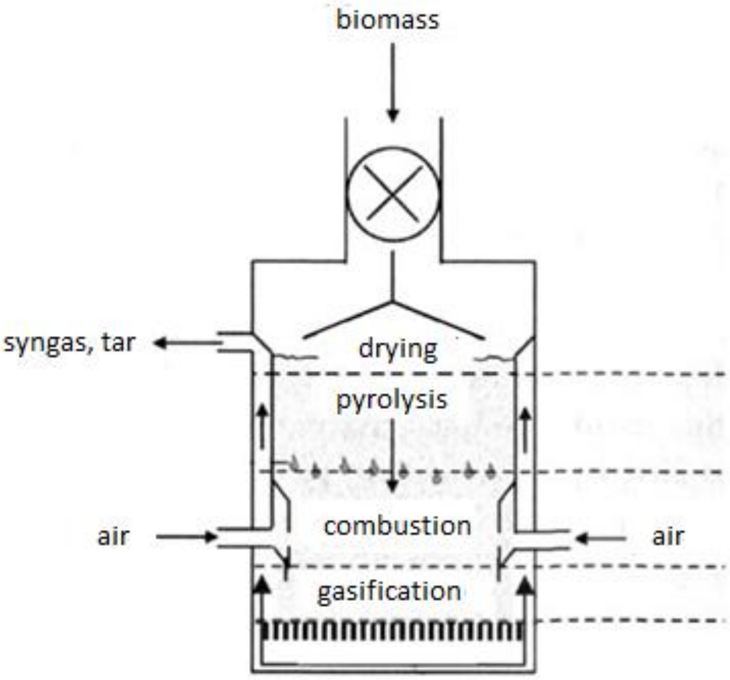

Fig. 3. Scheme of cocurrent fixed bed reactor [3]

4. EXPERIMENTAL STAND

Experimental studies were carried out in a small scale reactor with a height of 100 cm and the 22 cm diameter (Fig. 4). For the purposes of the research reactor was operated in batch mode.

Fig. 4. Small scale gasification reactor

The hot reactor was filled with char up to air nozzles, which are located at a distance of 45 cm from the top of the reactor. Next the reactor was filled up with wood chips (2.8 kg) and closed together with the measurement piston. The tests were performed for pine wood chips of 3–5 mm and a moisture content of 15%. Experiments were carried out for 5 different amounts of air supplied to the gasification process: 6.65, 11.07, 13.29, 15.51 and 19.94 Nm^3/h [4]. In each experiment time of piston settling on a distance about 5 cm was measured (Fig. 5). Reactor was filled up again with fresh fuel after settling of the piston with the fuel to the level of air nozzles.

The next part of the study was to analyze changes in the position of the combustion zone. During the experiments the temperature recorded at different heights in the reactor. The highest temperature was in a combustion zone located at the top of a moving bed. By registering times in which the highest temperature moved edge between thermocouples possible is description of the biomass settling. In this part of the study was checked the average speed of the char in the final stage of the experiment.

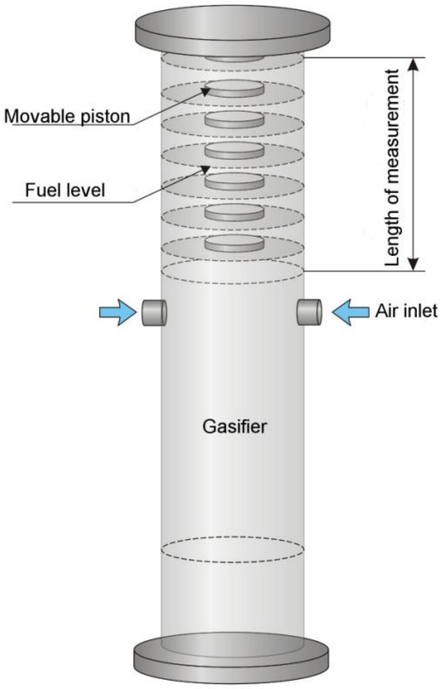

Fig. 5. Experimental Setup

5. RESULTS

The Table 2 summarizes the fuel settling time for particular experiments [4]. The results show that the shortest settling time of fuel occur at a height between 15 and 25 cm.

Table 2. The time of fuel settling in the gasifier for different various air flows

[Nm^3/h]	6.65	11.1	13.29	15.51	19.94
H [cm]	Fuel settling time [s]				
40	340	197	425	199	210
35	358	175	145	141	80
30	140	90	75	53	30
25	120	60	45	35	26
20	70	112	25	21	18
15	200	250	15	54	30
10	310	320	40	70	35
5	370	340	380	130	104

Settling fuel velocity in the reactor for individual cases of air supply to the gasification process are shown in Fig. 6. For the first measuring length settling velocity of the fuel for all cases are in the range of 0.01–0.025 cm/s. The largest increase of fuel settling velocity is at 15 cm measuring length for 13.29 Nm^3/h and 20 cm for other cases. This section is determined by the pyrolysis and oxidation of the volatiles. In the lower part, at measuring length 5 cm, the settling velocity of fuel fall down to 0.013 cm/s for 6.65, 11.07, 13.29 Nm^3/h, 0.038 cm/s for 15, 51 Nm^3/h and 0.048 cm/s for a 19.94 Nm^3/h.

The results show a significant effect of amount of air supply to gasifier on the settling fuel velocity. The results of biomass gasification in the reactor operating in batch mode showed that the increase of airflow effect on fuel consumption during gasification, which increased from 4.74 kg/h for 6.65 Nm^3/h to 17.00 kg/h for 19.94 Nm^3/h (Table 3).

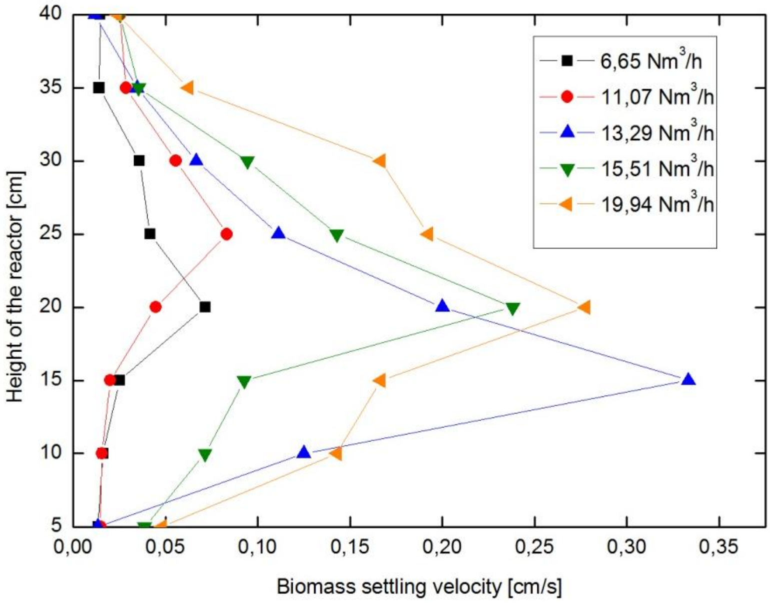

Fig. 6. Influence of amount of air supply to gasification process on the biomass settling velocity

Table 3. Fuel consumption during gasification of pine chips for various air flows

Airflow [Nm^3/h]	6.65	11.07	13.29	15.51	19.94
Biomass consumption [kg/h]	4.74	5.86	7.88	12.89	17

To check char settling was measure time of falling cobusion zone between thermocouples (180 mm). Averange time between offset of the zone was 2000 s. After calculation char decline time and distance between the thermocouple appointed speed 0,09 mm/s (Fig. 7.) In the graph consecutive numbers are thermocouples at different heights.

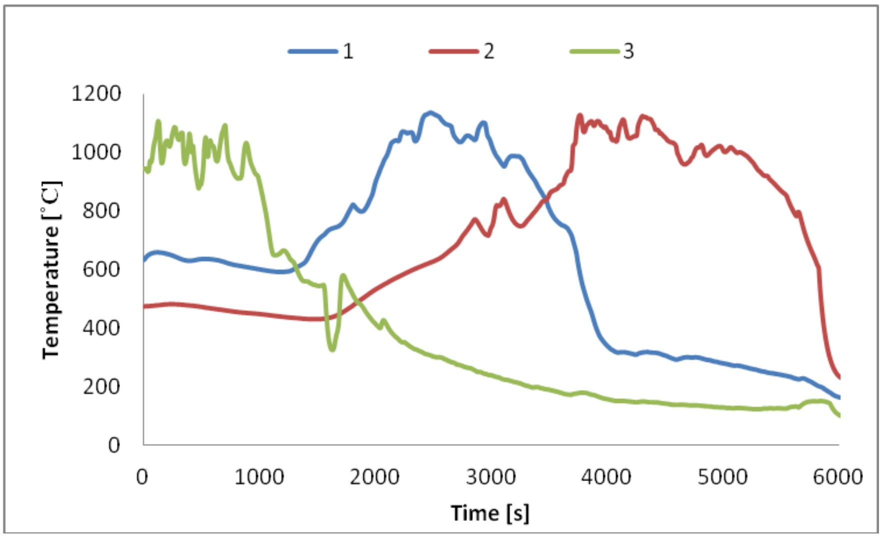

Fig. 7. Repositioning of the combustion zone during the experiment

6. CONCLUSION

Experimental work was carried out in the small scale reactor operating in batch mode. Tests of fuel settling were performed from the top of the reactor to the level of air nozles for different amount of air supply to the gasification process. The results show that the settling fuel velocity changes with the height of the reactor. The highest rate settling fuel was observed below zones of pyrolysis and above volatile combustion zone. It is associated with decrease of volume of fuel particles, which is caused by high temperature.

The experimental results indicate that the rate of biomass gasification process depends on the temperature and the amount of supplied air to the gasifier. These parameters have a direct impact on the rate of consumption of biomass and the velocity of the fuel settling in the reactor.

7. REFERENCES

1. ZAINAL Z.A., RIFAU A., QUADIR G.A., SEETHARAMU K.N., Experimental investigation of a downdraft biomass gasifier, *Biomass Bioenergy*, 23, pp. 283–289, 2002.
2. PLIS P., WILK R.K., Theoretical and experimental investigation of biomass gasification process in a fixed bed gasifier, *Energy*, 36, pp. 3838–3845, 2011.
3. BASU P., Biomass Gasification and Pyrolysis. Practical Design and Theory, Vol. 1: Elsevier, Oxford, 2010.
4. KLUSKA J., *The Course and Analysis of Physicochemical Processes in Downdraft Gasifier*. PhD Thesis, Institute of Fluid Flow Macinery Polish Academy of Sciences, 2015.

CYSENI 2016, May 26-27, Kaunas, Lithuania
ISSN 1822-7554, www.cyseni.com

ESTIMATION OF INDIRECT FUEL MOISTURE CONTENT FOR INTELLIGENT CONTROL OF BIOFUEL FURNACES

L. Vorotinskienė, N. Striūgas
Lithuanian Energy Institute
Breslaujos str. 3, LT-44403 Kaunas – Lithuania
Email: lina.vorotinskine@lei.lt

ABSTRACT

An important parameter for biofuel combustion is a moisture content which typically ranges from 30 to 55% by weight. Variable moisture content complicates furnace operation and influences combustion process. Fuel moisture content can be determined by direct measurement or by measuring moisture and oxygen content of the combustion flue gas. However, reliable and inexpensive methods for small and medium-sized boilers still not exists at the moment.

In order to maintain stable operation of moving grate combustion chamber, one important parameter is the moisture content, which usually varies with different batches of fuel. At the moment the standard procedure to determine the moisture content of the fuel in small and medium sized furnaces with grate is to analyse collected samples for each batch delivered examples. Such a simple method only serves as a rough estimation in order to calculate the price of an entire truck load. Furthermore, it is not accurate enough to predict the moisture content of the fuel-mix that continuously enters the furnace; a change in moisture content of the fuel-mix needs to be detected at high-frequent resolution to enable a correct response from the combustion – air system or to produce a response from the fuel-feed system within minutes. So, more accurate methods are necessary for monitoring the moisture content of the fuel.

Moisture content of fuel bends is determined by a direct and indirect measurement methods. Direct methods focus on the fuel, whereas indirect methods calculate the fuel moisture content from other measurement values, the flue gas and combustion air flow. In this work indirect biofuel moisture content measurement methods proposed by the world's scientists are reviewed; advantages and disadvantages of the methods are discussed, as well as the applicability for existing biofuel furnaces.

Keywords: biofuel, furnace, moisture content, combustion, intelligent control

CYSENI 2016, May 26-27, Kaunas, Lithuania
ISSN 1822-7554, www.cyseni.com

SCREENING OF NANOPOWDERS FOR CATALYTIC PYROLYSIS OF BUCKWHEAT STRAW BY USING TGA-FTIR METHOD

K. Lazdovica, V. Kampars, L. Vasarina
Institute of Applied Chemistry, Riga Technical University
Paula Valdena str. 3/7, LV-1048 Riga – Latvia
Email: kristinelazdovica@inbox.lv

J. Grabis
Institute of Inorganic Chemistry, Riga Technical University
Paula Valdena str. 3/7, LV-1048 Riga – Latvia

ABSTRACT

Pyrolysis plays a vital role in the biomass conversion as one of the most promising thermal conversion routes. Solid, liquid and gaseous products are obtained from biomass pyrolysis. The liquid is considered as perspective fuel; however, the direct use of bio-oil as fuel may present many difficulties due to its high viscosity, poor heating value and relative instability. This creates a significant economic barrier for production of transportation fuel by pyrolysis process. Catalytic pyrolysis has been widely used as a convenient method for the direct conversion of biomass into higher quality liquid bio-fuels.

In this study, pyrolysis of buckwheat straw without and with nanopowders (Ni/MgO, Ni/Al_2O_3, Fe_2NiO_4, $FeO \cdot Fe_2O_3$, $NiO \cdot Al_2O_3$, $NiO/MnO/Al_2O_3$) was investigated using a thermogravimetric analyzer STA 6000 combined with a FTIR Spectrum 100 (TGA-FTIR). The non-catalytic and catalytic pyrolysis experiments were performed by ramp the temperature from 30 to 700 °C at the heating rate of 100 °C/min and held at 700 °C for 10 minute in a pure nitrogen flow of 20 ml/min. The mass of sample without catalyst was 32 mg and the mass ratio of mixed catalyst and sample was 1:1. The transfer line and gas cell were heated to an internal temperature of 230 °C to avoid condensation or adsorption of the semi-volatile products. FTIR spectrum was recorded every 9 s in the spectral range between 4000 and 650 cm^{-1}.

All catalysts increased the yield of volatile products from 66.5% to 79.5%. Fe_2NiO_4 provided higher relative yield of aromatics and carbon dioxide compared to the Ni/MgO, Ni/Al_2O_3, $NiO/MnO/Al_2O_3$, whereas by using Ni/MgO, Ni/Al_2O_3, $NiO/MnO/Al_2O_3$ improved the relative yield of olefins and carbon monoxide. Fe_2NiO_4 catalyst affected not only the relative yield and composition of volatile products but also their evolution profiles.

Keywords: buckwheat straw, catalytic pyrolysis, TGA-FTIR method, nanopowders

1. INTRODUCTION

Alternative energy sources have been gaining an increased attention in the past years due to increase in consumption of fossil fuels, growing emission of greenhouse gases, environment and climate concerns. In this context, lignocellulosic biomass conversion into transportation fuels, chemical commodities, and power generation is getting growing interest and thus the biomass resources becoming as a very important source of renewable energy [1].

Pyrolysis of biomass is one of the most promising technologies to utilize renewable biomass resources, gases, bio-oil, and solid char are obtained. The composition of bio-oil is very complex and totally different from petroleum fuels. Bio-oil usually contains a complex mixture of acids, ketones, aldehydes, phenols, hydrocarbons and water. Therefore, it is a low-grade liquid fuel, because it is highly oxygenated, acidic and corrosive to common metals, chemically and thermally unstable, as well as non-miscible with petroleum fuels. As a result, it is difficult to use crude bio-oil in various thermal devices, especially internal combustion engines [2, 3].

Catalytic pyrolysis has been widely used as a convenient method for the direct conversion of biomass into high quality liquid bio-fuels. Zeolites (ZSM-5; HZSM-5) have been known as usable catalysts for direct conversion of biomass-derived carbohydrates into aromatics and light olefins, but many problems were encountered, such as fast deactivation of the catalysts by coke deposition and formation of polycyclic aromatic hydrocarbons [3]. Nano metal oxides have attracted extensive attention in various catalytic processes due to their unique properties, but they are even not widely used in catalytic treatment of biomass pyrolysis vapors [3]. Fabbri et al. studied the effect of nanopowder metal oxides (Al_2O_3, MgO, $TiSiO_4$, and $Al_2O_3TiO_2$) on the production of chiral anhydrosugars from cellulose. Nanopowder metal oxide exhibited a strong influence on the pyrolytic behaviour of cellulose [4]. Lu et al. investigated the influence of six nano metal oxides (MgO, CaO, TiO_2, Fe_2O_3, NiO, and ZnO) on the product distribution of wood fast pyrolysis vapors. CaO was the most effective catalyst in altering the pyrolytic products. The catalysis by Fe_2O_3 was capable of forming various hydrocarbons [3].

Analytical pyrolysis are valuable techniques to characterize biomass thermal conversion by combining pyrolysis with gas chromatography/mass spectroscopy (Py-GC/MS) or by using thermogravimetric analyzer coupled with Fourier transform infrared spectrometer (TGA-FTIR). The influence of CaO and MCM-41 on pyrolysis of corncob [5] and potassium inorganic and organic salts catalytic effect on the pyrolysis kinetics of cigarette paper [6] were studied by using TGA-FTIR.

In this study, the catalytic effect of six nanopowders (Ni/MgO, Ni/Al_2O_3, Fe_2NiO_4, Fe_3O_4, $NiAl_2O_4$, and NiO/MnO/Al_2O_3) on the pyrolysis of buckwheat straw were studied. We focusing only on composition of volatile compounds. The compositions of char and coke were not investigated.

2. MATERIALS AND METHODS

2.1. Materials

Raw material of buckwheat straw (BS) has been taken from Cooperative society of agricultural services “LATRAPS”. The biomass sample was dried at 105 °C for 24 h, then milled in a IKA A11 Basic mill, and completed by sifting through sieves with a wire mesh size of < 3.15 mm. In the experiments mean fraction of biomass with particles size of 0.15–0.25 mm was used. The study involves the full characterisation of raw materials by the proximate, ultimate and composition analysis and determination of the higher heating value (HHV) (see Table 1).

Table 1. The proximate, ultimate and composition analysis and HHV of BS

Proximate analysis (wt.%)[a]		**Ultimate analysis (wt)** [a]		**Composition analysis (wt.%)** [a]	
Volatile matter	74.70	Carbon	41.78	Cellulose	40.15
Fixed Carbon	15.60	Hydrogen	5.37	Hemicellulose[c]	26.05
Ash content	9.70	Nitrogen	0.61	Lignin	24.82
HHV, J/g [a]	16 500	Sulphur	0.24	Fat	1.56
Relative moisture (wt.%)	8.80	Oxygen[b]	42.30	Extractives	7.42

[a] Dry biomass
[b] Calculated by diference: O(wt.$_{\%}$) = 100% – (C% + H% + N% + S%) – Ash%
[c] Calculated by diference: Hemicellulose (wt.$_{\%}$) = 100%-cellulose%-lignin-fat%-extractives%-ash%

2.2. Catalysts

The nanocrystalline Ni/MgO, Ni/Al_2O_3, Fe_2NiO_4, Fe_3O_4, $NiAl_2O_4$, and NiO/MnO/Al_2O_3 nanopowders were prepared by introduction and evaporation of coarse grained commercially available oxides into a high-temperature inductively-coupled nitrogen plasma flame using apparatus described in [7]. The Fe_2O_3, FeO, NiO, Al_2O_3, MnO, MgO powders with particle size of 10–40 μm at different ratio of components were premixed and introduced into nitrogen plasma flame radially through four tubes (diameter 3 mm) welded into water cooled flange by nitrogen transporting gas. Formation of product phase composition and growth process of the produced nanoparticles was controlled by introducing cold nitrogen into reaction chamber in a region of vapours of oxides. Evaporation of raw oxides was achieved by varying the power of the radio frequency oscillator, the flow rate of the plasma forming gas, the feeding rate of the powder (in the range of 15–20 g/min), and their injection velocity.

The chemical and phase composition of the nanopowder was determined by X-ray diffraction analysis (XRD; 8Advanced, Bruker AXS). The specific surface area (SSA) was determined by argon adsorption-desorption method. The crystallite size of oxides was determined by X-ray line broadering method using the Scherrer equation. The particle size and shape was studied by transmission electronic microscopy (TEM).

Table 2. Phase composition, SSA and crystallite size d of prepared nanopowders

Raw powders	Products		
	XRD	SSA, m^2/g	crystallite size d, nm
Fe_2O_3, FeO	Fe_3O_4	31.0	14
Fe_2O_3, NiO	Fe_2NiO_4	26.5	16
Ni, Al_2O_3,	Ni/Al_2O_3	27.1	12
NiO, Al_2O_3	$NiAl_2O_4$	26.2	15
NiO, Al_2O_3, MnO	$NiO/MnO/Al_2O_3$	34.0	13
Ni, MgO	Ni/MgO	30.0	18

The TEM studies showed that particles with size in the range of 25–80 nm are close to spherical shape.

2.3. TGA-FTIR experiments

Thermogravimetric analyzer (PerkinElmer STA 6000) is coupled to the Fourier transform infra-red spectrometer (FTIR spectrometer PerkinElmer Spectrum 100) by a transfer line (TL8000) to investigate the mass loss of BS and formation of volatile products at the same time. Transfer line and gas cell are heated and maintained at an internal temperature of 230 °C to avoid condensation or adsorption of semi-volatile products during the thermal degradation process of biomass. The FTIR spectrum is recorded every 9 s in the spectral range between 4000 and 650 cm^{-1} with resolution factor of 4 cm^{-1}. There is an approximate 90 sec delay between the TGA result and the corresponding spectra. Dry biomass samples were heated from 30 up to 700 °C with heating rate of 100 °C/min and held for 10 min in a pure nitrogen flow of 20 ml/min supervised by a mass-flow controller. The mass of sample consists of 32 mg BS and 32 mg catalyst. In the non-catalytic experiments biomass sample was mixed with quartz sand. Each experiment was repeated three times.

2.4. Determination of chemical composition of biomass

Identification of main volatile products of BS pyrolysis was performed by TG-FTIR method and Spectrum Search Plus database library. The characteristic absorptions of the volatiles used to ascertain their formation in BS pyrolysis process are listed in Table 3.

Table 3. The characteristic IR spectra absorptions of the volatiles

Reference	**Absorption band (cm^{-1})**	**Peak (cm^{-1})**	**Assignment**	**Compounds**
[1]	2217–2391	2309	$\upsilon_{as}C = O$	CO_2
	2071–2207	2182	υC-O	CO
	2972–3018	3014	υC-H	CH_4
	650–900 728–770 (phenyl) 735–770 (ortho)	742.9	γC-H	Aromatics
	950–993 900–920 (vinyl)	950	$\gamma = CH_2$	Olefins

υ – stretching vibrations
υ_{as} – asymmetric stretching vibrations
γ – out-of plane bending

2.5. Volatile matter of biomass

The yield of volatile matter of BS received in catalytic pyrolysis process and amount of solid residue is calculated according to the literature [1].

2.6. The relative yield of the volatile compound

The typical output from TG-FTIR instrument are IR spectra as a function of time, that pre-programmed on temperature shows three-dimensional (3D) absorbance stack plot obtained from volatilized compounds of BS thermal decomposition in inert atmosphere.

During the process of pyrolysis all acquired TG-FTIR data are gathered and subsequently can be used for obtaining absorption spectra profile over the temperature range for each of the corresponding volatiles. In this study relative yield for each compound is assumed as an integral intensity of absorbance-temperature curve (2D curve) and calculated according to the literature [1].

The average value of three experiments is used to compare relative yield of obtained products during pyrolysis without and with catalyst. Probability of confidence interval was equal to p = 0.95, that complies with Student's distribution coefficient for three experiments – $t_{0.95;3} = 4.303$.

3. RESULTS AND DISCUSSION

3.1. Influence of catalysts on the thermal decomposition of buckwheat straw

The thermogravimetric (TG) and derivative thermogravimetric (DTG) curves of buckwheat straw pyrolysis with or without catalysts are present in Fig.1. The thermal degradation of buckwheat straw with quartz sand (non-catalytic) and with catalysts occurred in three major weight loss steps.The first weight loss step, which corresponds to the removal of moisture from buckwheat, occurred at the temperature range between 30 and 100 ºC.

The main weight loss step happened over a wide temperatures range from 180 to 430 ºC and is related to evaporation of extractives and degradation of hemicellulose, cellulose and partially lignin components of buckwheat straw. The thermal decomposition behavior of biomass components have been studied before and it is well known that the decomposition of hemicellulose, cellulose, and lignin occurred in the temperature range of 200–350, 300–450, and 250–1000 ºC, respectively [8, 9]. The main weight loss step referred as active pyrolysis zone because the mass loss rate is high. This step can be ascribed to the series of reactions involving dehydration, decarboxylation, and decarbonylation, fragmentation, and rearrangement. The inflection point (where

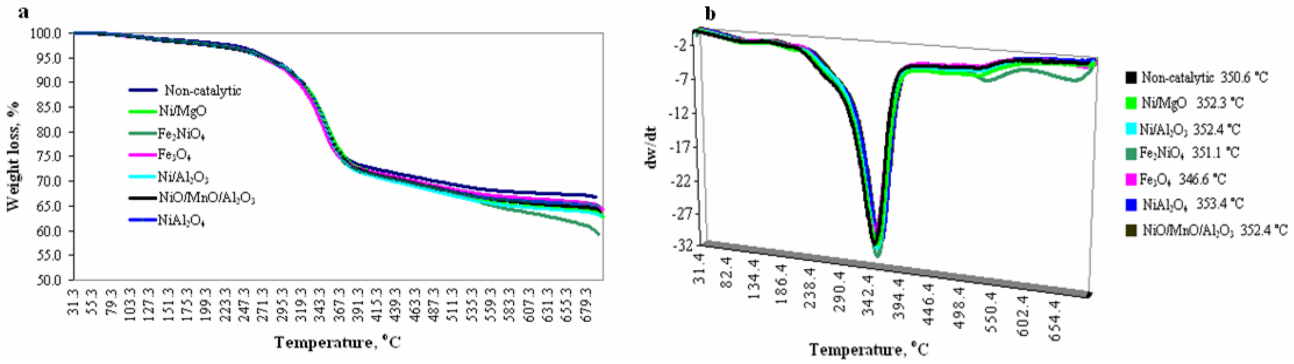

Fig. 1. TG (a) and DTG (b) curves of buckwheat straw pyrolysis with quartz (non-catalytic) and catalysts (mass ratio of quartz sand or catalyst and buckwheat straw = 1:1)

the rate of weight loss is maximum) of this step was 350.6 ºC for non-catalytic process. It was found that the inflection point remained almost the same or slightly changed when catalyst was present. The inflection point changed from 350.6 ºC to 352.3 ºC, 352.4 ºC, 351.1 ºC, 346.6 ºC, 353.4 ºC, 352.4 ºC under the nanopowder catalysts of Ni/MgO, Ni/Al_2O_3, Fe_2NiO_4, Fe_3O_4, $NiAl_2O_4$, and $NiO/MnO/Al_2O_3$, respectively. The final weight loss step observed at the temperature range from 430 to 700 ºC corresponds to the pyrolysis of lignin and cracking process of the residue. This stage can be described as the passive pyrolysis zone because the mass loss rate is low. The overall form of TG and DTG curves in the presence of all catalysts did not change, except nano-Fe_2NiO_4. It is clearly seen that buckwheat straw with nano-Fe_2NiO_4 showed the maximum mass loss and decreased the char formation. As shown in Fig. 1 b, the presence of nano-Fe_2NiO_4 showed two inflection points with T_{max} of 540.4 ºC and 673.4 ºC in the passive pyrolysis zone. The influence of catalysts on the yield of volatile products and solid residue are shown in Fig. 2.

It was found that the yield of volatile matter increased from 66.6% to 66.9%, 69.6%, 69.7%, 70.1%, 70.7%, and 79.5% and solid residue decreased from 23.7% to 23.4%, 20.7%, 20.6%, 20.2%, 19.6%, and 10.8% under the use of nanopowder catalysts of $NiAl_2O_4$, $NiO/MnO/Al_2O_3$, Fe_3O_4, Ni/MgO, Ni/Al_2O_3, and Fe_2NiO_4, respectively.

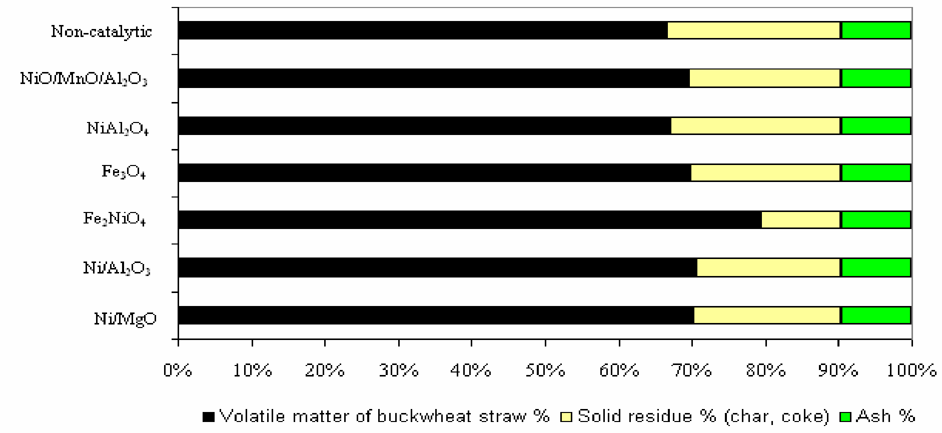

Fig. 2. The influence of catalysts on the yield of volatile products and solid residue of buckweat straw

3.2. Influence of the catalysts on the relative yield of non-condensable gases

According to the literature [10], the aromatics hydrocarbons are produced through a series of acid-catalyzed decarboxylation, decarbonylation, dehydration and oligomerization reactions of oxygenates, while oxygen is removed by the formation of water, carbon monoxide or carbon dioxide. The efficiency of the nanopowder catalysts was monitored by restricting the analysis to five compounds commonly associated with catalytic/non-catalytic pyrolysis of biomass, three non-condensable gases (methane, carbon dioxide, and carbon monoxide) and two hydrocarbons (aromatics and olefins).

The composition of the non-condensable gases resulting from the buckwheat straw treatment with different nanopowder catalysts is shown in Fig. 3.

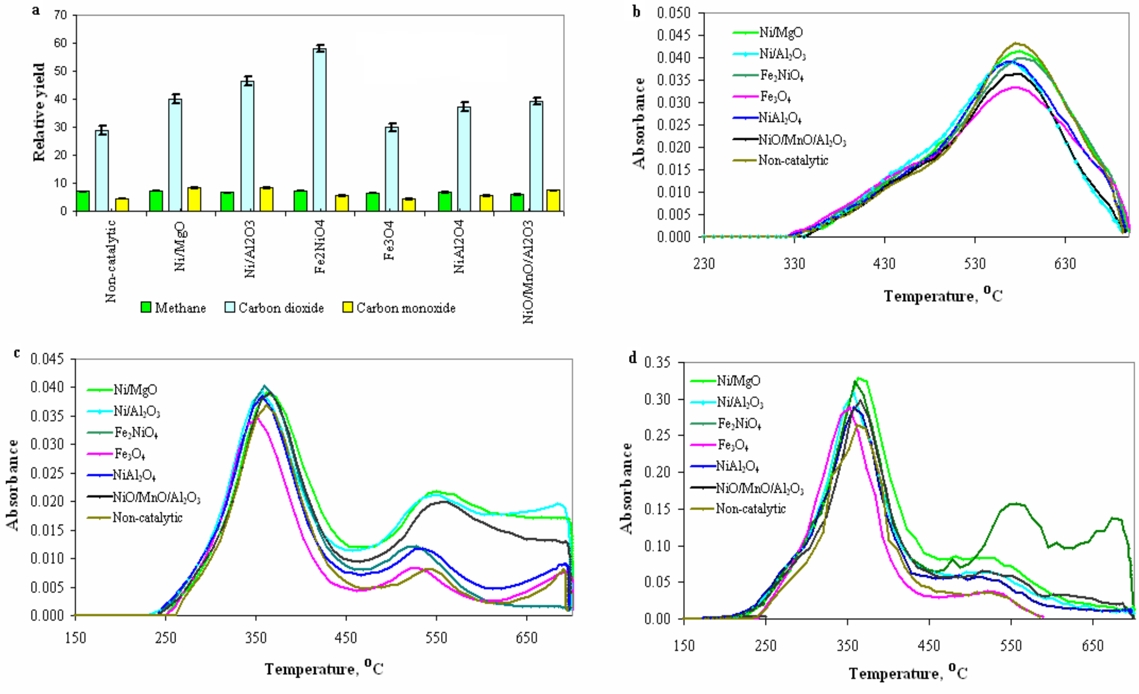

Fig. 3. The relative yield of non-condensable gases (a), the evolution of methane (b), carbon monoxide, (c) and carbon dioxide (d) during buckwheat straw pyrolysis without and with catalysts

As shown in Fig. 3, the relative yield of methane remained unaffected by using nano-Ni/MgO, nano-Ni/Al_2O_3, and nano-Fe_2NiO_4. By using nano-Fe_3O_4, nano-$NiAl_2O_4$, and nano-NiO/MnO/$Al_2O_{3,}$ the relative yield of methane slightly decreased 1.2, 1.2, and 1.3 times, respectively. The evolution curve of methane without and with nanopowder catalysts occured in the same range of temperature from 330 to 700 ºC with one wide peak at $T_{\max}$ of 574.4 ºC (non-catalytic), $T_{\max}$ of 579.0 ºC (nano-Ni/MgO), $T_{\max}$ of 573.0 ºC (nano-Ni/Al_2O_3), $T_{\max}$ of 585.5 ºC (nano-Fe_2NiO_4), and $T_{\max}$ of 579.2 ºC (nano-Fe_3O_4), $T_{\max}$ of 563.8 ºC (nano-$NiAl_2O_4$), $T_{\max}$ of 572.0 ºC (nano- NiO/MnO/Al_2O_3). Profiles of methane without and with nanopowder catalysts correspond to the formation of methane from thermal degradation of lignin.

As shown in Fig. 3, the relative yield of carbon monoxide increased 1.2, 1.2, 1.6, 1.8 and 1.8 times by using nano-Fe_2NiO_4, nano-$NiAl_2O_4$, nano- NiO/MnO/Al_2O_3, and nano-Ni/MgO, nano-Ni/Al_2O_3 whereas nano-Fe_3O_4 has not impacted the formation of above mentioned gas. The evolution curve of carbon monoxide (see Fig. 3) without and with nanopowder catalysts happened in the same and wide range of temperature from 250 to 700 ºC with two peaks $T_{\max}$ of 361.1 ºC and $T_{\max}$ of 540.1 ºC (non-catalytic), $T_{\max}$ of 362.1 ºC and $T_{\max}$ of 559.6 ºC (nano-Ni/MgO), $T_{\max}$ of 357.4 ºC and $T_{\max}$ of 549.8 ºC (nano-Ni/Al_2O_3), $T_{\max}$ of 358.9 ºC and $T_{\max}$ of 527.0 ºC (nano-Fe_2NiO_4), $T_{\max}$ of 352.4 ºC and $T_{\max}$ of 530.0 ºC (nano-Fe_3O_4), and $T_{\max}$ of 357.4 ºC and $T_{\max}$ of 534.8 ºC (nano-$NiAl_2O_4$), $T_{\max}$ of 365.8 ºC and $T_{\max}$ of 562.3 ºC (nano-NiO/MnO/Al_2O_3). Compared with methane, the releasing of carbon monoxide appeared to be more complicated. The formation of carbon monoxide below 450 ºC was the consequence of the cleavage of carbonyl, carboxyl, and ester groups in the side-chain of lignin and decarbonylation reactions of the low molecular weight products, especially the aldehyde-type compounds. According to the literature, for temperature higher than 450 ºC, the hemicellulose and cellulose are completely thermally degraded. Most of the initial bonds between monomer units of lignin have been broken, only the more stable such as the phenyl linkage and the ether linkage are still present. Pyrolysis of lignin releases an important amount of carbon monoxide between 500 and 800 ºC corresponding to the conversion of some oxygenated groups still present in the residue [11]. Shen et al. review indicates that nano-Ni catalyst on the support of γ-Al_2O_3 was ideal for tar removal in biomass catalytic gasification or pyrolysis, the content of hydrogen and carbon monoxide increased significantly at 800 ºC [12]. It is possible that the formation of carbon monoxide at higher temperatures in the presence of nano-Ni/MgO and nano-Ni/Al_2O_3 is certrainly due to the conversion of the residue which contain oxygenated groups.

As depicted in Fig. 3, carbon dioxide appears to be the most abundant product, relative yield of carbon dioxide increased 1.3 times with nano-$NiAl_2O_4$, 1.4 times with nano-Ni/MgO and nano-NiO/MnO/Al_2O_3, 1.6 and 2.0 times respectively by using nano-Ni/Al_2O_3, nano-Fe_2NiO_4, whereas nano-Fe_3O_4 has not impacted the formation of above mentioned gas.

It can be seen that nano-Fe_3O_4 compared to the nano-$NiAl_2O_4$, nano-NiO/MnO/Al_2O_3, nano-Ni/MgO, nano-Ni/Al_2O_3, and nano-Fe_2NiO_4 does not affect the formation of non-condensable gases, it is inactive. It was observed that during the pyrolysis nano-Fe_3O_4 change color from dark brown to reddish orange. This suggests that nano-Fe_3O_4 in presence of high temperature is able to do a phase transition from alpha iron (ferrite) to gamma iron (austenite) thereby the activity of catalyst decreased.

The evolution curve of carbon dioxide (see Fig. 3) with or without catalyst, except nano-Fe_2NiO_4, proceeded in a wide temperature range from 230 to 580 ºC with one peak at T_{max} of 352.4 ºC (nano-Fe_3O_4), T_{max} of 357.3 ºC (nano-$NiAl_2O_4$), T_{max} of 356.5 ºC (nano-Ni/Al_2O_3), T_{max} of 361.1 ºC (non-catalytic), T_{max} of 362.5 ºC (nano-Ni/MgO), and T_{max} of 365.8 ºC (nano-NiO/MnO/Al_2O_3).

The increase in the relative yield of carbon dioxide indicates that nanopowder catalysts are highly effective in the decarboxylation of biomass. When nano-Fe_2NiO_4 was used the evolution profile of carbon dioxide was noticeably different and was located in region from 230 to 700 ºC with three peaks at T_{max} of 358.9 ºC , T_{max} of 556.1 ºC, and T_{max} of 680.2 ºC.

3.3. Influence of the catalysts on the realtive yield of hydrocarbons

The effect of catalysts on the relative yield and evolution curve of hydrocarbons is shown in Fig. 4. It can be clearly seen that nano-Fe_2NiO_4 had substantial effect on production of aromatics whereas the relative yield of olefins was notably increased in presence of nano-Ni/MgO.

As depicted in Fig. 4, the relative yield of olefins increased 1.8 times with nano-Ni/MgO, 1.3 times with nano-Ni/Al_2O_3, 1.2 times with nano-$NiAl_2O_4$, but decreased 1.8 times with nano-Fe_2NiO_4 whereas nano-Fe_3O_4 and nano-NiO/MnO/Al_2O_3 have not impacted the formation of olefins. According to the literature, the formation of olefins is conected with the dehydration of alcohols. The dehydration of alcohols can be catalyzed by various types of acidic compounds including modified alumina, zeolites, and mesoporous materials [1].

As shown in Fig. 4, the evolution curve of aromatics with and without catalysts, except nano-Fe_2NiO_4, occurred in the similar range of temperature from 240 to 600 ºC with one peak at T_{max} of 352.4 ºC (nano-Fe_3O_4), T_{max} of 368.5 ºC (nano-$NiAl_2O_4$), T_{max} of 368.4 ºC (nano-Ni/Al_2O_3), T_{max} of 371.4 ºC (non-catalytic), T_{max} of 362.5 ºC (nano-Ni/MgO), and T_{max} of 365.8 ºC (nano-NiO/MnO/Al_2O_3). All catalysts increased the formation of aromatics, the relative yield of aromatics increased 1.5, 1.6, 1.6, 1.7, 1.8 and 2.6 times by using nano-Fe_3O_4, nano-$NiAl_2O_4$, nano-NiO/MnO/Al_2O_3, nano-Ni/Al_2O_3, and nano-Ni/MgO and nano-Fe_2NiO_4, respectively.

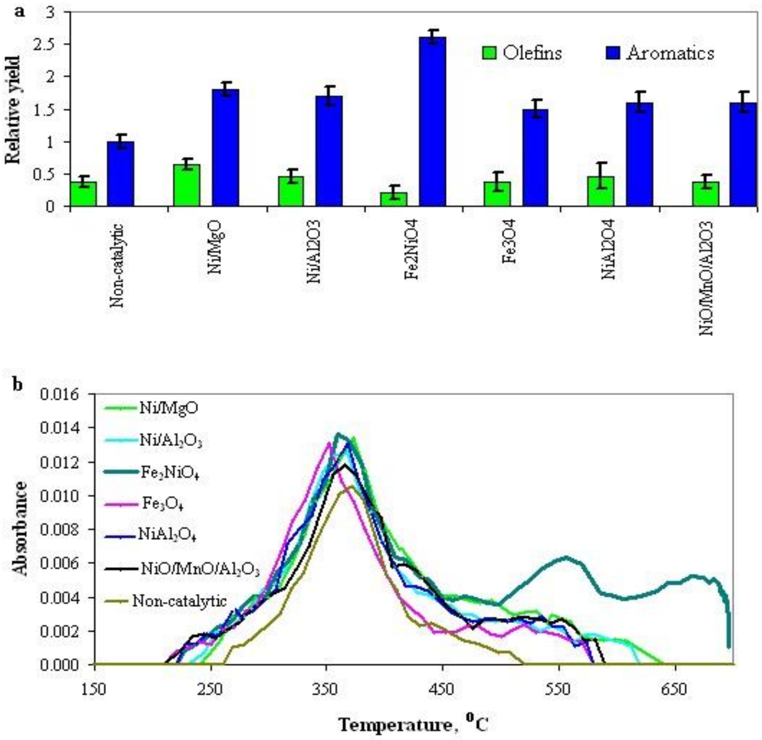

Fig. 4. The relative yields of olefins and aromatics (a), the evolution of aromatics during buckwheat straw pyrolysis without and with catalysts

Nano-Fe_2NiO_4 changed the evolution profile of aromatics like as in the case with carbon dioxide. It was located in region from 230 to 700 ºC with three peaks T_{max} of 358.4 ºC , T_{max} of 556.1 ºC, and T_{max} of 663.7 ºC.

4. CONCLUSIONS

All nanopowder catalysts $NiAl_2O_4$, $NiO/MnO/Al_2O_3$, Fe_3O_4, Ni/MgO, and Ni/Al_2O_3, except Fe_2NiO_4, didn't changed the overall tendency of TG and DTG curves of buckwheat straw, but the mass losses were clearly modified. All investigated catalysts increased the volatile matter of buckwheat straw, the highest improvement of volatile matter produced Fe_2NiO_4 (12.9%). Nano-Fe_2NiO_4 provided higher relative yield of aromatics and carbon dioxide compared to the catalysts nano-Ni/MgO, nano-Ni/Al_2O_3, nano-$NiO/MnO/Al_2O_3$, whereas by using nano-Ni/MgO, nano-Ni/Al_2O_3, nano-$NiO/MnO/Al_2O_3$ improved the relative yield of olefins and carbon monoxide. Nano-Fe_2NiO_4 catalyst affected not only the relative yield and composition of volatile products but also its evolution profiles.

5. ACKNOWLEDGEMENTS

This study is supported by the doctoral grants of Materials Science and Applied Chemistry of Riga Technical University (34-14000-DOK.MLĶF).

6. REFERENCES

1. LAZDOVICA, K., LIEPINA, L., KAMPARS, V. Comparative wheat straw catalytic pyrolysis in the presence of zeolites, Pt/C, and Pd/C by using TGA-FTIR method. *Fuel Processing Technology*, 2015, Vol. 138, p. 645–653.

2. GRAMS, J., NIEWIADOMSKI, M., RUPPERT, M. A., KWAPINSKI, W. Influence of Ni catalyst support on the product distribution of cellulose fast pyrolysis vapors upgrading. *Journal of Analytical and Applied Pyrolysis*, 2015, Vol. 113, p. 557–563.
3. LU, Q., ZHANG, F-Z., DONG, Q-C., ZHU, F-X. Catalytic Upgrading of Biomass Fast Pyrolysis Vapors with Nano Metal Oxides: An Analytical Py-GC/MS Study. *Energies*, 2010, Vol. 3, p. 1805–1820.
4. FABBRI, D., TORRI, C., BARAVELLI, V. Effect of zeolites and nanopowder metal oxide on the distribution of chiral anhydrosugars evolved from pyrolysis of cellulose: An analytical study. *Journal of Analytical and Applied Pyrolysis*, 2007, Vol. 80, p. 24–29.
5. WANG, D., XIAO, R., ZHANG, H., HE, G. Comparison of catalytic pyrolysis of biomass with MCM-41 and CaO catalysts by using TGA-FTIR analysis. *Journal of Analytical and Applied Pyrolysis*, 2010, Vol. 89, p. 171–177.
6. ZHAO, D., DAI, Y., CHEN, K., SUN, Y., YANG, F., CHEN, K. Effect of potassium inorganic and organic salts on the pyrolysis kinetics of cigarette paper. *Journal of Analytical and Applied Pyrolysis*, 2013, Vol. 102, p. 114–123.
7. GRABIS, J., KUZJUKEVICS, A., RASMANE, D., MORGENSEN, M., LINDERTH, S. Preparation of nanocrystalline YSZ powders by the plasma technique. *Journal of Materials Science*, 1998, Vol. 33, p. 723–728.
8. LIU, Q., WANG, S., ZHENG, Y., LUO, Z., CEN, K. Mechanism study of wood lignin pyrolysis by using TG-FTIR analysis. *Journal of Analytical and Applied Pyrolysis*, 2008, Vol. 82, p. 170–177.
9. LIU, Q., ZHONG, Z., WANG, S., LUO, Z. Interactions of biomass components during pyrolysis: A TG-FTIR study. *Journal of Analytical and Applied Pyrolysis*, 2011, Vol. 90, p. 213–218.
10. WANG, K., HO KIM, K., BROWN, C.R. Catalytic pyrolysis of individual components of lignocellulosic biomass. *Green Chemistry,* 2014, Vol. 16, p. 727–735.
11. COLLARD, X-F., BLIN, J. A review on pyrolysis of biomass constituents: Mechanisms and composition of the products obtained from the conversion of cellulose, hemicelluloses and lignin. *Renewable and Sustainable Energy Reviews*, 2014, Vol. 38, p. 594–608.
12. SHEN, Y., YOSHIKAWA, K. Recent progresses in catalytic tar elimination during biomass gasification or pyrolysis-A review. *Renewable and sustainable Energy Reviews*, 2013, Vol. 21, p. 371–392.

CYSENI 2016, May 26-27, Kaunas, Lithuania
ISSN 1822-7554, www.cyseni.com

THE APPLICATION OF AGRICULTURAL WASTE AND RECYCLING PRODUCTS FOR SMALL AND MEDIUM SCALE BOILERS

T. Vonžodas
Lithuanian Energy Institute
Breslaujos str. 3, LT-44403 Kaunas – Lithuania
Email: vonzodast@mail.lei.lt

ABSTRACT

In all the European countries, as well in Lithuania, the residential heating with biofuel is applied using a variety of heating equipment: water-heating boilers, stoves, open and closed fireplaces and air heater. However, most of the devices are technically obsolete, not adapted for firing particular type of biofuels or just not properly equipped, so the heating system with such devices operate inefficiently and significantly increase environmental pollution.

Biofuel consumption structure analysis shows that recently the large part of biofuel is consumed by households. It is therefore very important improve parameters of heating devices used for residential heating.

In this paper the improvement of combustion process in biomass stove combustion chamber was investigated in order to increase thermal efficiency and to minimize emissions of carbon monoxide (CO), hydrocarbons (C_xH_y), nitrogen oxides (NO_x) and particulate in the combustion products.

During the experiments thermal parameters and emissions in combustion products were continuously recorded to gather information for further development actions. Some design corrections and proper application of stage combustion could reduce the CO and H_xC_y emissions up to 60%,

Increasing the excess air ratio to $\lambda = 2.2$ the concentration of CO and H_xC_y decreased ~ 60%, but the NO_x concentration increased by almost 30%. Particulate concentrations of excess air ratio change had no effect. While increasing the coefficient of air excess, the coefficient of efficiency decreased by 3 present.

Keywords: Space-heating stove, Biomass-fired stove, Stove emission, Combustion; Excess air ratio, Thermal efficiency

1. INTRODUCTION

Biomass fuels in developing countries. Lithuania is currently the largest renewable energy potential of biofuels, especially wood and wood waste. Fuel wood and agricultural waste consumption structure analysis shows that in 2011. The largest part of the 60 percent was consumed by households. District heating companies' boilers and power plants consumed 25.8 per cent of fuel wood and agricultural waste. It is therefore very important that the household boilers are more efficient and less pollutant emission levels.

It is well known, that modern biomass combustion systems have already achieved a technological level which allows for an operation at comparably low emissions [1].

In a biomass stove combustion chamber, a number of physical and chemical processes occur in time and space during the combustion. The processes include: drying and preheating of the fuel, pyrolytic release of volatile flammable matter, flaming combustion of the pyrolyzates and glowing combustion of fixed carbon. Besides, the products of biomass combustion should generally contain carbon dioxide, water, ash, sulphur oxides, carbon monoxide, unburnt hydrocarbons, oxides of nitrogen, smoke and soot [2].

The formation of combustion emissions is influenced largely by the fuel properties, which can be determined by proximate analysis, and by the stove design parameters (e.g. excess air, particle size, fuel bed). The combustion air which is supplied by natural circulation depends very much on ambient conditions and the architectural configuration of the stove location [3].

In this article are presented in the flue emissions (CO, C_xH_y, NO_x) and the performance impact depending on the excess air ratio. It is also accompanied by the heater operating parameters.

2. MATERIALS AND METHODS

2.1. Experimental method

The goal was set as the outflowing gas concentrations (CO, CO_2, O_2, C_xH_y, NO_x), and the efficiency depends on the excess air ratio. The experiment was carried out in two different modes, it is the excess air ratio $\lambda = 2.2$ (120%), and $\lambda = 1.65$ (65%).

2.2. Combustion chamber

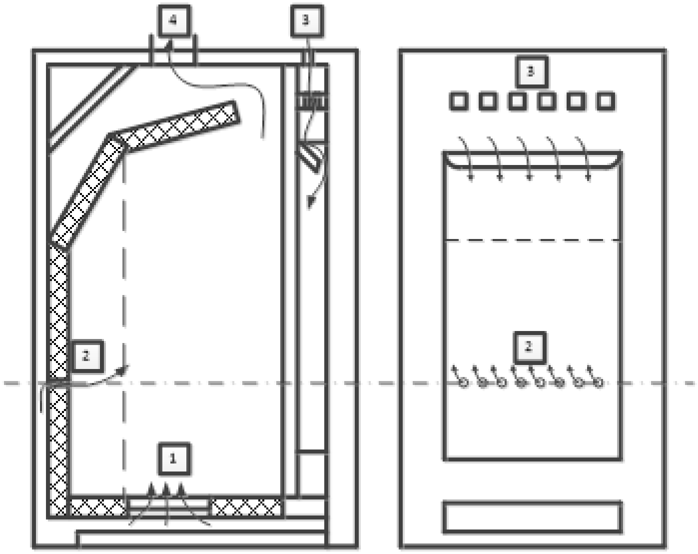

Fig. 1. Diagram of the combustion chamber. 1 – inflammation of the air, 2 – primary air, 3 – secondary air

The study investigated biomass-fired oven, which is produced by Lithuanian manufacturers. Oven is the main parts of a combustion chamber that is the bottom of the grate, through which dropped ach faeces fall into the ash bin. Primary and secondary air control levers. Oven is equipped with three air supply area. During the first air to enter the combustion chamber through the grate and immediately involved in the combustion process. In the second zone the air is fed to the glass door. The main purpose of the air supply to protect the glass from sooting. The third air is fed back of rear wall. The Air Support is a secondary combustion, thus significantly reducing emissions.

2.3. Efficiency and excess air ration calculation

2.3.1. Calculation of efficiency

In order to determine the thermal efficiency of a heater (in the stand) the total useful amount of a heat must be found. The amount which was produced in the heater during combustion is transferred to the room in the way of natural convection and radiation from hot surfaces of a heater and chimney.

The efficiency in the heaters is calculated in two ways – direct and inverse. The ratio of efficiency in a direct way is calculated when fuel properties are well known. Then in accordance with the calculated amount of a heat, which should be obtained after a fuel is burnt, and the ratio of the produced heat amount is calculated the ratio of efficiency. However it is very difficult to measure accurately the amount of produced heat. Therefore more often is used the inverse method for estimation of a heater efficiency. This calculation is done by summing heat losses which form together with the effluent smoke, chemical losses of incomplete combustion and losses due to incompletely burnt fuel.

Thus, the efficiency is calculated by the following formula:

$$\eta = 100 - (q_a + q_b + q_r),\ \%. \tag{1}$$

Thermal losses in the flue gas [4, 5]:

$$Q_a = (t_a - t_r)\cdot\left[\left[\frac{C_{pmd}\cdot(C - C_r)}{0.536\cdot(CO + CO_2)}\right] + \left[\frac{C_{pmH_2O}\cdot 1.224\cdot(9\cdot H + W)}{100}\right]\right],\ kJ/kg \tag{2}$$

$$q_a = 100\cdot\frac{Q_a}{H_U},\ \% \tag{2.1}$$

where H_u – Lower calorific value of the test fuel.

Chemical losses in the flue gas:

$$Q_b = 12644\cdot CO\cdot\frac{(C - C_r)}{(0.536\cdot(CO_2 + CO)\cdot 100)},\ kJ/kg \tag{3}$$

$$q_b = 100\cdot\frac{Q_b}{H_U},\ \% \tag{3.1}$$

Heat losses due to combustible constituents in the residue passing through the grate:

$$Q_r = 335\cdot\frac{b\cdot R}{100},\ kJ/kg \tag{4}$$

where b – combustible constituents (% of mass), R – residue passing through the grate, referred to the mass of the fired test fuel (%).

$$q_r = 100\cdot\frac{Q_r}{H_U},\ \% \tag{4.1}$$

The total heat output is calculated from the mass of fuel burned per hour, the calorific value of the test fuel and efficiency, using the formula: [4, 5]:

$$P = \frac{(\eta\cdot B\cdot H_U)}{100\cdot 3600},\ kW \tag{5}$$

2.3.2. Calculation of excess air ratio

To determine the excess air ration is first necessary to know what the maximum concentration of CO_2 is. CO_{2max} content is calculated by follows:

$$CO_{2\max} = \frac{1}{\left(1 + m_s + A\cdot\left(\frac{79}{21}\right)\right)}\cdot 100,\ \% \tag{6}$$

$$A = 1 + \frac{m_h}{4} - \frac{m_o}{2} + m_s,\ mol/mol \tag{6.1}$$

$$m_s = \frac{12}{32} \cdot \frac{S}{C}, \ mol \quad m_h = 12 \cdot \frac{H}{C}, \ mol \quad m_o = \frac{12}{16} \cdot \frac{O}{C}, \ mol \qquad (6.2, 6.3, 6.4)$$

Then the excess air coefficient is calculated according to the formula: [4]:

$$\lambda = \left[\left(\frac{CO_{2\ max}}{CO_{2\ calculate}}\right) - 1\right] \cdot 100, \% \qquad (7)$$

2.4. The measurement of emissions (of particulate matter (PM))

During this research all parameters were measured every 20 seconds. Emissions ((CO, CO_2, O_2, C_xH_y, NO_x) using a heated probe were measured in the position specified in the Figure 2. Concentrations of NO_x were calculated by analyser, as a sum of measured concentrations NO and NO_2. Particulate matter was measured using the method of isokinetic sampling. Isokinetic accumulation is when a rate of sample suction is equal to a rate of smoke in a chimney. Measurement probe was installed in the centre of smoke Chanel and a sample was collected 30 minutes using a filter which can collect 99.8% of smoke particles. The filter prior and after the measurement was dried in the temperature of 105 ^{o}C and then weighed with the accuracy of ±0,1 mg.

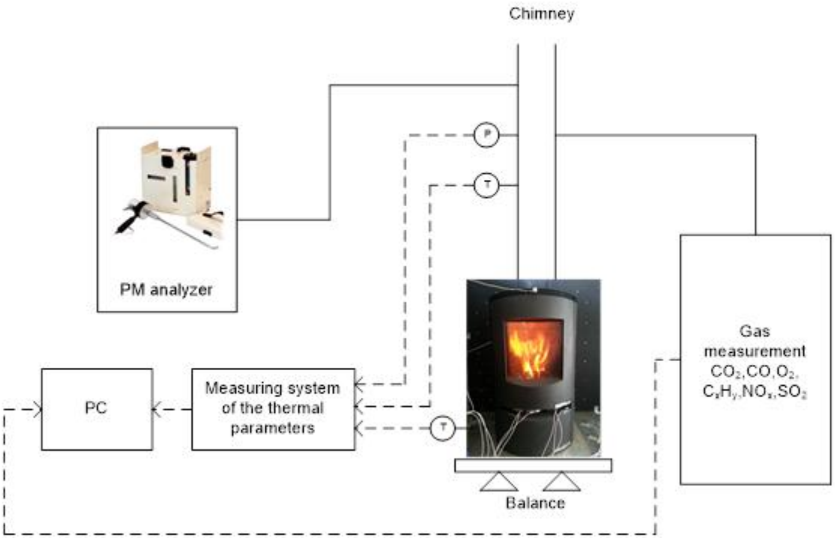

Fig. 2. Schematic diagram of experimental setup

2.5. Burning intervals

During performance of the research was performed as test of the heater heating (pre-test) on purpose to heat all surfaces up to operating temperatures and all other tests to be performed under equal conditions. Later were performed tests by changing the parameters in the way to reach the best performance results. And only then were performed the researches with different amounts of supplied air. In the first case the ratio of supplied air excess was λ = 2.2 and in another case λ = 1.65. With each different excess air ratio were performed at least two fuel loadings.

2.6. The fuel used during the research

During performance of calculations it is very important to know well the parameters of the fuel used during the researches. All fuel parameters were measured by ourselves, the main parameters are provided in the Table 1. The obtained results statistically reliably correlate with the results provided in the article [6].

Table 1. The main parameters of used fuel

Parameter	Units	Value	Expanded uncertainty, %
Lower calorific value of the wet fuel	kJ/g	**16.03**	± 1.31
Carbon (C) content	%	**49.10**	± 0.58
Oxygen (O) content	%	**42.81**	± 0.34
Hydrogen (H) content	%	**5.84**	± 0.33
Nitrogen (N) content	%	**0.27**	± 0.28
Sulphur (S) content	%	**0.12**	± 0.20
Ash content	%	**1.35**	± 0.38
Moisture content	%	**10.42**	± 0.20

3. RESULTS

The process of the heaters combustion is into three combustion phases: start-up phase, intermediate phase and the final burn-out phase. During start-up phase O_2 concentration in smoke decreases while the temperature of combustion chamber increases. While O_2 concentration and temperature of the heater is low, the combustion conditions are inadequate; therefore big concentrations of CO, C_xH_y are being detected. Once conditions of combustion stabilize, begins the intermediate phase of combustion. This phase is characterized by relatively stable concentration of O_2 and high temperature of combustion chamber, this creates appropriate conditions of combustion. During this phase concentrations of CO, C_xH_y and particulate matters are significantly lower in comparison with start-up phase. During burn-out phase the concentration of O_2 and the temperature of combustion chamber begin to decrease. Therefore again start to increase CO and C_xH_y concentrations in the smoke. The measurements of carbon monoxides and hydrocarbons were performed measuring their concentrations ppm (parts per million), and the mean values were calculated to mg/m^3 at the reference conditions (when – 13% O_2).

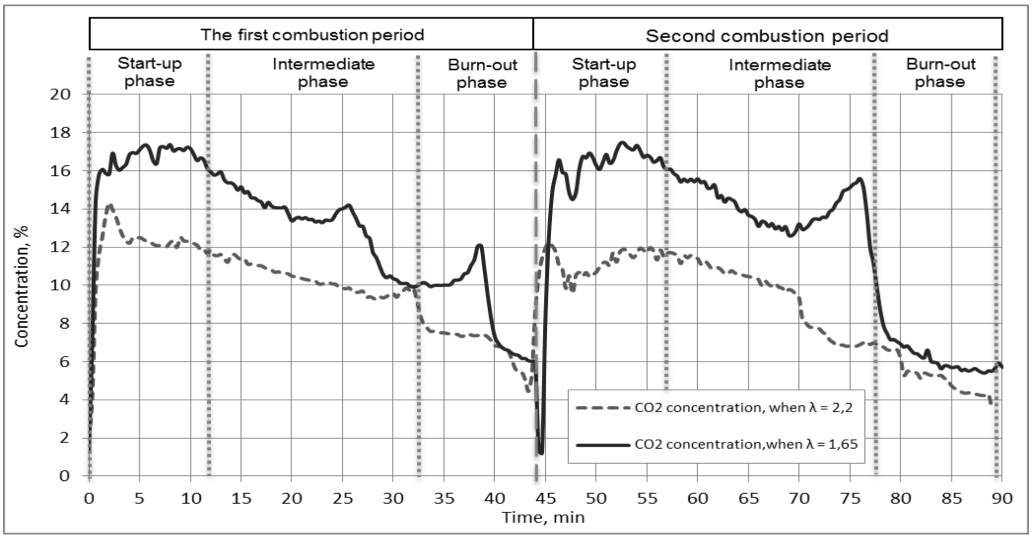

Fig. 3. The comparison of CO_2 concentrations at different excess air ratios

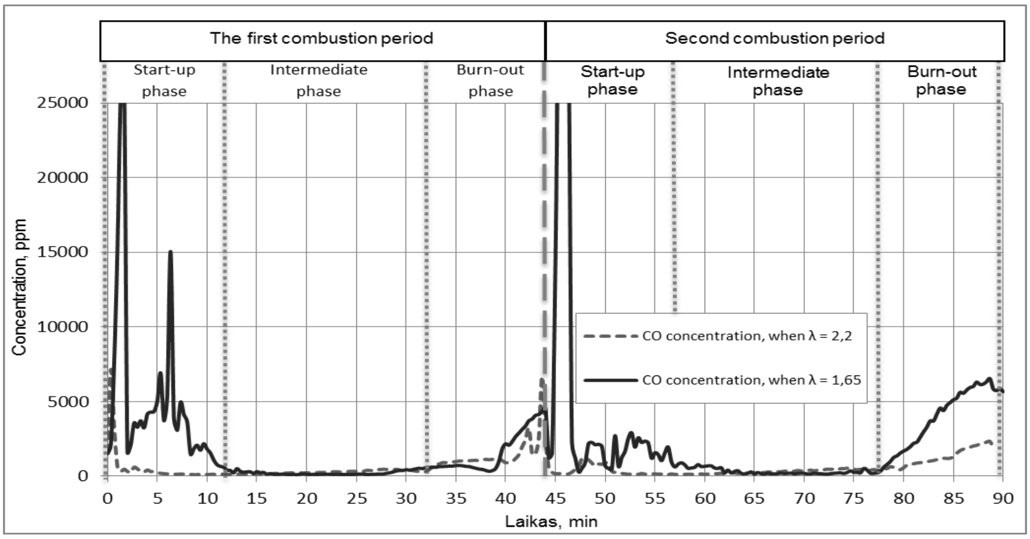

Fig. 4. The comparison of CO concentrations at different excess air ratios

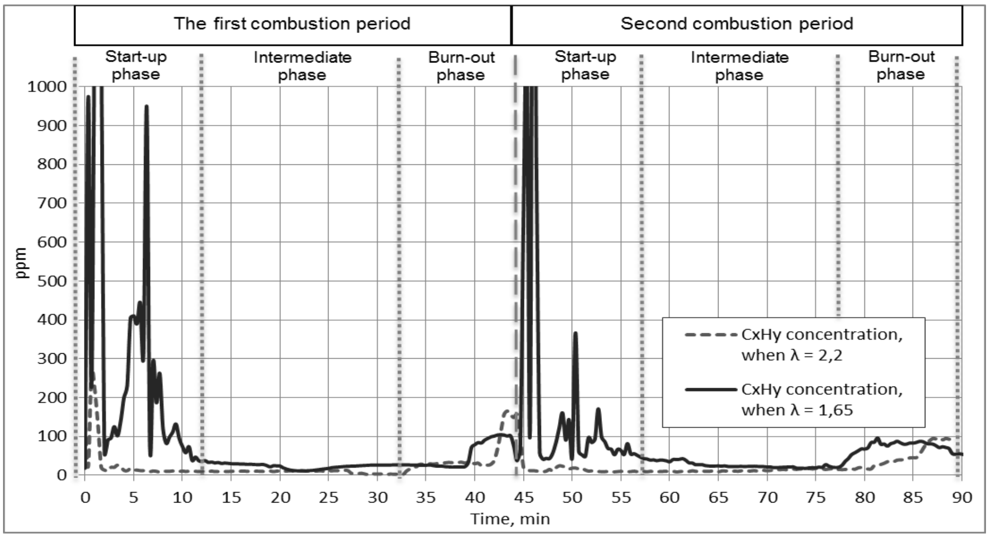

Fig. 5. The comparison of C_xH_y concentrations at different excess air ratios

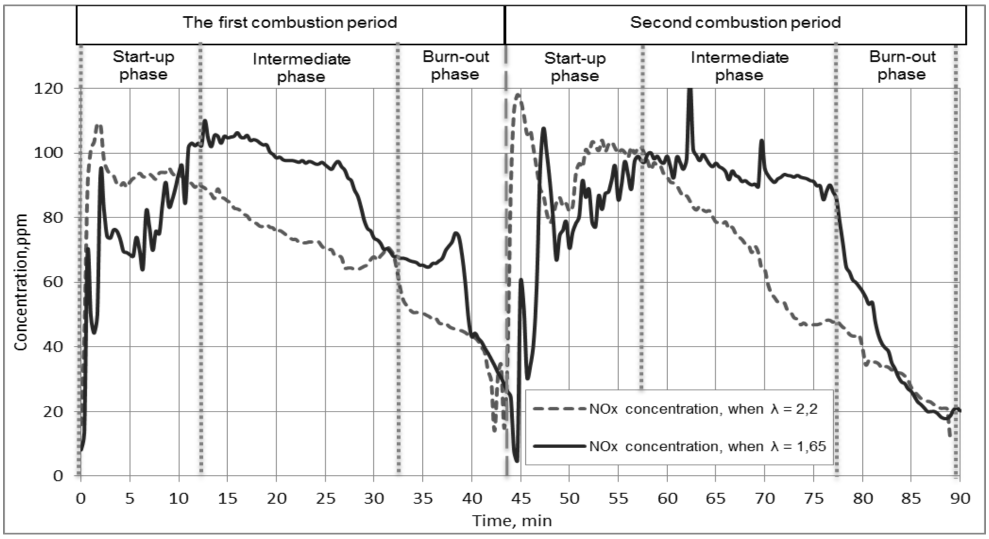

Fig. 6. The comparison of NO_x concentrations at different excess air ratios

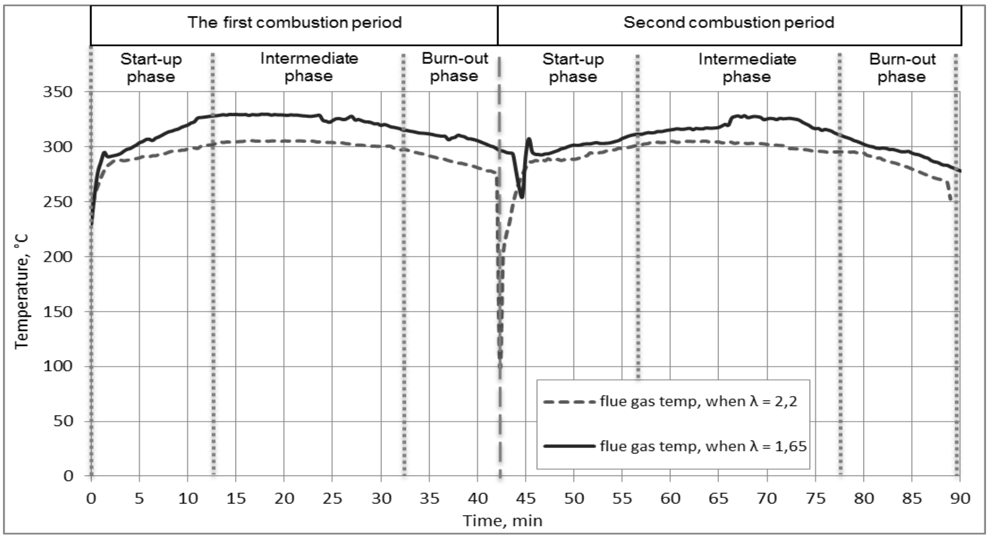

Fig. 7. The comparison of flue gas temperature at different excess air ratios

While increasing the excess air ratio the increasing amount of air passed through without being involved in the oxidation process. Therefore the air which hasn‘t involved in the process of combustion weakens the formed combustion products. This is well seen in the Fig. 7, which indicates that in case there is bigger excess air ratio the temperature of smoke is lower. However while calculating losses which have emerged due to the temperature of effluent smoke in accordance to the formula (2) is evaluated the flowing amount of air and the losses accordingly are when $\lambda = 2.2$ $q_a = 22.42\%$ and when $\lambda = 1.65$ $q_a = 18.08\%$. Therefore the formed 4.32% is very big and although at a higher excess air ratio forms significantly less products of incomplete combustion, however losses due to chemical incomplete combustion increase the ratio of combustion only by incomplete 1%.

Table 2. Concentration of emissions results

Combustion products	**Units**	**Result when $\lambda = 2.2$**	**Result when $\lambda = 1.65$**	**Expanded uncertainty, %**
CO_2	%	9.36	12.45	± 2.00
CO concentration at 13% O_2	mg/m^3	637.86	1760.72	± 2.02
NO_x concentration at 13% O_2	mg/m^3	119.93	91.35	± 2.52
C_xH_y concentration at 13% O_2	mg/m^3	32.43	91.94	± 4.04
Dust concentration at 13% O_2	mg/m^3	31.47	31.45	± 4.96

Table 3. The test results

Measured and calculated parameters	**Units**	**Result when $\lambda = 2.2$**	**Result when $\lambda = 1.65$**	**Expanded uncertainty, %**
Efficiency	%	77.02	80.60	± 2.62
Thermal losses in flue gas	%	22.42	18.08	---
Chemical losses	%	0.41	1.21	---
Heat losses due to unburnt constituents	%	0.14	0.12	---
Nominal heat output	kW	6.58	7.68	± 2.70 %
Flue gas temperature	°C	292.8	309.99	± 1.4 °C
Draft	Pa	11.52	10.32	± 2 Pa
The test duration	min	89	91.67	---
Fuel consumption	kg/h	1.92	2.14	---

The obtained results indicate that given the excess air ratio λ = 2.2 the concentrations of carbon monoxides and hydrocarbons which form in the products of combustion are 2.8 times lesser, however concentrations of nitrogen oxides have increased by approximately 30%. Due to bigger amount of supplied air are generated bigger "thermal" and "high-speed" nitrogen oxides. Thermal oxides form due to flame temperature – for the oxidation of air nitrogen the essential condition is a presence of atomic oxygen. The oxygen molecule can dissociate to atomic oxygen and atomic oxygen reacts with nitrogen molecule forming nitrogen oxides: $N_2 + O \leftrightarrow NO + N$. High-speed nitrogen oxides form due to reaction of the products radicals of hydrocarbons incomplete burning with nitrogen molecule. But as the main source of nitrogen oxides formation is nitrogen which is present in the fuel, because for separation of nitrogen atoms from fuel compounds is needed 1.5–4 lesser energy than for dissociation of oxygen molecule, therefore the formation of fuel nitrogen progresses at low temperatures. The patterns of nitrogen oxides are reflected in the obtained results. When is supplied the increased amount of air greater influence plays formation of thermal and high-speed nitrogen oxides, therefore the total amount of nitrogen oxides also increases up to 119.93 mg/m^3.

4. CONCLUSIONS

1. After increase of excess air ratio the concentrations of CO have decreased 2.7 times and the concentrations of H_xC_y have decreased 2.8 times, however the concentrations of NO_x have increased by almost 30%. Change of excess air ratio didn‘t influence the concentration of particulate matter.
2. Given the excess air ratio λ = 2.2, although the concentrations and losses of incomplete burning products CO and C_xH_y due to incomplete burning have decreased by almost 1%, however have increased the losses due to smoke temperature and the total ratio of efficiency has decreased by 3.5%.
3. The initial and secondary air in the heaters is adjusted manually, therefore it is essential to determine the limits in case to avoid excessive air feeding and to save fuel.

5. REFERENCES

1. BRUNNER, T., OBERNBERGER, I., SCHARLER, R. Primary measures for low-emission residential wood combustion – comparison of old with optimised modern systems. Proceedings o the 17th European Biomass Conference & Exhibition, June 2009, p. 1–10.
2. KOYUNCU, T., PINAR, Y. The emissions from a space-heating biomass stove. Biomass and Bioenergy, Vol. 31, Iss. 1, January 2007, p. 73–79.
3. NDIEMA, C.K.W., MPENDAZOE, F.M., WILLIAMS, A. Emission of pollutants from a biomass stove. Vol. 39, Iss. 13, 1 September 1998, p. 1357–1367.
4. Lietuvos standartas LST EN 13240. Roomheaters fired by solid fuel – Requirements and test methods. 2002. December.
5. ROYA, M. M., CORSCADDENB, K., W. An experimental study of combustion and emissions of biomass briquettes in a domestic wood stove. Applied Energy, Vol. 99, November 2012, p. 206–212.
6. VASSILEV, S. V., BAXTER, D., ANDERSEN, L. K., VASSILEVA, C. G. An overview of the chemical composition of biomass. Fuel. Vol. 89, Iss. 5, May 2010, p. 913–933.

CYSENI 2016, May 26-27, Kaunas, Lithuania
ISSN 1822-7554, www.cyseni.com

TOMOGRAPHIC RECONSTRUCTION OF THE FLAME TEMPERATURE FIELD BASED ON THE TALBOT IMAGES METHOD

I. N. Shatan
A.V. Luikov Heat and Mass Transfer Institute of National Academy of Sciences of Belarus
P. Brouki str. 15, BY-220072 Minsk – Republic of Belarus
E-mail: inshatan@gmail.com

ABSTRACT

Currently, there is a certain scientific interest in the possibility of using tomographic reconstruction techniques to measure the distribution of the various parameters in the reacting and non-reacting gas flows. The aim of this work was to develop a method of tomographic reconstruction of three-dimensional temperature distribution in the reacting gas flows on the basis of optical diagnostics by means of Talbot images. In this case, the results of the object diagnostic by Talbot images method are used as the projection data for reconstruction algorithm. The paper discusses the algorithms of experimental Talbot images processing and methods of the refractive index reconstruction based on the testing in several view directions. The results of the tomographic investigation of the premixed methane-air flame are presented. The system of gas flow formation consists of three converging cylindrical tubes. The tubes are equally spaced from each other. The two-dimensional field of deflection angles of the probe radiation was measured at different viewing angles by rotating the flow formation system. The filtered back projection algorithm was used to solve tomographic problem. The calculation of temperature field is based on the refractive index distribution.

Keywords: methane-air flame, Talbot images, tomography

1. INTRODUCTION

Currently, there is a certain scientific interest in the possibility of using tomographic reconstruction techniques for measuring the distribution of the various parameters in the reacting gas flows [1, 2]. A detailed description of such processes is often possible only with the three-dimensional distribution of physical and chemical parameters. The results of the tomographic investigation of such flows provide important information for a thorough understanding of combustion, for combustion processes improvement and for verification of computational gas dynamics methods. The results can include the dynamic of the flame front, the frequency of disturbances propagation, the distribution of free radicals or fuel-oxidizer ratio for operation of combined burners.

Tomographic reconstruction involves the use of a diagnostic method, based on which the physical parameters of the object can be measured in different directions of observation. In optical tomography for reacting and non-reacting gas flows absorption or interferometric methods are most commonly used. In the paper [3] the tomographic reconstruction of the density field in a supersonic jet was based on holographic interferometry. In [4] the possibility of using a holographic interferometer to restore the three-dimensional density field and for the study of turbulent structures in a subsonic and transonic jet was shown. In the [5] the tomography was based on the shearing interferometry. The optical system was constructed for the simultaneous diagnostic of turbulent flow in the six directions. In the paper [6] the ability to restore the refractive index of the field using a volumetric computed tomography algorithms based on the method of moire deflectometry was shown. In the [7] the tomographic reconstruction on the basis of moire deflectometry was used to reconstruct temperature distribution in a flame.

The aim of this work is to develop a method of tomographic reconstruction of the three-dimensional distribution of temperature in the reacting gas flow based on the method of Talbot images [8].

2. EXPERIMENTAL SETUP

The experimental setup consists of the reacting gas flow forming system and the optical system for Talbot images registration. Acquiring enough number of projections is a major technical problem. To simplify investigations the optical scheme has been selected, in which the projections in different viewing directions are registered by rotating the object.

The flame of three converged methane flows was chosen as the research object. The system of three cylindrical tubes was used. The position of tubes corresponds to the lateral edges of a frustum with an equilateral triangle in the base. Tubes were deflected from the vertical direction on 30 °. The top face of the frustum corresponds to the equilateral triangle with a side length of ~ 13 mm. The outer diameter of the tubes was 3 mm and the inner diameter was 2 mm. For the presented experiments a premixed methane-air gas with a stoichiometric ratio $\varphi = 2.0$ was used. The mixture flow was controlled by a gas flow controller. The flow rate was ~ 0.5 m/s.

Optical scheme of the experimental setup was built on the basis of a gas laser with a wavelength λ = 514.5 nm. As a Talbot grating, a glass plate with a reflective layer was used. Reflective layer comprises a matrix of circular holes with a diameter d = 50 μm located in the nodes of a square grid. The distance between the holes in the grid was p = 250 μm. For diagnostic a wide aperture laser beam 200 mm in diameter with an approximately flat wavefront was used. The grating was located normal to the vector of propagation of laser radiation behind the investigated flame and before the digital camera. Registration of the interference pattern in the plane of the first self-reproduction (L_T = 0.121 m) was carried out on the CCD camera "Nikon-D700" with the matrix size of 24 × 36 mm.

Measurement of a two-dimensional field of laser beam deflections was carried out under different viewing angles by rotation the nozzle. Projection data were obtained for observation angles ranging from 0 ° to 360 ° with 15 ° increments. For precise positioning flow forming system has been installed on the rotary table, which ensures the accuracy of the angle measurement up to 0.5'.

3. RESULTS

When using the method of Talbot images, coherent radiation after passing through the investigated object forms a distorted image of a two-dimensional diffraction grating. Numerical analysis of the distortion of an interference pattern in the plane of self-imaging relative to the reference pattern will determine the deflection angles of the probe radiation.

The task of experimental data processing consists of the following steps:

1) the recognition of spots structure corresponding to the structure of the Talbot grating;
2) determination of the single elements of the image;
3) deflection angles calculation on the basis of a comparison of the relevant elements of the reference and distorted Talbot images.

For the analysis of experimental data in the automatic regime, the set of software tools was developed. Fig. 1 shows a field of probe radiation deflection angles for one of the viewing directions.

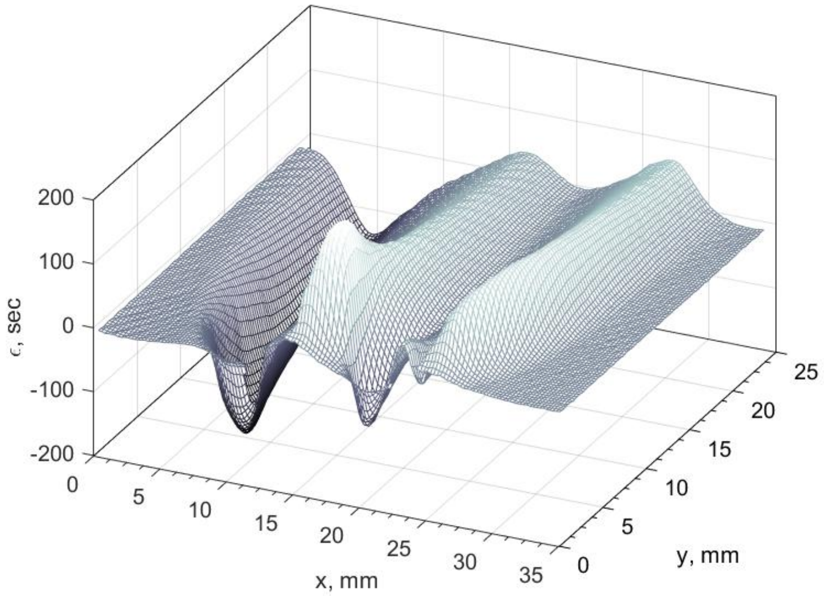

Fig. 1. The projection data as a field of deflection angles of the probe radiation

The three-dimensional field of refractive index can be restored on the basis of projection data in the form of a two-dimensional field of probe radiation deflections. The relation between refractive index distribution $n(x,y)$ and the field of probe radiation deflections $\varepsilon(t,\theta)$ can be expressed by the equation:

$$\varepsilon(t,\theta)=\int_{-\infty}^{+\infty}\int_{-\infty}^{+\infty}\frac{1}{n_0}\frac{dn(x,y)}{dt}\delta(x\cos\theta+y\sin\theta-t)\,dxdy\,, \qquad (1)$$

where deflections $\varepsilon(t,\theta)$ are measured for the angle of observation θ. The corresponding coordinate system st rotated through an angle θ relative to the starting system xy is shown in Fig. 2. The equation (1) differs from the Radon equation by a presence of a transverse gradient of the refractive index.

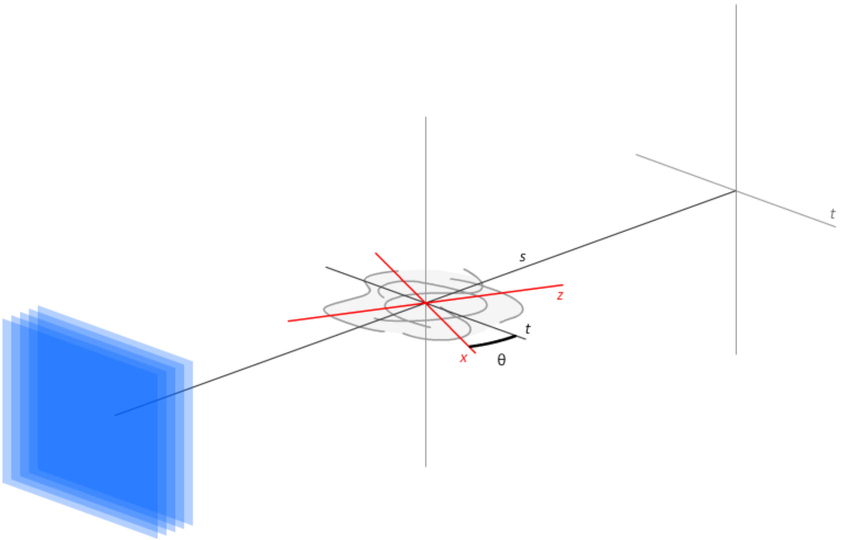

Fig. 2. The position of the coordinate systems for measuring projection data
at an angle θ

Fig. 3 shows the deflection angles of the probe radiation in the form of a sinogram for a horizontal section at the height of 10 mm from the nozzle exit.

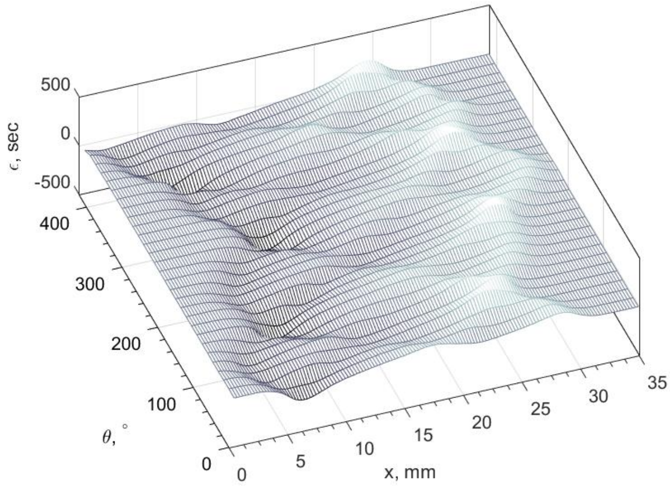

Fig. 3. Deflection angles of the probe radiation in the form of a sinogram for the horizontal slice at a distance of 10 mm from the exit of the nozzle

There are many different algorithms to solve the problem of tomography. For the purpose of this work the method of filtered back projections which is modified for the case of transverse gradient projections [9, 10] was selected. In this case, the solution can be presented in the form of equation:

$$n(x,y) = \int_0^{\pi} \left[\varepsilon(t,\theta) * k(t) \right]_{t=-x\sin\theta + y\cos\theta} d\theta , \tag{3}$$

where $k(t)$ is a filter function, which corresponds to the inverse Fourier transform of $-i\,\mathrm{sgn}(T)/2\pi$:

$$k(t) = \frac{1}{\pi^2 t} \sin^2\left(\frac{\pi t}{2\Delta t}\right), \tag{4}$$

and Δt is the spacing between samples in a projection.

The equation (3) was directly used for the reconstruction of the refractive index. The algorithm consists of two parts, the convolution process (filtering projection data) and the back projection process (the summation over all projections).

The chosen method allows restoring the two-dimensional distribution in any horizontal slice of the object. In order to obtain a three-dimensional distribution of the refractive index data between the slices was interpolated. The results of reconstruction of refractive index distribution in a horizontal section at a distance z = 2.5 mm from the edge of the nozzle are shown in Fig. 4.

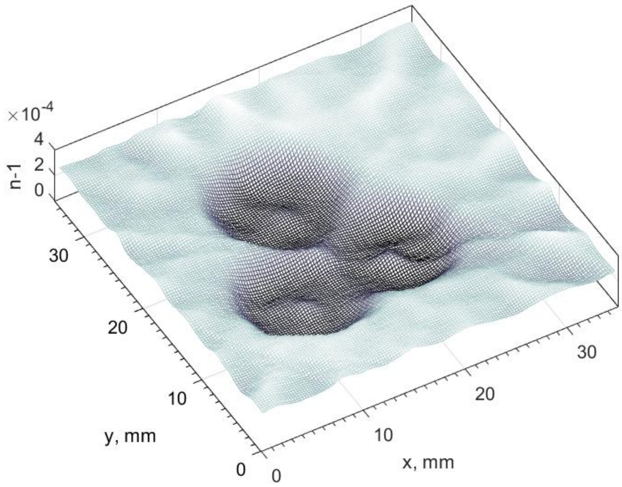

Fig. 4. The distribution of the refractive index in the horizontal slice z = 2.5 mm from the nozzle exit

For temperature field calculation the approach based on the neglecting of composition variation was selected. It can be used since for the combustion of lean mixtures in the air nitrogen molecules N_2 have a considerable influence on the refractive index variation in the entire area. So it can be assumed that the refractive index at each point of the flame corresponds to the refractive index of the air heated to the same temperature. In this case temperature T is inversely proportional to the refractive index of the flame:

$$T = T_0 \frac{(n_{av} - 1)}{(n - 1)} . \tag{5}$$

The results of calculation of the temperature field in the test flame are presented in Fig. 5.

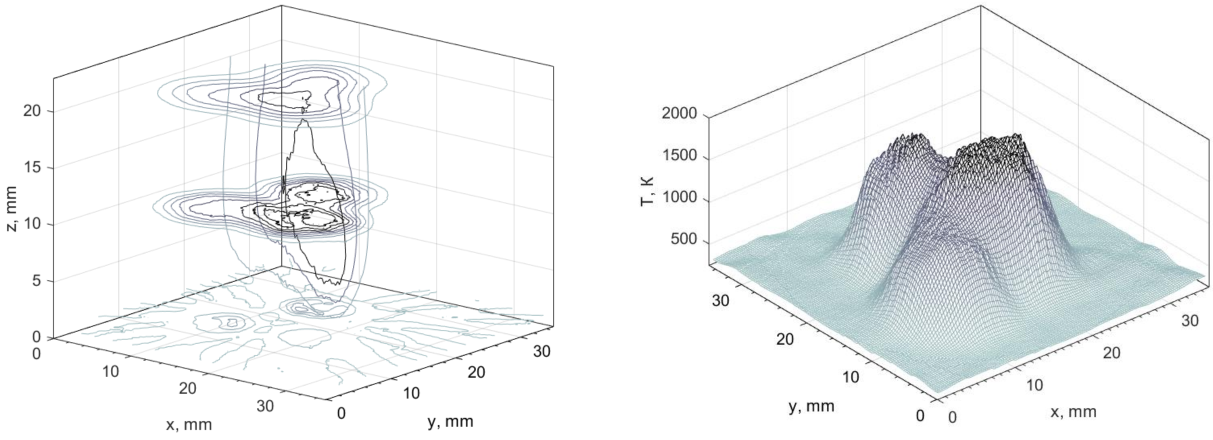

Fig. 5. The temperature distribution in the flame of three converging methane-air flows as a three-dimensional view (left) and as a horizontal section at a distance of 10 mm from the exit of the nozzle

4. CONCLUSIONS

The possibility of using the method of Talbot images for tomographic reconstruction of the field of local characteristics in three-dimensional gas flows are shown. The methodic was approved for measuring the temperature field in the flame. The experimental study was carried out for the rich premixed methane-air flame ($\varphi = 2.0$) of three converged methane flows. The temperature was calculated based on the distribution of refractive index. To calculate the temperature an approach based on the neglecting of composition variation was selected. The distribution of the refractive index in the flame was reconstructed from light deviation measurements by means of Talbot images. To obtain projection data along various viewing directions the nozzle was rotated. For tomographic reconstruction, the filtered back projections algorithm was chosen because it is one of the most common methods. The results of reconstruction have a good quality. As seen from the figures the internal structure of the flame is clearly seen.

According to the results and the characteristics of the optical scheme, the method of Talbot images can be used for tomographic investigation of reacting and non-reacting gas flows.

5. ACKNOWLEDGMENTS

This work was supported by Belarusian Republican Foundation for Fundamental Research (grant F14M-142).

6. REFERENCES

1. Yong YAN, Tian QIU, Gang LU, HOSSAINA, M.M., GILABERTA, G., Shi LIU. Recent advances in flame tomography. *Chinese Journal of Chemical Engineering*, 2012, Vol. 20. No. 2, p. 389–399.
2. KHAIRI, M.T.M., IBRAHIM, S., YUNUS, M.A.M., FARAMARZI, M. A review on applications of optical tomography in industrial process. *International journal on smart sensing and intelligent systems*, 2012, Vol. 5, No. 4, p. 767–798.
3. SÖLLER, C., WENSKUS, R., MIDDENDORF, P., MEIER, G. E. A., & OBERMEIER, F. Interferometric tomography for flow visualization of density fields in supersonic jets and convective flow. *Applied optics*, 1994, Vol. 33, No. 14, p. 2921–2932.
4. TIMMERMAN, B. H., WATT, D. W., & BRYANSTON-CROSS, P. J. Quantitative visualization of high-speed 3D turbulent flow structures using holographic interferometric tomography. *Optics & Laser Technology*, 1999, Vol. 31, No. 1, p. 53–65.
5. PELLICCIA-KRAFT, B. J., & WATT, D. W. Three-dimensional imaging of a turbulent jet using shearing interferometry and optical tomography. *Experiments in fluids*, 2000, Vol. 29, No. 6, p. 573–581.
6. WANG, J., SONG, Y., LI, Z. H., & HE, A. Z. Realization of volume optical computerized tomography by circular gratings. *Optik-International Journal for Light and Electron Optics*, 2013, Vol. 124, No. 22, p. 5822–5825.
7. ZHANG, B., WU, Z., & ZHAO, M. Deflection tomographic reconstructions of a three-dimensional flame structure and temperature distribution of premixed combustion. *Applied optics*, 2015, Vol. 54, No. 6, p. 1341–1349.
8. KHRAMTSOV, P. P., PENYAZKOV, O. G., SHATAN, I. N. Temperature measurements in an axisymmetric methane–air flame using Talbot images. *Experiments in Fluids*, 2015, Vol. 56, No. 2, p. 1–9.
9. FARIS, G.W., BYER, R.L. Three-dimensional beam-deflection optical tomography of a supersonic jet. *Applied optics*, 1988. Vol. 27, No. 24. p. 5202–5212.
10. AGRAWAL, A.K. et al. Three-dimensional rainbow schlieren tomography of a temperature field in gas flows. *Applied optics*, 1998. Vol. 37, No. 3. p. 479–485.

CYSENI 2016, May 26-27, Kaunas, Lithuania
ISSN 1822-7554, www.cyseni.com

ANALYSIS OF PRECIPITATED PARTICLES IN ESP AND CYCLONES OF SMALL AND MEDIUM SCALE BOILERS

V. Zaleskas, D. Valaitis
Lithuanian Energy Institute
Breslaujos str. 3, LT-44403 Kaunas – Lithuania
Email: vladas.zaleskas@lei.lt

ABSTRACT

Solid biomass combustion is getting substantial as a renewable energy source, but also is increasingly criticized for generating much higher particulate matter (PM) concentrations than alternatives. One of the main PM pollution sources are domestic and medium scale water boilers and heating appliances. More attention was dedicated to PM_{10} precipitation devices such as cyclones and electrostatic precipitators (ESP) after EU directive 1999/30/EC, which limits PM of size up to 10 micrometers (PM_{10}) concentration in the air. The objective of this paper is to get size distributions of particle that are precipitated in ESP and cyclones. Furthermore, to compare those distributions between particles from different power boilers as well as boilers using different fuel. All PM distributions show a peak at 0.2 μm. Samples of PM from water boilers burning wood chips and shale shows a secondary, more shallow peak at (2 to 20) μm for wood chips and (1 to 5) μm for shale. Said particle size distributions were acquired using PM spectrometer Promo 3000 H, which has two cells with particle diameter measuring intervals (0.2–10) μm and (2–105) μm.

Keywords: PM_{10}; particle size distribution; particle precipitation

1. INTRODUCTION

Solid biomass combustion is getting substantial as a renewable energy source, but also is increasingly criticized for generating much higher particulate matter (PM) concentrations than alternatives. Environment polluted with PM can cause serious health problems. Statistically it reduces life expectancy by a year [1]. That is mainly because of increased hazard of heart and blood-vessel and respiratory diseases, pulmonary cancer. PM impact on human health depends on:

- PM size;
- Time-frame of the effect;
- PM concentration;
- PM composition;
- Individual sensitivity, physical condition.

Smaller particles can penetrate deeper into the lungs:

- Larger than 10 μm particles precipitates in nasopharynx and is removed by sneezing;
- 5–10 μm particles settles down in trachea;
- Smaller than 5 μm particles reach bronchi;
- And smallest particles, $PM_{2.5}$ (less than 2.5 μm diameter particles) reaches alveoli.

Knowing that, we can understand how important it is not only to measure mass concentration of the PM but to measure particle distribution as well. Problem is that there are still used different methods for measuring particle distribution [2, 3] and results depends on the method used. The methods namely are:

- Heated Filter (HF). Sampling of particles on a heated filter, through a probe, from undiluted flue gas in the chimney;
- Full Flow Dilution Tunnel (FFDT). Sampling of filterable particles in a dilution tunnel with a filter holder gas temperature at e.g. < 35 °C (e.g. Norwegian standard NS 3058-2);
- Sampling of condensable organic matter in impinge traps at temperatures close to 0°C;

- Dilution sampling (DS). To mimic conditions in the ambient, sampling is performed in cold, highly diluted flue gas.

Studies [2, 3] emphasize that the amount of particles collected with the FFDT method was much higher (5.6 times on average in one of the studies) than the amount of particles collected on the HF, but sadly doesn't compare PM distrubutions. This shows, that the mass of condensables may significantly exceed the mass of solid particles.

Extensive investigation was done by Saxony Anhalt State Environmental Protection Agency and University of Stuttgart, Institute of Process Engineering and Power Plant Technology [4]. Over a 100 different measurement campaigns performed, PM distributions determined for various plants and combustion units firing wood, coal, oil. The number includes measurements of PM in industrial production factories like cement production, metallurgy, etc. Considering only industrial plants and domestic stoves it was found that in more than 70% of the emission measurements the PM10 portion amounted to more than 90% and the $PM_{2.5}$ portion between 50% and 90% of the total PM emission. To measure PM distribution two eight- or six-stage Anderson Impactors were used and they gave comparable results. PM distribution results were represented by both frequency distribution (Y) over the PM diameter and cumulative frequency particle size distribution (D) according to Rosin, Rammler, Sperling and Bennet (RRSB) of selected typical samples. The relation between the two:

$$Y = -dR/d(log\ d); \qquad (1)$$

here R is cumulative residue distribution, R = 1 – D; d – particle diameter.

The trends of PM distributions given in this study by fuel type will be discussed together with our results.

The purpose of this work was to make initial measurements of PM distribution of different type of combustion systems that are using different types of fuel. Samples were collected from different precipitators or filters under operating conditions or in laboratory.

2. METHODOLOGY

Aerosol spectrometer system Promo 3000 H with sensors welas 2100 HP and welas 2500 HP were used to measure PM distribution. Spectrometer illuminates measuring volume with white light and measures intensity of 90 degrees scattered light and calculates equivalent diameter of the sphere. Promo 3000 H use white light to avoid specific light wavelength dependant phenomena like diffraction or interferention. This way calibration curve – the reflected light intensity dependance on particle diameter – is even and clear. Particle concentration is calculated by evaluating number of analyzed particles and volume of illuminated flow. Maximum concentration that 2100 sensor can measure is 2×10^5 particles/cm^3 and 800 particles/cm^3 for 2500 sensor.

It is possible to switch measuring range for both sensors. Possible ranges for 2100 sensor are (0.2–10) µm, (0.3–17) µm and (0.6–40) µm. For 2500 sensor they are: (0.3–17) µm, (0.6–40) µm and (2–105) µm. In our experiments we usually used 2100 (0.2–10) µm and 2500 (2–105) µm measuring ranges to get maximum range coverage.

To this moment we only analyzed samples of particles collected in filters, cyclones and electrostatic precipitators (ESP). Samples were taken from PM bunker of precipitator or from filters of sampler used for measurement of PM mass concentration. Collected particle samples were put into a container and shook to create aerosol. Then one or the other welas sensor was placed inside the container so that suction would pull aerosol through the sensor. Suction velocity is constant at 5 l/min. Measurements were continuos and lasted 4–5 minutes each. The concentration of aerosol was monitored during the measurement and controled so it would be roughly 50 to 100% of the maximum concentration measured by welas sensors. Number of analysed particles during the measurement varied 30 to 300 thousand with each sensor.

When analyzing the data we plotted distributions of the same sample from different time intervals. We noticed that those distributions were similar despite the fluctuation in concentration and thereby – number of analysed particles per interval. Since it was initial measurements we were satisfied to get general trends of distributions of PM from different sources and didn't try to obtain very acurate results with small uncertainty.

Measurement data is presented as particle number distribution dN/N (number of particles in the interval / number of all particles). Important to note that particle diameter is in logarithmic scale, so diameter interval width is increasing exponentially with the diameter.

It is also possible to plot mass concentration distribution as we did in the second case party to show it is possible and partly to show how much it differs from number distribution. Mass concentration distribution is shown on secondary scale dCm/Cm. Here dCm is mass concentration of particles in the interval and Cm is mass concentration of all particles. Such denotation is used in Promo 3000 H software so we have used the same.

However, results were presented using particle number distribution more often than mass distribution in reviewed literature. Following that example we didn't plot mass distribution in other cases for fear of overcrowding the graphs.

Our future goal is to measure particle size distribution in situ, but that requires measuring significantly higher temperature samples from inside the chimney and that creates technical problems.

To avoid influence of working mode we measured particles collected from boilers working at standard condition during nominal power mode.

3. RESULTS AND DISCUSSION

3.1. Water heating boilers firing biofuel

3.1.1. Water heating boiler firing wood pellets

25 kW wood pellet firing unit without any PM precipitator was tested in laboratory conditions. PM mass concentration was measured with gravimetric method using isokinetic sampling. Calculated concentration was 196.92 mg/m^3, emission factor: 93.37 mg/MJ. The same glass wool filters that were used for gravimetric method were later re-used to obtain a sample for spectrometer. Obtained PM distributions can be seen in Fig. 1. From distribution No. 1 we can see that number of particles steadily increase with decreasing particle diameter. From 0.7 µm the rate of increase is even greater and peak is reached around 0.2 µm. Comparing (2 to 105) µm diameter particles we can see that the trend is the same as with distribution No.1 and there are only few particles larger than 20 µm. Very similar trend was given in [4] for the same type – wood pellet firing unit.

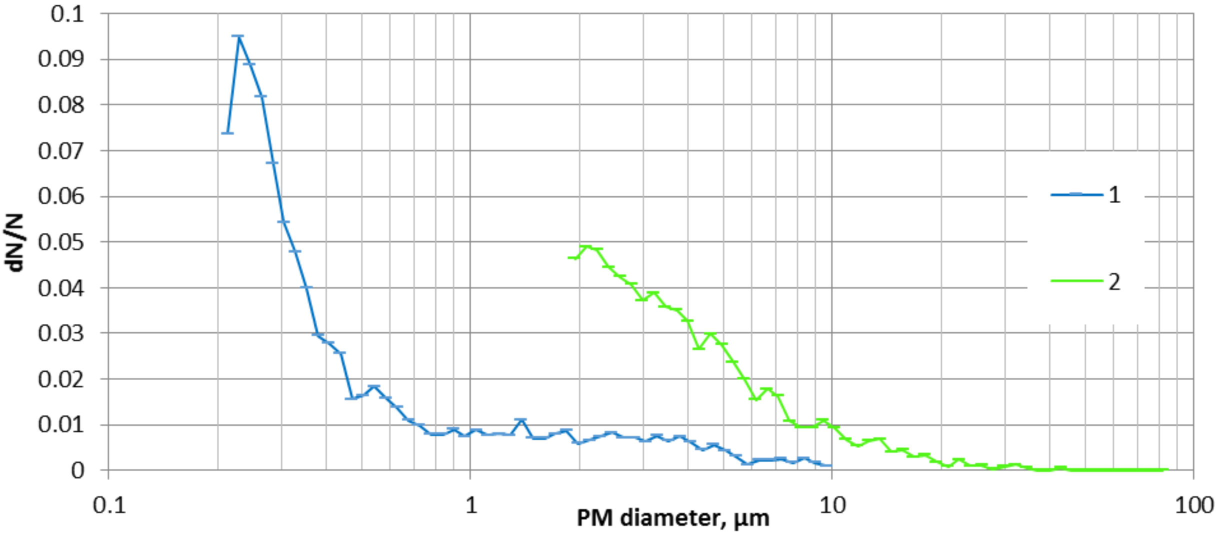

Fig. 1. PM distribution from filters used for 25 kW wood pellet firing unit testing: 1, 2 – PM distribution obtained with sensor 2100 using (0.2 to 10) µm measurement range and with sensor 2500 using (2 to 105) µm measurement range respectively

3.1.2. Water heating boiler firing wood chips

Test samples were taken from bunkers of multicyclones and ESP installed after 7 MW water boilers which are using wood chips as fuel. There were two identical water boilers followed by a multicyclone for each. After multicyclones exhaust channels merged and went through ESP outside. As we can see from PM distribution in Fig. 2 there are two peaks: sharp spike around 0.2 µm and shallow at (2 to 10) µm. Both [4] and [5] show that wood chip using boilers of different power emits PM with similar two peaks at (0.2 to 0.4) µm and (3 to 7) µm which well corresponds to our results.

Comparing ESP and multicyclones we can see that in (2 to 20) µm range there is notable difference: multicyclones cleanse the flow from larger particles – (5 to 20) µm diameter and ESP precipitates more of what’s left – (2 to 5) µm diameter particles.

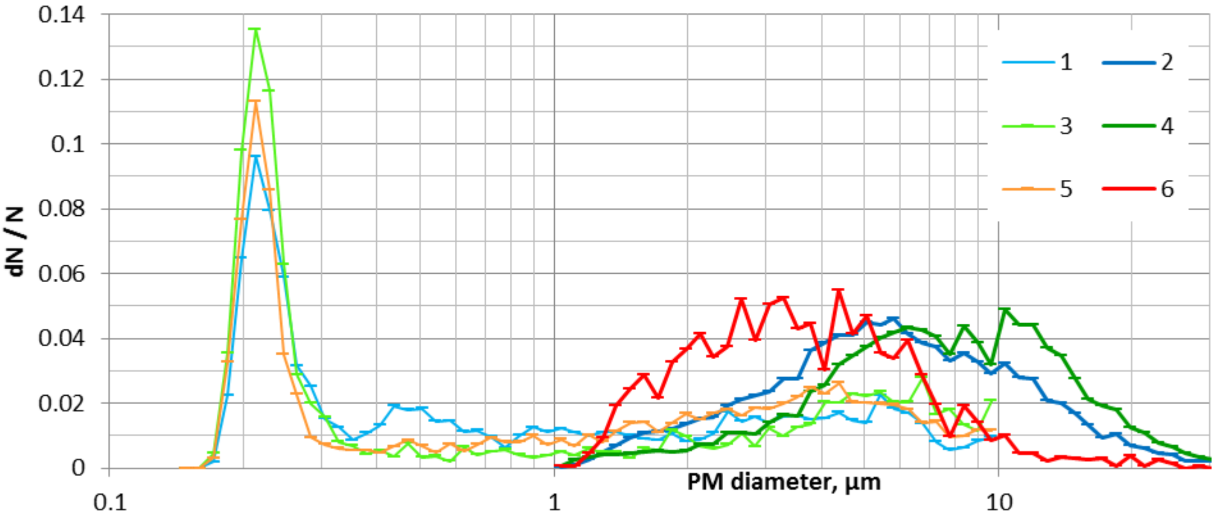

Fig. 2. PM distribution from 2 multicyclones and ESP after water heating boiler firing wood chips. PM distributions obtained with sensor 2100 using (0.2 to 10) µm measurement range: 1 – 1st multicyclone, 3 – 2nd multicyclone, 5 – ESP; PM distributions obtained with sensor 2500 using (2 to 105) µm measurement range: 2 – 1st multicyclone, 4 – 2nd multicyclone, 6 – ESP

3.2. Coal combustion system

Particles samples were taken from multicyclone installed after fine coal combustion system with a capacity of 3 MW to 10 MW. Particle number distribution is very similar to first case – wood pellet firing unit – it's obvious that the smaller diameter the more particles there are, but they constitute only small percentage of mass concentration as we can see from mass concentration distribution. 87% of particles are smaller than 2 µm, but they amount only to 1.5% of mass concentration and the peak is around 10 µm. This result doesn't conflict with the claim that $PM_{2.5}$ forms large part (50 to 90)% of total PM emission [4], because we have to keep in mind, that we analyzed from multicyclone and in [5] it was nicely shown that multicyclone precipitate only a fraction of $PM_{2.5}$. In fact, despite that, the trend is very similar to [4] PM frequency distribution for small firing plants using brown coal briquettes.

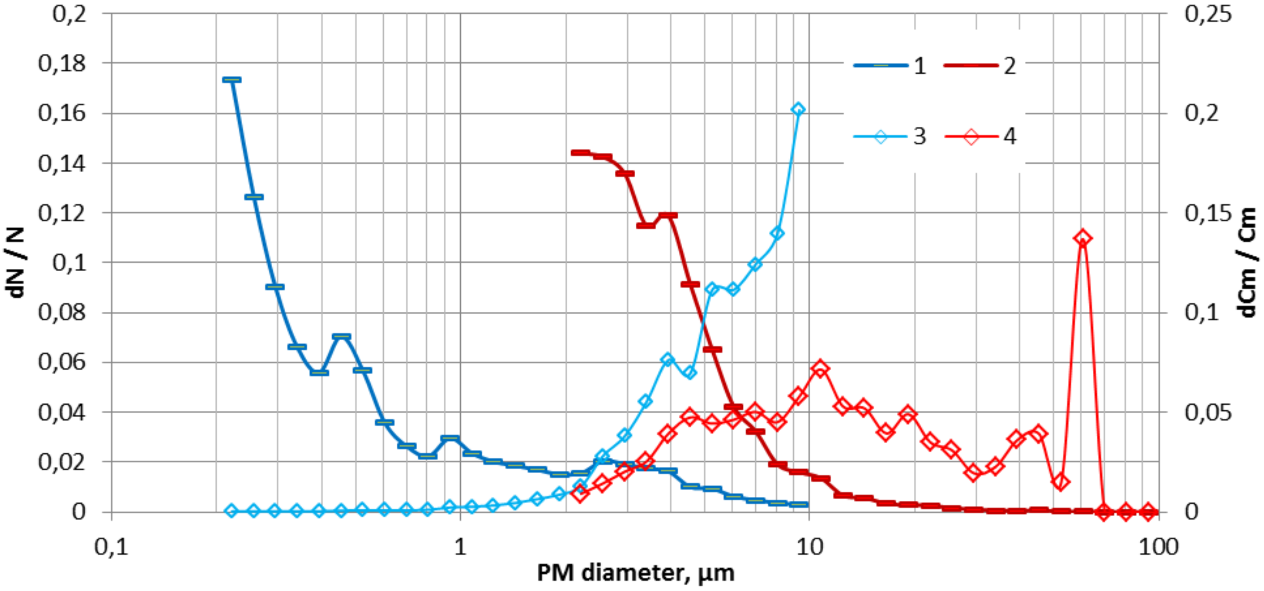

Fig. 3. PM distribution by number and mass concentration from multicyclone after coal combustion system. PM distributions obtained with sensor 2100 using (0.2 to 10) µm measurement range: 1 – number distribution, 3 – mass concentration distribution; PM distributions obtained with sensor 2500 using (2 to 105) µm measurement range: 2 – number distribution, 4 – mass concentration distribution

3.3. Water heating boiler firing shale

Last case: 115 MW water boiler that is using shale. Two samples were taken from two ESP, one in beginning of the set and another – in the end of the set. Results (see Fig. 4) are similar to water boiler firing wood chips, because both has two peaks and first one is (0.2 to 0.3) µm, but in this case second one is shifted to (1 to 5) µm. Also in this case second one is much more pronounced and first one isn't as sharp or high.

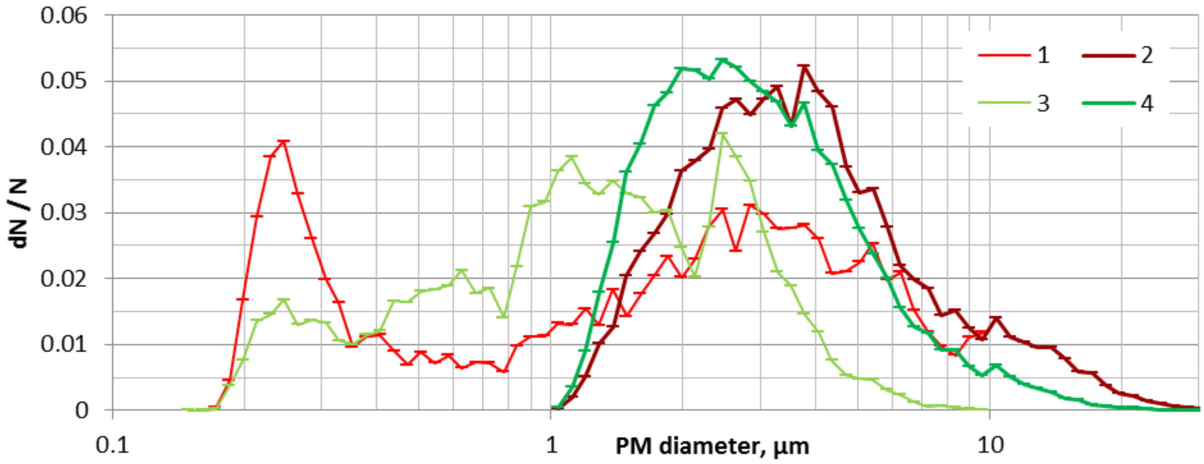

Fig. 4. PM distribution from ESP after water heating boiler firing shale. PM distributions obtained with sensor 2100 using (0.2 to 10) µm measurement range: 1 – sample No. 1, 3 – sample No. 2; PM distributions obtained with sensor 2500 using (2 to 105) µm measurement range: 2 – sample No. 1, 4 – sample No. 2

4. CONCLUSIONS

Samples for PM analysis were collected from different precipitators or without them. Samples were taken from PM bunkers or from filters of sampler used for measurement of PM mass concentration.

Among PM from wood pellet firing unit and fine coal combustion system fine particles dominates with single peak at around 0.2 µm particle diameter.

Samples of PM from water boilers burning wood chips and shale shows a secondary, more shallow peak at (2 to 20) µm for wood chips and (1 to 5) µm for shale.

These results well correlates with published PM distributions from combustion units of corresponding type.

From multicyclone and ESP comparison we can attest that multicyclones precipitate larger particles (> 2.5 µm) better and while ESP can precipitate $PM_{2.5}$ as well.

5. REFERENCES

1. http://www.am.lt/VI/files/File/Seminaras%20oro%20tarsa%202015-10-08/A.Ragoza_oro_tarsos_poveikis_sveikatai.ppt 2016-03-07.
2. SELJESKOG, M., SEVAULT, A., ØSTNOR, A., BIRGER RØNNING, B. Wood Emission measurements, CEN/TC 295 - Residential solid fuel burning appliances. SINTEF Energy Research and SP Fire Research Norway, 21st October 2015.
3. NUSSBAUMER, T., KLIPPEL, N., JOHANSSON, L. Survey on measurements and emission factors on particulate matter from biomass combustion in IEA countries. 16th European Biomass Conference and Exhibition 2008. Valencia, Spain. 2–6 June 2008.
4. EHRLICHA, C., NOLLA, G., KALKOFFA, W.-D., BAUMBACHB, G., DREISEIDLERB, A. PM_{10}, $PM_{2.5}$ and $PM_{1.0}$–Emissions from industrial plants–Results from measurement programmes in Germany. Atmospheric Environment 41 (2007) 6236–6254.
5. TONKONOGIJ, J., PEDIŠIUS, N., STANKEVIČIUS, A., TONKONOGOVAS, A. Mažos ir vidutinės galios kietuoju kuru kūrenamų įrenginių kietųjų dalelių emisijų tyrimas. Energetika. 2015. T. 61. Nr. 3–4. P. 119–130.

CYSENI 2016, May 26-27, Kaunas, Lithuania
ISSN 1822-7554, www.cyseni.com

LOW FLOW PROJECTIONS OF THE SOUTH-EASTERN LITHUANIAN RIVERS IN 21ST CENTURY

V. Akstinas
Lithuanian Energy Institute
Breslaujos str. 3, LT-44403 Kaunas – Lithuania
Email: vytautas.akstinas@lei.lt

ABSTRACT

The evaluation of hydrological extremes (floods and droughts) is very important for all kinds of human life aspects. The low flow is one of hydrological extremes which is characterised by average of the lowest river discharge in the 30 day period. This period is very important hydrological characteristic from which depends water quality, ecosystem condition and health of whole environment. For that reason it is important to find out low flow variation under climate change conditions. According to it the main task of this research is creation of the projections of warm season low flow in 21st century for three Lithuanian rivers (Neris, Merkys and Nemunas up to Druskininkai water gauging station (WGS)). In this study, for low flow future projections, meteorological data (precipitation and temperature) has been taken from two different regional climate models (RCM) which were generated according to A1B climate change scenario. Daily precipitation and temperature data of 21st century were performed by Bias Correction Change in mean (BCC) and Quantile Mapping (QM) methods, which are used to delete errors of RCM output. After performance, daily precipitation and temperature data were used for HBV hydrological modelling of the low flow in three Lithuanian rivers under climate change conditions in 21st century. The low flow projections showed very high amplitude in variance, but most of them have decreasing trends.

Keywords: Lithuanian rivers, projections of low flow, climate change, RCM, statistical downscaling

1. INTRODUCTION

Projection of hydrological extremes gives deeper knowledge about climate change impact on hydrological processes all over the world. This information is very important for management of water resources using, because in near future freshwater resources might be the major object in research field. The low flow determines river conditions during the dry period of the year [1]. In some cases these conditions are described as hydrological droughts. Prediction of hydrological drought events, their characteristics and changes allows for adequate adaptation to its impact [2]. Due to Lithuanian geographical conditions, two different low flow patterns are found: summer-autumn (warm season) and winter (cold season) low flow [3]. In this research only summer-autumn low flow type was analysed.

High frequency low flow events are the most prevalent in small and low elevation river catchments, but for bigger rivers it doesn't have such effect [4]. Normally low flow is derived from groundwater feeding or surface feeding from the lakes [1]. For this reason, it is important to take account of river feeding source in a catchment scale. Therefore evaluation of distribution of low flow parameters must include local physical geographical conditions. In analysis of changing low flow events, there is more important to estimate absolute values than changes of the mean. Due to climate change low flows have tendency to become more frequent but in generally they are becoming weaker [5]. Some tendencies of Czech Republic Rivers show the decrease of summer low flows, but the increase of winter low flows and duration of these events [6]. Lithuanian rivers runoff projections show other character when in the summer and autumn season it will have both increasing and decreasing tendencies [7]. According to historical data, several studies of Lithuanian rivers did not indicate clear tendencies of low flow distribution, because these results did not indicate any statistically significant trends, except Western part of Lithuania, where some rivers had positive trends [8, 9]. Detailed analysis of hydrological drought of Nemunas River catchment and its relation with meteorological droughts has been done too [10].

The main goal of this research is creation of the projections of warm season low flow in 21st century for three Lithuanian rivers (Neris, Merkys and Nemunas up to Druskininkai water gauging station (WGS)). To achieve this objective, regional climate model (RCM) RCA3, created by Swedish Meteorological and Hydrological Institute (SMHI), was used [11]. RCM is based on two driving general circulation models (GCM): ECHAM5-r3 and HadCM3Q3. Both GCM have been used for low flow projections under climate change [12]. According to some authors, A1B climate change scenario, which was used in this research, is suitable for low flow estimation, because other scenarios give higher precipitation amount combined with relatively small increase of temperature [13]. All potential results might be used for risk assessment for all kinds of human life aspects; therefore this study is based on low flow projection of three Lithuanian rivers under climate change conditions.

2. METHODOLOGY

2.1. Study area

Study area consists of three rivers catchments, which are located in south-eastern part of Lithuania (Fig. 1). The Neris River catchment is presented by Jonava water gauging station (WGS) and includes 24600 km^2 area (98.5% of whole catchment). Puvočiai WGS represents almost all the Merkys River catchment – 4300 km^2 of 4415.7 km^2. For evaluation of the Nemunas River runoff, there has been chosen catchment part up to Druskininkai WGS – 37100 km^2 (39% of whole catchment) All these catchments together characterise particular hydrological conditions of this region, because most of the rivers in generally have ground water feeding. Such hydrological situation is very important for study of low flow. During the warm season the area of south-eastern rivers do not have enough surface feeding from the rainfall, therefore these catchments will show common distribution characters of low flow in the whole region, which is marked by blue dashes in Fig. 1.

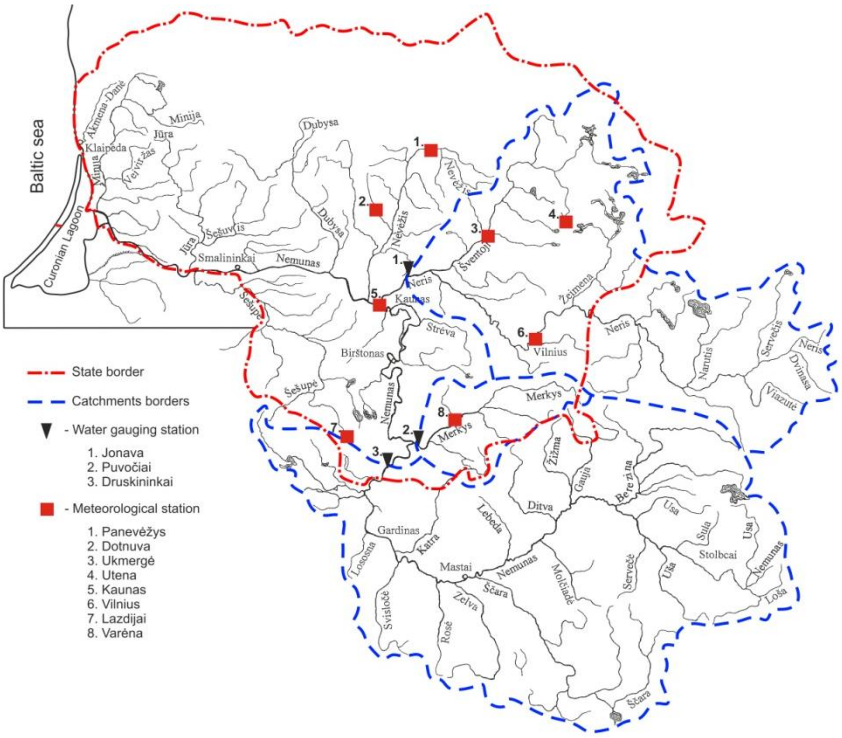

Fig. 1. Location of Neris (to Jonava WGS), Merkys (to Puvočiai WGS) and Nemunas (to Druskininkai WGS) rivers catchments

2.2. Meteorological data

Primary research data (in this case daily precipitation and temperature) for future projections has been taken from Ensembles project open access database (http://ensemblesrt3.dmi.dk). SMHI RCA3 is covering all Europe and has resolution with 25 km grid cell. All RCM area is consisting of 170 grid cells in horizontal axis and 190 grid cells in vertical axis. Lithuania enters from 108 to 123 cells in horizontal axis and from 111 to 122 cells in vertical axis. Meteorological data for hydrologic modelling has been taken from eight grid cells, which represent real points of meteorological stations (MS) (Fig. 2). Historical data of hydrological and meteorological parameters has been taken from Lithuanian Hydrometeorological Service.

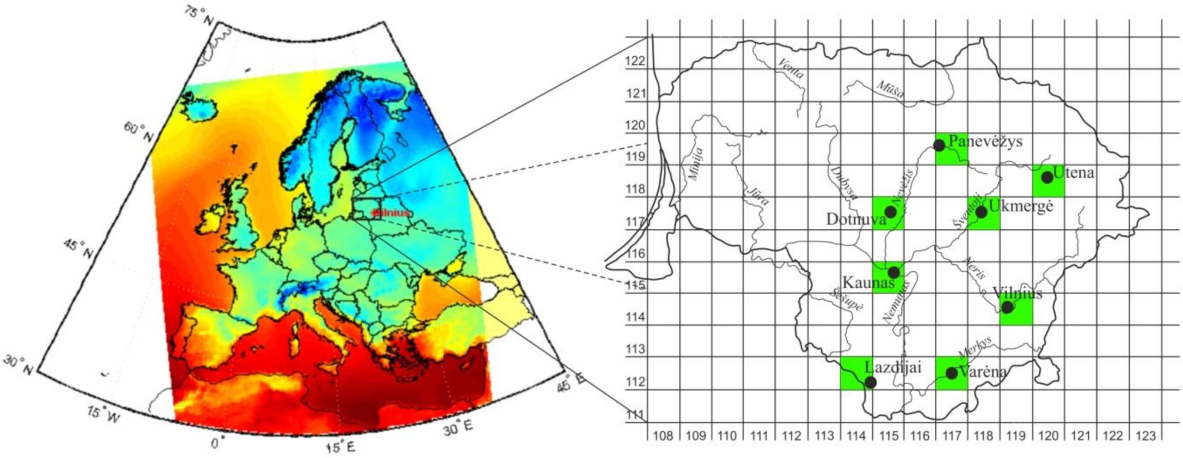

Fig. 2. Projection of RCA3 grid cells over Lithuania and location of MS

2.3. Statistical downscaling

Projection data of precipitation and temperature of the 21st century were prepared with Bias Correction Change in mean (BCC) and Quantile Mapping (QM) methods, which are used to delete errors of RCM output. These methods are used to downscale data from separate grid cell to concrete meteorological stations, which enters into boundaries of that cell. First of them BCC is based on such transformation

$$\mathrm{P}^{\mathrm{Fut}}_{y,j} = a_j(\mathrm{P}^{\mathrm{RCM\,Fut}}_{y,j}), \tag{1}$$

$$\mathrm{a}_{\mathrm{j}} = \frac{P^{Obs}_j}{P^{RCMCon}_j}, \tag{2}$$

where y is a year, j is the day of the year and a_j is estimated as a change factor parameter. This parameter is calculated in two steps. 61 days moving average, which is centred on day j, is set for $\mathrm{P}_j^{\mathrm{Obs}}$ and $\mathrm{P}_j^{\mathrm{RCM\ Con}}$ and then a_j is estimated as the mean of $\mathrm{P}_j^{\mathrm{Obs}}$ divided by the mean of $\mathrm{P}_j^{\mathrm{RCM\ Con}}$. QM method [14] is based on the concept of transformation h, such that

$$\mathrm{P}^{\mathrm{Obs}} = h(\mathrm{P}^{\mathrm{RCMCon}}) = ECDF^{\mathrm{Obs}-1}(ECDF^{\mathrm{RCMCon}}(\mathrm{P}^{\mathrm{RCMFut}})), \tag{3}$$

where P^{Obs} is observed meteorological parameter, $P^{RCM\ Con}$ is RCM output for control period, $P^{RCM\ Fut}$ is meteorological parameter, which is modeled by RCM for the future period. $ECDF^{Obs\text{-}1}$ is empyrical cumulative ditribution function for observed period and $ECDF^{RCM\ Con}$ is empyrical cumulative ditribution function for RCM control period. First, all the probabilities in $\mathrm{ECDF}^{\mathrm{Obs}}$ and $\mathrm{ECDF}^{\mathrm{RCMCon}}$ are calculated at a fixed interval of 0.01. Then, h in each interval is estimated as the relative difference between the two different ECDFs. Interpolation between the fixed values is based on a monotonic tricubic spline interpolation. For correction of the number of wet days were estimated from the empirical probability of non-zero values in P^{Obs}. After that all RCM values below this threshold were set to zero [15]. The method was implemented by *Python* sofware. After statistical downscaling, daily precipitation and temperature data were used for HBV hydrological modelling of three Lithuanian rivers. HBV model construction, calibration, validation and uncertainties have been analysed by other authors [16].

2.4. Climate change scenarios and low flow calculation

For the future low flow projections, one RCM RCA3, which is based on two driving GCM according to A1B official climate change scenario, was used. But in this research scenarios were called as projections of three different combinations of GCM's and statistical downscaling methods. These scenarios consist of ECHAM5 QM, ECHAM5 BCC and HadCM3 QM combinations. ECHAM5 and HadCM3 mean GCM. And the following compound (QM and BCC) describes the statistical downscaling method of precipitation corrections. All temperature data was prepared by QM method (because this method does not cause extreme changes).

In this research the low flow period is characterized by minimum discharge value of 30 days moving average and from each year the lowest value was selected and used for further estimation. These calculations were accomplished by Microsoft Excel, after that, obtained results were described by 30-day minimum discharge or just Q_{30}. Precipitation data was calculated at the same day of the year when Q_{30} was obtained, but the sum of precipitation rate was calculated (instead of the average precipitation) and called as sum of 30-day precipitation rate or P_{30}. Calculated projections of Q_{30} and P_{30} were expressed as deviation from the means of mentioned characteristics in 1961–1990 period (background period).

3. RESULTS AND DISCUSSION

3.1. Low flow projections of Neris river catchment

The 21st century precipitation, temperature and low flow projections of the Neris River were created by ECHAM5 QM, ECHAM5 BCC and HadCM3 QM scenarios. According to ECHAM5 QM scenario precipitation rate ranges in high amplitude, but it didn't have any trend during the hydrological drought. This tendency remains till the end of this century. Meanwhile at the beginning of the 21st century, 30% rise of 30-days minimum discharge (Q_{30}) of the Neris River is expected. At the end of 2011–2100 low flow decrease is projected, but it still is going to be 15% higher compared with 1961–1990 (Fig. 3 a). In average, ECHAM BCC scenario projected 15% lower precipitation rate in relation to background period and its trend has a slight upward tendency. In the first half of 21st century, 30-day minimum discharge of the Neris River presents 15% rise compared with background, but in the long term run Q_{30} has downward trend, while reaching background rate (Fig. 3 b).

According to HadCM3 QM scenario the amplitude of precipitation rate should increase, but during the whole period it wouldn't have any trend (Fig. 3 c). Values of the Neris River Q_{30} have quite similar character which was projected by the ECHAM BCC scenario.

In the 21st century projection of minimum Q_{30} expect up to 20 % higher values than in the background period. Throughout the century negative trend of the Neris River Q_{30} was predicted. In the Neris River catchment two scenarios project precipitation rate without any trend, but according to all scenarios, 30-day minimum discharge is characterized by increased values at the beginning of 21st century and slightly decreased till the end of the period of 2011–2100. In the Neris River catchment all scenarios project Q_{30} and P_{30} values with high range amplitude. For the future studies it is important to take note of precipitation conditions before the low flow period.

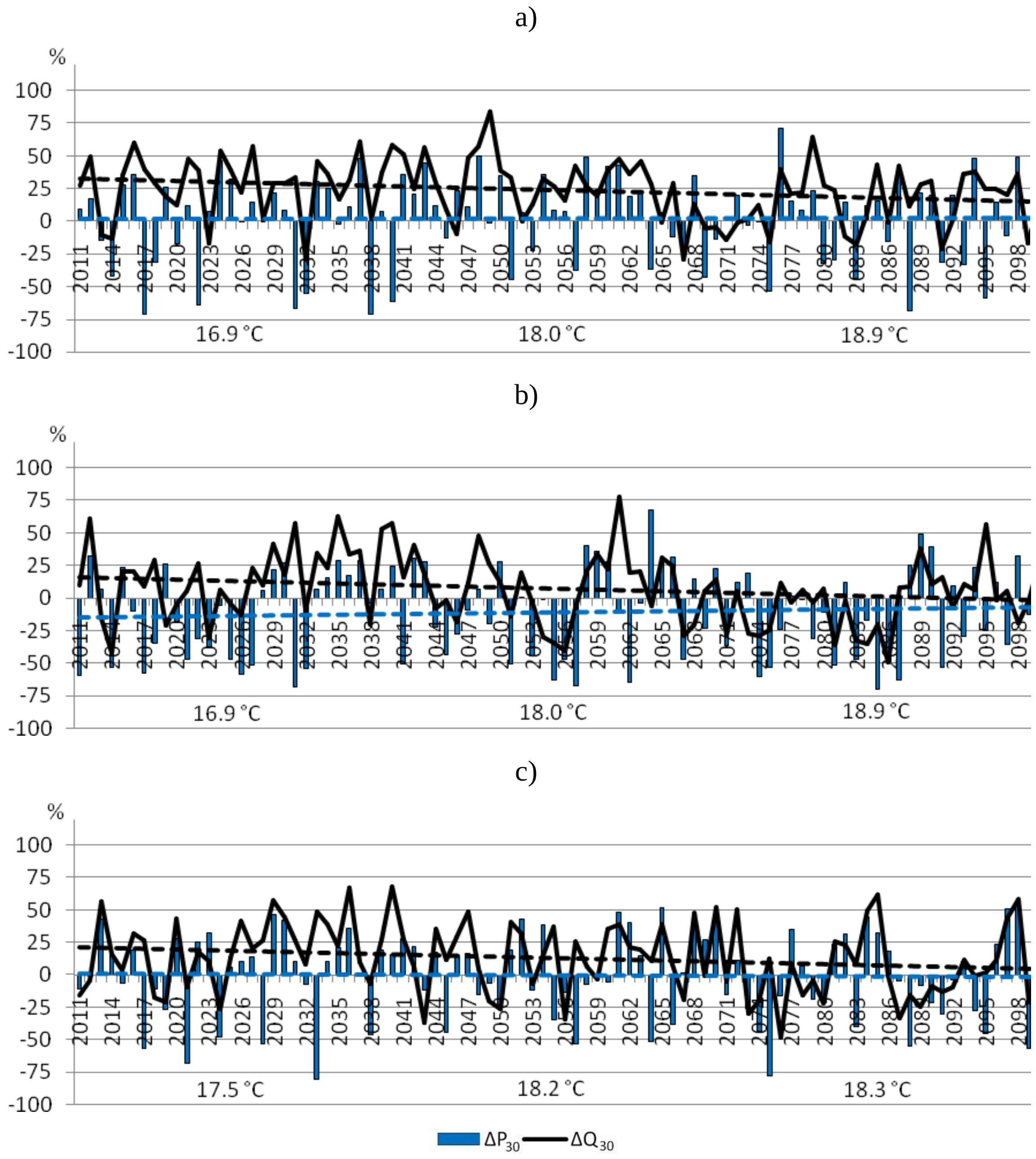

Fig. 3. Projections of the Q_{30} and P_{30} deviations from the background period in the Neris River and projected air temperature (at the beginning, middle and the end of 21st century) according to ECHAM5 QM (a), ECHAM5 BCC (b) and HadCM3 QM (c) scenarios

3.2. Low flow projections of Merkys river catchment

Projections of the Merkys River low flow in the 21st were created by three different scenarios (ECHAM5 QM, ECHAM5 BCC and HadCM3 QM). According to these scenarios, deviation of 30-day minimum discharge and 30-day precipitation sum was calculated. After that all results were compared with the data of 1961–1990. At the beginning of 2011–2100 ECHAM5 QM scenario projects in average 40% higher precipitation rate than in the background period, however at the end of this century the decrease trend of precipitation (up to 10% higher than background) is supposed (Fig. 4 a). Such pattern of precipitation distribution has an impact on 30-day minimum discharge in the Merkys river catchment. Since at the beginning of analyzed century Q_{30} in average exceeded the background period by 20% higher values, but it has declining trend and at the end of 21st century

Q_{30} is gaining negative deviation values. Quite different situation was projected according to ECHAM BCC scenario (Fig. 4 b), when precipitation rate should be 20% greater than in the background period and this tendency will keep till the end of analyzed period. Q_{30} of the Merkys River should slightly decrease from the norm of background period by 20% at the end of 2011–2100. HadCM3 QM scenario projects the increase of precipitation from 15 to 35% in relation to background period during the whole century. Q_{30} of the Merkys River shouldn't strongly change and remain close to the norm of 1961–1990.

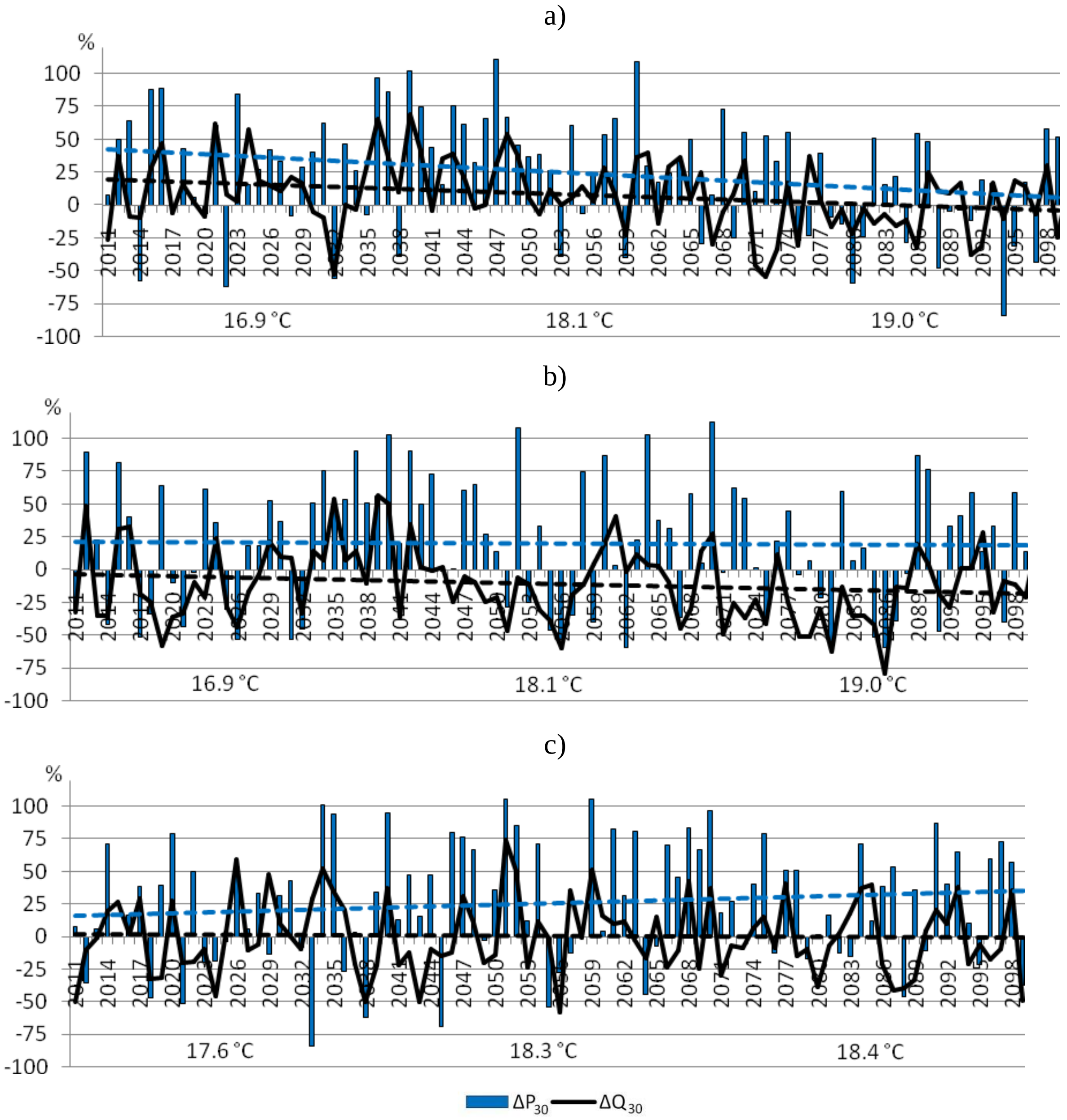

Fig. 4. Projections of the Q_{30} and P_{30} deviations from the background period in the Merkys River and projected air temperature (at the beginning, middle and the end of 21st century) according to ECHAM5 QM (a), ECHAM5 BCC (b) and HadCM3 QM (c) scenarios

All these changes are strongly related to average temperature of warm season. When at the end of 21st century average temperature of warm season will be higher than 19 °C, then evaporation will get rise, and water inflow into the river from surface runoff will decrease. It would have significant impact on low flow decline. Besides the changing meteorological conditions it is worth mentioning that projected low flow of the Merkys River becomes more extreme, because the amplitude between lowest and highest value sharply increases.

3.3. Low flow projections of the Nemunas (to Druskininkai WGS) River catchment

According to ECHAM5 QM, ECHAM5 BCC and HadCM3 QM scenarios 30-day minimum discharge of the Nemunas River and sum of 30-day precipitation rate over Nemunas River catchment were projected. All results were compared to the values of 1961–1990 period. After that deviation of Q_{30} and P_{30} was calculated. The obtained results showed differences between projections of various scenarios. At the beginning of the 21^{st} century ECHAM5 QM scenario showed 20% higher precipitation values than values of background period, but through all period this range should decrease to the rate of background period (Fig. 5 a). Greater changes were projected for minimum Q_{30}, when in the first half of the 21^{st} century it would be 40% higher than

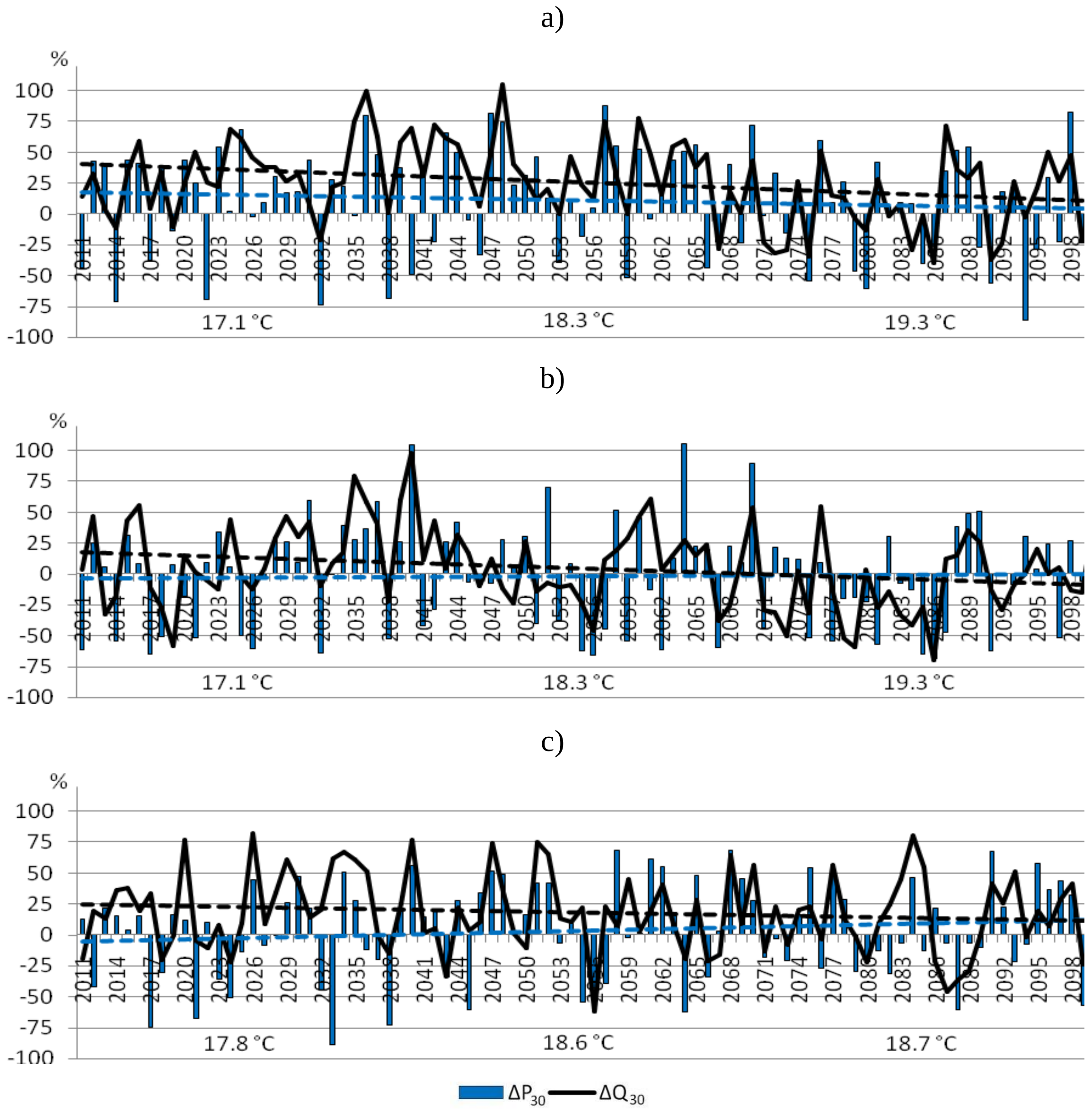

Fig. 5. Projections of the Q_{30} and P_{30} deviations from the background period in the Nemunas River (at the Druskininkai WGS) and projected air temperature (at the beginning, middle and the end of 21^{st} century) according to ECHAM5 QM (a), ECHAM5 BCC (b) and HadCM3 QM (c) scenarios

the rate of 1961–1990, however this tendency has negative trend and it would decline down to 10%, but will still remain higher than climate norm. According to projection of ECHAM5 BCC scenario, precipitation trend remains the same as in the background period and it persists unchanged through the century (Fig. 5 b). Q_{30} of the Nemunas River would have negative trend from 20% higher values at the beginning and -5% lower values at the end of the 21st century. Obtained negative trend showed deeper low flow projection than in the background period.

In the 21st century HadCM3 QM scenario projects that during the low flow period precipitation rate may slightly increase (at the end of the century it can reach up to 15% of the background period) (Fig. 5 c). Meanwhile, the minimum Q_{30} acquires negative trend during the whole 21st century. All climate scenarios project the increased amplitude of minimum Q_{30} and sum of 30-day precipitation rate (Fig. 5). The obtained results show an increase in amplitude of parameters of low flow formation and grow of extremes under climate change conditions.

4. CONCLUSIONS

During this study, the changes of projections of precipitation and 30-day minimum discharge were identified in the Neris, Merkys and Nemunas (up to Druskininkai WGS) rivers. In the Neris River almost all scenarios project that precipitation rates wouldn’t have any trends, but they should have great amplitude of variation. Q_{30} would rise at the beginning of the 21st century and slightly decrease to the norm of the background period (1961–1990) in the end of 21st century therefore Q_{30} would have high amplitude of variation as well as precipitation. Quite similar distributions of these parameters were obtained in the Nemunas River catchment. Identified similarities could be characterised by no trend variation of precipitation rate and higher values of low flow at the beginning of the 21st century and downward trend till the end of 2011–2100. According to all scenarios Q_{30} of the Nemunas River is higher than in the background period. From all catchments, the Merkys River catchment is the most distinctive one, because it has the opposite situation. In this catchment during the low flow period, higher precipitation values were projected. Depending on scenarios these tendencies may have positive or negative trends. Therefore values of Q_{30} in the Merkys River could vary within boundaries of the background period or that tendencies would have significant negative trends. In summary it is important to mention that all projections closely depend on the chosen GCM and statistical downscaling method, but one thing is certain that any combination of scenarios project the rise in the amplitude of analysed variables.

5. ACKNOWLEDGMENT

This study is supported by National Research Programme “Sustainability of agro-, forest and water ecosystems” according to the Project “Impact Assessment of Climate Change and Other Abiotic Environmental Factors on Aquatic Ecosystems” (SIT-11).

6. REFERENCES

1. SMAKHTIN, V.U. Low flow hydrology: a review. *Journal of Hydrology*, 2001, Vol. 240, p. 147–186.
2. HUIJGEVOORT, M.H.J., LANEN, H.A.J., TEULING, A.J., UIJLENHOET, R. Identification of changes in hydrological drought characteristics from a multi-GCM driven ensemble constrained by observed discharge. *Journal of Hydrology*, 2014, Vol. 512, p. 421–434.
3. GAILIUŠIS, Brunonas; JABLONSKIS, Jonas; KOVALENKOVIENĖ, Milda. *Lithuanian rivers. Hydrography and runoff.* Kaunas: Lithuanian Energy Institute, 2001. 792 p. ISBN 9986-492-64-5 [In Lithuanian].

4. STEWART, I. T., FICKLIN, D. L., CARRILLO, C. A., MCINTOSH, R. 21st century increases in the likelihood of extreme hydrologic conditions for the mountainous basins of the Southwestern United States. *Journal of Hydrology*, 2015, Vol. 529, p. 340–353.
5. BOÉ, J., TERRAY, L., MARTIN, E., HABETS, F. Projected changes in components of the hydrological cycle in French river basins during the 21st century. *Water resources research*, 2009, Vol. 45, W08426.
6. FIALA, T., OUARDA, T. B. M. J., HLADNÝ, J. Evolution of low flows in the Czech Republic. *Journal of Hydrology*, 2010, Vol. 393, p. 206–218.
7. KRIAUČIŪNIENĖ J., MEILUTYTĖ-BARAUSKIENĖ D., RIMKUS E., KAŽYS J., VINCEVIČIUS A. Climate change impact on hydrological processes in Lithuanian Nemunas river basin. *Baltica*, 2008, Vol. 21, No. 1–2, p. 51–61.
8. KRIAUČIŪNIENĖ, J., KOVALENKOVIENĖ, M., MEILUTYTĖ-BARAUSKIENĖ, D. Changes of the Low Flow in Lithuanian Rivers. *Aplinkos tyrimai, inžinerija ir vadyba*, 2007, Vol. 42, No. 4, p. 5–12.
9. REIHAN, A., KOLTSOVA, T., KRIAUCIUNIENE, J., LIZUMA, L., MEILUTYTE-BARAUSKIENE, D. Changes in water discharges of the Baltic states rivers in the 20th century and its relation to climate change. *Hydrology Research*, 2007, Vol. 38, No. 4–5, p. 401–412.
10. RIMKUS E., STONEVIČIUS E., KORNEEV V., KAŽYS J., VALIUŠKEVIČIUS G., PAKHOMAU A. Dynamics of meteorological and hydrological droughts in the Neman river basin. *Environmental Research Letters*, 2013, Vol. 8, No. 4, 045014 (10 p.).
11. KJELLSTRÖM, E., BÄRRING, L., GOLLVIK, S., HANSSON, U., JONES, C., SAMUELSSON, P., RUMMUKAINEN, M., ULLERSTIG, A., WILLÉN U., WYSER, K., 2005. A 140-year simulation of European climate with the new version of the Rossby Centre regional atmospheric climate model (RCA3). Reports Meteorology and Climatology, 108, SMHI, SE-60176 Norrköping, Sweden, 54 p.
12. PARAJKA, J., BLASCHKE, A. P., BLÖSCHL, G., HASLINGER, K., HEPP, G., LAAHA, G., SCHÖNER, W., TRAUTVETTER, H., VIGLIONE, A., ZESSNER, M. Uncertainty contributions to low flow projections in Austria. *Hydrology and Earth System Sciences*, 2015, Vol. 12, p. 12395–12431.
13. HUANG, S., KRYSANOVA, V., HATTERMANN, F. F. Projection of Low Flow Conditions in Germany under Climate Change by Combining Three RCMs and a Regional Hydrological Model. *Acta Geophysica*, 2013, Vol. 61, No. 1, p. 151–193.
14. GUDMUNDSSON, L., BREMNES, J. B., HAUGEN, J. E., ENGEN-SKAUGEN, T. Technical Note: Downscaling RCM precipitation to the station scale using statistical transformations – a comparison of methods. *Hydrology and Earth System Sciences*, 2012, Vol. 16, p. 3383–3390.
15. SUNYER, M. A., HUNDECHA, Y., LAWRENCE, D., MADSEN, H., WILLEMS, P., MARTINKOVA, M., VORMOOR, K., BÜRGER, G., KRIAUČIŪNIENĖ, J., LOUKAS, A., OSUCH, M., YÜCEL I. Inter-comparison of statistical downscaling methods for projection of extreme precipitation in Europe. *Hydrology and Earth System Sciences*, 2015, Vol. 19, p. 1827–1847.
16. KRIAUCIUNIENE J., JAKIMAVICIUS, D., SARAUSKIENE, D., KALIATKA, T. Estimation of uncertainty sources in the projections of Lithuanian river runoff. *Stochastic Environmental Research and Risk Assessment*, 2013, Vol. 27, p. 769–784.

CYSENI 2016, May 26-27, Kaunas, Lithuania
ISSN 1822-7554, www.cyseni.com

DIVERSITY AND IMPORTANCE OF ECOSYSTEM SERVICES ON WETLANDS: EXAMPLE OF BIEBRZA NATIONAL PARK AND WARTA MOUTH NATIONAL PARK, POLAND

L. Tylec
Warsaw University of Life Sciences
Nowoursynowska Str. 166, 02-787 Warsaw – Poland
Email: l.tylec@levis.sggw.pl

ABSTRACT

Biebrza National Park (BbPN) and Warta Mouth National Park (PNUW) are polish National Parks covered by wetlands. These wetlands are important in country and European scale (Ramsar Convention). Each area is concerned by restoration project which aims to improve hydrological conditions and to keep rich habitats. BbPN is located in east part and PNUW in west part of Poland. This two study areas were taken to analysis based on different land use and condition of existing wetlands. For both areas ecosystem services were identified. For further analysis the most important ES were chosen as: touristic, water storage, water quality, hay production. This ES are a part of three main groups of services: provisioning, regulating and cultural. To assess the importance of particular ES proper algorithms were created to add ES monetary values. In the final stage of the research all values were compared. The conception of ES has an big value in environment management and restoration project preparation by economical characterization of ecosystems.

Keywords: wetlands, ecosystem services, Biebrza, Warta

1. INTRODUCTION

Wetlands are very important ecosystems not only in European scale byt also on Worlds scale. Nowadays wetlands are degraded by drainage and agriculture [9] by what looses in quality and quantity. Ecosystem services, directly related to human well-being, are a way of perceiving a quality of the environment that is gaining popularity in recent days, also because it attempts to bridge the gap between social and natural sciences approaches. To use the services provided by the wetlands we need to prevent deterioration and improve the quality of wetland ecosystems. In a number of European countries actions to restore wetlands have been taken. International and national programs of restoration, and programs to verify the effects of restoration were created. The evaluation of wetland ecosystem service is a evaluation to convert the abstract service into monatary values more visible fo human. It is important to evaluate the value of wetlands in monetary value. It will help to make a proper restoration programme creating different scenarios of ecosystem services.

2. METHODOLOGY

2.1. Sites description

2.1.1. Biebrza National Park

Biebrza National Park (BbPN) is the largest park in north-east Poland created in 1993. Area of BbPN is the area of alkaline fens that are protected in European scale [1]. The area of the Park is 592.32 km^2. The area consist of forest (155 km^2), arable land (182 km^2) and water bodies (9 km^2). In the area of Biebrza National Park meets the aquatic communities, marsh, bog, rushes, and forest communities. Habitats were supplied groundwater and spring flooding.

2.1.2. Warta Mouth National Park

Warta Mouth National Park (PNUW) was created in 2001 near Warta mouth into Oder. The area of the park is 80.38 km^2. The area consists of forests (total area 82 ha), arable lands (total area 2662 ha) and water bodies (total area 297 ha). The PNUW is one of the most important breeding and feeding area for water and prey birds in Poland, Europe and World scale [3, 4]. So far found in the area around 60 plant communities and about 500 species of vascular plants. The largest areas in the Park occupied rushes with domination of: Phalaris arundinacea , Glyceria maxima. The PNUW is a Nature 2000 site (code PLC080001) and wetland protected on Earth inscribed on a Ramsar Convention list. More than 250 species of birds were recognized during research, wherein more than quarter of a million individuals may stay on this area. The top layer of the Park surface is mainly peat and gyttjas, which layer is obtained, in places, up to 6 m in thickness, and alluvial soils. Melioration works and interference of human on this area started over 2000 years ago. Network of drainage underwent continuous change until the age of 60, in which a project of currently functioning system was created [2].

2.2. Data

To assess the ecosystem services for both areas ArcGIS maps were used. Maps were created for vegetation, land use, soils and water bodies (Fig. 1, Fig. 2). Based on this this maps also the area [ha] of different study sites characteristic was calculated.

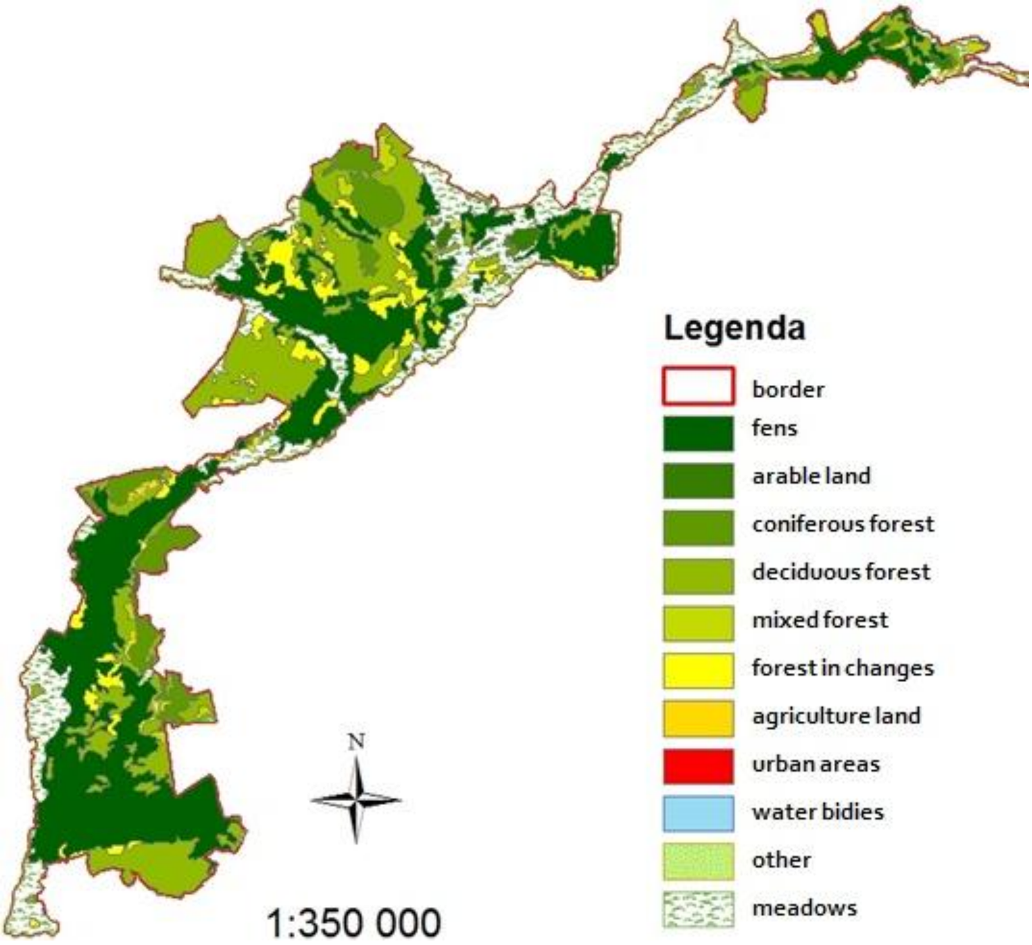

Fig. 1. Land use of Biebrza National Park, CORINE Land Cover 2006

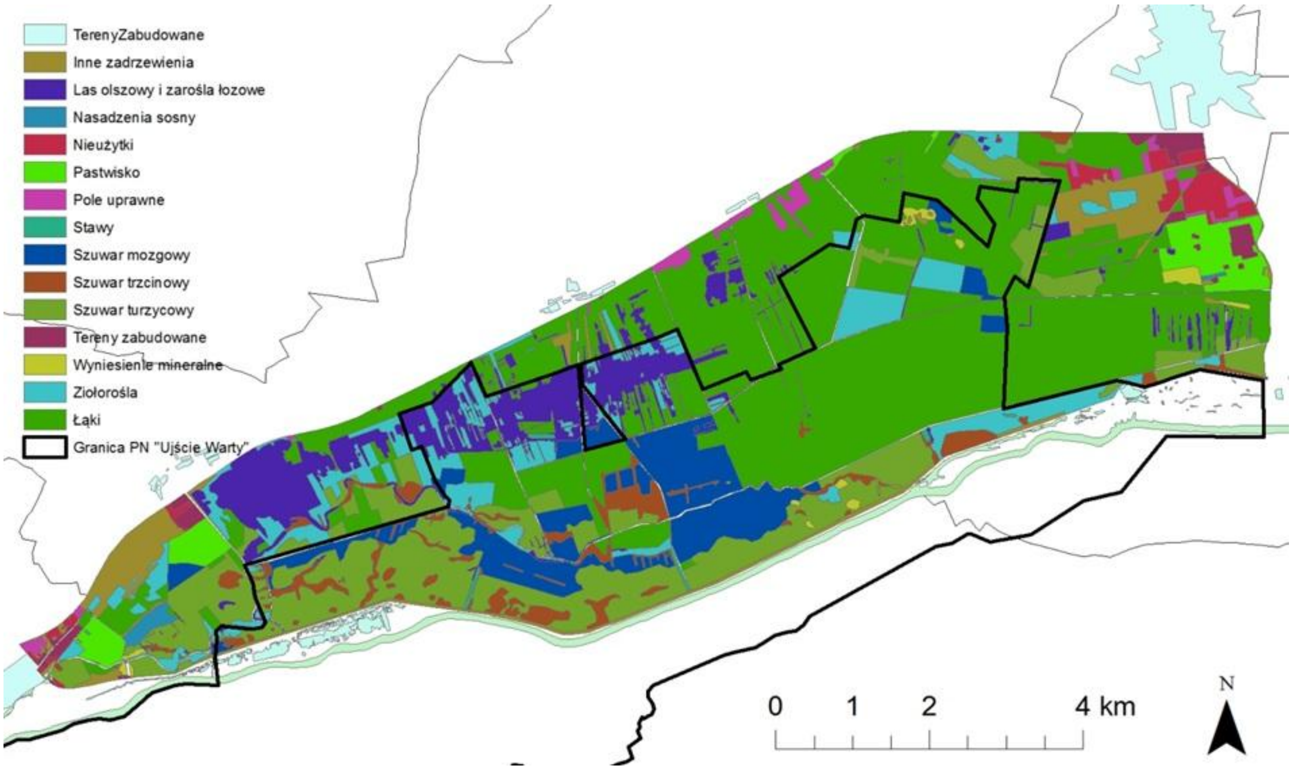

Fig. 2. Vegetation map of Warta Mouth National Park

For the economic analysis data from the Central Statistical Office (GUS) were used. Later on using data from Central Statistical Office and algorithms values were calculated for each ecosystem service in biophysical units (e.g. €/ha/year). Algorithms were created by research team. Assigning a monetary value allowed for comparison of the quality and quantity of services

2.3. Ecosystem services

In this research a Common International Classification of Ecosystem Services (CICES) was used. This is the one of three main ES classifications [8]. This classification is divided for three main groups of ES: provisioning, regulation and meintenance, cultural. Further on all three sections are divided on: division, group, class, class type. The recognized types of land use were assigned to the appropriate services ecosystems. In this research only the most important ES were assessd. The services used for calculations are in Table 1. Wood and hay production were chosen because of land use and agricultural character of these areas. Nutrient sotrage and removal, water purification, floodplain storage and carbon storage and removal because of peat which is covering almost whole area. Because this are Nature 2000 areas habitat for birds is very important service.

Table 1. Calculation algorithms

Service category	Division	Group	Ecosystem service	Calculation algorithm	Final unit
Provisioning	Materials	Biomass	Wood for timber	P x € / Ag	M€/yr
			Hay production	(No$_{mow}$ x A x € x Y) - A x €$_{labor}$	M€/yr
Regulation and maintenance	Maintenance of physical, chemical, biological conditions	Soil formation and composition	Nutrient storage in soils and forests		M€/yr
			Nutrient removal by wetlands	(Rr$_N$ x €$_{remov}$ + Rr$_P$ x €$_{remov}$) x A	M€/yr
			CO2 emission from degraded peatlands (negative)	A x € x CO2$_E$ / 1000000	M€/yr
		Water conditions	Water purification	(N$_{load}$ x €$_{remov}$) + (P$_{load}$ x €$_{remov}$) x A	M€/yr
			Floodplain water storage	V x t x € x 1000000	M€/yr
		Atmospheric composition and climate regulation	Carbon storage in soil	A x € x CO2$_R$ / 1000000	M€/yr
			Carbon storage in wood	P x A x W x €$_{remov}$ x CO2$_{RB}$ / 30	M€/yr
Cultural	Physical and intellectual interactions with biota, ecosystems, and land-/seascapes [environmental settings]	Physical and experiential interactions	Fishing	No$_{fish}$ x €	M€/yr
			Habitat conditions for birds		M€/yr

2.4. Calculations

Based on the gained data, field investigation, the main service functions were evaluated by the following methods. All used calculations are in Table 1. Value of wood for timber was evaluated by productivity of wood (depending on species and use) and age of trees (5 different classesss) [5]. The hay production as provisioning service was calculated based on number of moving, which depends on type of meadow [6] and vegetation, covered area and annual yeld of hay. Nutriens storage and nutrienty removal was calculated for soils and wood. It depends on type of soil and level of degradation and condition of forests and their age. Carbon dioxide emission is a negative service for degraded peatlands. It was assessd by use the area of degraded peatlands and amount of CO_2 emission. Water purification included two main substances: phosphorus and nitrogen [7] and its amount on both upstream and downstream points on Biebrza river. As a monetary value the price for removal was used. Floodplain water storage is the result of simulation of floods on this area and cost of demage removal. Carbon storage in soil and wood was calculated using area, prive for CO_2 removal, and in case of wood – age. In case of cultural services only fishing was easy to assess because of collected data: number of licenses per year. Habitat conditions for birds are very important service, but almost impossible to calculate. Table 2 is showing the meaning of the signs in algorithms.

Table 2. Algorithms explanations

Parameter	Units	Mark
Water storage volume	mln m^3	V
Time factor	[-]	t
Price	[€/ha]; [€/m^3]; [€/t/ha]	€
Number of mowing	[-]	No$_{mow}$
Area	[ha]	A

Yield	[t/ha]	Y
Payment for bird habitats	[€/ha/yr]	$P_€$
Payment for fens	[€/ha/yr]	$P_€$
Payment for molinion meadows	[€/ha/yr]	$P_€$
Productivity	[m^3/ha]	P
Number of fishing licenses	[-]	No_{fish}
Lump sum	[€]	Ls
Cost of removal	[€/kg]	$R_€$
Removal rate P	[mg/l]; [kg/ha/yr]	R_P
Removal rate N	[mg/l]; [kg/ha/yr]	R_N
CO2 retention in the soil	[g/ha]	$CO2_R$
CO2 evasion from the soil	[g/ha]	$CO2_E$
CO2 retention in the biomass	[kgCO2/Kg of dry wood]	$CO2_{RB}$
Mass of wood in the unit volume	[kg/m^3]	m_{wood}
Age	[yr]	Ag
Labor costs	[€/ha]	$L_€$
N load	[kg/ha/yr]	N_{load}
P load	[kg/ha/yr]	P_{load}
Wood mass	[kg/m^3]	m_w

3. RESULTS

In the Table 3 we can see the results of calculations. The values are given in M EUR per year. This results show only general comparison of values

Table 3. Values of ecosystem services

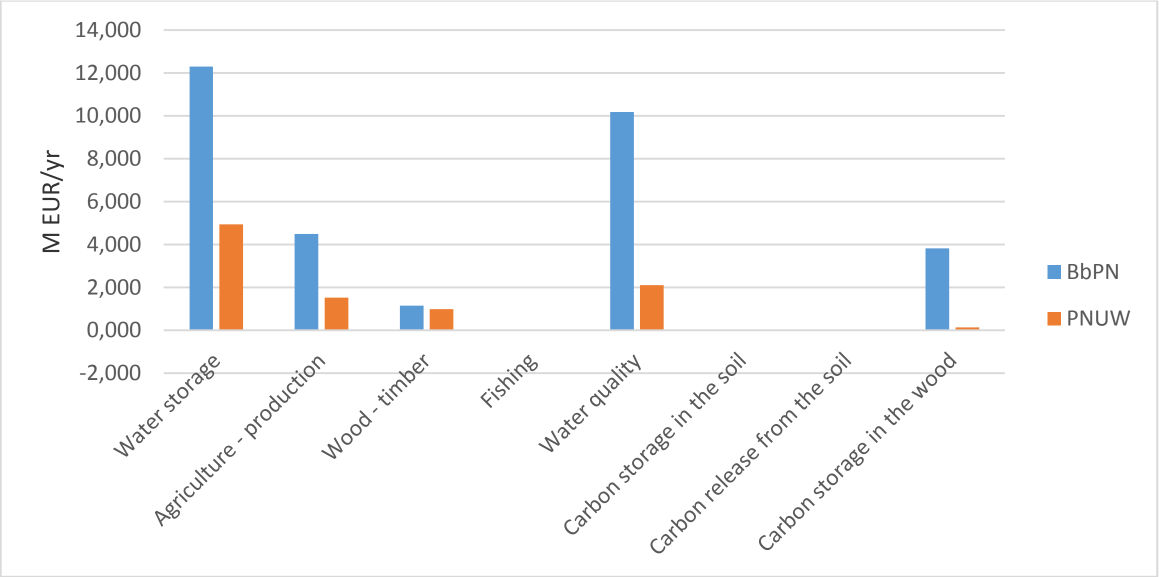

Results show us also the condition of study area. As we can see the most important ES in both areas is water storage. It is a result of peat soil which is covering almost whole area. Unfortunately peatlands on the PNUW area are more degraded than on BbPN. The amount of water storage is more than two times higher on BbPN. Than in case of Biebrza also very important ES is water quality. Peats have an ability to clear water from nutrients. Carbon storage in wood is higher on the BbPN area because of the forest condiotion and productivity. What is also important, the carbon release has a negative value. It is because the bad condition of wetlands. Degraded peat will release carbon into the atmosphere and we will pay for exceeding standards.

To sum up, Biebrza National Park is in a better condition than Warta Mouth National Park.

4. CONCLUSION

Wetlands in Europe were degraded what we can see by the calculations. By the results we can see dependence the values of ecosystem services from quality of the ecosystems. As higher the quality is the higher is value. Howewer not all services were considered in the valuation. For better perceiving of differences and results further models should incude as much services as possible. Also the algorithms should be more detailed. Values shows us that Biebrza national park has less degraded peat soils.

5. REFERENCES

1. GRYGORUK M., , BAŃKOWSKA A., JABŁOŃSKA E., JANAUER G., KUBRAK J., MIROSŁAW-ŚWIĄTEK D., KOTOWSKI W., *Assessing habitat exposure to eutrophication in restored wetlands: Model-supported ex-ante approach to rewetting drained mires*, Journal of Environmental Management, Vol. 152, 1 April 2015, p. 230–240.
2. OKRUSZKO T., 2009: *The concept of revitalization wet-meadow habitats in the Warta Mouth National Park - North Polder* [in polish], report, Warsaw.
3. SIDŁO P.O., BŁASZKOWSKA B. & CHYLARECKI P. (red.): *Important Bird Areas of European importance in Poland* [in polish], OTOP, Warsaw, 2004.
4. SIDŁO P. (red.): *Evaluation of birds' population in the areas covered by the Ramsar Convention. Report prepared for the Ministry of the Environment* [in polish], OTOP, Warsaw, 2005.
5. NASILR., WUNDER S. CAMPOS J., *A. FOREST ECOSYSTEM SERVICES: CAN THEY PAY OUR WAY OUT OF DEFORESTATION* discussion paper prepared for the GEF by for the Forestry Roundtable to be held in conjunction with the UNFF II, New York on March 11, 2002.
6. BJORKLUND J., LIMBURG K.E., TORBJORN E., *Impact of production intensity on the ability of the agricultural landscape to generate ecosystem services: an example from Sweden*, Ecological Economics 29 (1999) 269–291.
7. VYMAZAL J., *Removal of nutrients in various types of constructed wetlands*, Science of the Total Environment 380 (2007) 48–65.
8. DE GROOT R., WILLSON M., BOUMANS R., *A typology for the classification, description and valuation of ecosystem functions, goods and services*, Ecological Economics, Volume 41, Issue 3, June 2002, p. 393–408.
9. BULLOCK A., ACREMAN M.; *The role of wetlands in hydrological cycle*, Hydrology and Earth System Sciences, 2003, 7 (3), p. 358–389.

CYSENI 2016, May 26-27, Kaunas, Lithuania
ISSN 1822-7554, www.cyseni.com

NEUTRON ACTIVATION IN WATER COOLING SYSTEMS OF NUCLEAR FUSION DEVICES

A. Tidikas, G. Stankūnas
Lithuanian Energy Institute, Laboratory of Nuclear Installation Safety
Breslaujos str. 3, LT-44403 Kaunas – Lithuania
Email: andrius.tidikas@lei.lt

ABSTRACT

The examination of water cooling systems of fusion devices, which resemble to DEMO and ITER projects, due to the neutron irradiation is being carried out in this work. Main objects of interest are primary heat transfer systems for vacuum vessel, first wall/blankets and divertor as they are relatively close to the neutron source. Assessment of activity, contact dose rate and decay heat of water and functional materials such as SS316L(N)-IG and CuCrZr are estimated with respect to different localizations and structures. In addition, the possible influence of corrosion effects due to the neutron activation in water was investigated. The identification of dominant radionuclides was carried out. All calculations were performed with few assumptions: flow rate of coolant is steady and uniform; activated coolant does not mix in other cooling systems; coolant is being reused for full fusion device operation period. Irradiation was simulated with activation system program FISPACT. Obtained results showed good agreement with other works in the available literature.

Keywords: nuclear fusion, FISPACT, neutron activation, irradiation, water cooling systems

1. INTRODUCTION

Material activation induced by neutron irradiation is major concern for fusion power plants. Neutrons are required for tritium breeding and heat transfer in plant operation, however activation of materials is unwanted, but unavoidable process. Neutron activation effects could be mitigated by using certain design solutions or using low activation materials.

Coolant activation is important issue because it is not contained within vacuum vessel and flows through power plant facility heat transfer loop, leading to increased risk of personel and sensitive electronic component exposure to harmful radiation. Suffiecient shielding and leakage prevention should be taken into consideration when designening cooling sysyems. On top of that coolant might also transfer activated corrosion products.

2. METHODS AND MATERIALS

European Activation System: Easy-2007 is used as a main tool for the determination of dominant radionuclides in structural materials after irradiation. Its code FISPACT is being utilized for simulation of irradiation process[1]. Model of irradiation is simplified: infinite slab of material is being irradiated by neutron flux in pulses corresponding to operation of fusion device. FISPACT uses external libraries of reaction cross sections and decay data for all relevant nuclides to calculate nuclides produced as a result of the irradiation. Its output contains amount of radionuclide (number of atoms and grams), the activity (Bq), α-, β- and γ-energies (kW), γ dose-rate (Sv h^{-1}) as well as potential ingestion and inhalation doses (Sv) [1].

Input data: composition, density and mass can be expressed either as the percentage elemental composition or explicitly as the number of atoms of each nuclide.

Water Cooled Lithium Lead blanket (WCLL) is design based on water cooling, other prominent design is based on helium as coolant. It uses Eurofer reduced activation ferritic martensitic steel as structural material. Such blanket modules are formed by a directly cooled steel, utilizing C shape double-walled tubing in which the water coolant circulates. The water flows downstream in the tubes near the first wall and upstream near the back plate of the module. The first wall is cooled by pressurized water flowing in horizontal channels [2, 3, 5].

Water-cooled divertor is also under consideration, however in devices like DEMO such cooling systems might be not enough sufficient as divertor could be exposed to very high heat loads. Copper alloy CuCrZr has been suggested for heat sink material. Tungsten alloy was selected for armor material. Monoblock design so far showed best performance. In this design copper piping is being placed inside wolfram monoblock. Alternatively using martensic steel piping with pyrolitic graphite barrierier mounted in wolfram was also suggested [2, 3, 5].

SS316L(N)-IG steel which is main material for non critical cooling structural components for fusion devices will also be considered in this study [4, 6].

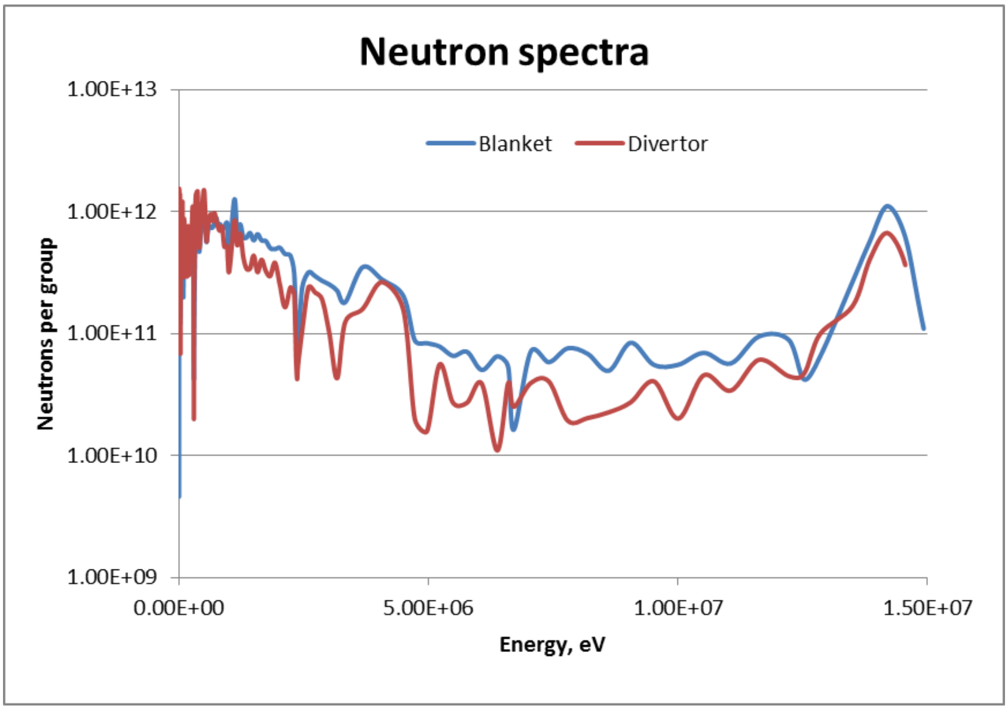

Fig. 1. Neutron spectra used for blanket and divertor irradiation

Neutron spectra are presented in (Fig. 1), they were used in calculation for divertor and blanket localizations (Fig. 2). Long time exposure and a series of neutron irradiation pulses were considered. First irradiation sequence is 1825 day long with 0,3 MW m^{-2} neutron load on the slab surface. Another sequence consists of 12 pulses: material is exposed to 1 MW m^{-2} load for 4 hours. Pulse sequences were performed one after another with one hour delay. Neutron flux for divertor irradiation was 2.60E+13 n/cm^2/s for long term exposure and 8.70E+13 n/cm^2/s for pulse mode. Respectively for blanket neutron flux values were at 4.88E+12 n/cm^2/s and 1.62804E+13 n/cm^2/s. Neutron activation related properties were analyzed for 100 years period after last irradiation sequence. Such period length was selected with regards to previous studies which dealt with recycling of materials of fusion devices [7].

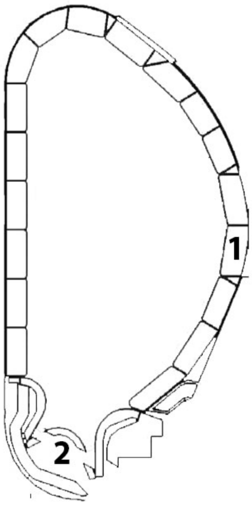

Fig. 2. Irradiation localizations, 1 – Blanket, 2 – Divertor

3. RESULTS AND DISCUSSION

Activity (Fig. 3) is one of the key characteristics in activation calculations, together with radionuclide composition (Figs. 4–6) it is possible derivation of all other characteristics such as decay heat and dose rate. From the graph in Fig. 3 it is evident that neutron flux is significantly higher in blanket module, however the magnitude of neutron flux moderation among examined materials is not same. Blanket/divertor activity ratio for Eurofer is ~2.8, for SS316L(N)-IG ~18.6 and for CuCrZr ~19.4. In CuCrZr alloy dominant radionuclides are Copper isotopes: Cu-64 and Cu-66, however their influence decreases significantly in 3 days period. Similarly in SS316L(N)-IG steel Mn-64 dominates for half a day after being undertaken by more Stable Cr-51 radionuclide. A bit different situation is shown Eurofer material. Dominance by Mn-56 radionuclide is not as significant and does not amount even half (42%) of activity (close to 75% in SS316L(N)-IG)). Such factor indicates that it is less dependent on neutron flux compared to other materials. This notion also confirms design considerations where Eurofer is considered in both divertor and blanket cooling structures, while copper alloy is only in divertor.

Table 1. Investigated materials and their chemical compositions

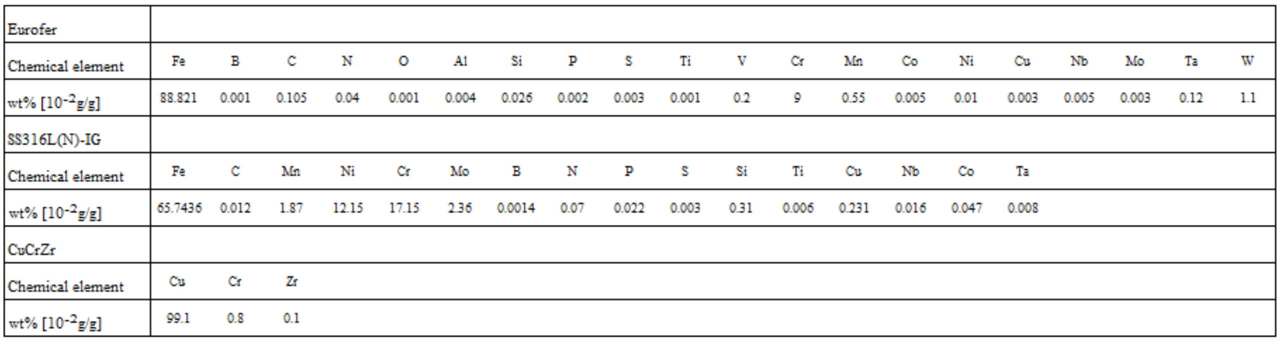

Eurofer																				
Chemical element	Fe	B	C	N	O	Al	Si	P	S	Ti	V	Cr	Mn	Co	Ni	Cu	Nb	Mo	Ta	W
wt% [10^{-2}g/g]	88.821	0.001	0.105	0.04	0.001	0.004	0.026	0.002	0.003	0.001	0.2	9	0.55	0.005	0.01	0.003	0.005	0.003	0.12	1.1
SS316L(N)-IG																				
Chemical element	Fe	C	Mn	Ni	Cr	Mo	B	N	P	S	Si	Ti	Cu	Nb	Co	Ta				
wt% [10^{-2}g/g]	65.7436	0.012	1.87	12.15	17.15	2.36	0.0014	0.07	0.022	0.003	0.31	0.006	0.231	0.016	0.047	0.008				
CuCrZr																				
Chemical element	Cu	Cr	Zr																	
wt% [10^{-2}g/g]	99.1	0.8	0.1																	

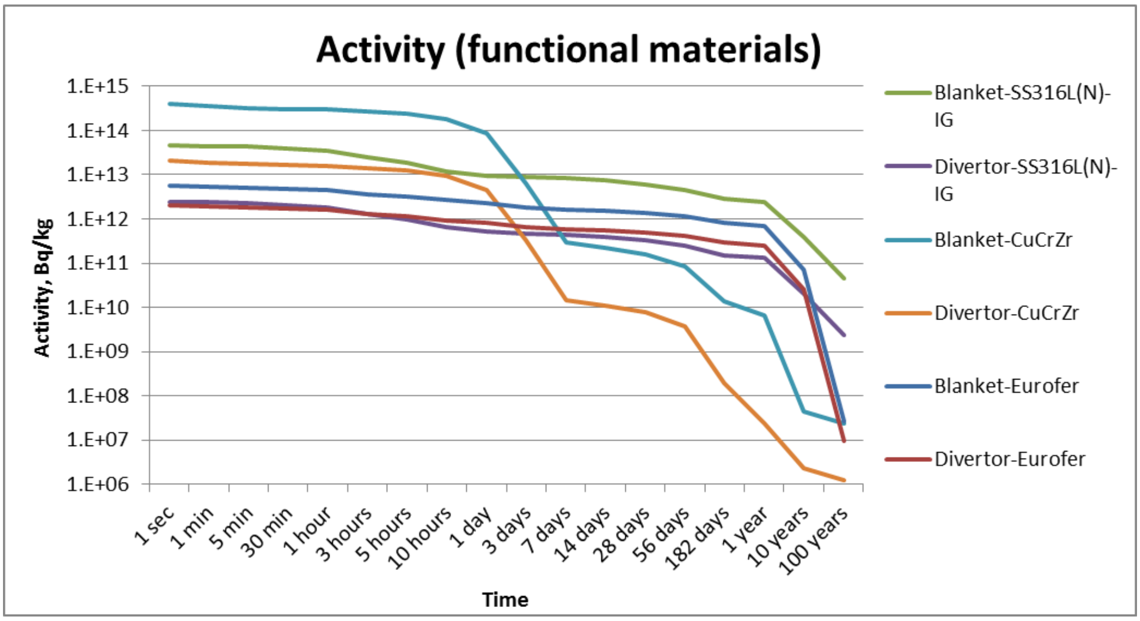

Fig. 3. Activity dependence on time after shut down

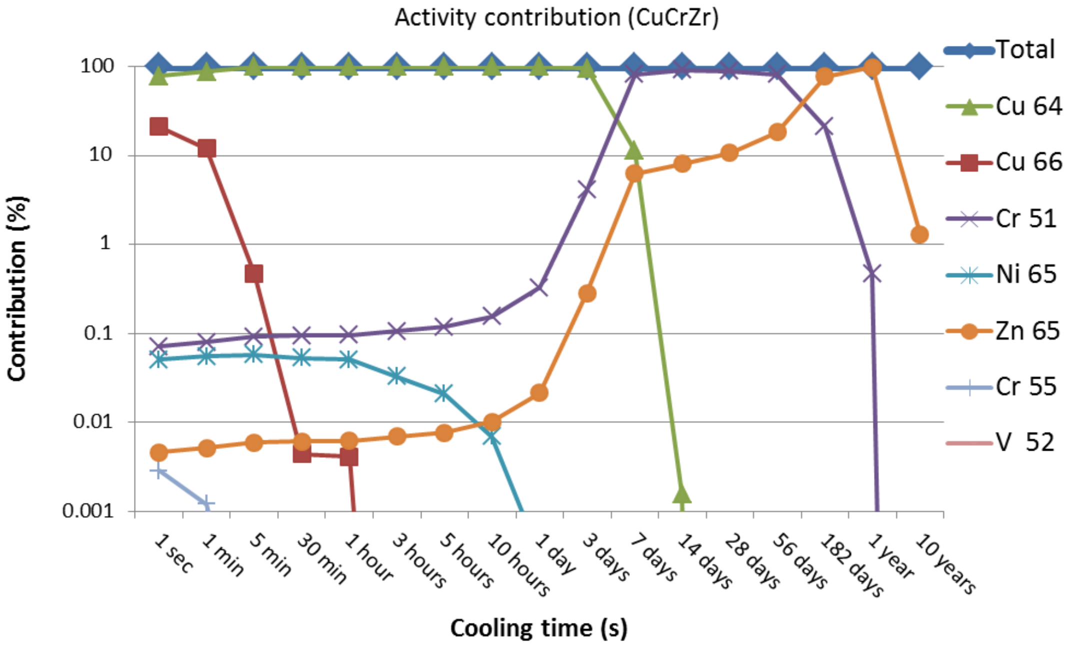

Fig. 4. Dominant radionuclides and activity contribution in blanket module localization (CuCrZr)

Highest activity in 1 week period after shutdown is exhibited by CuCrZr alloy approximately 8 times higher than SS316L(N)-IG and 60 times higher than Eurofer. Highest activity in later period up to 100 years is exhibited by SS316L(N)-IG which is approximately 5 times higher than Eurofer activity and few hundred times higher than CuCrZr activity. While copper alloy shows relatively good results it underperforms in other categories, lowest operation temperature and faster degradation of mechanical properties under high neutron flux. SS316L(N)-IG is still a primary material for piping in water cooling systems that are not exposed to high neutron flux.

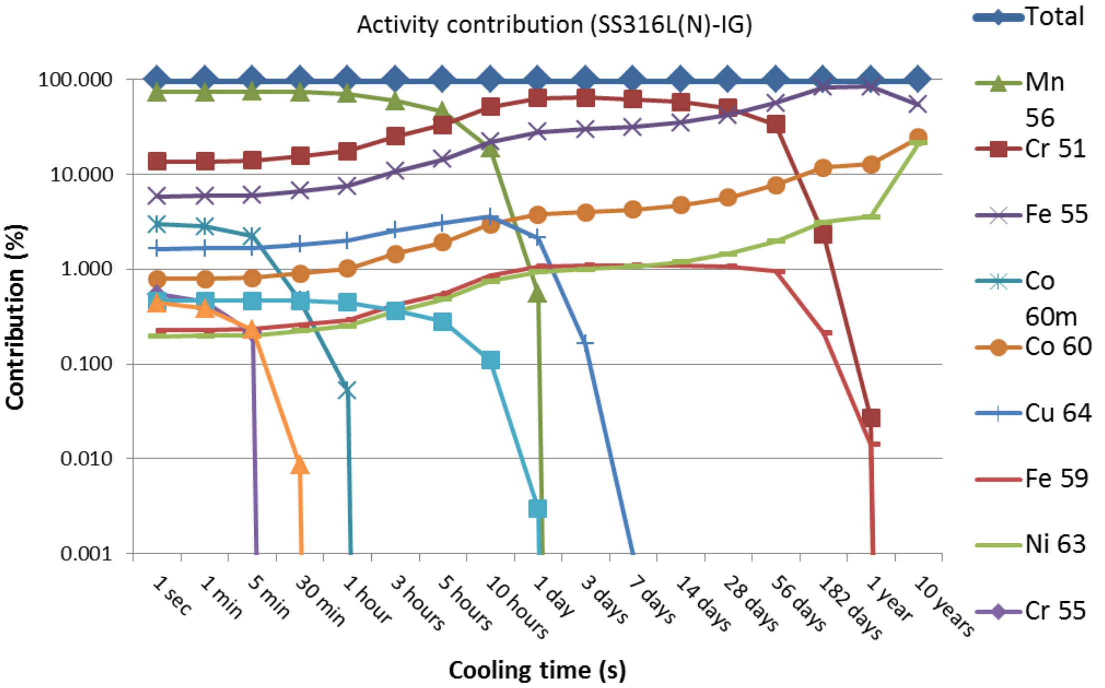

Fig. 5. Dominant radionuclides and activity contribution in blanket module localization (SS316L(N)-IG)

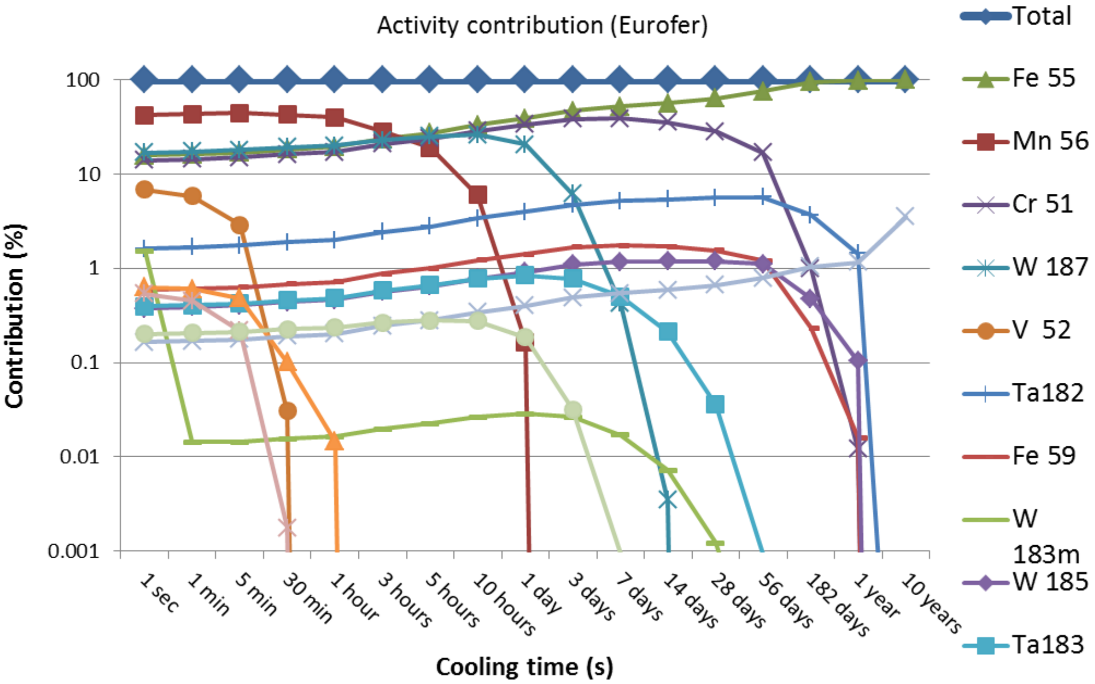

Fig. 6. Dominant radionuclides and activity contribution in blanket module localization (Eurofer)

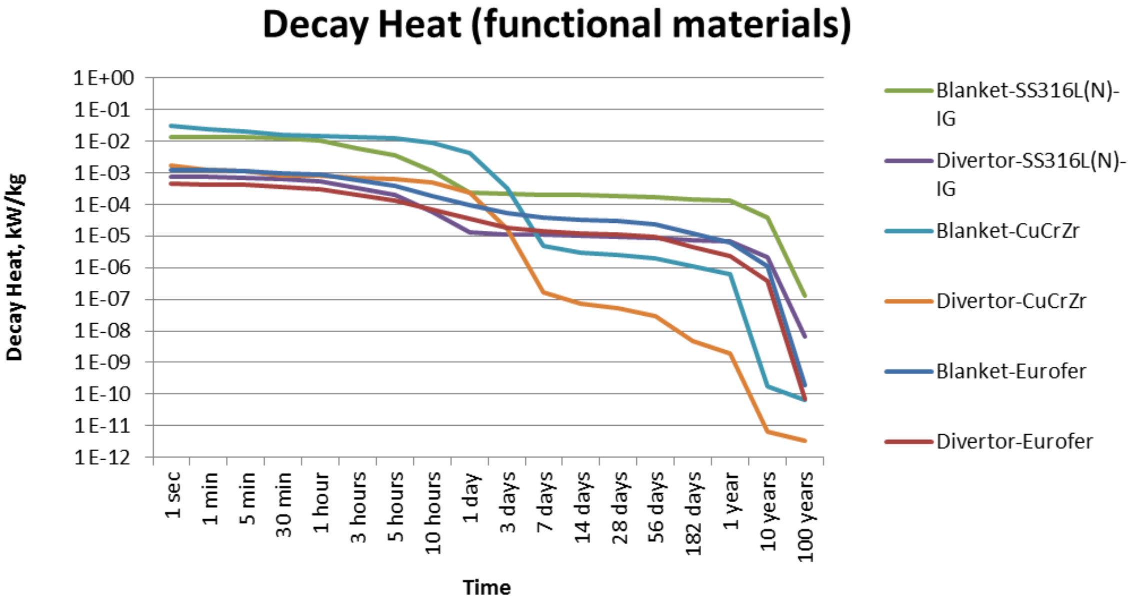

Fig. 7. Decay heat dependence on time after shut down

Decay heat is another characteristic that is really important in fusion device heat transfer system operation. Decay heat dependence on time for functional materials is shown in Fig. 7. Highest decay heat in 1 week after shut down is exhibited by CuCrZr and is 2 times higher than SS316L(N)-IG, however decay heat values in divertor localization are very similar, even though it still follows same trends with Eurofer exhibiting lowest decay heat. In later period highest decay heat is exhibited by SS316L(N)-IG and is respectively ~15 and ~150 times higher than Eurofer and CuCrZr decay heat.

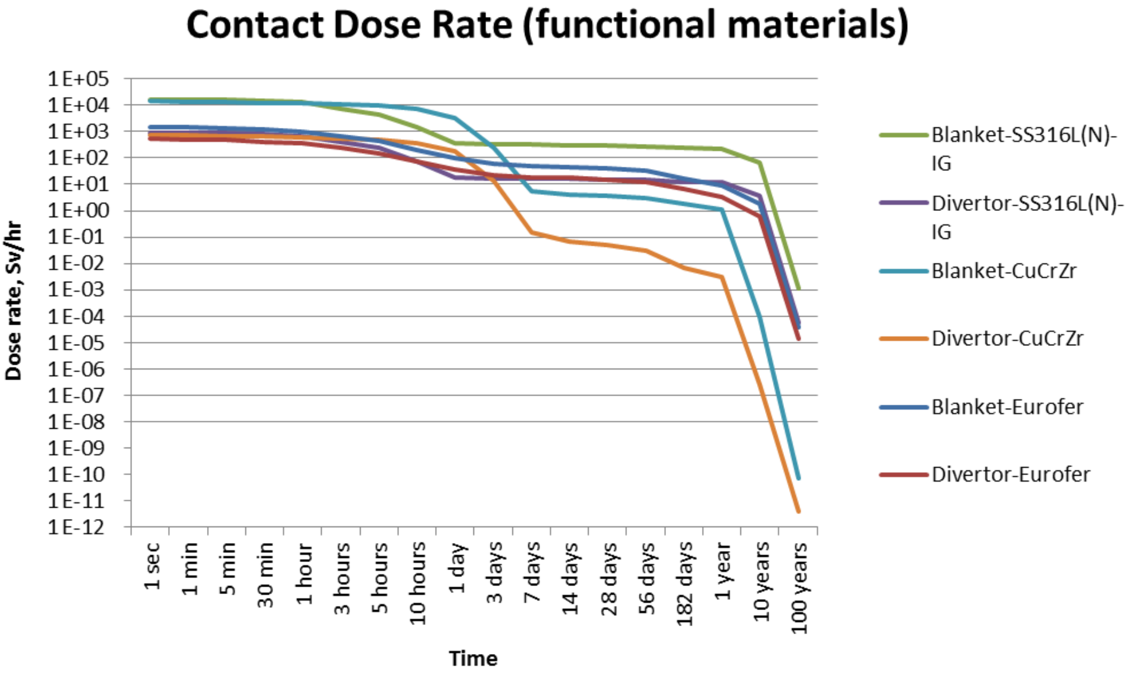

Fig. 8. Contact dose rate dependence on time after shut down

The contact dose rate was calculated near the surface of the slab. Fig. 8 shows that the highest dose rate in first week corresponds to CuCrZr which is marginally higher than SS316L(N)-IG and about 12 times higher than Eurofer dose rate. In later period highest dose is exhibited by SS316L(N)-IG is approximately 7 times higher than Eurofer and 12 times higher than CuCrZr dose rates.

Another part of research was focused on coolant – water. Molecularly pure water was examined (Hydrogen 11.19% Oxygen 88.81%). Results are shown in Figs. 9–11, It was found that main dominant radionuclide was tritium constituting ~96% of all activity in first minutes after shut down and increasing to 99% throughout rest of period. Second and third most active radionuclides were Oxygen-19.and Carbon-15 contributing respectively ~3 and 0.6 percent.

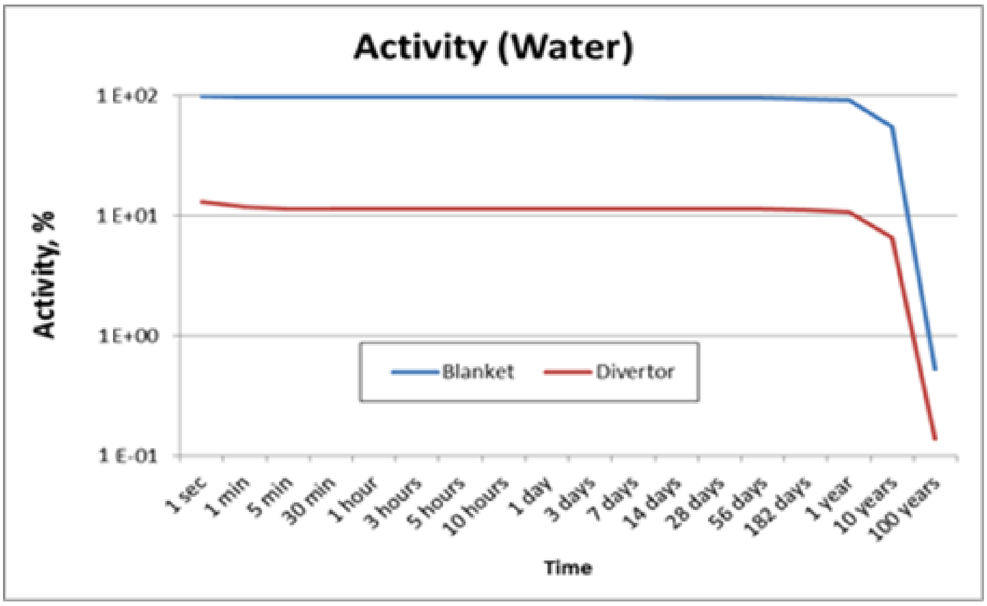

Fig. 9. Activity dependence on time after shut down

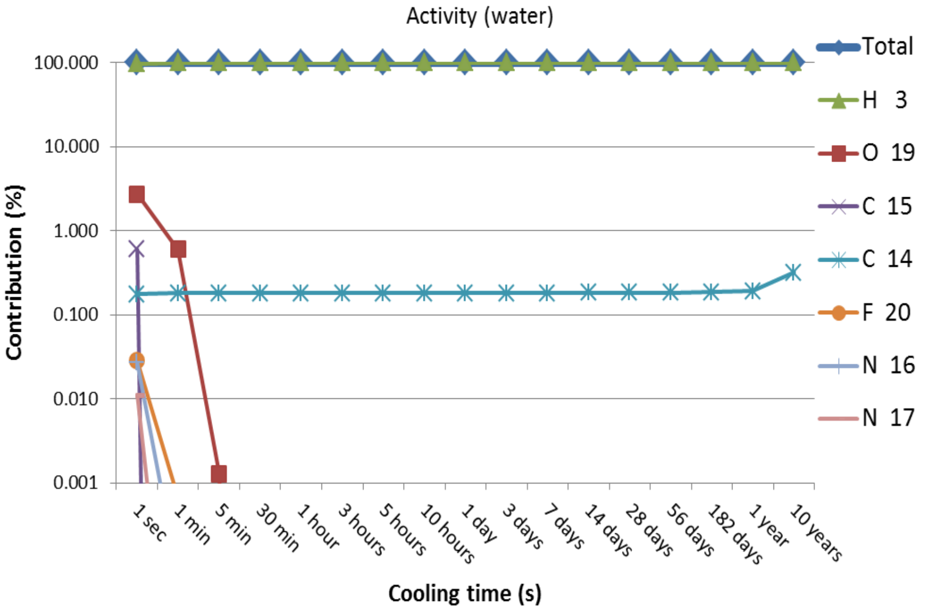

Fig. 10. Dominant radionuclides and activity contribution in blanket module localization (water)

Decaying tritium releases rather weak beta particles that should be contained within cooling system. Oxygen-19 produces both beta particles and gamma rays when undergoing decay. Another important factor contributing dose rate of coolant is Nitrogen-16 radionuclide, which is strong gamma source and is widely considered highest challenge in water cooling systems. In addition to that it is important to state that even though neutron activation is serious operational concern, short half-lives of previous radionuclides mitigate exposure risk. They are predominantly produced and located in close proximity to neutron source and their radiological effects become negligible in matter of minutes.

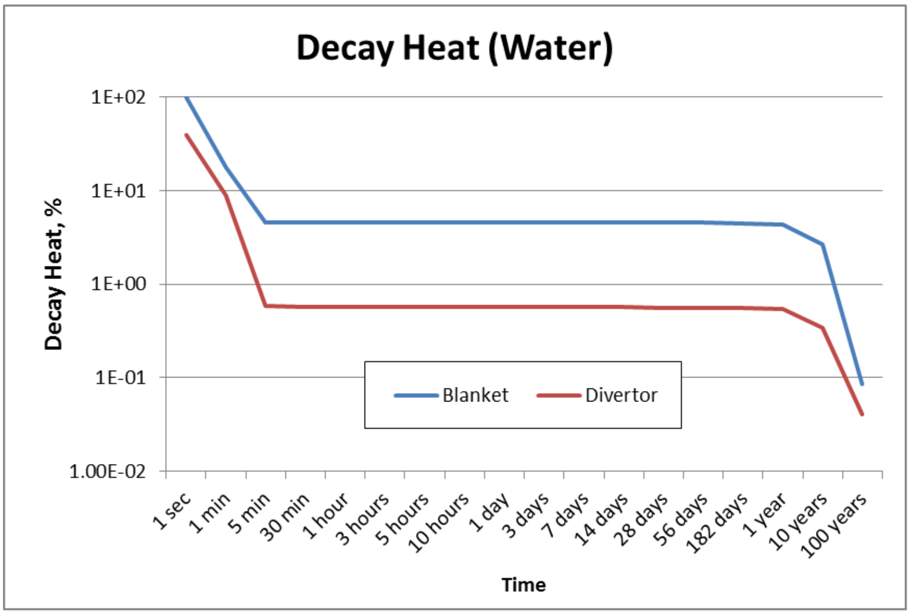

Fig. 11. Heat output dependence time after shut down (water)

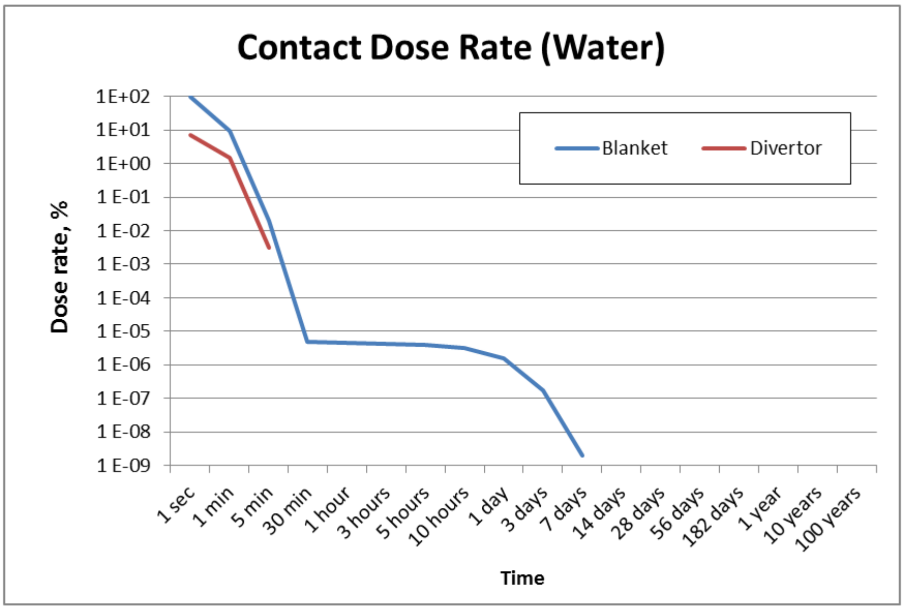

Fig. 12. Contact dose rate dependence time after shut down (water)

Activity ratio between blanket and divertor localizations was ~8.17 which is close to 6.76 from other study [2]. Such discrepancy might be result of different methodology, experiment setup. Dose rate estimation didn’t provided sufficient results as seen in Fig. 11. Solution of this issue might lie in methodology adjustment.

In addition to that possible activated corrosion products were identified that might pose additional risks for working in water cooling system. For Eurofer: Manganese-56, Vanadium 52,Tungsten-187, Tallium-182. For SS316L(N)-IG: Manganese-56, Cobalt-60, Iron-59, Cromium-51. For CuCrZr: Copper-64, Copper-66, Nickel-65, Zinc-65.

4. CONCLUSIONS

Effective cooling still raise many questions for scientists and engineers working on future fusion reactor designs. In this study two irradiation scenarios were investigated: one for blanket and one for divertor localizations, focusing on cooling system component materials and coolant. Activity ratio between blanket and divertor for water was determined to be close to one that was found in previous studies reffered in Loughlin M. et. al. paper [2]. Obtained value was 17% larger, but that might be a result of different experimental setup, conditions.

In this experimental setup activated water due to short half lives of gamma sources and low activity were not considered as major risk in the system. However more thorough examination is still needed. Activated corrosion products that are potentially dangerous gamma sources were identified. Manganese-56 attribute ~80% of dose rate for Eurofer alloy and ~95% for SS316L(N)-IG steel during one day period after irradiation. For CuCrZr dose rate key contributor is Copper-64 radionuclide attributing ~ 85% of dose rate.

Examination of different potential functional materials alloys was conducted in terms of their activity, dose rate, heat output. These values were calculated for the period of 100 year after neutron irradiation sequences. Eurofer 97 steel, SS316L(N)-IG steel and CuCrZr copper alloy were examined. In one week after irradiation period CuCrZr exhibits at least ~8 times higher activity than other two examined materials as well as 2 times higher decay heat. Difference in contact dose rate between CuCrZr and SS316L(N)-IG is only slight. In later period SS316L(N)-IG exhibit at least ~5 times higher activity than other examined materials, ~15 times higher decay heat and ~7 times higher contact dose rate. In the end CuCrZr material ,according to neutron activation analysis only, would be better suited material for water cooling systems, particularly in divertor localization, where neutron flux is significantly smaller.

5. REFERENCES

1. FOREST R. A. *FISPACT-2007: User manual.* EURATOM/UKAEA Fusion Association, Culham Science Centre, Abingdon, Oxfordshire UK 234 2007.
2. LOUGHLIN M. et. al. *Status and verification strategy for ITER neutronics.* Fusion Engineering and Design, 2014.
3. STORK D. et al. *Developing structural, high-heat flux and plasma facing materials for a near-term DEMO fusion power plant: The EU assessment.* Journal of Nuclear Materials 455 277–291, 2014.
4. SARDAIN P. et. al. *European Concepts of First Generation Fusion Power Plants*. KN2-PPCA1, 2004.
5. YOUSSEF M., RUSSELL F. *Neutronics Analysis of the International Thermonuclear Experimental Reactor (ITER) MCNP "Benchmark CAD Model withthe ATTILA Discrete Ordinance Code*. Technical Report 2007.
6. STORK D. et al. *Materials R&D for a timely DEMO: Key findings and recommendations of the EU Roadmap Materials Assessment Group.* Fusion Engineering and Design 89 1586–1594 2014.
7. COOK I. *Et al, European Fusion Power Plant Studies, Euratom/UKAEA Fusion Association, Culham Science Centre, 2004.*

CYSENI 2016, May 26-27, Kaunas, Lithuania
ISSN 1822-7554, www.cyseni.com

CFD SIMULATING THE HEAT REMOVAL FROM FUEL ASSEMBLY LOCATED IN A SPENT FUEL POOL

A. Graževičius
Lithuanian Energy Institute
Breslaujos str. 3, LT-44403 Kaunas – Lithuania
Email: audrius.grazevicius@lei.lt

ABSTRACT

Spent fuel (SF) storage facilities have to provide for the safe, stable and secure SF storage before it is reprocessed or disposed of as radioactive waste. Fukushima Daiichi nuclear accident shows that is necessary to study heat removal from the spent fuel assemblies (SFA) located in a spent fuel pool (SFP). For analysis of heat removal from SFAs have been chosen 8x8 configuration SFA, which is located in SFP of boiling water reactor 4 (BWR 4) MARK I containment. Most of SFAs in this type of SFPs are storage in 6 rings by the time of defueling from the reactor core and distribution of decay heat. Using ANSYS Fluent computer code were created detail 1/4 SFP model with SFAs, which is adopted "porous media" function. For this model analysis of thermal-hydraulic processes has been performed, then are lost heat removal and circulation systems. The results of SFP calculations showed that, at accident case, water through SFAs flows by natural circulation to the top of SFP and flow down near pool walls. The water velocity in SFA depends due to distribution on decay heat. For analysis of heat removal in SFA detail model of SFA were created and studied six different distributions of decay heat at accident case.

Keywords: spent fuel pool, spent fuel assembly, heat removal, ANSYS Fluent

1. INTRODUCTION

After Fukushima accident on March 11 of 2011, researchers pay more attention for the loss of heat removal systems for spent fuel pool (SFP). Usually SFP have residual heat removal system and could be cooled by external cooling systems. If cooling capabilities of SFP is unavailable, the temperature of pool water and fuel rods increase due to distribution of decay heat. The water level in the SFP starts to decrease, causing the uncovering of spent fuel rods and even the oxidation of zircaloy cladding. Therefore, it is important to investigate the thermal-hydraulic process in the fuel assembly, then are lost SFP cooling systems.

Nuclear regulatory commission using FLUENT CFD code, investigated thermal-hydraulic processes in the boiling water reactor (BWR) pool after a complete loss of spent fuel pool cooling water. The SFP, which is filled 4200 SFA of various ages and for this case were used porous media approach [1]. In the other study nuclear regulatory commission were analyzed loss of cooland accident (LOCA) and many other accidents using MELCORE code. Were analyzed a lot of cases: different distribution of decay heat, different spent fuel assemblies SFA storage methods and etc. In this study was found that then is loss heat removal system, water start to boil after 20 hours. Were investigated small, big leaks and cladding temperatures [2]. Researchers from Taiwan investigated the thermal–hydraulic characteristics in a spent nuclear fuel assembly (17×17) located in a Maanshan nuclear power plant SFP under the loss of external cooling system accident. The SFA can obtain the localized distributions of the flow and heat transfer during the accident [3].

2. MODEL DESCRIPTIONS

The thermal-hydraulic processes in the SFP and SFA were simulated using ANSYS Fluent 14.0v software [4]. For detail analysis were chosen SFP of boiling water reactor 4 (BWR4) and mostly in this type pool storage 8 × 8 fuel configuration SFA.

2.1. Spent fuel domain and simulation conditions

In the SFP there is 3819 cells for SFA storing. The 764 cells are always empty due to reactor accident in which all fuel assemblies from reactor core are loaded in the SFP, until the accident will be removed. SFP is 12.2 m wide, 10.8 m length, 11.8 m deep. Water level is about 11.0 m above the SFP floor (1510 cubic meters of water). SFP walls are made from 1.2–2.4 m concreate [2, 104 p.]. SFA are defueling from the reactor going every 12–18 months. At defueling process are removed 254 SFA from the reactor and moved to the SFP through the water channel. SFA in the pool must be storage not less than 3 or 5 years, but due to a lot of reasons, SFA are storage in pool until 15 or 30 years. SFA are storage in the racks, which is on the pool floor. The full pool consists of 3055 SFA [2, 112 p.]. All assemblies in the pool is grouped by the time of defueling from the reactor, for storage is using 1x4 method and assemblies is grouped in 6 rings by distribution of decay heat and time of discharge. The thermal-hydraulic analysis was performed at the biggest distribution of decay heat in full loaded SFP 3,567 MW. The configuration of full loaded SFP are shown in Fig. 1.

In the 1 and 3 rings are storage 284 SFA from the most recent offload, this ring is surrounded by 352 old assemblies in 2 ring. The 5 ring contains the last offload. Rings 2, 4, and 6 have a total of 2456 assemblies with their total distribution of decay heat in each ring scaled by the number of assemblies. 7 ring is empty and don‘t has distribution of decay heat. This ring is empty due to not expected reactor accident in which all assemblies must be loaded in the SFP. In the LOCA accident the 7 ring is used for better cooling by airflow. This empty ring ensures better air flow between racks and pool floor. Distribution of decay heat in SFA are shown in Table 1 and Table 2.

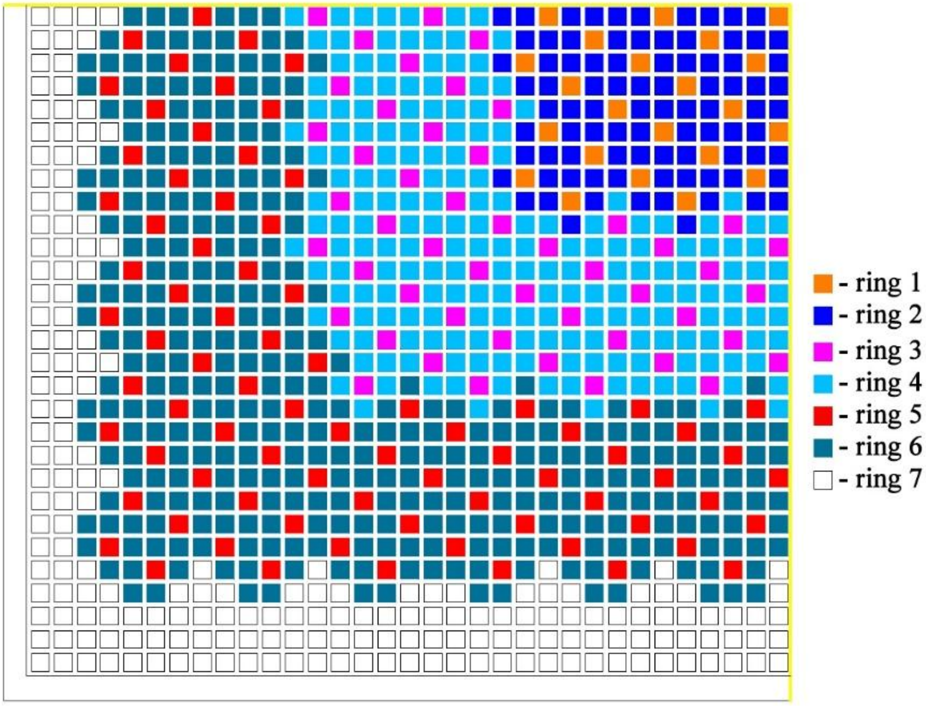

Fig.1. Full spent fuel pool

Table 1. Distribution of decay heat in the SFP [2, 112 p.]

Spent Fuel Pool (kW)						
Ring 1 (88)	Ring 2 (352)	Ring 3 (196)	Ring 4 (784)	Ring 5 (315)	Ring 6 (1320)	Total (3055)
1144	80	1533	178	332	300	3567

* number of SFA in the ring.

In the pool all SFA is individual, therefore, is necessary to transfer each ring decay heat to volume decay heat by equation:

$$Q_A = \frac{Q_R}{k_A} = \frac{1144}{88} = 13\ kW; \tag{1}$$

here: Q_A – distribution of decay heat of one SFA, kW; Q_R –distribution of decay heat in ring, kW; k_A – number of SFA in ring.

Volume decay heat for one SFA:

$$Q_V = \frac{Q_A}{V} = \frac{13000}{0.07168} = 181359.31\ W/m^3; \tag{2}$$

here: Q_V – volume decay heat, W/m^3. V – volume of simplified SFA, m^3.

Table 2. Conversion from decay heat to volume decay heat for one SFA

Ring No.	Distribution of decay heat of one SFA, W	Distribution of volume decay heat of one SFA, W/m^3
1	13000.00	181359.31
2	227.27	3170.58
3	7821.43	109114.55
4	227.04	3167.37
5	1053.97	14703.64
6	227.27	3170.58
7	–	–

For numerical investigation were created ¼ model of SFP in ANSYS Fluent. For SFP model was created 10.2 million elements mesh (see Fig. 2). For SFA are used “porous media” function, this function let to simplified the complicated geometries and use values of viscous and inertial loses. For calculation are used standard $k - \varepsilon$ model with standard wall functions for the near-wall treatment is chosen. This model is a common turbulence model and is known to be suitable for free-shear layer flows with relatively small pressure gradients. The method of solution was a SIMPLE-based pressure-velocity coupling, pressure equation was body-force-weighted. SFP wall are made from concreate with 2.0 m thickness, thermal conductivity is 2.5 $W/m \cdot K$. The racks are not modeled and due to selected geometry are modelated 3828 SFA. Gap between SFA is 4.0 cm and 26.0 cm above from the floor. Initial water temperature 28 ℃. Calculation is transient and results are analyzing after 20 hours, then was lost residual heat removal system.

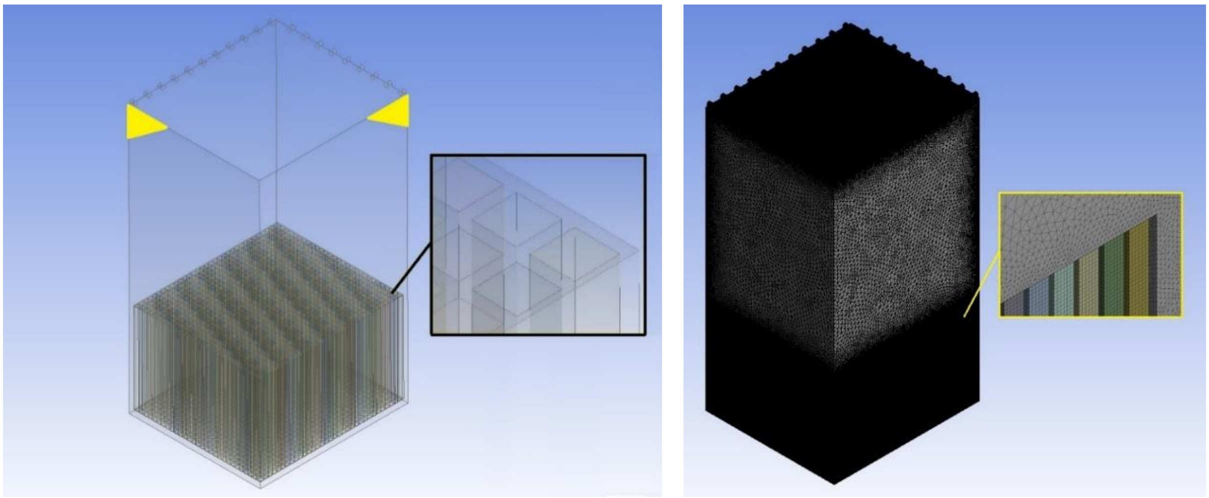

a) b)

Fig. 2. The spent fuel assembly model in ANSYS Fluent: a) ¼ according the planes of symmetry (yellow collar); b) spent fuel assembly mesh

2.2. Spent fuel assembly domain and simulation conditions

For numerical investigation of the thermal-hydraulic processes in the SFA, which is located in the SFP, were created ¼ model of 8x8 configuration SFA. Assembly consist of 60 fuel rods and 1 guide tube. The geometry and dimensions of SFA are shown in Fig. 3. The active fuel length is 3.708 m, fluid region around the assembly and through water channel is not modeled. The SFA mesh consist of 10 million elements (see Fig. 4). For calculations are used standard $k-\varepsilon$ model with standard wall functions for the near – wall treatment. The method of solution was a SIMPLE – based, pressure – velocity coupling, pressure equation – standard. Calculation is steady state.

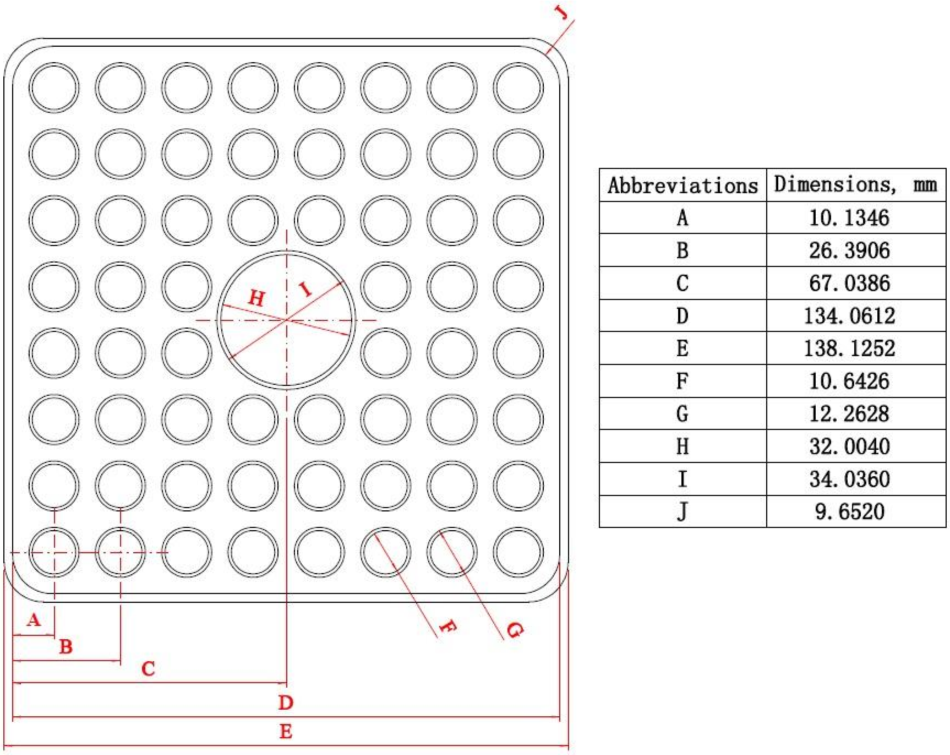

Abbreviations	Dimensions, mm
A	10.1346
B	26.3906
C	67.0386
D	134.0612
E	138.1252
F	10.6426
G	12.2628
H	32.0040
I	34.0360
J	9.6520

Fig. 3. Section of 8 × 8 configuration spent fuel assembly [5]

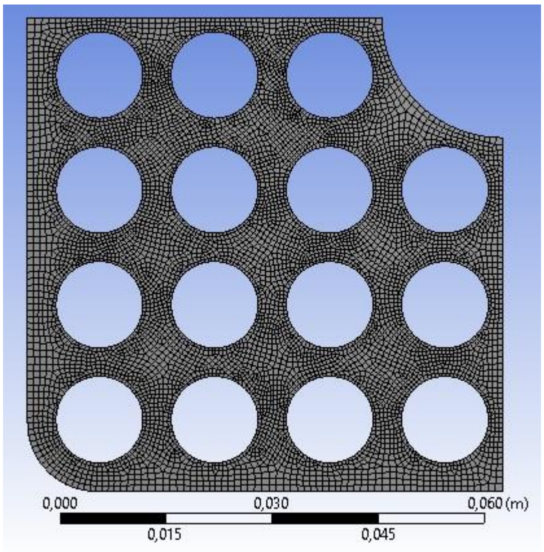

Fig. 4. Spent fuel assembly mesh

3. RESULTS AND DISCUSION

Fig. 5 shows cooling water temperature in sections from the top and from the side of SFP, at 20 hours after accident (loss of residual removal heat system). The highest temperature is in rings (1, 3 and 5 ring), which has a biggest distribution of decay heat, approximately 69–76 °C. The temperature in 2, 4 and 6 rings are similar, approximately 66 °C. Fig. 6 shows cooling water speeds, which form due to distribution of decay heat (natural circulation). The biggest speed is in 1 and 3 rings (0.015 m/s). The lower speed is 5 ring (0.005 m/s). In the other rings cooling water speed is very low. Cooling water temperature in the above of SFA is 68 °C.

Fig. 7 shows cooling water temperature in the end of SFA. In all rings water not start to boil. The lowest temperature is in the middle of SFA, aproxximity 72 °C. The higest temperature in the assemblies, which are storaged in 1 ring. Temperature about fuel rod is 78 °C. The Fig. 8 shows temperature growing throuht all height in all SFAs.

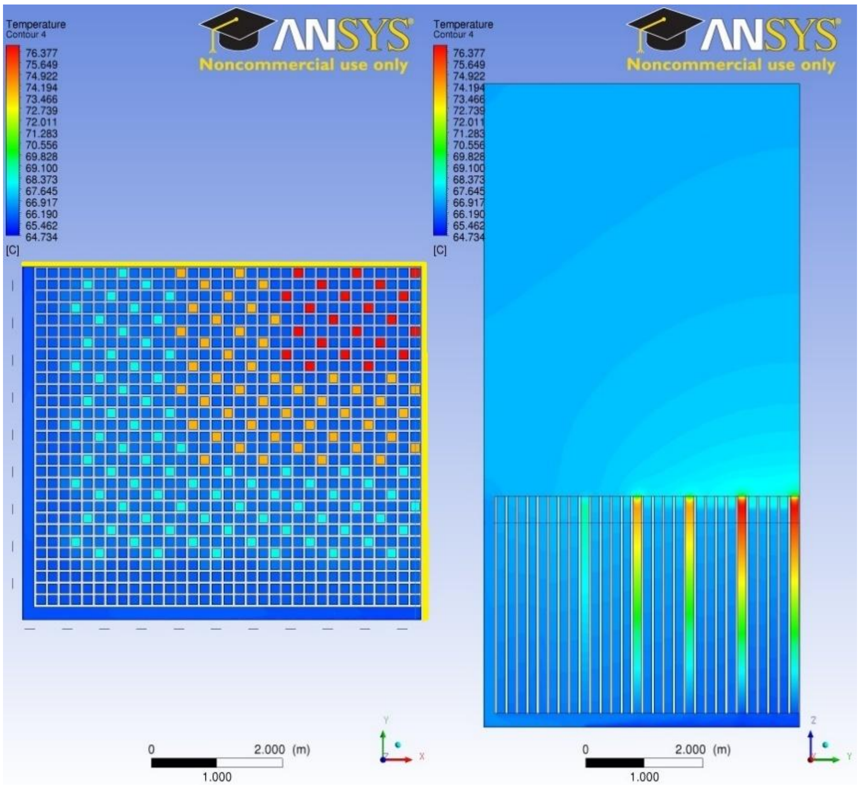

Fig. 5. Water temperature after 20 hours

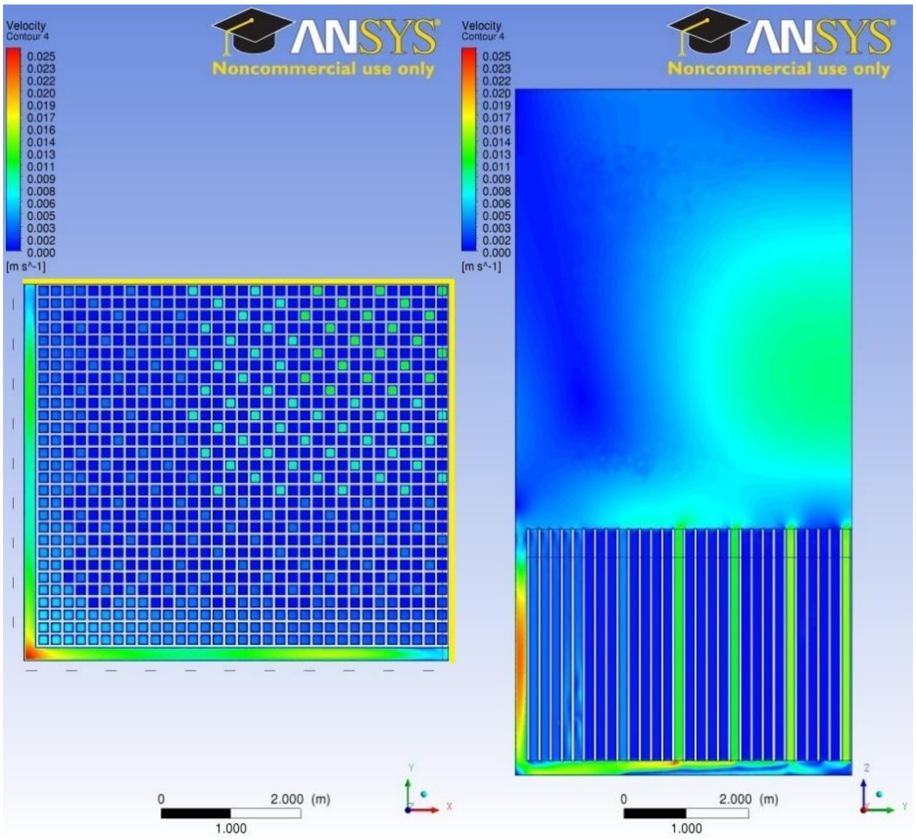

Fig. 6. Water velocity after 20 hours

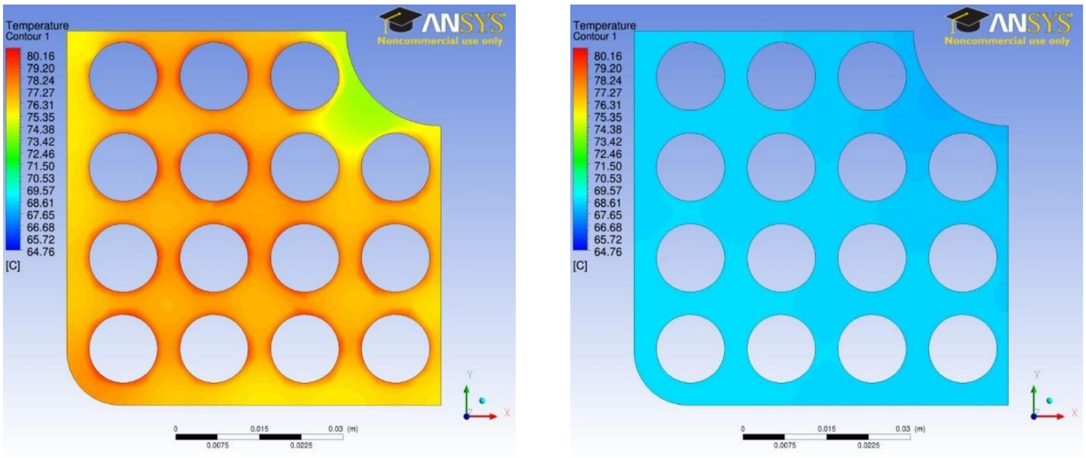

1 ring 2 ring

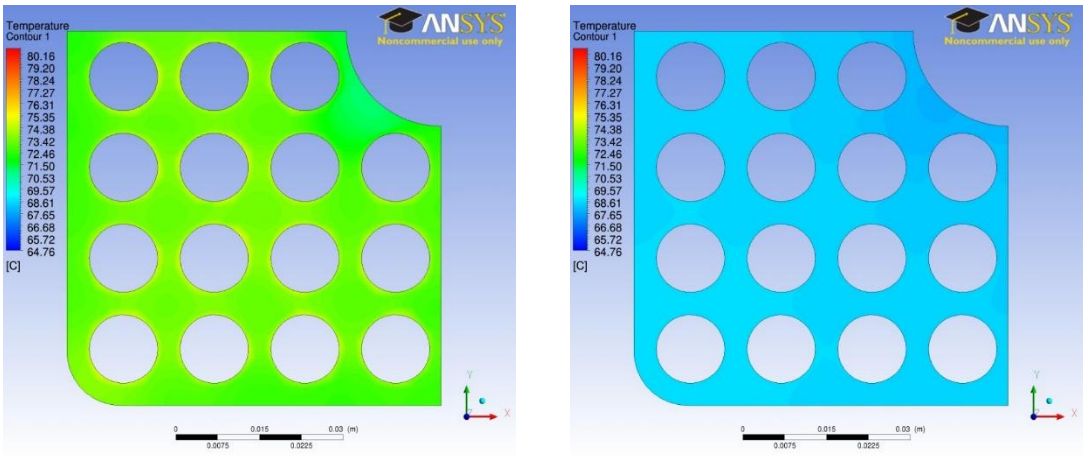

3 ring 4 ring

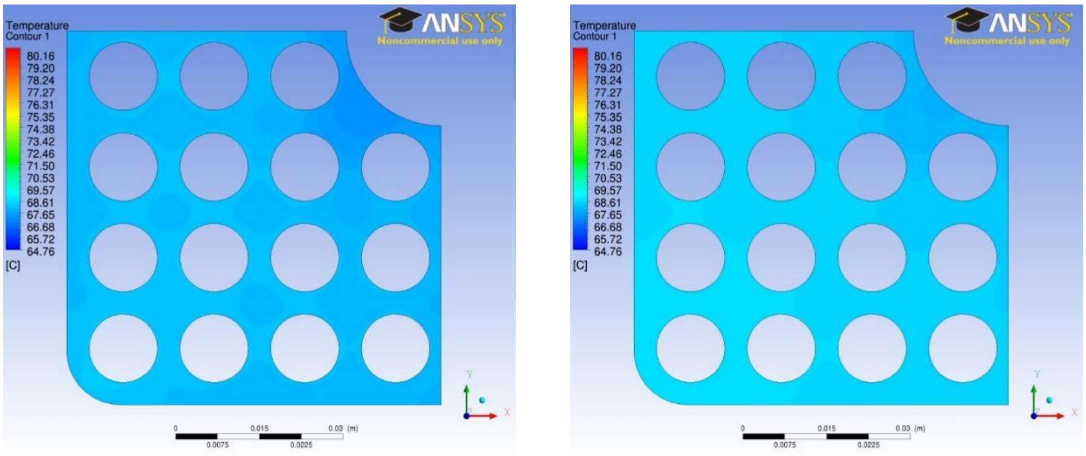

5 ring 6 ring

Fig. 7. Section in the end of SFAs in the different rings

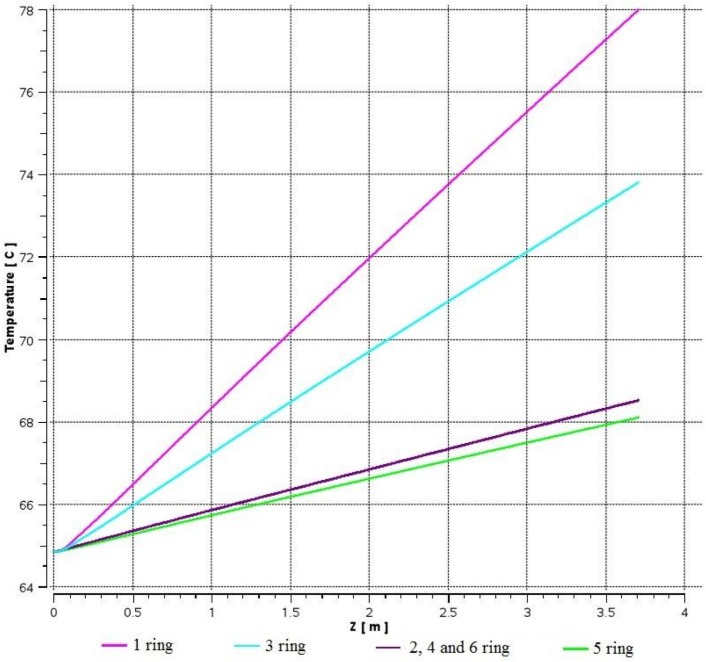

Fig. 8. Temperature growing through the height of spent fuel assembly

4. CONCLUSION

This paper simulates transient behavior of SFP and steady state behavior of 8x8 configuration SFA at 20 hour, when are lost residual heat removal system. Several important conclusions can be drawn from the simulation results:

1. Due to distribution of decay heat, water starts to flow through SFA. The highest speed and temperature in the SFA at 20 hour after accident is 0.015 m/s and 78 ℃.
2. After 20 hours water in SFA, which has the biggest distribution of decay heat not start to boil and around fuel rods not occur the boiling crisis.
3. After the 20 hours the operation of residual heat removal system must to be renewed.
4. The cooling water in the SFP warm only due to SFA, which is storage in 1, 3 and 5 rings.

5. REFERENCES

1. Division of Systems Analysis and Regulatory Effectiveness Office of Nuclear Regulatory Research U.S. Nuclear Regulatory Commission Washington, DC 20555-0001, 2000. Link to the internet <http://pbadupws.nrc.gov/docs/ML0037/ML003727905.pdf>.
2. Office of Nuclear Regulatory Research US Nuclear Regulatory Commission, 2013. Link to the internet <http://www.nrc.gov/reading-rm/doc-collections/commission/secys/2013/2013-0112scy.pdf>
3. *Annals of nuclear energy*. Taiwan Power Company, Institute of Nuclear Engineering and Science, Department of Engineering, System Science, Department of Mechanical and Biomedical Engineering, 2014. Link to the internet <http://ac.els-cdn.com/S030645491400317X/1-s2.0-S030645491400317X-main.pdf?_tid=88e68d40-e38e-11e5-9455-00000aab0f02&acdnat=1457263882_9acb645eefd862dab5a4dd655021dab2>
4. ANSYS, Inc. ANSYS FLUENT Getting Started Guide. Release 14.0. Southpointe. November 2011.
5. U.S. Department of energy, 2015. Link to the internet <http://www.casl.gov/docs/CASL-U-2015-0040-000.pdf>

CYSENI 2016, May 26-27, Kaunas, Lithuania
ISSN 1822-7554, www.cyseni.com

REGIONAL REGULATION EFFECT ON THE URANIUM MARKET PRICE

A. Auzans, A. Teder, A. H. Tkaczyk
University of Tartu
Ravila 14C, 50411 Tartu – Estonia
Email: aris.auzans@gmail.com

ABSTRACT

This paper demonstrates the effect of regional regulations on the natural uranium (NU) market price based on real market supply and demand analysis. The uranium (U) market is modelled as a front-end nuclear fuel cycle, where the final low-enriched uranium (LEU) consumers are nuclear reactors with relatively stable demand. Enrichment facilities are supplied with NU from U mines. The aim of this paper is to demonstrate a more realistic U mine-based front-end nuclear fuel cycle simulation, which applies additional constraints on regional or local level, thereby creating additional U market price fluctuations.

Government policy has direct effects on U mine competitiveness in the U market and individual mine production decisions. NU market price can change in a short and long time period; price fluctuations can cause changes in demand, new U mine opening or technology changes. Local governments regulate U mine licensing and can limit annual production ratio [1]. It is possible for government regulation to directly affect the U market price.

A mine-based U market clearing model was used for simulations [2, 3]. The model is built around databases of primary and secondary U supply as a time-dependent simulation that determines the U and enrichment market conditions by calculating the intersection between the supply and demand curves in each user-defined time period (usually one year). The model simulates a time period from 2010 until 2030.

Keywords: uranium supply, market modelling, nuclear fuel cycle economics

1. INTRODUCTION

In this paper we propose improvements to the mine-based U market clearing model for the front-end U market and enrichment industries [2, 3]. The initial model analyses U market price impact on individual U mine production output and takes into account the decision making ability based on the U market conditions such as demand and U market price. The initial model has demand side decision strategy based on price and stability of the U supply in the previous periods as well as a rollback algorithm to test negative price effect after new U mine opening.

Before introducing improvements to the model, it is important to provide a general description of the dynamics of the U market. The majority of natural uranium (NU) is consumed by enrichment services to meet nuclear reactor U235 isotope concentration needs for commercial electricity production. The market demand for NU is the sum of the demand functions.

Since nuclear reactors require many years to modify their demand for low enriched uranium (LEU) fuel, the LEU requirement per unit of installed nuclear capacity is treated as fixed. Utilities, however, can substitute natural uranium (NU) for enrichment services, so the model’s uranium and enrichment demand curves exhibit considerable short run price elasticity while still meeting LEU requirements. Each demand curve is a locus of cost-minimizing tradeoffs between uranium and enrichment services over the range of feasible production levels of those commodities.

Investments in nuclear reactors for electricity production have long payback periods and are often of a strategic importance to the country, so we expect the demand for U to remain relatively stable regardless of the price (the demand is non-elastic). The market supply of U is the sum of the supply functions of all individual U producers with their respective marginal costs.

Improvements presented in this paper reflect a more realistic behavior of U miners and a more realistic price adjustment in the U market. More specifically the paper introduces regional level constraints which regulates how much U each mine can produce annually. The hypotheses to be tested in the paper are as follows. We expect that these changes to the model will firstly reduce the supply of U. Secondly we expect the market supply and price to be much more volatile since model limits U overproduction. These characteristics will be tested in the paper. Such kind of research has not been previously conducted with an agent based U mine decision making model. Therefore the outcome will have a more conceptual meaning and will allow to create more realistic front-end U market simulations in the future.

The methodology section will contain general information about changes made in the model. Then two test cases, presented in Section 3 and Results. The first test case includes five U mines to evaluate and demonstrate changes in the fuel cycle simulation model. The second test case implements the realistic depiction of the world U and enrichment markets.

2. METHODOLOGY

The work presented here builds on a mine based market clearing model of the U and enrichment industries described in the reference [3]. A market clearing conditions means that supply of U is equal to demand, so there is no oversupply or undersupply. The model is built around a database of primary and secondary U resources. The primary U databases contain information about more than 360 U mines in different development stages across the globe. The reference model demonstrates an agent based modelling concept which is used to simulate individual U mine's decision making strategy.

Fig. 1 shows the economic concept and ground rules on which U mine’s operational decisions are based, as described in [4]. The marginal cost (MC) is the variable cost incurred by producing one additional unit of output. The average variable cost (AVC) is the average value of the MC for all units of output produced. The average total cost (ATC) is the AVC plus the amortized capital cost (ACC) divided by the number of units of output. For a mine to operate, its economic costs must be covered. The MC curve crosses ATC at its lowest point (E_1) because the MC is of producing an additional unit of output is averaged into the ATC. When the MC is less than the ATC, each new unit of output lowers the ATC. A new mine will not begin to operate unless its average total cost of producing U is less than or equal to the mine’s MC. This point is known as the short-run breakeven point (E_1 in Fig. 1). If a mine is currently operating it will continue to operate until the market price drops below the minimum value of its AVC. This is known as the long-run industry exiting point (E_2).

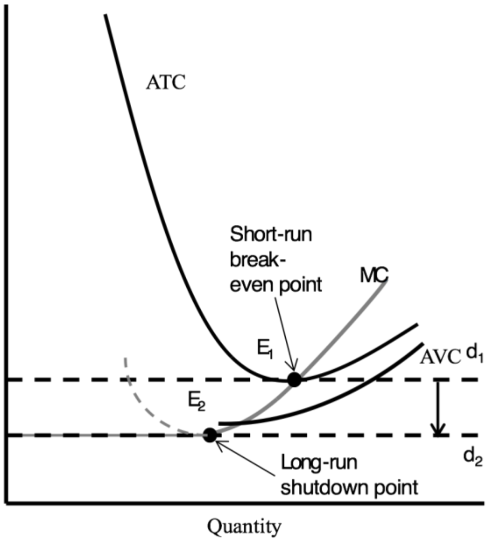

Fig.1. Cost curves for a single U mine

The reference model assumes that producing each next unit of output will also quite significantly raise the ATC. Such overproduction will not be economical and also will raise the U market price. But, as shown in certain market conditions, U mines exceed annual extraction rates and theoretically an individual mine can sell all U reserves in a single year. In the U mining industry additional licensing is needed to increase production output. Licensing depends from regional policy and local authorities. This work introduces regional level regulation to the mining industry and imposes additional constraints. An individual U mine cannot sell more U than is defined by local regulator.

3. RESULTS

3.1. Test Case Conditions

The experiment demonstrates the effect of regional level regulation on the U market price. The simulation runs from 2010 to 2030 under a growing NU demand of 2.6% per year and a start demand of 6790 tons/year of 4.5% enriched U and 3390 t/year of natural U to supply Canada Deuterium Uranium (CANDU) and other NU-fueled reactors. As simplifications for this test case, the enrichment price is fixed at $100/SWU and no secondary supplies of U are made available.

Based on the reference model, the experimental data of Q (quantity at which the marginal cost of producing the next unit) and P (the marginal cost at that quantity) are normalized against the reference quantity and cost respectively, so that $Q_2 = 0.5$ and $P = 0.7$, meaning that the mine's marginal cost is minimized at 50% of its reference production level, at which the level of its MC is 70% of the reference value. The same configuration will be used for a test case with five U mines and for the real world scenario. The model setup allows to restart U mine operations after bankruptcy in 3 years, if market conditions satisfy individual U mine's economic characteristics.

Table 1 contains data of five made-up U mines, which are intended to illustrate the model's behavior. One U mine has large reserves and is supposed to supply U over the whole simulation period. We expect that other U mines will produce depending from market conditions. In Table 2 are coefficients, which regulate actual production rate in a single simulation time frame. For the test case only three coefficients are used. These are made-up and aim only to demonstrate the model's behavior. In the test case regulations are applied to 10 regions. This number is fixed in the current case, but does not work as a mandatory constraint, i.e. constraints can be determined for each country.

Table 1. Initial U mine data

U mine	Total Reserves & Resources tU	Reference Annual Extraction Rate tU/year	Year Available	Reference Cost $/kg U	Country
A	150,000	15,000	2009	75	AUS
B	300,000	15,000	2009	100	AUS
C	200,000	20,000	2009	120	USA
D	150,000	15,000	2018	60	CAN
E	10,000,000	30,000	2009	50	KAZ

Table 2. Regional regulation settings

Country	**Coefficient**
USA	2.5
CAN	2.5
NIG	3
AUS	2
KAZ	3
CHN	3
RUS	1.5
SAF	1.5
MON	1.5
IND	1.5

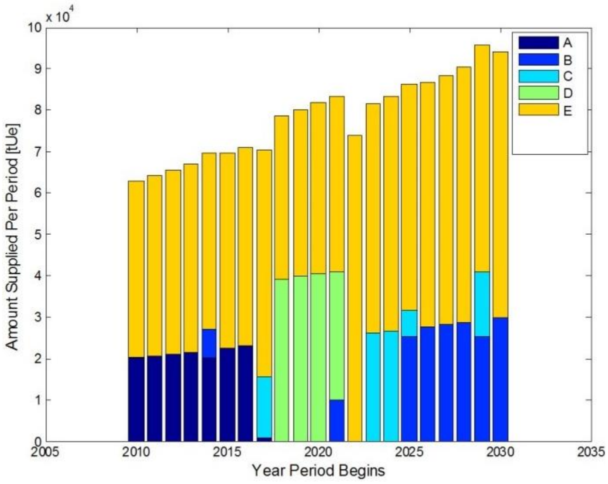

Fig. 2. Amount of NU supplied per 20 year period

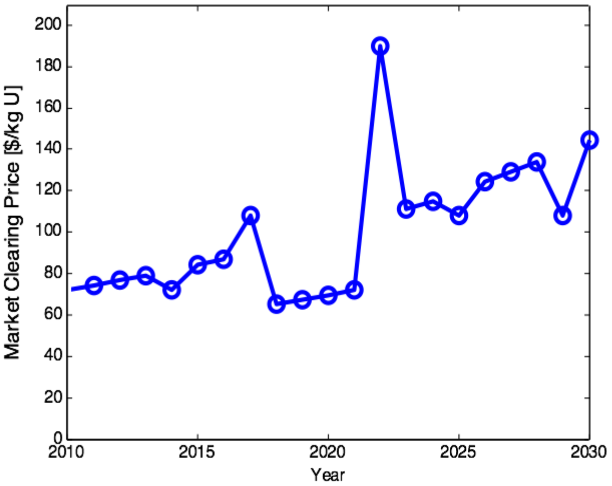

Fig. 3. U market clearing price

Fig. 2 and Fig. 3 represent test case results. Fig. 2 shows supplied amount of NU from mines A, B, C, D and E. We can see that U mines are operating whenever market condition satisfies requirements and model configuration. If the U mine is shut down due to a low market price, then it can start operation only after 3 years. In the current test case U mine C and B was down due to low U market price. U mine B is opened and shut down in year 2017. It is because the market price did not satisfy mine's requirements, i.e. market price was below the individual mine's long run shutdown point (Fig. 1). The reason of such price fall was the opening of U mine D in year 2018. In year 2021 mine D runs out of resources and is shut down. As expected U mine E fulfils the base supply function. Regional level regulations decrease maximum individual U mine's annual output rate. In such a way U market prices are more volatile and become more realistic. So, we confirmed that model behaves as expected.

3.2. World Case Test

The world case test conditions are described in the reference model [2]. Regional level coefficients are taken from Table 2. The hypotheses to be tested in the paper were as follows. Firstly, we expected that the changes in the model would lead to a reduction of supply and overall tougher conditions for U producers, also reflected in higher market clearing price for U. Secondly, we expected the market price to be much more volatile. Fig. 4 represents the world test case scenario and Fig. 5 shows the reference model world test case scenario. As it is demonstrated in Fig. 4 and Fig. 5, market price is more volatile and U price increases faster compared to the reference model world test case.

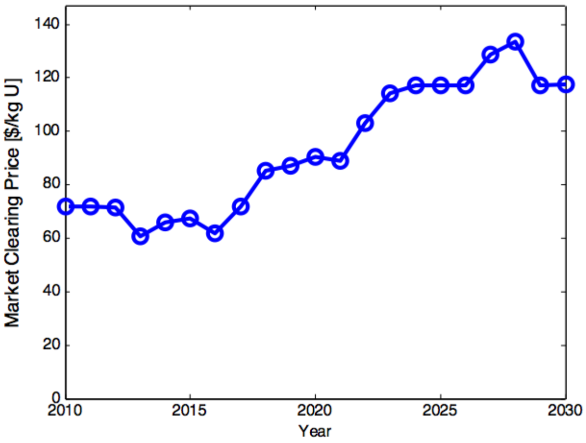

Fig. 4. Market clearing price

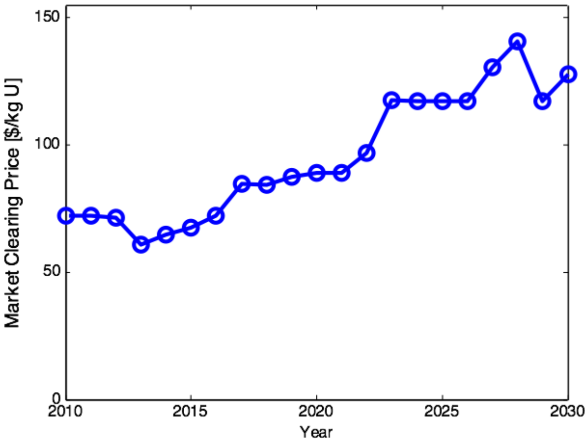

Fig. 5. Reference model market clearing price

4. CONCLUSIONS

An updated version of a mine based U market clearing model provides ability to test regional level government regulation and evaluate U market price effects. The model assumes that regulations might differ in each country and region. Although this work demonstrates only one kind of regional level constraint, it does not limit to extend regulations. Regulations are important because overproduction in the mining industry has significant environmental effects.

The results show that the improvements made to the model made the conditions much tougher for miners to operate in, causing the prices in the market to increase on average. We were also able to confirm that the improvements increased U market price volatility. In such a way we can confirm that regional governments can directly affect the world U market price by applying new regulations or taxes. This model can be used to measure policy change effect on U market price. This model demonstrates the effects of regional level regulation on an agent based front-end nuclear fuel cycle, which increases the model's accuracy. The next logical step is to extend the regulation constraints to each country and calculate the economic effects on the U market price.

5. ACKNOWLEDGMENTS

This research was supported by European Social Fund’s Doctoral Studies and Internationalisation Programme DoRa. We acknowledge support from the Estonian Research Council under ETF award 22/2011.

6. REFERENCES

1. SÖDERHOLMA, K., SÖDERHOLMA, P., HELENIUSB, H., PETTERSSONA, M., VIKLUNDA, R., MASLOBOEVC, V., MINGALEVAC, T., PETROVC. V. Environmental

regulation and competitiveness in the mining industry: Permitting processes with special focus on Finland, Sweden and Russia. *Resources Policy*. 2015, 43, 130–142.

2. SCHNEIDER, E.A., PHATHANAPIROM, U., EGGERT, B.R., SEGAL, E. A market-clearing model of the uranium and enrichment industries. *Nuclear Technology*. 2013, 183, 160–177.
3. AUZANS, Aris; SCHNEIDER, Erich A.; FLANAGAN, Robert; TKACZYK, Alan H. (2014). A Mine-Based Uranium Market Clearing Model. *Energies*, 7(11), 7673–7693.
4. NECHYBA, T.J. Microeconomics, an Intuitive Approach with Calculus; South-Western Cengage Learning: Mason, USA, 2011.

CYSENI 2016, May 26-27, Kaunas, Lithuania
ISSN 1822-7554, www.cyseni.com

DYNAMIC MODEL FOR ASSESSMENT OF SUSTAINABLE DEVELOPMENT LEVEL

A. E. Lutynska
Vytautas Magnus University
Vileikos str. 8, LT-44404 Kaunas – Lithuania
Email: a.lutynska@if.vdu.lt

ABSTRACT

Sustainable development and problems related to it become more and more relevant and important issue in the entire world. A comprehensive social progress can be achieved in balancing factors of environmental protection, economical efficiency and social equity. These factors are combined together according to the basis of sustainable development concept. This concept can be understood as meeting the needs of present generations without compromising the ability of future generations to meet their needs. It is difficult to define with precision and to measure sustainable development. There has been noticed rapid increase in numbers of methods and indicators to measure sustainability in last two decades. An indicator is a special index, which provides numerical values to important factors of the investigated sector. Sustainability indicators have multiple motivations, which include decision making and management, consensus building, etc. In this article, the integrated sustainability indicator is used to assess sustainable development level.

Sustainable development is a cross-cutting issue. It is covering economic, social and environmental fields. Energy plays a very important role in each of these areas. Models of different processes take into account various factors that are time-dependent and depend on each other. Thus, it is advisable to construct a dynamic model in order to describe these dependencies. The methodology for the dynamic indicator model construction and forecasting of indicators for the assessment of sustainable development level is presented in this article. Also, it is advisable to elaborate tools to predict sustainable development level. The developed dynamic model enables to forecast indicators' variation taking into account changes in system configuration.

Keywords: sustainability indicators, assessing sustainable development

1. INTRODUCTION

Sustainable development is one of the most important and frequently used subjects worldwide in the 21st century. Since it was introduced in 1987 by The World Commission on Environment and Development, the sustainable development theory has been developed continuously. According to the Brundtland Report, Sustainable Development is "the development that meets the needs of the present without compromising the ability of future generations to meet their own needs" [1].

Currently there are more than 60 definitions and interpretations of 'sustainable development' [2]. Beyond the pattern of definitions, sustainable development is the one that provides a framework through which communities can use resources in an efficient way, create efficient infrastructures, protect and improve the quality of life, create new activities to strengthen the economy, finally helping to create healthy communities that can support both this generation and the next one [2]. Sustainable development is based on a three-pillar framework: economic and social development, and environmental protection – that are interdependent, mutually reinforcing and must be satisfied jointly.

Sustainable development is a dynamic concept, with many dimensions and interpretations, seen as a process of permanent change [3]. It is very important to create a suitable framework that takes into account the correlation of development with the environment. In this case, science plays an essential role for sustainable development starting from informing about evidence-based targets, to assessing progress, testing solutions, identifying emerging risks and opportunities.

The main objective of this paper is to present the model for assessing sustainable development level. Research is focused on differential equations system of sustainable development indicators for sustainability assessment. Presented dynamic model is merging the well-known probabilistic, statistical and differential equation methods. Furthermore, this model enables to include the expert judgement on indicators' variation taking into account changes in system configuration. Since technical parameters of new objects are not exactly known, these uncertainties should be reflected in the initial conditions. Thus, in such conditions, the values of indicators are random variables and we have the ordinary differential equations system with random initial data. Another way to involve the expert opinion of the influence of new factors on indicators is to apply the Bayesian method to the solution of differential equations system. This model may be useful for estimating the level of sustainable development level in the future. In this way, it is a tool for decision-makers in planning variuos scenarios for development when it is necesseary to evaluate technical, economic and environmental aspects individually or as a complex task.

2. BRIEFLY OF SUSTAINABLE DEVELOPMENT

The term of sustainability appeared in the early 1970s as the rapid growth of the human race and the environmental degradation. Finding a way for consent between environment, advancement and well-being of the world's poor was discussed in the United Nation's 1972 Stockholm Conference. The conflicts between environment and development were acknowledged for the first time there. In the 1982 The World Commission on Environment and Development meeting was chaired by then-Prime Minister of Norway Gro Harlem Brundtland. As Brundtland argued "the environment does not exist as a sphere separate from human actions, ambitions, and needs, and attempts to defend it in isolation from human concerns" [1]. As with previous efforts, the report was followed by major international meetings. The United Nations Conference on Environment and Development (UNCED) in Rio de Janeiro in 1992 issued declaration principles, a detailed Agenda 21. Chapter 40 of Agenda 21 encourages the nations to introduce indicators of sustainable development to provide a solid basis "for decision-making at all levels and to contribute to a self-regulating sustainability of integrated environment and development systems" [4]. Ten years later, in 2002, at the World Summit on Sustainable Development in Johannesburg, South Africa, the commitment to sustainable development was reaffirmed. There was marked a further expansion of the standard definition with the widely used three pillars of sustainable development: economic, social, and environmental. The Johannesburg Declaration created "a collective responsibility to advance and strengthen the interdependent and mutually reinforcing pillars of sustainable development – economic development, social development and environmental protection – at local, national, regional and global levels" [4].

UNCED had another meeting in Rio de Janeiro in 2012. Rio +20 Conference focused on two topics: the green economy in the context of sustainable development and poverty eradication and the institutional framework for sustainable development [5].

Since 1980s, the sustainable development theory has been studied extensively by a large number of international organizations, governments, and research institutes. Significant progress has been made in terms of indicators system. An indicator is a special index, which provides numerical values to important factors for the investigated sector. However, there are a lot of empirical literature about methods to elaborate sustainable development indexes. But no set of indicators can be final and definite [6]. Indicators and synthetic indexes could be useful for monitoring progress toward sustainability as well as communicating information to the policy-makers. With the progress of research on the index system, more index evaluation methods are emerging. Listing technique is the most commonly used method for the sustainability evaluation [7]. It mainly includes a typical framework and typical index. Progress also had been made in sustainability assessment. The number of tools, methodologies and processes for assessing sustainability is in the hundreds [8].

Measuring sustainability is a major issue. It is need to determine whether the current actions are sustainable and, if not, how to change them in order to make sustainable. Finding the appropriative assessment instrument is critical to match theory with practice, and to have successful outcomes in improving sustainability.

2.1. Assessing sustainability

In the last decades, sustainable development has been one of the key guiding principles in the European Union strategy. Europe 2020 emphasizes the importance to make European Union more sustainable by means of the establishment of a long term approaches with a clear guidance to climate change [9]. Integrated sustainability assessment indicator (*ISI*) is developed for monitoring progress of implementing the Sustainable Development Strategy and sustainability assessment of policies and measures seeking to reflect the main issues of sustainable development set in the National Sustainable Development Strategy. *ISI* is constructed from a wide range of specific structural social, economic and environmental indicators aim to evaluate important features of the investigated social, economic and environmental issues. At the same time they indicate how the changes of structural indicators influence dynamics of an integrated indicator. Few methods for assessing sustainable development level are preseted in the paper [10]. But it also highlighted that integrated sustainability indicator gets numerical values and can be used the most widely. Using this method it is possible to analyze the trends of an integrated sustainability indicator and assess progress of the sustainable development path.

Integrated sustainability indicator can be calculated by summing the weighted indices of all indicators [11]:

$$ISI_t = \sum w_i I_{it}\ , \tag{1}$$

where ISI_t – integrated indicator for sustainability assessment at time moment *t*, I_{it} – index of sustainability indicator *i* at time moment *t*, w_i – weight of indicator *i* in the integrated indicator.

If indicator decrease (e.g. external costs or private cost) is positive in terms of sustainability assessment, the indices of such indicators are integrated as inverted indices:

$$I_{it} = 1/I_{it}\,. \tag{2}$$

3. DYNAMIC MODEL OF SUSTAINABLE DEVELOPMENT INDICATORS

According to the papers [12–14] dynamic model for indicators can be described by system of linear homogeneous differential equations

$$\begin{cases} \dfrac{\mathrm{d}I_1(t)}{dt} = a_{11}I_1(t) + a_{12}I_2(t) + \ldots + a_{1N}I_N(t), \\ \ldots \\ \dfrac{\mathrm{d}I_N(t)}{dt} = a_{N1}I_1(t) + a_{N2}I_2(t) + \ldots + a_{NN}I_N(t), \end{cases} \tag{3}$$

where, I_i, $i = 1,\ldots,N$, are indicators, describing factors of different areas, a_{ij}– coefficients that can be calculated employing statistical and algebraic methods.

Values of each indicator are taken in the certain time moments t_k, $k = 1,\ldots,n$, and then indicators are defined $I_{ik} = I_i(t_k)$, $i = 1,\ldots,N$.

Calculation of the coefficients of a system of Eq. (3) a_{ij}, $i,j = 1,\ldots,N$, is a complex task. Due to heterogeneity of data, one of the methods of estimating the coefficients is the standardization of the initial data. Therefore, it is further assumed that the initial data (indicators) are standardized. In the paper [12] several methods for calculation of coefficients a_{ij}, $i,j = 1,\ldots,N$, are proposed. Algebraic method has major limitation: the number of indicators and moments of time (when the values of indictors are recorded) has to be equal.

Augutis et al. [14] have shown that coefficients obtained by Ordinary Least Square Method (OLS) and applying Bayesian Method (BM) practically correspond, if moments of time $n \geq N - 1$. BM allows calculating all estimates of random parameters of the analyzed mathematical model with at least one observation value.

The expression of the solution of the system of differential Eq. (3) depends on eigenvalues λ of matrix A [15]. If eigenvalues are real and different numbers, the solution may be found according to the formula (4)

$$\mathrm{I}(t) = \sum_{\mathrm{j=1}}^{\mathrm{N}} C_j B_j e^{\lambda_j t} , \tag{4}$$

and if eigenvalues are complex numbers $\lambda_{2j-1} = x_j + iy_j$, $\lambda_{2j} = x_j - iy_j$, j = 1,…,N/2 (N is even number in this case) the solution may be found according to the formula (5)

$$\mathrm{I}(t) = \sum_{\mathrm{j=1}}^{\mathrm{N/2}} (\tilde{C}_{2j-1} B_{2j-1} e^{\lambda_{2j-1} t} + \tilde{C}_{2j} B_{2j} e^{\lambda_{2j-1} t}) , \tag{5}$$

where $B = (b_1, …, b_n)^{\mathrm{T}}$ – vector of constants, C_j – constants, $\tilde{C}_j$ – complex constants.

Also the solution for the system of Eq. (4) may be the combination of expressions from formulas (4) and (5).

In order to find a separate solution for the system of differential Eq. (3), i.e. particular expression of each indicator as a function depending on time, it is necessary to formulate the initial conditions. Constants C_j, j=1,…,N, at the time moment t_0, of general solution (4) and (5) may be obtained from the initial conditions

$$I_1(t_0) = I_1^0, …, I_N(t_0) = I_N^0 , \tag{6}$$

where I_i^0, i = 1,…, N, – standardized factual value of indicator at time moment t_0.

Assume that coefficient matrix A of differential Eq. (3) is normal, i.e., $\mathrm{P}^{-1}=\mathrm{P}^*$, here P is a matrix composed from eigenvectors of matrix A, P^* – joint matrix to matrix P. And if

$$\lambda_1 \leq … \leq \lambda_k < 0 \leq \lambda_{k+1} \leq … \leq \lambda_N ,$$

then evaluation of stability of the solution of the system (3) is

$$\|\mathrm{I}(t)\|_2 \leq \mathrm{e}^{|\lambda_1| t} \|\mathrm{I}(0)\|_2 . \tag{7}$$

The future changes of any indicator in the system can be estimated by employing the created dynamic model. Furthermore, data and influence of various new objects that will be constructed can be involved in this model.

The data of small new objects, the construction on which is planned in the nearest future, may be included in the dynamic model via the initial conditions (6). In that case, a new separate solution for the system of differential Eq. (3) should be found using the parameters of the new objects as initial conditions. However, the application of this method requires having the estimates of all indicators in case of the new object without any uncertainties.

Since technical parameters of new objects are not exactly known, these uncertainties should be reflected in the initial conditions. Thus, in such conditions, the values of indicators are random variables. Consequently, the solution (4) is also a random variable and $\{I_i(t)\}_{t \geq 0}$ a stochastic process [16]. For any t≥0, let as denote the probability density function of the probability distribution of $\mathrm{I}_i(t)$:

$$\mathrm{P}[\mathrm{I_i}(t) \leq x] = \int_{-\infty}^{x} u_i(t_0, s)\mathrm{d}s\,. \tag{8}$$

Assume that the initial values (6) are random variables and have a known probability distributions with density $u_i(t_0)$. The probability density function $u_i(t)$ associated with the random state $I_i(t)$ on a finite interval $t \in [0,T]$ represents a separate solution for the system of differentia Eq. (3).

In probability theory it is well known that Bayesian method (BM) allows a combination of two kinds of information: prior (for instance, generic statistic data, subjective option of experts) and measurements or observations. Application of BM allows taking into consideration the uncertainties, which are related to indicator values given by experts. Moreover, BM can serve for calculation of all specified estimates of model parameters when at least one value of the analyzed indicator system is available (does not require having a new information on the values of all factors involved in the model). In this case, non-stationary process (NP) is analyzed, as the values of indicators depend on time t, i.e., are expressed by functions, dependent on time t.

Expert judgment – probable mean values of indicators time t^*: $I(t^*) = (I_1^*, \ldots, I_N^*)$, with standard deviations σ_i, $i = 1, \ldots, N$, that represent uncertainties. C_i , $i = 1, \ldots, N$, in (4) or (5) solution for the system of differentia Eq. (3) are independent random variables, with prior probability density functions (pdfs) $p_i\,(x_i)$, $i = 1, \ldots, N$.

In this way, posterior probability density function

$$u(x_1,\ldots,x_n \mid I_k^*) = \frac{u(x_1,\ldots,x_n)\cdot L_k(I_k^* \mid x_1,\ldots,x_n)}{\int\limits_{D_1}\ldots\int\limits_{D_n} u(u_1,\ldots,u_n)\cdot L_k(I_k^* \mid u_1,\ldots,u_n)\mathrm{d}u_1\ldots\mathrm{d}u_n}, \tag{9}$$

where D_i – the range of values of random C_i , $i = 1,\ldots,N$; $\mathrm{L_k}(\cdot)$ – likelihood function.

It should be noted that Bayes' formula, which was defined by Eq. (9), could be used for recalculating of random C_i density function when a new value of indicator I_k is obtained: assuming the posterior density function as a prior.

4. NUMERICAL EXAMPLE

Sustainable development become one of the key guiding principles in the European Union strategy. Currently, the vision of European Commission on sustainable, low-carbon, climate friendly, competitive economy requires establishment of the Energy Union. A key question in sustainable development policies is to establish suitable indicators in order to simplify, quantify, analyze and communicate complex and complicated information. Statistical Office of the European Communities (Eurostat) is one of the international organizations, which are concerned about sustainable development indicators. One can easily find statistical data of classified indicators its' website.

Sustainable development indicators from Eurostat database will be analyzed as an example. Four indicators (Lithuanian case) were chosen for the presentation of proposed method. Indicator I_1 (main Gross Domestic Product (GDP) euro per capita) is related to socioeconomic development, indicator I_2 (employment rate of older workers) describe demographic changes, indicator I_3 (greenhouse gas emissions) and I_4 (primary energy consumption) are related to environmental development. The standardized statistical data on those indicators in Lithuania in 1998–2013 were used for calculations.

Coefficients a_{ij}, $i,j = 1,\ldots,4$, of a system of differential Eq. (3) were calculated using the Ordinary Least Square (OLS) method. It is applied assuming that the elements in main diagonal of the system matrix are $a_{ij} = 0$, $i = j = 1,\ldots,4$. OLS can be applied in case the number of factual values of observed indicators n = 16: $n \geq N - 1 = 3$. In this case, all collected statistical data on analyzed indicator values can be used for calculations. Obtained matrix $A = \{a_{ij}\}_{i,j=\overline{1,4}}$ is normal.

Two secenarios were investigated regarding practical demonstration of the proposed method on how to involved changes in system configuration i.e. expert judgement, into a model:

Scenario 1 (SC1) – basic scenario, which means that there are no changes in the future;

Scenario 2 (SC2) – in 2014 GDP increses by 10% (in comparison with indicators values in 2013) and others values not changed at all.

According to the SC1 (if changes in the system do not apear at all) the separate solution of the system (3) is calculated with the initial conditions (6) using standatrized factual data of the year 2013.

The influence of SC2 on sustainability indicators values were performed in two ways: using BM and analyzing system of Eq. (3) with random initial conditions.

Suppose that at the time moment t, probability distributions of indicators $I_i(t)$ are normal, their mean values satisfy Eq. (4).

Applying BM we assume that C_i, i = 1,2,3,4, are independent random variables. In case of normal distribution of indicators, probability distributions of random variables C_i are normal as well with means equal to values that are calculated for 2013, i.e. general solution of the system of Eq. (3).

Using the stability estimate of the solution of the system of differential Eq. (7), the stability of solution of all dynamic models was checked, and it was revealed that all solutions are stable.

The results of forecasted values of four sustainable development indicators are presented in Fig. 1. Solid line curves represent indicators values in case of SC1 (without any changes in the future). Another two line curves describe indicators behaviour in case of SC2: dashed was obtained applying BM, doted – using dynamic model with random initial (RI) conditions.

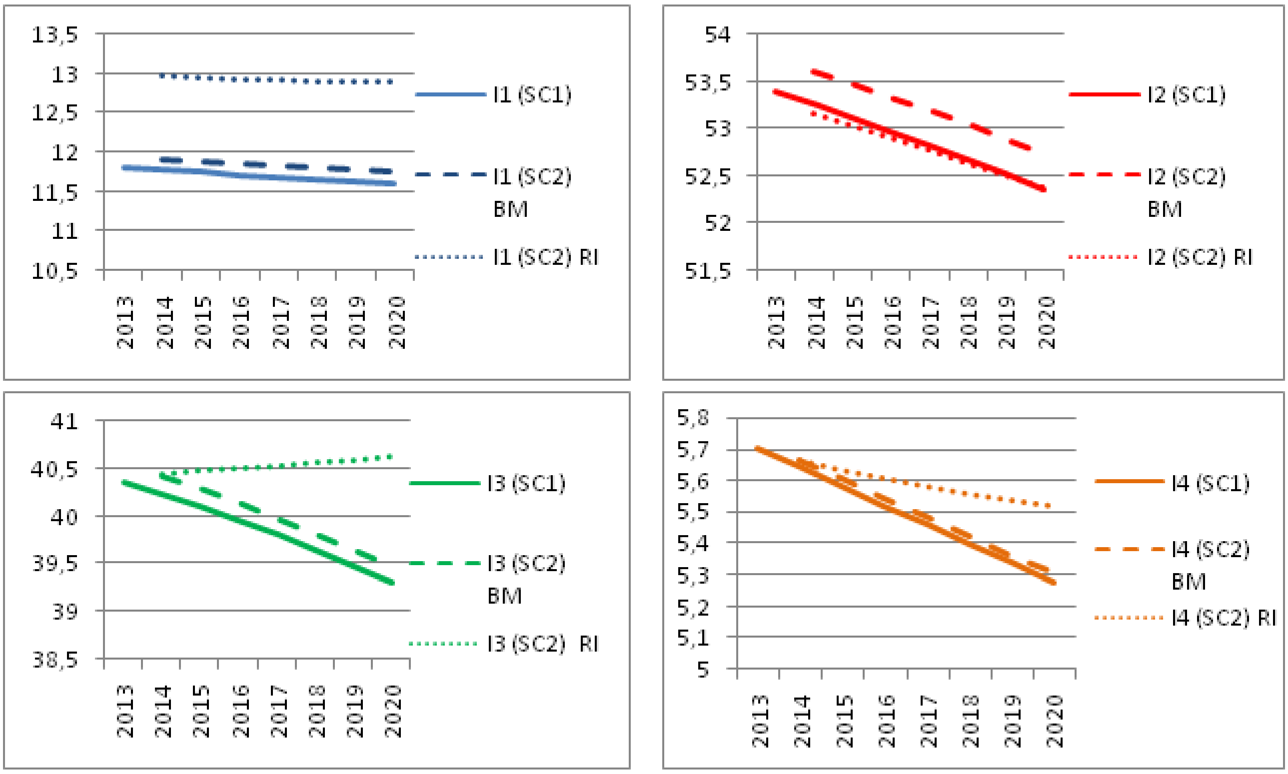

Fig. 1. Forecasted values of indicators

In case of both scenarios the forecasted values of indicator I_2 are almost the same, also we can observe that I_2 values are decreasing. In case of SC1 and SC2 applaying BM indicators I_1, I_3, I_4 retain the same decreasing tendency and their values are almost the same. SC2 include the rise in I_1.

This assumption become visible in forecasted values of I_1 using dynamic model with random initial conditions. In Fig. 1 we can observe that if I_1 is growing I_3 and I_4 will also increase.

The obtained values of sustainability indicators can be used for assessment of sustainable development level according to the Eq. (1). Integrated sustainability indicator (*ISI*) was calculated in three ways and results are presented in Fig. 2. Considered on SC2 the *ISI* undeniably should increase. If we take into account indicators values which were obtained using BM, we can see (in Fig. 2) that *ISI* become lower compared with SC1. This type of situation is inappropriate. Therefore, it is advisable to use dynamic model with random initial conditions in order to forecast sustainability indicators values in case of any impact on the system.

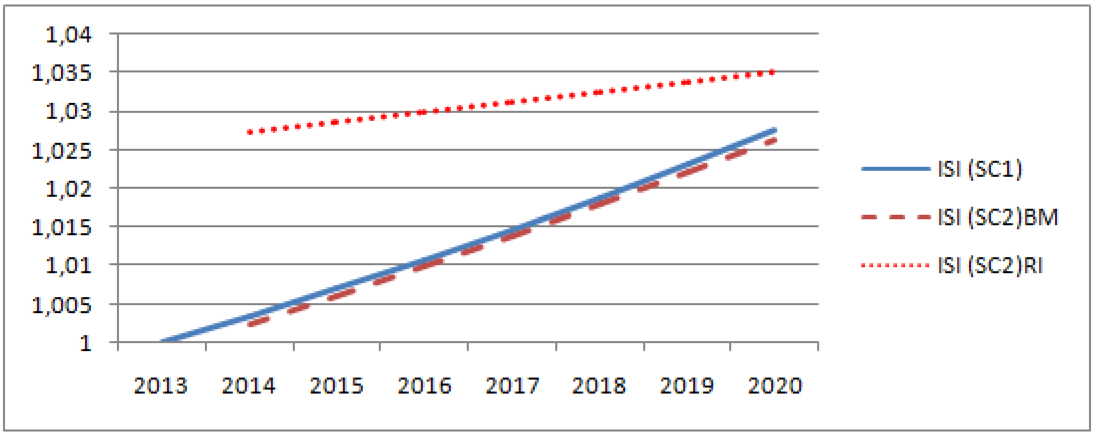

Fig. 2. Forecast of integrated sustainability indicator

5. CONCLUSIONS

One of the most important concerns of society is a decision making especially on sustainable development issues. However, we do not know if we are becoming more sustainable without finding a way to measure it. There are many methodologies, models, approaches, and appraisals for assessing sustainability. Many of research analyzed only monitoring for sustainable development. In a monitoring process, calculations of the sustainable indicators help us to understand in which area action is needed. Furthermore, we should find the way to evaluate the consequences of this interaction. It is advisable to have forecasting methods for sustainable development indicators. In this article the use of dynamic model is proposed. As an example, dynamic model of four indicators in Lithuania was used to present the impact of two scenarios on integrated sustainability assessment indicator (ISI) in the future. If we do not change anything (SC1) we can notice slow growth of ISI. If there will be changes in the system, we should use the dynamic model with random initial conditions for predicting values of sustainability indicators. According to the second scenario ISI instantly grew in 2014 and it is continuing to increase.

6. REFERENCES

1. World Commission on Environment and Development (WCED), *Our Common Future*, New York: Oxford University Press, 1987, 8 p.
2. KATES, R. W., PARRIS, T. M., LEISEROWITZ, A. A. What is Sustainable Development? Goals, indicators, values, and practice. April 2005 issue of Environment: Science and Policy for Sustainable Development, 2005, Vol. 47, No. 3, p 8–21.
3. NEAG, M. –M., BUCATA, G. Globalization and Sustainable Development. *Revista Academiei Fortelor Terestre*, 2015, Vol. 77, No. 1, p. 16–19.

4. United Nations. *The Johannesburg Declaration on Sustainable Development*. New York: NGO Committee on Education, 2002.
5. *The Future We Want Rio+20 Outcome Document.* United Nations, 2012- [referred on the 14th of January 2016 y.]. Link to the internet <http://www.slideshare.net/uncsd2012/the-future-we-want-rio20-outcome-document>.
6. International Atomic Energy Agency. *Energy indicators for sustainable development: guidelines and methodologies*. Vienna: IAEA, 2005.
7. WANG, Q., YUAN, X., ZHANG, J., GAO, Y., HONG, J., ZUO, J., LIU, W. Assessment of the Sustainable Development Capacity with the Entropy Weight Coefficient Method. *Sustainability*, 2015, Vol. 7, p. 13542–13563.
8. POVEDA, C.A., LIPSETT, M. G. A Review of Sustainability Assessment an Sustainability/Environmental Rating Systems and Credit Weighting Tools. *Journal of Sustainable Development*, 2001, Vol. 4, No. 6, p. 36–55.
9. GARCIA-ALVAREZ, M. T., MORENO, B., SOARES I. Analyzing the sustainable energy development in the EU-15 by an aggregated synthetic index. *Ecological Indicators*, 2016, Vol. 60, p. 996–1007.
10. LUTYNSKA, A. E. Review of methods for measuring sustainable development. CYSENI 2015. Proceedings of annual conference of young scientists on energy issues. [CD]. Kaunas: Lithuanian Energy Institute. 2015 May 27–28.
11. ŠTREIMIKIENĖ, D., GIRDZIJAUSKAS, S., STOŠKUS, L. Sustainability Assessment Methods and Their Application to Harmonization of Policies and Sustainability Monitoring. *Environmental Research, Engineering and Management*, 2009, Vol. 48, No. 2, p. 51–62.
12. AUGUTIS, J., KRIKŠTOLAITIS, R., LUTYNSKA, A. E., PEČIULYTĖ, S., ŽUTAUTAITĖ, I. Evaluation of Coefficients for Energy Security Indicators System. SAFE – 2013. Proceedings of the 5th international conference on safety and security engineering. Rome. 2013 September 17–19.
13. KRIKŠTOLAITIS, R., LUTYNSKA, A. E., PEČIULYTĖ, S., ŽUTAUTAITĖ, I. Involvement of expert judgement in dynamic model. ESREL 2014. Proceedings of the European Safety and Reliability Conference. Wroclaw. 2014 September 14–18.
14. AUGUTIS, J., KRIKŠTOLAITIS, R., PEČIULYTĖ, S., ŽUTAUTAITĖ, I. Dynamic model based on Bayesian method for energy security assessment. *Energy Conversion and Management*, 2015, Vol. 101, p. 66–72.
15. GOLOKVOSČIUS P. *Diferencialinės lygtys*. Vilnius, TEV, 2000.
16. WEIßE, A. Y. *Global Sensitivity Analysis of Ordinary Differential Equations*. Berlin, 2009.

CYSENI 2016, May 26-27, Kaunas, Lithuania
ISSN 1822-7554, www.cyseni.com

EFFECT OF GEOMETRICAL SHAPE AND BOUNDARY CONDITION ON STRESS DISTRIBUTION AND DEFORMATION IN OPHTHALMIC ARTERY NUMERICAL MODEL

Edgaras Misiulis, Algis Džiugys
Lithuanian Energy Institute
Laboratory of Combustion Processes
Breslaujos str. 3, LT-44403 Kaunas – Lithuania
Email: edgaras.misiulis@lei.lt

ABSTRACT

Intracranial pressure (ICP) – is a pressure inside human skull and thus in the brain tissue and cerebrospinal fluid (CSF). Increased ICP values could lead to irreversible secondary brain damage. Two-Depth Transcranial Doppler non-invasive measurement method (nICP) allows absolute intracranial pressure determination by implementing blood flow velocity measurement at different ophthalmic artery (OA) segments and then calculating any measurement angle independent index etc. pulsatility index (PI), resistivity index (RI), which in turn correlates with ICP. nICP method was clinically tested in conjunction with invasive gold standard CSF pressure measurement technique and it was found that nICP works within clinically accepted tolerance range, although it is fundamentally important to investigate error occurrence patterns. These errors may occur due to indexes etc. PI dependence on many parameters such as arterial pressure pulsatility, cerebral resistance, compliance of the big vessels and also on the stress distribution induced cross-sectional area differences of ophthalmic artery at different measurement sites of OA.
In this paper commercial COMSOL module Fluid-Structure Interaction (FSI) was used to study stress distribution induced cross-sectional area differences in OA's intracranial and extracranial parts. Two models were created: 1) ophthalmic artery's lengths of its different parts were unequal (intracranial part, optic canal, extracranial part lengths were 4, 12, 10 mm accordingly. 2) all parts were 10 mm in length. Internal and external pressures were changed according to reviewed other authors works.

Keywords: hemodynamics, fluid-structure interaction (FSI), intracranial pressure (ICP), ophthalmic artery (OA)

1. INTRODUCTION

Assessed clinical research has shown that in most case human ophthalmic artery crosses several different segments; intracranial segment, which is inside the skull, optic canal segment, which is in between the intracranial and extracranial segments, and extracranial segment, which lies in the eye socket [1]. These segments are affected by different pressures - *ICP* (intracranial pressure) affects intracranial segment, *Pe* (Pressure external) affects extracranial segment. Since the ophthalmic artery is relatively short (up to 3 mm length), it is assumed, that mechanical properties does not vary across artery's length and pressure acting on different artery segments, on average, will deform uniformly, and average velocity will change dependently, if the operating environment mechanical properties are similar [2]. Using these features Kaunas Technology University researchers in cooperation with the Lithuanian Energy Institute researchers have developed a device permitting indirect measurement of absolute intracranial pressure. A special mask is put on a patient's head and pressure *Pe* is raised following near stepwise function while simultaneous measurements of blood flow velocity in a different ophthalmic artery segments are carried out. Comparative non-dimensional indices (CNI) are calculated, for example PI (pulsatility index), RI (resistivity index) or others. Clinical assessments have shown, that approximately similar CNI value at different segments corresponds to the condition, when *ICP* = *Pe* [3], although influence of ophthalmic artery's mechanical properties due to applied pressure is still in need of further research For this purpose we performed numerical investigation.

A theoretical one dimensional model of blood flow in an arteries using finite element method was implemented by *Tomas Tekorius* [4]. *Harvey Ho et. al.* [5] employed an open source software CMGUI (www.cmiss.org/cmgui) to digitize centreline of the ophthalmic artery and a few other major arteries (ICA, ACA, MCA) using key nodes and a one-dimensional cubic Hermite mesh from a Computed Tomography Angiography (CTA) image. Although in their study patient-specific case was investigated, though for simplicity artery wall was assumed as rigid.

F. Auricchio [6] investigated two different mechanical models for artery tissue behaviour: model HI – homogeneous, single-layer, isotropic model and model HA – non-homogeneous, single-layer, fiber-reinforced anisotropic model. Although luminal blood pressure was neglected.

The aim of this work is to investigate ophthalmic artery numerical models boundary conditions influence on arterial mechanical deformations and stress distribution.

2. METHOD

To achieve the aim, primary numerical fluid-structure interaction model of three-dimensional ophthalmic artery was implemented using COMSOL Multiphysics software package. Four studies, in which ophthalmic artery's length [1, 7, 8] was changed, were carried out: a) intracranial: 4 mm, optic canal: 12 mm, extracranial: 10 mm, b) all three segments are of equal length: 8.667 mm, and also a1), b1) near stepwise raise function was implemented in an inner part of ophthalmic artery, when outside pressure was held constant, and in a cases of a2), b2) near stepwise raise function was implemented in an outer part of ophthalmic artery when inside pressure was held constant.

2.1. Lengths of ophthalmic artery segments are non-equal a1) and a2) cases. Stationary case study

a1), a2) ophthalmic artery segments length: intracranial $L_{IOA} =$ 4 mm, optic canal $L_{OC} =$ 12 mm, extracranial $L_{EOA} =$ 10 mm, the total artery length $L_{OA} =$ 26 mm; artery diameter $d_{OA} =$ 1.45 mm. Initial pressure acting on a system was equal to 1 standard atmosphere, absolute pressure was equal the sum of initial pressure and added or applied pressure. In the a1) study, the added inner pressure was changed by stepwise function in a range from 0 to 120 mmHg with a step of 20 mmHg, outer added pressure was held constant and equal to 0 mmHg. In the a2) case the added outer pressure was held constant and equal to 0 mmHg, while added inner pressure was changed by stepwise function in a range from 0 to 120 mmHg with a step of 20 mmHg.

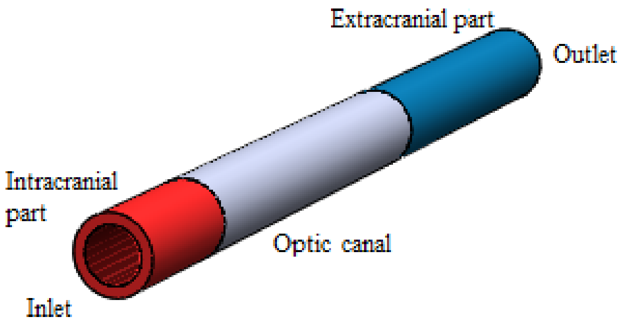

Fig. 1. Ophthalmic artery geometry in a1) and a2) case, when segments are of non-equal lengths

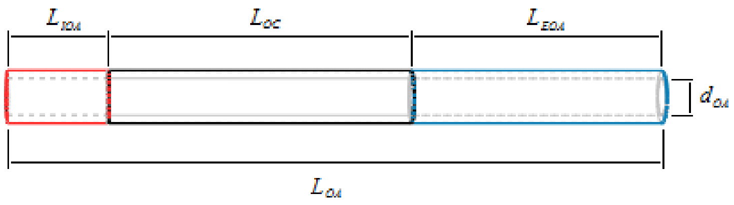

Fig. 2. a1), a2) geometry scheme

2.2. Equal arterial segments lengths of b1) and b2). Stationary case study

b1), b2) ophthalmic artery segments length were equal: intracranial $L_{IOA} = 8.667$ mm, optic canal $L_{OC} = 8.667$ mm, extracranial $L_{EOA} = 8.667$ mm, the total artery length $L_{OA} = 26$ mm; artery diameter $d_{OA} = 1.45$ mm. Initial pressure acting on a system was equal to 1 standard atmosphere, absolute pressure was equal the sum of initial pressure and added or applied pressure. In the b1) study, the added inner pressure was changed by stepwise function in a range from 0 to 120 mmHg with a step of 20 mmHg, outer added pressure was held constant and equal to 0 mmHg. In the b2) case the added outer pressure was held constant and equal to 0 mmHg, while added inner pressure was changed by stepwise function in a range from 0 to 120 mmHg with a step of 20 mmHg.

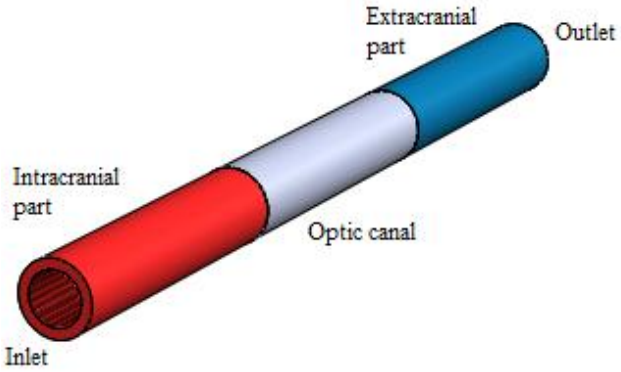

Fig. 3. Ophthalmic artery geometry in a b1) and b2) case, when segments are of equal lengths

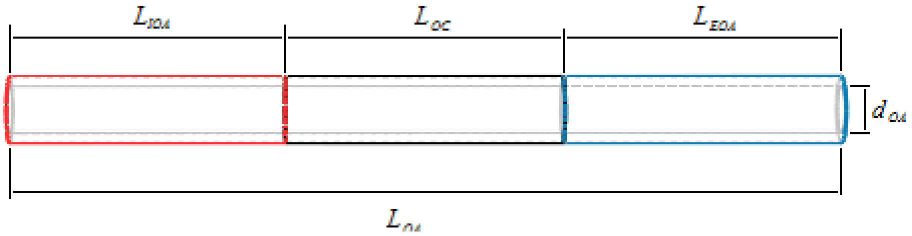

Fig. 4. b1), b2) geometry scheme

2.3. Boundary conditions of ophthalmic artery numerical model

Numerical model was implemented following assumptions, that arterial wall is homogeneous, isotropic, incompressible and exhibits hyperelastic properties [6]. Fluid is assumed to be homogeneous, nearly incompressible and with constant viscosity (Newtonian fluid) [9].

Boundary conditions for numerical studies a1), a2), b1), b2) differed in outer artery wall and inlet boundary conditions. The summary of the boundary conditions used are provided in Table 1. Initial conditions: fluid velocity in all directions was equal to 0, system was exposed to 1 standard atmospheric pressure and initial arterial wall movement in all directions was equal to 0.

Table 1. Implemented boundary conditions

Boundary condition	Range (initial value; step value; final value)	Units
Inlet pressure a1), b1)	(40;20;120)	mmHg
Outlet pressure a1), b1)	(40;20;120)	mmHg
Intracranial pressure (ICP) a2), b2)	(40;20;120)	mmHg
Extracranial pressure (Pe) a2), b2)	(40;20;120)	mmHg
Outer wall of the optic canal	Free movement	-
Inner fluid-structure interaction boundary	$u_{fluid} = 0$	-
Fluid mesh movement in the inlet and outlet boundaries	Displacement is equal to 0 in x direction	-

Numerical model was implemented using COMSOL Multiphysics software package, which solves following Navier-Stokes equations [10]:

Momentum equation:

$$\rho(\mathrm{u}_{\mathrm{fluid}} \cdot \nabla)\mathrm{u}_{\mathrm{fluid}} = \nabla \cdot [-p\mathrm{I} + \mu(\nabla \mathrm{u}_{\mathrm{fluid}} + (\nabla \mathrm{u}_{\mathrm{fluid}})^T)] + \mathrm{F} \tag{1}$$

where ρ – the density of the fluid, $\mathbf{u}_{\mathrm{fluid}}$ – the velocity of the fluid, p – pressure, ∇ – nabla operator (in this case $\left(\frac{\partial}{\partial x}, \frac{\partial}{\partial y}, \frac{\partial}{\partial z}\right)$), **I** – identity matrix, μ – dynamic viscosity.

Continuity equation:

$$\rho \nabla \cdot \mathrm{u}_{\mathrm{fluid}} = 0 \tag{2}$$

Equations describing mechanical properties of hyperelastic body [10]:

Volumetric deformation equation:

$$-\nabla \cdot \sigma = \mathrm{F}_{\mathrm{V}} \tag{3}$$

where $\mathbf{F}_{\mathrm{V}}$ – tensor of volumetric deformation.

Cauchy stress tensor:

$$\sigma = \mathrm{J}^{-1}\mathrm{FSF}^T, \tag{4}$$

where **F** – deformation gradient tensor, **S** – second Piola-Kirchhoff stress, J – determinant of deformation gradient tensor.

$$\mathrm{F} = (\mathrm{I} + \nabla \mathrm{u}_{\mathrm{solid}}), \tag{5}$$

$$\mathrm{J} = \det(\mathrm{F}), \tag{6}$$

$$S = \frac{\partial W_s}{\partial \epsilon}, \tag{7}$$

where W_s – elastic strain energy density.

Neo-Hookean model for nearly incompressible material uses following equation:

$$W_s = \frac{1}{2}\mu(\bar{I}_1 - 3) + \frac{1}{2}\kappa(J_{el} - 1)^2, \tag{8}$$

where μ – second Lame parameter, κ – initial bulk modulus, $\bar{I}_1$ – isochoric invariant, J_{el} – elastic volume ratio.

$$\epsilon = \frac{1}{2}[(\nabla \mathrm{u}_{\mathrm{solid}})^T + \nabla \mathrm{u}_{\mathrm{solid}} + (\nabla \mathrm{u}_{\mathrm{solid}})^T \nabla \mathrm{u}_{\mathrm{solid}}], \tag{9}$$

where ϵ – strain tensor.

Mechanical properties of different ophthalmic artery segments as also different mechanical properties of operating environment, or numerical models boundary conditions could influence $ICP = Pe$ condition. Assuming that mechanical properties of ophthalmic artery and operating environment are similar, only numerical model boundary conditions influence on $ICP = Pe$ condition remains. In this paper boundary condition, influence is labelled as ΔPe. Intracranial pressure equation then can be written as:

$$ICP = Pe + \Delta p + \Delta Pe, \tag{10}$$

where Δp is pressure drop across measurement zones.

2.4. Mesh verification

Mesh verification was performed to check its influence on numerical simulation results. In accordance with exponential functions presented in (Table 2), 15 Mesh parameters were parametrically changed. Considered case, when additional pressure in all segments was zero. Mesh consisted of tetrahedral, prism, triangular, quadrilateral, edge and vertex elements. Element count was increased in accordance with relative mesh element count, in a range from 0 to 3 with step 1, then up until 4 with a step of 0.5 and the final calculation was performed on 4.3 with a step of 0.3, where 0 corresponds to 14696 elements and element fraction volume 0.05157, and 4.3 corresponds to 688444 element and element fraction volume 0.003284. Verification parameter was ophthalmic artery centre's cross-sectional area.

Further investigation on ophthalmic artery wall deformation and stress distribution was carried out with a mesh generated using relative mesh element count value of 3.

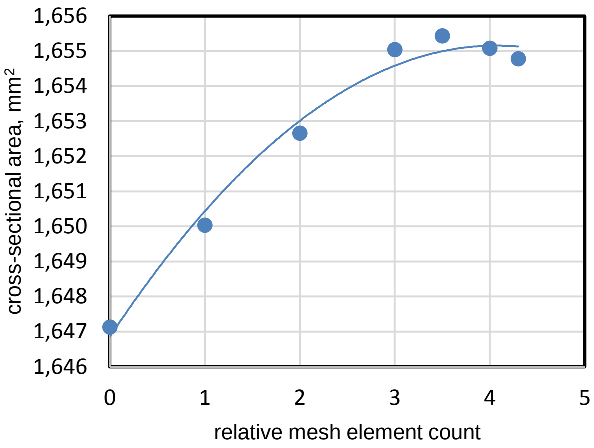

Fig. 5. Cross-sectional area dependence on relative mesh element count

Table 2. Mesh parameters

Parameter usage	System parameter	Function
Artery wall	max. element size	$0.0055e^{-0.374*mq}$
	min. element size	$0.0017e^{-0.664*mq}$
	max. element growth rate	$1.9215e^{-0.053*mq}$
	curvature factor	$1.1496e^{-0.191*mq}$
	resolution of narrow regions	$0.1488e^{0.2609*mq}$
Fluid	max. element size	$0.0009e^{-0.359*mq}$
	min. element size	$0.0004e^{-0.525*mq}$
	max. element growth rate	$1.4055e^{-0.036*mq}$
	curvature factor	$1.2857e^{-0.167*mq}$
	resolution of narrow regions	$0.2891e^{0.1629*mq}$
Fluid-structure interface	max. element size	$0.0004e^{-0.356*mq}$
	min. element size	$0.000045e^{-0.405*mq}$
	max. element growth rate	$1.274e^{-0.027*mq}$
	curvature factor	$1.0153e^{-0.205*mq}$
	resolution of narrow regions	$0.4591e^{0.1152*mq}$

3. RESULTS

Ophthalmic artery deformation and stress distribution due to different pressure added at different segments is presented in (Fig. 7).

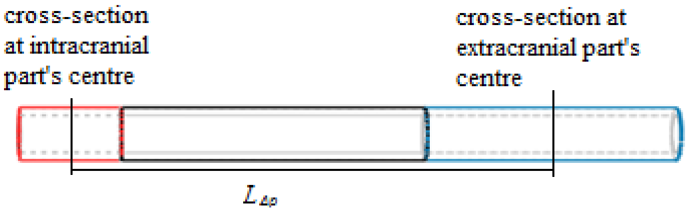

Fig. 6. Centre cross-sections of intracranial and extracranial parts of ophthalmic artery

Estimated Δp value was equal to 1.32 mmHg. Δp corresponds to pressure drop in a LΔp distance, which directly influences absolute pressure in a segment. Boundary condition influence ΔPe was estimated by solving equation (10) $ICP = Pe + \Delta p + \Delta Pe$, results shown in (Fig. 8).

It was found that in a1), a2), b2) cases the absolute value of ΔPe was increasing due to increasing boundary condition affection on different parts of the ophthalmic artery. The average ratio of applied pressure and resulting ΔPe in a two geometrically similar cases, when segments of ophthalmic artery were of non-equal lengths (a1) and a2) cases), was 0.5% and 0.35% respectively, while in b1) and b2) cases, when segments of ophthalmic artery were of equal lengths, was 0.05% and 0.04% respectively. In either case ΔPe was not of a significant cause in the equation (10), only more than 4% would introduce marginal erroneous contribution to the model results.

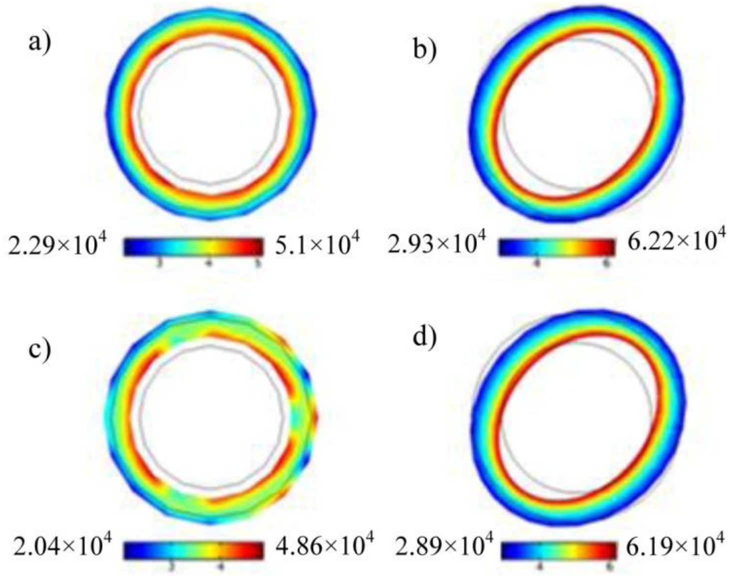

Fig. 7. Ophthalmic artery wall stress (Pa) and deformation at the centres of cross-sectional areas (Fig. 6), due to different added pressures. Grey circles indicate the artery shape before deformation. Fig. 7 a and c shows a cross-section that goes through intracranial part centre in a1) and a2) cases, when inside pressure was equal to 60 mmHg, outside 0 mmHg. Fig. 7 b and d shows cross-section that goes through extracranial part's centre in b1) and b2) cases, outside pressure was equal to 60 mmHg, inside pressure to 0 mmHg

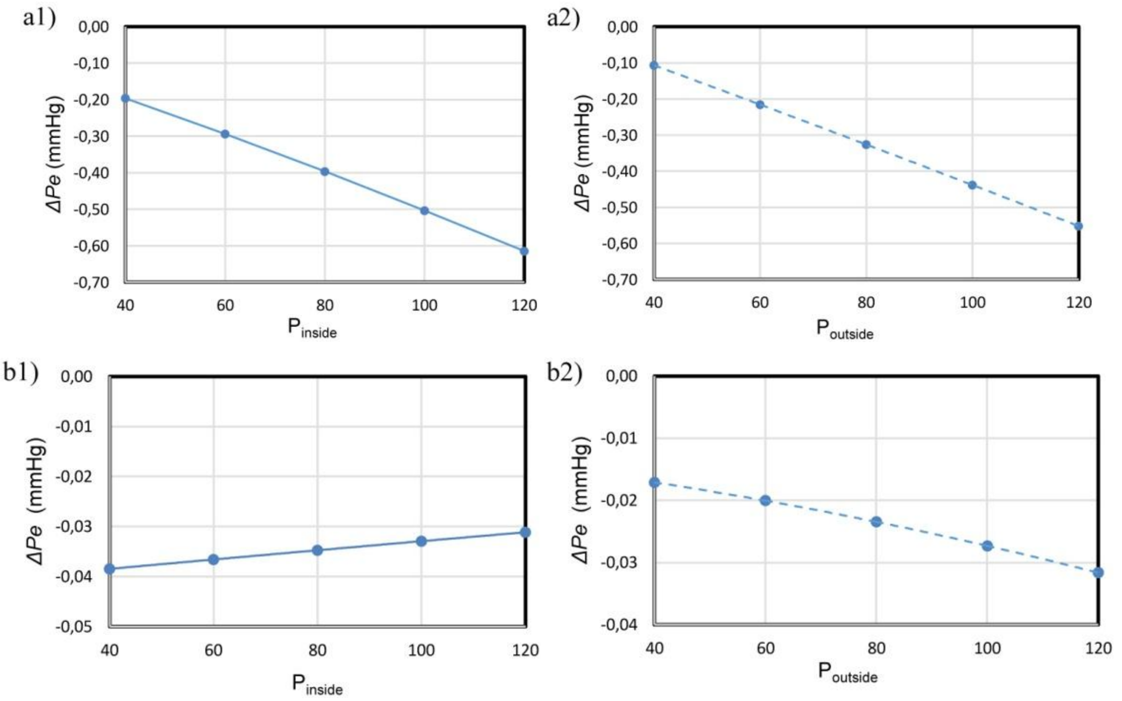

Fig. 8. Presented research on $\boldsymbol{\Delta Pe}$ (boundary conditions influence) dependence on the operating system when additional pressure is added in a1), a2), b1), b2) cases

In the b1) case absolute value of ΔPe decrease could be related to mesh reconfiguration, although the average ratio of applied pressure and resulting ΔPe is non marginal (0.05%).

4. CONCLUSIONS

1. Cross-sectional area changes according to acting inside pressure, while maintaining its primal geometrical shape (a circle). External pressure forces ophthalmic artery to change it to oval shape. Stresses in both cases are higher on the artery’s inside part and decreases going towards the outer part.
2. It was found that when the segments lenghts are equal, resulting boundary condition influence – ΔPe values are lower (-0.04 to -0.016 mmHg, when P varies from 40 to 120 mmHg) than at different segments of lengths (0.61 to -0.1, P varies from 40 to 120 mmHg).
3. Boundary condition induced stresses and influence on $ICP = Pe + \Delta p + \Delta Pe$ was not of a significant cause: 0.5% and 0.35% in a1) and a2) cases respectively, and 0.05% and 0.04% for the b1) and b2) cases respectively. Only more than 4% would introduce marginal erroneous contribution to the model results.

5. REFERENCES

1. HAYREH, S. S. Orbital vascular anatomy. Eye, 2006, Vol. 20, pp. 1130–1144.
2. RAGAUSKAS, A., DAUBARIS, G., DZIUGYS A. Innovative non-invasive method for absolute intracranial pressure measurement without calibration. Acta Neurochir. Suppl., 2005, Vol. 95, p. 357-361.2011. Vol. 25. No.6. P. 2469–2480.
3. RAGAUSKAS, A., MATIJOSAITIS, V., ZAKELIS, R. Clinical assessment of noninvasive intracranial pressure absolute value measurement method. Neurology, 2012, Vol. 78, p. 1684–1691.
4. TEKORIUS, T., “Investigation of mathematical model of blood vessel”, Biomedicininė inžinerija, pp. 44–47, 1997.

5. HO, H., MCGHEE, C., HUNTER, P., “Numerical analysis for the blood flow in a patient-specific ophthalmic artery”, Medical Engineering and Physics, No. 34, pp. 123–127, 2012.
6. AURICCHIO, F., CONTI, M., FERRARA, A., MORGANTI, S., REALI, A. Patient-specific finite element analysis of carotid artery stenting: a focus on vessel modeling. International Journal for Numerical Methods in Biomedical Engineering, 2012.
7. X. LIU IR C. ZHOU, „CT anatomic measurement of the optic canal its clinical significance”, 2000.
8. N. KOCABIYIK, F. YAZAR, „The intraorbital course of ophthalmic artery and its relationship with the optic nerve”, Neuroanatomy, t. 8, pp. 36–38, 2009.
9. K. AMBARKI,P. HALLBERG, „Blood Flow of Ophthalmic Artery in Healthy Individuals Determined by Phase-Contrast Magnetic Resonance Imaging“, Investigative Ophthalmology & Visual Science, t. 54, nr. 4, pp. 2738–2745, April 2013.
10. COMSOL Manual on One-Phase Fluid Flow; Hyperelastic material models, 2016.

CYSENI 2016, May 26-27, Kaunas, Lithuania
ISSN 1822-7554, www.cyseni.com

CASE STUDY – THE IMPORTANCE AND THE IMPACT OF THE COGENERATION PROJECT IN REDUCING ATMOSPHERIC EMISSIONS IN THE CITY OF PRISTINA

Fisnik Osmani
University of Mitrovica, Faculty of Mechanical Engineering and Computers,
Address: Fabrika e Akumulatorëve, 40000 Mitrovica – Kosovo
E-mail: fisnik.osmani@umib.net

Atanas Kochov
University of Skopje, Macedonia
Karpos II b.b. P.O.Box 464, 1000 Skopje – Macedonia
E-mail: atanas.kochov@mf.edu.mk

ABSTRACT

As we know, the term cogeneration means the combined production of electricity and thermal energy. Undoubtedly, we are living at a time when the demand for energy is at its peak. Today, we cannot imagine living without energy, whether it is electrical, thermal or of any other form. However, the production of energy is not always friendly to the environment, especially when the raw material used for energy is heavy oil, as in our case study. Last year Pristina, has started supplying thermal energy through cogeneration project, project which has two thermal stations, one at the TPP Kosovo B (HES – Heat Extracted Station) where steam is extracted from medium and low pressure turbines and than heat exchange will take place through a system of steam-water exchange at the heat exchanger , and the other station (HRS – Heat Recived Station) constructed at the District Heating "Termokos" where heat exchange will take place through a system of water-water exchange. Surely the entire system is traversed by pre-insulated pipes of DN 600/800 with a total length of 11.4 km.

We focused on the role played by co-generation project on the preservation of the environment in general, particularly in improving air quality, removing the production of thermal energy from heavy oil, and replacing it with the installation of the system co-generation. Of course, in addition to many other benefits that the project of co-generation has for the city, among the most important benefits is the improvement of the air quality, considering that for 14 years, on average 12,000 of heavy oil were spent per season.

Also, we will analyse the thermal energy production in Prishtina throughout 14 years starting with the heating season of 2001/2002 until the heating season of 2014/2015, when heating in Prishtina started operating the new co-generation system

Keywords: Environmental, Air Pollutant, Energy, Cogeneration Project, Analyse

1. INTRODUCTION

During the burning of different fuels in air different pollutants are emitted, such as, sulfur dioxide, carbon monoxide, nitrogen oxides and others who endanger the quality of the air. Researching and monitoring air quality in urban and industrial areas is one of the basic steps of the solution, where in most countries of the world, the problem of air polution is present. Monitoring and controling air quality aims to reduce the content of harmful substances in it. Air pollution affects not only air quality, but also indirectly the quality of groundwater, land, vegetation, forest and climate [1].

In the city of Prishtina, air pollution appears from burning coal (lignite) in Kosovo power plant and fuel oil combustion in the heat of the city, which releases a considerable amount of sulfur. Conditions for maintaining air quality in this area are very unfavorable due to high emissions of SO2, dust, and other pollutants, as well as due to unfavorable terrain.

The most reliable method for determining the emissions of pollutants discharged into the air is measurement. The values obtained by measuring the concentration of SO_2, NOx and CO gasses are necessary to recalculate the content reference oxygen from 3% to 3% liquid fuel compared with the limit values set out in the Regulation on limit values for emissions into the air from combustion plants [2]. Emissions are calculated depending on the amount of fuel consumed and the corresponding emission factor. For the calculation of emissions of pollutants the approach “bottom-up” is used, by which the total emissions in any territory (region) is determined by the aggregation (joining) of the emissions of all the individual sources in the defined territory.

In this paper our focus is on emissions caused by heating of Prishtina “Termokos”, as enterprise specialized in providing heat. Data on the quantities of spent fuel (fuel oil) and measured direct emissions of SO_2, NOx and CO have been taken from the table overview of the measurement results.The city’s “District Heating” supplies about 12,000 customers (about 11,500 households and 1,000 business entities-public institutions) [3]. This heating of hot objects approximately 1/5 of Prishtina and the rest, heating use traditional fuels (wood, coal, fuel oil, oil, electricity, etc.). Two years ago they started using cogeneration heating process in the city. This project is expanding and it has has brought benefits to the city in terms of environmental protection because the heat is not combustion in boilers, and therefore it has impacted environmental protection. Through this paper we will demonstrate the importance of the project in providing heat cogeneration Prishtina city and in reducing pollution.

2. PHYSICO-CHEMICAL ANALYSIS OF FUEL OIL AND THE EMISSIONS FROM A BOILER

For the heating of the city of Pristina crude oil of various qualities is used. Monitoring the quality of liquid petroleum fuel is spread in three segments of control: Customs, the retail sales points and deposits of petroleum importers. Method of determining the quality of liquid petroleum derivatives and determination of their quality, appointed by the Administrative Instruction, is done by lab. testing which applies standard testing methods.

Table 1. Physico-chemical analysis of heavy oil (mazut) for 2008–2011

Sample	**Density gr/cm^3**		**Viscosity cSt**		**t_n °C**	**W %**	**S %**	**Ashes %**	**Low heating value H_u, kJ/kg**
	50 °C	**15 °C**	**100 °C**	**50 °C**					
1	0.929	0.951	29.1	225.8	187	0.030	1.400	0.040	42723
2	0.931	0.953	30.4	239.5	198	0.037	1.350	0.037	41185
3	0.929	0.951	29.1	225.8	187	0.030	1.400	0.040	42793
4	0.931	0.953	30.4	239.5	198	0.050	1.350	0.037	41185
5	0.955	0.976	9.2	74.1	132	0.030	1.870	0.043	36827
6	0.921	0.943	30.3	239.3	178	0.030	1.450	0.021	40787
7	0.924	0.946	29.7	233.1	175	0.030	1.310	0.028	41041
8	0.914	0.936	20.9	142.0	170	0.030	1.660	0.030	40946
9	0.924	0.946	29.3	227.7	179	0.030	1.540	0.020	41976
10	0.911	0.933	7.6	29.2	200	0.050	0.100	0.034	36450
11	0.928	0.950	30.6	241.3	188	0.041	1.510	0.050	41968
12	0.921	0.942	19.4	115.4	140	0.010	1.330	0.043	41353
13	0.910	0.923	24.3	75.6	190	0.020	1.190	0.035	41968
14	0.925	0.947	22.3	155.8	180	0.500	1.410	0.035	43015

15	0.928	0.950	30.1	235.9	185	0.700	1.570	0.031	42336
16	0.930	0.952	33.5	274.3	205	0.220	1.430	0.037	41717
17	0.928	0.950	26.7	199.7	188	0.060	1.470	0.036	41754
18	0.926	0.948	29.0	225.0	205	0.200	1.530	0.037	41738
19	0.924	0.946	32.2	260.0	200	0.050	1.410	0.036	40888
20	0.920	0.942	32.5	263.1	203	0.150	1.520	0.045	40616
21	0.929	0.951	29.1	225.8	187	0.030	1.400	0.040	42793
22	0.942	0.964	32.8	265.8	158	0.280	1.510	0.045	39665

From the statistical data on the content of fuel oil components Table 1, the table is arranged in the form suitable for the respective anlalysis of calculated indicators: average value, maximum value, minimum, median, fashion, variance and standard deviation. These calculations are made for the purpose of determining the standard deviation and distribution of components for subsequent analysis. The results obtained arranged are shown in Table 2.

Table 2. Cumulative features of heavy oil (mazut) analysis

	S **%**	**Ashes** **%**	**H_u** **kJ/kg**
Count	22	22	22
Maximum	1.87000	0.05000	43015
Minimum	1.19000	0.02000	36450
Average	1.45591	0.03636	41169
Median	1.42500	0.03700	41535
Mod	1.40000	0.03700	41185
Variance	0.01880	0.00005	2827082
Standard deviation	0.13710	0.00729	1681

Based on the results obtained from the observations during the analysis of the emissions of boiler components, as well as of distribution and normal deviation, according to the following equation , we can also obtain the equations of the normal distribution

$$f(x)=\frac{N}{\sigma\sqrt{2\pi}}\exp\left[-(x-\mu)^2/2\sigma\right]. \tag{1}$$

After replacing the values of the statistical model of normal distribution curves we come up with the following results for S, H and Hu:

$$f(x)_S=\frac{22}{0.13710\sqrt{2\pi}}\exp\left[-(x-1.45591)^2/2\cdot 0.13710\right], \tag{2}$$

$$f(x)_H=\frac{22}{0.0729\sqrt{2\pi}}\exp\left[-(x-0.03636)^2/2\cdot 0.0729\right], \tag{3}$$

$$f(x)_{Hu}=\frac{22}{1681\sqrt{2\pi}}\exp\left[-(x-41169)^2/2\cdot 1681\right]. \tag{4}$$

The measurement of concentrations of SO_2 emissions, CO and NOx in exhaust gases discharged from boilers smoke is carried out using a gas analyzer TEST 350 xl [5]. This analyzer serves to analyze the composition of gases generated by burning fuel, pressure measurement, determining the gas flow speed and efficiency (utilization rate) of the combustion process. Self measurement is performed with electrochemical cells. Smoke gases analyzer with measurement probes is shown in Fig. 1.

Fig. 1. The gas analyzer for smoke measuring

Table 3 gives an overview of the average me asured values of pollutant emissions from heavy fuel released by boilers between certain limits in order to assess the emission of pollutants discharged into the air in the valley of Pristina.

Table 3. Average limit values of emissions from heavy oil (mazut) boiler

Average limit values of emissions			
	SO_2	CO	Nox
Unit	mg/m_N^3	mg/m_N^3	mg/m_N^3
Value	43.5	60.45	120.17
Limit values	1700	1700	195

The values of fuel consumption for heating seasons during 2004–2015 are given in Table 4, and the values of thermal energy for the same period in Table 5.

Table 4. Consumption of heavy fuel oil (mazut) for heating seasons

	Heating seasons	Oct.	Nov.	Dec.	Jan.	Feb.	Mar.	Apr.	Total
	Unit	**[ton]**	**[ton]**	**[ton]**	**[ton]**	**[ton]**	**[ton]**	**[ton]**	**[ton]**
1	2001/02	1000.00	1698.00	2755.00	2425.00	1510.00	1607.00	707.00	11702.00
2	2002/03	382.00	1006.00	1926.00	1877.00	2126.00	1311.00	416.00	9044.00
3	2003/04	489.00	1409.00	2332.00	3106.00	2576.00	1795.00	594.00	12301.00
4	2004/05	1810.80	1580.17	2585.22	2883.48	2491.63	1921.19	825.60	14098.09
5	2005/06	360.00	1682.87	2956.69	3625.21	2660.82	2087.54	570.00	13943.13
6	2006/07	538.11	1988.60	2772.10	2491.44	2135.61	1811.54	365.00	12102.40
7	2007/08	689.80	1865.55	1973.96	2249.45	1636.75	858.85	45.80	9320.16
8	2008/09	25.13	1534.20	2300.80	3084.19	2494.33	2168.57	536.12	12143.34
9	2009/10	750.96	1675.20	2290.85	2223.60	1827.03	569.37	0.00	9337.00
10	2010/11	570.00	876.84	1368.16	549.95	621.40	0.00	0.00	3986.35
11	2011/12	0.00	855.48	1621.04	1699.94	853.94	20.00	0.00	5050.40
12	2012/13	10.00	211.54	1890.24	1895.82	970.42	10.00	0.00	4988.02
13	2013/14	18.62	794.24	1703.86	1359.33	983.56	533.74	0.00	5393.35
14	2014/15	0.00	20.00	0.00	0.00	340.00	0.00	230.00	590.00

Table 5. Thermal energy production divided into heating seasons

Heating seasons	**Oct.**	**Nov.**	**Dec.**	**Jan.**	**Feb.**	**Mar.**	**Apr.**	**Total**
	MWh	**MWh**	**MWh**	**MWh**	**MWh**	**MWh**	**MWh**	**MWh**
2006/07	5531.42	19318.38	25310.70	23497.54	20102.01	22899.90	3746.02	120405.96
2007/08	7150.98	17918.60	16237.00	20846.07	16198.29	8082.09	128.51	86561.53
2008/09	0.00	14631.25	23045.47	28520.18	24732.75	24622.80	5965.01	121517.46
2009/10	7221.87	16090.20	22003.61	21357.68	18537.78	0.00	0.00	85211.14
2010/11	5783.45	8719.30	12662.74	5956.19	4997.10	0.00	0.00	38118.78
2011/12	0.00	8509.57	16119.62	16904.20	8491.58	0.00	0.00	50024.97
2012/13	0.00	2031.84	18155.76	18209.40	9320.89	0.00	0.00	47717.89
2013/14	0.00	7628.67	16365.57	13056.36	9447.09	5030.52	0.00	51528.21
2014/15	0.00	0.00	37250.00	42223.00	34675.96	35621.00	8144.12	157914.08
								759000.02

3. CALCULATION OF EMISSIONS POLLUTANTS IN THE AIR

For the purpose of analysis the method for calculating emissions of pollutants discharged into the air as follows is used: sulfur oxides expressed as sulfur dioxide (SO_2), nitrogen oxides (NOx) and carbon monoxide (CO) by CORINAIR (Core Inventory of Air emissions in Europe) [6] emissions calculation methodology that provides accurate calculation, comprehensive and sustainable emission of pollutants.

3.1. SO_2 Emission Calculations

SO_2 emissions calculated according formula (5):

$$E = B \times w(S) \times \left(\mathrm{steh} \frac{SO_2}{S} \right) \times (1 - \eta_{\mathrm{des}}) , \tag{5}$$

where:

E – SO_2 emissions (kg SO_2/vit),
B – Amount of fuel consumption (kg/year),
w (S) – general content of secondary for sulfur in fuel,
$\mathrm{steh}\frac{SO_2}{S}$ – stehiometric report of molecular wheight for SO_2/S, is 64/32 or 2,
η_{des} – rate action desulphurization system.

3.2. CO Emission Calculations

CO emissions calculated according formula (6):

$$E = \frac{B \times H_u \times EF}{1000000} , \tag{6}$$

where:

B – Amount of fuel consumption (kg/year),
EF – the CO emission factor for heating and industrial oilers is 73, [4],
Hu – Low heating value for heavy oil (mazut) 40000 kJ/kg.

3.3. NOx Emission Calculation

NOx emissions calculated according formula (7):

$$E = \frac{B \times H_u \times EF}{1000000}, \qquad (7)$$

where:

B – Amount of fuel consumption (kg/year),
EF – the NOx emission factor for heating and industrial boilers is 155, [4],
Hu – Low heating value for heavy oil (mazut) 29000 kJ/kg.

3.4. Emissions Calculating of ashes and gases thrown of the smoke stacg output

Ashes emissions calculated according formula (8)

$$E = B \times A \times \left(1 - \frac{\alpha_u}{100}\right), \qquad (8)$$

where:

B (t/season) – the amount of fuel that burned for season
A (%) – The ash conent in fuel
α_u - amount of ash that remains in the furnace and chimneys.

According to this calculation, using a variety of data and the type of fuel consumption and emission factors are calculated air emissions in tons / 6months for boilers discussed in Termokos Pristina. Based on these results it is clear that emissions during the heating season (the period of six months) in the air of the valley of Pristina by boilers analyzed is significant and it can be seen from Table 6 and histograms shown in Fig. 2.

Table 6. Total quantities of emissions from boilers in heating seasons

Heating seasons	**The average monthly consumption of fuel B**	**Calculation of emissions released into the air**			
		E_{SO2}	E_{CO}	ENox	$E_{\text{Hiri dhe cagja}}$
	t/6 months	t/6months	t/6months	t/6months	t/6months
2001/02	11702.00	337.33	4817.63	79490.87	4.24
2002/03	9044.00	260.71	3723.35	61435.26	3.28
2003/04	12301.00	354.60	5064.23	83559.83	4.46
2004/05	14098.09	406.41	5804.08	95767.34	5.11
2005/06	13943.13	401.94	5740.29	94714.71	5.06
2006/07	12102.40	348.88	4982.47	82210.76	4.39
2007/08	9320.16	268.67	3837.04	63311.19	3.38
2008/09	12143.34	350.06	4999.32	82488.86	4.40
2009/010	9337.00	269.16	3843.97	63425.59	3.39
2010/2011	3986.35	114.91	1641.15	27079.00	1.45
2011/2012	5050.40	145.59	2079.21	34307.01	1.83
2012/2013	4988.02	143.79	2053.53	33883.27	1.81
2013/2014	5393.35	155.47	2220.40	36636.65	1.96
2014/2015	590.00	17.01	242.90	4007.83	0.21

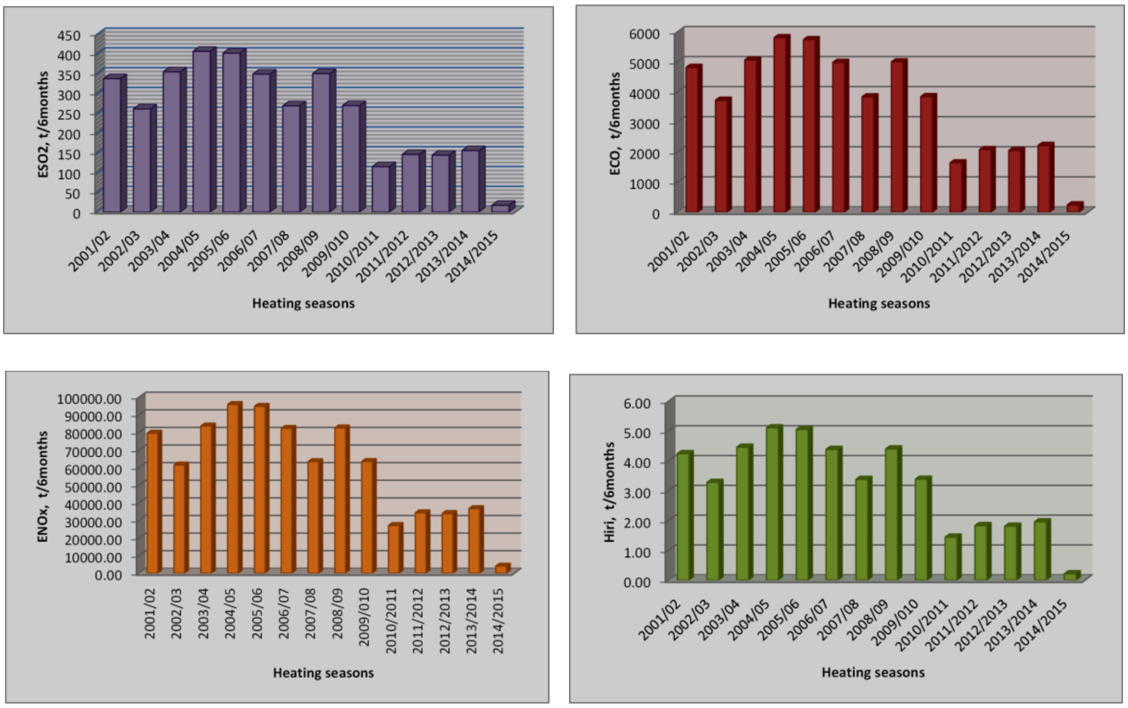

Fig. 2. The quantities of pollutants emitted into the air of the valley of Pristina by boilers during the heating season (the period of six months)

Quantities emissions SO_2, CO, NOx and ash function S, Hu and B for the respective borders of smoke gases discharged from boilers are given in Fig. 3.

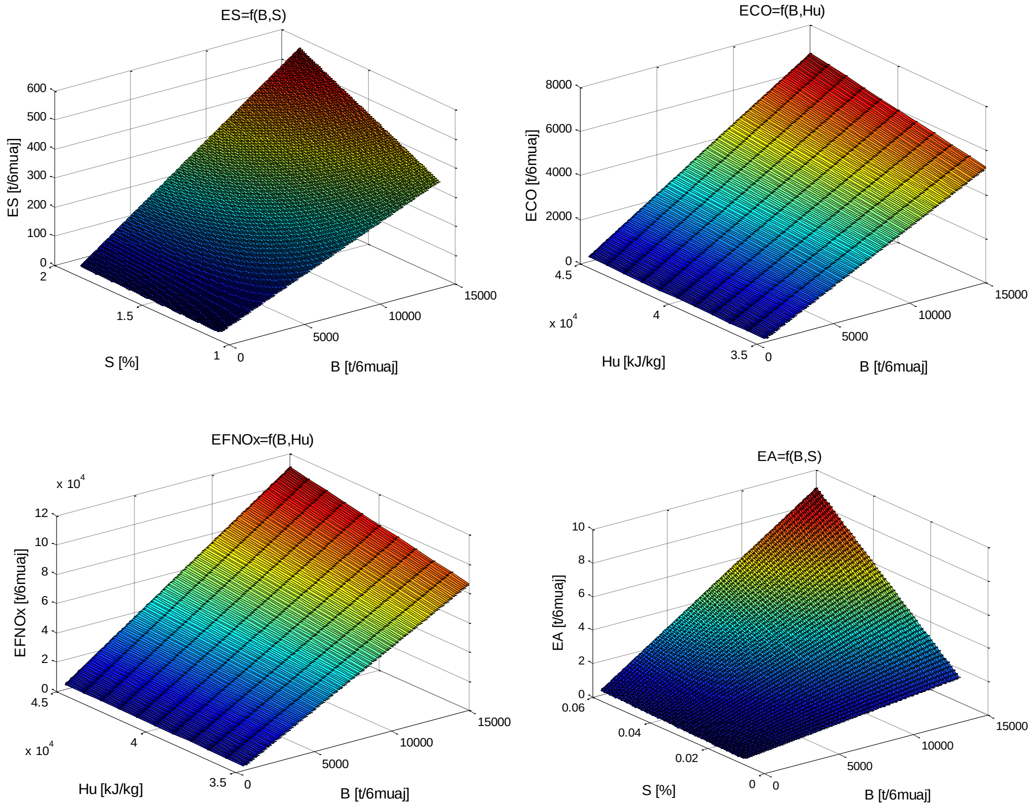

Fig. 3. Emissions Quantites ES = F(B, S), ECO = F(B, Hu), ENOx = F(B, Hu), EA = F(B, S)

4. ANALYSIS OF DATA PROCESSING

According to the analysis of the results obtained, we can see that the average values of SO_2 emissions from boilers reach a value of 255.32 tons / 6 months. Emissions of CO, reach the average values of 3629.0 tonnes / 6 months. Nox emissions achieve the average values of up to 60165.58 tons / 6 months, while the average values of grace and average value dross 3.21 mark ton / 6 months. Maximum contamination occurred in the heating season 2004/05 amounts of pollutant emissions as follows:

- Total SO_2 emissions = 406.41 t / 6 m,
- Total emissions of CO = 5804.08 t / 6 m,
- Total NOx emissions = 18 779 t / 6 m,
- Total emissions of ash and 5.11 dross = t / 6 m.

5. CONCLUSION

According to indicators of overall emissions of SO_2, NOx and CO, obtained based on the measurement, analysis and calculation methodology CORINAIR it is noted that much greater emissions are from the boilers. The main cause of the increase of SO_2 emissions from boilers is sulfur content in fuel oil. The main causes of increased emissions of CO are inadequate combustion conditions and the condition of the combustion chamber and chimney. Overall emissions of NOx boilers are lower than the estimated value of the boiler as a result of low temperatures in the combustion chamber. High emissions of CO discharged from boilers are due to poor combustion and therefore it is necessary to take appropriate technical and technological solutions to reduce emissions of CO to protect public health. NOx emissions are minimal, and SO_2 emissions occur as a result of fuel quality and low temperatures in the combustion chamber. The average values of SO_2, CO and NOx from fuel oil to heat the boilers are significantly lower than the prescribed limit values, which can be seen from Tables 1 and 3. Limit values for emissions of gaseous pollutants are mainly the result of fuel quality and combustion conditions, namely the relatively good technical condition and technological boiler.

From the results obtained, we suggest that the extension of heating network for the city of Pristina should intensify and increase the capacity of the system of cogeneration and reduce the number of boilers and bodies heating with solid fuels and liquid in parts of the city of Prishtina.

6. REFERENCES

1. ZHONGCHAO, T. Air Pollution and Greenhouse Gases – From Basic Concepts to Engineering Applications for Air Emissions Control. Springer Singapor + Business Media Singapore 2014.
2. Law on integrated prevention pollution control: LAW NO. 03/L-043.
3. District Heating “Termokos” JSC Prishtinë – Data from archive of D.H “Termokos” (schemes of principle operation and information materials).
4. BIRHADIC, V., SISIC, M., GOLETIC, Š., IMAMOVIC, N. Comparative analysis of the measured and calculated values of air emissions from local boiler. Naučno-stručni skup sa međunarodnim učešćem “KVALITET 2013”, Neum, B&H, 06. 08. Juni 2013.
5. www.testo350.com – Portable Emission Analyzers.
6. www.eea.europa.eu – European Environment Agency.